Vol. 61A

Boletín de la Asociación Argentina de Astronomía

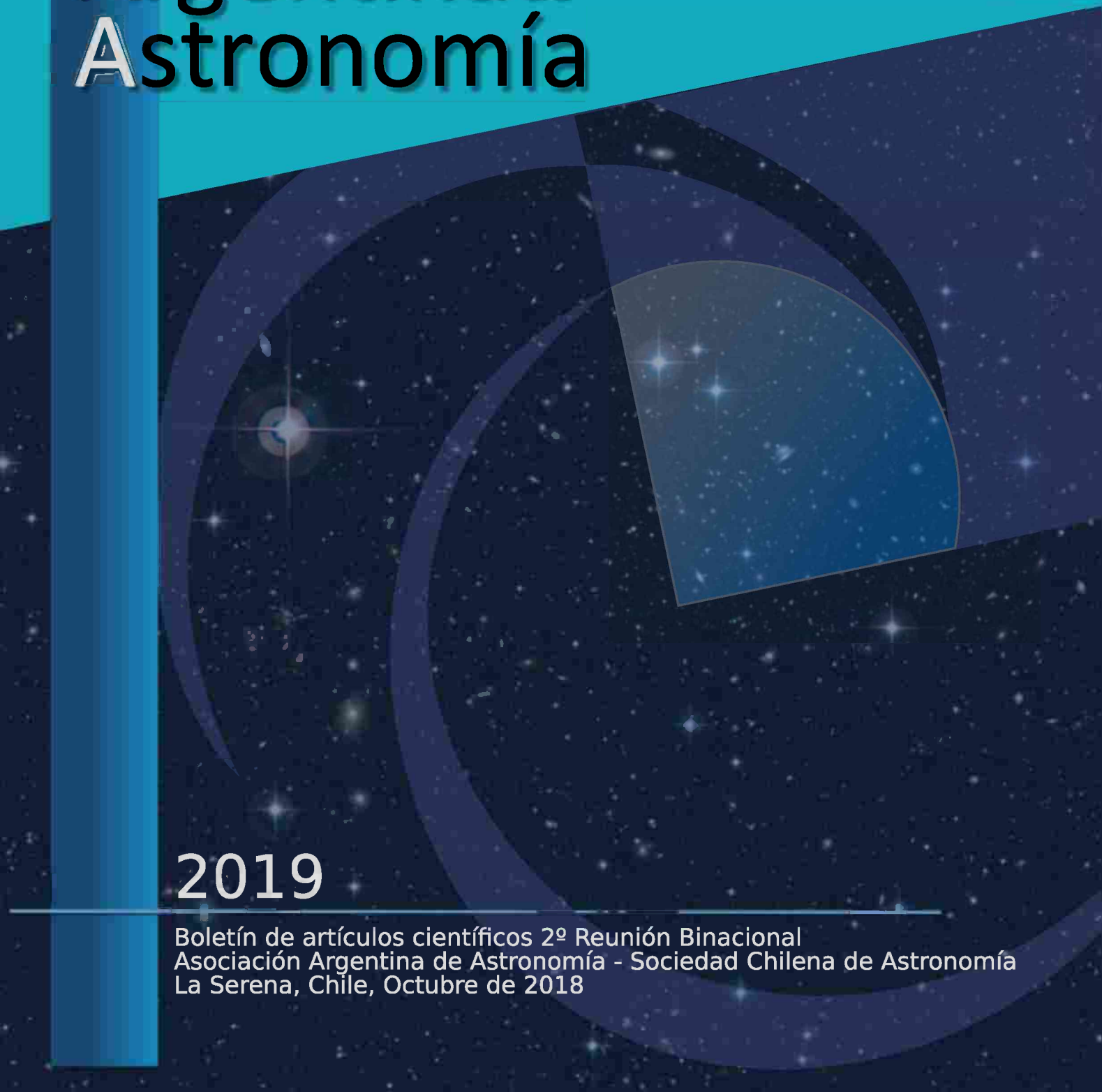

2019

Boletín de artículos científicos 2º Reunión Binacional
Asociación Argentina de Astronomía - Sociedad Chilena de Astronomía
La Serena, Chile, Octubre de 2018

Boletín de la Asociación Argentina de Astronomía

BAAA, Vol. 61A

Asociación Argentina de Astronomía. Comité Editorial BAAA Vol. 61A, correspondiente a la reunión anual 2018: Roberto Gamen (Editor en Jefe), Celeste Parisi (Editora Invitada), Nelson Padilla (Editor Invitado), Francisco Iglesias (Secretario Editorial) y Mario Agustín Sgró (Técnico Editorial)

Segunda Reunión Binacional AAA - SOCHIAS

La Serena, 7 al 12 de Octubre de 2018
Organizada por el Departamente de Física y Astronomía de la Facultad de Ciencia - Universidad de La Serena.

Publicado por
Asociación Argentina de Astronomía
Paseo del Bosque s/n, La Plata, Buenos Aires, Argentina

ISSN 1669-9521 (versión digital)
ISSN 0571-3285 (versión impresa)

Créditos:
Diseño de portada: Adrián Rovero y Andrea León
Foto grupal: Elise Miley
Confeccionado con la clase "confproc" en LaTeX

Impreso en Buenos Aires, julio de 2019

www.astronomiaargentina.org.ar

Prefacio

El presente volumen del Boletín de la Asociación Argentina de Astronomía contiene los trabajos correspondientes a la Segunda Reunión Binacional AAA-SOCHIAS[1], la cual tuvo lugar en el Hotel Club La Serena de la ciudad de La Serena, Chile, del 7 al 12 de octubre de 2018. La reunión fue organizada por la Sociedad Chilena de Astronomía, en conjunto con la Asociación Argentina de Astronomía.

La Reunión Anual convocó a más de 260 participantes. Reconocidos expertos invitados tuvieron a su cargo interesantes charlas de revisión, que complementaron las habituales presentaciones de trabajos, orales y murales. De estas últimas, el Comité Editorial recibió 70 contribuciones entre las que, luego del proceso de arbitraje por pares externos y de correcciones editoriales, finalmente son aquí publicadas 67.

Durante la reunión se entregaron dos de los premios que otorga la Asociación Argentina de Astronomía: el premio Jorge Sahade a la trayectoria y el premio Carlos M. Varsavsky a la mejor Tesis Doctoral. Los ganadores fueron el Dr. Félix Mirabel y la Dra. María Paula Ronco, respectivamente, quienes acompañaron la recepción del galardón con sendas contribuciones invitadas que forman parte del presente volumen e invitamos a leer especialmente.

Deseamos agradecer en esta entrega del Boletín a todos los autores que contribuyeron a enriquecerlo y a los colegas que han llevado a cabo serias tareas de arbitraje –algunos de ellos por primera vez para el BAAA.

La Plata, 3 de mayo de 2019.

Roberto Gamen
Editor en Jefe

Celeste Parisi
Editora Invitada

Nelson Padilla
Editor Invitado

Francisco Iglesias
Secretario Editorial

Mario Agustín Sgró
Técnico Editorial

[1] Ver nota de la CD incluida en este volumen.

Nota de la Comisión Directiva AAA

Estimados socios:

La denominación "Segunda Reunión Binacional AAA-Sochias"que se ha dado a la presente Reunión, sin que se le haya asignado un ordinal como es costumbre, tiene como objetivo corregir un error histórico que se ha mantenido durante muchos años. A continuación damos una breve reseña de cómo se han numerado las Reuniones y los Boletines, para poder apreciar cómo ha surgido el mencionado error y cómo la Asamblea decidió corregirlo.

Desde 1958 hasta 1982, las reuniones y los boletines llevaron la misma numeración.

En 1983, la participación argentina en la III Reunión Latinoamericana de Buenos Aires se consideró como equivalente a la 29ª Reunión de la AAA. Sin embargo, el BAAA 29 no se editó. Para mantener la numeración entre reuniones y boletines, se consideró que hubo un BAAA 29 "no editado".

En 1989 se produjo el primer deslizamiento numérico. En ese año, la Reunión (que hubiera sido la 35ª) se suspendió por superposición con la VI Reunión Latinoamericana. Sin embargo, se editó un BAAA 35 con contribuciones ad hoc.

En 1990, se realizó la 35ª Reunión, editándose el BAAA 36. Con motivo del desfasaje numérico, se decidió que las Reuniones no se designarían más con un número, sino solo con el lugar y el año: Reunión de San Juan 1990"fue el nombre de ese año.

En 1991, con motivo de la Asamblea General de la UAI en Buenos Aires, no hubo Reunión ni BAAA.

Entre 1992 y 1994, se siguió con el esquema de nombrar a las Reuniones con lugar y año, y los BAAA siguieron con su numeración.

En 1995, con motivo de la VIII Reunión Latinoamericana, otra vez no hubo Reunión ni BAAA.

Entre 1996 y 2004, en la denominación de las Reuniones se eliminó de facto el lugar, y pasaron a nombrarse solo con el año: Reunión Anual 1996"hasta Reunión Anual 2004". La excepción fue 2001, año en el cual no hubo Reunión ni BAAA por superposición con la X Reunión Latinoamericana.

En 2005 se produjo el primer error de denominación: a la Reunión se la llamó "48ª Reunión Anual", probablemente porque el BAAA de ese año era el número 48 y no había referencia cercana del número correcto de la Reunión, ya que hacía rato que no venían siendo numeradas. Pero esa Reunión fue en realidad la 47ª.

Entre 2006 y 2008 las Reuniones volvieron a llamarse con lugar y año.

A partir de 2009 hasta la actualidad, las Reuniones volvieron a denominarse con número, pero con la numeración corrida tal como había sucedido en 2005. Así, en 2009 la Reunión se denominó "Quincuagésima segunda Reunión Anual", cuando en realidad fue la 51ª, y así siguiendo hasta 2017, año en que la Reunión fue llamada "60ª Reunión Anual", cuando en realidad fue la 59ª.

Para corregir el error en la numeración de las Reuniones, y además para volver a sincronizarlas con la numeración del BAAA, se propuso y se aprobó en la Asamblea de 2018:

a) Denominar a la Reunión 2018 como "Segunda Reunión Binacional AAA-Sochias", sin asignarle número alguno. Contando las Reuniones desde 1958, a esta Reunión le hubiera correspondido ser la 60ª, pero ese número ya fue asignado erróneamente a la Reunión 2017, y volver a usar dicho número para designar a otra Reunión produciría una gran confusión. El BAAA debería ser el 61, siguiendo con la numeración propia. Pero en tal caso, seguiría desfasado con respecto a las reuniones, desfase iniciado en 1989. Por tal motivo, se decide denominarlo "61A", para permitir la repetición del número al año siguiente.

b) Denominar a la Reunión 2019 como "61ª Reunión Anual", con lo cual la numeración pasa a ser la correcta. El BAAA correspondiente llevará la denominación "61B", con lo cual, a partir de 2020, Reuniones y Boletines volverán a la numeración correcta y sincronizada que tuvieron hasta 1989.

Índice general

Memorias de mis investigaciones en Astronomía

I.F. Mirabel[1]

[1] *Instituto de Astronomía y Física del Espacio, CONICET–Universidad de Buenos Aires, Argentina*

Contacto / mirabel@iafe.uba.ar; felix.mirabel@cea.fr

Resumen / Presentación oral en ocasión de recibir el Premio a la Trayectoria 2018 otorgado por la Asociación Argentina de Astronomía en reunión conjunta con la Sociedad Chilena de Astronomía.

Abstract / Talk in the occasion of receiving the 2018 Life Achievement Prize awarded by the Argentinean Astronomical Association at a joint meeting with the Chilean Astronomical Society.

Keywords / history and philosophy of astronomy — Galaxy: general — galaxies: active — stars: black holes — intergalactic medium — cosmology

1. Introducción

Para mí es un gran honor y motivo de enorme satisfacción y orgullo recibir el "Premio a la Trayectoria" de la Asociación Argentina de Astronomía (A.A.A.), por lo cual agradezco profundamente a su Comisión Directiva. Según la Comisión este premio se otorga por "los aportes en el descubrimiento y comprensión de las galaxias infrarrojas ultraluminosas, de las galaxias enanas de marea, de la existencia de movimientos aparentemente superlumínicos en la Vía Láctea, y de los microcuásares, campo del que la comunidad internacional lo considera fundador". Por lo tanto en mi exposición haré eje en el proceso que llevó a estos descubrimientos científicos y sus implicaciones. También haré referencia al aporte principal en gestión científica que de acuerdo a la comisión quizás sea "el aporte más significativo para nuestra comunidad, la concepción y gestión política del Proyecto "Large Latin American Millimeter Array" (LLAMA), del cual fue mentor, y a cuya promoción dedicó más de una década".

De las incursiones en nuevas áreas de la Astronomía que menciona la Comisión Directiva de nuestra Asociación, permanecen anclados en mi memoria no solo los resultados científicos, los cuales se pueden encontrar fácilmente en las publicaciones. También están presentes en mi memoria las circunstancias del comienzo de cada investigación, la sorpresa ante lo inesperado, la emoción al trascender la frontera de lo conocido para confrontar lo desconocido, la fraternidad forjada en el trabajo de investigación científica con colegas de otras culturas y regiones del mundo. Por ello, en esta presentación recuerdo en forma especial a colegas que han hecho aportes significativos, y con los cuales he compartido las experiencias vividas durante esas investigaciones.

2. Motivación, circunstancias y azar

La palabra "Trayectoria" en este "Premio a la Trayectoria" con el que me honra la A.A.A., podría tácitamente hacer alusión a una trayectoria continua, ordenada, de acuerdo a una planificación racional. En realidad, mi camino hacia la astronomía y posteriormente dentro de sus subdisciplinas, ha sido desde su comienzo y hasta la actualidad, un camino accidentado, como naturalmente es toda exploración. Por tal razón, más que una trayectoria continua y planificada en un área específica de la astronomía, mi tránsito hacia y en la astronomía ha consistido en un conjunto de diferentes exploraciones.

Mi motivación por el saber en general ha sido sintetizada por Nikos Kazantzakis en un parágrafo del "El jardín de las rocas": "Soy una criatura efímera, pero dentro de mí, siento arremolinarse todas las fuerzas del Universo. Quiero, por un instante, antes de que me quebranten, abrir los ojos y verlas". Desde muy temprano sentí curiosidad por conocer los misterios de la existencia y de este mundo, y como adolescente tuve la ilusión de que la Filosofía podría revelar esos misterios, o por lo menos, ayudarme para "abrir los ojos y ver las fuerzas del Universo", como dice Kazantzakis.

Uruguay, mi país natal, después de la bonanza de la posguerra, entra en recesión en la década de los años '60. Mi padre, ingeniero del politécnico alemán de Dresden, pierde su trabajo, por lo que al finalizar los estudios secundarios debo emigrar a Buenos Aires para trabajar y participar en el sustento familiar. En aquellos años, la Universidad Tecnológica es la única posibilidad, para la gente que trabaja, de realizar estudios nocturnos y gratuitos a nivel terciario. Curso hasta el tercer año de ingeniería industrial. Me maravilla la capacidad de la Física, que por medio de pocas ecuaciones ha podido sintetizar y predecir la enorme diversidad de los fenómenos de la Mecánica y el Electromagnetismo. Me siento profundamente atraído por la racionalidad de la Física, que contrasta con el absurdo y caos de nuestro mundo. Más tarde, cuando los problemas económicos más acuciantes son resueltos, para poder "abrir los ojos y ver las fuerzas del Universo", ingreso a la Facultad de Filosofía y Letras de la UBA. Siendo la Física el modelo paradigmático del conocimiento, solicito en el departamento de Física equivalencias para continuar los estudios de

Figura 1: Carlos Varsavsky (izq.) y Carlos Jaschek (der.)

Figura 2: Antenas de 30 m del Instituto Argentino de Radioastronomía.

ciencia. Nunca tuve una respuesta, ni siquiera negativa.

Casualmente, por una publicación de la editorial EUDEBA de la UBA me entero sobre los sorprendentes descubrimientos en astrofísica y cosmología ocurridos en el siglo XX: la expansión del Universo, su evolución química por reacciones nucleares en el centro de las estrellas, los pulsares, el destino final de las estrellas más masivas como estrellas de neutrones y agujeros negros. Motivado por esa y otras lecturas ingreso como alumno en la Escuela de Astronomía y Geofísica del Observatorio de la Universidad de La Plata (UNLP). Poco tiempo después, la UNLP me otorga una beca que me permite continuar, sin tener que trabajar, estudios simultáneos de Filosofía en la UBA y de Astronomía en la UNLP.

Dos profesores impactan en mi formación. En Filosofía, Saúl Katz, un ayudante de trabajos prácticos de quien aprendo que la Filosofía, además de una disciplina formal, puede ser una forma de vida. Carlos Jaschek (Fig. 1) me introduce en dos aspectos de la investigación astronómica que serán esenciales para mi formación como investigador científico. Por una parte, la elaboración e integración de las observaciones en todo el espectro electromagnético, o sea, la investigación "multifrecuencia", que actualmente se llama investigación "multimensajera", porque además de la radiación en todo el espectro electromagnético, integra la emisión de partículas, neutrinos y ondas gravitacionales. Por otra parte, de Jaschek también aprendo la necesidad de la integración multidisciplinaria entre las diferentes áreas de la astrofísica. En aquella época, el astrónomo observacional todavía conserva una relación "artesanal" con el instrumento de observación y cierta empatía con la vastedad del cielo estrellado. Esas enseñanzas anticipan las "observaciones de servicio" de los grandes observatorios, el incremento de grupos numerosos de investigación, y el carácter de empresa cuasi–industrial de la "Gran Ciencia", y en particular, de los grupos de investigación astronómica en la actualidad.

Al finalizar las carreras de Filosofía en la UBA y de Astronomía en la UNLP, intento realizar una tesis doctoral en Filosofía en la UBA sobre la Teoría del Conocimiento en la "Critica de la Razón Pura" de Kant. La idea es contrastar esa teoría del conocimiento que tiene como paradigma la Física Clásica, con la Teoría de la Relatividad y la Física Cuántica. Ese proyecto de tesis doctoral lo podría haber realizado rápidamente, ya que durante los últimos dos años de la carrera de Filosofía estudié con gran dedicación la "Critica de la Razón Pura", y a su vez cursé Física Relativista y Física Cuántica en el departamento de Física de la UNLP. Pero el proyecto de tesis doctoral en Filosofía se frustra por el golpe de estado de junio de 1966, que derroca al presidente electo Arturo Illia, y un general llamado Onganía ocupa la presidencia. La UBA es intervenida, y los mejores profesores de la Facultad de Filosofía y Letras renuncian o son expulsados.

Como la astronomía se ocupa de "cuestiones celestiales", en el contexto político de aquel momento es considerada como una actividad políticamente "inocente". En ese contexto postulo bajo la dirección de Carlos Varsavsky (Fig. 1) a una beca doctoral del CONICET en astronomía, con lugar de trabajo en el Instituto Argentino de Radioastronomía (IAR, Fig. 2). De hecho, me convierto en el primer egresado de una escuela de astronomía en Argentina que postula para realizar una tesis doctoral en el IAR, el cual había sido concebido y desarrollado por físicos de la UBA, en colaboración con la institución Carnegie de los Estados Unidos. Obtengo la beca, pero ocurre "la noche de los bastones largos", Varsavsky renuncia como profesor de la UBA y luego es expulsado como director del IAR.

3. Mis investigaciones en áreas establecidas de la Astronomía

3.1. Tesis doctoral: Acreción de hidrógeno atómico hacia la Galaxia (1971–1975)

Ken Turner de la fundación Carnegie, asume la dirección del IAR y de mi tesis doctoral. Inicialmente esta consiste en una búsqueda en la línea de 21 cm del hidrógeno atómico de un "puente de gas" entre las Nubes de Magallanes y la Vía Láctea. Ese gas debería ser sustraído de las Nubes de Magallanes por las fuerzas de marea de la Galaxia sobre las galaxias satélites, y estar actualmente cayendo hacia la Vía Láctea. Por la vastedad de la región del cielo a explorar, las limitaciones en sensibilidad del receptor y falta de automatización del radiotelescopio del IAR, se decide observar las

Figura 3: Celebración con colegas de trabajo del IAR por la defensa de mi tesis doctoral a fines de 1975.

Figura 4: Junta militar toma el poder en Argentina el 24 de marzo de 1976.

regiones del cielo donde ese gas debería estar ubicado de acuerdo a un modelo del matemático computacional norteamericano Alar Toomre. La primera publicación es sobre los resultados negativos de esa búsqueda (Mirabel & Turner, 1973). Astrónomos australianos con instrumentación más avanzada realizan rápidamente un relevamiento general de todo el cielo Sur y encuentran la llamada "Corriente de Magallanes", en una región del cielo diferente a la predicha por el modelo de Toomre. A partir de entonces concentro mis investigaciones en la caída de gas atómico hacia la región central de la Galaxia y después de varias publicaciones, en 1975 ingreso a la carrera del investigador científico del CONICET.

Por los trabajos en el IAR establezco relación epistolar con el profesor Rodney Davies del Laboratorio de radioastronomía Jodrell Bank de la Universidad de Manchester, quien me apoya para la obtención de becas postdoctorales del British Council y de la Universidad de Manchester. Por otra parte, Jorge Sahade sugiere que postule a un subsidio de la Unión Astronómica Internacional (UAI) para financiar el costo del viaje, el cual es otorgado. Así puedo continuar mis investigaciones sobre nubes de hidrógeno atómico de alta velocidad en Inglaterra.

Debido a la inminencia de un nuevo golpe de estado militar, solicito poder defender con urgencia la tesis doctoral en diciembre de 1975, la que se organiza en los sótanos del Observatorio de La Plata. Parto hacia Inglaterra el 10 de marzo. Un golpe de estado ocurre dos semanas después (Fig. 4).

3.2. Jodrell Bank. Universidad de Manchester (1976–1978)

Sir Bernard Lovell, director de los laboratorios de radioastronomía de la Universidad de Manchester en Jodrell Bank fue integrante del equipo científico-técnico que concibió, construyó, y puso por primera vez en operación radares en suelo británico durante la segunda guerra mundial. Al llegar a Manchester me sorprende la estima de los ingleses de la región hacia los científicos en general, y en particular, hacia los radioastrónomos de Jodrell Bank. El descubrimiento del radar impactó profundamente en sus vidas, ya que por su operación permitió disminuir los bombardeos alemanes en el noroeste industrial de Inglaterra.

3.2.1. Gas en el halo de la Galaxia y en el medio intergaláctico del Grupo Local

En Jodrell Bank realizo investigaciones bajo la dirección del profesor Rodney Davies y en colaboración con Jim Cohen, sobre hidrógeno atómico en el halo y en el Grupo Local de galaxias. Los hallazgos principales en esta área de investigación con los radiotelescopios Mark II (38×25 m) y Lovell de 89 m de diámetro, en ese momento el radiotelescopio *fully stereable* más grande del mundo, son:

- La estructura fina del gas atómico en el halo de la Galaxia, la cual sugiere la existencia de tres fases térmicas del gas en el halo de la Galaxia y medio intergaláctico. De particular importancia es la inferencia de gas intergaláctico ionizado con temperaturas de $\sim 10^5$ K a fin de hacer posible la estabilidad de las nubes de hidrógeno atómico. Ese gas ionizado es difícil de observar directamente y se ha propuesto que puede constituir una fracción importante de la masa bariónica del Universo (Cohen & Mirabel, 1979).
- La observación de nubes de gas neutro en el medio intergaláctico del Grupo Local de galaxias con posible rotación, sin población estelar visible hasta ese entonces (Mirabel & Cohen, 1979).

3.2.2. Cosmología

Como me interesa aprender y trabajar en Cosmología, una disciplina que no se enseñaba en la carrera de astronomía de la UNLP, solicito al profesor Davies colaborar en un proyecto de investigación, lo cual amablemente aceptó. En colaboración con Rodney Davies y Alan Pedlar realizamos una primera búsqueda de hidrógeno atómico en protocúmulos de galaxias a distancias cosmológicas correspondientes a corrimientos al rojo de $z = 3.3$ y 4.9. Mi contribución consiste en desarrollar un programa de cómputo para identificar interferencias y eliminarlas en forma automática por interpolación de canales adyacentes del espectrómetro. No se detectó ningún protocúmulo de galaxias a esas distancias cosmológicas, pero disfruté la lectura de los trabajos teóricos de Sunyaev & Zeldovich sobre la posible existencia de tales protocúmulos.

Llegando a su fin el financiamiento de la posición postdoctoral debo dejar Inglaterra. Hacia fines de 1978

Figura 5: *De izq. a der.*: Tomas Gergely, Andrew Wilson y Ricardo Morras.

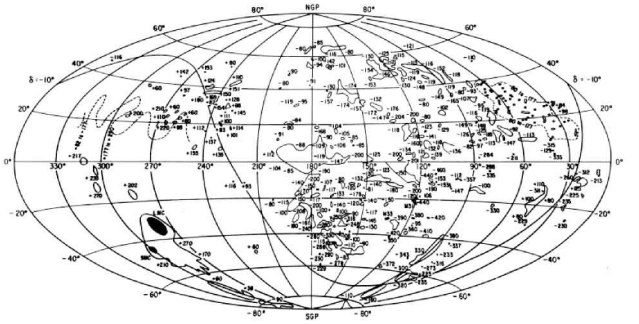

Figura 6: Distribución en coordenadas galácticas de Nubes de H I de Alta Velocidad observadas en la línea de 21 cm. Exposición invitada en la segunda Reunión Regional Latinoamericana de la Unión Astronómica Internacional. Reproducción de Revista Mexicana de Astronomía y Astrofísica. (Mirabel, 1981a).

la información sobre la situación en Argentina en el exterior es muy fragmentaria. En ese contexto y ante la ausencia de posibilidad de obtener otro postdoctorado en Europa, planifico volver a la Argentina. Tomas Gergely (Fig. 5), colega y amigo húngaro-argentino con el que había compartido oficina en el IAR y que en ese momento está en la Universidad de Maryland, me advierte y aconseja no volver a la Argentina en ese momento. Tomas me pone en contacto con Frank Kerr, decano de la Facultad de Ciencias de la Universidad de Maryland, el cual me ofrece una posición postdoctoral. Tomas provee una ayuda inestimable para la instalación con mi familia en Estados Unidos.

3.3. Universidad de Maryland, College Park (1978–1979)

En la época de mi primer postdoctorado en el Reino Unido, la investigación científica en ese país tiene una estructura vertical. Las propuestas de investigación solamente son formuladas por "Professors" (jefes de grupo), y la iniciativa de los jóvenes ocupa un rol secundario, son los ejecutores de proyectos concebidos por los "Professors". Al llegar a Estados Unidos, inmediatamente experimento en la práctica, que Estados Unidos es país de inmigrantes. Por lo menos para mí, después de la estadía en Inglaterra, ofrece muchas más oportunidades.

El salario de mi posición postdoctoral en la Universidad de Maryland proviene de un subsidio de la *National Science Foundation* (NSF) otorgado a Frank Kerr. En la primera entrevista, Kerr me informa que el 50 % del tiempo debo dedicarlo a la docencia y a colaborar con el desarrollo de sus proyectos que me explica en detalle. Luego, para mi sorpresa, después de casi tres años en Inglaterra, me pregunta: "¿Qué ideas tiene usted para el 50 % restante?"

3.3.1. Acreción de gas hacia la Vía Láctea

Relevamientos preliminares de hidrógeno atómico en la región interior de la Galaxia con el radiotelescopio de 42 m de NRAO, revelan una clara preponderancia de gas con altas velocidades de caída hacia el disco galáctico, a una tasa estimada de 0.2–1.0 $M_\odot$ a^{-1}. Esa tasa de acreción es suficiente para sostener la tasa de formación estelar en la Vía Láctea (de $\sim$1 $M_\odot$ a^{-1}). A raíz de este resultado recibo una carta de felicitación del célebre astrónomo holandés Jan Oort, lo cual constituye un estímulo importante. Por estos trabajos, soy invitado por primera vez a presentar un artículo de síntesis sobre las Nubes de Hidrógeno de Alta Velocidad en un congreso internacional (Fig 6).

3.3.2. Astronomía extragaláctica: galaxias activas

En la Argentina de la década del '70, la Astronomía Extragaláctica, tanto a nivel de docencia como de investigación, es exclusividad del Observatorio de Córdoba. A fin de aprender sobre esta área, le propuse a Andrew Wilson, astrónomo británico de la Universidad de Maryland, colaborar con sus investigaciones. Mi aporte consistió en el conocimiento de las técnicas radioastronómicas de observación que aprendí en el IAR y perfeccioné en Jodrell Bank. Varias publicaciones sobre hidrógeno atómico en galaxias Seyfert y Radio Galaxias fueron realizadas en colaboración con Andrew Wilson, basadas en observaciones iniciadas con el radiotelescopio de 92 m de NRAO, que luego son continuadas con el radiotelescopio de 305 m de Arecibo.

3.3.3. Cosmología: búsqueda de H I en protocúmulos a z=9

Esta búsqueda de protocúmulos de galaxias fue realizada con el radiotelescopio de 92 m de NRAO, en colaboración con otros postdoctorados de la Universidad de Maryland, luego continuada en Arecibo. En aquel momento dio resultados negativos, pero en este proyecto cosmológico perfecciono mi conocimiento de técnicas de observación radioastronómicas, y en particular, como sintonizar los receptores para observaciones extragalácticas a distancias cosmológicas. Una presentación corta de estos proyectos se realiza en la Reunión Regional de la Unión Astronómica Internacional (Mirabel, 1981b).

3.3.4. Astronomía galáctica, extragaláctica y cosmología en el Observatorio de Arecibo

Como postdoctorando en la Universidad de Maryland someto varias propuestas de observación en Arecibo para diversos estudios relacionados con la línea de 21 cm

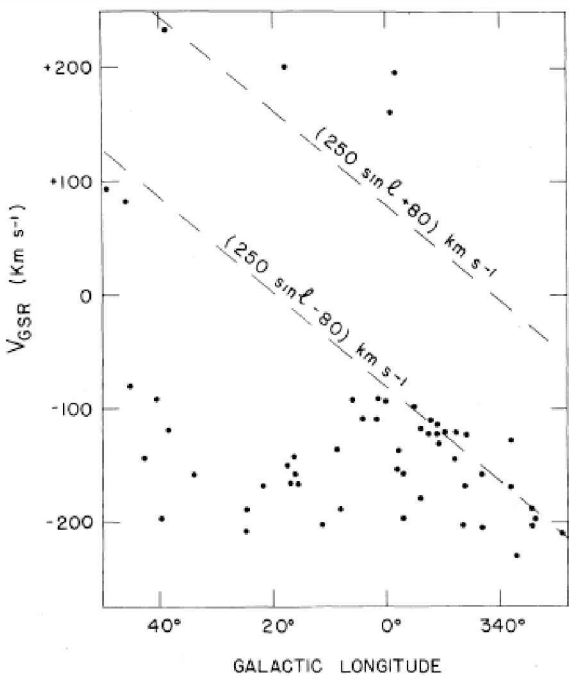

Figura 7: Evidencia del influjo de H I hacia la Galaxia. Velocidades radiales galacto-céntricas de Nubes de NRAO en dirección de la región interior de la Vía Láctea. Reproducción de Astrophysical Journal (Mirabel & Morras, 1984).

del hidrógeno atómico, en astronomía galáctica, galaxias activas, y cosmología. Todas las propuestas son aprobadas. En ese contexto, el decano de la Universidad de Puerto Rico (Estado Libre Asociado de los EEUU), me invita a dar una conferencia en el campus de San Juan. Luego de esa conferencia me ofrecen una posición de profesor "*tenure track*" en el departamento de Física, un apartamento en el campus de la universidad sin costo de arriendo, y la tramitación de la "*Green Card*".

La NSF aprueba un subsidio para financiar las investigaciones en curso con los radiotelescopios de Arecibo y NRAO. Con esos fondos se financia una posición postdoctoral en Puerto Rico de Ricardo Morras y una visita de Marcelo Arnal para colaborar con observaciones en Arecibo. Con Morras (Fig. 5) continuamos un proyecto sobre nubes de alta velocidad de hidrógeno atómico con los radiotelescopios de Arecibo y NRAO.

3.3.5. Acreción de gas atómico en la región central de la Galaxia

Uno de los problemas principales para determinar si existe adquisición de materia hacia la Vía Láctea, radica en la sustracción del movimiento del sistema solar en la determinación de las velocidades radiales, lo cual dificulta la interpretación de las observaciones. Como la componente radial del movimiento del sistema solar en las direcciones del centro y anticentro de la Galaxia es relativamente pequeña, propongo relevamientos profundos de H I en esas dos regiones. En la dirección del centro, con el radiotelescopio de 42 m del Observatorio Nacional de Radioastronomía de los EEUU en West Virginia, y en la dirección del anticentro, con Arecibo. En la

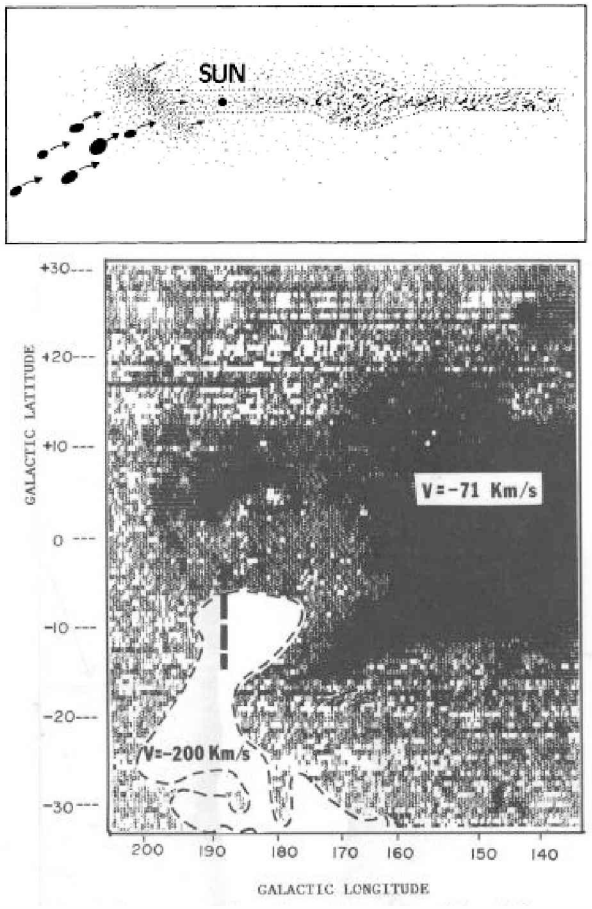

Figura 8: *(Arriba)*: Esquema de la corriente de H I impactando en la región del anticentro de la Vía Láctea; *(Abajo)*: Supercáscara causada por el impacto de esa corriente. Sobre la base de observaciones con el radiotelescopio de 305 m de Arecibo. Reproducciones de Astrophysical Journal (Mirabel & Morras, 1990).

Fig. 7 se ilustra la clara preponderancia de gas cayendo hacia la Vía Láctea en la región del centro galáctico.

3.3.6. Acreción de gas atómico en la región del anticentro de la Galaxia y formación de "supercáscaras"

Sobre la base de observaciones con el radiotelescopio de Arecibo se estima que la acreción de H I en el anticentro es de 4×10^5 $M_\odot$ a una velocidad de 200 km s^{-1}, lo cual corresponde a una inyección de energía de 2.5×10^{53} erg. Esta energía es equivalente a la de la explosión de centenas de supernovas, y da origen a la supercáscara de H I en el anticentro galáctico. En estos trabajos se concluye que si bien la inyección de energía por acreción de gas atómico, en la totalidad del disco galáctico, es menor a la que inyectan las supernovas, la deposición de energía por acreción de gas extragaláctico puede ser mucho mayor en las regiones donde tienen lugar los impactos de nubes de alta velocidad (Fig. 8).

El 10 de diciembre de 1983 retorna la democracia en Argentina y solicito mi reincorporación al CONICET. El proceso administrativo dura unos dos años. Finalmente

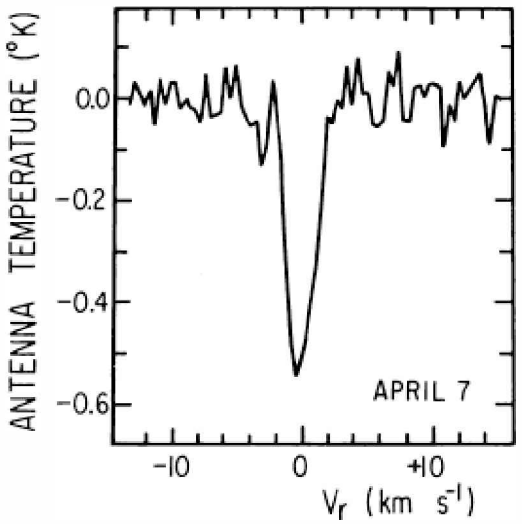

Figura 9: Prototipo de espectros de absorción del radical OH en la línea de 18 cm, observados con la antena del IAR, en la coma del cometa Halley, durante su pasaje frente a fuentes galácticas de radio continuo. Reproducción de la Publicación Especial de la European Space Agency sobre la incursión hacia el interior del sistema solar del cometa Halley en febrero–abril de 1986. Mirabel, Bajaja, Arnal et al. (1986).

soy reincorporado a fines de 1985, a tiempo para involucrarme en observaciones del cometa Halley durante su última incursión en la región central del sistema solar.

3.3.7. Astronomía del Sistema Solar en el IAR: Perihelio del cometa Halley

Para las observaciones del cometa Halley (durante febrero–abril 1986) se obtiene un subsidio de la NSF de los EEUU a fin de determinar la tasa de inyección de gas hacia la coma del cometa por medio de la absorción del radical OH de fuentes de radio continuo en el plano galáctico (Fig. 9). Se observan varias eyecciones discretas a una tasa media de $(4.6\pm0.2)\times10^{29}$ moléculas s^{-1}. El subsidio incluye la donación al IAR del autocorrelador de 1024 canales del observatorio de Arecibo, cuyo costo de construcción había sido estimado en centenas de miles de dólares.

3.3.8. SETI: Búsqueda de señales provenientes de civilizaciones extraterrestres

El primer simposio de la UAI sobre Exobiología en la Universidad de Boston tuvo un carácter interdisciplinario. En el participaron astrónomos, físicos, químicos, biólogos, historiadores, especialistas de la comunicación, etc. Esa reunión internacional fue una de las más motivantes de las que he participado. Para dar un ejemplo, la reflexión sobre cuál debería ser nuestra actitud ante el encuentro con una alteridad tan radical como la de seres extraterrestres con una capacidad científica y tecnológica equivalente o superior a la nuestra, se convirtió en aquel congreso en una reflexión profunda sobre la historia de nuestras propias civilizaciones terrestres, y en particular, sobre las consecuencias de sus múltiples encuentros. En aquella oportunidad adherí como miembro fundador de la comisión 51 de Exobiología de la UAI.

En general se ha supuesto que si existen civilizaciones extraterrestres en nuestra Galaxia los canales de comunicación por medio de radioondas deberían estar en lo que se designa como "pozo de agua". Esta es la región del espectro electromagnético más cercana a la temperatura del fondo cósmico de microondas, la cual podría servir como canal de comunicación por medio de ondas de radio entre civilizaciones galácticas. Por tal razón, las búsquedas de tales señales han sido cercanas a las frecuencias de 1420 MHz del hidrógeno atómico o entre 1620 y 1720 MHz del radical OH, donde tanto nosotros como las posibles civilizaciones extraterrestres deberían tener sistemas receptores de alta sensibilidad, y transmisores de alta potencia.

Un canal alternativo que no había sido explorado es el de la transición a 4.8 GHz de la molécula de H_2CO (formaldehído), que por un mecanismo antimáser es observada en absorción contra el fondo de microondas de 2.7 K. Esto hace que ese pozo de absorción sería el canal más "frío" para las comunicaciones por radioondas entre civilizaciones. Por tal razón envío una propuesta al Observatorio Nacional de Radioastronomía de los EEUU para realizar observaciones durante una semana con el radiotelescopio de 42 m en West Virginia, en la dirección de un conjunto de estrellas de tipo espectral similar al sol. Los cuatro evaluadores acuerdan que la idea es original, dos están a favor de conceder el tiempo de observación solicitado, pero los otros dos están en contra. Estos últimos argumentan que no se debe utilizar una facilidad nacional sobresubscripta para un *shoot in the dark*, con tan baja probabilidad de detección. Pero el director del observatorio toma la decisión de conceder una semana entera de observación.

En las últimas horas de observación, observando una de las estrellas del programa se registra una posible señal con forma de delta de Dirac, solamente en uno de los canales. Eso podría ser el llamado de atención esperado, ya que concentrando toda la energía del sistema transmisor en el rango más estrecho posible de frecuencias, y en el menor intervalo de tiempo posible, se obtiene la mayor potencia de transmisión. Cuando el director ve el registro de esa señal sugiere conceder tiempo de observación discrecional, aconsejándome permanecer por el resto de mi vida observando esa estrella. Cambio la reserva de los vuelos de regreso para poder continuar con las observaciones unos días más y, mientras tanto, exploro el bosque circundante. Repentinamente me pregunto si en las adyacencias de la delta de Dirac se pueden observar los armónicos producidos por el sistema de recepción, lo cual confirmaría que la señal realmente provino del exterior del sistema receptor. Vuelvo rápidamente, tomo la cinta magnética de respaldo y al leer los datos registrados en el otro edificio del observatorio, la señal no está. En Argentina promuevo SETI mediante la organización de un simposio en la UBA, se publican entrevistas en periódicos y revistas y un artículo corto en Revista Astronómica (Mirabel, 1984).

3.3.9. Flujos bipolares en regiones de formación estelar

El estudio de flujos bipolares se lleva a cabo con la antena de Arecibo y el VLA observando transiciones de H I y OH en ondas centimétricas, y con varios telescopios milimétricos (CO, CS, NH_3) en colaboración con Luis F. Rodríguez y Jorge Cantó de la Universidad Nacional Autónoma de México. La integración de estas observaciones multifrecuencia, que se muestra en la Fig. 10, es presentada en varios congresos y publicada en Mirabel et al. (1985) y Rodríguez et al. (1989).

4. Apertura de nuevas áreas en Astronomía

4.1. Galaxias infrarrojas ultraluminosas

4.1.1. El descubrimiento

Quizás por haber desarrollado la tesis doctoral en Argentina, lejos de los principales centros de investigación del mundo, durante los primeros años de formación como investigador científico no pude participar en ningún congreso internacional. Siendo consciente de que la ciencia es una actividad social, desde un comienzo adquiero el hábito de leer y disfrutar la lectura de publicaciones en revistas de astronomía, durante una o dos horas diarias. Esta disciplina de lector la fui adquiriendo no solo respecto a publicaciones directamente relacionadas a mis investigaciones, ya que desde temprano tuve la convicción del carácter interdisciplinario de la investigación científica, y de la importancia de transitar hacia nuevas áreas con nuevas preguntas, sin los prejuicios preestablecidos en las mismas.

A comienzos de la década del '80, leo en "The Astrophysical Journal" que astrónomos del NRAO de los EEUU habían encontrado, por medio de observaciones en el continuo de radio, un tipo de galaxias que designan como "Radio Bright Spiral Galaxies". Esas galaxias llaman mi atención, ya que la emisión intensa en radioondas no proviene mayoritariamente de la región nuclear como en las galaxias con núcleos activos (AGN, por sus siglas en inglés). Contrariamente a lo habitual en galaxias activas, la emisión intensa de radio es tan extendida como la población estelar del disco. Ese tipo de galaxias muy prominentes en el continuo de radioondas son tenues en el óptico, por lo que en su gran mayoría hasta entonces habían pasado desapercibidas. Observaciones de esos objetos con los telescopios más grandes tanto en la línea de 21 cm del H I como en transiciones del gas molecular eran inexistentes.

Mi hipótesis fue que se puede tratar de galaxias con brotes muy intensos de formación de estrellas masivas con una alta tasa de explosión de supernovas, lo que produce emisión sincrotrón en radioondas extendida en todo el disco estelar. Paradójicamente, ahora pienso que quizás los agujeros negros y estrellas de neutrones en sistemas binarios de alta masa pueden producir un flujo mayor en radioondas que las supernovas. Cuestión a explorar. Obviamente, solo puede haber intensos brotes de formación de estrellas masivas si hay disponibles grandes cantidades de gas atómico y molecular. Sobre la base de esa hipótesis simple, someto propuestas para observar una veintena de estas "radio bright spiral galaxies" en la línea de 21 cm con el radiotelescopio de 305 m de Arecibo, y en la transición CO(1–0) de la molécula de monóxido de carbono en la longitud de onda de 3 mm con la antena de 12 m del NRAO en Arizona.

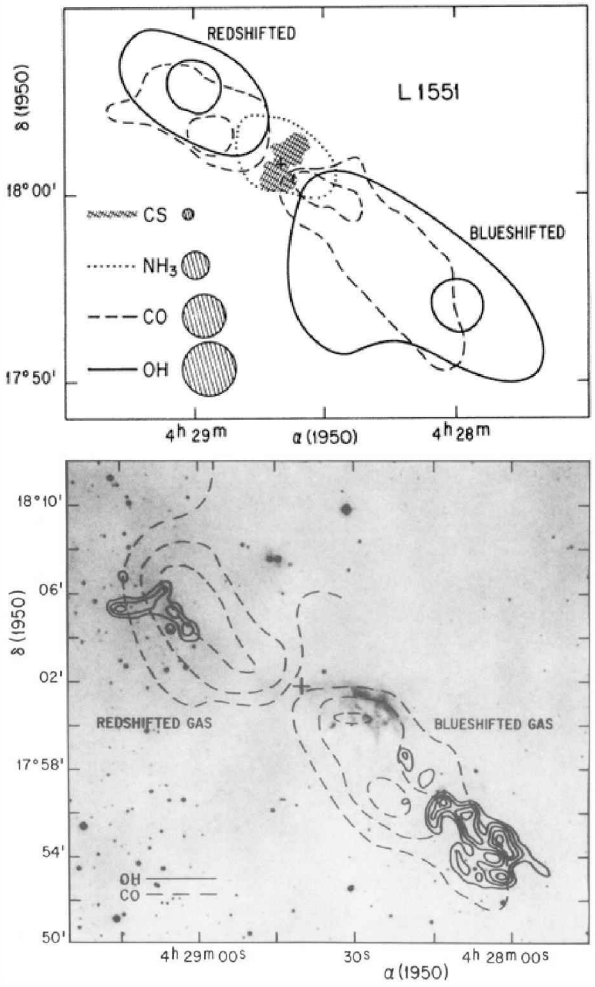

Figura 10: *Arriba*: Superposición de las transiciones de 1667 y 1665 MHz del radical OH observadas con el radiotelescopio de 305 m de Arecibo, sobre diferentes transiciones moleculares en el flujo bipolar de la región de formación estelar L1551. La absorción del OH representa la parte más tenue de flujo bipolar de alta velocidad. Reproducción de Astrophysical Journal Letters, Mirabel, Rodríguez, Cantó et al. (1985). *Abajo*: Radical OH de alta velocidad observado con el VLA de NRAO en absorción (línea continua) superpuesto sobre un mapa del CO de alta velocidad (línea a trazos) en el flujo bipolar de la región de formación estelar L 1551. El OH es producido en las extremidades del flujo molecular por disociación de H_2O debida a la radiación estelar en el medio interestelar. Reproducción de Astrophysical Journal, Rodríguez, Mirabel, Cantó, et al. (1989).

Las observaciones en H I revelan espectros sorprendentes, nunca vistos, muy complejos. En algunos casos con completa y profunda absorción en H I, como es el caso de Arp 220/IC 4553 (Mirabel, 1982). La propuesta para las observaciones de CO(1–0) con la antena del NRAO es aprobada para todo el tiempo solicitado, pero diferida por un año debido al cambio ya programado de la superficie del radiotelescopio.

Para estas observaciones de gas molecular necesitaría la colaboración de un experto en observaciones milimétricas. Asisto a un simposio de la UAI en Amsterdam, Países Bajos, sobre los resultados de la radioastronomía del medio interestelar en la Vía Láctea, y en particular, sobre la incipiente radioastronomía milimétrica, cuya técnica de observación desconozco, ya que difiere en varios aspectos de la técnica de observación en ondas centimétricas y métricas.

En la sala de embarque para el vuelo de retorno a los Estados Unidos identifico a Dave Sanders (Fig. 11), quien en el congreso realizó una exposición sobre nubes gigantes de gas molecular en la Vía Láctea, que me había llamado la atención. En aquel entonces, Dave era astrónomo postdoctorado en la Universidad de Massachusetts, especialista en observaciones milimétricas de gas molecular en la Vía Láctea. Al ver que se cerraba el vuelo y el número escaso de pasajeros permitiría solicitar asientos adyacentes, luego de consultar con Dave, cambio de asiento para poder explicarle durante el vuelo transatlántico, la propuesta ya aceptada sobre observaciones de gas molecular en las "radio bright spiral galaxies". Dave no conoce ese tipo de galaxias y tampoco ha leído mi trabajo sobre las observaciones de H I en Arecibo.

Hasta ese momento las observaciones de transiciones moleculares en ondas milimétricas se habían limitado a la Vía Láctea y recién se comenzaba a realizar observaciones de las galaxias más próximas como Andrómeda o Messier 81. En este contexto se establece una nueva colaboración, donde Dave contribuye con su conocimiento de las técnicas de observación en ondas milimétricas, yo con la lista de galaxias a observar, y en particular, con las precauciones que se deben tomar cuando se sintonizan los receptores de radioondas para observaciones de galaxias lejanas. De hecho, por mis investigaciones en cosmología y galaxias activas aprendí que en los observatorios radioastronómicos no se usa la definición óptica del corrimiento al rojo para calcular la frecuencia de "sintonía del cielo".

La conjugación de ambas experiencias es la clave para la primera detección exitosa de todas las galaxias observadas. Por el contrario, los primeros intentos de detección de transiciones moleculares de este tipo de galaxias lejanas por parte de grupos de investigación de Estados Unidos, Europa y Japón utilizando otros radiotelescopios milimétricos resultan infructuosos. Simplemente porque sintonizan los receptores a frecuencias equivocadas, ya que utilizan la definición radioastronómica del corrimiento al rojo óptico inserta en el software de todos los radio observatorios, en lugar de utilizar la definición óptica del mismo. Por esa razón, dejan la emisión molecular de las galaxias lejanas fuera del rango de frecuencias del espectrómetro.

En 1984 debo repentinamente limitar mi participación en las misiones de observación ya programadas sobre galaxias infrarrojas luminosas en observatorios de Estados Unidos, América del Sur, Europa y Japón. A pesar de la productividad en investigación científica, reconocida por distinciones y subsidios de la NSF, debo reducir mis ausencias de la Universidad para poder cumplir con una dedicación docente de tres cursos de Física por semestre. En este contexto, propongo a Dave Sanders que él tome el liderazgo en la continuación de esta área de investigación. Ese mismo año, Dave pasa a ocupar una nueva posición postdoctoral en Caltech, donde tiene acceso directo a los datos del satélite *IRAS*. Las observaciones de este satélite revelan que esas galaxias son tan luminosas en el infrarrojo como los cuásares. Inmediatamente realizamos la primera publicación sobre las Galaxias Infrarrojas Ultraluminosas (ULIRGs, por sus siglas en inglès), y la relación en este tipo de galaxias entre el contenido de gas molecular, continuo de radioondas y emisión en el infrarrojo por el polvo (Sanders & Mirabel, 1985).

Figura 11: Equipo de trabajo sobre la relación entre Galaxias Infrarrojas Ultraluminosas (ULIRGs) y Galaxias con Núcleos Activos (AGN). De izquierda a derecha: Dick Sramek (NRAO), Peter Barthel (U. de Groningen), Félix Mirabel, Dave Sanders (Caltech), Rick Edelson (U. de Maryland). Frente al Museo de Arte de China en Taiwan a mediados de los años '90.

Para profundizar las investigaciones sobre esta nueva clase de galaxias me otorgan la beca Guggenheim para trabajar dos años en el California Institute of Technology (Caltech), donde conozco la práctica de la investigación de frontera en astrofísica.

Además de realizar estudios en diferentes longitudes de onda de las listas de galaxias luminosas provenientes de las observaciones con *IRAS*, también se estudia en forma integral casos individuales paradigmáticos de estas galaxias luminosas en el infrarrojo. Para ello se deben realizar observaciones en el rango óptico y en el infrarrojo cercano a 2 μm, por lo que solicito colaboración a José Maza, profesor de astronomía de la Universidad de Chile para las observaciones espectroscópicas en el óptico, y a Dieter Lutz del Instituto Max Planck en Garching Bei München, para las observaciones de las imágenes ópticas y del infrarrojo cercano. La Superantena, prototipo de ULIRG, es llamada así porque entre las extremidades de las colas de marea hay una distancia de 350 kpc. En la Fig. 12 se muestra un núcleo Seyfert y un núcleo *starburst* de dos galaxias en estado de fusión avanzada. Los núcleos se encuentran a una distancia entre sí de solo 10 kpc. La publicación Mirabel et al. (1991) será mencionada en un News & Views de la revista Nature.

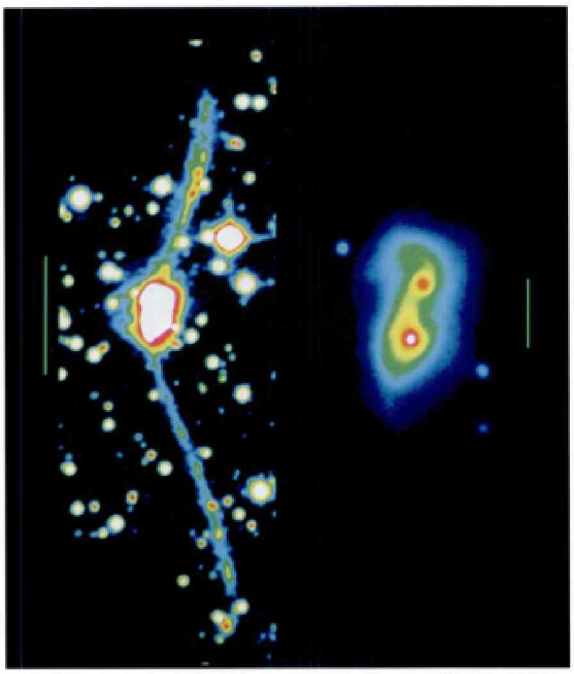

Figura 12: La Superantena, prototipo de galaxia ultraluminosa en radiación infrarroja ($> 10^{12}$ $L_{\odot}$). Esta galaxia consiste en la colisión de dos galaxias espirales, como Andrómeda y la Vía Láctea, que por acción de marea han eyectado materia hasta distancias, entre sus extremidades, de 350 kpc. En la derecha se muestra una imagen de la zona central con un núcleo activo (Seyfert) y un núcleo con brote de formación estelar (*starburst*), que se han aproximado entre sí a una distancia de 10 kpc. Reproducción de Astronomy & Astrophysics. Mirabel, Lutz & Maza (1991).

Diferentes proyectos de investigación son realizados sobre esta nueva clase de galaxias con *IRAS*, Arecibo, VLA y varios radiotelescopios milimétricos: ver por ejemplo: OH Megamasers in Luminous IRAS Galaxies (Mirabel & Sanders, 1987); SEST observations of CO(1–0) in ultraluminous infrared galaxies (Mirabel et al., 1988); NTT images of ultraluminous infrared galaxies (Melnick & Mirabel, 1990).

Del conjunto de estas y otras investigaciones se concluye que las ULIRGs son galaxias ricas en gas y polvo que se encuentran en estado de fusión avanzada. Estas galaxias producen en el infrarrojo tanta energía como los cuásares ($> 10^{12}$ $L_{\odot}$). Esa radiación infrarroja es emisión térmica de polvo calentado por la energía generada en intensos brotes de formación estelar y acreción hacia agujeros negros supermasivos.

De hecho, algunas de las galaxias infrarrojas más cercanas se encuentran en el "Atlas and Catalog of Interacting Galaxies"(Vorontsov-Velyaminov, 1959) y en el "Atlas of Peculiar Galaxies" (Arp, 1966), publicado siete años después. Para planificar observaciones ópticas e infrarrojas de las galaxias de *IRAS* con telescopios de 4 m encuentro fácilmente el catálogo de Arp, pero no el de Vorontsov-Velyaminov, que finalmente hallo en una noche nublada durante un proyecto de observaciones en la biblioteca del observatorio de Monte Palomar . Para mi sorpresa, en esa publicación se representa la morfología de las galaxias interactuantes dibujadas a mano!

Figura 13: Catherine Cesarsky y Laurent Vigroux.

Años después, durante la Perestroïka que impulsa Mijail Gorbachov soy invitado a participar en un simposio en el Instituto Sternberg de Moscú, donde encuentro a Vorontsov-Velyaminov. En la conversación me cuenta las limitaciones que ha tenido para desarrollar sus investigaciones científicas, carencia de placas fotográficas, carencia de *reprints* de su trabajo original, falta de fotocopiadora, y otras muchas más, que en varios aspectos hallo análogas a las dificultades encontradas durante mi trabajo de tesis doctoral en Argentina.

En un simposio de la UAI en Kentucky doy una conferencia invitada sobre las ULIRGs. Geoffrey Burbidge, editor de Annual Review of Astronomy and Astrophysics (ARAA) escucha mi exposición sentado en primera fila. Pero cuando comienzo a exponer mi interpretación de las superantenas como originadas por interacción de marea entre dos galaxias en colisión, súbitamente me interrumpe y me demanda en voz alta una justificación de la misma. De hecho, Burbidge conjuntamente con Arp desarrollaron una interpretación de las galaxias que se encuentran en el plano del cielo alrededor de cuásares, como objetos eyectados desde los cuásares. No sé si mi explicación lo convenció. De todas maneras, luego de mi disertación, Burbidge me invita a escribir un artículo para ARAA, y yo a su vez invito a Dave Sanders como colaborador. Hasta la fecha el trabajo, Sanders & Mirabel (1996), ha sido citado en más de 2300 publicaciones.

4.2. Continuación de investigaciones extragalácticas con el Infrared Space Observatory

Cuando la beca Guggenheim en Caltech llega a su término, mi colega francés Ilya Kazès me cuenta que en la Comisión de Energías Atómica y Alternativas de Paris-Saclay se abre una nueva posición *tenure track*. Postulo a esa posición, ya que me daría la posibilidad de continuar la línea de investigación sobre ULIRGs. De hecho, se solicita un investigador confirmado para trabajar en el programa extragaláctico de tiempo garantido con la cámara para imágenes infrarrojas ISOCAM (Investigadora principal: Catherine Cesarsky; Director técnico: Laurent Vigroux; Fig. 13) del "Infrared Space Observatory" (*ISO*) de la Agencia Espacial Europea. En el Departamento de Astrofísica de CEA-Saclay-Paris que es dirigido por Cesarsky y luego lo será por Vigroux, encuentro la libertad y condiciones ideales para desarrollar investigación científica.

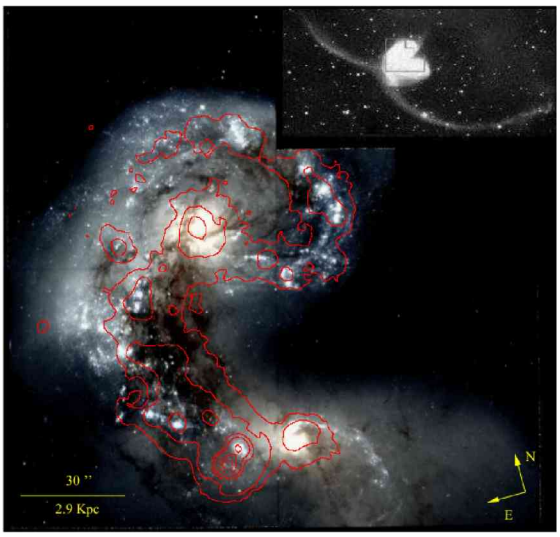

Figura 14: Superposición de la emisión en el infrarrojo intermedio (12–17 μm, contornos en rojo) de Las Antenas obtenida con ISOCAM del *Infrared Space Observatory*, sobre la imagen compuesta en los filtros V (5252 Å) e I (8269 Å) de la base de datos del HST. La emisión infrarroja más intensa proviene de una región marginalmente visible en el óptico. La formación estelar más intensa en estas galaxias en colisión tiene lugar en regiones ópticamente oscuras, todavía envueltas en grandes cantidades de polvo y gas. Reproducción de Astronomy & Astrophysics. Mirabel, Vigroux, Charmandaris et al. (1998b).

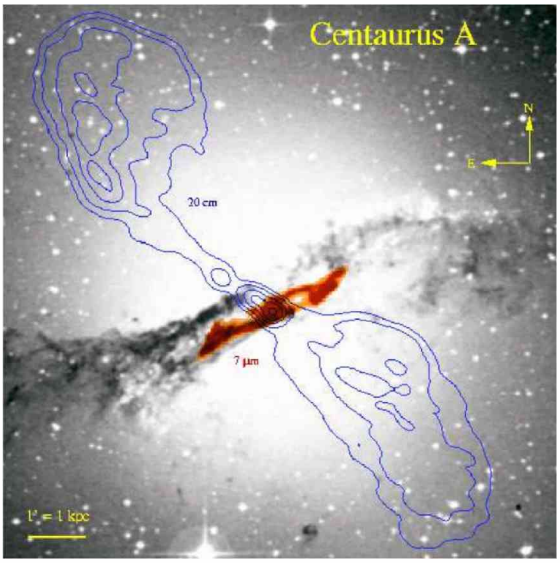

Figura 15: Imagen obtenida con ISOCAM en 7 μm (color rojo) y emisión en el continuo en 20 cm de los archivos de NRAO-VLA (contornos azules), superpuestas sobre una imagen óptica (negro y blanco) del *Palomar Sky Survey*. Mientras el gas asociado a la espiral bicónica en la región central rota a una velocidad radial máxima de 250 km s^{-1}, la componente estelar elipsoidal rota lentamente, aproximadamente en dirección perpendicular al plano que contiene la estructura espiral de polvo. Reproducción de Astronomy & Astrophysics, Mirabel, Laurent, Sanders et al. (1999).

Contrariamente a lo que supongo antes de llegar a Saclay, la sensibilidad de ISOCAM no es suficiente para estudiar galaxias infrarrojas muy lejanas. Sin embargo, es un instrumento adecuado para estudiar regiones de formación estelar inmersas en polvo en galaxias cercanas. Tal es el caso de la región más intensa de formación estelar en la región ópticamente oscura, donde tiene lugar la colisión de los discos de dos galaxias espirales Sc en Las Antenas (Fig. 14), y de la estructura espiral del polvo y gas molecular en Centauro A (Fig. 15).

Figura 16: Horacio Dottori, Dieter Lutz, y Pierre-Alain Duc.

4.3. Galaxias enanas de marea

La primera evidencia firme sobre la formación de esta nueva clase de galaxias enanas se obtiene por las observaciones con el telescopio de 3.6 m del observatorio La Silla, ESO, Chile, en colaboración con Horacio Dottori de la Universidad de Rio Grande do Sud, Brasil, y Dieter Lutz del Instituto Max Planck en Garching Bei München, Alemania (Fig. 16). Las Antenas son galaxias espirales Sc en colisión, y las propiedades del objeto en la extremidad de la cola de marea son comparables a las propiedades de las galaxias enanas IC 1604 y NGC 6822 del Grupo Local. La primera confirmación observacional sobre la existencia de esta clase de objetos se encuentra en la Fig. 17.

Cuando el manuscrito de esa publicación aún estaba siendo evaluado por los árbitros, propongo una búsqueda sistemática de este tipo de objetos como proyecto de tesis doctoral. Para el comité encargado de decidir sobre el financiamiento del proyecto, el tema parece riesgoso, inusual y de resultado incierto para una tesis doctoral. Por ello en primera instancia recibo un cuestionamiento. Pero finalmente, quizás por la reputación de trabajos anteriores, se otorga el financiamiento de la beca doctoral. Pierre-Alain Duc es seleccionado como becario y pasa a liderar esa área de investigación. En su tesis doctoral y trabajos posteriores como post-doc en Cambridge, Inglaterra, encuentra una diversidad de galaxias enanas de marea, empezando por Arp 105: "La Guitarra" (Fig. 18). Actualmente, Pierre-Alain es director del Observatorio de Estrasburgo.

Cuestiones de actualidad en esta área: 1) ¿Son las galaxias enanas de marea sistemas gravitacionalmente estables?; 2) Si son estables, ¿esto quiere decir que se pueden formar galaxias sin materia oscura?; 3) ¿Qué fracción de las galaxias enanas irregulares pueden haberse formado como galaxias enanas de marea?

4.4. Microcuásares en astrofísica de altas energías y cosmología

Los microcuásares son objetos de la astrofísica de altas energías relacionados a dos aspectos de la Física Rela-

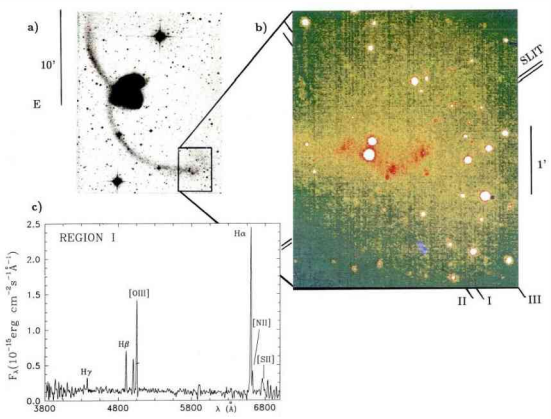

Figura 17: Galaxia Enana de Marea en Las Antenas. Imagen óptica del extremo sur de las Antenas obtenida con el telescopio de 3.6 m de ESO. Esta imagen en colores artificiales muestra en rojo una cadena de regiones H II, los círculos en color blanco son estrellas de la Vía Láctea. Las regiones H II se encuentran inmersas en un fondo difuso de emisión estelar. La región H II más luminosa alcanza a tener una luminosidad equivalente a 300 veces la luminosidad de la región H II de Orión en la Vía Láctea. Las estrellas ionizantes tienen edades menores a 2×10^6 a, las cuales son inferidas a partir del espectro de la región. Estas observaciones muestran que a 100 kpc de las galaxias NGC 4038/39, se forma un objeto similar a las galaxias enanas irregulares como IC 1604 y NGC 6822, a partir de los desechos de la colisión expulsados por acción de marea. Reproducción de Astronomy & Astrophysics, Mirabel, Dottori & Lutz. (1992a).

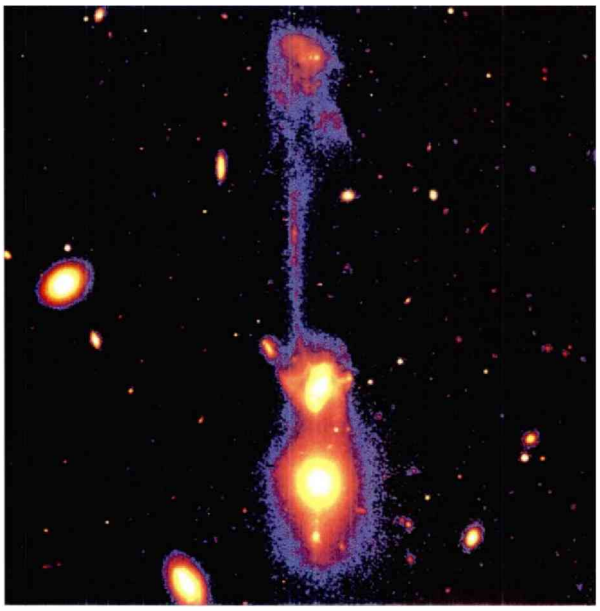

Figura 18: Galaxias enanas de Marea en Arp 105. Imagen CCD en banda V con el Canada-France-Hawaii Telescope. Arp 105, es una galaxia espiral que está siendo descuartizada por una galaxia elíptica gigante en la región central del cumulo de galaxias Abel 1185. En los extremos de las colas de marea se encuentran una galaxia enana compacta y una galaxia irregular que se asemeja a las nubes de Magallanes. Se propone que estas galaxias enanas son objetos reciclados a partir de los desechos expulsados hacia el espacio intergaláctico por acción de mareas sobre la galaxia espiral. La dimensión de la imagen corresponde a un tamaño físico de 190×190 kpc^2. Reproducción de Astronomy & Astrophysics, Duc & Mirabel (1994).

tivista: los agujeros negros y jets relativistas. La primera detección de jets relativistas en la Galaxia fue en la binaria compacta de alta masa SS 433 (Margon et al., 1979), donde se observan variaciones Doppler periódicas en las frecuencias de líneas espectrales ópticas, debidas a la precesión de jets con velocidades de $0.26c$. Varios años después, a partir de los '90, a partir de observaciones en ondas de radio de las fuentes compactas de radiación X descubiertas por satélites espaciales, se comienza a identificar nuevas fuentes de jets relativistas en la Vía Láctea llamados microcuásares. Estos son laboratorios cercanos que sirven para el estudio de los jets relativistas y fenómenos de alta energía que se observan en todo el universo, convirtiéndose en una nueva área de la astrofísica de altas energías. Desde entonces ha habido diez congresos internacionales sobre microcuásares, siendo uno de los temas principales de un simposio de la UAI sobre jets en el universo que tuvo lugar en Buenos Aires en el año 2010.

4.4.1. El descubrimiento de los microcuásares

En diciembre de 1989 una colaboración entre la Unión Soviética, Francia y Dinamarca pone en órbita el satélite *GRANAT* para la observación de fuentes de radiación X dura y radiación gamma. Contrariamente a lo esperado, se encuentra que la fuente más intensa de radiación de altas energías en la región del centro galáctico no es Sgr A*, sino una fuente previamente descubierta por el satélite *Einstein* llamada 1E 1740.7–2942. Inmediatamente se sospecha que esta es la fuente responsable de una emisión variable en 511 keV tentativamente reportada por experimentos con globos de la NASA, la cual es atribuida a la aniquilación de materia y antimateria (e^- e^+). Por tal razón, esta fuente es bautizada por una editorial de la revista Physics Today como "El Gran Aniquilador de materia y antimateria". La posición precisa y naturaleza de la fuente es aún desconocida.

Razono que una fuente de fotones de alta energía como el "Gran Aniquilador" también debe ser fuente de partículas de altas energías, que en interacción con campos magnéticos producen emisión sincrotrón en radioondas. A fin de localizar la posición en el cielo del "Gran Aniquilador" 1E 1740.7-2942 con una precisión mejor que un segundo de arco, se me ocurre realizar observaciones en radioondas con el interferómetro VLA, simultáneamente con observaciones del satélite *GRANAT*. Jacques Paul, Stephane Corbel y François Lebrun de CEA-Saclay, Francia, proveen la información sobre las observaciones con *GRANAT*. Para las observaciones con el VLA propongo a Luis Felipe Rodríguez colaborar en este proyecto. Luis Felipe es especialista en observaciones con el VLA, con el cual ya había colaborado en estudios de flujos bipolares en regiones de formación estelar utilizando Arecibo y el VLA (ver Sec. 3.3.9.). Entonces, enviamos nuevamente una propuesta al VLA, esta vez para monitorear el círculo de error de la emisión de altas energías del "Gran Aniquilador" observado con

Figura 19: (*izq a der.*) Mirabel, Rodríguez, Cordier et al. (1992b); Rodríguez & Mirabel (Saclay 1998); Mirabel & Rodríguez (1994).

GRANAT.

En primer lugar, el monitoreo simultáneo en radioondas y radiación X y gamma mostró que las variaciones de una fuente de radio compacta observada con el VLA están correlacionadas con variaciones de la fuente de alta energía observada con *GRANAT*, lo cual permitió confirmar que 1E 1740.7–2942 es la fuente de emisión gamma y localizar la posición del "Gran Aniquilador" con una precisión mejor a un segundo de arco.

En segundo lugar, a medida que vamos adicionando los datos del monitoreo con el VLA, para nuestra sorpresa, aparecen condensaciones de emisión alineadas a ambos lados de la fuente compacta, las cuales se asemejan a los jets observados en los cuásares y radio galaxias. Al consultar los archivos del VLA vemos que existen observaciones de 1E 1740.7–2942 (P.I. Shri Kulkarni) de dominio público, ya que tenían más de dos años de antigüedad. De todas maneras solicitamos y obtenemos permiso de Kulkarni para la utilización de esas observaciones, que se incorporan a las de nuestro monitoreo para producir la imagen de 1E 1740.7–2942, como fuente compacta en el centro de los jets que se muestran en la tapa de la revista Nature (Fig. 19; Mirabel et al., 1992b). Además, en la misma tapa la editorial reproduce el término *microquasar* que se menciona en el texto.

El término "microcuásar" sugiere una analogía más que morfológica, o sea, una analogía conceptual basada en la universalidad de la Física en el entorno de los agujeros negros. Propone implícitamente que la fenomenología en las inmediaciones de los agujeros negros puede ser descripta por un único sistema de ecuaciones, independientemente de las masas de los agujeros negros, con la salvedad que las escalas de espacio y de tiempo son proporcionales a las masas de los agujeros negros. Esta idea será desarrollada más explícitamente en otra publicación en Nature (Fig. 21; Mirabel & Rodríguez, 1998), una vez confirmada por observaciones adicionales que la fenomenología de la acreción-eyección es análoga en microcuásares y cuásares, tal como se sugiere en la publicación de 1992.

El descubrimiento de los microcuásares y la constitución de esta nueva área de investigación, en su comienzo fue motivado por observaciones con globos de la NASA desde la alta atmósfera de una posible variación de la intensidad global de la línea de aniquilación electrón-positrón de 511 keV proveniente de la región del centro galáctico. La búsqueda del "Gran Aniquilador", o sea, de la fuente compacta responsable de esa supuesta variación nos llevó a 1E 1740.7–2942, que si bien es una fuente variable de emisión en ese rango de energías, no puede dar cuenta de la intensa variación global detectada por las observaciones con globos. De hecho, el satélite *INTEGRAL*, sucesor de *GRANAT*, tampoco ha detectado dicha variabilidad. Por una suposición que resultó ser errónea, se encuentra y constituye un nuevo territorio de investigación. Esto muestra que en ciencia experimental/observacional, a partir de suposiciones erróneas se pueden encontrar nuevas verdades. En ciencia, y quizás también en la vida, el miedo al error es miedo a la verdad.

4.5. Movimientos superlumínicos aparentes en la Galaxia

Si la analogía microcuásar-cuásar es correcta, con Luis Felipe Rodríguez nos preguntamos, en 1992, si los microcuásares podrían producir jets con movimientos aparentes superlumínicos, tal como se observan en los cuásares y radiogalaxias, con velocidades aparentes de hasta decenas de veces la velocidad de la luz. Hasta ese momento, en los cuásares se detectan jets solamente de un lado de la fuente compacta, lo cual no permite determinar con certeza los parámetros físicos de los jets relativistas, como ser, la velocidad intrínseca y la potencia de los jets.

Una noche, colegas franceses de la misión *GRANAT* me informan en Saclay sobre el descubrimiento de un objeto en el plano galáctico que, repentinamente, había comenzado a producir radiación X y gamma intensa. Esa fuente se llama GRS 1915+105 ("GR"=GRANAT; "S"=Source; 1915+105=coordenadas ecuatoriales). Sospechando que esa radiación de alta energía puede estar asociada a la génesis de potentes jets

relativistas, suponemos que GRS 1915+105 puede ser el candidato esperado para la detección de movimientos aparentes superlumínicos en la Galaxia. Comienzo a escribir una propuesta para monitorear GRS 1915+105 con el VLA de NRAO, pero descubro que en unas horas más, a medianoche del uso horario en el Este de los Estados Unidos, a las cinco de la mañana del día siguiente correspondiente al uso horario europeo, se cumple el tiempo límite para la recepción de propuestas de observación con el VLA de NRAO. Rápidamente escribo la propuesta de observación para este nuevo "blanco de oportunidad" (*target of oportunity*). Afortunadamente, la propuesta entra a tiempo en el fax de la oficina de NRAO en Charlottesville, estado de Virginia. Sin embargo, me llama la atención que días después no recibo acuso de recepción de la propuesta.

A comienzos de los años '90 los observatorios ópticos-infrarrojos y radioastronómicos todavía no estaban habituados a realizar las observaciones de blancos de oportunidad necesarias para una comprensión integral de las fuentes cósmicas de altas energías, que en general se caracterizan por ser altamente variables. En aquel tiempo, yo ya había comenzado a realizar ese tipo de observaciones, primero con Arecibo, y luego con el radiotelescopio milimétrico de 30 m de IRAM en la Sierra Nevada de Andalucía. GRS 1915+105 además de ser monitoreado con *GRANAT*, también lo es con el satélite de NASA llamado Rossi X-Ray Timing Explorer (*RXTE*), de radiación X en cuatro bandas y de gran campo. *RXTE* provee información sobre las observaciones en tiempo casi real. Por el análisis de los datos que vamos analizando de *GRANAT* y *RXTE*, se comienza a intuir con cierta anticipación, por los cambios de intensidad e índice espectral de la radiación X, cuando se producirá una nueva eyección de potentes jets.

Algunos meses después llega el momento en que se anticipa la posibilidad de una nueva erupción, por lo que solicito la utilización del tiempo de observación de la propuesta. Sin embargo, el director de operaciones del VLA responde que no han recibido ninguna propuesta para justificar la ejecución de las observaciones que solicito. Llamo a la oficina de NRAO en Charlottesville y la secretaria recuerda muy bien haber recibido el fax de la propuesta y haberlo reenviado a la oficina de recepción de propuestas en Socorro, Nuevo México. En realidad yo había enviado por error el fax de la propuesta a la oficina en Virginia en vez de enviarla a la oficina de NRAO en Socorro. Llamo por teléfono a Miller Goss, director de operaciones del VLA, constata la recepción de la propuesta a tiempo y concede en forma discrecional el tiempo de observación. A partir de ese momento, por un tiempo permanecemos al acecho de un brote de alta energía y de una intensa emisión en radioondas proveniente de GRS 1915+105. Por azar se producen circunstancias favorables para el proyecto. En ese momento, Luis Felipe Rodríguez está en año sabático en el sitio del VLA, en el estado de Nuevo México, a fin de instalar receptores de 7 mm en diez antenas. Por lo tanto quedan disponibles para otros proyectos las 17 antenas restantes. Observaciones de archivo con el VLA de la región del cielo que contiene GRS 1915+105 en diferentes épocas, y observaciones de monitoreo en el contexto de nuestra propuesta, muestran la aparición y desaparición de fragmentos de emisión en radioondas alrededor de la fuente. Aun no se puede saber si esos fragmentos se deben a emisiones isotrópicas análogas a "fuegos artificiales", distribuidas aleatoriamente alrededor de la fuente compacta, o a eyecciones colimadas de jets relativistas.

Un fin de semana, Luis Felipe me comunica que la fuente compacta de radioondas había aparecido por primera vez con gran intensidad y con forma ligeramente ovalada. Además, la atmósfera tenía un nivel de humedad alto, por lo que las observaciones en 7 mm son interrumpidas y, consecuentemente, las 17 antenas restantes se pueden utilizar para las observaciones en 3.6 cm de nuestro proyecto. Unos días después aparecen un par de condensaciones que se han desprendido de la fuente compacta y manifiestan asimetría en brillo y velocidad. Esto es inmediatamente interpretado como debido a *Doppler boosting* relativista. La condensación del lado "izquierdo", que se mueve más rápido y es más brillante, se mueve hacia el observador, y la condensación menos luminosa, que parece moverse más lentamente hacia el lado derecho, se debe a *de-boosting* porque se aleja del observador (Fig. 19, 1994).

Esto confirma que se trata de una eyección relativista antisimétrica de nubes de plasma gemelas hacia ambos lados de la fuente central. Es la primera vez que se observan jets relativistas hacia ambos lados de una fuente, con velocidades aparentes mayores que la velocidad de la luz. En ese momento saco pasaje de avión para Socorro, en Nuevo México, a fin de seguir las observaciones del movimiento de los jets, hasta su desaparición un mes y medio después. Luis Felipe se encarga de hacer una exposición de este descubrimiento en el instituto de NRAO. Al terminar la exposición, el director Miller Goss declara que este es el descubrimiento más importante realizado con el VLA de NRAO.

Las asimetrías aparentes en brillo y velocidad de los jets son explicadas en términos de una eyección antisimétrica de jets gemelos a una velocidad de 95 % de la velocidad de la luz (c), a lo largo de una dirección que forma un ángulo de 70° con la línea de la visual. Si la velocidad de la eyección es de $0.95c$ y suponiendo que en las eyecciones hay un protón por cada electrón, los cuales deben tener factores de Lorentz de 10^3 para producir emisión sincrotrón, se infiere que la energía cinética de la eyección es enorme, de 3×10^{46} erg, equivalente a la energía cinética de un tercio de la masa de la Luna moviéndose al 95 % de la velocidad de la luz.

Comprender cabalmente las observaciones en términos de la relatividad restringida nos lleva varios días. Luego nos enteramos que este es el primer problema formulado en las Olimpiadas Internacionales de Física que tienen lugar en Suecia, unos meses después de la publicación Mirabel & Rodríguez (Fig. 19; 1994). En la competencia olímpica los jóvenes deben resolver este mismo problema en algunas decenas de minutos, cuando a nosotros nos llevó días, lo cual nos llamó la atención. Pero pensándolo bien, una cosa es resolver un problema dado, y otra es llegar a formular el problema para luego resolverlo.

Mirabel & Rodríguez (1994) proponen un nuevo

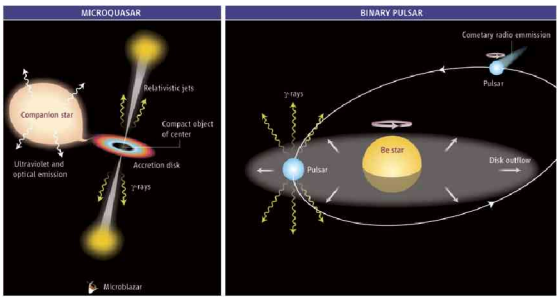

Figura 20: Microcuásares y pulsares en sistemas binarios de alta masa, son fuentes de radiación de alta energía (GeVs y TeVs). Reproducción de Science. Mirabel (2006).

método para la determinación de distancias de las fuentes de eyecciones relativistas en el Universo. Este método es correcto desde el punto de vista teórico pero actualmente difícil de implementar en la práctica. Si hay protones en las eyecciones, es factible la producción de líneas espectrales provenientes de iones, las que combinadas con los movimientos propios, permitirían determinar las distancias a las que se encuentran las fuentes de eyecciones relativistas. Por ello, en el mismo momento en que aparece la publicación, el 1 de septiembre de 1994, ya estoy en el observatorio de Mauna Kea, Hawaii, realizando la búsqueda de líneas espectrales provenientes de los jets de GRS 1915+105. Esta búsqueda resulta infructuosa por dos razones posibles: o los jets son puramente leptónicos y no hay iones en los jets para observar líneas espectrales de recombinación, o si las hay, las líneas espectrales quizás son tan anchas en frecuencia que desbordan el rango de detección del espectrómetro. Quizás vale la pena intentar nuevamente usando el nuevo espectrómetro X-SHOOTER de ESO, que tiene un ancho de banda que cubre longitudes de onda de UV-ópticas-infrarrojas (300–2500 nm). Mirabel & Rodríguez (1994) ha sido citado en mas de 940 publicaciones.

Mientras estoy intentando la detección de esas posibles líneas espectrales a 4200 m s.n.m., en el telescopio UKIRT en Mauna Kea, Hawaii, periodistas del diario Clarín, el de mayor tiraje en Argentina, intentan contactarme sin éxito para una nota sobre los movimientos superlumínicos aparentes. Al no poder localizarme, la editorial de ese diario simula en una publicación a dos carillas completas, una entrevista insertando una foto de archivo. En esa publicación se anuncia que "un astrónomo argentino destrona la teoría de la relatividad de Einstein", ya que ha encontrado velocidades superiores a la de la luz... Averiguo que la especialidad periodística del que ha hecho la nota es el fútbol. A partir de aquel momento, en el año 1994, descubrí que Clarín no es un periódico serio, y que (al menos en este caso), con el fin de lograr sensacionalismo, falsea la realidad.

Más adelante, con el desarrollo de la astrofísica observacional para radiación de altas energías por medio de satélites y de observatorios Cherenkov, se detecta emisión en GeVs y TeVs proveniente de objetos compactos (agujeros negros y estrellas de neutrones) en sistemas binarios de alta masa (Fig. 20 Mirabel, 2006, 2012).

4.6. Acreción y génesis de jets relativistas en agujeros negros

Como la escala de tiempo de los fenómenos en el entorno de agujeros negros es proporcional a la masa del agujero negro, en el lapso de una hora se puede observar en una binaria X con un agujero negro de 10 $M_\odot$ como GRS 1915+105, la relación entre las inestabilidades en el disco de acreción asociadas a la génesis de jets relativistas (Fig. 21). En dicha figura se muestran las observaciones simultáneas con *RXTE* en radiación X (color negro), con UKIRT en Hawaii en el IR a 2.2 μm (color rojo), y en radio a 3.6 cm (color azul) con el VLA. La emisión en X proviene del disco de acreción que después de amplias inestabilidades, decrece súbitamente en energías equivalentes a 10^6 $L_\odot$, al mismo tiempo que el índice espectral cambia en radiación X del estado *low-hard* a *high-soft*. Durante algunos minutos permanece en este estado hasta que un pico de emisión en la radiación X asociado a una reversión del índice espectral, marca el inicio de una eyección que primero se observa como emisión sincrotrón a 2 μm, y luego, con un retardo de $\sim$15 minutos se observa con el VLA a 3.6 cm. Estas son las primeras observaciones simultáneas multifrecuencia (en X, IR y radio) de un fenómeno de acreción–eyección en el entorno de un agujero negro. Este resultado se obtiene luego de más de una decena de intentos, con una tasa de fracasos mayor al 90 %. Para estas observaciones es necesario coordinar la disponibilidad simultánea de los tres instrumentos en observatorios diferentes. Además, una vez que se obtiene la disponibilidad simultánea para obtener las observaciones en los tres dominios de longitud de onda, la fuente debe "colaborar", es decir, debe generar una eyección en el preciso momento en que las condiciones de observación están dadas.

La interpretación de estas observaciones es la siguiente: el disco de acreción entra en un proceso de fuertes inestabilidades, y súbitamente la parte interior del mismo desaparece más allá del horizonte hacia el agujero negro. Luego, la parte interior del disco de acreción comienza a rellenarse hasta que 5 minutos después, asociado a la inversión del índice espectral, se produce un pico en radiación X, que marca la iniciación del jet. Este consiste en un plasma denso que a medida que se expande adiabáticamente deviene progresivamente transparente para longitudes de onda cada vez mayores, primero en radiación X "soft", luego la emisión sincrotrón a 2 μm, y con un tiempo de retardo de 15 min en ondas centimétricas. Es interesante señalar que el tiempo de retardo observado entre el pico de emisión en onda de radio a 3.6 cm, respecto al pico de la emisión en el IR a 2 μm, es el mismo que se infiere utilizando ecuaciones formuladas en el año 1966 para eyecciones relativistas en cuásares, suponiendo expansión adiabática de los jets (van der Laan, 1966). Por otra parte, una relación análoga entre inestabilidades en el disco de acreción y la eyección de jets relativistas en el cuásar 3C 120, son publicadas cuatro años más tarde, pero en intervalos de años en vez de minutos (Marscher et al., 2002), como predice la analogía cuásar–microcuásar (Fig. 21 centro). Estos trabajos teóricos previos y observaciones posteriores confirman definitivamente la analogía cuásar–microcuásar

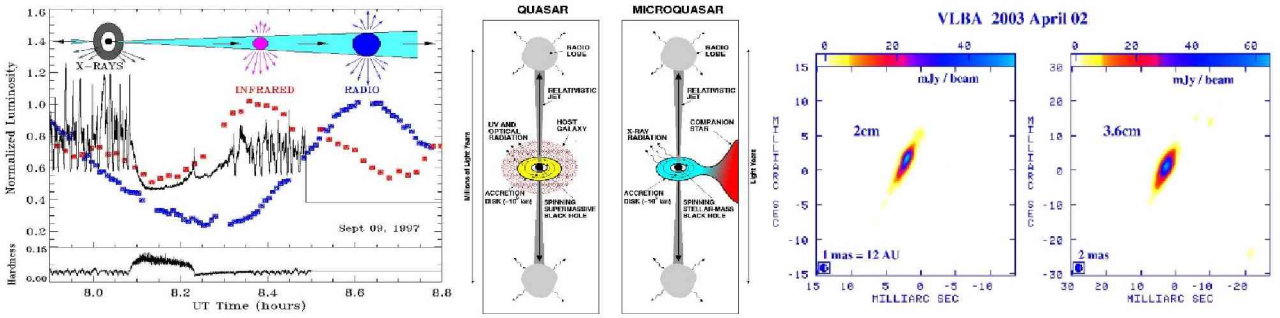

Figura 21: De *izq.* a *der.*): Curvas de luminosidad en X con RXTE (color negro), IR con UKIRT (rojo) y radio con el VLA (azul) del microcuásar GRS 1915+105. Reproducción de Astronomy & Astrophysics: Mirabel, Dhawan, Chaty et al. (Mirabel et al., 1998a). Representación esquemática de la analogía de la analogía Cuásar–Microcuásar. Reproducción de Nature (Mirabel & Rodríguez, 1998). Jets compactos en el microcuásar GRS 1915+105 con tamaños de unas pocas centenas de unidades astronómicas. Reproducción de Astrophysical Journal, Dhawan, Mirabel & Rodríguez (2000).

propuesta por Mirabel & Rodríguez (1998).

En el extremo derecho de la Fig. 21 se muestran imágenes de los jets generados durante las mini-eyecciones. Estas imágenes fueron obtenidas con el interferómetro VLBA de NRAO, que consiste en diez antenas distribuidas en territorio de los EEUU, entre Hawaii y las Islas Vírgenes en el mar Caribe. Estos jets son compactos, de tamaños de algunas pocas centenas de unidades astronómicas, colimados en la misma dirección de las potentes eyecciones del tipo que se muestra en la Fig. 19 (panel derecho). Las investigaciones sobre microcuásares hasta el año 1998 han sido sintetizadas en la revista Annual Review of Astronomy and Astrophysics (Mirabel & Rodríguez, 1999), que hasta la fecha ha sido mencionada en 730 publicaciones.

4.7. Formación de agujeros negros estelares

En colaboración con Irapuan Rodrigues (Fig. 22), doctorado en la Universidad de Rio Grande do Sul, actualmente profesor en la Universidad do Vale do Paraiba en el estado de San Pablo, iniciamos el análisis de observaciones de agujeros negros en sistemas binarios de radiación X, para determinar su cinemática e inferir el mecanismo de formación de agujeros negros estelares. Una de las cuestiones a dilucidar consiste en saber si los agujeros negros estelares se forman como remanentes de estrellas masivas que terminan su vida explotando como supernovas energéticas, tal como habitualmente se supone. De ser así, los agujeros negros en sistemas binarios de radiación X deberían ser despedidos de su lugar de formación, y observar que se mueven con velocidades espaciales anómalas respecto al medio circundante.

Para obtener la velocidad espacial en tres dimensiones utilizamos los jets compactos observados en los microcuásares para determinar los movimientos propios, las velocidades radiales determinadas a partir de espectros de las estrellas compañeras, y las distancias determinadas por diferentes medios. Los datos disponibles nos permitieron inferir las velocidades espaciales para solo cinco sistemas con agujeros negros. La conclusión tentativa a partir de esta pequeña muestra es que los agujeros negros con masas ≥ 10 M$_\odot$ se forman por implosión total o casi total, sin supernovas energéticas, como es el caso del agujero negro de ~ 15 M$_\odot$ en Cygnus X-1, el cual ha permanecido anclado y se mueve conjuntamente con su asociación estelar de origen Cygnus OB3 (Fig. 22 Mirabel & Rodrigues, 2003).

Es posible que agujeros negros con masas < 10 M$_\odot$ se formen a través de explosiones de supernovas, como es el caso de las estrellas de neutrones. Un ejemplo de ello podría ser XTE J1118+480 (Fig. 22), el primer agujero negro en una binaria X identificado en el halo de nuestra Galaxia. Se ha propuesto que este sistema habría sido catapultado desde el disco hacia el halo galáctico por la explosión de una supernova. Sin embargo, no se puede excluir que el agujero negro en XTE J1118+480 haya sido eyectado por interacción dinámica de una región de alta densidad estelar en un cúmulo globular, atrapando una pequeña estrella para su largo viaje por el halo galáctico. La contribución de Vivek Dhawan (Fig. 22), de origen indio, y en aquel entonces *Project manager* del VLBA de NRAO, ha sido esencial para la programación, ejecución y análisis de las observaciones con el VLBA.

Actualmente, esta línea de investigación iniciada con Irapuan Rodrigues y Vivek Dahwan es desarrollada por diferentes grupos de investigación. Utilizando observaciones VLBI de los jets compactos en radioondas, y más recientemente con los datos de creciente precisión que se están obteniendo con *GAIA* en el óptico, se pueden determinar paralajes trigonométricas y movimientos propios con mayor precisión. Nuestra conclusión tentativa sobre la formación por implosión de agujeros negros de más de 10 M$_\odot$ (Cygnus X-1 y GRS 1915+105), ha sido confirmada por diferentes grupos de investigación utilizando nuevas observaciones. En Mirabel (2017) se presenta una síntesis de los resultados de esta línea de investigación sobre la formación de agujeros negros estelares en binarias X y agujeros negros binarios.

4.8. Agujeros negros estelares en el albor del Universo

En el año 2010 recibo una invitación para asistir a una reunión en la Universidad de Maryland a fin de realizar una exposición general sobre microcuásares. En esa oportunidad presento una nueva hipótesis: en los albores

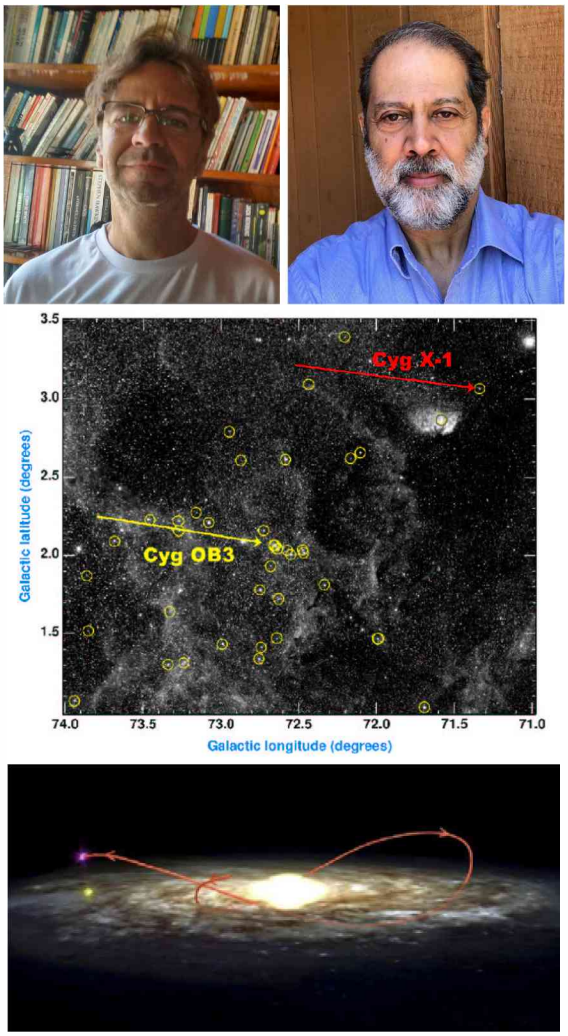

Figura 22: (*Arriba*): Izq. Irapuan Rodrigues, der. Vivek Dhawan; (*centro*): Imagen óptica del cielo que contiene a Cygnus X-1 y la asociación de estrellas masivas Cygnus OB3. Las flechas roja y amarilla muestran las magnitudes y direcciones de los movimiento en el plano del cielo de la contraparte de radio de Cygnus X-1 y el movimiento promedio de Cygnus OB3, respectivamente, durante los últimos 0.5 Ma. Luego de la formación del agujero negro, Cygnus X-1 permaneció anclado en la asociación estelar madre Cygnus OB3, de lo cual se infiere que el agujero negro se formó por implosión de una estrella de 40 $M_\odot$. Reproducción de Science, Mirabel & Rodrigues (2003); (*abajo*): Representación esquemática de la órbita de XTE J1118+480 (curva roja) durante los últimos 240 Ma, lo que corresponde al periodo orbital del sistema solar (curva amarilla) alrededor del centro galáctico. Reproducción de Nature, Mirabel, Dhawan, Mignani et al. (2001).

del Universo deberían haberse formado en forma prolífica, a partir de las estrellas masivas de primera generación, agujeros negros estelares en sistemas binarios de alta masa. Por su retroacción en radiación X y jets relativistas deberían impactar en la física del medio interestelar en la época oscura y de reionización que tuvo lugar entre los primeros 400 000 y 1000 Ma del Universo (Fig. 23)

Esta hipótesis surge a partir de las observaciones que sustentan la formación de agujeros negros por colapso

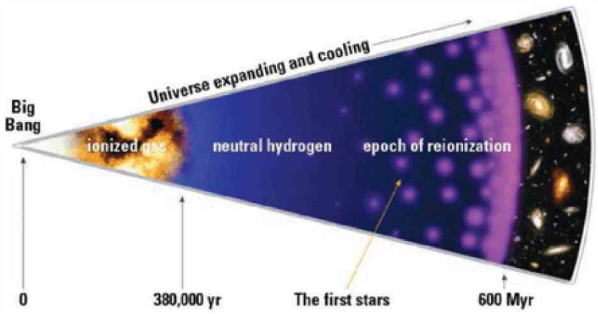

Figura 23: Evolución cósmica durante los primeros 800 Ma. Crédito WMAP. A partir de resultados teóricos y observacionales en diferente áreas de la astrofísica, se propone que los agujeros negros en sistemas estelares múltiples de alta masa tienen un impacto importante en la era de reionización del universo, y en la formación de agujeros negros binarios detectados por LIGO (Mirabel, 2019).

directo de estrellas masivas, sin explosión de supernovas energéticas. Esto implica que los remanentes de binarias estelares con masas mayores a unas 18 $M_\odot$ deberían permanecer gravitacionalmente ligados. Esta hipótesis la voy desarrollando con la incorporación y síntesis de resultados teóricos y observacionales en otras áreas de la astrofísica. Como ser, que más del 80 % de las estrellas masivas se forman en sistemas múltiples, el aumento de la pérdida de masa en estrellas masivas con el aumento de la metalicidad, lo que implica la formación de agujeros negros más masivos y más frecuente en épocas tempranas del Universo, la observación de una alta tasa de formación de binarias compactas de alta masa en galaxias enanas irregulares del universo local. En este contexto propongo que, además de la radiación UV de las estrellas masivas de las primeras generaciones, la radiación X y jets relativistas de los remanentes de estrellas masivas en el albor del universo, o sea, agujeros negros en binarias X de alta masa, también deberían impactar en épocas tempranas del Universo.

En la pausa de café de aquella reunión en Maryland, Avi Loeb de origen israelí (Fig. 24), director del Departamento de Astrofísica Teórica de Harvard, manifiesta interés por esta hipótesis. Luego de una breve conversación ofrece su colaboración para el desarrollo teórico, con participación de sus investigadores post-doctorales, Mark Diskra, de origen holandés y actualmente profesor en la Universidad de Oslo, y Jonathan Pritchard, de origen inglés, actualmente *lecturer* en el Imperial College de Londres (Fig. 24). Por mi parte, invito a participar en esta colaboración a Philippe Laurent de origen francés y miembro de APC-Universidad de Paris y CEA-Saclay. Philippe contribuye con su conocimiento de Cygnus X-1. Mark con la formulación de las ecuaciones que comparan el calentamiento e ionización del medio intergaláctico por la radiación X de las binarias compactas, con la radiación ultravioleta de las estrellas progenitoras. Jonathan contribuye con el cálculo de la evolución térmica del medio intergaláctico y temperatura de brillo de la transición de 21 cm del hidrógeno atómico, incorporando la retroacción de los agujeros negros en binarias X de alta masa (BH-HMXBs).

Este trabajo interdisciplinario, que incorpora nuevos

Figura 24: Colaboradores en el trabajo "Agujeros negros estelares en el albor del universo"publicado en Astronomy & Astrophysics (Mirabel et al. 2011) que motiva un News and Views in Nature. De izq. a der.: Avi Loeb, Mark Diskra, Philippe Laurent y Jonathan Pritchard.

resultados de diferentes áreas de la astrofísica en una de las cuestiones de frontera en la cosmología actual, es publicado en Mirabel et al. (2011), y motiva un News & Views en Nature (Haiman, 2011). Las predicciones derivadas de este trabajo podrán ser contrastadas por los muchos experimentos destinados a revelar las propiedades de la emisión en 21 cm del hidrógeno atómico en la era de pre-reionizacion y reionización, con las configuraciones de radiotelescopios como LOFAR, SKA, HERA, y los experimentos con dipolo único destinados a observar la señal global de 21 cm, como DARE, EDGES, LEDA. Recientemente, he propuesto que si la absorción de hidrógeno atómico reportada por EDGES* (Bowman et al., 2018) a z=17 es confirmada, esta observación sería la primera indicación cuasidirecta de la existencia de numerosas poblaciones de BH-HMXB-Microcuásares, entre los primeros 200 y 260 Ma después del Big Bang (Mirabel, 2019).

4.9. Agujeros negros binarios y fuentes de ondas gravitacionales

La formación de agujeros negros binarios (BBHs) es una cuestión de suma actualidad para la incipiente astrofísica de ondas gravitacionales. BBHs en fusión son las primeras fuentes cósmicas detectadas en ondas gravitacionales. Estas ondas gravitacionales fueron predichas por Einstein hace un siglo, y han sido recientemente detectadas por la colaboración LIGO-Virgo. En la Fig. 25 se muestra uno de los dos posibles canales de formación de BBHs, a partir de binarias estelares masivas y a través de la fase intermedia de BH-HMXB. El canal alternativo propuesto para la formación de BBHs es por interacción dinámica en cúmulos estelares de alta densidad (Mirabel, 2017). Las altas masas de hasta 40 $M_\odot$ de los agujeros negros descubiertos por medio de ondas gravitacionales, en relación a las masas de los agujeros negros identificados en el universo local a partir de la radiación X que producen, y las altas tasas de fusión de agujeros negros encontrada por la colaboración LIGO–Virgo, son naturalmente explicadas en el contexto de la hipótesis de una alta tasa de formación de BH-HMXBs en el albor del Universo, formulada por primera vez por Mirabel et al. (2011).

*Experiment to Detect the Global EoR Signature.

5. Gestión y difusión de la Astronomía en América del Sur

Durante mi trayectoria científica he realizado múltiples tareas para la difusión y gestión de la astronomía y de la ciencia en general. En cuanto a difusión en América del Sur, y en Argentina en particular, cabe mencionar conferencias en el Planetario de la ciudad de Buenos Aires y la Universidad de Buenos Aires; la iniciación en colaboración con la periodista Nora Bar de Cafés Científicos en el Tortoni de Buenos Aires, auspiciados por la Academia Nacional de Matemáticas y Ciencias Físicas y Naturales de Argentina; la iniciación de los Cafés Científicos en las ciudades de Santiago y Antofagasta, y la organización de la Primera Escuela Latinoamericana de Astrofísica en Santiago de Chile, con la participación de más de 300 jóvenes provenientes de más de diez países de América del Sur, Central y el Caribe, durante mi gestión como Representante y Director de la Oficina de Ciencias del Observatorio Europeo Austral (ESO).

En cuanto a la gestión, cabe mencionar: la donación al IAR del autocorrelador del Observatorio de Arecibo en el contexto de un subsidio de la NSF, y la exploración realizada en los '80 y '90 por iniciativa individual en las provincias de Salta y Jujuy para la posible instalación de instrumentos astronómicos. En la atribución de este premio a la trayectoria, la Comisión Directiva de la Asociación Argentina de Astronomía menciona el "incansable trabajo en pos de insertar a la Argentina en proyectos astronómicos internacionales de primer nivel, como el *Cherenkov Telescope Array*. Quizás su aporte más significativo a nuestra comunidad sea la concepción y gestión política del Proyecto *Large Latin American Millimeter Array* (LLAMA), del cual fue mentor, y a cuya promoción dedicó más de una década".

5.1. Proyecto LLAMA

El territorio argentino puede ser de interés internacional para la instalación de proyectos astronómicos en el hemisferio sur que no requieren atmósfera de baja turbulencia, ya que el Norte de Chile ofrece los mejores sitios para observaciones en los rangos de longitudes de onda óptica e infrarrojo cercano. Por tal razón, en la década del 90 comienzo a explorar la Puna Salteña para la posible instalación de facilidades astronómicas a más de 3 800 m s.n.m.

Por iniciativa personal realizo una primera búsqueda de sitio para el proyecto europeo Large Submillimeter

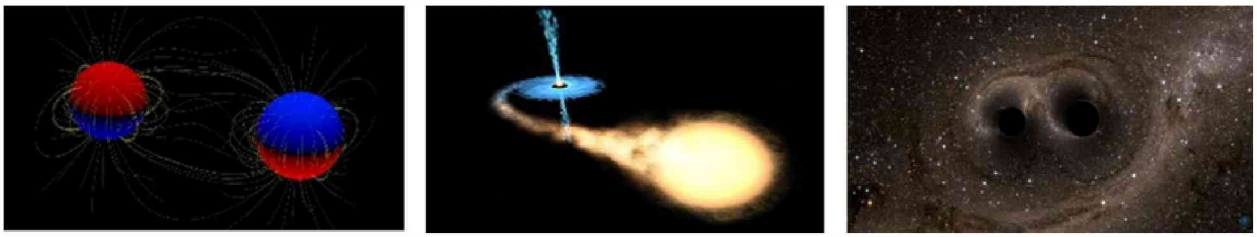

Figura 25: Formación de agujeros negros binarios a partir de sistemas binarios de estrellas masivas. Reproducción de New Astronomy Reviews, Mirabel (2017).

Array (LSA). Este proyecto consiste en un arreglo de radiotelescopios de ∼20 m capaces de observar galaxias como la Vía Láctea a corrimientos al rojo $z > 6$, cuando el Universo tenía menos de un billón de años. Como el sitio debe consistir en un área plana y extensa en alturas a 3500–4000 m, durante diez días realizo una búsqueda a lo largo de la vía del Tren de las Nubes, hasta cercanías de la frontera con Chile, e incluso en la provincia de Catamarca. Para ello el gobernador de Salta provee un vehículo 4x4 con un conductor y un geólogo, conocedores de la Puna.

En esta primera exploración se identifican diferentes sitios posibles para el LSA, como ser el llano al pie de Macón. Un informe completo sobre los sitios posibles es enviado al Instituto de Radioastronomía Milimétrica europeo (IRAM), que lidera LSA. Sin embargo, por una combinación del liderazgo norteamericano en astronomía milimétrica y razones políticas, los europeos deciden plegarse al proyecto americano Millimeter Array (MMA), y desarrollar conjuntamente con EEUU y Japón el proyecto ALMA (Atacama Large Millimeter Array), en Chajnantor (Chile) a 5200 m s.n.m. Este proyecto requiere una inversión de $\sim 1.4 \times 10^9$ USD para su construcción, y para su operación posterior ∼10 % anual de esa inversión inicial. Si bien ALMA es un observatorio que ha producido resultados científicos de gran impacto, en la decisión de construir ALMA en Chajnantor a 5200 m en lugar de desarrollar este proyecto en alturas menores, han prevalecido razones científicas y políticas.

En el periodo 2004–2009 desempeño funciones en el Observatorio Europeo del Sur (ESO): Representante y Director de la oficina de Ciencias de ESO en Chile. La primera función incluye la responsabilidad como Ejecutivo por ESO en el proyecto ALMA. En 2004 comienzo a concebir LLAMA para integrar la astronomía en Argentina a la ciencia de frontera generada por ALMA. La instalación de dos antenas en la Puna, a ∼ 180 km de ALMA hará posible incrementar la resolución angular de las observaciones con ALMA en un orden de magnitud, lo cual será una necesidad futura para la continuación de proyectos científicos en diferentes áreas de la astrofísica desarrollados con ALMA. De este modo se podrá intervenir en la ciencia con ALMA, a un costo relativamente bajo, respecto al costo que implica entrar formalmente como país miembro de las organizaciones internacionales que financian ALMA.

En 2007 presento un manuscrito sobre la idea de LLAMA a Thijs de Graauw, director de ALMA, el cual me recomienda implementar la idea. La misma semana de la creación del Ministerio de Ciencia, Tecnología e Innovación Productiva (MinCyT), presento el manuscrito al Dr. Charreaux, presidente del CONICET, y al flamante ministro Lino Barañao. En el contexto de integración regional de aquella época, Barañao recomienda desarrollar LLAMA en colaboración con Brasil, por lo que propongo esa colaboración a Jacques Lepine de la Universidad de San Pablo. Se firma un convenio entre MinCyT y la fundación FAPESP del estado de San Pablo, donde se toma el compromiso de una inversión equivalente por cada una de esas dos instituciones. En la asamblea de la A.A.A. de 2008 LLAMA es definido como proyecto prioritario de la astronomía en Argentina y también es considerado prioritario en la hoja de ruta del MinCyT. El año siguiente organizamos con Marcelo Arnal y Ricardo Morras por Argentina, y Jacques Lepine, Zulema Abraham y Bete Gouveira Dal Pino por Brasil, un *workshop* sobre LLAMA en la Asamblea General de la UAI en Rio de Janeiro, donde LLAMA es presentado como una ventana de oportunidad para la astronomía en Sudamérica (Fig. 26).

Hasta la fecha (abril de 2019) se ha construido el camino hasta el sitio de la primera antena en Alto Chorrillos, Salta, a 4850 m.s.n.m. Todos los componentes de la antena se encuentran en ese sitio, excepto una pieza dañada por accidente durante su transporte, que es repuesta a nueva por la aseguradora. Además, se ha finalizado la construcción del edificio en San Antonio de los Cobres cuya función será la de servir como base de operaciones. El costo total estimado de construcción es de 20×10^6 USD. Hasta marzo de 2019 se ha invertido un total estimado de $\sim 15 \times 10^6$ USD (10×10^6 por FAPESP-Brasil, 1×10^6 por la provincia de Salta y 3.5×10^6 por MinCyT). Lamentablemente, en 2018 el MinCyT es degradado a la categoría de Secretaría, y hasta abril de 2019 el financiamiento por parte de la Secretaria de Ciencia y Técnica de Argentina para este proyecto se encuentra demorado desde 2017.

Si LLAMA hubiera estado operacional en 2017 podría haber integrado el Event Horizon Telescope (EHT), colaboración internacional que incluye ALMA, y que ha logrado obtener la primera imagen de un agujero negro supermasivo (Event Horizon Telescope Collaboration et al., 2019). Aunque el avance del proyecto LLAMA se encuentra demorado, este constituye una ventana de oportunidad única para el futuro de la astronomía argentina. Tarde o temprano primará la razón y LLAMA será realidad.

MONDAY, AUGUST 10th, 2009 — DAY 6

A WINDOW OF OPPORTUNITY FOR
SOUTH AMERICAN ASTRONOMY

The possibility of installing two radio telescopes for millimeter and sub-millimeter wavelengths, in the Argentinean side of the Atacama desert at distances of 180-210 km from Chajnantor (the site of ALMA), and altitudes greater than 4700 meters, has been discussed among astronomers of Argentina and Brazil.

The support to this idea has been ratified in September 2008 by the Argentinean Astronomical Assembly. In Brazil it is being studied as one of the possible key science goals of the recently approved Astrophysics National Science Institute by the Brazilian National Council of Research - CNPq. Top authorities of Science and Technology in Argentina informed that in the context of regional integration, funds may be available for original projects on basic sciences, with technology transfer components.

The initial US$ 20 million investment of LLAMA would allow Argentine and Brazilian scientists to develop millimeter and sub-millimeter single dish radio astronomy, as well as integration in global experiments with Very Long Baseline Interferometer networks. Of particular interest may be VLBI with already existing radio telescopes in Chajnantor (APEX and ASTE), and in the long run with elements of the ALMA array. Site testing in Argentina has been carried out for three years in Macón (4600m, 180km SE of ALMA) with equipment provided by UNAM (México), and further site testing started at other site 180 km SE of Chajnantor (see attached map). A proposal for initial funding to carry on the in depth study of this project will be submitted by December 2009.

We invite you for an open meeting on this project that will take place on Tuesday August 11 at 17:30 in room 2.11.

LF. MIRABEL, M. ARNAL, R. MORRAS, G. ROMERO, J. LEPINE, Z. ABRAHAM, EL. M. DE GOUVEIRA DAL PINO

LOCATION OF CHAJNANTOR, MACÓN AND CHURRILLOS. THE YELLOW LINE SHOWS THE BORDER BETWEEN ARGENTINA AND CHILE, THE BLACK LINE THE RAILWAY TRACK SALTA-ANTOFAGASTA.

Figura 26: LLAMA: una ventana de oportunidad para la Astronomía en América del Sur. Diario de la UAI en la Asamblea General de la UAI en Rio de Janciro, 2009.

6. Epílogo

En el casi medio siglo de mi trabajo como investigador científico he sido testigo de dos transformaciones en la investigación astronómica: 1) la emergencia progresiva y arrolladora de lo que se llama "Gran Ciencia"; y 2) el incremento del trabajo interdisciplinario en la investigación astronómica, a través de la síntesis de observaciones multifrecuencia del espectro electromagnético, y recientemente, por la integración de nuevas ventanas multimensajeras.

La "Gran Ciencia" se ha desarrollado de modo espectacular en las últimas décadas. Esta consiste en la ejecución de proyectos científicos a través de organizaciones y colaboraciones científico–tecnológicas formadas por equipos numerosos, de hasta centenas y en algunos casos, miles de científicos, ingenieros y técnicos. Esta tendencia es consecuencia de la creciente complejidad de las cuestiones científicas, cuya resolución requiere grandes colaboraciones interdisciplinarias entre especialistas en diferentes dominios de la ciencia y tecnología. La "Gran Ciencia" es necesaria para ejecutar proyectos de gran complejidad, de fuerte carácter industrial, única manera de dar respuesta a ciertas cuestiones fundamentales de las ciencias.

Sin embargo, la "Gran Ciencia" ha llegado acompañada con un significativo detraimiento financiero de las actividades científicas de investigadores solitarios y pequeños grupos, lo cual es cuestionable. Las nuevas ideas tienen origen en soledad y usualmente son concretadas a través de pequeños grupos de investigadores. Además, usualmente las nuevas ideas requieren ser contrastadas observacional/experimentalmente a costos relativamente bajos, por lo que cierto equilibrio entre el financiamiento de la "Gran Ciencia" y la ciencia que podríamos llamar "artesanal" es importante.

En el momento de esta disertación (4/11/2018) el futuro del desarrollo científico en Argentina se ha tornado oscuro. El MinCyT ha sido degradado a Secretaria, y en el caso particular de LLAMA, su continuidad se ha tornado incierta, a pesar de haber sido definido como prioritario para el desarrollo de la astronomía en Argentina, con una inversión ya realizada de $15{\times}10^6$ de dólares, en el contexto de un acuerdo internacional con Brasil.

No obstante las dificultades, invertir tiempo y esfuerzo en investigación científica y educación es uno de los mejores legados para el futuro de Argentina. Mi experiencia personal ha sido que la investigación científica consiste en una vida profesional apasionante, gestando a través del trabajo, amistad con colegas provenientes de diversas culturas y regiones del mundo.

Agradecimientos: A todos los colegas y amigos con los que he colaborado y compartido las emociones de la investigación científica. A Roberto Gamen, editor del Boletín de la Asociación Argentina de Astronomía, por la lectura critica, paciente ayuda, y excelente trabajo de incorporación de la versión original del manuscrito en el formato del Boletín.

Referencias

Arp H., 1966, *Atlas of peculiar galaxies*
Bowman J.D., et al., 2018, Nature, 555, 67
Cohen R.J., Mirabel I.F., 1979, MNRAS, 186, 217
Dhawan V., Mirabel I.F., Rodríguez L.F., 2000, ApJ, 543, 373
Duc P.A., Mirabel I.F., 1994, A&A, 289, 83
Event Horizon Telescope Collaboration, et al., 2019, ApJL, 875, L1
Haiman Z., 2011, Nature, 472, 47
Margon B., et al., 1979, ApJ, 230, L41
Marscher A.P., et al., 2002, Nature, 417, 625
Melnick J., Mirabel I.F., 1990, A&A, 231, L19
Mirabel I.F., 1981a, RMxAA, 6, 245
Mirabel I.F., 1981b, RMxAA, 6, 7
Mirabel I.F., 1982, ApJ, 260, 75
Mirabel I.F., 1984, Revista Astronómica, Órgano de la Asociación Argentina Amigos de la Astronomía, 56, 2
Mirabel I.F., 2006, Science, 312, 1759
Mirabel I.F., 2012, Science, 335, 175
Mirabel I.F., 2017, NewAR, 78, 1
Mirabel I.F., 2019, arXiv e-prints
Mirabel I.F., Cohen R.J., 1979, MNRAS, 188, 219
Mirabel I.F., Dottori H., Lutz D., 1992a, A&A, 256, L19
Mirabel I.F., Lutz D., Maza J., 1991, A&A, 243, 367
Mirabel I.F., Morras R., 1984, ApJ, 279, 86
Mirabel I.F., Morras R., 1990, ApJ, 356, 130
Mirabel I.F., Rodrigues I., 2003, Science, 300, 1119
Mirabel I.F., Rodríguez L.F., 1994, Nature, 371, 46
Mirabel I.F., Rodríguez L.F., 1998, Nature, 392, 673
Mirabel I.F., Rodríguez L.F., 1999, ARA&A, 37, 409
Mirabel I.F., Sanders D.B., 1987, ApJ, 322, 688
Mirabel I.F., Turner K.C., 1973, A&A, 22, 437
Mirabel I.F., et al., 1985, ApJL, 294, L39
Mirabel I.F., et al., 1986, B. Battrick, E.J. Rolfe, R. Reinhard (Eds.), *ESLAB Symposium on the Exploration of Halley's Comet, ESA Special Publication*, vol. 250
Mirabel I.F., et al., 1988, A&A, 206, L20
Mirabel I.F., et al., 1992b, Nature, 358, 215
Mirabel I.F., et al., 1998a, A&A, 330, L9
Mirabel I.F., et al., 1998b, A&A, 333, L1
Mirabel I.F., et al., 1999, A&A, 341, 667
Mirabel I.F., et al., 2001, Nature, 413, 139
Mirabel I.F., et al., 2011, A&A, 528, A149
Rodríguez L.F., et al., 1989, ApJ, 337, 712
Sanders D.B., Mirabel I.F., 1985, ApJL, 298, L31
Sanders D.B., Mirabel I.F., 1996, ARA&A, 34, 749
van der Laan H., 1966, Nature, 211, 1131
Vorontsov-Velyaminov B.A., 1959, *Atlas and catalog of interacting galaxies (1959)*

Formation of Planetary Systems through population synthesis and N-body simulations

M.P. Ronco[1,2,3]

[1] *Instituto de Astrofísica, Pontificia Universidad Católica de Chile, Núcleo Milenio de Formación Planetaria, Chile*
[2] *Instituto de Astrofísica de La Plata, CONICET–UNLP, Argentina*
[3] *Facultad de Ciencias Astronómicas y Geofísicas, UNLP, Argentina*

Contact / mronco@astro.puc.cl

Resumen / En este documento describimos brevemente los resultados más importantes de los trabajos de investigación realizados durante mi doctorado. Este proyecto estuvo dedicado a estudiar la formación y evolución de diferentes tipos de sistemas planetarios tanto durante la etapa gaseosa de formación, que involucra los primeros millones de años de vida de un sistema planetario, como durante la era post-gas en la cual priman las interacciones gravitatorias entre los proto-planetas y planetesimales que se formaron al final de la primera etapa. Enfocamos nuestro análisis en la formación de planetas rocosos en las regiones internas del disco, particularmente en la zona de habitabilidad, prestando especial atención a los procesos y fuentes de acreción de agua durante toda la evolución de los sistemas. El mayor desafío del proyecto fue estudiar la formación de sistemas planetarios similares al nuestro con el objetivo de obtener un mejor entendimiento sobre cómo pudo haberse formado el Sistema solar, combinando diferentes etapas de la formación planetaria.

Abstract / In this manuscript we briefly describe the main results of the research works developed during my PhD. This project was dedicated to study the formation and evolution of different kinds of planetary systems, both during the gaseous formation stage, which involves the first million years of life of a planetary system, and during the post-gas stage, where the gravitational interactions between the proto-planets and planetesimals formed at the end of the first stage play a key role. We focused our analysis on the formation of rocky planets in the inner regions of the disk, particularly within the habitable zone, paying special attention to the water accretion processes and sources throughout the whole evolution of the planetary systems. The main challenge of this project was to analyze the formation of systems similar to our own with the aim of having a better understanding on how the Solar system could had formed combining different stages of planet formation.

Keywords / planets and satellites: dynamical evolution and stability — planets and satellites: formation — methods: numerical

1. Introduction

Since the discovery of the first extrasolar planet orbiting a solar-type star (Mayor & Queloz, 1995), the study of planetary formation, which until then had been limited only to our Solar system, had a significant growth. Up to March 2019, and with the increase in the quantity and quality of the different missions, 3997 exoplanets of great variety have been discovered orbiting nearby stars (`http://exoplanet.eu/` Schneider et al., 2011). Much of these planets form part of more than 650 multiple planet systems, and in many cases, the central star of these systems is similar to our Sun. However, we have not yet been able to find a Solar System Analog (SSA): a planetary system formed simultaneously by rocky planets in the inner regions of the disk and by at least a gas giant planet similar to Saturn or Jupiter in the outer zones of the disk.

These multiple planetary systems represent the final snapshot of different complex processes and stages of planet formation and have triggered theoretical studies about the formation and evolution of different kinds of planetary systems.

For the last ten years different models of planet formation have been developed to study the first stages of the formation of planetary systems when the protoplanetary disk still presents a gaseous component. Population synthesis works, like the pioneer works of Ida & Lin (2004a,b, 2008), have been performed with the aim to reproduce the mass vs. semimajor-axis diagrams of the current sample of exoplanets, and to better understand the main processes of planetary formation (see Benz et al., 2014, for a detailed review and references therein).

On the other hand, several works have studied the formation of terrestrial planets in the post-oligarchic growth regime, via purely N-body calculations, in different dynamical scenarios or within the framework of the formation of our Solar system (Raymond et al., 2004, 2009; O'Brien et al., 2006; Ronco & de Elía, 2014). However, the initial embryo and planetesimal distributions adopted to analyze the late accretion stage of planet formation are typically selected arbitrarily without linking them with previous evolutionary stages.

Raymond et al. (2004, 2006) studied the formation

of terrestrial planets around solar-type stars affected by the perturbational effects of a Jovian planet located in the outer regions of the disk. Then, Mandell et al. (2007) explored the same scenario but including a migrating gas giant planet, and later Fogg & Nelson (2009) showed that this phenomenon does not prevent rocky planet formation in the inner regions. More recently Zain et al. (2018) considered different dynamical environments around solar-type stars, harboring different kinds of planets as the main perturbers of the systems, with the aim of analyzing the rocky planet formation and water delivery within the habitable zone. They found that the formation of water-rich planets in the habitable zone seems to be a common process in all the studied scenarios.

The original goal of this project was to analyse the formation of different kinds of planetary systems during the post-gas phase through the development of pure N-body simulations. However, we were aware that, in order to get more reliable results, we had to link different stages of planetary formation to avoid starting our post-gas phase simulations from arbitrary initial conditions. To do that we improved our model of planet formation including some of the most relevant physical phenomena that take place in the formation of a planetary system during the gaseous phase, and we then performed a planetary population synthesis to determine the main properties of the disks that lead to the formation of SSA. The last stage of this project consisted in the development of N-body simulations of SSA starting from the planetary and planetesimal distributions that resulted at the end of the gaseous phase. During this part of the work we analyzed the formation of rocky planets within the habitable zone and their final water contents. Here we summarize the main results and conclusions of this PhD Thesis, but for the readers interest, the complete manuscript can be found in the Repositorio Institucional de la UNLP* (Spanish version).

2. Results

The first stages of this work were dedicated to study the formation of rocky worlds in planetary systems without gaseous giant planets. Previous observational (Cumming et al., 2008) and theoretical works (Mordasini et al., 2009; Miguel et al., 2011) had suggested that this kind of planetary systems would be common in the Universe. Following these results we first developed N-body simulations to analyze the late accretion stage of rocky planet formation (Ronco & de Elía, 2014) considering arbitrary initial conditions, i.e. arbitrary planetesimal and embryo distributions. Later, we improved this study using a planet formation code (Guilera et al., 2010) able to compute the formation of a planetary system during the gaseous phase and adopted the results of this stage as initial conditions for the late accretion stage N-body simulations (Ronco et al., 2015). The main conclusion of this last work was that, although the final outcomes of our simulations of planet formation were globally similar both using arbitrary or more realistic initial conditions, the use of initial conditions obtained from a model of planet formation resulted in different accretion histories for each of the final rocky planets of our simulations, particularly for those that remained within the habitable zone. Therefore, they presented different characteristics in terms of their final masses and final water contents which could significantly change the resulting planetary systems.

2.1. Population synthesis of planetary systems

Motivated by these results we improved our model of planet formation (Guilera et al., 2010, 2011, 2014), which we now call PlanetaLP, and we applied it to the study of the formation and evolution of SSA with the aim of getting better initial conditions to then study the long term evolution of this kind of systems. Following our definition, an SSA is a planetary system that presents rocky planets in the inner region of the disk and presents at least one gas giant planet, like Jupiter or Saturn, beyond the current Mars location, that is, beyond 1.5 au.

The 1D planet formation code PlanetaLP describes the time evolution of a planetary system during the gaseous phase and incorporates important physical phenomena for the formation of planetary systems. The model presents a protoplanetary disk characterized by two components: a gaseous disk that evolves in time due to an α-viscosity driven accretion (Pringle, 1981; Shakura & Sunyaev, 1973) and due to EUV photoevaporation by the central star (Dullemond et al., 2007; D'Angelo & Marzari, 2012), and a solid component represented by a planetesimal population that suffers accretion, scattering (Alibert et al., 2005) and ejection by the embryos (Ida & Lin, 2004a), and radial drift due to the gas drag. Moreover, PlanetaLP takes into account the evolution of the eccentricities and inclinations of the planetesimals affected by embryo gravitational excitations (Ohtsuki et al., 2002) and by the damping due to the nebular gas drag (Rafikov, 2004; Chambers, 2008).

The gaseous component, characterized by a gas surface density, is given by

$$\Sigma_{\rm g}(R) = \Sigma_{\rm g}^0 \left(\frac{R}{R_{\rm c}}\right)^{-\gamma} e^{-\left(\frac{R}{R_{\rm c}}\right)^{2-\gamma}}, \quad (1)$$

where R is the radial coordinate in the midplane of the disk, $R_{\rm c}$ is a characteristic radius of the disk, γ is the exponent that represents the surface density gradient and $\Sigma_{\rm g}^0$ is a normalization constant. The planetesimal surface density profile is given by

$$\Sigma_{\rm p}(R) = \Sigma_{\rm p}^0 \eta_{\rm ice} \left(\frac{R}{R_{\rm c}}\right)^{-\gamma} e^{-\left(\frac{R}{R_{\rm c}}\right)^{2-\gamma}}, \quad (2)$$

where $\Sigma_{\rm p}^0 \sim 0.01\Sigma_{\rm g}^0$, and $\eta_{\rm ice}$ is a function that represents an increase in the amount of solid material due to the condensation of water beyond the iceline; this represents the location in the disk beyond which water condensates, at ~ 2.7 au (Hayashi, 1981).

In addition, the model presents an embryo population which grows by accretion of planetesimals (Inaba et al., 2001), gas, and due to their fusion taking into account their atmospheres (Inamdar & Schlichting,

*http://sedici.unlp.edu.ar/handle/10915/66476

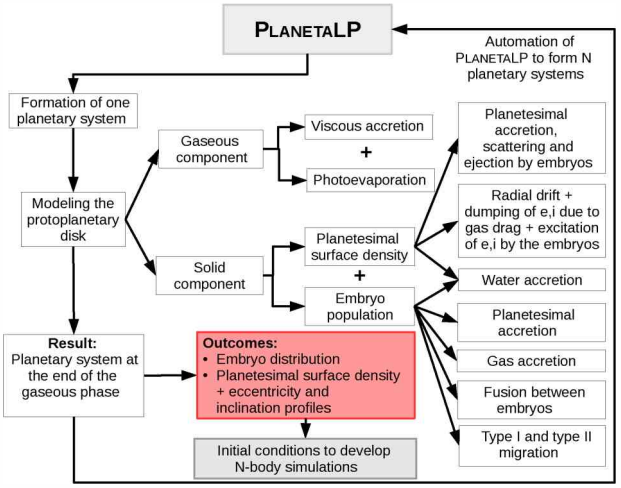

Figure 1: Diagram showing the operation of PLANETALP. The details of the implementation of each physical process can be found in Ronco et al. (2017)

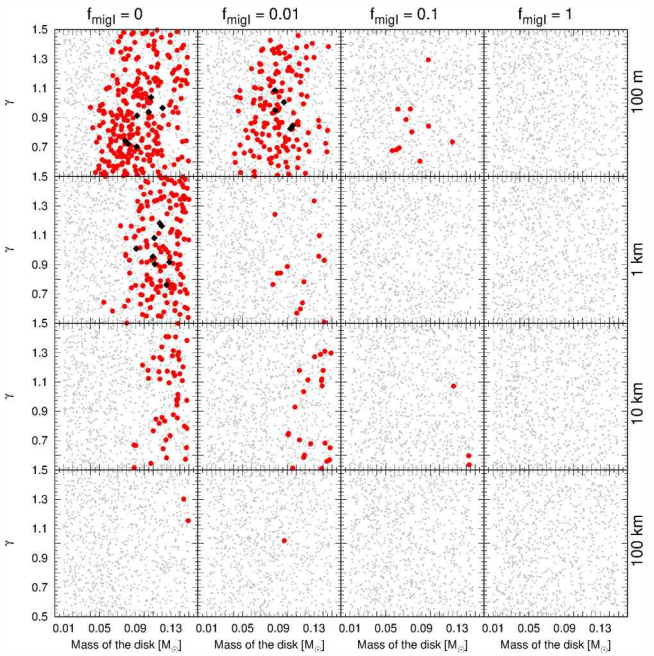

Figure 2: Results of the population synthesis developed with PLANETALP. Each block corresponds to a particular formation scenario with different type I migration rates and different planetesimal sizes, and each point represents a set of disk parameters for a particular planetary system in the $M_{\rm d} - \gamma$ plane. The red points represent sets of disk parameters that formed SSA at the end of the gaseous stage. Grey points represent the rest of the systems that are not SSA. Particularly, the black diamonds are SSAs that present all their disk parameters between $\pm\sigma$, simultaneously.

2015). When these planets are not massive enough to open a gap in the gaseous disk they suffer type I migration, which in idealized vertically isothermal disks like the ones we considered, always produces fast and inward migration rates (Tanaka et al., 2002). When the planets are massive enough to open a clear gap in the gas surface density (Crida et al., 2006) they suffer type II migration (Armitage, 2007). Both, planetesimal and embryo populations, also incorporate a water radial distribution. The initial percentage per unit mass of water in embryos and planetesimals is 0% inside the iceline and a percentage that can randomly vary between 10% and 66% beyond the iceline.

Fig. 1 summarizes the operation of the code. The details of the implementation of all these phenomena can be found in Ronco et al. (2017) and in previous versions of this code (Guilera et al., 2010, 2011, 2014).

With the aim of determining which are the most suitable formation scenarios and disk parameters of SSA, we automated PLANETALP to perform thousands of simulations and to do a population synthesis analysis. It is important to remark that the main goal of this population synthesis, unlike previous works of similar kind (Ida & Lin, 2004a; Mordasini et al., 2009; Alibert et al., 2013), was not to reproduce the mass vs. semimajor-axis diagram of the current exoplanet population, but to see what kind of planetary systems can be formed without following any observable distribution in the disk parameters. Thus, the disk parameters, such as the mass $M_{\rm d}$ and the characteristic radius $R_{\rm c}$ of the disk, the γ exponent of the density profile and the α-viscosity parameter among others, were randomly selected from uniform distributions and for which the values of the ranges were extracted mainly from previous observational works (Andrews et al., 2009, 2010). It is also important to remark that the selected disk parameters for each protoplanetary disk were combined in such a way that the gas disk always dissipated in timescales ranging from 1 to 12 Myr, in agreement with observational works (Pfalzner et al., 2014).

Fig. 2 shows the results of the population synthesis. Each square block represents a different formation scenario with different type I migration rates and different planetesimal sizes. As type I migration can be very fast, following Miguel et al. (2011) we introduced a reduction factor $f_{\rm migI}$ which considers possible mechanisms that can cancel or reduce the planet inward migration 10 and 100 times. The size of the planetesimals is still uncertain within the standard model of core accretion. Thus, as in Fortier et al. (2013), we considered single sizes of planetesimals of 100 m, 1 km, 10 km and 100 km per simulation. Each point in each block represents a planetary system formed from a particular set of disk parameters. The red points represent those systems that became SSA at the end of the gaseous phase. The small grey points represent all the other kinds of formed planetary systems (see Sec. 4.1 in Ronco et al., 2017, for more details). We developed 1000 simulations per each block, representing a total of 16000 simulations, but the SSA only represented a 4.3% of all of them, and the most suitable formation scenarios to get them were those formed from small planetesimals and with low/null type I migration rates. However, we found SSA throughout the whole range of disk parameters except for disk masses smaller than $0.04 M_{\odot}$. Therefore, SSA could only form in relatively massive disks.

An important finding to highlight, that serendipi-

tously arose during the analysis of the population synthesis (Ronco et al., 2017), was that a very small percentage of the total of the performed simulations, indeed only 6 from the total of 16000, presented a gas giant planet in an extended orbit at the end of the gaseous phase, beyond 40 au and up to 100 au. A detailed analysis of these results showed us that these planets were migrating outwards in synchrony with the outer boundary of the gas surface density gap opened by the photoevaporation process. This finding naturally explains the possible formation of gas giant planets in stable wide orbits and was latter studied in detail by Guilera et al. (2017) who computed the vertical structure of the disk and included type I migration rates for non-isothermal disks (Paardekooper et al., 2010, 2011).

Fig. 3 shows an example of the time evolution of one of the modeled planetary systems that ended up being an SSA once the gas disk had dissipated. Panel a) shows the time evolution, represented by the color scale, of the gaseous component as a function of the distance to the central star due to viscous accretion and photoevaporation. Panel b) shows the planetesimal surface density evolution due to radial drift, ejection, scattering and accretion by the embryos. Finally panel c) shows the time evolution of an embryo population distributed between 0.1 au and 30 au in a mass vs. semimajor-axis plane. The embryos grow by accreting gas and planetesimals, and via mergers between them. This planetary system formed from planetesimals of 1 km and in an scenario without type I migration. The disk parameters are $M_{\rm d} = 0.13 M_{\odot}$, $\gamma = 0.9$, $R_{\rm c} = 34$ au, $\alpha = 1.1 \times 10^{-3}$, and the dissipation timescale is $\tau = 6.65$ Myr.

Finally, Fig. 4 shows the configurations of ten different SSA formed from different planetesimal sizes and with different type I migration rates. These planetary configurations present the planet distribution (colored points) and the remnant of the planetesimal surface density after the gas completely dissipated (black curve) which would later be used as initial conditions to analyze the late accretion stage of planet formation. The big black and grey points represent Jupiter-like planets and Saturn analogs, respectively, while the colored points with black borders are Neptune-like planets. The rest of the colored points represent planetary embryos with different masses and different fractions of water by mass. As it can be seen, none of the formed embryos of the inner regions are water-rich at the end of this stage.

2.2. Long term evolution of SSA

The main goal of this part of the project was to analyze the long term evolution of SSAs once the gas had dissipated, through the development of N-body simulations. We focused primarily on the formation of rocky planets and their water contents in the inner regions of the disk, particularly within the habitable zone (HZ) (see Sec. 5.1 in Ronco & de Elía, 2018, for details about the considered limits of this region). We then made use of the results of the population synthesis as the initial conditions for our N-body simulations. Thus, the planetesimal remnant and embryo distributions at the end of the gas stage were our starting points to study the late accretion stage of SSA formation.

As we mentioned in the previous section, SSAs represent only a 4.3% of all the population synthesis simulations, this is only 688 SSAs. However, and due to the high computational cost of the N-body simulations of this kind, it was not viable to develop simulations for all of them. We show in Fig. 4 the most representative SSA for each formation scenario that were chosen to be simulated.

To carry out our simulations we used the hybrid integrator of the MERCURY code which uses a symplectic algorithm for the treatment of the interaction between objects with separations greater than three Hill radii, and a Burlisch–Stoer method for close encounters(Chambers, 1999). This version of the code does not include planet or planetesimal fragmentation, thus, collisions between all the bodies were treated as inelastic mergers, which conserved mass and water contents. Due to the high numerical cost of the N-body simulations we only considered gravitational interactions between planets and between planets and planetesimals, but planetesimals were not self-interacting. The number of planetary embryos depend on the results of the previous formation stage but is in the range of 40 to 90. The available mass in planetesimals also depends on the results of planet formation model, however we always considered 1000 planetesimals per simulation with semimajor-axis selected using an acceptance–rejection method that follows their surface density profile. Planetary embryos and planetesimals present physical densities of 3 gr cm^{-3} and 1.5 gr cm^{-3}, respectively.

We integrated each simulation for 200 Myr assuming that the rocky planets in our Solar system may have formed within this timescale (Touboul et al., 2007; Jacobson et al., 2014) and we considered a 6 day timestep to compute the inner orbit with enough precision. The energy conservation in our simulations was better than one part in 10^3. Embryos and gas giant planets were considered in circular and coplanar orbits. However the orbital eccentricities and inclinations for the planetesimal population were results of the gas-phase evolution. The rest of the orbital parameters, such as the argument of pericentre ω, the longitude of ascending node Ω, and the mean anomaly M, were taken randomly between 0° and 360° for all the solid bodies. We performed at least 10 simulations for each of the formation scenarios of Fig. 4 since the accretion process is very stochastic.

We first analyzed the long term evolution of four reference scenarios, which are the planetary systems formed from planetesimals of 100 km, 10 km, 1 km, and 100 m and without suffering type I migration during the gaseous phase (S_1, S_4, S_6 and S_9 scenarios of Fig. 4). We then developed simulations for the rest of the planetary systems, affected by different type I migration rates, and studying how this phenomenon could change the previous results.

The detailed description of the dynamical evolution of each of the four reference scenarios is not included here but can be found in Sect. 5.2 of Ronco & de Elía (2018). Here we only highlight their most important differences and similarities focusing on the regions where

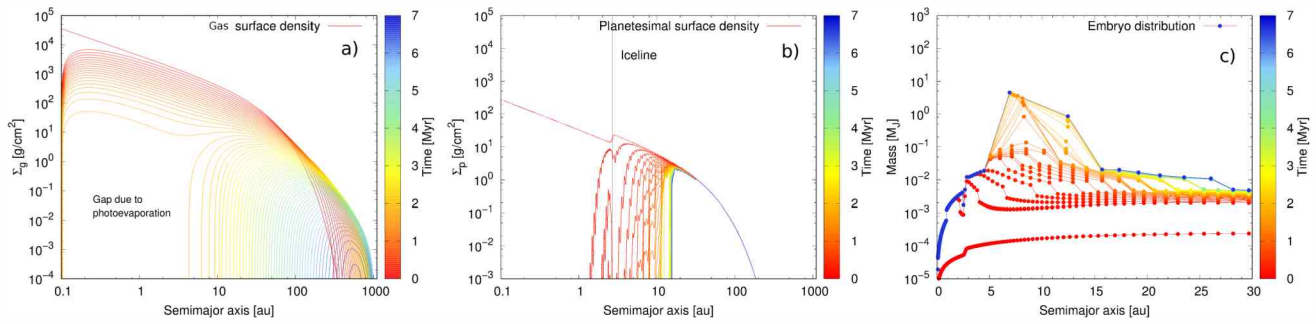

Figure 3: Example of the time evolution of the gas surface density (a), the planetesimal surface density (b) and the embryo distribution (c) of a planetary system similar to our own plotted every 0.1 Myr. The disk parameters for this system are: $M_{\rm d} = 0.13 M_{\odot}$, $\gamma = 0.92$, $R_{\rm c} = 34$ au, and $\alpha = 10^{-3}$. The dissipation timescale for this particular disk is $\tau = 6.65$ Myr.

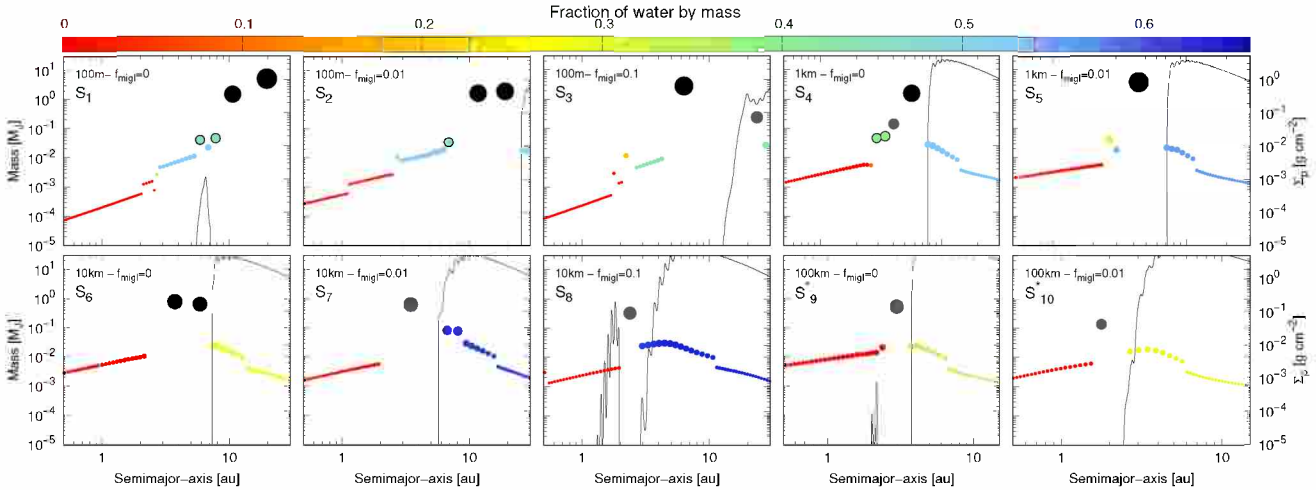

Figure 4: Ten SSA configurations at the end of the gaseous phase obtained with the population synthesis. Each panel shows a mass vs. semimajor-axis vs. planetesimal surface density plane for SSA formed in different formation scenarios. Each colored point represents a planetary embryo, the black and grey big points represent Jupiter and Saturn analogs, respectively, while the colored points with black borders are icy giants, like Neptune. The solid black line in all the planetary systems represents the remnant of planetesimal when the gas is completely dissipated. The colorscale represents the final amounts of water by mass in each planet and the size of each planet is represented in logarithmic-scale.

potentially habitable planets** (PHP) could form.

It can be seen from Fig. 4 that the mass of the gas giant planets of the different scenarios grows as the size of the planetesimals decreases. In those formation scenarios with low-mass gas giants, like S_9, the Saturn-like planet suffered a significant inward embryo-driven migration during the N-body simulations that located this planet at the outer edge of the HZ, preventing PHP from forming. Thus, formation scenarios formed from big planetesimals did not present any particular interest.

The general configuration at the end of the gaseous phase of those scenarios formed with planetesimals of 1 km, 10 km, and 100 km are quite different from the one formed with planetesimals of 100 m. By inspecting and comparing scenarios S_1, S_4, S_6 and S_9 of Fig. 4 it can be seen that the planetesimal population is located inside the giants positions in S_1, instead of outside, the gas giant planets are further away from the central star than in $_4$, S_6 and S_9, and a water-rich embryo population is directly next to the dry one, in the inner region of the disk. These differences conducted to different results in the final configurations of the N-body simulations.

The main similarities between all the formation scenarios were related to the mass remotion (embryos and planetesimals) mechanisms. Mass ejection from the systems was the most efficient remotion process, both for embryos and planetesimals, and to a lesser extent, accretion and collisions with the central star.

The configuration of the inner regions of all the scenarios was in general a quick process that occured within the first 1 Myr of evolution for scenarios of 100 km and 10 km, and within the first 10 Myr and 50 Myr for scenarios of 1 km and 100 m, respectively.

The analysis of the final planetary configurations showed us that the efficiency in the formation of PHPs seems to be higher for planetary systems formed from small planetesimals than from bigger ones, being completely null for planetesimals of 100 km. Fig. 5 shows three snapshots in time for an N-body simulation of

**Our definition of a potentially habitable planet (PHP) is that of a planet that remains within the limits of the HZ. A PHP will be of astrobiological interest if it is capable of harboring a water content superior to that estimated on Earth, which is $\sim 0.1\%$ by mass.

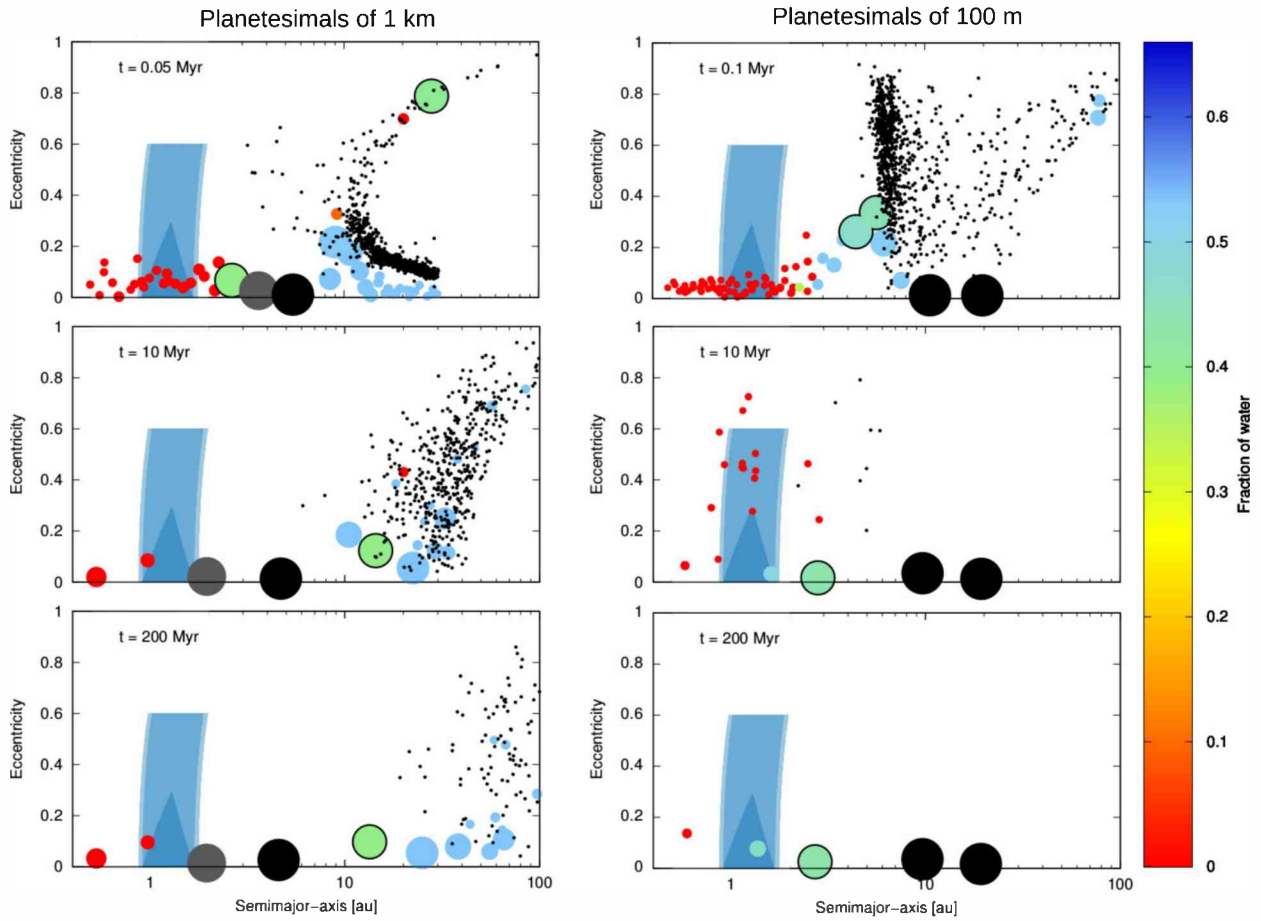

Figure 5: Time evolution of one of the ten developed simulations of planetary configuration S_4 (left) and S_1 (right) from Fig. 4. The shaded areas represent the HZ regions. Planets are plotted as coloured circles, planetesimals as black dots and the giant planets are represented in grey (Saturn-like planets) and black (Jupiter-like planets). The big coloured planets with black borders represent Neptune-like planets. The size of the planets is represented by a lineal relation between the mass and the size, where the size for the smallest embryo is the double of the size of the planetesimals. The giant planets do not follow this relation. The colorscale represents the fraction of water by mass.

scenario S_4 (left) formed from planetesimals of 1 km and for scenario S_1 (right) formed from planetesimals of 100 m. It can be seen how both scenarios formed PHP but with different characteristics. While the masses of those PHPs of S_1 were in the range of the Super-Earths ($2M_\oplus - 8M_\oplus$), the masses of the PHPs in the other scenarios were in the range of the Super and Mega-Earths ($8M_\oplus - 30M_\oplus$) . Besides, scenarios formed from planetesimals of 100 m were the only ones capable of forming PHPs of real interest that presented high water contents. And although considering the four reference scenarios the most common type of PHPs seemed to be the dry ones, since they were formed in three of four scenarios, considering all the developed simulations water-rich PHPs were the most abundant, representing more than 65% of the whole simulated PHP population. Finally, for the N-body simulations of planetary systems that were affected by type I migration rates during the gaseous phase, the general result was that this phenomenon seems to favour the formation of PHPs in planetary systems formed from small planetesimals, but avoids their formation in systems formed from big planetesimals.

The PHPs formed within our simulations were contrasted in mass, and radius, vs. semimajor-axis diagrams with the current discovered PHPs around Solar-type stars (PHLs Exoplanet Catalog of the Planetary Habitability Laboratory - `http://phl.upr.edu`). Fig. 6 shows that there is an overlap of both populations, the detected and the simulated ones. Although this is not a confident comparison since none of these observed PHPs are confirmed part of a planetary system similar to our own, we were able to form PHPs in regions of the diagrams that were already explored and where exoplanets were discovered.

3. Main Conclusions

We improved and automated our new planet formation code PlanetaLP, including several important physical phenomena for the planet formacion process, in order to perform a population synthesis analysis. The primary goal of this study was to find suitable formation scenarios and protoplanetary disk parameters for the for-

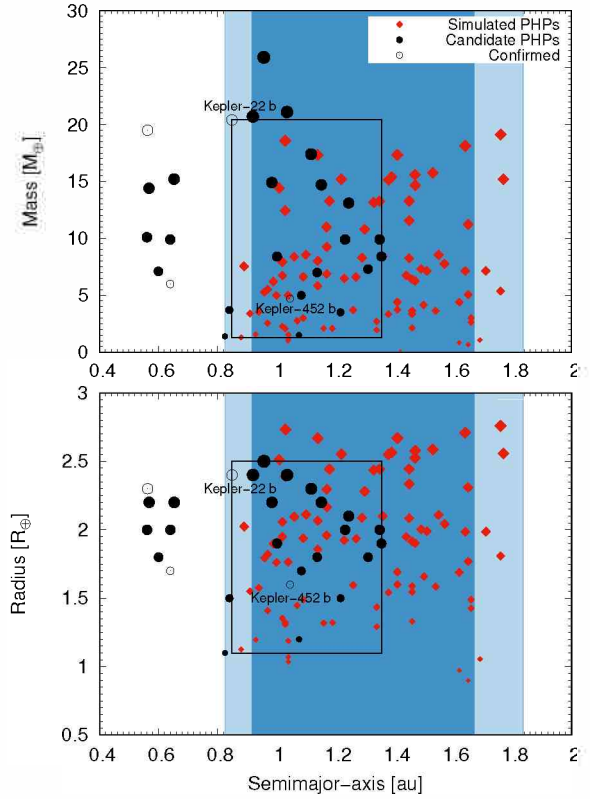

Figure 6: Mass (top) and radius (bottom) vs. semimajor-axis diagrams for the simulated PHPs (red diamonds) and the observed PHPs around solar-type stars (black points). The shaded areas represent the HZ and the black square delimits the region in where we find both, the observed and the simulated planetes. Kepler-452 b and Kepler-22 b are the only two confirmed exoplanets within this region.

mation of SSAs, this is, planetary systems with rocky planets in the inner region of the disk and at least a gas giant planet beyond 1.5 au. Then we used the final SSA planet and planetesimal configurations as initial conditions with the aim of studying the long term evolution of those systems with N-body simulations once the gas of the disk had dissipated.

The population synthesis analysis showed us that the formation of SSA is not common. In fact only 4.3% of the developed simulations resulted in planetary systems with this arquitecture. However we found SSA throughout the whole range of disk parameters considered, except in scenarios with disks less massive than $0.04 M_{\odot}$. The configurations found in these systems were quite diverse. The most representative ones presented between 1 and 3 gaseous giant planets, like Jupiter or Saturn, between 0 and 4 icy giant planets, like Neptune, and between 100 and 200 rocky planets throughout the protoplanetary disk. Finally, the most favorable formation scenarios for SSA were those formed from small planetesimals, with sizes between 100 m and 1 km, and with low and null type I migration rates.

Using the results after the dissipation of the gas disk as starting point, we performed more than 200 N-body simulations to analyze the long term evolution of some of the SSA configurations obtained with the population synthesis. The main goal of this part of the work was to study how do rocky planets form in this kind of systems, and how many of them and with what percentages of water by mass remain within the habitable zone. The reference formation scenarios, formed from planetesimals of 100 m, 1 km, 10 km and 100 km without type I migration showed that the efficiency in the formation of PHP strongly depends on the size of the planetesimals from which they were formed. The SSA formed from small planetesimals were the most efficient ones in the formation of PHP, being completely null for the SSA formed from large planetesimals (100 km).

Another important result was that those SSA that suffered moderate type I migration rates during the gas stage of planet formation showed the same tendency: the efficiency in the formation of PHP is higher for those planetary systems formed from small planetesimals. Two kinds of PHP were formed during our simulations: dry and water-rich. By considering the four reference scenarios, the most common type of PHPs seem to be the dry ones since we formed them in three of four scenarios. However, considering the final number of PHPs formed within all the developed simulations, the result is just the other way around: water-rich are the most common ones since they represent most of the PHPs population (more than 65%).

Acknowledgements: I would first like to thank mi PhD Advisor, Dr. Gonzalo C. de Elía, for his support and guidance during these first years of investigation. I thank the Facultad de Ciencias Astronómicas y Geofísicas where I developed my PhD and also the Consejo Nacional de Investigaciones Científicas y Técnicas de la República Argentina (CONICET) who awarded me with a PhD fellowship. Finally, I would like to thank the Varsavsky Foundation and the Asociación Argentina de Astronomía for the "Carlos M. Varsavsky" award received during the last Second Binational Meeting, and the AAA for the economic assistance that facilitated my participation during the meeting.

References

Alibert Y., et al., 2005, A&A, 434, 343
Alibert Y., et al., 2013, A&A, 558, A109
Andrews S.M., et al., 2009, ApJ, 700, 1502
Andrews S.M., et al., 2010, ApJ, 723, 1241
Armitage P.J., 2007, ApJ, 665, 1381
Benz W., et al., 2014, Protostars and Planets VI, 691–713
Chambers J., 2008, Icarus, 198, 256
Chambers J.E., 1999, MNRAS, 304, 793
Crida A., Morbidelli A., Masset F., 2006, Icarus, 181, 587
Cumming A., et al., 2008, PASP, 120, 531
D'Angelo G., Marzari F., 2012, ApJ, 757, 50
Dullemond C.P., et al., 2007, Protostars and Planets V, 555–572
Fogg M.J., Nelson R.P., 2009, A&A, 498, 575
Fortier A., et al., 2013, A&A, 549, A44
Guilera O.M., Brunini A., Benvenuto O.G., 2010, A&A, 521, A50
Guilera O.M., Miller Bertolami M.M., Ronco M.P., 2017, MNRAS, 471, L16
Guilera O.M., et al., 2011, A&A, 532, A142
Guilera O.M., et al., 2014, A&A, 565, A96
Hayashi C., 1981, Progress of Theoretical Physics Supplement, 70, 35
Ida S., Lin D.N.C., 2004a, ApJ, 604, 388

Ida S., Lin D.N.C., 2004b, ApJ, 616, 567
Ida S., Lin D.N.C., 2008, ApJ, 685, 584-595
Inaba S., et al., 2001, Icarus, 149, 235
Inamdar N.K., Schlichting H.E., 2015, MNRAS, 448, 1751
Jacobson S.A., et al., 2014, Nature, 508, 84
Mandell A.M., Raymond S.N., Sigurdsson S., 2007, ApJ, 660, 823
Mayor M., Queloz D., 1995, Nature, 378, 355
Miguel Y., Guilera O.M., Brunini A., 2011, MNRAS, 417, 314
Mordasini C., et al., 2009, A&A, 501, 1161
O'Brien D.P., Morbidelli A., Levison H.F., 2006, Icarus, 184, 39
Ohtsuki K., Stewart G.R., Ida S., 2002, Icarus, 155, 436
Paardekooper S.J., Baruteau C., Kley W., 2011, MNRAS, 410, 293
Paardekooper S.J., et al., 2010, MNRAS, 401, 1950
Pfalzner S., Steinhausen M., Menten K., 2014, ApJl, 793, L34
Pringle J.E., 1981, ARAA, 19, 137
Rafikov R.R., 2004, AJ, 128, 1348
Raymond S.N., Quinn T., Lunine J.I., 2004, Icarus, 168, 1
Raymond S.N., Quinn T., Lunine J.I., 2006, Icarus, 183, 265
Raymond S.N., et al., 2009, Icarus, 203, 644
Ronco M.P., de Elía G.C., 2014, A&A, 567, A54
Ronco M.P., de Elía G.C., 2018, MNRAS, 479, 5362
Ronco M.P., de Elía G.C., Guilera O.M., 2015, A&A, 584, A47
Ronco M.P., Guilera O.M., de Elía G.C., 2017, MNRAS, 471, 2753
Schneider J., et al., 2011, A&A, 532, A79
Shakura N.I., Sunyaev R.A., 1973, A&A, 24, 337
Tanaka H., Takeuchi T., Ward W.R., 2002, ApJ, 565, 1257
Touboul M., et al., 2007, Nature, 450, 1206
Zain P.S., et al., 2018, A&A, 609, A76

Magnetic energy release and topology in solar active phenomena

C.H. Mandrini[1,2]

[1] *Instituto de Astronomía y Física del Espacio, CONICET–UBA, Argentina*
[2] *Facultad de Ciencias Exactas y Naturales, UBA, Argentina*

Contact / mandrini@iafe.uba.ar

Resumen / La energía liberada durante los eventos activos, que ocurren en la atmósfera solar, está contenida en las corrientes asociadas al campo magnético que ha emergido luego de atravesar la zona convectiva. Una vez que el flujo magnético alcanza la fotósfera, el mismo puede ser forzado aún más a través de los movimientos en esta capa atmosférica inferior. Se acepta, en general, que la reconexión magnética es el mecanismo a través del cual la energía magnética almacenada se transforma en energía cinética de partículas aceleradas y flujos de masa y energía radiativa a lo largo de todo el espectro electromagnético. Aunque este mecanismo es eficiente sólo en escalas espaciales muy pequeñas, el mismo puede implicar una restructuración a gran escala del campo magnético; esta restructuración se puede inferir del análisis combinado de las observaciones, el modelado del campo coronal y el cálculo de su topología. Los eventos resultado de la liberación de energía van desde nanofulguraciones, aún indetectables a la resolución espacial de las observaciones actuales, a poderosas fulguraciones, que pueden ir acompañadas de la expulsión de grandes cantidades de plasma y campo magnético en eventos llamados eyecciones coronales de masa (CMEs), y fenómenos estacionarios como el viento solar lento. En este trabajo discutiremos cómo el cálculo y análisis de la topología del campo magnético, aplicada a la variedad más amplia de configuraciones magnéticas observadas, se puede utilizar para identificar las zonas de liberación de energía y sus características físicas.

Abstract / The energy released during active atmospheric events in the Sun is contained in current-carrying magnetic fields that have emerged after traversing the solar convective zone. Once the magnetic flux reaches the photosphere, it may be further stressed via motions in this lower atmospheric layer. Magnetic field reconnection is thought to be the mechanism through which the stored magnetic energy is transformed into kinetic energy of accelerated particles and mass flows, and radiative energy along the whole electromagnetic spectrum. Though this mechanism is efficient only at very small spatial scales, it may imply a large-scale restructuring of the magnetic field which is inferred from the combined analysis of observations, models of the coronal magnetic field, and computation of its topology. The consequences of energy release include events that range from nano-flares, still below our present observational spatial resolution, to powerful flares that may be accompanied by the ejection of large amounts of plasma and magnetic field in events called coronal mass ejections (CMEs), and stationary phenomena like the slow solar wind. We will discuss how the computation and analysis of the magnetic field topology, applied to the widest variety of observed magnetic configurations, can be used to identify the energy release locations and their physical characteristics.

Keywords / Sun: magnetic field — Sun: magnetic topology — Sun: flares — Sun: coronal mass ejections (CMEs)

1. Introduction

It is generally admitted that the energy released in solar active phenomena is taken from the magnetic field energy where the event occurs. However, a potential magnetic field is a minimum energy state and cannot be the source of the released energy. Therefore, free magnetic energy has to be accumulated in the non-potential part of the field in the form of electric currents flowing in the solar atmosphere. How and where this energy is released may greatly depend on the connectivity of the magnetic field lines in the corona (i.e. its topology). The earliest works connecting the topology of a magnetic field with flux systems separated by magnetic field lines in 2D (and surfaces in 3D) were the ones of Sweet (1958, 1969). A magnetic null point is present at the intersection of these field lines. Sweet suggested that a current, when formed, should be centered at this intersection. In 3D surfaces, separatrices are present instead of field lines and the intersection of these surfaces is a line, called the separator. It was shown that the separator is a singular line where the frozen-in condition does not apply and electric currents could flow (see works as early as Syrovatskii, 1981). Separatrix surfaces divide the magnetic volume into topologically distinct regions, in the sense that any of them contains only field lines that start at a particular magnetic flux source and end up at another particular flux source (see Figure 1 in Mandrini et al., 1991). When magnetic reconnection occurs, magnetic flux is transferred from one region to another and magnetic energy can be released (see e.g. the review work by Longcope, 2005, and references therein). A large number of articles invoked this 3D topological scenario to interpret solar flares and

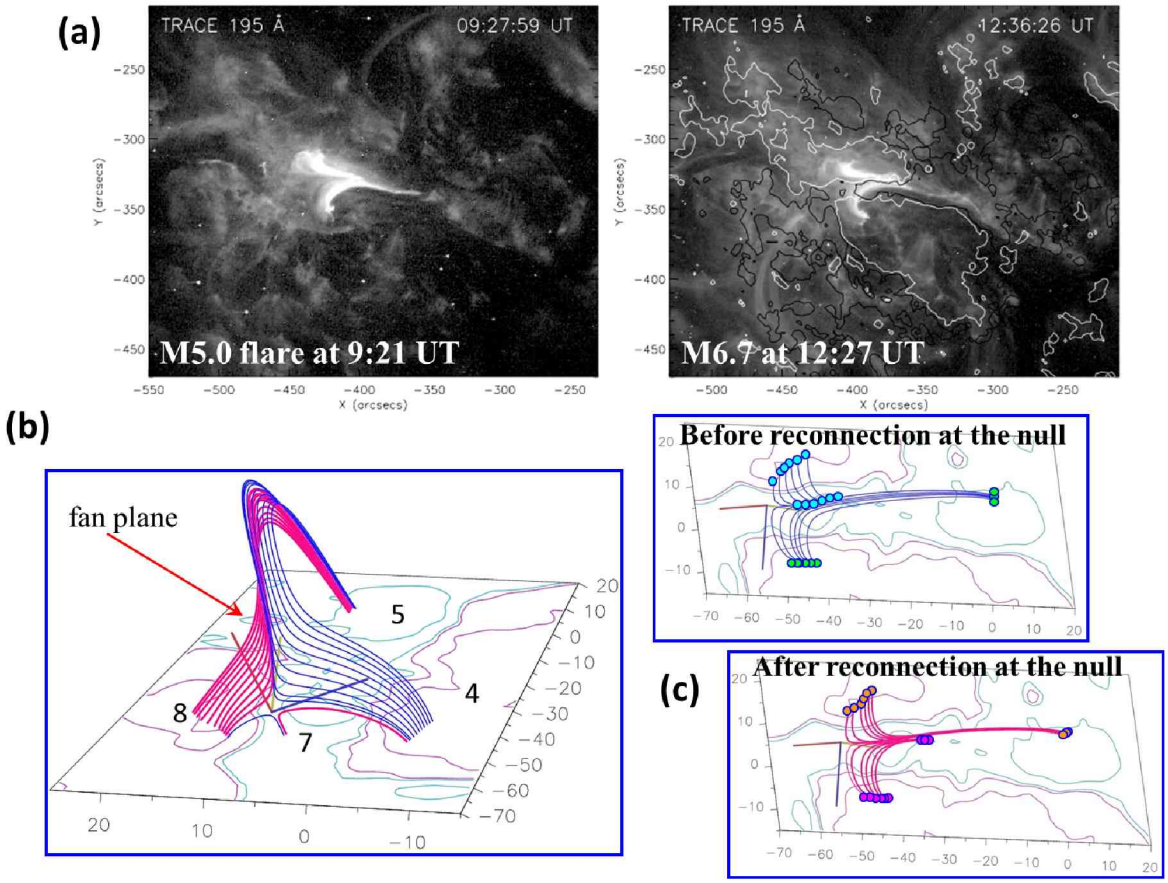

Figure 1: (a) Transition Region and Coronal Explorer (TRACE) images in 195 Å showing the flare loop brightenings at coronal level of both M-class flares. A Michelson Doppler Imager (MDI) magnetogram (at 12:47 UT) isocontour of ±100 G (white/black continuous line corresponds to the positive/negative field value) has been overlaid on the image on the right as reference. The field of view is the same in both panels. (b) Shows the magnetic null point location in AR 10486 coronal field from a 3D perspective. The null point height is 3.1 Mm. Field lines in this panel have been computed starting integration at finite distances from the null. A set of blue continuous lines follow roughly the direction of the eigenvector with the lowest eigenvalue in the fan plane. These have footpoints at polarities 4 and 5. These field lines could reconnect at the null with field lines linking 7 to 8, these are represented by only one short blue continuous line. After reconnection, we would have the set of red continuous field lines that have footpoints at 8 and 5 and those that connect 4 and 7 (the latest are represented by only one short continuous field line). The three eigenvectors of the Jacobian field matrix have been depicted at the null location. (c) Coronal magnetic field model of AR 10486 close to the magnetic null. The top and bottom panels show the field lines drawn in (b) in the observer's point of view before and after reconnection. Notice that the shape of these lines follows closely the shape of TRACE loops. Several short field lines have been added as compared to those in (b). We also depict the location of the null. In (b) and (c) the negative/positive field isocontours are shown in continuous magenta/cyan thin lines, their values are ±100, 1000 G. The axes are labeled in Mm. Adapted from Luoni et al. (2007).

other energetic phenomena and found that flare brightenings were located at the intersection of separatrices with the photosphere as a proof of magnetic energy release (Gorbachev & Somov, 1988, 1989; Mandrini et al., 1991, 1993; Démoulin et al., 1994; Bagalá et al., 1995; Longcope, 1996). In all these examples, and the ones we will discuss later, magnetic reconnection is understood as a change in magnetic connectivity through which the magnetic configuration goes from a higher energy state to a lower one with the consequent release of energy. The coronal magnetic field was at first modelled using sub-photospheric sources to represent the photospheric flux concentrations (see the review by Mandrini et al., 1997) and later a force-free approach was used, in all cases the observed photospheric magnetic field was taken as boundary condition (see e.g. Mandrini et al., 1996; Démoulin et al., 1997).

Other topological structures, apart from null points, where the magnetic field connectivity is discontinuous are the so-called bald patches or BPs (Titov et al., 1993). At a BP the field lines are curved upward and the horizontal component of the magnetic field crosses the photospheric inversion line (PIL) from the negative to the positive polarity (i.e. in the opposite way when compared to normal portions of the PIL). Bald patches define separatrices where current layers can develop (see e.g. Vekstein et al., 1991; Aly & Amari, 1997). More recently, Pariat et al. (2009) showed that currents

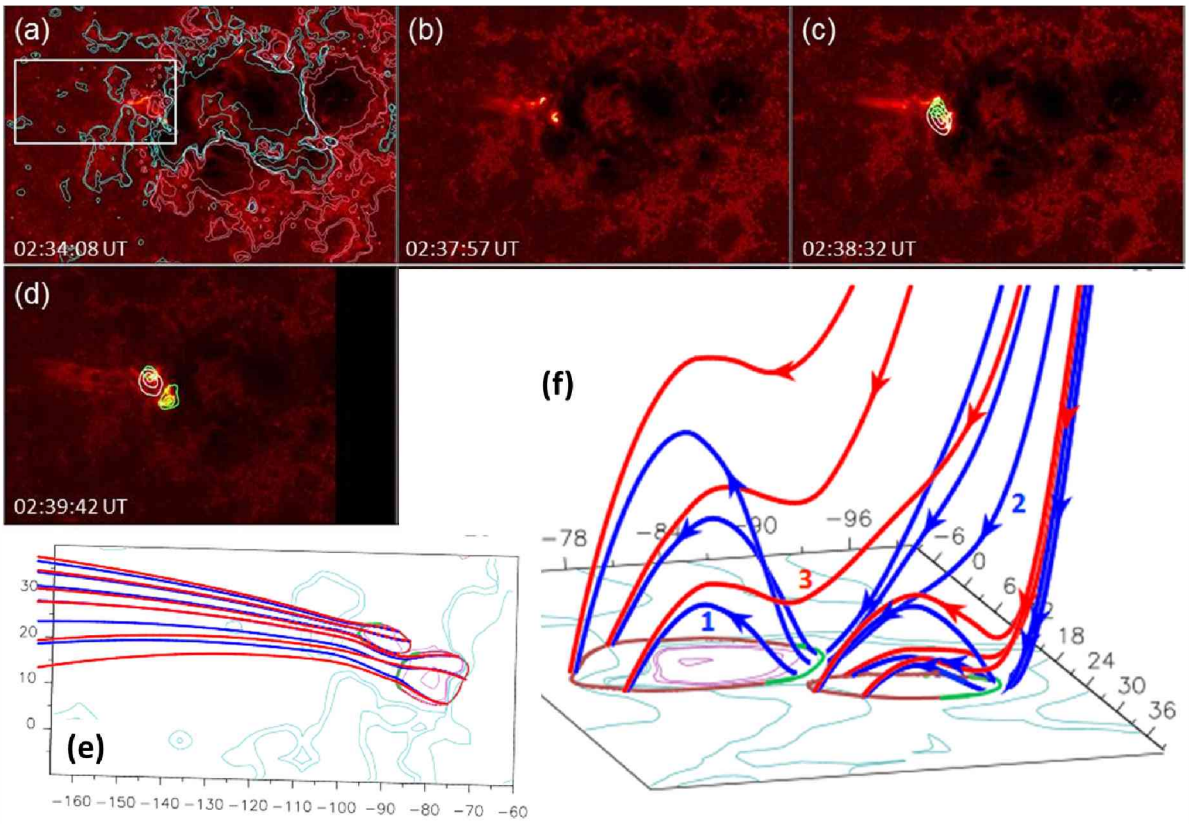

Figure 2: (a, b, c, d) Sequence of TRACE 1700 Å images, showing the blowout jet and the M2.4 flare on 23 October 2003, overlaid by cotemporal Reuven Ramaty High-Energy Solar Spectroscopic Imager (RHESSI) X-ray contours. The yellow/light-green contours correspond to the 10–15/50–100 keV range. MDI isocountors of $\pm 50, 100, 500$ G (magnetogram at 01:35 UT) have been overlaid to panel (a), shown in continuous magenta/cyan line for positive/negative field. The white rectangle in panel (a) indicates the FOV shown in panel (e). (e) Magnetic field model showing the two BPs found in the AR configuration and a set of pre-reconnected and reconnected field lines as inferred when comparing with observations. The blue solid lines would correspond to the situation before reconnection, while the set of red continuous lines issued from the BP separatrices, located at the photospheric level, would correspond to the lines after reconnection. This panel is shown from the observer point of view. (f) This is the same set of field lines as in panel (e) drawn from a different 3D perspective so that the field connectivity becomes clear. We have also added arrows to the computed lines to indicate the direction of the magnetic field and numbers to some of them to explain how reconnection can proceed (1 would reconnect to 2 and give 3). The height of these field lines was multiplied by a factor of four so that they can be clearly distinguished. Notice the agreement between the reconnected field lines and the shape and direction of the jet, as well as the location of flare kernels on the BP separtrices. The conventions for the field isocontours are as in panel (a). The axes are in Mm. BPs are shown as thick green continuous lines, while the magenta thick continuous lines correspond to the photospheric trace of BP separatrices. Adapted from Chandra et al. (2017).

can accumulate at BPs and their separatrices in magnetohydrodynamic (MHD) numercial simulations. Other simulations like those by Archontis & Hood (2013) or Takasao et al. (2015) have shown the development of magnetic reconnection at BPs during the build up of active regions (ARs).

However, after computing the magnetic topology of a large number of magnetic configurations with various boundary magnetic field distributions (from quadrupolar to bipolar ARs with an S-shaped PIL and even with a nearly potential field and an almost straight PIL), it was found that the presence of magnetic nulls or BPs was not a necessary condition for having an active event and that, in some cases, if a null was present, it could be at any place along the separator and not necessarily related to the region where the energy was released (see e.g. Démoulin et al., 1994; Schmieder et al., 2007). These results and theoretical developments aiming to understand magnetic reconnection in 3D led Démoulin et al. (1996) to propose that magnetic reconnection may occur in the absence of null points at quasi-separatix layers (QSLs). These are 3D thin volumes where the coronal field-line connectivity experiences a drastic change. QSLs are preferred sites for the formation of current layers and are therefore locations where magnetic reconnection is prone to occur. Several numerical experiments support this idea (see e.g. Milano et al., 1999; Aulanier et al., 2005; Pariat et al., 2006; Wilmot-Smith et al., 2009; Effenberger et al., 2011; Savcheva et al., 2012; Janvier et al., 2013).

In Sec. 2. we will show examples of observed magnetic configurations in which the magnetic connectivity

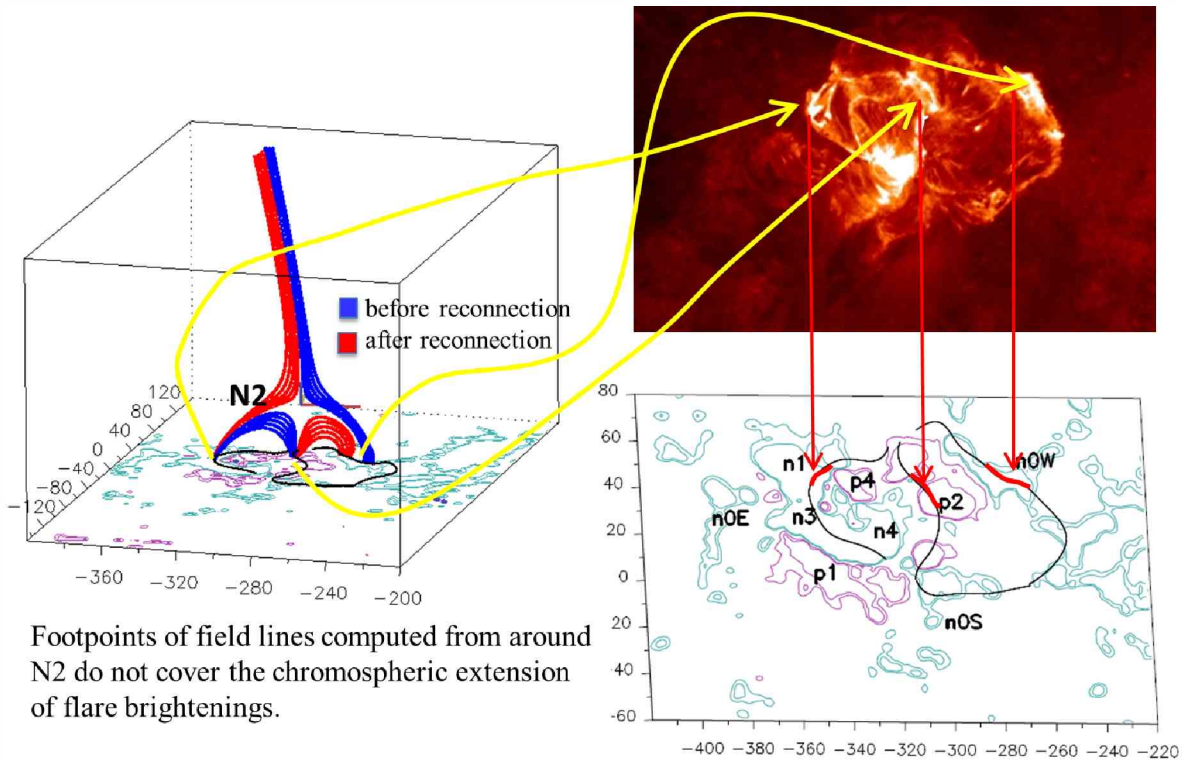

Figure 3: Coronal magnetic-field model in the close vicinity of a magnetic null point, called N2 (height of 14 Mm), in AR 11123. The 3D view to the left shows two sets of field lines representing the pre-reconnected lines (in blue color) and reconnected lines (in red color), as inferred from the observed evolution described in Mandrini et al. (2014b). In this panel and the one on the bottom right, the black continuous lines correspond to the photospheric trace of QSLs computed from a LFFF model. The top panel corresponds to an Atmospheric Imaging Assembly (AIA) image in the 304 Å band showing the brightenings of a confined flare that occurred on 11 November 2010 at 7:42 UT. Following the yellow and red arrows, we can see that the reconnected field lines associated to N2, with photospheric footpoints along the null separatrices, extend only along a short portion of flare brightenings. This implies that reconnection at the null point cannot explain all of the flare extension. The letters and numbers identify the different polarities in the AR. All axes are in Mm and the isocontours of the field correspond to $\pm 50, 100$ G in continuous magenta/cyan style for the positive/negative values (magnetogram at 07:06 UT). See also Fig. 4. Adapted from Mandrini et al. (2014b).

is discontinuous, i.e. active events can be explained by magnetic reconnection in either magnetic null points or BPs and associated separatrices. In Sec. 3. we will show an example of a flare in which a null point was present but only QSLs can explain the full extension of flare brightenings. In Sec. 4. we will discuss how magnetic reconnection proceeds at QSLs using the results of MHD simulations that resemble the photospheric field distribution in ARs and, finally, in Sec. 5. we will summarize the findings in this area of research.

2. Solar phenomena and discontinuous magnetic field connectivity

The field connectivity in the neighbourhood of a null point displays a structure that is characterized by the so-called spines and fans (see e.g. Longcope, 2005; Pontin et al., 2011). From an observational point of view, the origin of several flares has been associated to magnetic reconnection in the fan or spine structure of null points (see e.g. Mandrini et al., 1991, 1993, 2006, 2014b; Parnell et al., 1994; Aulanier et al., 2000; Manoharan & Kundu, 2005; Luoni et al., 2007; Reid et al., 2012). Furthermore, magnetic null points have been found in the global coronal magnetic field computed using potential-field source suface (PFSS) models; reconnection in their vicinity has been proposed as a way to drive the coronal plasma into the slow solar wind (van Driel-Gesztelyi et al., 2012; Mandrini et al., 2014a).

From a mathematical point of view, the neighbourhood of a magnetic null point can be described by the linear term in the local Taylor expansion of the magnetic field (see Démoulin et al., 1994, and references therein). Diagonalisation of the Jacobian field-matrix gives three eigenvectors and the corresponding eigenvalues, which add up to zero to locally satisfy the divergence-free condition on the field. Under coronal conditions, the eigenvalues are real (Lau & Finn, 1990). A positive null point has two positive fan eigenvalues and conversely for a negative null. When a null point is present, the coronal volume is divided into two connectivity domains, which are separated by the surface of the fan. In each of these domains a spine is present, separating again each volume in two others. Fig. 1 shows the magnetic connectivity in the neighborhood of a null point found in AR 10486 by Luoni et al. (2007). Two M-class homologous flares oc-

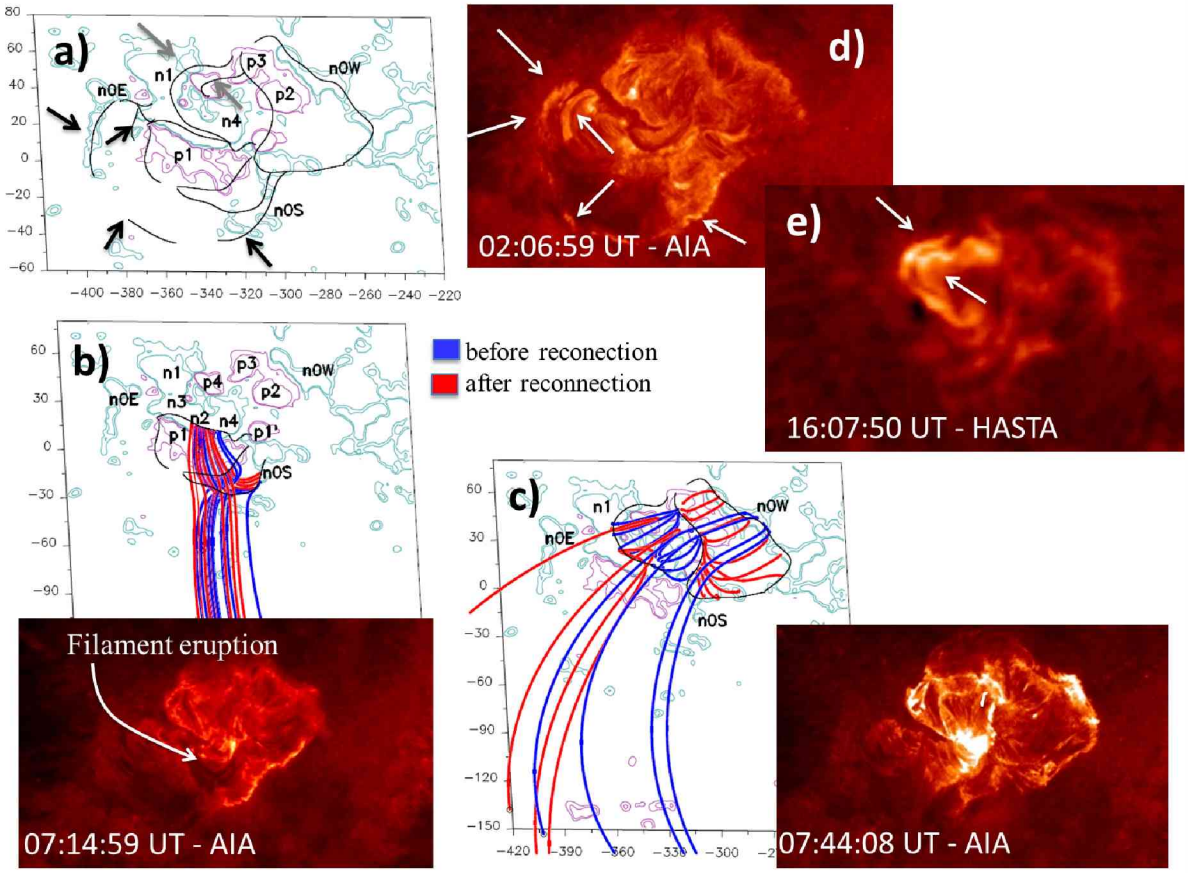

Figure 4: (a) Trace of all the QSLs on the photosphere (solid black lines) superimposed on the contours ($\pm 50, 100$ G, magenta/cyan for positive/negative values) of the magnetic field of AR 11123 observed by the Helioseismic and Magnetic Imager on 11 Novmeber 2010. (b) Subset of QSLs associated with the ejection of a filament at the start of the flare at 07:16 UT. In red and blue, field lines with bases are shown at both sides of QSLs. By reconnection between the two sets of blue lines, the magnetic field above the filament it would be modified allowing its ejection. The red lines correspond to the lines resulting from the reconnection process. An image of AIA is shown superimposed on the field model at 304 Å. (c) Idem panel (a) for the confined flare at 07:42 UT with an image of the same to its bottom right. (d) Brightenings corresponding to the flare at 01:58 TU observed by AIA in the 304 Å band. (e) Brightenings of the flare at 15:53 TU observed with the Hα Solar Telescope for Argentina (HASTA). Notice in all cases the spatial coincidence between the brightenings and the QSLs. All these QSL traces are computed using the same magnetogram (at 07:06 UT), which emphasizes that QSLs indicate the location of flare ribbons once the magnetic configuration is established. The black and grey arrows in (a) indicate which sections of the QSLs are associated with the brightenings in panels (d) and (e). The letters and numbers identify the different polarities in the AR. Adapted from Mandrini (2016). The axes of the model are in Mm.

cured at 09:21 UT and at 12:27 UT on 27 October 2003 in this active region. The different panels in Fig. 1 show the bright EUV loops for each flare and the field lines computed in the close vicinity of the null point derived from a linear force-free field (LFFF) coronal model. Notice that the shape of the field lines match closely the shape of the bright EUV loops as a proof of reconnection occurring at the null point and associated separatices.

Apart from cases in which magnetic nulls are present, separatrices appear in magnetic configurations with BPs. Combining observations and magnetic field modelling, BPs were found asociated to different kinds of events. Aulanier et al. (1998) found a close association between BP separatrices and a small flare. Delannée & Aulanier (1999) studied a flare in a BP configuration, where reconnection could have given place to a CME; while Wang et al. (2002) found elongated bright features linked to BPs before an X-class flare and CME. Fletcher et al. (2001) studied transition region (TR) brightenings related to BPs. Mandrini et al. (2002) presented a non-classical scenario in which interacting BPs were related to the formation of arch-filament systems and a Hα surge. Pariat et al. (2004) discussed the importance of BPs for the emergence of undulatory flux tubes and Ellerman bombs. We show in Fig. 2 the first clear example of a series blowout jets, that evolved into narrow CMEs, occurring in a BP topology in AR 10484 on 21–24 October 2003 (the figure illustrates one event). In order to explain the series of jets, some of which were accompanied by intense flares, Chandra et al. (2017) proposed that magnetic reconnection could occur at the BP separatrices forced by the destabilization of a flux rope underlying them. This process could bring the cool flux-rope material into the reconnected open field lines

driving the series of recurrent blowout jets and accompanying CMEs.

3. Quasi-separatrix layers and active events

Though the presence of null points and BPs can help us interpret where magnetic free energy is released in several solar phenomena, in a large number of cases, as discussed in Sec. 1., more general topological structures are needed. As an example Fig. 3 shows that if we compute field lines starting integration in the neighborhood of a null point, the footpoints of these lines lie at the intersection of the null-point separatices with the photosphere; however, in this case the separatrix traces cover only a portion of flare brightenings implying that most of the elongated flare ribbons cannot be explained by energy release in the null point vicinity.

The original method to determine the location of QSLs was described by Démoulin et al. (1996). QSLs were defined using the norm of the Jacobian matrix of the field-line mapping; the value of the norm depends on the direction chosen to compute the mapping (positive to negative polarities or the reverse). In this case, the norm has different values at the two footpoints of a field line in the photosphere. This ambiguity in the method was solved by Titov et al. (2002), who defined the squashing degree, Q, which is independent of the mapping direction. Q is the norm squared divided by the ratio of the vertical component of the photospheric field at both ends of a field line. In this way, Q could be assigned to have a constant value along each field line.

The computation of QSLs, which in their definition include null points and BPs as exterme cases, helps to understand where flare kernels or other energy release manifestations should be found in the solar atmosphere (see e.g. Démoulin et al., 1997; Bagalá et al., 2000; Mandrini et al., 2006, 2014b, 2015; Cristiani et al., 2007; Savcheva et al., 2015; Janvier et al., 2016; Polito et al., 2017; Joshi et al., 2017; López Fuentes et al., 2018). In some of the just mentioned studies, photospheric currents derived from vector magnetograms where found at QSLs, emphasizing the role of QSLs as places where currents can build up. Fig. 4 shows an example of several flares that can be explained by reconnection at QSLs.

If the observed magnetic field structure is moderately sheared or twisted, the characteristics of QSLs in complex configurations depend strongly on the surface (i.e. photosphere) distribution of the line-of-sight field component and weakly on the details of the coronal field model. This means that QSLs are a good tool to understand where energy release will happen and to learn about the properties of energy release sites (see the reviews by Longcope, 2005; Démoulin, 2006; Mandrini, 2010).

4. Magnetic reconnection at QSLs

The just described examples provide a static view of the relationship between the magnetic field topology and solar active phenomena. We start with a photospheric magnetogram at a given time, in general we choose the closest in time to the event we want to analyze. This magnetogram is taken as boundary condition to compute a coronal magnetic field model that is in general static (a potential, LFFF or non-LFFF model). The next step is to find either magnetic null points, as discussed in Sec. 2., BPs following their definition or, in a more general case, to determine the locations of QSLs. QSLs are computed by integrating an extremely high number of field lines in a very precise way. To decrease the computation time, we use an adaptive mesh to progressively refine the computation of field lines where Q has the highest values (i.e. where the connectivity changes more drastically). We follow this iterative method until the QSL is locally well resolved or when the limit of the integration precision is reached (see more details in Mandrini et al., 2015). We then compare the location of QSLs to flare brightenings and conclude on the role of any of the just mentioned topological structures as the location where reconnection occurs, i.e. we can understand where energy release happens but not how it happens or how the magnetic field evolves as it reconnects at QSLs.

To answer questions such as: are currents formed at QSLs as the magnetic field evolves before reconnetion? or how do the field lines evolve when reconnection occurs at QSLs?, we need to build an MHD model of the coronal field that includes its dynamics. Aulanier et al. (2005) performed zero-β resistive MHD simulations of the development of electric currents in magnetic configurations which were driven by smooth and large-scale sub-Alfvénic boundary motions. The magnetic configurations had QSLs in their potential state. Extended electric currents formed naturally in the configurations as well as narrow current layers at small scales all around the QSLs. For long-time motions, the strongest currents developed where the QSLs were thinnest, the region which would correspond to the generalization of the separator concept. These simulations self-consistently accounted for the long-duration energy storage prior to a flare, followed by the start of reconnection when the currents reached the dissipative scale. These results led the authors to conjecture that physically, current layers must always form at the QSL scale.

As a next step, Aulanier et al. (2006) studied the characteristics of 3D reconnection in thin QSLs. They analyzed magnetic configurations that had been weakly stressed by asymmetric line-tied twisting motions and whose potential fields already had thin QSLs. When the driving was suppressed, magnetic reconnection occurred due to the self-pinching and dissipation of narrow current layers formed previously along the QSLs. They found that a property of this reconnection process was the continuous slippage of magnetic field lines along each other, while they pass through the current layers (see also Janvier et al., 2013). This behavior is contrary to standard null point reconnection, in which field lines clearly reconnect by pairs that abruptly exchange their connectivities. These authors concluded that QSLs can physically behave as real separatrices at MHD time scales, because magnetic lines can change their connectivity on time scales much shorter than the travel-time of Alfvén waves along them.

Several MHD simulations where perfomed to analyze the charateristics of QSLs and the development and evolution of electric currents formed at their locations (see e.g. Janvier et al., 2014; Savcheva et al., 2012; Aulanier et al., 2010; Masson et al., 2009). Concerning observations showing evidence of slip-running reconnection, the first example was presented by Aulanier et al. (2007); while other cases were discussed (see e.g. Sobotka et al., 2016; Li & Zhang, 2015, 2014; Dudik et al., 2014; Chandra et al., 2011; Schmieder et al., 2009). Observation of this process is difficult because high-spatial and temporal resolution data are required .

5. Summary

We have shown that there is a close link between the magnetic field topology, understood in terms of the connectivity of its field lines, and the location where solar active phenomena occur. These locations are either regions where the magnetic field line connectivity is discontinous (null points or BPs) or where it suffers a drastic change (QSLs). In this sense QSLs are a generalization of separatrices. We have also shown that once the photospheric configuration is set and does not evolve abruptly, we can compute QSLs and determine beforehand where we should expect that an event happens.

Furthermore, both observations and MHD simulations indicate that as the magnetic configuration evolves currents are formed at QSLs. In MHD simulations, at some point during the evolution of the modelled configuration, magnetic reconnection and the consequent energy release starts. The magnetic reconnection process is characterized by the slipping of magnetic field lines across QSLs. In this sense, clues have been found of the appearance of brightening displacements along flare ribbons that lie at QSLs. Work in this line continues both observationally and combining observations with numerical simulations.

Acknowledgements: CHM is a member of the Carrera del Investigador Científico (CONICET). The author thanks the Organizing Committees of the Second Binational Meeting AAA-SOCHIAS 2018 for the invitation to give the talk associated to this article and for the support received.

References

Aly J.J., Amari T., 1997, A&A, 319, 699
Archontis V., Hood A.W., 2013, ApJL, 769, L21
Aulanier G., Pariat E., Démoulin P., 2005, A&A, 444, 961
Aulanier G., et al., 1998, SoPh, 183, 369
Aulanier G., et al., 2000, ApJ, 540, 1126
Aulanier G., et al., 2006, SoPh, 238, 347
Aulanier G., et al., 2007, Science, 318, 1588
Aulanier G., et al., 2010, ApJ, 708, 314
Bagalá L.G., et al., 1995, SoPh, 161, 103
Bagalá L.G., et al., 2000, A&A, 363, 779
Chandra R., et al., 2011, SoPh, 269, 83
Chandra R., et al., 2017, A&A, 598, A41
Cristiani G., et al., 2007, SoPh, 240, 271
Delannée C., Aulanier G., 1999, SoPh, 190, 107
Démoulin P., 2006, Adv. Space Res., 37, 1269
Démoulin P., Henoux J.C., Mandrini C.H., 1994, A&A, 285
Démoulin P., et al., 1996, A&A, 308, 643
Démoulin P., et al., 1997, A&A, 325, 305
Dudik J., et al., 2014, ApJ, 784, 144
Effenberger F., et al., 2011, Physics of Plasmas, 18, 032902
Fletcher L., et al., 2001, SoPh, 203, 255
Gorbachev V.S., Somov B.V., 1988, SoPh, 117, 77
Gorbachev V.S., Somov B.V., 1989, Soviet Ast., 33, 57
Janvier M., et al., 2013, A&A, 555, A77
Janvier M., et al., 2014, ApJ, 788, 60
Janvier M., et al., 2016, A&A, 591, A141
Joshi N.C., et al., 2017, ApJ, 845, 26
Lau Y.T., Finn J.M., 1990, ApJ, 350, 672
Li T., Zhang J., 2014, ApJL, 791, L13
Li T., Zhang J., 2015, ApJL, 804, L8
Longcope D.W., 1996, SoPh, 169, 91
Longcope D.W., 2005, Liv. Rev. Solar Phys., 2, 7
López Fuentes M., et al., 2018, SoPh, 293, 166
Luoni M.L., et al., 2007, Adv. Space Res., 39, 1382
Mandrini C.H., 2010, A.G. Kosovichev, A.H. Andrei, J.P. Rozelot (Eds.), *Solar and Stellar Variability: Impact on Earth and Planets*, *IAU Symposium*, vol. 264, 257–266
Mandrini C.H., 2016, BAAA, 58, 256
Mandrini C.H., et al., 1991, A&A, 250, 541
Mandrini C.H., et al., 1993, A&A, 272, 609
Mandrini C.H., et al., 1996, SoPh, 168, 115
Mandrini C.H., et al., 1997, SoPh, 174, 229
Mandrini C.H., et al., 2002, A&A, 391, 317
Mandrini C.H., et al., 2006, SoPh, 238, 293
Mandrini C.H., et al., 2014a, SoPh, 289, 4151
Mandrini C.H., et al., 2014b, SoPh, 289, 2041
Mandrini C.H., et al., 2015, ApJ, 809, 73
Manoharan P.K., Kundu M.R., 2005, Adv. Space Res., 35, 70
Masson S., et al., 2009, ApJ, 700, 559
Milano L.J., et al., 1999, ApJ, 521, 889
Pariat E., Aulanier G., Démoulin P., 2006, D. Barret, F. Casoli, G. Lagache, A. Lecavelier, L. Pagani (Eds.), *SF2A-2006: Semaine de l'Astrophysique Francaise*, 559
Pariat E., Masson S., Aulanier G., 2009, ApJ, 701, 1911
Pariat E., et al., 2004, ApJ, 614, 1099
Parnell C.E., Priest E.R., Golub L., 1994, SoPh, 151, 57
Polito V., et al., 2017, A&A, 601, A39
Pontin D.I., Al-Hachami A.K., Galsgaard K., 2011, A&A, 533, A78
Reid H.A.S., et al., 2012, A&A, 547, A52
Savcheva A., et al., 2012, ApJ, 750, 15
Savcheva A., et al., 2015, ApJ, 810, 96
Schmieder B., et al., 2007, Adv. Space Res., 39, 1840
Schmieder B., et al., 2009, Earth, Planets, and Space, 61, 565
Sobotka M., et al., 2016, A&A, 596, A1
Sweet P.A., 1958, B. Lehnert (Ed.), *Electromagnetic Phenomena in Cosmical Physics*, *IAU Symposium*, vol. 6, 123
Sweet P.A., 1969, ARA&A, 7, 149
Syrovatskii S.I., 1981, ARA&A, 19, 163
Takasao S., et al., 2015, ApJ, 813, 112
Titov V.S., Hornig G., Démoulin P., 2002, Journal of Geophysical Research (Space Physics), 107, 1164
Titov V.S., Priest E.R., Démoulin P., 1993, A&A, 276, 564
van Driel-Gesztelyi L., et al., 2012, SoPh, 281, 237
Vekstein G., Priest E.R., Amari T., 1991, A&A, 243, 492
Wang T., et al., 2002, ApJ, 572, 580
Wilmot-Smith A., Hornig G., Pontin D.I., 2009, ApJ, 696, 1339

Tomography of the Solar Corona with Multiple Instruments: First Steps

D.G. Lloveras[1], A.M. Vásquez[1,2], E. Landi[3] & R.A. Frazin[3]

[1] *Insituto de Astronomía y Física del Espacio, CONICET–UBA, Argentina*
[2] *Departamento de Ciencia y Tecnología, UNTREF, Argentina*
[3] *Department of Climate and Space Sciences and Engineering, University of Michigan, USA*

Contact / dlloveras@iafe.uba.ar

Resumen / La tomografía solar rotacional es una técnica observacional de la corona solar que permite la reconstrucción de la distribución tridimensional (3D) global de algunos de sus parámetros fundamentales, como por ejemplo la densidad electrónica. La tomografía basada en EUV es aplicada regularmente a datos obtenidos con telescopios espaciales, cubriendo típicamente el rango de alturas heliocéntricas $\approx 1.02-1.25$ $R_\odot$. Este rango solapa parcialmente el del campo de visión del coronógrafo de luz blanca K-coronagraph (KCOR), en el High Altitude Observatory (HAO), que cubre el rango $\approx 1.05-3.0$ $R_\odot$. En este trabajo presentamos resultados preliminares de la primer comparación de una reconstrucción de la densidad electrónica coronal obtenida utilizando imágenes EUV con la obtenida utilizando imágenes en luz blanca. Los resultados de la comparación son discutidos en términos de las diversas características de los datos utilizados, así como de los diferentes factores físicos que afectan cada análisis.

Abstract / Solar rotational tomography is an observational technique of the solar corona that allows the reconstruction of the global three-dimensional distribution of some of its fundamental physical parameters, such as electron density. EUV tomography is routinely applied to data provided by spaceborne telescopes, typically covering the range of heliocentric heights $\approx 1.02 - 1.25$ $R_\odot$. This range partially overlaps with the field of view of the white light K-coronagraph (KCOR) instrument, at the High Altitude Observatory (HAO), which covers the range $\approx 1.05 - 3.0$ $R_\odot$. In this work we show preliminary results of the first comparison of tomographic reconstruction of the coronal electron density based on EUV images, with the reconstruction based on white light images. The results are discussed in terms of the diverse characteristics of the used data sets, as well as the different physical factors that affect each analysis.

Keywords / Sun: corona — Sun: fundamental parameters — Sun: UV radiation — Sun: abundances

1. Introduction

Solar rotational tomography (SRT) was initially developed by Altschuler & Perry (1972) to reconstruct the three-dimensional (3D) distribution of the coronal electron density based on white light (WL) data. Frazin & Janzen (2002) developed a modern, robust, regularized, positive method for tomographic inversion of the coronal electron density from WL data, used in this work. A thorough review on WL tomography can be found in those references.

More recently, Frazin et al. (2009) developed the differential emission measure tomography (DEMT) technique. DEMT combines EUV tomography in several pass-bands with local DEM analysis, to reconstruct the 3D distribution of both the coronal electron density and temperature. A recent review by Vásquez (2016) summarizes the existing solar physics literature based on DEMT analysis. More recent DEMT-based studies include that by Lloveras et al. (2017), who carried out a comparative analysis of the coronal structure at the solar minima between solar cycles (SC-)22/23 and 23/24.

DEMT research has been carried out based on data provided by several generations of spaceborne EUV telescopes. The latest one is the Atmospheric Imaging Assembly (*AIA*) instrument, on board the Solar Dynamics Observatory (*SDO*), whose data is used in this work.

While the electron density determined from EUV tomography is dependent on the assumed iron coronal abundance, as well as affected by the so-called coronal filling factor (Frazin et al., 2009), that determined from WL tomography is not (Frazin et al., 2010). So far, no comparison has been carried out between results obtained with both techniques. Here, the tomographic reconstruction of the coronal electron density for a given period is carried out using both methods and their results are compared for the first time.

2. Data and Methodology

Carrington rotation (CR-)2198 (03 December 2017, 14:37 UT – 30 December 2017, 22:25 UT), selected as target for our analysis, is a relatively quiet rotation in the declining activity phase of SC-24. Low latitudes were dominated by the equatorial streamer belt, with a complex of active regions (ARs) located in the longitude range $\approx 80^\circ - 200^\circ$, and high latitudes were dominated by polar coronal holes (CHs).

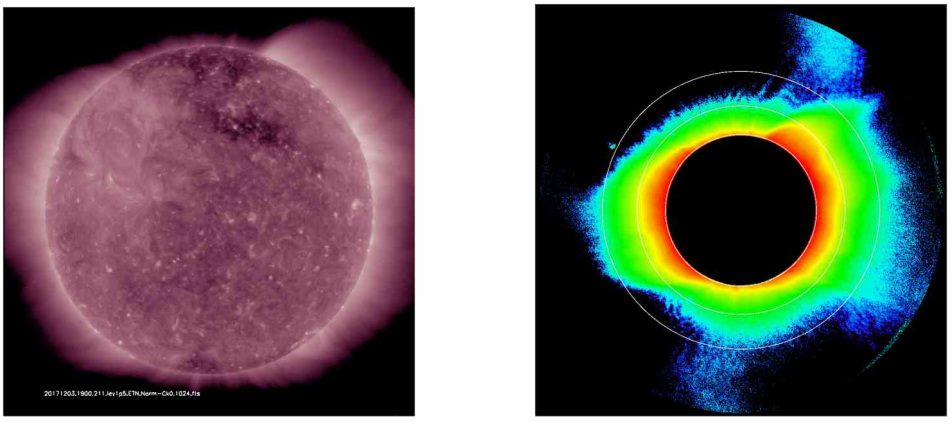

Figure 1: Example of images used for tomographic reconstruction of the coronal electron density of CR-2198 (see text), both corresponding to 2017 December 03 UT 18:00-19:00. Left panel: *SDO/AIA* coronal EUV image in the 211 Å band. Right panel: HAO/KCOR coronal pB image, with white rings indicating heliocentric heights 1.09, 1.50, and 2.0 $R_\odot$.

In this work, tomography is carried out using WL coronagraph data from KCOR, and blocking the disk in the case of EUV images (i.e. only using off-limb data). As a result, in both cases the data required to provide observations of the corona at all Carrington longitudes is gathered over a lapse equal to half solar synodic rotational period. Specifically, KCOR and *AIA* images were obtained for the period December 03 through December 17, 2017. In the case of *AIA*, images for all the coronal bands 171, 193, and 211 Å are obtained every 1 hr, and processed with our own tomographic data preprocessing tools, which make use of the SolarSoft *AIA* software in its latest version. In particular, images are averaged over 6 hr long bins, so that a total of about 55 images are used. In the case of KCOR, one 10-minute average coronal polarized brightness (pB) image for each day, obtained using its best observational window, was requested to the instrument team.

Fig. 1 shows examples of the coronal images used for this work. The left panel shows an *AIA* coronal EUV image taken in its 211 Å band. The right panel shows a KCOR coronal pB WL image. Both images were taken nearly-simultaneously on 2017 December 03 UT 18:00-19:00. This is roughly the beginning of CR-2198, so the longitude of the disk center in these images is $\approx 0^\circ$, so the ARs are not seen and the images are dominated by the quiet Sun streamer belt and the CHs.

Both the WL and EUV tomographic reconstructions were performed on the same resolution, with computational voxels having uniform radial size of 0.01 $R_\odot$ and angular size of 2° in both latitude and longitude. Solutions were computed with a 3D regularization scheme.

3. Results

For the specific data sets of this rotation, the coronal electron density structure was reconstructed in the height range $1.02-1.20$ $R_\odot$ from EUV tomography, and $1.09-1.80$ $R_\odot$ from WL tomography. Fig. 2 shows Carrington maps of both reconstructions at heliocentric height $r = 1.105$ $R_\odot$. The white boxes in the maps indicate two regions selected for quantitative comparison. The region in the Southern hemisphere is a high-density quiet Sun region within the equatorial streamer belt. The region in the Northern hemisphere is a lower density region at subpolar latitudes in the northern CH.

The quantitative comparison of the electron density determined from both tomographic analyses at each computational voxel of the two selected regions is shown in Fig. 3. For each region, the top panel shows the histogram of the ratio of electron density as determined from both tomographic analyses for all voxels within the common reconstructed coronal volume, i.e. in the range of heights $1.09-1.20$ $R_\odot$. For each region, the bottom panel shows the average radial dependence of the electron density determined from both analyses.

4. Discussion and Future Work

The coronal electron density determined from WL tomography is systematically larger than that determined from EUV tomography. The characteristic (median) WL-to-EUV electron density ratio is ~ 2.0 in the quiet Sun streamer belt region and ~ 1.6 in the subpolar region within the CH.

This difference may be partly explained by the fact that the KCOR data is affected by the sky brightness which was not subtracted in the specific data set used for this first work, as the required procedures were being revised by the HAO team at the moment of this analysis. Once a sky subtraction is applied, the electron density as determined from WL tomography will systematically decrease. If systematic differences persist, they can be attributable to physical factors.

Regarding EUV emissivity, firstly, its value determined at each voxel from tomographic analysis is proportional to the local mean squared electron density, i.e. $E_{\rm EUV} \propto \langle N_e^2 \rangle = f \, \langle N_e \rangle^2$, where the *filling factor* is here defined as $f \equiv \langle N_e^2 \rangle \, / \, \langle N_e \rangle^2 > 1$. As the WL emission is due to Thompson scattering, its voxel emissivity is proportional to the local average electron density, i.e. $E_{\rm WL} \propto \langle N_e \rangle$. Then: $\langle N_e \rangle_{\rm WL} \, / \, \langle N_e \rangle_{\rm EUV} \propto \sqrt{f}$.

If differences in the results are solely attributed to the filling factor f, then $f \sim 4.0$ in the quiet Sun re-

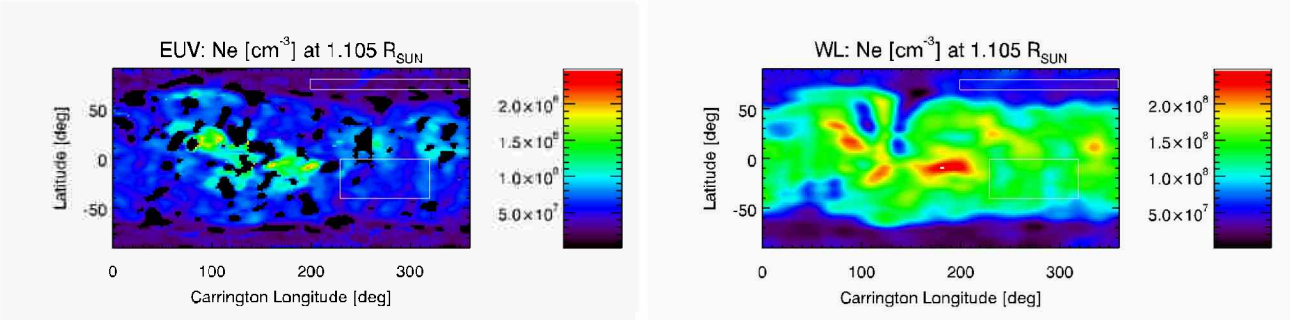

Figure 2: Example results of the tomographic reconstruction of the coronal electron density for CR-2198. Carrington maps of the reconstructed electron density are shown at an heliocentric height of $r = 1.105$ $R_\odot$. Left panel: reconstruction based on EUV data. Right panel: reconstruction based on WL data. The white boxes indicate two ranges of longitudes and latitudes selected for quantitative comparison (see text).

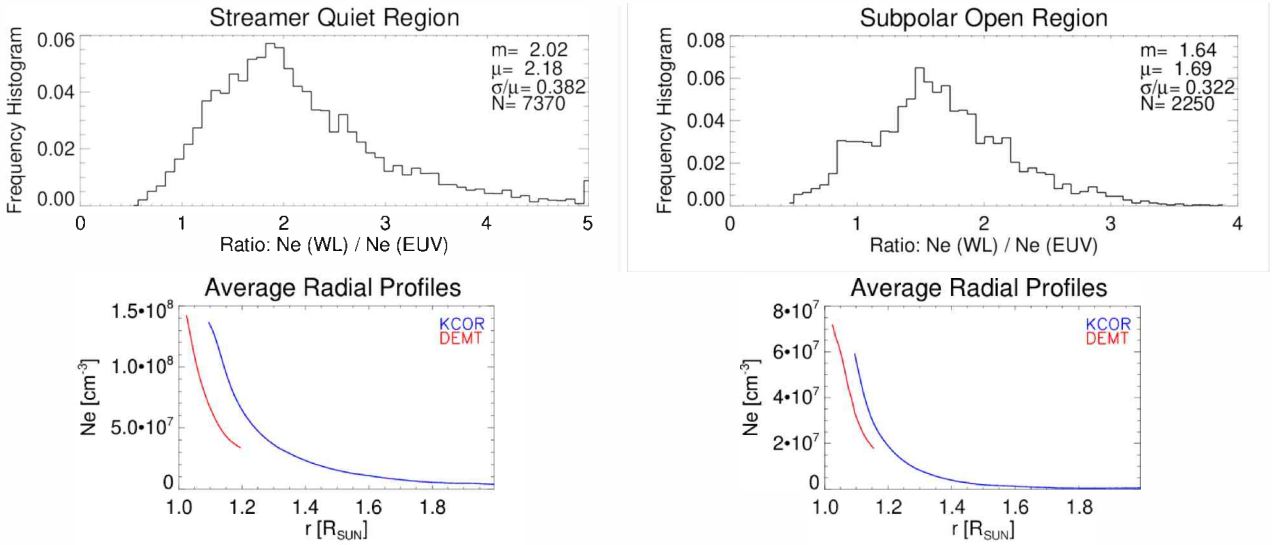

Figure 3: Quantitative comparison between the results of the two tomographic reconstructions of the coronal electron density of CR-2198 in the two selected regions indicated in Fig. 2. Left panels show the results in the quiet Sun region of the southern hemisphere within the streamer belt. Right panels show the results in the subpolar open region within the northern CH. For each region, the top panel shows the histogram of the ratio of the electron density value obtained in each computational voxel from the WL and EUV tomographic analyses. For each region, the bottom panel shows the average radial profile of the electron density based on the EUV (red) and WL (blue) tomographic reconstructions.

gion of the streamer belt, and $f \sim 2.5$ in the subpolar region of the CH. As for any probability distribution, $\sigma^2_{Ne} \equiv \mathrm{Var(N_e)} = \langle \mathrm{N_e^2} \rangle - \langle \mathrm{N_e} \rangle^2 = \langle \mathrm{N_e} \rangle^2 \, (\mathrm{f} - 1)$, then $\sigma_{Ne} / \langle N_e \rangle = \sqrt{f-1}$. With this interpretation, where f is larger (quiet Sun region) the electron density probability distribution has a larger variance.

Secondly, the EUV emissivity determined from tomography is proportional to the assumed iron coronal abundance [Fe]. As a result, the EUV tomography estimate of the average squared electron density scales as $\langle N_e^2 \rangle \propto 1/[\mathrm{Fe}]$ (Frazin et al., 2009).

The work summarized here is a first step towards the development of a new methodology capable of jointly determining the coronal 3D distribution of the electron density and temperature, as well as the filling factor and iron abundance. The technique, dubbed multi-instrument tomography (MIT) and currently under development by us, will involve joint analysis of tomographic products based on data provided by multiple instruments. These include white-light coronagraphs, EUV telescopes, and visible emission line coronagraphs. In particular, MIT will attempt to combine KCOR, *AIA* and data from the (soon to be operative) Upgraded Coronal Multichannel Polarimeter (UCoMP) instrument (Landi et al., 2016).

References

Altschuler M.D., Perry R.M., 1972, SoPh, 23, 410
Frazin R.A., Janzen P., 2002, ApJ, 570, 408
Frazin R.A., Vásquez A.M., Kamalabadi F., 2009, ApJ, 701, 547
Frazin R.A., et al., 2010, SoPh, 265, 19
Landi E., Habbal S.R., Tomczyk S., 2016, Journal of Geophysical Research (Space Physics), 121, 8237
Lloveras D.G., et al., 2017, SoPh, 292, 153
Vásquez A.M., 2016, Advances in Space Research, 57, 1286

Development of pre-processing techniques for the new 30 THz infrared telescope

F. Manini[1,2], C. Francile[1,2], F.M. López[1,3], R.F. Hidalgo Ramirez[4], A.S. Kudaka[4] & J.P. Raulin[4]

[1] *Facultad de Ciencias Exactas, Físicas y Naturales, UNSJ, Argentina.*
[2] *Observatorio Astronómico Félix Aguilar, UNSJ, Argentina*
[3] *Instituto de Ciencias Astronómicas, de la Tierra y del Espacio, CONICET–UNSJ, Argentina.*
[4] *Centro de Rádio Astronomia e Astrofísica Mackenzie, Universidade Presbiteriana Mackenzie, São Pablo, Brasil*

Contact / francoamaninig@gmail.com

Resumen / En el presente trabajo se reporta el desarrollo de técnicas de preprocesamiento de imágenes para el nuevo telescopio solar de 30 THz ubicado en la Estación Astronómica C. Cesco, El Leoncito, San Juan, Argentina. Esto incluye: corrección por campo plano, corrección por oscurecimiento al limbo, centrado y rotación de las imágenes respecto al norte solar, creación del encabezado para cada archivo de imágen bajo estándares Solar SoftWare (SSW), salida en formato estándar FITS y la automatización de los procesos anteriores, con la creación de una interfaz gráfica. Esto será usado para investigar fenómenos solares transitorios en esta banda asociados a regiones activas y estructuras fotosféricas tales como manchas solares y plages.

Abstract / In this work we report on the development of image pre-processing techniques for the new 30 THz solar telescope located in the Estación Astronómica C. Cesco, El Leoncito, San Juan, Argentina. This includes: flat fielding correction, limb darkening correction, centering and north rotation of the images, header creation for each image under Solar SoftWare (SSW) standards, FITS standard format for the output images and automation of the processes, also with the creation of a graphic user interface. These data will be used to study transitory solar phenomena associated with active regions and photospheric structures such as sunspots and plagues.

Keywords / Sun: photosphere — Sun: infrared — Methods: observational

1. Introduction

A new 20 cm infrared telescope was recently installed in the Estación Astronómica C. Cesco for solar photospheric observations at 30 THz (10 μm). The investigation of the Sun in this region of the spectrum is in growing development due to the rise of new technologies in cameras and detectors. This telescope has an infrared camera which is ideal to study sunspots evolution, plages and transient events such as flares. Since this is a new instrument, a pre-processing routine package is not available yet for flat-field correction, limb darkening, image registration (centering and image orientation), and generation of FITS (Flexible Image Transport System) standard format files, with heading under Solar SoftWare (SSW) standards. Because of this, the development of pre-processing techniques for the images acquired with the camera is of fundamental interest to improve the scientific study of the Sun in this region of the spectrum.

Technical details about the instrument can be found in Manini et al. (2017). One of the events that we use in this report occurred on September 4th, 2017, when two active regions were present: AR12673 (north) and AR12674 (south). We will use these images to show how we apply the pre-processing routines and how sunspots are seen in infrared.

2. Pre-processing techniques

Once the raw images have been acquired and saved in Flir Public Format (FPF), which is the proprietary format of the camera, we can start with the following pre-processing steps:

2.1. Flat-field correction

The fact that there are no extended and homogeneous radiation sources similar in intensity to the Sun, and with temperatures like those found on the Solar photosphere (4000-6000 K), requires the implementation of synthetic methods to obtain flat-field images. In this work we applied a process that creates a flat mask for the 30 THz camera using the method developed by Kuhn et al. (1991).

The process to obtain the images begins when the operator of the telescope gets the images which are going to be used to construct the flat image. For this, the operator moves the solar disk over the camera frame in a random manner with the manual control while approximately 200 images are taken. 100 of them will be randomly selected to perform the flat-fielding process. This quantities were determined empirically, given that with a higher or lower amount, the result worsen. The process needs to be done in favorable conditions (no clouds near the Sun, and no solar activity, if possible).

Once the FPF images are saved, the flat creation process begins, with an IDL routine which applies the method developed by Kuhn et al. (1991) described below:

To begin with, the routine creates a circular mask with a radius of 330 pixels that is used to eliminate the edges of the image, i.e leave the solar limb outside (because of its high intensity gradient which introduces spurious values in the algorithm). Then 100 images are randomly selected from the total set. After that, it begins to iterate, reading the offset from the solar disk center respect to the center of the image. The *roberts* filter (Davis, 1975) is used, which is a function that returns the approximate value of the Roberts operator, that serves to highlight the edges.

The routine then finds the pixels that define the solar limb, and generates an array where the limb is defined. Then a circumference is interpolated to the limb position with the *mpfit* package (Markwardt, 2009), this function returns an array with the parameters of the circumference, in our case, the x-y position of the center and the radius. In the set of images, it saves the central sector of the selected image using the mask.

Being the image set defined with its respective centers, the routine creates the flat, using the function *mk kuhn flat* from SSW. It requires the spatially displaced set of images previously found, and a threshold value, over which the image data and the iteration number are considered valid. Empirically, a threshold of 0.1 and an iteration number of 10 are used to get a good results. It was determined that applying the process for a second time to the flat corrected images considerably improves the results, for which the final flat image is obtained as $flat = flat_{step1} * flat_{step2}$. This method assumes that the source (Sun) does not change between frames, thus the signal observed in an image i in a pixel x can be expressed as:

$$D_i(x) = G(x)S_i(x), \tag{1}$$

where $G(x)$ is the detector gain and $S(x)$ the source. A detector gain matrix can be built from misaligned images i,j from the Sun, by minimizing the expression:

$$\sum_{i>j,x} [D_i(x+a_i) - D_j(x+a_j) - G(x+a_i) + G(x+a_j)]^2, \tag{2}$$

with a_i, a_j being the displacement vectors. Kuhn et al. (1991) developed an iterative algorithm to calculate the gain mask of the array as follows:

$$G^{r+1}(x) = K(x)\frac{1}{n(x)}\sum_{i<j}[G^r(x - a_i + a_j) + G^r(x - a_j + a_i)], \tag{3}$$

where

$$K(x) = \frac{1}{n(x)}\sum_{i<j}[D_i(x) - D_j(x - a_i + a_j)] + [D_j(x) - D_i(x - a_j + a_i)]. \tag{4}$$

This way, through successive iterations, and considering the threshold level, a gain mask of sufficient precision is obtained. Then, the images are corrected by dividing each raw image by the created flat. The results of the application of this method are shown in Fig. 1.

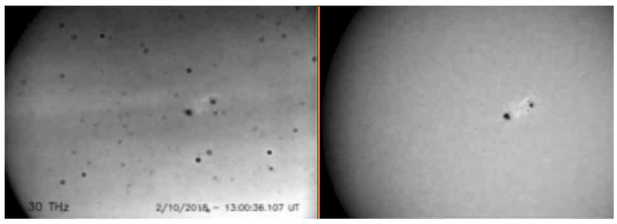

Figure 1: 30 THz image from February 10th, 2018. Left: No flat fielding is applied, tiny black dots are seen on the image, which are produced by dust particles over the camera. Right: Once the flat fielding is applied, the dust is removed and two sunspots are clearly visible.

2.2. Image registration: Centering and orientation of the images

Image registration consists of two steps: one is centering the image, which means to match the center of the Sun with the central pixel of the image frame; the other is rotation, which brings the solar north upwards aligned with the vertical axis of the frame, and the solar west to the rightmost of the frame (Thompson, 2006). This serves as a reference for the final user. The first step in this process is to open the flat corrected image, and through the *sxpar* function, extract from the header the x and y coordinates of the solar rotational axis in the ecliptic coordinates system, the position angle of the solar center, $P0$, and the measured deviation angle of the camera, of -15.574 °, taken from Manini et al. (2017). The original size of the frame is 640x480 pixels^2, and the pixel whose coordinates are (0,0) in IDL, is located on the lower left corner of it. The full solar disk does not fit in in a frame, the solar radius of 15.994 arcmin and a pixel scale of 2.55 arcsec obtained for the observation (Manini et al., 2017) results in a solar radius of 376 pixels.

The process continues by reversing the image horizontally, so as to leave the west to the right of the frame, using the function *reverse*. This is due to the image reflection in a mirror situated in front of the camera. Then, the array containing the frame is enlarged to 1280x960 pixels^2, because when performing the rotation, some portions of the solar disk might be lost. The displacement of the image is done, placing the center of the Sun in the center of the new frame, and then the image is rotated with the function *rot*, which needs the rotation angle (clock-wards), defined as the sum of the deviation angle of the camera and the position angle $P0$, as well as the position of the pixel that defines the center of rotation. The function uses a cubic interpolation approach.

2.3. Limb darkening correction

The method to correct the images by limb darkening was previously published in Manini et al. (2017). The results of the method can be seen in Fig. 3.

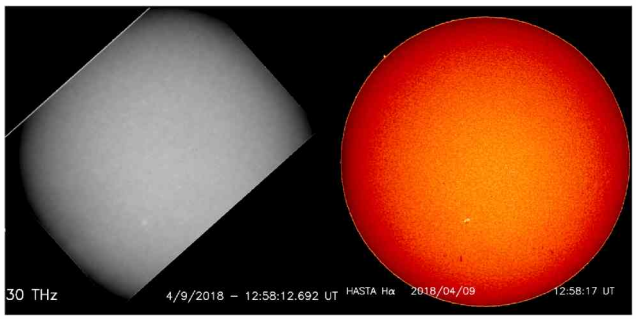

Figure 2: To the left: 30 THz rotated image. To the right: H_α image obtained by the HASTA telescope. Both images are centered, with the solar north upwards, and were taken on April 8th, 2018. In both pictures a small plage is observed.

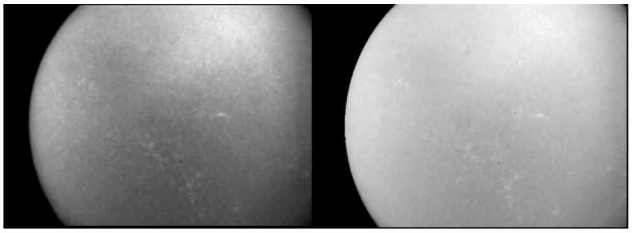

Figure 3: Limb darkening correction. Left: Raw 30 THz image without correction. Right: Same image corrected by limb darkening with the method by Manini et al. (2017). The image was acquired on May 21st, 2017.

2.4. Output in FITS standard format and automation of the processes.

All previous routines were automated in order to simplify the process. An IDL program was created, which selects the FPF images of the day from a specified folder and then performs the flat correction for this set of images, with an option to convert to FITS format. Once the image format is selected, its up to the operator's choice whether to correct the images by limb darkening using the method previously mentioned, and to rotate them. At the same time, a header is created for each image using the routine *mkhdr* where some parameters are added using the *sxaddpar* function, having almost 70 parameters for each image. This was made taking into account the SSW standards (S.L.Freeland, 1999; Hanisch et al., 2001).

3. Results and conclusions

In Fig. 4 the full pre-processing applied to a 30 THz image taken on September 4th, 2017 where two group of sunspots are seen. To compare and verify the accuracy of the results, we show a continuum image from the *Solar Dynamic Observatory (SDO)*. A graphic user interface is being developed, in which all the routines are automated to simplify the user operation.

The proposed preprocessing method has proven to be accurate, as it has also been tested with images taken

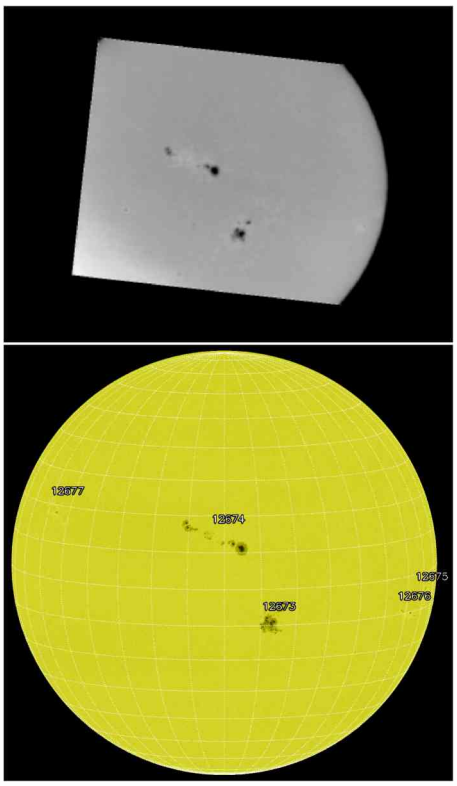

Figure 4: Upper panel: Final image obtained in 10 μm after the application of our pre-processing methodology. Lower panel: A 617,3 nm solar image obtained by *HMI/SDO*. Image from www.solarmonitor.org. Both images correspond to September 4th, 2017.

in different times of the year, and compared with calibrated images from several telescopes. So, it is an easy, fast and practical way for the user to pre-process the images taken with this instrument. Given that the telescope is new, the preprocessed images are now ready to be used to provide new insights for the Sun at this wavelength.

References

Davis L., 1975, Computer Graphics and Image Processing, 4, 248

Hanisch R.J., et al., 2001, Astronomy and Astrophysics, 376, 359

Kuhn J., Lin H., Loranz D., 1991, Publications of the astronomical society of the pacific, 103, 1097

Manini F., et al., 2017, BAAA

Markwardt C., 2009, D. Bohlender, D. Durand, P. Dowler (Eds.), *Astronomical Data Analysis Software and Systems XVIII*, *Astronomical Society of the Pacific Conference Series*, vol. 411, 251

S.L.Freeland, 1999, *SSW Keyword/Tag Definitions*

Thompson W.T., 2006, Astronomy and Astrophysics, 449, 791

Expansión y autosimilitud de eyecciones coronales de masa a partir de observaciones estereoscópicas

H. Cremades[1,2], F.A. Iglesias[1,2], L.A. Merenda[2], F.M. López[3] & I. Cabello[1,2]

[1] *Consejo Nacional de Investigaciones Científicas y Técnicas, Argentina*
[2] *Facultad Regional Mendoza, UTN, Argentina*
[3] *Instituto de Ciencias Astronómicas, de la Tierra y del Espacio, CONICET–UNSJ, Argentina*

Contacto / hebe.cremades@frm.utn.edu.ar

Resumen / Las eyecciones coronales de masa (ECMs) constituyen los eventos dinámicos más espectaculares del sistema solar, y juegan un papel fundamental en la determinación de las condiciones de la meteorología del espacio. Dado que la ocurrencia de una ECM ha sido hasta el momento imposible de predecir, en el mejor de los casos es posible elaborar pronósticos que intenten evaluar su grado de impacto. En este respecto, es crucial comprender cómo están organizados los campos magnéticos dentro de ECMs, y cómo evolucionan desde la baja corona hacia la heliósfera. Misiones solares excepcionales, como *STEREO*, *SOHO*, y *SDO*, brindan una oportunidad privilegiada para examinar este aspecto. Las imágenes de vista e*STEREO*scópica provistas por el paquete de instrumentos *STEREO/SECCHI* en combinación con imágenes desde la perspectiva terrestre captadas por *SDO/AIA* y *SOHO*/LASCO permiten el análisis de la evolución de ECMs desde su nacimiento en la baja corona. El grupo de ECMs bajo estudio surge de una combinación apropiada entre los puntos de observación de las naves y la dirección de propagación de ECMs, fundamental para reducir incertidumbres en su modelado. Estos eventos son analizados cuidadosamente en sus comienzos en la baja corona mediante observaciones simultáneas de *STEREO/EUVI* y *SDO/AIA*, y seguidos hasta el final del campo visual de los coronógrafos a bordo de *STEREO* y *SOHO*. En particular, examinamos la evolución de la configuración global de su campo magnético, y cómo se expanden en la dirección de su eje principal de simetría y en aquella perpendicular a éste.

Abstract / Coronal mass ejections (CMEs) constitute the most spectacular dynamic events in the solar system, and are key players in determining space weather conditions. Given that the ocurrence of a CME has so far been impossible to predict, the best attempt at forecasting is then to assess their impact with the best possible accuracy. In this respect, understanding how magnetic fields are organized within CMEs, and how they evolve from the low corona into the heliosphere, is crucial. Exceptional ongoing solar missions, such as *STEREO*, *SOHO*, and *SDO*, provide a unique opportunity to shed light into this aspect. The *STEREO*scopic-view images provided by the *STEREO/SECCHI* suite in combination with images from Earth's perspective recorded by *SDO/AIA* and *SOHO*/LASCO enable the analysis of CME evolution from their birth in the low corona. The set of CMEs uder study arises from an appropriate combination of spacecraft vantage points and CME propagation direction, which is helpful to reduce uncertainties in their forward modeling. These events are carefully analyzed as they originate low in the corona by means of simultaneous observations of *STEREO/EUVI* and *SDO/AIA*, and followed up to the outer fields of view of the *STEREO* and *SOHO* coronagraphs. In particular, we examine the evolution of their global magnetic field configuration, and how CMEs expand along the direction of their main symmetry axis and orthogonal to it.

Keywords / Sun: coronal mass ejections (CMEs) — Sun: corona — Sun: dynamics

1. Introducción

Las eyecciones coronales de masa (ECMs) son descomunales burbujas de plasma y campos magnéticos, eyectadas por el Sol en todas direcciones. Están asociadas a variedad de fenómenos solares como fulguraciones, protuberancias y oscurecimientos coronales, a su vez relacionados a procesos de liberación de energía, aceleración de partículas, y remoción del flujo magnético solar. Por otro lado, su capacidad de interactuar con la magnetósfera terrestre las torna un objeto imperativo de estudio, al poder afectar sistemas de comunicaciones y de navegación, líneas de transmisión de energía eléctrica, satélites, y astronautas en paseos extravehiculares, entre otros.

El estudio de la morfología de ECMs, por su parte, resulta de particular interés por su estrecha relación con la configuración de sus campos magnéticos. De esta manera, tanto la morfología como su evolución, son la llave para comprender procesos físicos involucrados en la iniciación de ECMs, para asociar la configuración de sus regiones fuente con estructuras *in situ*, y para mejorar predicciones de meteorología del espacio en base a configuraciones pre-eruptivas u observaciones coronográficas. Debido a las limitaciones imperantes en la elaboración de pronósticos de meteorología del espacio, el poder conocer cómo están organizados los campos magnéticos asociados a ECMs es clave para determinar si la magnetósfera terrestre será perturbada y en que medida.

El principal instrumento empleado para el análisis

de ECMs es el coronógrafo, capaz de detectar el brillo dispersado por los electrones presentes en la corona solar mediante el efecto de Thomson *scattering*. Desde el descubrimiento de las ECMs, la sensibilidad y resolución espacial y temporal de los coronógrafos ha mejorado formidablemente. A pesar de esto, una restricción fundamental prevalece: al registrar el brillo integrado a lo largo de la línea de la visual, los coronógrafos brindan una proyección bidimensional de una entidad tridimensional, como lo son las ECMs. Fundamentalmente por esta razón, la interpretación de las imágenes coronográficas se ve considerablemente dificultada.

En la actualidad, es mayormente aceptado que las ECMs están organizadas a lo largo de un eje principal de simetría, consistente con una cuerda de flujo magnético retorcida. Evidencia de campos magnéticos helicoidales puede encontrarse en cantidad de imágenes coronográficas de ECMs (Dere et al., 1999; Wood et al., 1999, *v.g.*), mientras que Moran & Davila (2004) encontraron una configuración de arcadas con simetría cilíndrica en base a imágenes polarizadas de la corona solar. Cremades & Bothmer (2004), por su parte, notaron que las vistas de ECMs proyectadas en la corona, dependen de la inclinación y ubicación de las líneas neutras asociadas a sus regiones fuente, también en acuerdo con una configuración de simetría cilíndrica. No fue hasta el trabajo de Cabello et al. (2016b), que pudieron visualizarse simultáneamente la vista axial y lateral de una misma ECM, es decir a lo largo y a lo ancho de su eje principal, como prueba de esta configuración. El concepto de cuerda de flujo también explica la manera en que están organizados los campos magnéticos de estructuras interplanetarias como las nubes magnéticas, contrapartes de ECMs detectadas *in situ* por misiones espaciales.

Como fuera señalado por Mierla et al. (2009), la reconstrucción tridimensional de la morfología de una ECM a partir de imágenes coronográficas disponibles es una tarea intrínsecamente indeterminada, dado que una reconstrucción tomográfica adecuada requiere un gran número de imágenes de una misma ECM desde numerosos puntos de observación diferentes. No obstante, la simultaneidad de misiones espaciales dedicadas al monitoreo solar desde puntos de observación diferentes, se transformó en una realidad con la Misión *STEREO* (Kaiser et al., 2008, Solar-Terrestrial Relations Observatory). Las imágenes de la corona solar tomadas desde sus naves gemelas, sumadas a las de la vista terrestre provistas por la Misión *SOHO* (Domingo et al., 1995, Solar and Heliospheric Observatory), conforman un triplete que resta subjetividad a la reconstrucción tridimensional de la morfología de ECMs, permitiendo la investigación de su evolución desde sus inicios en la baja corona.

2. Datos y métodos

Los datos primordialmente empleados en este análisis consisten en imágenes de la corona solar en luz blanca, provistas por los coronógrafos *COR1* y *COR2* del paquete *SECCHI* (Howard et al., 2008, *Sun–Earth Connection Coronal and Heliospheric Investigation*) a bordo de las naves de la misión *STEREO*. La tercer vista de la corona en luz blanca es provista por el coronógrafo *LASCO C2* (Brueckner et al., 1995, *Large Angle Spectroscopic Coronagraph*) a bordo de la legendaria Misión *SOHO*, que brinda la perspectiva terrestre. Los instantes iniciales de la evolución de las ECMs son investigados mediante datos de la baja corona en el extremo ultravioleta (EUV) registrados por los telescopios *SECCHI/EUVI* de la Misión *STEREO* y *AIA* (Lemen et al., 2012, Atmospheric Imaging Assembly) a bordo de la nave *SDO* (Pesnell et al., 2012, Solary Dynamics Observatory).

Con el objetivo fundamental de caracterizar la morfología de un puñado de ECMs minimizando incertezas por efectos de proyección, los eventos bajo estudio se seleccionaron siguiendo una serie de cuidadosos criterios. De otra manera, tres vistas del mismo evento no serán suficientes para discernir correctamente la orientación de su eje principal de simetría ni la configuración global de su campo magnético. Por un lado, los eventos bajo estudio fueron identificados durante épocas de cuadratura entre naves: noviembre de 2010 – julio de 2011 (cuadratura de las naves de *STEREO* con *SOHO*) y diciembre de 2012 – junio de 2013 (cuadratura entre las dos naves de *STEREO*). Siguiendo el mismo criterio utilizado por Cabello et al. (2016b), además se condicionó la selección a ECMs cuya dirección de propagación fuese aproximadamente ortogonal al plano que contiene las naves (la eclíptica para *STEREO*, *SOHO* y *SDO*), es decir, que se propagasen a altas latitudes. Dado que gran parte de las ECMs se origina en los dos cinturones de actividad situados a ± 20 deg, los eventos polares son relativamente poco frecuentes.

Como primera aproximación para identificar los eventos que cumplieran con estos criterios, se investigó el *SOHO*/LASCO CME Catalog (Yashiro et al., 2004, `http://cdaw.gsfc.nasa.gov/CME_list`) en búsqueda de ECMs con ángulo de posición central (APC) dentro de ± 25 deg con respecto a un APC $= 0$ deg (polo norte) y un APC $= 180$ deg (polo sur), durante los dos períodos de cuadratura mencionados. Se encontraron un total de ~ 35 eventos que cumplieron estos criterios. Sin embargo, como uno de los objetivos fundamentales de este trabajo es estudiar la evolución de ECMs desde sus inicios en la baja corona, aquí sólo se consideran aquellos cuya erupción pudo visualizarse por los instrumentos *STEREO/SECCHI EUVI* y *SDO/AIA*.

Como fuera mencionado en la Sec.1., la configuración general de las ECMs está de acuerdo con la de una cuerda de flujo magnético retorcida de manera helicoidal, con simetría aproximadamente cilíndrica. El modelo GCS propuesto por Thernisien et al. (2009) es una herramienta de modelado capaz de ajustar una figura tridimensional *ad hoc* representativa de una cuerda de flujo a dos o tres vistas estereoscópicas de la corona solar. Este modelo es un avance de la versión desarrollada por Thernisien et al. (2006), en base a los descubrimientos de Cremades & Bothmer (2004). La estructura *ad hoc* que es ajustada a las imágenes consiste de una figura tubular organizada sobre un eje principal, curvada en sus extremos y sostenida por dos conos que representan las "patas", de manera que todo el conjunto se parece a una medialuna de confitería (ver Fig. 1). A

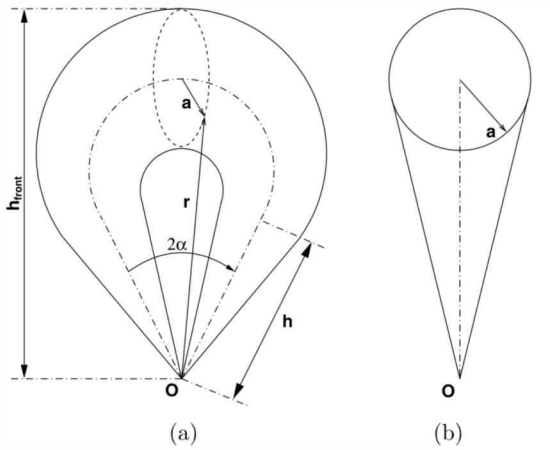

Figura 1: Representación del modelo GCS (a) de frente, mostrando su eje principal con una línea punteada, y (b) de costado. Adaptado de Thernisien et al. (2009).

pesar de ser vastamente usado, la correcta aplicación de este modelo no es trivial, debido a que dos (o tres) vistas estereoscópicas de una misma ECM pueden no ser suficientes si su dirección de propagación yace cerca del plano que contiene a las naves, y diversas soluciones pueden parecer ajustar a la misma ECM.

3. Resultados

Las vistas simultáneas de la ECM del 5 de junio de 2011 se muestran a modo de ejemplo para dos instantes de tiempo en la Fig. 2, uno durante su inicio en la baja corona (panel superior) y otro momentos después, a mayor altura (panel inferior). Las filas primera y tercera muestran a la ECM sin ajustar, mientras que las filas segunda y cuarta muestran en verde la malla de la figura ajustada con el modelo GCS. Este tipo de ajustes se repitió para cada instante de tiempo en que la ECM fuera observada, desde su inicio en la baja corona y durante su paso por el campo visual de los coronógrafos *STEREO*/COR y *SOHO*/LASCO. La evolución de los parámetros ajustados por el modelo GCS, y de otros derivados a partir de éstos, se grafica en la Fig. 3, de arriba a abajo y de izquierda a derecha: altura, ángulo medio entre las "patas", longitud central, latitud central, relación de aspecto, inclinación, ancho angular en la dirección del eje principal, ancho angular en la dirección perpendicular al eje, derivada de las dos anteriores, y diferencia entre las derivadas.

Gráficas como las de la Fig. 3 fueron confeccionadas para siete eventos más a altas latitudes cuya erupción pudo seguirse desde la baja corona. Para comprender cómo se expanden las ECMs en la dirección de su eje principal, y en la perpendicular a éste, resultan de particular interés los valores de AW_L y AW_D. Éstos son representativos del ancho angular en ambas direcciones, y se corresponden con los de las vistas esquematizadas en la Fig. 1. El ancho angular de una ECM en la dirección del eje principal de su cuerda de flujo se determina como $AW_L = 2(\alpha + asin(\kappa))$, mientras que el ancho angular en la dirección perpendicular al eje se calcula

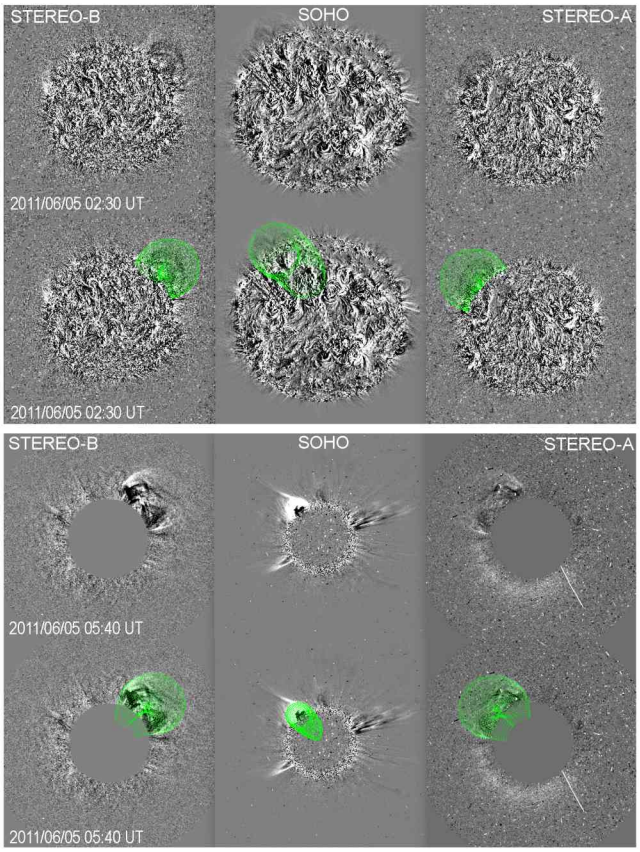

Figura 2: ECM del 5 de junio de 2011 en imágenes diferenciales de la corona solar, desde las perspectivas de *STEREO-B* (columna izquierda), *SOHO* (columna central), y *STEREO-A* (columna derecha). Panel superior: baja corona en el extremo ultravioleta a las 02:30 UT, arriba sin ajustar y abajo con el ajuste del modelo GCS. Panel inferior: corona de luz blanca a las 05:40 UT, arriba sin ajustar y abajo con el ajuste del modelo GCS.

como $AW_D = 2asin(\kappa)$. El ángulo α es el ángulo medio entre el eje de los conos que conforman las "patas" de la estructura, mientras que la relación de aspecto κ está dada por $\kappa = a(r)/r$, con a(r) siendo el radio variable de la sección transversal de la estructura a una distancia r del Sol (Fig. 1).

Una relación entre los anchos angulares AW_L y AW_D de ECMs distinta de la unidad, fue propuesta por Cremades & Bothmer (2005), quienes obtuvieron un valor de 1.6. Sin embargo, esta relación surge de comparar los AW_L y AW_D promedios determinados para diferentes eventos, ya que en ese momento no se contaba con vistas estereoscópicas de la corona solar. Los primeros casos para los que fue posible determinar AW_L/AW_D a partir de la misma ECM, fueron presentados en Cabello et al. (2016b,a). En la Fig. 4 se muestra, para las ECMs bajo estudio, la evolución de esta relación en función de la altura. Puede notarse que esta relación cambia en los primeros instantes de su evolución, y hasta unos ∼3 radios solares. A partir de esta altura, la relación AW_L/AW_D se estabiliza y se alcanza la autosimilitud. Además, el valor en el que se estabiliza esta relación varía significativamente de evento a evento, entre ∼1.2 y 2.5.

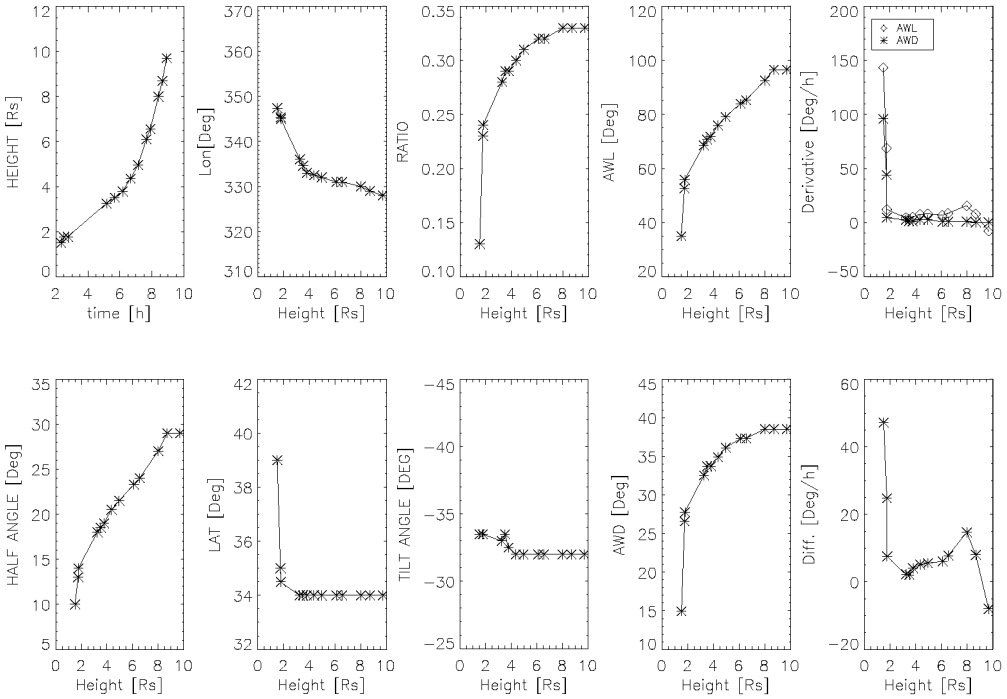

Figura 3: Evolución de los parámetros ajustados mediante el modelo GCS al evento del 5 de junio de 2011.

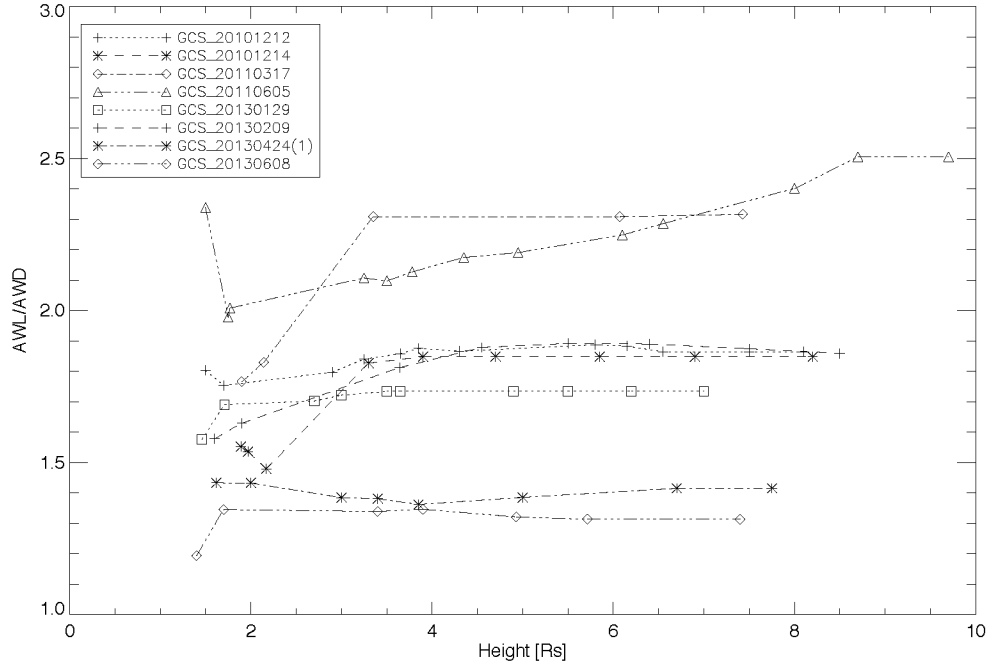

Figura 4: Relación entre los anchos angulares AW_L y AW_D como función de la altura de las ECMs.

En búsqueda de asimetrías entre la manera que se expanden las ECMs a lo largo de su eje y perpendicular a éste, en la Fig. 5 se muestra, en grados por hora, la diferencia entre las derivadas de AW_L y AW_D. Puede notarse que, al ser esta diferencia siempre positiva, todos los eventos se expanden más rápidamente en la dirección de su eje que en la perpendicular a éste. Además, esta asimetría se da mayormente en la baja corona, ya que más allá de ~ 4 radios solares ambas tasas de expansión y su diferencia se vuelven despreciables.

4. Discusión y perspectivas futuras

Las vistas estereoscópicas provistas por naves de monitoreo solar desplazadas con respecto a la línea Sol-Tierra permiten restringir apropiadamente los parámetros mor-

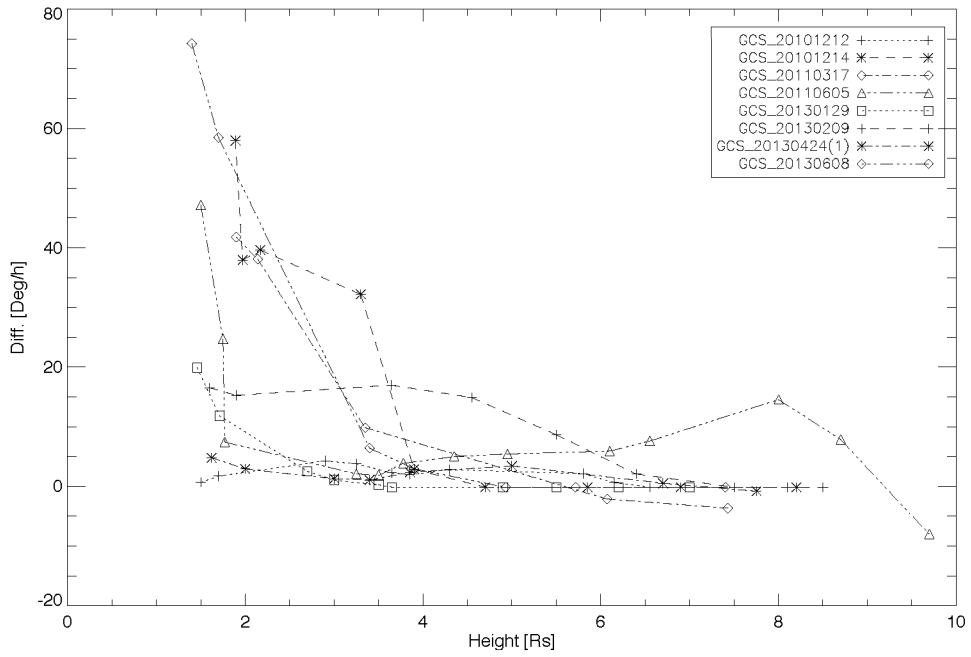

Figura 5: Diferencia entre las derivadas de AW_L y AW_D como función de la altura. Los distintos trazos y puntos representan los diferentes eventos analizados.

fológicos principales de ECMs. De todas maneras, debe tenerse en cuenta que el modelado tridimensional de la morfología de ECMs es un problema para el que existen múltiples soluciones posibles dependiendo de la ubicación de las naves y de la dirección de propagación de las ECMs. En este trabajo se han analizado ocho eventos aproximadamente polares, ocurridos durante épocas de cuadratura, y cuya erupción pudo visualizarse también en la baja corona.

Según los resultados obtenidos, la autosimilitud, un atributo comúnmente considerado inherente a ECMs, no puede garantizarse por debajo de ∼3 radios solares. A partir de esta altura, la relación AW_L/AW_D se estabiliza en valores que van de ∼1.2 hasta 2.5 dependiendo del evento. Además, pudo comprobarse que existe una asimetría considerable entre las velocidades de expansión en la dirección de su eje principal de simetría y en la perpendicular a éste, siendo mucho mayor en la dirección del eje.

Si bien aquí se presentan resultados que surgen del análisis de ocho eventos, en la actualidad se busca ampliar la muestra. Mejorando el contraste de las estructuras en las imágenes de la baja corona, será posible estudiar para mayor cantidad de eventos los instantes iniciales de las erupciones, que como se ha visto son los más importantes en cuanto a cambios de morfología. Misiones fuera de la eclíptica, como Solar Orbiter, permitirán además extender este tipo de análisis a eventos propagándose cerca de este plano, y en particular, a ECMs dirigidas hacia la Tierra.

Agradecimientos: HC agradece a los Comités Organizadores de la Segunda Reunión Binacional entre la Asociación Argentina de Astronomía y la Sociedad Chilena de Astronomía por su invitación a presentar este informe y por la ayuda brindada para asistir a esta reunión. HC e IC son miembros de la Carrera del Investigador Científico (CONICET). FAI y FML son becarios de CONICET, y LAM becario del Consejo Interuniversitario Nacional. Los autores agradecen financiamiento de los proyectos UTN UTI4035TC y UTI4915TC. Los autores reconocen el uso de datos de *STEREO* (NASA), *SDO* (NASA), *SOHO* (ESA/NASA), y Wind (NASA).

Referencias

Brueckner G.E., et al., 1995, SoPh, 162, 357
Cabello I., et al., 2016a, BAAA, 58, 263
Cabello I., et al., 2016b, SoPh, 291, 1799
Cremades H., Bothmer V., 2004, A&A, 422, 307
Cremades H., Bothmer V., 2005, K. Dere, J. Wang, Y. Yan (Eds.), *Coronal and Stellar Mass Ejections*, *IAU Symposium*, vol. 226, 48–54
Dere K.P., et al., 1999, ApJ, 516, 465
Domingo V., Fleck B., Poland A.I., 1995, SoPh, 162, 1
Howard R.A., et al., 2008, SSRv, 136, 67
Kaiser M.L., et al., 2008, SSRv, 136, 5
Lemen J.R., et al., 2012, SoPh, 275, 17
Mierla M., et al., 2009, SoPh, 259, 123
Moran T.G., Davila J.M., 2004, Science, 305, 66
Pesnell W.D., Thompson B.J., Chamberlin P.C., 2012, SoPh, 275, 3
Thernisien A., Vourlidas A., Howard R.A., 2009, SoPh, 256, 111
Thernisien A.F.R., Howard R.A., Vourlidas A., 2006, ApJ, 652, 763
Wood B.E., et al., 1999, ApJ, 512, 484
Yashiro S., et al., 2004, J. Geophys. Res. (Space Physics), 109, A07105

Exoplanetas en torno de estrellas pequeñas y la búsqueda de vida fuera del Sistema Solar

R.F. Díaz[1,2]

[1] *Facultad de Ciencias Exactas y Naturales, UBA, Argentina*
[2] *Instituto de Astronomía y Física del Espacio, CONICET–UBA, Argentina*

Contacto / rodrigo@iafe.uba.ar

Resumen / El campo de exoplanetas está experimentando una transformación. Las detecciones en grandes números y los descubrimientos asombrosos están dejando lugar a una caracterización detallada de los planetas descubiertos. En particular, la caracterización de las atmósferas es un área de gran desarrollo, pero limitada, por ahora, a los planetas gigantes. Sin embargo, se espera poder estudiar las atmósferas en planetas rocosos, parecidos a la Tierra, en el futuro cercano.
En esta contribución señalamos las ventajas de estudiar los planetas en órbita alrededor de estrellas de tipo M de baja masa con respecto a aquellos en órbita alrededor de estrellas más calientes y parecidas al Sol. En particular, discutimos las posibilidades de caracterizar la atmósfera de estos planetas y de buscar indicadores de vida.

Abstract / The field of exoplanet research is changing. Detections in large numbers and amazing discoveries are gradually giving way to the detailed characterisation of these discovered planets. In particular, atmospheric characterisation is an area developing rapidly, but mostly limited up to now to giant planets. It is expected, though, that studying the atmospheres of rocky planets, similar to Earth, will become feasible in the near future. In this contribution we show the advantages of studying planets in orbit around low-mass M-type stars with respect to those orbiting hotter stars similar to the Sun. In particular, we discuss the possibilities of characterising their atmospheres and searching for proxies of life.

Keywords / planets and satellites: terrestrial planets, planets and satellites: detection, planets and satellites: atmospheres, techniques: radial velocities, techniques: photometric

1. Introducción

Suele decirse que la detección de los primeros planetas fuera del Sistema Solar a mediados de la década del noventa (por ejemplo, Mayor & Queloz, 1995; Marcy & Butler, 1996; Butler et al., 1997), inició una revolución en la astronomía y la astrofísica. Cuando se considera la cantidad de modificaciones a las teorías de formación y evolución de los sistemas planetarios que se produjeron desde la fecha de los primeros descubrimientos de esos exoplanetas, y el rápido avance que aun experimenta este campo, la expresión no resulta una exageración. En efecto, el estudio de los planetas extrasolares generó una nueva perspectiva sobre cómo se forman y evolucionan los sistemas planetarios, sobre sus interacciones dinámicas, y sobre su estructura interna y atmósferas (por ejemplo, Mordasini et al., 2009; Chambers, 2009; Beaugé et al., 2012; Dorn et al., 2017).

Es posible identificar dos vías en la exploración de los sistemas extrasolares. Por un lado, se encuentra la empresa de comprender los fenómenos físicos asociados con la formación y evolución de los sistemas planetarios, y de obtener información precisa sobre la tasa de aparición de planetas. Esta via requiere de una gran cantidad de detecciones, que cubra la mayor parte posible del espacio de parámetros (períodos orbitales, excentricidad, etc.). Esta tarea se ha visto fuertemente favorecida por misiones espaciales como *Kepler* (Borucki et al., 2010; Koch et al., 2010), lanzada en 2009, y cuya duración de poco más de cuatro años, su altísima precisión fotométrica, y su observación prácticamente ininterrumpida de más de 150 000 estrellas, entre otros factores, permitieron la detección de miles de objetos de diversas características (por ejemplo, Thompson et al., 2018; Coughlin et al., 2016), algunos de radios extremadamente pequeños (por ejemplo, Borucki et al., 2013; Barclay et al., 2015; Almenara et al., 2018).

Sin embargo, en los últimos años, el campo de exoplanetas se está transformando lentamente. Donde antes el objetivo principal consistía en detectar una gran cantidad de objetos para poder realizar estudios estadísticos, ahora el hincapié está puesto en caracterizar en detalle algunos exoplanetas particularmente favorables. Esta es la segunda vía, que si bien siempre convivió con la primera, está ganando intensidad desde hace unos años. Se dice que la era de descubrimiento está dando lugar a una era de caracterización. Es por esta razón que las misiones espaciales de búsqueda de tránsitos, como TESS (Ricker et al., 2014), lanzada en abril de 2018 y CHEOPS (Broeg et al., 2013), programada para ser lanzada a fines de 2019, se enfocan en detectar planetas cuya caracterización detallada sea posible. Para esto, se concentran en la búsqueda en torno de estrellas brillantes. Algo similar ocurre con los relevos de velocidad radial, cuyo paradigma cambia lentamente de las búsquedas en grandes catálogos limitados en

volumen a las búsquedas enfocadas en estrellas cercanas (Anglada-Escudé et al., 2016; Bonfils et al., 2018). Estos esfuerzos buscan, en particular, caracterizar las atmósferas de planetas rocosos, y más precisamente de aquellos que se encuentren en la zona de habitabilidad (ZH; Kasting et al., 1993; Buccino et al., 2006; Kopparapu et al., 2013). Este camino permitiría, en principio, estudiar la presencia de vida en las superficies de estos exoplanetas.

El objetivo principal de este artículo es señalar las ventajas de las estrellas de baja masa (tipo M o más frías) en esta empresa. Como veremos, los planetas en órbita alrededor de estrellas de baja masa son más fáciles de detectar y las señales que permiten caracterizar sus atmósferas son mayores. Además, más allá de las ventajas teóricas, es sabido que la fracción de estrellas M que albergan planetas rocosos es alta. En la Sec. 2. discutimos las tasas de aparición de planetas en torno de estrellas de baja masa. La Sec. 3. es el centro de la contribución y presenta las diferentes ventajas de estas estrellas. En la Sec. 4. se discuten las dificultades asociadas al bajo brillo intrínseco de las estrellas de baja masa, y en la Sec. 5. se presentan las posibilidades de detectar vida a través del estudio de las atmósferas de los planetas extrasolares.

2. Ocurrencia de planetas

Las detecciones y los datos acumulados durante más de veinte años de investigación en el campo de planetas extrasolares han permitido deducir la tasa de presencia de planetas en torno de estrellas frías de la secuencia principal*, en base a estudios estadísticos. Esto se logró gracias, por un lado, a las observaciones de relevos de velocidad radial llevados a cabo con espectrógrafos como HARPS (Mayor et al., 2009), HIRES (Howard et al., 2010), o SOPHIE (Santerne et al., 2012) y por el otro gracias a la misión *Kepler* (Youdin, 2011; Howard et al., 2012; Fressin et al., 2013; Petigura et al., 2013; Burke et al., 2015, entre muchos otros).

Los relevos de velocidad radial son sensibles a la masa de los objetos detectados (ver, por ejemplo, Díaz, 2017, 2018), y la misión *Kepler*, que utilizó el método de los tránsitos es sensible a los tamaños de los planetas detectados (ver, igualmente, Díaz, 2017). Pero ambas técnicas coinciden: los planetas extrasolares más pequeños y menos masivos son comunes. Mayor et al. (2009) encuentran que más de la mitad de las estrellas de tipo solar albergan al menos un planeta con masa inferior a la masa de Neptuno. Burke et al. (2015) calcularon que existen entre 0.3 y 1.9 planetas por estrella (media 0.77), con radios entre 0.75 $R_\oplus$ y 2.5 $R_\oplus$ en órbitas con períodos inferiores a 300 días. Además, pareciera que la tasa de aparición aumenta para planetas más pequeños, y todavía no está claro si esa tendencia se revierte para planetas con radios inferiores a aproximadamente un radio terrestre o no.

*Existen también trabajos respecto de la tasa de aparición de planetas en torno de estrellas evolucionadas (por ejemplo Reffert et al., 2015), pero se basan en un número mucho menor de detecciones, y por lo tanto sufren de incertezas mucho mayores.

Las estrellas de tipo M no son la excepción. Si bien la tasa de ocurrencia de planetas gigantes alrededor de estas estrellas es menor a la de las estrellas de tipo solar (Bonfils et al., 2013)**, los planetas rocosos son abundantes. Basados en los resultados del relevo de HARPS, Bonfils et al. (2013) reportaron que la tasa de aparición de planetas de tipo super Tierras con períodos orbitales entre 10 y 100 días es mayor al 50 %; Dressing & Charbonneau (2015) estudiaron la fotometría de *Kepler* y encontraron un promedio de 2.5 planetas con radios entre uno y cuatro radios terrestres, por cada estrella M, en órbitas con períodos menores a los 200 días; Gaidos et al. (2016) concluyeron que las estrellas M tienen un promedio de 2.2 planetas por estrella con períodos entre 1.5 y 100 días.

Además, los planetas en la ZH de las estrellas de baja masa también son relativamente comunes. Dressing & Charbonneau (2015) indicaron un promedio de entre 0.16 y 0.24 planetas con el tamaño de la Tierra en la ZH de estrellas M, mientras que Bonfils et al. (2013) reportaron una fracción de $0.41^{+0.54}_{-0.13}$, aunque este número se encuentra probablemente sobreestimado ligeramente.

En conclusión, las observaciones muestran que los planetas rocosos en torno de las estrellas de baja masa son comunes, y que, en particular, una importante fracción de ellos se encuentra en la ZH. Se sabe además que los planetas rocosos en torno de estrellas M forman en general sistemas múltiples (Mayor et al., 2009; Bonfils et al., 2013).

3. Ventajas de las estrellas de tipo M

Como mencionamos en la introducción, la detección de planetas extrasolares de baja masa y radio en torno de estrellas de tipo M es relativamente más sencilla que en torno de estrellas más calientes. En esta sección detallamos la ventaja para dos métodos de detección: los tránsitos y las velocidades radiales. Además argumentamos que los planetas en la ZH de estrellas M son mucho más fáciles de detectar que los planetas que reciben una irradiación equivalente de estrellas de tipo solar.

3.1. Profundidad de los tránsitos

El método de los tránsitos consiste en detectar la disminución periódica del brillo de la estrella cuando el planeta pasa por deltante del disco estelar. Estos tránsitos tienen una profundidad, ΔF, que, despreciando el efecto del oscurecimiento al limbo, resulta aproximadamente igual a

$$\Delta F = \left(\frac{R_p}{R_s}\right)^2 \quad ,$$

donde R_p es el radio del planeta y R_s es el radio de la estrella (Seager & Mallén-Ornelas, 2003). Resulta evidente, entonces, que un planeta dado producirá una disminución de flujo mayor si orbita alrededor de una estrella

**Se cree que esta diferencia está relacionada con la menor masa del disco protoplanetario en torno a las estrellas de menor masa, que no dificultaría la formación de objetos masivos.

Tabla 1: Cociente de áreas para distintas combinaciones de estrellas y planetas. El cociente de áreas es aproximadamente igual a la profundidad de los tránsitos centrales.

		Estrellas		
		Sol (G2)	GJ 411 (M0)	TRAPPIST-1 (M8)
Planeta	Radio	1 $R_\odot$	0.39 $R_\odot$	0.12 $R_\odot$
Tierra	1 $R_\oplus$	8.4×10^{-5}	5.5×10^{-4}	5.8×10^{-3}
Neptuno	3.9 $R_\oplus$	1.3×10^{-3}	8.3×10^{-3}	8.7×10^{-2}
Júpiter	11.2$R_\oplus$	0.01	0.07	0.73

de tipo M, cuyo radio puede ser hasta 10 % del radio solar, que si lo hace en torno de una estrella similar al Sol.

En la Tabla 1 se presentan algunos valores del cociente de tamaños para diferentes estrellas y planetas. Se ve que mientras que el tránsito de un planeta como la Tierra frente a una estrella como el Sol produce una disminución de apenas 80 ppm (partes por millón), un planeta del mismo tamaño en torno de una estrella tipo M8 produce una disminución de casi 0.6 %. Es entonces posible detectar tránsitos de planetas del tamaño de la Tierra sin tener que recurrir a instrumentos en el espacio si la estrella huésped es una estrella pequeña. De hecho, dos de los sistemas más interesantes en términos de caracterización atmosférica (ver más abajo) son TRAPPIST-1, una estrella ultra-fría (tipo espectral M8V), que alberga al menos siete planetas de radios inferiorers a 1.2 $R_\oplus$, detectados inicialmente con un telescopio de 60 cm en el observatorio La Silla (Gillon et al., 2016, 2017), y LHS 1140 (Dittmann et al., 2017), de tipo espectral M4.5V, que alberga un planeta rocoso en la ZH, y que fue detectado por los telescopios Mearth, de tan sólo 40 cm de apertura.

3.2. Señal de velocidad radial

El método de las velocidades radiales también se ve favorecido por las estrellas de baja masa. Esta técnica detecta las variaciones en la velocidad de la estrella, proyectada en la línea de la visual, producidas por un planeta a lo largo de su órbita. Si se supone que la masa del planeta es despreciable frente a la de la estrella, es decir $1 + M_p/M_s \sim 1$, la expresión de la amplitud de la velocidad radial es:

$$K \sim \left(\frac{2\pi G}{P}\right)^{1/3} \frac{1}{\sqrt{1-e^2}} \frac{m_{\rm p} \sin i}{m_{\rm s}^{2/3}} \quad ,$$

donde G es la constante de gravitación universal, e es la excentricidad orbital, P es el período orbital, i es la inclinación del plano orbital con respecto al plano del cielo, y $m_{\rm s}$ and $m_{\rm p}$ son la masa de la estrella y del planeta, respectivamente. Una derivación detallada de esta formula se encuentra en Murray & Dermott (2000), Murray & Correia (2010), y en Díaz (2018).

La amplitud de la señal es entonces aproximadamente proporcional a $m_{\rm s}^{-2/3}$, por lo que estrellas más frías exhibirán mayor variación en su velocidad, para un planeta y una órbita dados. En la tabla 2 presentamos la amplitud de velocidad radial de una serie de combinaciones de planetas y estrellas, para períodos orbitales que corresponden a la ZH de estrellas de distinto tipo espectral. Se puede ver que para un planeta y un periodo dado, la amplitud aumenta para estrellas menos masivas. No sorprende entonces que la mayor parte de los planetas de baja masa que han sido detectados hasta el momento se encuentra en torno de estrellas de tipo M, como puede verse en la Fig. 1. La misma figura deja ver también la dificultad de detectar objetos con amplitudes inferiores a 1 m/s. En este rango de amplitudes, los efectos de la actividad estelar, no completamente comprendidos y de difícil corrección, se vuelven dominantes.

3.3. Zona de habitabilidad

La distancia de la estrella a la que un planeta rocoso puede, en principio, albergar agua líquida en la superficie fue estimada, por primera vez, por Kasting et al. (1993). Con la premisa básica de que la habitabilidad necesita de la presencia de agua líquida, esta zona recibe el nombre de zona de habitabilidad (ZH). Para calcular la distancias de la estrella entre las que se extiende la zona de habitabilidad, se supone además que los planetas tienen una composición atmosférica similar a la de la Tierra actual (CO_2, H_2O, y N_2). Los modelos de Kasting et al. (1993) fueron ampliados más recientemente por Kopparapu et al. (2013).

Hay una serie de factores no considerados en los modelos de Kopparapu et al. (2013) que tienen el potencial de modificar la ubicación y extensión de la ZH sensiblemente. Por ejemplo, usando modelos de clima global, Yang et al. (2013) mostraron que la presencia de nubes en la atmósfera permitiría a planetas sincronizados por efectos de marea ser habitables, incluso al recibir cerca del doble del flujo estelar que el modelo básico indica como el límite superior para albergar agua líquida. Por otro lado, Pierrehumbert & Gaidos (2011) estudiaron los efectos de una composición atmosférica diferente a la supuesta por Kasting et al. (1993) o Kopparapu et al. (2013). Concluyen que el hidrógeno molecular puede actuar como un gas de efecto invernadero, y que la ZH de una estrella G podría extenderse, entonces, hasta los 10 AU. Los autores muestran también que atmósferas primordiales de He-H_2 son posibles, y que esas atmósferas pueden persistir en el tiempo si el planeta tiene campos magnéticos que la protejan. Por último, el efecto de la excentricidad y la oblicuidad de las órbitas de los planetas en la extensión de la ZH fue explorada por, por ejemplo, Linsenmeier et al. (2015), quienes concluyen que la oblicuidad puede tener el efecto de expandir la frontera externa de la ZH.

En todos los casos, es claro que en las estrellas menos

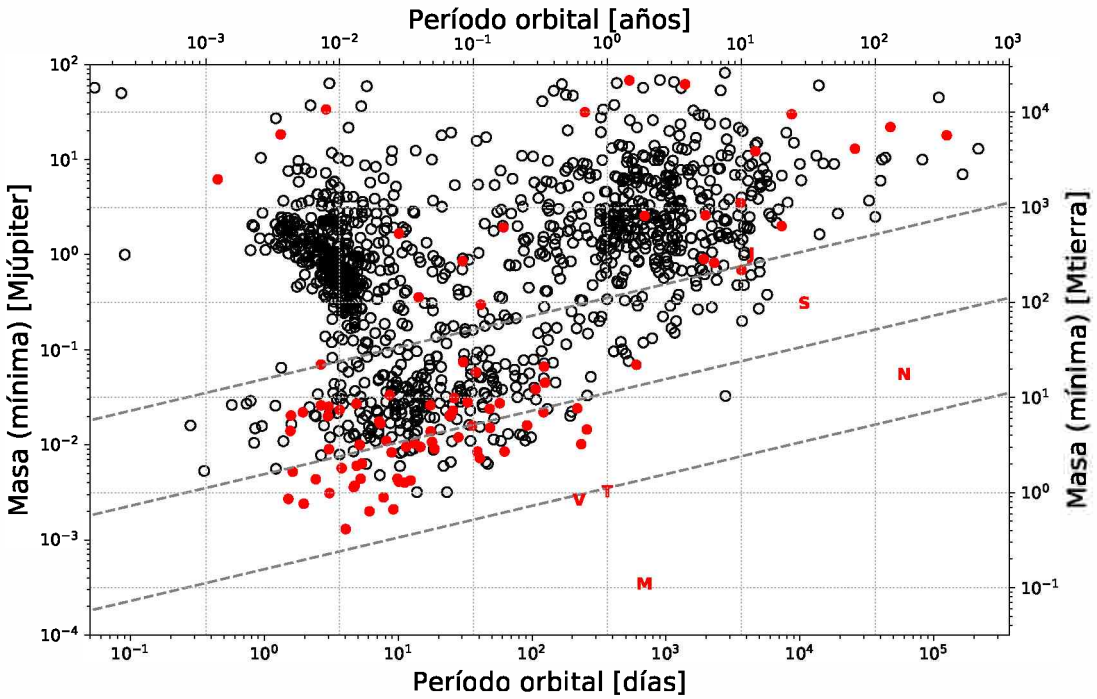

Figura 1: Diagrama masa-período para los exoplanetas listados en `exoplanet.eu` con masas medidas mejor que al 100 %. Los exoplanetas en torno a estrellas con masas inferiores a 0.5 $M_\odot$ se indican en rojo. Se indica además la posición de los planetas del Sistema Solar con sus iniciales. Las líneas discontínuas señalan la ubicación de los objetos que producen amplitudes de velocidad radial de (de arriba para abajo) 10 cm/s, 1 m/s y 10 m/s.

Tabla 2: Amplitud de la variación de velocidad radial (en m/s) experimentada por distintas estrellas en presencia de distintos planetas a períodos orbitales correspondientes a la ZH de distintas estrellas. Se supone que las órbitas son circulares y que $i = 90°$.

		Estrellas		
		Sol (G2)	GJ 411 (M0)	TRAPPIST-1 (M8)
Planeta	Masa	1 $M_\odot$	0.40 $M_\odot$	0.089 $M_\odot$
$P = 9.2$ d		Zona de habitabilidad de una estrella tipo M8		
Tierra	1 $M_\oplus$	0.31	0.56	1.5
Neptuno	17.2 $M_\oplus$	5.2	9.7	26
Júpiter	318$M_\oplus$	97	178	483
$P = 67$ d		Zona de habitabilidad de una estrella tipo M0		
Tierra	1 $M_\oplus$	0.16	0.29	0.79
Neptuno	17.2 $M_\oplus$	2.7	5.0	13.5
Júpiter	318$M_\oplus$	50	92	249
$P = 365$ d		Zona de habitabilidad de una estrella tipo G2		
Tierra	1 $M_\oplus$	0.09	0.16	0.45
Neptuno	17.2 $M_\oplus$	1.5	2.8	7.7
Júpiter	318$M_\oplus$	28	52	142

brillantes, la ZH se encontrará más cerca de la estrella. Tomando el modelo de Kopparapu et al. (2013), en la Fig. 2 mostramos la extensión de la zona de habitabilidad para estrellas de distinto tipo espectral. Los límites interno y externo corresponden, respectivamente, a la distancia a la que la irradiación desata el efecto invernadero en cadena, y a la distancia en la que el agua se congela, incluso suponiendo un efecto invernadero máximo.

Las estrellas M, entonces, presentan una serie de ventajas adicionales al presentar la ZH más cerca de su estrella. En primer lugar, un planeta ubicado en la ZH de una estrella M producirá una señal de velocidad radial mayor que si estuviera en la ZH de estrellas más ca-

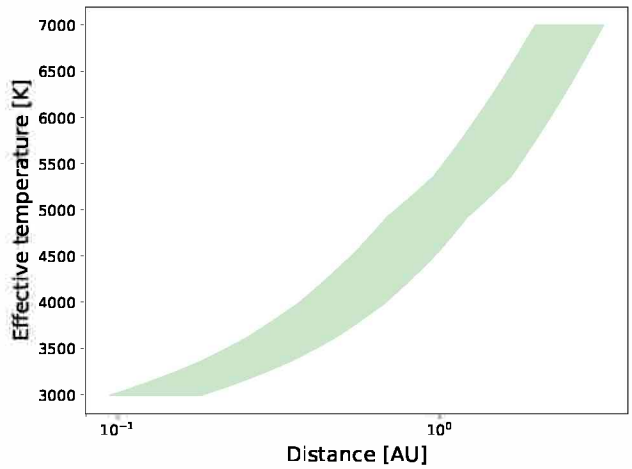

Figura 2: Evolución de la zona de habitabilidad para estrellas de distinto tipo espectral. La franja verde representa la posición de la ZH, en la que puede existir agua líquida en la superficie de cuerpos rocosos. Calculado para los límites de efecto invernadero en cadena (interno) y de máximo efecto invernadero (zona externa),.

lientes (ver Tabla 2), lo que facilita la detección de estos objetos. Además, si el planeta transita, una mayor cantidad de tránsitos serán observables en un período dado, lo que facilita también la detección. Estos dos efectos hacen que los planetas en la ZH de estrellas de tipo M sean más fácilmente detectables y caracterizables.

3.4. Caracterización atmosférica

El estudio de las atmósferas de los planetas extrasolares puede hacerse a través de varios métodos diferentes. El más evidente es la espectroscopía de un planeta resuelto espacialmente. Este método, sin embargo, sólo puede llevarse a cabo para planetas muy alejados de sus estrellas, para los cuales se pueda usar la técnica de imagen directa. Esa técnica fue empleada para los planetas del sistema HR 8799 (por ejemplo, Zurlo et al., 2016; Oppenheimer et al., 2013; Janson et al., 2010). No se espera que esta técnica permita obtener el espectro de planetas en la ZH en un futuro cercano.

Por otro lado, si el planeta transita puede utilizarse la técnica de tránsito espectroscópico, que consiste en medir la señal espectroscópica dejada por la atmósfera del planeta en la luz de la estrella que se filtra a través de ella durante un tránsito. Para esto, se mide precisamente la profundidad de los tránsitos planetarios en distintas bandas espectrales. La hipótesis es que en cada una de esas bandas, la luz de la estrella será absorbida o dispersada por la atmósfera de manera diferente, dependiendo, entre otras cosas, de la composición química, por lo que la profundidad de los tránsitos variará ligeramente. Puede entonces obtenerse un espectro de transmisión atmosférica de esta manera (Ehrenreich, 2018). En este caso, la amplitud de la señal que se busca detectar, δ_H, que corresponde a la superficie de un anillo alrededor del planeta, de ancho igual a la altura de escala, puede aproximarse (Ehrenreich, 2018):

$$\delta_H \sim (R_s)^{-2} \rho^{-1} \mu^{-1} T \ ,$$

donde R_s es el radio de la estrella, ρ es la densidad media del planeta, μ es el peso molecular medio de la especie que esté absorbiendo, y T es la temperatura de la atmósfera. La dependencia inversa con el cuadrado del radio estelar implica que para un planeta dado, la señal será mayor si la estrella huésped tiene menor tamaño. Esto constituye una gran ventaja de las estrellas M para realizar la caracterización atmosférica de planetas extrasolares. De hecho, si bien se pudo estudiar las atmósferas de planetas gigantes alrededor de estrellas de tipo solar o más calientes (por ejemplo, ver, Sing et al., 2016), los pocos planetas rocosos que han sido objeto de este tipo de mediciones se encuentran alrededor de estrellas frías. Por ejemplo, de Wit et al. (2016, 2018) obtuvieron espectros de los planetas del sistema TRAPPIST-1, tres de los cuales se encuentran en la ZH. Con la precisión actual, las observaciones muestran un espectro plano, sin ningún rasgo espectral. Esto permitió a los autores descartar la existencia de una atmósfera rica en hidrógeno y libre de nubes, pero existe una gran cantidad de posibilidades de composiciones que aún son compatibles con los datos. El futuro telescopio espacial James Webb proveerá observaciones de mayor precisión, que posiblemente permitirán echar luz sobre las atmósferas de los planetas de TRAPPIST-1(ver Sect. 5.).

Otro método de caracterización atmosférica utiliza espectroscopía de alta resolución para separar las líneas (o bandas moleculares resueltas gracias a la alta resolución) de las atmósferas planetarias de aquellas de la estrella. Se aprovecha el hecho de que a las grandes velocidades orbitales que experimentan los planetas sus líneas espectrales se separan de aquellas de la estrella o de la atmósfera terrestre, que se mantienen casi estáticas, a lo largo de pocas horas de observación (Snellen et al., 2014). La ventaja de esta técnica es que puede utilizarse para planetas no transitantes. Por otro lado, el más grande inconveniente es, claramente, el gran contraste entre la estrella y el planeta, que limita la señal que puede detectarse con esta técnica. Actualmente, se han obtenido contrastes del orden de 10^{-5}, que corresponde a la señal de la atmósfera de planetas de tipo Júpiter caliente (por ejemplo, Brogi et al., 2012). La detección de especies químicas en planetas de menor tamaño requiere contrastes varios órdenes de magnitud menores, y parece ser inviable usando sólo esta técnica (Snellen et al., 2013; Rodler & López-Morales, 2014).

Sin embargo, la combinación de alta resolución angular con las espectroscopia de alta resolución (HRI+HDS, por sus siglas en inglés) resulta una técnica prometedora para estudiar las atmósferas de planetas rocosos en torno de las estrellas más cercanas al Sol (Snellen et al., 2015). Esta técnica fue propuesta por Sparks & Ford (2002), y puesta en práctica por, por ejemplo, Snellen et al. (2014), Schwarz et al. (2016), y Birkby et al. (2017), para medir la rotación y la composición atmosférica de planetas gigantes. Su máximo potencial será alcanzado con la nueva generación de telescopios gigantes (de alrededor de 30 metros de diámetro), que

podrán resolver la luz de los planetas en órbita alrededor de las estrellas más cercanas al Sol. Snellen et al. (2014) realizaron simulaciones tanto en el óptico como en el infrarrojo. En el primer caso, la limitación viene dada por la calidad de la óptica adaptativa en este rango de frecuencias, y en el segundo por el brillo del cielo. De todas maneras, observaciones en el óptico permitirían caracterizar la atmósfera de planetas rocosos en la ZH de las estrellas M más cercanas a la Tierra.

3.5. Cercanía

La técnica de HRI+HDS no necesita que los planetas transiten delante de su estrella, pero requiere que los sistemas observados se encuentren relativamente cerca, para que su luz pueda ser resulta en la mayor medida posible. Por ejemplo, para los sistemas cercanos Proxima b (Anglada-Escudé et al., 2016) y Gl 411 b (Díaz et al., 2019), la distancia estrella planeta subtiende aproximadamente 0.03 - 0.04 segundos de arco, que corresponde a $2\lambda/D$ para telescopios de 10 metros, con $\lambda = 750$ nm. De manera que es necesario esperar a la aparición de la nueva generación de telescopios, para utilizar la técnica de HRI+HDS en los sistemas más cercanos. En particular, para el E-ELT, el instrumento METIS será propicio para este tipo de observaciones en el infrarrojo (Snellen et al., 2014)***.

Las estrellas M son también en este sentido un blanco atractivo, porque constituyen una importante fracción de las estrellas más cercanas al sistema solar. En los últimos años, la cantidad de planetas en torno de estrellas de baja masa a menos de 5 pc de distancia aumentó sensiblemente, y los cuatro planetas más cercanos al Sistema Solar se encuentran en órbita en torno de estrellas de tipo M: Proxima b (Anglada-Escudé et al., 2016), Barnard b (Ribas et al., 2018), Gl 411 b (Díaz et al., 2019), y Ross 128 b (Bonfils et al., 2018). Se destaca, además, el sistema múltiple YZ Cet (Astudillo-Defru et al., 2017). Todos estos sistemas serán objetivos principales de la nueva generación de instrumentos, montados en telescopios de 30 o 40 metros de diámetro.

4. Una desventaja y una solución

Hasta aquí hemos señalado un número de ventajas de estudiar los planetas extrasolares en torno de estrellas de tipo M, con respecto a aquellos que se encuentran en estrellas más calientes. Existe, sin embargo, una gran desventaja. Las estrellas frías son intrínsecamente más débiles. Debido a esto, sólo se conoce un pequeño número de planetas en torno de estrellas muy frías ($T_{\rm eff} \lesssim 3200$ K). La razón principal es que la mayor parte de los espectrógrafos actuales funcionan en el óptico, donde las estrellas M son tres órdenes de mangnitud menos brillantes que las estrellas de tipo solar****.

Sin embargo, en el infrarrojo las estrellas M son relativamente más brillantes. Esta es la razón por la que un gran número de espectrógrafos recientes o planeados trabajan en el infrarrojo. Entre ellos se cuentan CARMENES (Quirrenbach et al., 2018), SPIRou (Donati et al., 2018), y el Habitable-zone Planet Finder (HPF Mahadevan et al., 2014), que ya se encuentran en funcionamiento. Existen además otros proyectos, como NIRPS (Wildi et al., 2017), que será instalado en La Silla y funcionará simultáneamente con HARPS, que ampliarán las posibilidades instrumentales en estas longitudes de onda más largas. Por lo tanto, existen instrumentos que permiten sobreponerse a esta importante limitación de las estrellas de baja masa.

5. La búsqueda de vida

Además del interés por comprender los mecanismos físicos que actúan y dan forma a las atmósferas exoplanetarias, su caracterización detallada permitirá, se espera, estudiar la presencia de vida en los exoplanetas. La actividad biótica deja marcas en las atmósferas planetarias, en forma de elementos químicos que no podrían persistir en la atmósfera de otra manera. A estos elementos se los llama biomarcadores, y su estudio es un campo en rápida expansión dentro de la astrobiología†. Un artículo de revisión reciente sobre las posibilidades de detectar vida de forma remota puede encontrarse en Schwieterman et al. (2018).

En el futuro cercano, el telescopio espacial James Webb (JWST) permitirá realizar mediciones de las atmósferas de planetas en tránsito de mucha precisión. La detección de los planetas que serán propicios para la caracterización con el JWST se está produciendo ahora, principlamente gracias a las observaciones de la misión TESS, pero también a partir de relevos desde tierra.

Muchos estudios recientes exploran el desempeño del JWST para la detección de oxígeno (y su derivados, el ozono) en las atmósferas de planetas extrasolares en órbita alrededor de estrellas M (por ejemplo, Greene et al., 2016; Meadows et al., 2018). Esto se debe a que el oxígeno es un excelente biomarcador, difícil de producir de forma abiótica. Sin embargo, Krissansen-Totton et al. (2018) argumenta que es posible que muchas atmósferas sean anóxicas (es decir, que no posean grandes cantidades de oxígeno), pero que de todas maneras soporten vida, como la que conoció la Tierra temprana (Krissansen-Totton et al., 2018). En este estudio, se evalúa la capacidad de JWST para detectar biomarcadores basados en el CO_2 y el CH_4 en un planeta como TRAPPIST-1 e. Los autores concluyen que la observación de diez tránsitos son en principio suficiente para realizar una medición precisa, que permita descartar con 90 % de confianza los escenarios de generación abiótica de metano.

En la era de la caracterización de los planetas extrasolares, aquellos en órbita alrededor de estrellas de tipo

***La resolución espectral de EPICS, un instrumento óptico, es demasiado baja, pero su diseño no está definido aún.

****Precisamente, la diferencia de brillo en la banda V entre una estrella M5V y una estrella G2V es de más de 7 magnitudes.

†Ver, por ejemplo, la importante contribución de la NASA a este campo, a través de la creación de un centro de estudio que involucra a un gran número de instituciones norteamericanas (`https://nexss.info/about/about-nexss`)

M jugarán un rol central. No sólo son objetos que se detectan con mayor facilidad, sino que también se encuentran en una situación ventajosa para caracterizar sus atmósferas. Esto aplica especialmente a los planetas en la ZH. Si bien las estrellas frías son intrínsecamente débiles, la nueva generación de instrumentos infrarrojos, tanto en tierra como en el espacio, proveen un paliativo a este problema. Los planetas en torno de estrellas de baja masa constituirán los primeros objetivos de las observaciones realizadas con estos instrumentos. Entonces, por primera vez en la historia de la Humanidad, estaremos buscando respuestas de manera científica a la pregunta sobre la existencia de vida fuera del Sistema Solar.

Agradecimientos: Agradecemos a los organizadores de la reunión binacional AAA-SOCHIAS, por la invitación a presentar el Informe Invitado en el que se basa esta contribución y por el apoyo financiero que nos permitió asistir. Además, agradecemos a los editores del Boletín por su paciencia y flexibilidad.

Referencias

Almenara J.M., et al., 2018, MNRAS, 478, 460
Anglada-Escudé G., et al., 2016, Nature, 536, 437
Astudillo-Defru N., et al., 2017, ArXiv e-prints
Barclay T., et al., 2015, ApJ, 800, 46
Beaugé C., Ferraz-Mello S., Michtchenko T.A., 2012, Research in Astronomy and Astrophysics, 12, 1044
Birkby J.L., et al., 2017, AJ, 153, 138
Bonfils X., et al., 2013, A&A, 549, A109
Bonfils X., et al., 2018, A&A, 613, A25
Borucki W.J., et al., 2010, Science, 327, 977
Borucki W.J., et al., 2013, Science, 340, 587
Broeg C., et al., 2013, *European Physical Journal Web of Conferences*, *European Physical Journal Web of Conferences*, vol. 47, 03005
Brogi M., et al., 2012, Nature, 486, 502
Buccino A.P., Lemarchand G.A., Mauas P.J.D., 2006, Icarus, 183, 491
Burke C.J., et al., 2015, ApJ, 809, 8
Butler R.P., et al., 1997, ApJL, 474, L115
Chambers J.E., 2009, Annual Review of Earth and Planetary Sciences, 37, 321
Coughlin J.L., et al., 2016, ApJS, 224, 12
de Wit J., et al., 2016, Nature, 537, 69
de Wit J., et al., 2018, Nature Astronomy, 2, 214
Díaz R.F., 2017, BAAA, 59, 183
Díaz R.F., 2018, Asteroseismology and Exoplanets: Listening to the Stars and Searching for New Worlds, 49, 199
Díaz R.F., et al., 2019, arXiv e-prints
Dittmann J.A., et al., 2017, Nature, 544, 333
Donati J.F., et al., 2018, *SPIRou: A NIR Spectropolarimeter/High-Precision Velocimeter for the CFHT*, 107
Dorn C., et al., 2017, A&A, 597, A37
Dressing C.D., Charbonneau D., 2015, ApJ, 807, 45
Ehrenreich D., 2018, Asteroseismology and Exoplanets: Listening to the Stars and Searching for New Worlds, 49, 251
Fressin F., et al., 2013, ApJ, 766, 81
Gaidos E., et al., 2016, MNRAS, 457, 2877
Gillon M., et al., 2016, Nature, 533, 221
Gillon M., et al., 2017, Nature, 542, 456
Greene T.P., et al., 2016, ApJ, 817, 17
Howard A.W., et al., 2010, Science, 330, 653
Howard A.W., et al., 2012, ApJS, 201, 15
Janson M., et al., 2010, ApJL, 710, L35
Kasting J.F., Whitmire D.P., Reynolds R.T., 1993, Icarus, 101, 108
Koch D.G., et al., 2010, ApJL, 713, L79
Kopparapu R.K., et al., 2013, ApJ, 765, 131
Krissansen-Totton J., et al., 2018, AJ, 156, 114
Linsenmeier M., Pascale S., Lucarini V., 2015, Planet. Space Sci., 105, 43
Mahadevan S., et al., 2014, *Ground-based and Airborne Instrumentation for Astronomy V*, *Proc. SPIE*, vol. 9147, 91471G
Marcy G.W., Butler R.P., 1996, ApJL, 464, L147
Mayor M., Queloz D., 1995, Nature, 378, 355
Mayor M., et al., 2009, A&A, 493, 639
Meadows V.S., et al., 2018, Astrobiology, 18, 133
Mordasini C., et al., 2009, A&A, 501, 1161
Murray C.D., Correia A.C.M., 2010, *Keplerian Orbits and Dynamics of Exoplanets*, 15–23, University of Arizona Press
Murray C.D., Dermott S.F., 2000, *Solar System Dynamics*, Cambridge University Press
Oppenheimer B.R., et al., 2013, ApJ, 768, 24
Petigura E.A., Howard A.W., Marcy G.W., 2013, Proceedings of the National Academy of Science, 110, 19273
Pierrehumbert R., Gaidos E., 2011, ApJL, 734, L13
Quirrenbach A., et al., 2018, *Ground-based and Airborne Instrumentation for Astronomy VII*, *Society of Photo-Optical Instrumentation Engineers (SPIE) Conference Series*, vol. 10702, 107020W
Reffert S., et al., 2015, A&A, 574, A116
Ribas I., et al., 2018, Nature, 563, 365
Ricker G.R., et al., 2014, *Space Telescopes and Instrumentation 2014: Optical, Infrared, and Millimeter Wave*, *Proc. SPIE*, vol. 9143, 914320
Rodler F., López-Morales M., 2014, ApJ, 781, 54
Santerne A., et al., 2012, A&A, 545, A76
Schwarz H., et al., 2016, A&A, 593, A74
Schwieterman E.W., et al., 2018, Astrobiology, 18, 663
Seager S., Mallén-Ornelas G., 2003, ApJ, 585, 1038
Sing D.K., et al., 2016, Nature, 529, 59
Snellen I., et al., 2015, A&A, 576, A59
Snellen I.A.G., et al., 2013, ApJ, 764, 182
Snellen I.A.G., et al., 2014, Nature, 509, 63
Sparks W.B., Ford H.C., 2002, ApJ, 578, 543
Thompson S.E., et al., 2018, ApJS, 235, 38
Wildi F., et al., 2017, *Society of Photo-Optical Instrumentation Engineers (SPIE) Conference Series*, *Society of Photo-Optical Instrumentation Engineers (SPIE) Conference Series*, vol. 10400, 1040018
Yang J., Cowan N.B., Abbot D.S., 2013, ApJL, 771, L45
Youdin A.N., 2011, ApJ, 742, 38
Zurlo A., et al., 2016, A&A, 587, A57

Los satélites pequeños de Saturno: origen y craterización

N.L. Rossignoli[1], R.P. Di Sisto[1,2] & M. Zanardi[1]

[1] *Instituto de Astrofísica de La Plata, CONICET–UNLP, Argentina*
[2] *Facultad de Ciencias Astronómicas y Geofísicas, UNLP, Argentina*

Contacto / nrossignoli@fcaglp.unlp.edu.ar

Resumen / En este trabajo estudiamos el proceso de craterización en los satélites pequeños de Saturno debido a objetos Centauros. Modelamos la producción de cráteres en sus superficies considerando dos índices para la distribución diferencial de tamaños de los Centauros pequeños y obtenemos que la distribución de cráteres correspondiente al índice $s_2 = 3.5$ se ajusta mejor a las observaciones realizadas por las misiones Voyager y Cassini. En los casos de disrupción de satélites debido a una colisión catastrófica, encontramos que entre este grupo de satélites pequeños, los más grandes podrían ser primordiales, mientras que los más pequeños no podrían haber sobrevivido a las colisiones producidas por Centauros en la configuración actual del Sistema Solar.

Abstract / We study the cratering process by Centaur objects on Saturn's small satellites. We model the crater production on their surfaces considering two indexes of the differential size distribution of Centaurs for small sizes and find that the crater counts corresponding to the $s_2 = 3.5$ index fit better the observations made by the Voyager and Cassini missions. In the cases of satellite disruption due to a catastrophic collision, we find that among this group of ''small satellites", the largest ones may be primordial, while the smallest ones could not have survived the collisions by Centaurs in the present configuration of the Solar System.

Keywords / Kuiper belt: general — Planets and satellites: individual: Saturn — Planets and satellites: surfaces

1. Introducción

En nuestro Sistema Solar existen numerosas evidencias de actividad colisional presentes tanto en los planetas como en los satélites y pequeños cuerpos. Los planetas exteriores han sido estudiados por varias misiones espaciales en los últimos años. Recientemente, la misión *Cassini-Huygens* exploró el sistema de satélites de Saturno obteniendo numerosos resultados y observaciones con gran resolución de los cráteres en las superficies de los mismos (Thomas et al., 2013).

Se piensa que los cráteres en los satélites de los planetas gigantes se podrían haber formado por impactores heliocéntricos y/o planetocéntricos. Este último grupo lo constituirían objetos en órbita alrededor del planeta del tamaño de al menos decenas de metros, como para provocar cráteres observables. Sin embargo, no se ha observado tal fuente y hasta el momento no es posible cuantificarla. La principal fuente heliocéntrica de cráteres serían los objetos Centauros provenientes del Disco Dispersado (SD) en la Región Transneptuniana, ya que son los pequeños cuerpos que cruzan las órbitas de los planetas gigantes.

En base a simulaciones numéricas previas, Di Sisto & Brunini (2011) desarrollaron un modelo de craterización que fue aplicado al satélite de Saturno Phoebe, asumiendo como fuente principal los Centauros del SD. En este trabajo, aplicamos dicho modelo a los satélites pequeños de Saturno y lo contrastamos con las observaciones disponibles, para obtener así restricciones sobre el origen y evolución de cada uno de estos cuerpos.

Los satélites pequeños de Saturno

Los satélites pequeños de Saturno presentan una gran variedad de formas y tamaños, con radios que oscilan entre los 300 m y los 135 km. En general son cuerpos de alta porosidad y baja densidad, aproximadamente la mitad de la del agua (Thomas et al., 2013). Sus parámetros físicos y dinámicos se muestran en la Tabla 1.

La mayoría de estos satélites están fuertemente relacionados con el sistema de anillos de Saturno. Pan, Daphnis y Atlas están vinculados al anillo A; Prometheus y Pandora orbitan dentro y fuera del anillo F respectivamente; Janus y Epimetheus son satélites coorbitales; entre ellos y Enceladus se encuentran los muy pequeños Aegaeon, Methone, Anthe y Pallene embebidos en "arcos de escombros"; Telesto y Calypso son Troyanos de Tethys y Helene y Polydeuces, Troyanos de Dione; y el más grande del grupo es Hyperion.

La misión Cassini obtuvo numerosas observaciones de estos cuerpos, descubriendo características físicas y dinámicas nunca antes vistas en el Sistema Solar. En los casos en los que se obtuvieron imágenes con gran resolución, se develaron detalles sorprendentes de sus superficies, motivando numerosos estudios sobre los procesos físicos y químicos que ocurren en estos objetos y su relación con su entorno dinámico.

2. Métodos

Para estudiar la producción teórica de cráteres es necesario caracterizar la población impactora. Consideramos como fuente principal los Centauros provenientes del SD, y seguimos el modelo de Di Sisto & Brunini

(2011). De esta manera, la distribución acumulada de tamaños (CSD) de la población impactora estará dada por:

$$N(>d) = C_0 \left(\frac{1\text{km}}{d}\right)^{s_2-1} \text{ para } d \leq 60 \text{ km},$$
$$N(>d) = 3.5\times 10^5 \left(\frac{100\text{km}}{d}\right)^{s_1-1} \text{ para } d > 60 \text{ km}, \quad (1)$$

donde $C_0 = 3.5 \times 10^5 \times 100^{s_1-1} \times (60)^{s_2-s_1}$. Consideramos un quiebre en la CSD en $d = 60$ km, siendo $s_1 = 4.7$ el índice de la distribución diferencial para $d > 60$ km y 2 posibles valores para s_2 : 2.5 y 3.5 (ver Di Sisto & Brunini (2011) para un análisis detallado).

Calculamos el número de colisiones sobre cada satélite con el método de Di Sisto & Brunini (2011) y Di Sisto & Zanardi (2013). Estos autores usan los archivos de encuentros de Centauros con Saturno y mediante la aproximación de partícula en una caja, calculan el número de colisiones entre Centauros y satélites. De esta manera, el número acumulado de colisiones sobre cada satélite en función de la CSD de los impactores es:

$$N_c(>d) = \frac{v_i\, R_G^2}{v\,(R_\text{H})\, R_\text{H}^2} 10.257\, N(>d), \quad (2)$$

donde v_i es la velocidad de colisión relativa sobre cada satélite, $v(R_\text{H})$ es la velocidad media de encuentro de los Centauros al entrar a la esfera de Hill (de radio R_H) de Saturno y R_G es el radio gravitacional del satélite dado por: $R_G = R_s(1 + (v_{esc}/v(R_\text{H}))^2)^{1/2}$.

Para obtener la producción de cráteres usamos la ley de escala de Holsapple & Housen (2007) que da el diámetro D_t del cráter generado por un impactor de diámetro d dada por:

$$D_\text{t} = K_1 d \left[\left(\frac{gd}{2v_\text{i}^2}\right)\left(\frac{\rho_\text{t}}{\rho_\text{i}}\right)^{\frac{2\nu}{\mu}} + K_2 \left(\frac{Y}{\rho_\text{t} v_\text{i}^2}\right)^{\frac{2+\mu}{2}} \left(\frac{\rho_\text{t}}{\rho_\text{i}}\right)^{\frac{\nu(2+\mu)}{\mu}}\right]^{-\frac{\mu}{2+\mu}}, \quad (3)$$

donde $\mu = 0.38$, $\nu = 0.397$, $K_1 = 1.67$, $K_2 = 0.351$ y el coeficiente de cohesión es $Y = 1.5 \times 10^5$ dyn/cm^2 (Di Sisto & Zanardi, 2013). El primer término en la Ec. 3 refiere a la importancia de la gravedad del blanco (régimen gravitatorio) y el segundo a la importancia de la fuerza de cohesión del mismo (régimen de cohesión). Al igualar ambos términos se obtiene el diámetro de transición entre ambos regímenes (D_l, d_l).

Algunos de los satélites estudiados son muy pequeños, por lo cual estudiamos los casos en los que una colisión catastrófica puede producir su ruptura. Para ello nos basamos en el trabajo de Benz & Asphaug (1999) donde, mediante experimentos de laboratorio, los autores encuentran una expresión analítica para la energía cinética de la colisión por unidad de masa para un evento dispersivo dada por:

$$Q_D^* = Q_0 \left(\frac{R_\text{s}}{1\text{cm}}\right)^{\alpha} + B\,\rho \left(\frac{R_\text{s}}{1\text{cm}}\right)^{\beta}, \quad (4)$$

donde R_s es el radio en cm y ρ la densidad del blanco en g/cm^3. Q_0, B, α y β son constantes que para el hielo valen: Q_0=1.6x10^7 erg/g, B=1.2 erg.cm^3/g^2, α=-0.39 y β=1.26.

Q_D^* es la energía específica requerida para dispersar los fragmentos de la colisión considerando reacumulación y dejando el mayor fragmento con masa igual a la mitad de la masa del blanco. Igualando esta expresión a la energía cinética de la colisión por unidad de masa dada por $Q = \frac{1}{2}\left(\frac{M_\text{p}}{M_\text{s}+M_\text{p}}\right) v_\text{i}^2$, es posible obtener el radio del proyectil que fragmenta catastróficamente el blanco:

$$R_\text{p} = \left[\frac{6Q_D^* M_\text{s}}{4\pi\rho_\text{p}(v_\text{i}^2 - 2Q_D^*)}\right]^{\frac{1}{3}}. \quad (5)$$

Para los satélites que sufren una o más colisiones catastróficas, es posible calcular sus edades siguiendo los lineamientos del trabajo de Di Sisto & Zanardi (2016) (Eq. 5), donde las autoras encuentran que el número acumulado de cráteres en función del tiempo es:

$$N_c(>D,t) = F(t) N_c(>D), \quad (6)$$

donde $N_c(>D)$ es el número total de cráteres con diámetros mayores a D producidos a lo largo de la edad del Sistema Solar (que se obtiene de las Ec. 2 y 3) y $F(t) = a \ln t + b$, con a=0.198406 $\pm$ 0.0002257 y b=-3.41872 $\pm$ 0.004477. Así, si $d_{rup} = 2R_p$, la última colisión que fragmentó catastróficamente el satélite se producirá a un tiempo t que puede obtenerse de la condición $N_c(>D_{rup}, t_f) - N_c(>D_{rup}, t) = 1$, donde D_{rup} es el diámetro del cráter correspondiente a un impactor de diámetro d_{rup}. De esta forma, la edad del satélite, es decir el lapso de tiempo desde su formación al presente está dada por:

$$\tau = t_f - t = t_f \left[1 - e^{-\frac{1}{aN_c(>D_{rup})}}\right], \quad (7)$$

donde $t_f = 4.5$ Gyr es la edad del Sistema Solar.

3. Resultados y conclusiones

Siguiendo el método descrito, calculamos la producción de cráteres en los satélites pequeños durante la edad del Sistema Solar por objetos Centauros. Nuestros resultados se muestran en la Fig. 1 para los dos valores del índice de distribución del tamaño de los impactores ($s_2 = 2.5$ y $s_2 = 3.5$). Para analizar y comparar nuestros resultados teóricos, utilizamos los conteos de cráteres disponibles en la literatura, fundamentalmente de Thomas et al. (2013), Hirata et al. (2014) y Plescia & Boyce (1985). En general y a pesar de que cada pequeño satélite tiene un ambiente peculiar, encontramos que la distribución de tamaños de la población impactora con $s_2 = 3.5$ es la más consistente con las observaciones. Por lo tanto, el análisis de los resultados corresponde a este caso.

Se calcularon el tamaño del impactor (d_m) que produce el cráter más grande (D_m) y el diámetro del cráter de transición entre los regímenes gravitatorio y de cohesión (D_l), presentados en la Tabla 1. Algunos de estos satélites son muy pequeños; es el caso de Pan, Daphnis, Atlas, Aegaeon, Methone, Anthe, Pallene, Calypso y Polydeuces. Encontramos que estos satélites sufren una o más colisiones catastróficas durante la edad del Sistema Solar.

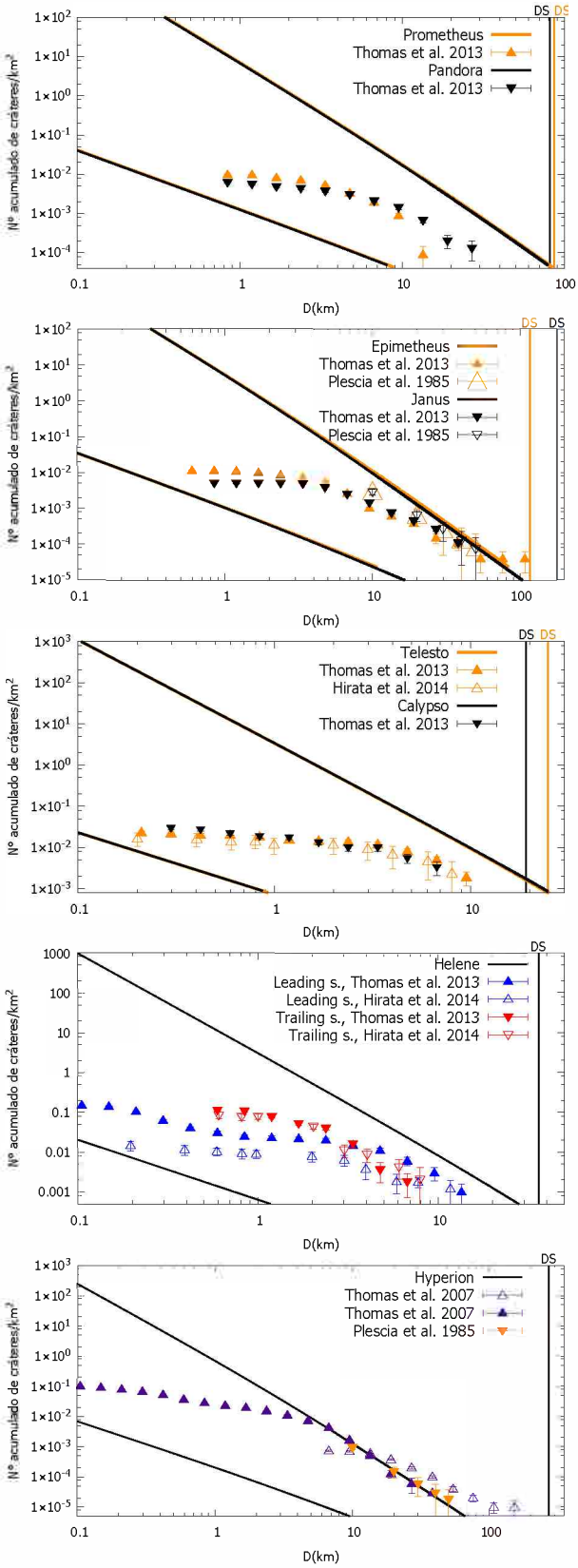

Figura 1: Número acumulado de cráteres por km^2 vs D. Las líneas continuas corresponden a nuestro modelo para s_2=3.5 (superior) y s_2=2.5 (inferior). Los puntos representan las observaciones citadas en cada figura. Los diámetros de cada satélite "DS" se indican con líneas verticales.

En consecuencia, calculamos el diámetro del impactor que fragmentó el satélite y luego la edad del mismo (ver Tabla 1). Posiblemente, estos satélites se formaron después de la formación planetaria y de sus satélites regulares. Esto implicaría la existencia de material disponible a partir del cual estos satélites se puedan haber formado recientemente. De hecho, Charnoz et al. (2010) estudian la formación de las lunas pequeñas más allá del límite de Roche a partir del material de los anillos. Se puede observar que las edades dependen tanto del tamaño del satélite (cuanto más pequeño, más joven) como del grupo al que pertenecen, siendo los más jóvenes los asociados a arcos.

Cada grupo de satélites es particular, tanto sus características como su entorno y por tanto cada caso es diferente. Sin embargo, en general podemos observar de la Fig. 1 que la distribución observada de cráteres se hace más plana y se desvía de la curva teórica para diámetros de cráteres pequeños. Esta desviación podría deberse a una combinación de procesos de erosión de cráteres por partículas de los anillos y/o saturación, dependiendo de la posición del satélite y las características de su entorno.

Tabla 1: Radio medio del satélite R_s [km], densidad media del satélite ρ [Kg/m^3], diámetro del cráter de transición D_l [km], diámetro del impactor más grande d_m [km] y del cráter más grande D_m [km] considerando s_2=3.5. En los casos de ruptura catastrófica, figuran el diámetro del impactor d_{rup} [km] y la edad del satélite τ [10^9 años].

Satélite	R_s	ρ	a	D_l	d_m	D_m	d_{rup}	τ
Pan	14.0	430	133584	25.7	0.55	45.9	0.4	4.04
Daphnis	3.8	340	136504	153.8	0.06	5.9	0.06	0.9
Atlas	15.1	460	137670	20.9	0.58	46.5	0.47	4.27
Prometheus	43.1	470	139380	6.9	1.33	83.7	-	-
Pandora	40.6	490	141720	6.8	1.26	79.2	-	-
Epimetheus	58.2	640	151410	2.8	1.66	82.6	-	-
Janus	89.2	630	151460	1.9	2.34	103.7	-	-
Aegaeon	0.33	540	167425	938	0.03	2.3	0.003	0.12
Methone	1.45	310	194440	210	0.08	7.8	0.01	0.32
Anthe	0.5	500	197700	93	0.03	3.0	0.005	0.19
Pallene	2.23	250	212280	168	0.11	11.1	0.02	0.43
Telesto	12.4	500	294710	12.6	0.42	29.2	-	-
Calypso	9.6	500	294710	16.3	0.35	24.8	0.33	4.45
Polydeuces	1.3	500	377200	209	0.07	5.1	0.02	1.03
Helene	18.0	400	377420	10.9	0.55	36.0	-	-
Hyperion	135.5	544	1500933	1.7	2.14	68.9	-	-

Agradecimientos: A Naoyuki Hirata y Peter C. Thomas por proveer datos observacionales y aportar comentarios que ayudaron a mejorar el trabajo, y al COL y COC de la Reunión Binacional Sochias-AAA por su invitación a presentar este informe.

Referencias

Benz W., Asphaug E., 1999, Icarus, 142, 5
Charnoz S., Salmon J., Crida A., 2010, Nature, 465, 752
Di Sisto R.P., Brunini A., 2011, A&A, 534, A68
Di Sisto R.P., Zanardi M., 2013, A&A, 553, A79
Di Sisto R.P., Zanardi M., 2016, Icarus, 264, 90
Hirata N., Miyamoto H., Showman A.P., 2014, Geophys. Res. Lett., 41, 4135
Holsapple K.A., Housen K.R., 2007, Icarus, 187, 345
Plescia J.B., Boyce J.M., 1985, J. Geophys. Res., 90, 2029
Thomas P.C., et al., 2013, Icarus, 226, 999

The Pampa-A strewn field, Antofagasta Region, Northern Chile

G. Pinto[1,2], A. Menzies[1], R. Martinez[3] & M. Valenzuela[2,4,5]

[1] *Facultad de Ingeniería y Ciencias Geológicas, Universidad Católica del Norte, Antofagasta, Chile*
[2] *Grupo de Meteoritos y Ciencias Planetarias, Sociedad Geológica de Chile, Santiago, Chile*
[3] *Museo del Meteorito, San Pedro de Atacama, Chile*
[4] *Unidad de Geopatrimonio, Dp. Geología aplicada, Servicio Nacional de Geología y Minería, Santiago, Chile*
[5] *Instituto Milenio de Astrofísica, Santiago, Chile*

Contact / gpinto.mo@gmail.com

Resumen / La elipse de dispersión puede ser definida interpretando las características de los diferentes fragmentos del meteoroide pertenecientes al mismo evento de caída. Presentamos el estudio de una caída múltiple de meteoritos descubierta en 1986 por coleccionistas privados en Pampa de Mejillones, norte de Chile. El meteorito, Pampa-A, fue clasificado como una Condrita Ordinaria tipo L6 / S4 / W2, y está compuesto por 16 fragmentos, 14 de los cuales corresponden al mismo evento de caída. Ellos fueron emparejados de acuerdo a sus características físicas, petrográficas y/o químicas. La forma de la elipse cubre un área de 1.5.5 km^2. Basado en la dispersión de los fragmentos en la superficie inferimos una entrada desde el NW al SE con un buzamiento de 106° desde el norte. Para estimar el tamaño pre-atmosférico del meteoroide asumimos una forma esférica y una pérdida de material debido a la ablación entre 90 % y 99 % del peso inicial. Por lo tanto el diámetro del meteoroide se estimó en 16.7 cm y 36 cm, respectivamente. Esto debería ser considerado diámetro estimado mínimo, ya que en el área de caída algunos fragmentos pueden permanecer sin ser encontrados o informados.

Abstract / The strewn field can be defined interpreting the characteristics of the different fragments of the meteoroid belonging to the same fall event. We present the study of a multiple meteorite fall discovered in 1986 by private collectors in Pampa de Mejillones, in northern Chile. The meteorite, Pampa-A, was classified as an Ordinary Chondrite type L6 / S4 / W2, and is composed of 16 fragments, 14 of which correspond to the same fall event. They were paired according to their physical, petrographic and / or chemical characteristics. The shape of the ellipse covers an area of 1.5×0.5 km^2. Based in the dispersion of the fragments on the surface we can infer an entry from the NW to the SE with a dip of 106° from the north. For estimating the pre-atmospheric size of the meteoroid we assumed spherical shape and a loss of material duo to the ablation between 90 % and 99 % of its initial weight. Therefore the diameter of the meteoroid was estimated at 16.7 cm and 36 cm, respectively. This should be consider the minimum estimated diameter as some fragments can remained not found or not reported in the fall area.

Keywords / meteorites, meteors, meteoroids

1. Introduction

In the past two decades, a big number of meteorites have been collected from hot deserts around the world, including the Sahara desert (Bischoff & Geiger, 1995), Mojave desert (Kring et al., 2001), Oman desert (Gnos et al., 2009), and Atacama desert (Hutzler et al., 2016).

The meteorite strewn fields found in hot deserts are still relatively rare (Zeng et al., 2018). The few rare examples include the Vaca Muerta strewn field (Pedersen et al., 1992), the Gold Basin strewn field (Kring et al., 2001), and the Jiddat al Harasis (JAH) 073 strewn field (Gnos et al., 2009).

In the Pampa de Mejillones there are 27 official meteorites published by the Meteoritical Bulleting*.

The fragments in areas of high accumulation may contain cross-scatters of different fall events at different times. The Pampa-A meteorite was the first found in this area in 1986 (Graham, 1987).

Here we present the characterization of the physical properties of the 14 fragments recognized as Pampa A.

The main mineralogy of all samples as well as the description of their surface morphology was established through a macroscopic inspection.

Eleven of the samples were selected for a microscope study to define their texture and minerals in five of them and the chemical compositions, including whole rock and specific minerals of this five samples.

2. Samples and Methods

In the Pampa de Mejillones area, located ∼ 9 km south of the city of Mejillones, sixteen rock pieces have been collected as part of a same fall, named Pampa-A (Fig. 1). The total mass reached 904 g. In this research fourteen fragments were analyzed (PMP-A1 to PMP-A14), with a total mass of 841 g.

Five of these fragments are complete (a single pieces with fusion-crusted) and nine are fractions of the total

*https://www.lpi.usra.edu/meteor

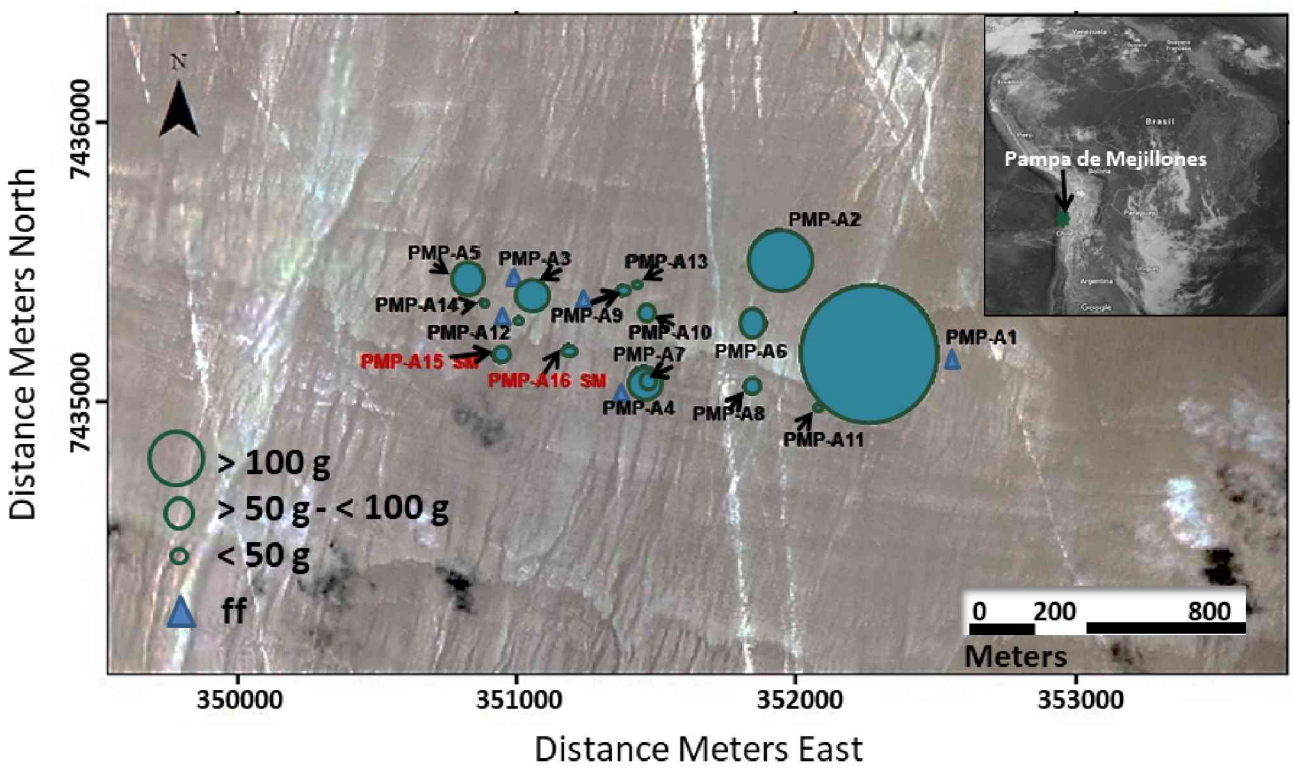

Figure 1: Map of the strewn field in the Pampa-A area, Atacama Desert, north of Chile. The samples in red show the material not available for investigation. The samples with triangle show the full fragments (ff).

sample. Only five of these fractions (PMP-A2, PMP-A4, PMP-A5, PMP-A8 and PMP-A10) were selected to make polished thin section (PTS) for microscopic description and chemical analysis.

The magnetic susceptibility was measured with the SM30 equipment, covering three different directions that allow homogenizing the variation of clasts/minerals in each fragments. The density was calculated using the volume measured by the Dial-0-Gram (Ohaus) -310 g-precision to the hundredth of a gram. The porosity was measured in proportion to its porous space through mineralogical maps using QEMSCAN.

The description of the macroscopic petrography was made with a Nikon SMZ645 steroscopic zoom microscope, focusing on the fusion crust and surface alterations. Five PTS were studied in the optical microscope OLYMPUS BL to define the petrographic textures and the abundance (in percentages ratios) of chondrules, crystals and matrix.

The chemical analysis were carried out using a QEMSCAN E430 model, which is based on a scanning electron microscope (SEM) ZEISS EVO 50 combined with energy dispersive spectrometer (EDS) detectors to analyze the elemental components and mineral phases. The measurements were made in alloys of Fe-Ni (21); SFe: troilite (50); silicates: plagioclase (2), olivine (50) and pyroxene (7).

3. Results

3.1. Physical properties

The average magnetic susceptibility (in log χ 10–9 m^3 kg^{-1}) is 4.41, with a standard deviation of 0.17. The average bulk density is 3.44 g cc-1, with a standard deviation of 0.25. The average porosity is 3.21 vol%.

3.2. Petrography

The meteorites are mostly composed of crystals (∼15%) with sizes greater than 0.5 mm. The presence of Chondrules in the studied thin section vary from 15 to 20 % with apparent diameters from 0.3 mm to 3 mm. Their textures types are porphyritic olivine (PO), porphyritic olivine pyroxene (POP) and barred olivine (BO). The matrix covers ∼65% of the samples with crystals having less than 0.3 mm in size. Concerning the mineralogy, the samples are mainly composed of two main phases, olivine (∼55 %) and pyroxene (∼30 %) with minor amounts of troilite (∼4 %), chromite (∼1%), kamacite (∼4 %), taenite (∼1 %) plagioclase (∼2 %), zircon (∼1 %) and apatite (∼1 %).

The absence of chondrules with well defines borders and the presence of chromite, plagioclase and apatite among other features, indicate a thermal metamorphism degree marching the type 6 (Van Schmus & Wood, 1967).

With regard to the shock degree, the presence of irregular and planar fractures, some primary veinlets filled with opaque minerals as well as undulating extinc-

tion and incipient mosaicism present in olivine point towards a degree of shock between S3-S4. In addition presence of Fe oxides that can be replacing primary opaques phases between 0 and 100 %, with an average of 45 to 55 % in different samples. Also it can be observed in most of the samples the development of secondary weathering veins filled with Fe oxides. These observations support an alteration degree of W2.

3.3. Chemical composition

The chemical composition of Fe^0/ Fe has ranges between 0.37 and 0.33, with a total Fe content between 22.1 and 23.8 $wt\%$. This allows classifications of the sample as an ordinary chondrite type L. The average chemical composition of the main mineral phases is: olivine Fa_{24}; orthopyroxene $En_{70}Wo_{1.7}$ and plagioclase $An_{10}Al_{80}$.

4. Discussion

4.1. Pairing

The criteria used for the pairing of Pampa A fragments included physical properties, petrography descriptions and chemical composition, all of them described and explained in previous works (Benoit et al., 2000; Hutzler et al., 2016).

The physical characteristics of the samples as their different shapes and sizes point towards slight dispersions, as described by (Consolmagno et al., 2006). The petrographic studies show that all samples share the same components, varying in slight percentages due to the heterogeneity that is typical for ordinary chondrites (Hutchison, 2004). The [Fe^0/ Fe] ratio and total Fe content of the analyzed samples range in the values assigned to type L ordinary chondrites 0.33 ± 0.07, as established in Van Schmus & Wood (1967).

According to our results, when samples paired the three criteria, that is: chemical analysis, mineralogy and physical characteristics, the certainty in pairing samples increase. While in the studied fragments in which only the physical features could be measured, the pairing is less precise. However, one of the determinant features for matching meteorites is their closeness in the distribution area (Benoit et al., 2000).

4.2. Strewn field and entrance

The dispersion of the fragments on the surface has an elliptical shape, with the major axis in NW-SE direction. The larger pieces are at the SE end, because they flew a large distance due to their great inertia (Fig. 1). This indicates an entry from the NW to the SE with a dip of 106° from the north. The ellipse covers an area of 1.5×0.5 km^2 relatively small if compared to others which can reach dozens of km on its major axis (Hutchison, 2004). The absence of impact structures in the surface related to the fragments is a robust argument to propose a low speed entrance of the meteoroid. In addition, the direction of the fall match that of the terrestrial rotation direction.

For estimating the pre-atmospheric size of the meteoroid we took into account the average density of the fourteen fragments of Pampa-A (3.44 g cc-1) and the total mass collected (841 g), similarly to what has been done for the JAH 073 Strewn field (Gnos et al., 2009). In addition, we assumed a spherical shape and a loss of material due to the ablation varying between 90 % and 99 % of its pre-atmospheric weight, like the principal ablation percentage in ordinary chondrite (Sears et al., 2016). Therefore, the diameter of the meteoroid was estimated at 16.7 cm (90 %) and 36 cm (99 %). This should be consider the minimum estimated diameter as several fragments can remained not found or not reported in the fall area.

References

Benoit P.H., et al., 2000, Meteoritics & Planetary Science, 35, 393

Bischoff A., Geiger T., 1995, Meteoritics, 30, 113

Consolmagno G., et al., 2006, Meteoritics & Planetary Science, 41, 331

Gnos E., et al., 2009, Meteoritics & Planetary Science, 44, 375

Graham A., 1987, Meteoritics, 22, 157

Hutchison R., 2004, *Meteorites: A petrologic, chemical and isotopic synthesis*, Cambridge University Press

Hutzler A., et al., 2016, Meteoritics & Planetary Science, 51, 468

Kring D.A., et al., 2001, Meteoritics & Planetary Science, 36, 1057

Pedersen H., de Bon C.C., Lindgren H., 1992, Meteoritics, 27, 126

Sears D.W., et al., 2016, Planetary and Space Science, 124, 105

Van Schmus W., Wood J.A., 1967, Geochimica et Cosmochimica Acta, 31, 747

Zeng X., et al., 2018, Meteoritics & planetary science

Zooming out: what a broader view is telling us about stellar and substellar conglomerates

K. Peña Ramírez[1]

[1] *Centro de Astronomía (CITEVA), Universidad de Antofagasta, Chile*

Contacto / karla.pena@uantof.cl

Resumen / La medición de distribuciones de edades y masas de estrellas de baja masa y objetos subestelares en diversos ambientes jóvenes requiere de un censo minucioso de esta población en particular. Tradicionalmente, los estudios que se llevan a cabo en este sentido buscan miembros en conglomerados definidos usando rasgos de juventud (variabilidad, líneas de emisión, exceso de emisión infrarroja, emisión en rayos X), movimientos propios y diagramas color-magnitud en el óptico y el infrarrojo. Dado el acceso a los más recientes relevamientos de cielo completo, se cuenta ahora con un mayor número de objetos bajo estudio y una serie de desafíos teóricos y observacionales se mantienen latentes dentro del campo. La definición de funciones de luminosidad en conglomerados delineados sufre modificaciones ante un cubrimiento espacial mayor y homogéneo de su población de objetos ultra fríos. Algunos ejemplos recientes son presentados.

Abstract / Measuring the distributions of ages and masses of low-mass stars and substellar sources in different young environments requires a thorough census of this specific population. Typically, studies have searched for defined conglomerate members using signatures of youth (variability, emission lines, infrared (IR) excess emission, X-ray emission), proper motions, and optical and near-IR color-magnitude diagrams. Given the access to the most recent all-sky surveys, better statistics are now in place, and a series of observational and theoretical challenges keep the field ongoing. Given a wider and uniform spatial coverage of ultra-cool dwarf sources, the diversity of spatial structures and the traditional definition of luminosity functions in spatially-delineated conglomerates should be revisited. Some recent examples are presented.

Keywords / open clusters and associations — stars: kinematics and dynamics — stars: pre-main sequence

1. Introduction

With the advent of large photometric/astrometric/spectroscopic surveys, the panorama of the physical processes beneath the formation and dynamics of low mass stars and massive brown dwarfs has changed radically. The low mass population of our Milky Way is mainly populated by ultra-cool dwarfs being the bridges between the stellar and the substellar population of the Galaxy. There are not only new insights about the specific features relevant to the stellar/substellar transition but in the definitions of the environments where these kinds of sources lie. The defining boundaries of star-forming regions, open clusters, associations, moving groups at ages of less than a few Myr are no longer clear, making even harder to arise conclusions of a specific population in a determined spatial portion of space.

2. Spatial location

Ultra-cool dwarfs (sources of about M7 spectral type or later) have been found mainly as field old dwarfs, young members of star-forming regions, clusters and associations as well as members of young moving groups. In terms of detected ultra-cool dwarfs as not members of gravitationally bound structures, before Gaia Data Release 2 (DR2, Gaia Collaboration et al., 2018) the number of known dwarfs in the field was about 4300. This number has increased considerably with recent works using Gaia data. One example is the photometric selection done by Reylé (2018), in which the number of filed ultra-cool dwarfs would rise to more than 13 700 sources. Even more, the discovery of three L-type dwarfs at about 10-19 pc (Scholz & Bell, 2018) suggests that there exist remaining undiscovered objects in this volume.

The census of ultra-cool dwarfs in very young star-forming regions has been reaching a few Jupiter masses in several locations: λ Orionis (e.g., Barrado y Navascués et al., 2007; Bayo et al., 2011); NGC 1333 (e.g., Scholz et al., 2009, 2012; Luhman et al., 2016); IC 348 (e.g., Alves de Oliveira et al., 2013; Burgess et al., 2009; Luhman et al., 2016); σ Orionis (e.g., Zapatero Osorio et al., 2000; Caballero et al., 2007; Bihain et al., 2009; Peña Ramírez et al., 2011, 2012, 2015); Orion Nebular Cluster (e.g., Lucas et al., 2001; Weights et al., 2009; Hillenbrand et al., 2013; Ingraham et al., 2014; Suenaga et al., 2014), ρ Ophiuchus (e.g., Geers et al., 2011; Mužić et al., 2012; Alves & Bouy, 2012; Chiang & Chen, 2015); Upper Scorpius (e.g., Ardila et al., 2000; Slesnick et al., 2006; Peña Ramírez et al., 2016; Best et al., 2017; Lodieu et al., 2018); 25 Orionis (e.g., Suárez et al., 2017); Taurus (e.g., Luhman et al., 2006; Slesnick et al., 2006; Esplin et al., 2017; Luhman, 2018), among others. Being this kind of environments the most suitable ones to pursue studies on the formation and evolution of ultra-cool dwarfs given the premise of a common origin for all the

cloud members.

Low mass dwarfs have also been reported as members of co-moving groups. Now, we count with low mass populations of various young moving groups as close as ∼150 pc. Given that these are sparse, low-density populations the membership studies and age assessment of the low mass content of young moving groups is a demanding task. Recent studies suggest that there are about 900 ultra-cool dwarfs of spectral types as late as L2 in the seven nearest young co-moving groups (Gagné & Faherty, 2018).

3. Challenges

Given the increased amount of observational data, the field has faced a series of challenges trying to reconcile not only all the observational efforts among themselves but also to give an appropriate theoretical description of the physical processes beneath the formation and evolution of the low mass stellar/substellar galactic population.

In that sense, there has been a vast improvement from the first evolutionary models (e.g., Baraffe et al., 1998) describing the mass regime of about 0.075 to 1 $M_\odot$ (not even describing the massive extreme of the substellar regime) at optical wavelengths and using the interior physics and non-grey atmosphere models available at the time. Missing sources of opacity in the optical together with the limited treatment of grain formation accounted for some of the discrepancies among observational sequences and theoretical isochrones. We do count now, twenty years later, with models with updated molecular lists, updated solar abundances, and the inclusion of atmospheric convection parameters calibrated on 2D/3D radiative hydrodynamics simulations in the near infrared (e.g., Baraffe et al., 2015). An example of the improvement can be seen in Fig 1 where the σ Orionis cluster sequence (Peña Ramírez et al., 2012) is compared with the set isochrones of Baraffe et al. (1998) and Baraffe et al. (2015). The new set of isochrones and the observational sequence are in agreement specially for the massive brown dwarfs in the cluster. The situation becomes worse for the faintest sources, in particular in the $J - K$ color, possibly related with the presence of infrared excesses due to circun(sub)stellar disk of these young sources.

A similar panorama faces the theoretical work of synthetic spectra of ultra-cool dwarfs. There have been tremendous efforts in the modeling of atmosphere models and the derivation of synthetic spectra. The BT-Settl (Allard et al., 2012; Allard, 2014) synthetic spectra, for example, aim to describe the atmospheres of low-mass stars, brown dwarfs, and planets without irradiation. They include a cloud model by accounting for the formation and gravitational settling of dust grains for $T_{\rm eff} \leq 2700$ K. As can be seen in Fig.2 the over-all aspect of the optical and near-infrared data is successfully reproduced by the theoretical spectra, implying that no relevant molecule or atomic element is missing from the atmospheric computations. Synthetic spectra still face limitations on reproducing specific spectroscopic features of ultra-cool dwarfs in part due to the limited signal

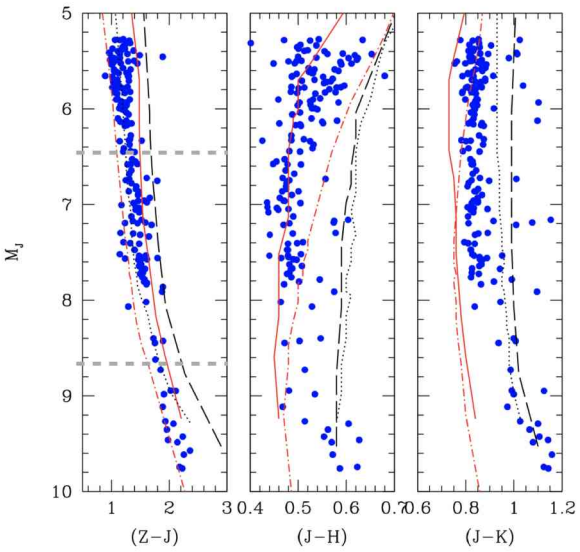

Figura 1: Comparison of models with observations in the σ Orionis cluster in various color-magnitude diagrams. Isochrones of 1 Myr and 10 Myr are displayed for various sets of models. Baraffe et al. (2015) (red): solid (1 Myr) and dash-dot (10 Myr). Baraffe et al. (1998) models (black): long dashed (1 Myr) and dot (10 Myr). The data (blue dots) are from Peña Ramírez et al. (2012). Figure from Baraffe et al. (2015).

to noise achieved of intrinsically faint sources, even at large astronomical facilities. From Fig 2, the VO features are typically less intense in observed data, water opacities can be related with the not so accurate H-peak shape, and the noise level at K-band prevents us from comparing observations from synthetic spectra associated with the CO band. The models do reproduce the relative fluxes between the optical, J-, H-, and K-bands, which can be understood as evidence in favor of a proper treatment of the gas and dust condensation chemistry and the dust opacity at these low temperatures and surface gravities (Zapatero Osorio et al., 2017).

Different approaches have been undertaken to define a precise sequence of spectral types among low-mass dwarfs. The definition of standardized datasets either at optical or infrared wavelengths as well as the quest of homogeneity in involved instrumentation and reduction techniques has been one of the main drivers in recent works. The mentioned challenges in the atmospheres of the ultra-cool dwarfs led to several difficulties on the spectral type determination. As an example, the recent work of Luhman (2018) redefines the sequence of dwarfs entirely later than M6 spectral type in the Upper Scorpius association deriving a tighter sequence of members, including the faintest ones (Peña Ramírez et al., 2016). The comparison of dwarfs found in different environments has also been benefited from the large statistic now available. In Best et al. (2018), authors made a global comparison among different color combinations of ultra-cool dwarfs from the field, from young environments, binaries, and subdwarfs. The work mentioned above includes near ten thousand field dwarfs found in the Pan-STARRS1 3π Survey (Chambers et al., 2016). As a result, there seems to be a surprising diversity of

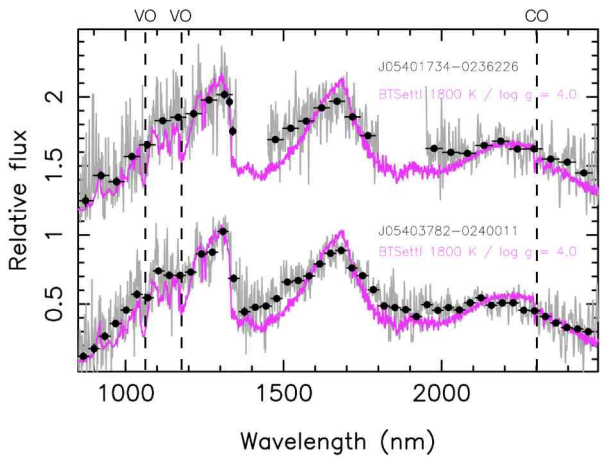

Figura 2: Best-fit BT-Settl synthetic spectra (magenta lines) plotted together with the observed spectra (gray lines) of a couple of faint σ Orionis ultra-cool dwarfs (J=19.5, 19.9 mag). The rebinned data are shown with black dots. All models are computed for solar metallicity and log g = 4.0 (cm s^{-2}). Spectra are normalized to unity at 1.28-1.32 μm and offset vertically by a constant. Figure from Zapatero Osorio et al. (2017).

L-type colors in the near infrared. Theoretically, this diversity is explained by dust dispersal that includes both a sudden sinking of the entire cloud deck into the deep, unobservable atmosphere or breakup of the cloud into scattered patches (as seen on Jupiter and Saturn, Crossfield et al. (2014)). Until recently, observations of brown dwarfs have been limited to globally integrated measurements; such measurements can reveal surface inhomogeneities but cannot unambiguously resolve surface features. Crossfield et al. (2014), presented a two-dimensional map of large scale bright and dark features possibly related to patchy clouds in the Luhman 16AB system at two pc (Luhman, 2013). This early T-dwarf presents constant temporal variability with a rotation period of ∼5 h, brightness variations of ±10 % and even a bright spot in the pole. The work of Apai et al. (2017) presents a long-term Spitzer Space Telescope infrared monitoring campaign of three brown dwarfs to constrain cloud cover variations over a total of 192 rotations along 1.5 years. As a result, authors support the presence of zonal temperature and wind speed variations which would help to explain puzzling behaviors seen in brown dwarf brightness variations.

The mass determination of ultra-cool dwarfs is one of its biggest challenges. The work on dynamical masses of Dieterich et al. (2018) in the system ϵ Indi B and C gave us a recent example. Both sources are close to the theoretical hydrogen burning minimum mass limit a key point of transition between the stellar and the substellar regime. The reported mass for ϵ Indi B, a T1.5 dwarf, is 75±0.8 M_{Jup}, while the mass assigned to ϵ Indi C, a T6 dwarf, is 70.1±0.7 M_{Jup}. Given that for a mid-T dwarf its mass value can range between ∼20 M_{Jup} for a source with 500 Myr to ∼60 M_{Jup} for a source with an age of 10 Gyr; the dynamical mass values found by Dieterich et al. (2018) are extremely high. Unknown molecule and cloud formation, poor knowledge of opacities that affect the rate of cooling are among the reasons for this discrepancy. Authors claim that it is clear that the current models under-predict the upper mass limit and (or) the necessary cooling rates for ϵ Indi B and C, with less opaque models coming closer to replicating the observed parameters.

Finally, it is relevant to mention the gap observed in the Hertzsprung-Russell diagram of field early-type M dwarfs based on Gaia DR2 measurements (Jao et al., 2018). A gap introduces a diagonal feature that dips toward lower luminosities at redder colors. It is seen at various distances (<130 pc) and it is not tight to Gaia photometry. The gap is near the luminosity-temperature regime where M dwarf stars transition from partially to fully convective, i.e., near spectral type M3.0V. This gap was possible to detect given the massive amount of red dwarfs detected by the satellite (more than 250.000 sources). From the theoretical perspective, Baraffe & Chabrier (2018) and MacDonald & Gizis (2018) relate the gap to a complex interplay between the production of ^{3}He and its transport by convection. With a vast amount of high-quality data, the Hertzsprung-Russell diagram could thus provide a deep insight into the interior structure of low mass stars.

4. Substellar formation scenarios and observational constrains

Currently the substellar formation mechanisms scenario counts with five main theoretical proposals: hierarchical fragmentation (Bonnell et al., 2008), gravo-turbulent fragmentation (Padoan & Nordlund, 2004), disc fragmentation (Bate et al., 2002, 2003; Goodwin et al., 2004), ejection of protostellar embryos (Reipurth & Clarke, 2001) and photo erosion (Hester et al., 1996; Whitworth & Zinnecker, 2004). There are different observational constraints to the theoretical models: the shape of the low-mass initial mass function and its minimum mass, (sub)stellar multiplicity, spatial and kinematic distributions at birth, prevalence and sizes of circum(sub)stellar disks and envelopes and, the dependence of these properties on the star-forming environment.

Changes in the shape of the initial mass function, independently of its functional form, are related with different dominant formation processes in a given mass regime. For substellar sources, there has been a steady effort in nearby young star-forming regions trying to asses its impact in the mass function (system initial mass function). There is a consensus of a universal initial mass function down to the ∼0.03 $M_\odot$, described as a lognormal distribution it would have a characteristic mass around the 0.25 $M_\odot$ and σ ∼0.5. Under the mentioned conditions the initial mass function in different young star-forming regions is consistent among each other within the quoted uncertainties. Various initiatives have tried to preserve uniformity of analysis in terms of instrumentations, study, applied corrections (e.g., mass segregation) and used models for the mass-luminosity relationship (de Wit et al., 2006; Moraux et al., 2003,

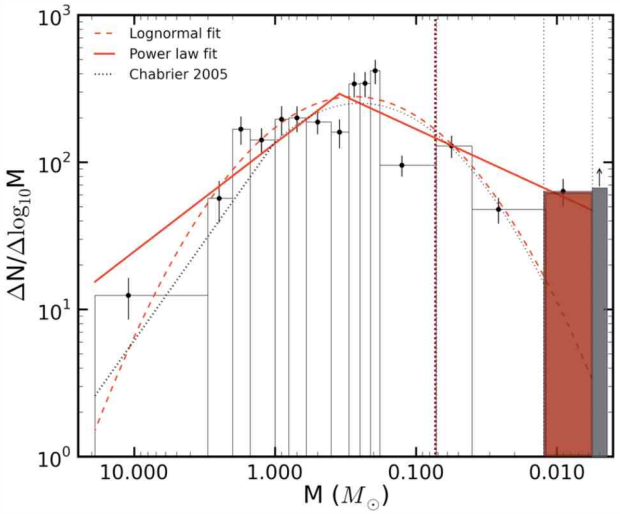

Figura 3: The σ Orionis mass function. The best lognormal fit to our data is depicted with a dashed line, the double power-law fit from our mass spectrum is illustrated with a continuous line, and the Chabrier (2005) mass function normalized to the total number of sources is plotted as a dotted line. Vertical error bars stand for the Poisson uncertainties. The highlighted mass bins account for the new substellar candidate members. Vertical dashed lines represent the classical stellar/substellar regime, the planetary mass regime and, our completeness level. Figure from Peña Ramírez et al. (2012).

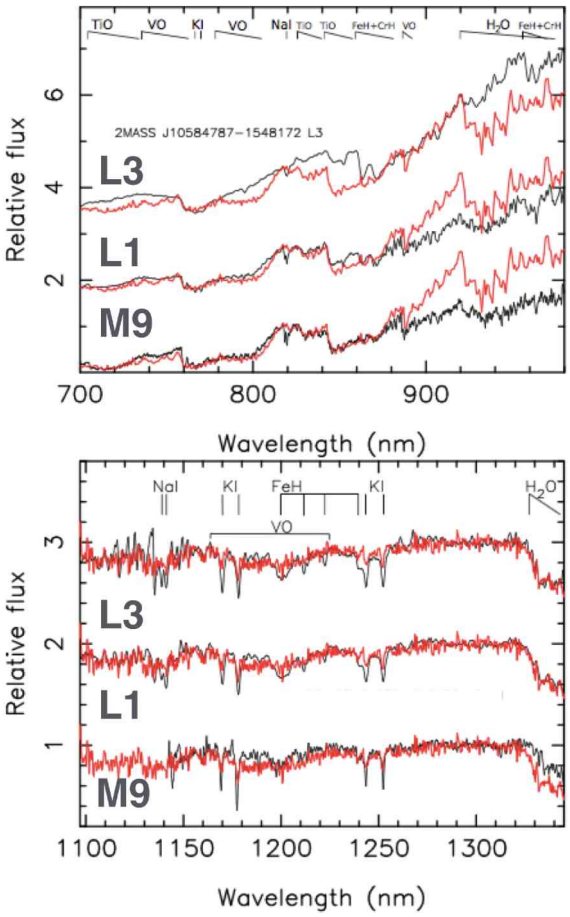

Figura 4: Combination of all spectroscopic data in optical and near-infrared of the faintest σ Orionis members, shown in red. The field high-gravity spectral standards are plotted as black lines. All spectra have the same wavelength resolution for a proper comparison. The most prominent features are labeled. Optical and near-infrared spectra are normalized to unity at 814-817.5 nm and 1.28-1.32 μm. The data are vertically shifted by a constant. Figure from Zapatero Osorio et al. (2017).

2007; Scholz et al., 2009, 2012, 2013; Mužić et al., 2011, 2012, 2014, 2015). At lower masses, below the 0.03 $M_\odot$ there is uncertainty in the initial mass function variations and its low-mass cut-off. Residual contamination, incompleteness, mass segregation and substantial uncertainties in the mass-luminosity relationship account among the factors that affect any assessment about the mass function shape at such low masses.

The case of the σ Orionis cluster (~3 Myr, ~400 pc) is representative. The most recent study of its mass function (Peña Ramírez et al., 2012) used about 400 sources to cover the cluster mass range 19-0.004 $M_\odot$ in an area of about 2800 arcmin^2, see Fig. 3. The discovery of 23 new sources as substellar members that gave hints of variations in the mass function below the 0.03 $M_\odot$ led to an observational effort concluded in Zapatero Osorio et al. (2017), where about the half of those new candidates were confirmed as young clusters members given its optical and near-infrared spectra as seen in Fig. 4. For the faintest cluster candidate members, the T-type sources identified in the cluster line of sight, the studies of Peña Ramírez et al. (2011, 2015) shows that none of the T-dwarfs is a possible σ Orionis member. Either planetary-mass objects with masses below ~4 M_{Jup} may not exist free-floating in the cluster, or they may lie at fainter near-infrared magnitudes than those of the targets (i.e., $H > 20.6$ mag), thus remaining unidentified to date.

Another observational constraint to the substellar formation scenarios looks for its dependence on star-forming environments. In that sense the work of Mužić et al. (2017) focusses on RCW38 (~1 Myr, ~1.7 kpc, ~300 sources), a dense environment (2500 pc^{-2}), twice denser than the Orion Nebular Cluster or 10 times denser than NGC1333. Their results are in agreement with the values found in other young star-forming regions, revealing no evidence that a combination of high stellar densities and the presence of numerous massive stars affect the formation efficiency of brown dwarfs and very-low-mass stars. An ongoing effort, under the same premise, is focussed in the young massive cluster NGC2244 (~2 Myr, ~1.6 kpc), located in the Rosette nebula (Mužić et al., 2019).

Broadly speaking, to obtain an initial mass function a luminosity function must be derived, using a mass-luminosity relation and applying the relevant corrections due to the dynamical evolution and multiplicity of the members. There are a series of caveats that arise in the process. In terms of the mass-luminosity relation, there is a direct dependence on the theoretical uncertainties and models are tied to a specific age, distance, and metallicity. The theoretical treatment of the low

mass is homogeneous, therefore claims about the accretion history affecting the early stellar evolution for ages less than 10 Myr is usually not taken into account (Baraffe et al., 2017). Effects such as rotation will inflate the radius determination and therefore modify the inferred luminosity value. Also at including magnetic activity, it can be produced cool spots reducing the T_{eff} and consequently the mass estimation.

Regarding corrections of dynamical evolution, effects such as mass segregation and loss of low-mass members can impact the mass function derivation, although usually it is not considered when dealing with very young environments. Deriving the luminosity function requires a large sample of clean members, deal with contaminants, completeness, and extinction plus it needs to understand the processes of conglomerate assembly, equilibration, and dissolution. Additionally, the source movements in the youngest environments should reflect the dominant conglomerate formation process. At this stage, it therefore critical to fully account the entire population of interest.

5. A wider view

Just until recently ultra-cool dwarf studies in substellar/stellar conglomerates (e.g., young star-forming regions, associations, young moving groups) have been mapped under the limitation of relatively small field coverage. Telescopes such as VISTA at Paranal, Chile have been able to map uniformly in the near-infrared vast regions of different star forming regions and open clusters with surveys such as Vista Variables de la Vía Láctea (eXtended) (Minniti et al., 2010) VVV(X) or the VISTA Star Formation Atlas (VISIONS) which is focused in the ultra-cool dwarf population of various star-forming complexes. When completed, VISIONS will be the most sensitive and complete near-infrared survey of local star formation and will feed the next generation of telescopes with new targets for star and planet formation studies. Alternative approaches such as the Dynamical Analysis of Nearby ClustErs (DANCE, Bouy et al., 2013) aimed at deriving a comprehensive and homogeneous census of the stellar and substellar content of a number of nearby (<1 kpc) young (<500 Myr) associations re-reducing in an uniform manner data from different facilities to increase spatial coverage offers combined multi-epoch deep wide field images.

In the last year, with the advent of Gaia DR2 data, the concept of a wider view mapping substellar/stellar conglomerates achieved a new level. For example in the Vela OB2 region (∼10 Myr, ∼336 pc), the first surveys with contoured X-ray data gave a selection of pre-main sequence stars with lithium detections (Pozzo et al., 2000). Studies in a larger area like the ones presented by Jeffries et al. (2014) and Sacco et al. (2015) shows evidence of a bimodal radial velocity distribution, product of a mixed population with a nearby structure. Last year only, using Gaia DR2 data, Franciosini et al. (2018) confirmed two populations separated ∼38 pc from each other along our line of sight. Beccari et al. (2018), in a 10 × 5 deg^2 field conclude that there are stars of the age of Vela OB2 plus four different subgroups. Cantat-Gaudin et al. (2018), have confirmed the subclustering, updated the mass budget of the conglomerate from ∼1000 $M_\odot$ to ∼2330 $M_\odot$, connect the complex with the IRAS Vela Shell as well as conclude that there is no presence of mass segregation effects. Even at lower masses (∼0.16 $M_\odot$) the work of Armstrong et al. (2018) using previously known low mass members in a small region of Vela OB2, designed a selection criteria that combine Gaia and 2MASS photometry, independently of any astrometric information, to identify low-mass stars detecting a widespread population across the whole area of the association. The authors claim that there are apparent differences in the spatial distributions of the low-mass and the high-mass OB populations, suggesting either that the structure and dynamics of these populations have evolved separately or that the initial mass function can vary considerably on small scales within a single association.

The Scorpius-Centaurus OB2 region (∼5-11 Myr, ∼120-160 pc) is another conglomerate where a wider view has given us exciting results. Given its large extension (∼2000 deg^2), this complex of B-type stars is usually referred to as an association. To derive a complete mass function in such a vast region is a challenge. It is separated in the Upper Scorpius, Upper Centaurus Lupus and Lower Centaurus Crux regions. Nevertheless, the work of Damiani (2018), presents a spatial density map indicating the boundaries of the traditional conglomerates known in Scorpius-Centaurus OB2 plus enhanced low-density areas. This gives a new picture of the region with a series of new clusters identified within the main conglomerate(s). Authors conclude that kinematically diffuse groups are older whereas compact groups are younger with a significant age spread among the groups. At lower masses (∼0.02 $M_\odot$) in Lower Centaurus Crux, the study of Goldman et al. (2018) add about 1800 new intermediate- and low-mass young stellar objects and brown dwarfs, that escaped identification until Gaia DR2. The discoveries will add up to a total mass of about 700 $M_\odot$ in the complex, grouped the new members in four denser subgroups, which have an increasing age from 7 to 10 Myr, surrounded by "free-floating" young stars with mixed ages. In the case of the Upper Scorpius region, the survey of Luhman (2018) adds more than a thousand of additional low mass candidate members to the region. The census now encompasses a large portion of early L dwarfs, excluding the ρ Ophiuchus star-forming region.

Finally, one of the most studied star-forming regions, the Orion complex, has also been recently revisited with a wider perspective. The study of Großschedl et al. (2018) uses the Gaia DR2 distances of about 700 mid-infrared selected young stellar objects in the benchmark giant molecular cloud Orion A to infer its 3D shape and orientation. These authors find a denser and enhanced star-forming (bent) *head*, and a lower density and star-formation quieter ∼75 pc long *tail* across the area studied. With this results, Großschedl et al. (2018) find that the current cloud and young stellar object masses toward the *tail* can be underestimated by about 30 % to 40 % under the common assumption of a single constant distance to Orion A. Also very recently, Briceno et al.

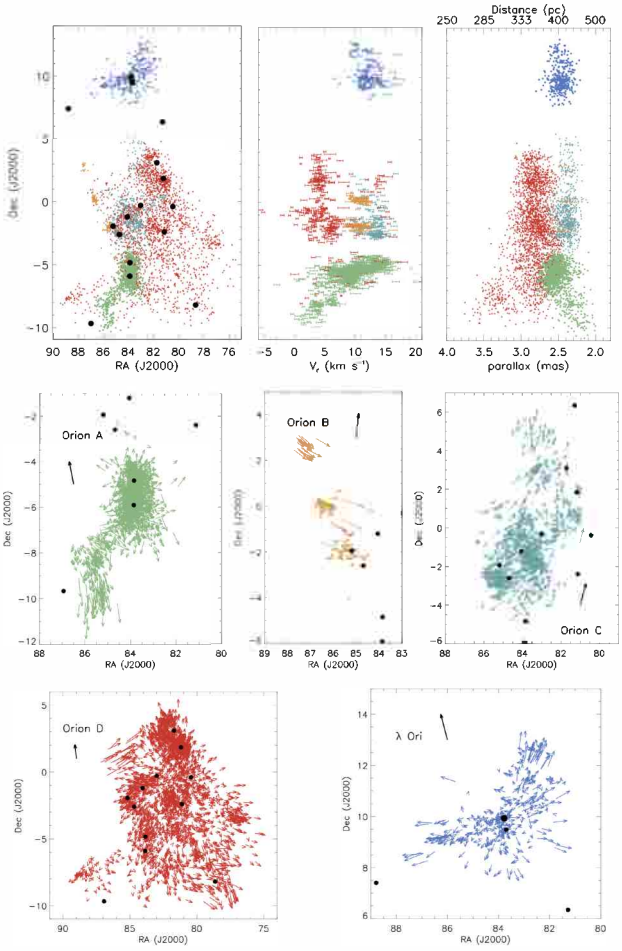

Figura 5: Distribution of stars identified as members Orion A (green), Orion B (orange), Orion C (cyan), Orion D (red), and λ Ori (blue). Proper motions of the stars identified as members of the complex, relative to the average proper motion in each structure are also shown. The length of the vectors correspond to the motion of over 1.2 Myr. Figure from Kounkel et al. (2018).

(2018) pursued a vast photometric study ($\sim$180 deg^2) across the Orion OB1 association, complemented with extensive follow up spectroscopy. They mapped and characterized the off-cloud, low-mass, pre-main sequence populations uniformly. Their main conclusion is that the spatial distribution of the young stars across Orion OB1 is far from uniform, but rather has a significant degree of substructure. This feature has also been acknowledged in the work of Kounkel et al. (2018). Using together physical information from Gaia DR2 and the Apache Point Observatory Galactic Evolution Experiment (APOGEE Gunn et al., 2006; Blanton et al., 2017) spectrograph, the authors gave an unprecedented 6-dimensional view of the entire Orion complex as can be seen in Fig.5. It was possible the identification of spatially and kinematically distinct groups of young stellar objects with ages ranging from 1 to 12 Myr. Among other results, two separate populations towards OriOB1 (d, RV) were identified: Orion C (3 formation epochs, 2-10 Myr, σ Orionis associated) and Orion D. Both spans the full extent of the OB1ab region. There were also found several peculiar substructures, the radial expansion of λ Orionis was confirmed as well as the movement of various groups in Orion B towards NGC 2024.

Agradecimientos: I gratefully acknowledge the local organizers and staff members of the Second Binational Meeting AAA-SOCHIAS meeting for all the work done. I also acknowledge CONICYT PAI Concurso Nacional de Inserción en la Academia, Convocatoria 2016 Folio PAI79160052.

Referencias

Allard F., 2014, M. Booth, B.C. Matthews, J.R. Graham (Eds.), *Exploring the Formation and Evolution of Planetary Systems*, *IAU Symposium*, vol. 299, 271–272
Allard F., Homeier D., Freytag B., 2012, Philosophical Transactions of the Royal Society of London Series A, 370, 2765
Alves J., Bouy H., 2012, A&A, 547, A97
Alves de Oliveira C., et al., 2013, A&A, 549, A123
Apai D., et al., 2017, Science, 357, 683
Ardila D., Martín E., Basri G., 2000, AJ, 120, 479
Armstrong J.J., Wright N.J., Jeffries R.D., 2018, MNRAS, 480, L121
Baraffe I., Chabrier G., 2018, A&A, 619, A177
Baraffe I., et al., 1998, A&A, 337, 403
Baraffe I., et al., 2015, A&A, 577, A42
Baraffe I., et al., 2017, A&A, 597, A19
Barrado y Navascués D., et al., 2007, ApJ, 664, 481
Bate M.R., Bonnell I.A., Bromm V., 2002, MNRAS, 332, L65
Bate M.R., Bonnell I.A., Bromm V., 2003, MNRAS, 339, 577
Bayo A., et al., 2011, A&A, 536, A63
Beccari G., et al., 2018, MNRAS, 481, L11
Best W.M.J., et al., 2017, ApJ, 837, 95
Best W.M.J., et al., 2018, ApJS, 234, 1
Bihain G., et al., 2009, A&A, 506, 1169
Blanton M.R., et al., 2017, AJ, 154, 28
Bonnell I.A., Clark P., Bate M.R., 2008, MNRAS, 389, 1556
Bouy H., et al., 2013, A&A, 554, A101
Briceno C., et al., 2018, arXiv e-prints
Burgess A.S.M., et al., 2009, A&A, 508, 823
Caballero J.A., et al., 2007, A&A, 470, 903
Cantat-Gaudin T., et al., 2018, arXiv e-prints
Chabrier G., 2005, E. Corbelli, F. Palla, & H. Zinnecker (Ed.), *The Initial Mass Function 50 Years Later*, *Astrophysics and Space Science Library*, vol. 327, 41
Chambers K.C., et al., 2016, arXiv e-prints
Chiang P., Chen W.P., 2015, ApJL, 811, L16
Crossfield I.J.M., et al., 2014, Nature, 505, 654
Damiani F., 2018, A&A, 615, A148
de Wit W.J., et al., 2006, A&A, 448, 189
Dieterich S.B., et al., 2018, ApJ, 865, 28
Esplin T.L., et al., 2017, AJ, 154, 46
Franciosini E., et al., 2018, A&A, 616, L12
Gagné J., Faherty J.K., 2018, ApJ, 862, 138
Gaia Collaboration, et al., 2018, A&A, 616, A1
Geers V., et al., 2011, ApJ, 726, 23
Goldman B., et al., 2018, ApJ, 868, 32
Goodwin S.P., Whitworth A.P., Ward-Thompson D., 2004, A&A, 414, 633
Großschedl J.E., et al., 2018, A&A, 619, A106
Gunn J.E., et al., 2006, AJ, 131, 2332
Hester J.J., et al., 1996, AJ, 111, 2349

Hillenbrand L.A., Hoffer A.S., Herczeg G.J., 2013, AJ, 146, 85
Ingraham P., et al., 2014, ApJ, 782, 8
Jao W.C., et al., 2018, ApJL, 861, L11
Jeffries R.D., et al., 2014, A&A, 563, A94
Kounkel M., et al., 2018, AJ, 156, 84
Lodieu N., et al., 2018, MNRAS, 473, 2020
Lucas P.W., et al., 2001, MNRAS, 326, 695
Luhman K.L., 2013, ApJL, 767, L1
Luhman K.L., 2018, AJ, 156, 271
Luhman K.L., Esplin T.L., Loutrel N.P., 2016, ApJ, 827, 52
Luhman K.L., et al., 2006, ApJ, 647, 1180
MacDonald J., Gizis J., 2018, MNRAS, 480, 1711
Minniti D., et al., 2010, NewA, 15, 433
Moraux E., et al., 2003, A&A, 400, 891
Moraux E., et al., 2007, A&A, 471, 499
Mužić K., et al., 2011, ApJ, 732, 86
Mužić K., et al., 2012, ApJ, 744, 134
Mužić K., et al., 2014, ApJ, 785, 159
Mužić K., et al., 2015, ApJ, 810, 159
Mužić K., et al., 2017, MNRAS, 471, 3699
Mužić K., et al., 2019, Apj. Submitted
Padoan P., Nordlund Å., 2004, ApJ, 617, 559
Peña Ramírez K., Béjar V.J.S., Zapatero Osorio M.R., 2016, A&A, 586, A157
Peña Ramírez K., Zapatero Osorio M.R., Béjar V.J.S., 2015, A&A, 574, A118
Peña Ramírez K., et al., 2011, A&A, 532, A42
Peña Ramírez K., et al., 2012, ApJ, 754, 30
Pozzo M., et al., 2000, MNRAS, 313, L23
Reipurth B., Clarke C., 2001, AJ, 122, 432
Reylé C., 2018, A&A, 619, L8
Sacco G.G., et al., 2015, A&A, 574, L7
Scholz A., et al., 2009, ApJ, 702, 805
Scholz A., et al., 2012, ApJ, 744, 6
Scholz A., et al., 2013, ApJ, 775, 138
Scholz R.D., Bell C.P.M., 2018, Research Notes of the American Astronomical Society, 2, 33
Slesnick C.L., Carpenter J.M., Hillenbrand L.A., 2006, AJ, 131, 3016
Suárez G., et al., 2017, AJ, 154, 14
Suenaga T., et al., 2014, PASJ, 66, 33
Weights D.J., et al., 2009, MNRAS, 392, 817
Whitworth A.P., Zinnecker H., 2004, A&A, 427, 299
Zapatero Osorio M.R., Béjar V.J.S., Peña Ramírez K., 2017, ApJ, 842, 65
Zapatero Osorio M.R., et al., 2000, Science, 290, 103

Star formation at high redshift

P. FFibla[1], S. Bovino[1], R. Riaz[1], V.B. Díaz[1], C. Olave[1], S. Vanaverbeke[2] & D.R.G. Schleicher[1]

[1] *Departamento de Astronomía, Universidad de Concepción, Concepción, Chile*
[2] *Centre for mathematical Plasma-Astrophysics, Department of Mathematics, KU Leuven, Heverlee, Belgium*

Contact / pfibla@udec.cl

Resumen / La importancia del uso de modelos químicos detallados para comprender la formación estelar a baja metalicidad ha sido ampliamente reconocida, como se resalta en recientes investigaciones.
Presentamos aquí simulaciones tridimensionales hidrodinámicas para formación estelar. Nuestro objetivo es explorar el efecto del enfriamiento de la línea de metal sobre la termodinámica del proceso de formación estelar. Exploramos el efecto de cambiar la metalicidad del gas desde $Z/Z_\odot = 10^{-4}$ hasta $Z/Z_\odot = 10^{-2}$. Además, exploramos las implicancias de utilizar el patrón de abundancia observacional de una estrella CEMP-no, las cuales han sido propuestas como estrellas de segunda-generación.
Para lograr nuestro objetivo, modelamos la micro-física utilizando el paquete público de astroquímica KROME, usando una red química que incluye dieciséis especies químicas (H I, H II, H^-, He I, He II, He III, e^-, H_2 I, H_2 II, C I, C II, O I, O II, Si I, Si II, and Si III). Juntamos KROME con el código basado en *Smoothed-particle hydrodynamics* (SPH) tridimiensional hidrodinámico GRADSPH. En este contexto, investigamos el colapso de una nube enriquecida en metales, explorando el proceso de fragmentación y formación estelar.
Encontramos que la metalicidad tiene un claro impacto en la termodinámica del colapso, permitiendo que la nube alcance la temperatura de piso del CMB a una metalicidad $Z/Z_\odot = 10^{-2}$, la cual concuerda con trabajos anteriores. Además, encontramos que al utilizar el patrón de abundancia de la estrella Keller, el comportamiento termodinámico de la nube es bastante similar a aquellas simulaciones con metalicidad $Z/Z_\odot = 10^{-2}$, debido a la alta presencia de carbón. Mientras solo el enfriamiento de la línea de metal sea considerado, los resultados obtenidos confirman el límite de metalicidad propuesto en trabajos anteriores, el cual es muy probable que regule los primeros episodios de fragmentación y potencialmente determine las masas de los conjuntos de estrellas resultantes. Para un modelado completo del IMF y su evolución, notamos también que el enfriamiento producido por el polvo necesita ser considerado.

Abstract / The importance of detailed chemical models to understand low-metallicity star formation is widely recognized, as reflected also in recent investigations. We present here a three-dimensional hydrodynamical simulation for star formation. Our aim is to explore the effect of the metal-line cooling on the thermodynamics of the star-formation process. We explore the effect of changing the metallicity of the gas from $Z/Z_\odot = 10^{-4}$ to $Z/Z_\odot = 10^{-2}$. Furthermore, we explore the implications of using the observational abundance pattern of a CEMP-no star, which have been considered to be the missing second-generation stars.
In order to pursue our aim, we modeled the microphysics by employing the public astrochemistry package KROME, using a chemical network which includes sixteen chemical species (H I, H II, H^-, He I, He II, He III, e^-, H_2 I, H_2 II, C I, C II, O I, O II, Si I, Si II, and Si III). We couple KROME with the fully three-dimensional, smoothed-particle hydrodynamics (SPH) code GRADSPH. With this framework we investigate the collapse of a metal-enhanced cloud, exploring the fragmentation process and the formation of stars.
We found that the metallicity has a clear impact on the thermodynamics of the collapse, allowing the cloud to reach the CMB temperature floor for a metallicity $Z/Z_\odot = 10^{-2}$, which is in agreement with previous works. Moreover, we found that adopting the abundance pattern given by the Keller star, the thermodynamics behavior is very similar to simulations with a metallicity of $Z/Z_\odot = 10^{-2}$, due to the high carbon abundance. As long as only metal line cooling is considered, our results support the metallicity threshold proposed by previous works, which will very likely regulate the first episode of fragmentation and potentially determine the masses of the resulting star clusters. For a complete modeling of the IMF and its evolution, we expect that also dust cooling needs to be taken into account.

Keywords / cosmology: early universe, stars: formation, stars: carbon, stars: Population III, stars: abundances

1. Introduction

The birth of the very first stars in the Universe must have occurred at redshifts $z \sim 15 - 30$ in dark matter mini-halos with $\sim 10^6$ solar masses (e.g., Haiman et al. (1996), Tegmark et al. (1997)). Such mini-halos were composed from a primordial gas of a few chemical species where the main coolant was molecular hydrogen (Galli & Palla (1998)). Thus, the expected temperature for these primordial clouds is about 300 K, which is thirty times greater than the temperature in typical present-day clouds. The Jeans mass associated with these clouds is therefore greater when compared to their present-day counterparts, as well as the mass of the collapsing objects.
From hydrodynamical simulations, it has been shown

that several stars could be born from a single dark matter mini-halo, contrary to past results that pointed towards the formation of a single star per dark matter mini-halo. Moreover, the clear impact of some chemical species in the star formation process has been established. In particular, Bromm et al. (2001) proposed that the presence of metals triggers fragmentation in metal deficient primordial clouds up to a metallicity $Z/Z_o = 10^{-3.5}$, which has been confirmed by recent investigations, e.g, Bovino et al. (2014), Safranek-Shrader et al. (2014). But, although the qualitative picture of the formation of the Pop III.1 stars is rather well known, how the star formation mode shifts from extremely massive stars with 100-1000 solar masses to present-day stars is still unclear. The development of surveys searching for the most metal-deficient stars has shown that the ratio between oxygen, carbon and nitrogen is enhanced compared to iron for around one-quarter of all the known stars with [Fe/H] < -2.0 (Beers & Christlieb (2005)). These particular stars are now collectively known as carbon-enhanced metal poor (CEMP) stars, and arbitrarily have been defined to have [C/Fe] $> +0.7$. Furthermore, subsequent studies have grouped the stars falling into the CEMP-definition into four different subgroups on the basis of the abundances of their electron-capture associated species. The CEMP-s stars show an overabundance of chemical species produced by the s-process, the CEMP-r stars show an overabundance of chemical species produced by the r-process, the CEMP-s/r stars show an overabundance of elements related to both processes, while the CEMP-no stars do not show an overabundance of elements, neither related to the s-process or related to the r-process.

Abundances for the s-group are well explained by means of mass transfer in a binary system from an AGB star to a secondary smaller star which is the one observed today. For the CEMP-no group the panorama is a bit more complicated as several progenitors have been proposed by different authors. As has been found by Hansen et al. (2016), CEMP-no stars seem to be bona-fide, second-generation stars. This has been proposed on the basis of multiple observational findings (e.g., Cooke et al. (2011), Cooke et al. (2012)), Carollo et al. (2012), Yoon et al. (2016), Hansen et al. (2016)).

This paper is structured as follows. Sec. 2. describes the computational scheme employed in our simulations, as well as the initial conditions for all our models and its features. Sec. 3. contains a description from our results, while our conclusions are presented in Sec. 4..

2. Methods

Simulations were carried out by combining two different codes. One was GRADSPH, developed by Vanaverbeke et al. (2009), a parallel fully three-dimensional TREESPH code designed to evolve self-gravitating astrophysical fluids. The other one was KROME, developed by Grassi et al. (2014), a novel astrochemical open-source package to treat the microphysics of the collapse, such as the temperature and the evolution of the chemical species included in the networks used. Such framework has been already used by Riaz et al. (2018c), to investigate primordial star formation and its binaries properties. GRADSPH has been further tested on star formation and their evolution in Riaz et al. (2018a) and Riaz et al. (2018b).

We perform several one-zone model simulations using KROME, varying the initial metallicity of the cloud from a primordial case to $Z/Z_\odot = 10^{-2}$, including the one given by the observational pattern of the Keller star (Keller et al., 2014), assuming the solar metallicity given by Asplund et al. (2009). Likewise, hydrodynamical simulations were carried out assuming a primordial abundance and the Keller star abundance pattern by coupling KROME with GRADSPH (the results from the later are still in preparation). All simulations were started assuming an spherical cloud, at the same redshift $z = 15.0$, an initial temperature T = 300 K, and following Bovino et al. (2014) an initial density $\rho = 10^{-22}$ g $\cdot$ cm^{-3}, from which, in order to assure the gravitational collapse of the clouds, the initial mass was set as M $= 2.912 \times 10^6$ M$_\odot$, with a radius R $= 2.4 \times 10^{20}$ cm. Thus, following the criteria from Riaz et al. (2018c), we get a mass resolution $M_{\rm resolution} = 529\ M_\odot$. Moreover, we defined two groups of simulations based on their chemical pattern, labeled as p-runs, for the one using a primordial network which includes nine chemical species: H I, H II, He I, He II, He III, e$^-$, H_2 I, H_2 II, and H^-; and the m-runs, for the ones using a metal-enriched network which includes the already named species for the p-run, plus the metal-species C I, C II, O I, O II, Si I, Si II, and Si III. All species were initialized in number densities, with a value of almost zero ($n_X = 10^{-40}$ cm^{-3}), with the exception of H I, He I, H_2 I, H II, e$^-$, C II (carbon was assumed as totally ionized), O I, and Si I. The non-metal species were initialized in number densities as $n_{\rm H} = 44.81$ cm^{-3}, $n_{\rm He} = 3.72$ cm^{-3}, $n_{\rm H_2} = 2.98 \times 10^{-2}$ cm^{-3}, and $n_{\rm HII} = 4.90 \times 10^{-5}$ cm^{-3}. The metal species were computed on-the-fly by KROME for models met2 ($Z/Z_\odot = 10^{-2}$) and met3 ($Z/Z_\odot = 10^{-3}$) and scaled according to their metallicities, in the Keller model the reported observed abundances (Keller et al. (2014)) were used. The initial abundance of the electrons was computed on-the-fly by KROME for all models, such that the positive charge of the species was balanced.

3. Results

Fig. 1 shows the density profile of the temperature evolution for different cloud models resulting from the one-zone simulations. The dotted line represents the primordial model, the dotted-dashed line the met3 model, the dashed line the met2 model, and the solid line the Keller model. The red bottom line represents the CMB floor temperature given by the initial redshift of the simulations. The temperature is given in K, while the number density in cm^{-3}. From the figure, the enhancement in the cooling rate for the cloud is evident, as even for a slight presence of metals as $Z/Z_\odot = 10^{-3}$ the temperature of the cloud drops drastically compared to the primordial model at densities of $\sim 10^3$ cm^{-3}. Moreover, for a metallicity $Z/Z_\odot = 10^{-2}$ the cloud is already able to reach the CMB floor temperature, in agreement with

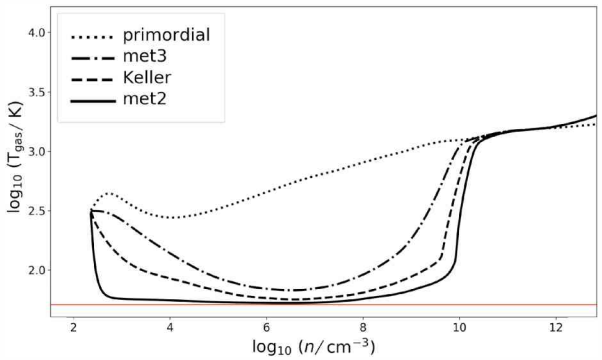

Figure 1: Phase diagram log(T) vs log(n) of prestellar clouds with different chemical species abundances. The dotted line represents the primordial model, the dotted-dashed line the met3 model, the dashed line the met2 model, and the solid line the Keller model. The red bottom line represents the CMB floor temperature given by the initial redshift of the simulations.

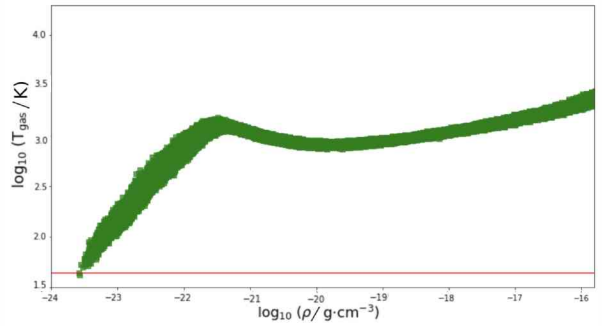

Figure 2: Phase diagram log(T) vs log(n) of the prestellar cloud of the primordial model resulting from the hydrodynamical runs. The red bottom line represents the CMB floor temperature given by the initial redshift of the simulations. Note the plateau at high densities.

previous results. Further, the temperature evolution of the Keller model is very similar to the met2 model, due to the high presence of carbon. Fig. 2 shows the density profile of the temperature evolution for the primordial model resulting from the hydrodynamical runs. The red solid bottom line represents the CMB floor temperature.

4. Discussion

We have presented the coupling between KROME and GRADSPH (Fig. 2), as well as results using only the former (Fig. 1). By looking at Fig. 1 the enhancement in the cooling of the clouds it is evident, which is consistent with previous results (e.g., Bovino et al. (2014)). Further, the results from the one-zone runs are in agreement with the metallicity threshold proposed by Bromm et al. (2001), showing that for a metallicity $Z/Z_{\odot} = 10^{-2}$, clouds are already able to reach the CMB floor temperature. In addition, the high presence of ionized carbon and neutral oxygen in the Keller model allows to the cloud to follow closely the temperature evolution of the met2 model. This reflects their major contribution as cooling channels at high redshift star-forming conditions, which is in agreement with previous results.

In order to improve the accuracy of the results generated by the simulation it is necessary to include further physical processes such as the presence of a UV radiation background or the treatment of a dust grain distribution. The former has been proven to have a lesser impact on the thermodynamics of the collapse of a cloud, but this need to be confirmed by further studies. The latter has been shown to have major impact of the thermodynamics of a collapsing cloud by several authors, showing its great impact as a catalyzer for several chemical reactions that are impossible without the presence of a third-body, or acting as a shield for the external radiation that hits the cloud.

Acknowledgements: The simulations were performed with resources provided by the Kultrun Astronomy Hybrid Cluster via the projects Conicyt Programa de Astronomia Fondo Quimal 2017 (project code QUIMAL170001), Conicyt PIA (project code ACT172033), and Fondecyt Iniciacion (project code 11170268). Powered@NLHPC: This research was partially supported by the supercomputing infrastructure of the NLHPC (ECM-02). The author thanks the referee for his useful and pertinent comments. DRGS, SB, VD, CO and FF thank for funding via CONICYT PIA ACT172033. DRGS and SB acknowledge funding through CONICYT project Basal AFB-170002. RR, CO, FF and DRGS thank for funding through the 'Concurso Proyectos Internacionales de Investigación, Convocatoria 2015' (project code PII20150171). DRGS, SB and VBD thank for funding via CONICYT PIA ACT172033. FF and VBD thank for funding through Fondecyt regular (project code 1161247). VBD thanks to Conicyt for financial support on her master studies (CONICYT-PFECHA/MagísterNacional/2017-22171293).

References

Asplund M., et al., 2009, ARA&A, 47, 481
Beers T.C., Christlieb N., 2005, ARA&A, 43, 531
Bovino S., et al., 2014, ApJL, 790, L35
Bromm V., et al., 2001, MNRAS, 328, 969
Carollo D., et al., 2012, ApJ, 744, 195
Cooke R., Pettini M., Murphy M.T., 2012, MNRAS, 425, 347
Cooke R., et al., 2011, MNRAS, 412, 1047
Galli D., Palla F., 1998, A&A, 335, 403
Grassi T., et al., 2014, MNRAS, 439, 2386
Haiman Z., Thoul A.A., Loeb A., 1996, ApJ, 464, 523
Hansen T.T., et al., 2016, A&A, 586, A160
Keller S.C., et al., 2014, Nature, 506, 463
Riaz R., Vanaverbeke S., Schleicher D.R.G., 2018a, A&A, 614, A53
Riaz R., Vanaverbeke S., Schleicher D.R.G., 2018b, MNRAS, 478, 5460
Riaz R., et al., 2018c, MNRAS, 479, 667
Safranek-Shrader C., Milosavljević M., Bromm V., 2014, MNRAS, 438, 1669
Tegmark M., et al., 1997, ApJ, 474, 1
Vanaverbeke S., et al., 2009, Computer Physics Communications, 180, 1164
Yoon J., et al., 2016, ApJ, 833, 20

Correlational study between model variables and observable quantities of magnetar-powered H-rich supernovae

N.P. Maffione[1,2], M. Orellana[1,2] & M.C. Bersten[3,4,5]

[1] *Laboratorio de Procesamiento de Señales Aplicado y Computación de Alto Rendimiento, Sede Andina, UNRN, Argentina*
[2] *Consejo Nacional de Investigaciones Científicas y Técnicas, Argentina*
[3] *Instituto de Astrofísica de La Plata, CONICET–UNLP, Argentina*
[4] *Kavli Institute for the Physics and Mathematics of the Universe, The University of Tokyo, Japan*
[5] *Facultad de Ciencias Astronómicas y Geofísicas, UNLP, Argentina*

Contact / npmaffione@unrn.edu.ar

Resumen / Aún no ha sido posible identificar la presencia de un magnetar en una explosión de supernova (SN). Sólo conocemos piezas en un escenario desafiante que nos presenta interrogantes sumamente trascendentes. Si tuviéramos un magnetar con una velocidad de rotación suficientemente alta en una dada SN, este debería contribuir a la misma con una fuente adicional de energía. Esta fuente podría incluso superar la energía liberada por los mecanismos más usuales, dando lugar al nacimiento de una SN superluminosa.
Recientemente se ha construido una grilla de modelos hidrodinámicos (con un tratamiento simple de los procesos radiativos) para un progenitor rico en hidrógeno y masa $M_{ZAMS} = 15\ M_\odot$. Las curvas de luz (LC por sus siglas en inglés) obtenidas muestran evidencia indirecta de las propiedades del magnetar. Por medio de un análisis correlacional sencillo investigamos la existencia de relaciones entre las variables usadas para definir los modelos (energía inicial de rotación y tiempo de frenado) y cantidades observables derivadas de las LCs. Esta clase de estudios podrían ayudar a definir estrategias para la búsqueda de magnetares en SNs con buen seguimiento fotométrico. En este trabajo presentamos algunos resultados preliminares.

Abstract / Up to date, it has not been possible to identify the presence of a magnetar in a supernova (SN) explosion. We know only pieces of a challenging scenario that poses ahead extremely important questions. If a magnetar with a sufficiently high rotation speed is actually present in a given SN, it would contribute as an additional energy source. That power source may overcome the energy released by otherwise usual mechanisms, so a magnetar could give birth to a superluminous SN.
A grid of hydrodynamic models (with a simple treatment for radiative processes) has been recently computed for a hydrogen-rich progenitor of $M_{ZAMS} = 15\ M_\odot$. The corresponding light curves (LCs) show indirect evidence of the properties of the magnetar. By means of a simple correlational analysis, we investigate the existence of a correspondence between the variables used to define the models (initial rotation energy and spin-down timescale) and the observable quantities derived from the LCs. This type of analyisis might help to define search strategies to obtain evidence of the magnetar engine working into SNe, with good photometric data. Herein we present some preliminary results.

Keywords / supernovae : general — stars : magnetars — methods : statistical

1. Introduction

It has been suggested that some supernovae (SNe) may be powered by a magnetar formed at the moment of the explosion. The additional energy provided by the magnetar may result in an extra bright light curve (LC). In the context of hydrogen-rich (H-rich) progenitors, magnetar powered LCs have not been deeply studied in the literature (Bersten & Benvenuto, 2016; Orellana et al., 2018, and references therein). We investigate here the correlation matrices between intrinsic properties (parameterized with model variables) of an hypothetical magnetar and plausible observable quantities from the LC. Our goal is to test the connection between these two types of data.

2. Numerical model and model variables

A grid of hydrodynamic models (with a simple treatment for radiative processes) has been computed for an H-rich progenitor, with the following characteristics: (a) main sequence mass of 15 $M_\odot$ consistently evolved until core collapse by Nomoto & Hashimoto (1988), (b) the pre-SNe model shows a transition between H-rich to He-rich at a layer of $\simeq 3.2\ M_\odot$, (c) the pre-explosion radius is 500 $R_\odot$ and (d) the surface metallicity is $Z \sim 0.02$. To parameterize the magnetar source, Orellana et al. (2018) used the spin-down timescale (t_p) and the initial rotation energy (E_{rot}) as the model free parameters (hereinafter MFPs). In Fig. 1 we present the corresponding bolometric LCs. In the presence of a magnetar, an early short phase of increasing luminosity precedes the maximum (in some cases, the maximum is a plateau). Ac-

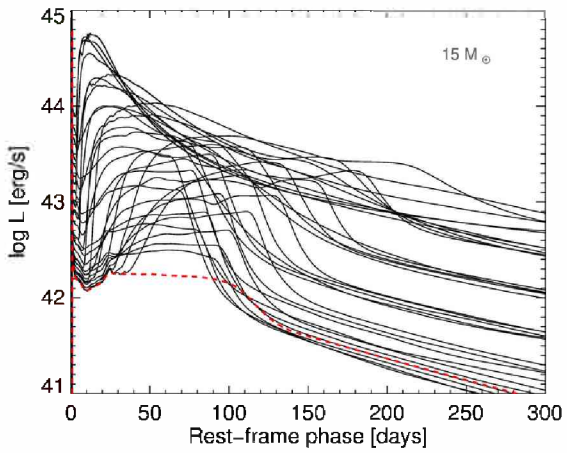

Figure 1: Bolometric LCs for the grid of hydrodynamic models. For comparison, we show the same SN model without a magnetar in red dashed line.

cording to these results, the LC is much steeper during this rise than in the case without the magnetar, producing a larger luminosity variation. This seems to be a unique characteristic of the magnetar models that can help us to identify such power source.

3. Definition of observable quantities

For a quantitative study of the LCs we follow Orellana et al. (2018) and use a set of own-defined quantities obtained from the bolometric LCs (see an example in Fig. 2). This set is composed of two quantities introduced in that paper, namely (a) $\log(L_{max})$: the mean value of the local maxima produced after the shock peak and (b) Δ_t: the time interval over which $\log(L) > \log(L_{max}) - 0.2$ dex (or the plateau duration). We introduce three new quantities, measured in the same plane: (i) $d_{min-SBO}$: the normalized distance of the minimum point after the shock break-out (where the normalization is with respect to the scale of the plot and the origin in time is associated with the energy injection that produce the SN), (ii) $d_{ini-plateau}$: the normalized distance of the initial point of Δ_t and (iii) $d_{min-ini}$: the normalized distance between the minimum point after the shock break-out and the initial point of the plateau phase. Whether these are plausible observables depends strongly on the photometric follow up of the SN.

Now we are in position to study the existence of connections among the MFPs and our plausible observables (POs). In next section we compute the corresponding Spearman and Pearson correlation matrices.

4. Correlation matrices

The Spearman correlation matrix (indicative of a monotonic relationship) among the MFPs: t_p and E_{rot} and the set of POs presents the largest values for the following subset of parameter-observable (MFP-PO) pairs: t_p with $d_{min-ini}$ (0.92) and E_{rot} with Δ_t (-0.85) and

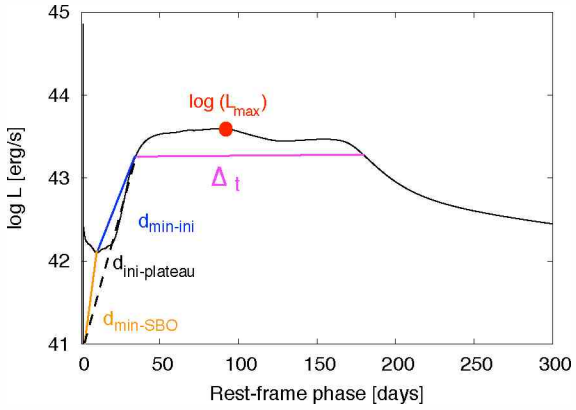

Figure 2: Definition of plausible observables. (a) In red, $\log(L_{max})$: the mean value of the local maxima produced after the shock peak and (b) in purple, Δ_t: which characterizes its duration. Also, the newly defined (i) in orange, $d_{min-SBO}$: the normalized distance of the minimum point after the shock break-out; (ii) in black dashed line, $d_{ini-plateau}$: the normalized distance of the initial point of the plateau phase (defined by the intersection of Δ_t with the light curve) and (iii) in blue, $d_{min-ini}$: the normalized distance between the minimum point after the shock break-out and the initial point of the plateau phase.

$\log(L_{max})$ (0.88) and $d_{min-SBO}$ (0.89) and $d_{ini-plateau}$ (0.84). Notice that a negative Spearman coefficient means a monotonic function that reverse order, while a positive coefficient preserves order. All Spearman coefficients are rather large which means strong evidence of a monotonic function behind the MFP-PO pairs from the subset.

In Fig. 3 we present the Pearson correlation matrix (indicative of a linear relationship) for the complete set of parameters and observables, to visualize if there is further indication of a stronger dependence (i.e. not only monotonic but linear) among such quantities. Blue and red pies (below the main diagonal) correspond to a positive and negative slope, respectively. Scatter plots (above the main diagonal) are also included in order to visualize the actual distribution of the data. The aforementioned subset of MFP-PO pairs (i.e. those with the largest values of the Spearman coefficient) are framed in the figure, with their Pearson coefficient also included. Rather large (absolute) values of the Pearson coefficient are observed for almost every pair from the selected subset.

Notice the strong linear dependence (according to their Pearson coefficient, ~ 1) between two of the POs: $\log(L_{max})$ and $d_{ini-plateau}$ which means that they can be used interchangeably.

4.1. Connecting the model variables with the observable quantities

From the subset of MFP-PO pairs, we kept those with the largest Spearman and/or Pearson coefficients. For instance, the pair (t_p, $d_{min-ini}$) has the largest Spearman coefficient (0.92) and the only one from the sample that includes the MFP t_p and has an (absolute)

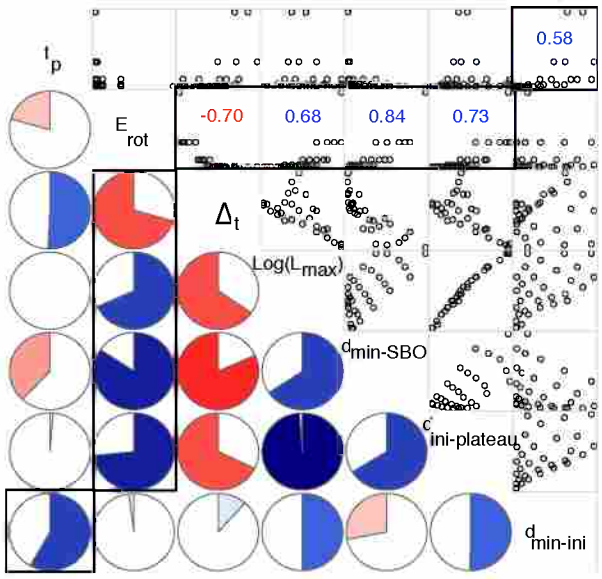

Figure 3: Pearson correlation matrix (indicative of a linear relationship) for the complete set of parameters and observables under study. The subset of parameter-observable pairs with the largest values of the Spearman coefficient is framed and the value of their Pearson coefficient is also included.

value of the Spearman coefficient larger than 0.7. On the other hand, the MFP E_{rot} has large values of the Spearman coefficient for many of the selected POs, being the largest (0.89), the one associated with the pair (E_{rot}, $d_{min-SBO}$). Their Pearson coefficient is also large ($\sim$ 0.84, see Fig. 3). However, there is some level of unwanted degeneracy in their relationship as it can be seen from the middle panel of Fig. 4, where we present two candidates for suitable MFP-PO pairs to re-parameterize the grid of hydrodynamic models (Section 2.). The second largest Spearman coefficient (0.88) is for (E_{rot}, $\log(L_{max})$). The latter also presents a rather large Pearson coefficient, $\sim$ 0.68. The bottom panel of Fig. 4 shows the behavior of such election in re-parameterizing the grid. There is no sign of degeneracy, thus probing to be the most suitable MFP-PO pair.

5. Conclusions and forthcoming research

By means of a correlational analysis we found the existence of a possible one-to-one correspondence (with rather large Spearman and Pearson coefficients) between the free parameters used to define the models (spin-down timescale and initial rotation energy of the magnetar) and a couple of own-defined (and plausible observable) quantities. Such pair of observable counterparts extracted from the synthetic light curves is given by $d_{min-ini}$ and $\log(L_{max})$. The former component can be difficult to observe, though. Then, we are evaluating the possibility to replace that observable with another one easier to detect.

Acknouledgements: This research was partially supported by PI2017-40B531 of Universidad Nacional de Río Negro.

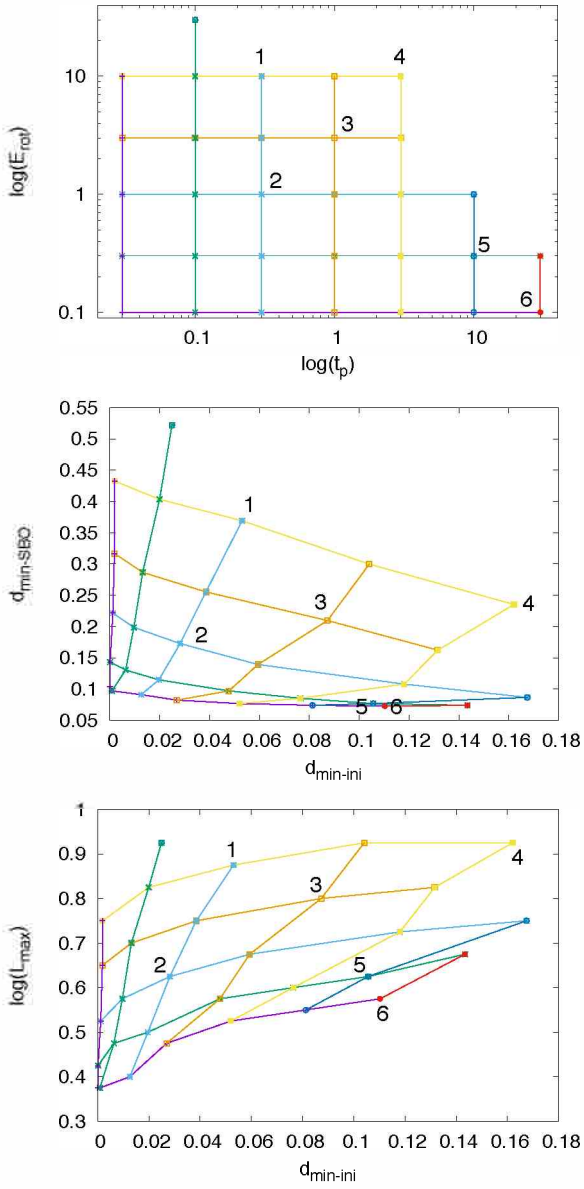

Figure 4: Examples of parameter-observable pairs. Top panel: grid of hydrodynamic models parameterized by model free parameters: spin-down timescale (t_p) and the initial rotation energy (E_{rot}) of the magnetar (in log scale). Middle panel: re-parameterization of the grid by two of our own-defined observables: $d_{min-ini}$ and $d_{min-SBO}$. Bottom panel: idem middle panel but using the following observables: $d_{min-ini}$ and $\log(L_{max})$. The bottom panel shows a parameter-observable pair satisfying a one-to-one relation: there is no sign of degeneracy in the transformation (see the correspondence of the colours in the electronic version, or the numbered points in the B&W printed version of the paper).

References

Bersten M.C., Benvenuto O.G., 2016, BAAA, 58, 246
Nomoto K., Hashimoto M., 1988, PhR, 163, 13
Orellana M., Bersten M.C., Moriya T.J., 2018, A&A, 619, A145

Properties of massive stars in Galactic binary systems

C. Sabín-Sanjulián[1], R.H. Barbá[1], R. Gamen[2] & J.A. Arias[1]

[1] *Departamento de Física y Astronomía, Universidad de La Serena, La Serena, Chile*
[2] *Instituto de Astrofísica de La Plata, CONICET–UNLP, La Plata, Argentina*

Contact / cssj@dfuls.cl

Resumen / En el marco del proyecto OWN, usamos datos espectroscópicos de alta resolución de la binaria masiva HD 54662 para medir velocidades radiales y desentramar los espectros de las dos componentes del sistema, que hemos clasificado como O6.5 Vz(n) y O7.5 Vz. Obtenemos una nueva solución orbital espectroscópica para el sistema, con un periodo de 5.50 ± 0.02 años. Usamos datos astrométricos publicados para calcular masas estelares absolutas de 24 ± 1 y $20 \pm 1\,M_\odot$ para las componentes A y B, respectivamente. Analizamos cuantitativamente los espectros desentramados con modelos FASTWIND de atmósferas estelares y calculamos masas evolutivas actuales usando la herramienta BONNSAI. Obtenemos masas evolutivas demasiado altas, lo cual podría estar relacionado con el problema de discrepancia de masas.

Abstract / Within the OWN project, we use high resolution spectroscopic data of the massive binary system HD 54662 to measure accurate radial velocities and disentangle the spectra of the two components, which we classify as O6.5 Vz(n) and O7.5 Vz. We obtain a new spectroscopic orbital solution of the system, with a period of $P = 5.50 \pm 0.02$ yr. We use published astrometric data to derive absolute stellar masses of 24 ± 1 and $20 \pm 1\,M_\odot$ for components A and B, respectively. We analyze quantitatively the disentangled spectra using FASTWIND stellar atmosphere models and infer current evolutionary masses using the BONNSAI tool. We find too high evolutionary masses, which could be related to the mass discrepancy problem.

Keywords / stars: massive — stars: binaries — stars: atmospheres — stars: fundamental parameters

1. Introduction

Massive stars are considered cosmic engines that shape the physical and chemical structure of their host galaxies. Several mechanisms, such as rotation and stellar winds, affect the life of these extreme objects. Multiplicity is a crucial factor in massive stars, since more than half of them are expected to be born in a binary or multiple system (Sana et al., 2013; Sota et al., 2014; Barbá et al., 2017), and it affects their evolution by means of binary interaction processes and mergers (Langer, 2012; de Mink et al., 2013).

HD 54662 is an O-type double-lined spectroscopic binary located in the Seagull Nebula complex. Its binary nature was first revealed by (Boyajian et al., 2007, hereafter B07), who estimated an orbital period of ~ 560 d. Recently, Le Bouquin et al. (2017, LB17 hereafter) used VLTI interferometric data and radial velocity (RV) measurements by B07 to derive a period of 2100 d, confirming that HD 54662 is one of the spectroscopic binaries with the longest periods known to date. These authors provided a 3D solution for the orbit, estimating excessively high absolute stellar masses of $316\,M_\odot$ and $58\,M_\odot$ for the primary and the secondary components, respectively. On the other hand, Mossoux et al. (2018, M18 hereafter) used new spectroscopic observations and the results from LB17 to derive absolute stellar masses below $10\,M_\odot$, too low for O-type stars.

In this work, we use high-quality, multi-epoch spectroscopic data in order to obtain a new orbital solution for HD 54662 and characterize the properties of both components of the system via stellar atmosphere and evolutionary models.

2. Observations

We have used the spectroscopic data gathered by the OWN Survey (Barbá et al., 2017), a project devoted to study the multiplicity status of Galactic massive stars. It has obtained more than 7 000 high-resolution, optical spectra of O-type and WR stars in the Southern hemisphere, using 2-m class telescopes in Chile (La Silla, Las Campanas and CTIO) and Argentina (CASLEO). For HD 54662, we have used $\sim$50 spectra with $R = 15\,000$ – $50\,000$ and S/N > 100 with a good phase coverage (see Fig. 1 in Sec. 3.).

3. Spectral disentangling and orbital solution

HD 54662 has two components: one with broad lines (component A, which is the most massive of the system) and one with narrower lines (component B), which are highly blended. Using the iterative method by González & Levato (2006), we performed a spectral disentangling process to obtain the individual spectra of the components and accurate RV measurements (uncertainties below ~ 2 km s^{-1}). We used the MGB tool (Maíz Apellániz et al., 2012) to classify component A as O6.5 Vz(n) and component B as O7.5 Vz.

Fig. 1 shows the disentangled spectra of both components. Residuals from the disentangling process are

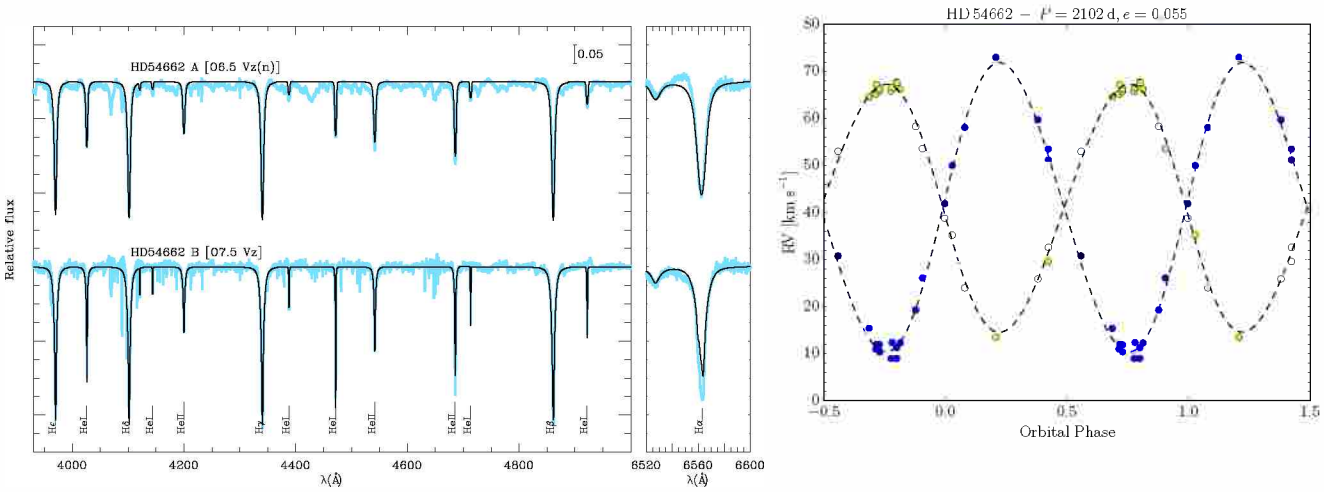

Figure 1: Results from the spectral disentangling and orbital solution. *Left:* Individual disentangled spectra of the components of HD 54662 (light blue). In black, best fitting FASTWIND spectrum from the quantitative spectroscopic analysis ($T_{\rm eff} = 39$ kK, $\log g = 3.90$ dex for component A; $T_{\rm eff} = 39$ kK, $\log g = 4.00$ dex for component B). Optical H and He diagnostic lines are indicated. *Right:* Spectroscopic orbital solution for HD 54662. RV measurements for components A (broad-lined) and B (narrow-lined) are plotted in yellow and blue, respectively.

present, mainly affecting the wings of the H Balmer lines, which is an important factor in the determination of surface gravities with synthetic spectra (see Sec. 4.).

We used RV measurements and the GBART code (improved version of Bertiau & Grobben, 1969, by F. Bareilles) to derive an orbital solution for the system (see Fig. 1, which shows a remarkably good fitting of the RV curve). We obtained a period of $P = 2012 \pm 9$ d, in agreement with previous results (LB17, M18). We derived RV semi-amplitudes of $K_{\rm A} = 26.4 \pm 0.3$ and $K_{\rm B} = 30.7 \pm 0.3\,{\rm km\,s^{-1}}$, which differ significantly from LB17 ($K_{\rm A} = 17.8 \pm 0.8$ and $K_{\rm B} = 98.0 \pm 18.0\,{\rm km\,s^{-1}}$) and M18 ($K_{\rm A} = 19.3 \pm 0.6$ and $K_{\rm B} = 22.9 \pm 0.7\,{\rm km\,s^{-1}}$). This discrepancy could be likely related to different assumptions in the Gaussian models used to fit the line profiles when measuring RVs.

Additionally, we used our RV estimates and the astrometric data from LB17 to compute a 3D solution for the orbit using the ORBIT* code by A. Tokovinin. We estimated an inclination angle of the orbit of $i = 75 \pm 0.5^\circ$ (almost the same as LB17) and a distance to the system of 1087 ± 25 pc, in agreement with LB17 and Gaia DR2 (Bailer-Jones et al., 2018). We derived absolute stellar masses of 24 ± 1 and $20 \pm 1\,{\rm M}_\odot$ for components A and B, respectively, which are consistent with the expected stellar masses for O-type stars, and differ significantly with the results from LB17 and M18 due to the differences in the estimated RV semi-amplitudes.

4. Quantitative spectroscopic analysis

We performed a quantitative analysis of the individual spectra in order to estimate the physical properties of each component. In a first step, we characterized the broadening of the line profiles by means of the IACOB-BROAD tool (Simón-Díaz & Herrero, 2014). We used the O III λ 5592 line to derive a projected rotational velocity ($v \sin i$) of 160 and 40 ${\rm km\,s^{-1}}$ for components A and B, respectively. This remarkable difference in $v \sin i$ between both components of HD 54662 is one of various cases discovered within the OWN Survey (see,e.g. Putkuri et al., 2018). This phenomenon could be related to asynchronism or non-parallel rotation axes (see, e.g. Hut, 1981), representing a key factor to consider when modeling massive stars in binary systems.

In a second step, we utilized IACOB-GBAT (Simón-Díaz et al., 2011) to determine mean values and uncertainties for stellar parameters (effective temperatures, surface gravities, helium abundances and wind parameters, see Sec. 5.). This automatic tool is based on a large grid of precomputed FASTWIND (Santolaya-Rey et al., 1997; Puls et al., 2005) stellar atmosphere models. Fig. 1 shows the synthetic models from the grid that best fit the individual spectra.

Stellar radii, spectroscopic masses and luminosities were computed using IACOB-GBAT by means of the absolute magnitudes in the V-band, which were estimated using the apparent magnitude of the system ($m_V = 6.21$, see Ducati, 2002), the brightness factors from the disentangling process and our estimation of distance (Sec. 3.). We used the Bayesian tool BONNSAI (Schneider et al., 2014) to compute current evolutionary masses (see Sec. 6.).

5. Properties and evolutionary status of HD 54662

We obtained effective temperatures ($T_{\rm eff}$) of 39.1 ± 1.0 and 39.0 ± 0.6 kK, and surface gravities ($\log g$) of 3.90 ± 0.10 and 4.00 ± 0.10 for components A and B, respectively. These results slightly differ with those from M18, who obtained 37.5 ± 1.0 and 37.7 ± 1.0 kK for $T_{\rm eff}$, and 3.81 ± 0.10 and 3.96 ± 0.10 for $\log g$, for components

*https://doi.org/10.5281/zenodo.61119.

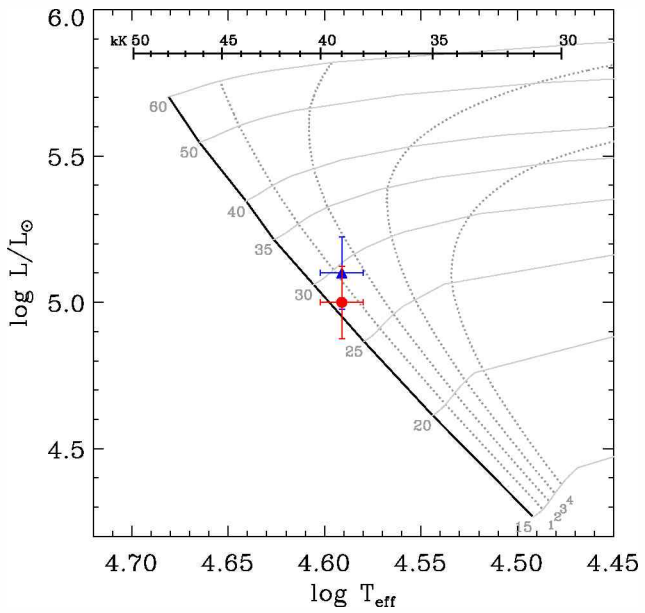

Figure 2: Location of both components of HD 54662 in the Hertzsprung–Russell diagram. The blue triangle and the red circle correspond to the primary and secondary components, respectively. Evolutionary tracks and isochrones for single stars with solar metallicity are taken from Brott et al. (2011), with an initial rotational velocity of $v_{ini} = 166\,\mathrm{km\,s^{-1}}$. Initial stellar masses (in solar masses) and ages (in Myr) are shown. The thick black isochrone corresponds to the *Zero Age Main Sequence* (ZAMS).

Table 1: Dynamical, spectroscopic and evolutionary masses for both components of HD 54662.

Stellar mass	A	B	Unit
$M_{\rm dyn}$	24 ± 1	20 ± 1	$M_\odot$
$M_{\rm sp}$	24 ± 5	19 ± 5	$M_\odot$
$M_{\rm ev}$	30 ± 2	28 ± 2	$M_\odot$

A and B, respectively. Differences in the disentangling process and the distortions of the line profiles, as commented in Sec. 3., could explain this discrepancy.

Fig. 2 shows the position of the stars of HD 54662 in the H–R diagram. Both components are very young objects (with ages ~ 1 Myr), in agreement with their Vz characteristic (Sabín-Sanjulián et al., 2014; Arias et al., 2016). The young age of HD 54662 makes a tidal synchronization or mass transfer improbable, so the inconsistency of the rotational velocities between both components (Sec. 4.) could be related to their formation process.

6. Mass discrepancy

In this work we have used three different methodologies to estimate stellar masses (see Table 1): *dynamical masses*, using RV measurements and astrometric data by LB17; *spectroscopic masses*, using FASTWIND stellar atmosphere models, and *evolutionary masses*, using evolutionary models from Brott et al. (2011).

Dynamical and spectroscopic masses agree within the error bars. However, evolutionary masses are $\sim$20–50 % higher than the other masses in both stars, which could be related to the long-standing *mass discrepancy problem* (Herrero et al., 1992, 2002). Sabín-Sanjulián et al. (2017) and Markova et al. (2018) have recently shown that evolutionary masses tend to be higher than the spectroscopic ones in the low mass regime ($M_* \lesssim 20$–$30\,M_\odot$), and the discrepancy is present in environments of different metallicities. A detailed quantitative study of a large number of binaries is needed to reach a compelling conclusion on the mass discrepancy problem.

Acknowledgements: C.S.-S. acknowledges support from CONICYT-Chile through the FONDECYT Postdoctoral Project 3170778.

References

Arias J.I., et al., 2016, AJ, 152, 31
Bailer-Jones C.A.L., et al., 2018, AJ, 156, 58
Barbá R.H., et al., 2017, J.J. Eldridge, J.C. Bray, L.A.S. McClelland, L. Xiao (Eds.), *The Lives and Death-Throes of Massive Stars*, *IAUS*, vol. 329, 89–96
Bertiau F.C., Grobben J., 1969, Ric. Astronomiche, 8, 1
Boyajian T.S., et al., 2007, ApJ, 664, 1121
Brott I., et al., 2011, A&A, 530, A115
de Mink S.E., et al., 2013, ApJ, 764, 166
Ducati J.R., 2002, VizieR Online Data Catalog, 2237, 0
González J.F., Levato H., 2006, A&A, 448, 283
Herrero A., Puls J., Najarro F., 2002, A&A, 396, 949
Herrero A., et al., 1992, A&A, 261, 209
Hut P., 1981, A&A, 99, 126
Langer N., 2012, ARA&A, 50, 107
Le Bouquin J.B., et al., 2017, A&A, 601, A34
Maíz Apellániz J., et al., 2012, L. Drissen, C. Rubert, N. St-Louis, A.F.J. Moffat (Eds.), *Scientific Meeting in Honor of Anthony Moffat*, *ASP Conf. Series*, vol. 465, 484
Markova N., Puls J., Langer N., 2018, A&A, 613, A12
Mossoux E., Mahy L., Rauw G., 2018, A&A, 615, A19
Puls J., et al., 2005, A&A, 435, 669
Putkuri C., et al., 2018, A&A, 618, A174
Sabín-Sanjulián C., et al., 2014, A&A, 564, A39
Sabín-Sanjulián C., et al., 2017, A&A, 601, A79
Sana H., et al., 2013, G. Pugliese, A. de Koter, M. Wijburg (Eds.), *370 Years of Astronomy in Utrecht*, *ASP Conf. Series*, vol. 470, 141
Santolaya-Rey A.E., et al., 1997, A&A, 323, 488
Schneider F.R.N., et al., 2014, A&A, 570, A66
Simón-Díaz S., Herrero A., 2014, A&A, 562, A135
Simón-Díaz S., et al., 2011, JPCS, 328, 012021
Sota A., et al., 2014, ApJS, 211, 10

Analyzing ι Ori Aa through high resolution spectroscopy: Orbital solution and apsidal motion

J. Eguren Brown,[1], G. Ferrero[1,2] & S. Simón Díaz[3,4]

[1] *Facultad de Ciencias Astronómicas y Geofísicas, UNLP, Argentina*
[2] *Instituto de Astrofísica de La Plata, CONICET–UNLP, Argentina*
[3] *Instituto de Astrofísica de Canarias, Tenerife, Spain.*
[4] *Departamento de Astrofísica, Universidad de La Laguna, Tenerife, Spain*

Contact / jordi@carina.fcaglp.unlp.edu.ar

Resumen / El sistema binario ι Ori Aa ha sido estudiado con diversas técnicas y desde diferentes puntos de vista. Las determinaciones de sus parámetros orbitales, realizadas por varios autores, son consistentes aunque difieren en la longitud del periastro. Aún así, la existencia de movimiento apsidal era dudosa. En este trabajo obtenemos un nuevo conjunto de velocidades radiales a partir de espectros de alta resolución, ajustamos una nueva solución orbital, separamos los espectros de sus componentes, mostramos que el movimiento apsidal claramente existe, y calculamos su velocidad.

Abstract / The binary system ι Ori Aa has been studied with different techniques and approaches. The orbital parameters determined by different authors are consistent, but differ in the value of the periastron longitude. However, the existence of apsidal motion in the system was quite controversial. In this work, we obtain a new set of radial velocities from high resolution spectra, fit a new orbital solution, separate the spectra of the two components, show that apsidal motion clearly exists, and calculate its rate.

Keywords / binaries: close — binaries: spectroscopic — stars: early-type — stars: individual: HD 37043

1. Introduction

ι Ori Aa (HD 37043, $\alpha = 05^h\ 35^m\ 25.98^s$, $\delta = -05^\circ\ 54'\ 35.64''$) is a massive, double line spectroscopic binary composed of an O9 III and a B1 IV-V star. Its first orbital solution was obtained by Plaskett & Harper (1909) and was later improved by Miczaika (1951) and Pearce (1953). It was noted by Gies & Bolton (1986) that the two components of the binary could not be coevals. This consideration, together with the high eccentricity of its orbit ($e \sim 0.7$), has led some authors (Bagnuolo et al., 2001) to propose that these components could have originally belonged to two different binary systems, and that the collision of said systems could have originated our object of study and the two close-by O9.5 V runaway stars AE Aur and μ Col. Later, Gualandris et al. (2004) postulated that both systems may have originated in the Trapezium cluster. Astroseismic activity of ι Ori Aa was studied using photometric data from the *BRITE Constellation* mission by Pablo et al. (2017) who discovered tidally excited oscillations in the primary star of the system, seen for the first time in an O-type star. Apsidal motion in the system was first proposed and measured by Stickland et al. (1987) and later rejected by Hilditch et al. (1991) due to unreliable measurements. It was reconsidered and measured by Marchenko et al. (2000) and finally by Ferrero (2016), who calculated the apsidal motion rate by fitting together all previous radial velocities (RVs) measurements in a single orbital solution. We intend to perform a thorough quantitative spectroscopic analysis of the two components of ι Ori Aa as well as of AE Aur and μ Col to shed light over this issue. As a first step, we present in this work the result of the orbital analysis of a new, high-quality spectroscopic dataset, including the results of the disentangling process and a new result for apsidal motion of the system.

2. Observations

This work is based on 63 high-resolution optical spectra obtained in the framework of the IACOB project (Simón-Díaz et al., 2015). In particular, the spectra were acquired with the HERMES instrument (Raskin et al., 2004) attached to the Mercator Telescope at the Roque de Los Muchachos Observatory on La Palma, Spain, during nights of the 2016 and 2017 season with a resolution of $R \sim$85 000, and typical signal to noise ratio $S/N \sim 300$.

3. Spectral disentangling

We measured the RVs and separated the spectra of the system components using the disentangling technique described by González & Levato (2006).

To obtain a first estimation of the RVs, we measured the position of the baricenter of the spectral lines He I $\lambda\lambda$5015 and 5875. The fact that these lines are not contaminated by other lines and are located in a spectral region free from telluric absorption made them ideal

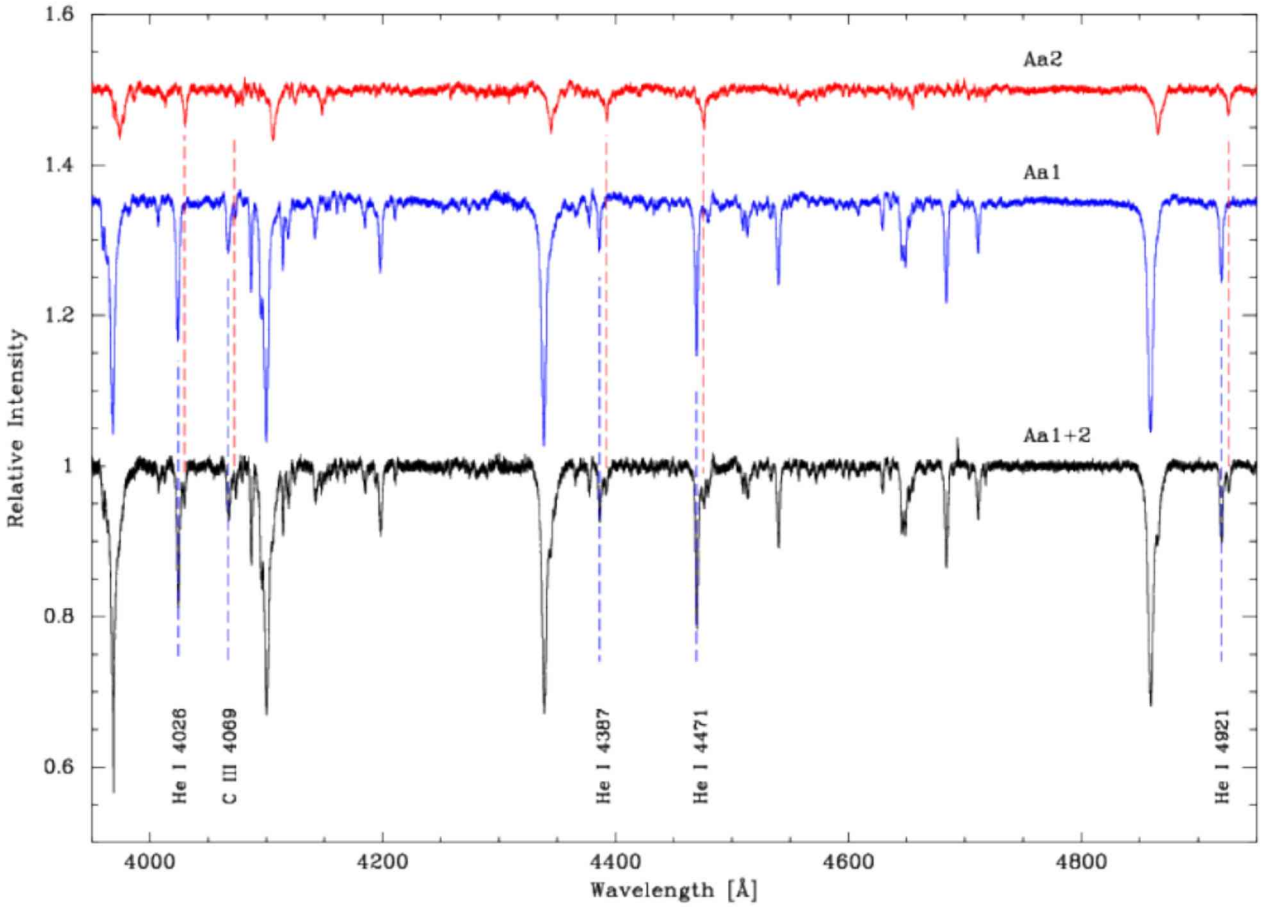

Figure 1: Disentangled spectra of both components in ι Ori Aa, and one of the composite ones.

candidates for these measurements. As a first step, we fitted Gaussian functions to the line profiles by mean of the NGAUSS task within IRAF. RV measurements of the secondary component were only possible for phases close to the quadratures due to line blending. Because of the high eccentricity of the system there were just ten spectra that fulfill this condition. Even so, the resulting separated spectra have a satisfactory S/N of ~ 700 (see Fig. 1).

4. Spectral classification

Following the criteria from Sota et al. (2011), since in the primary He II λ4542 > He I λ4388, He II λ4200 > He I λ4144 and He II λ4686 is in strong absorption, we propose to classify it as O8 III. For the secondary, according to Walborn & Fitzpatrick (1990), since the He II λ4686 line is present and considering the ratio Si III λ4552/He I λ4388, we propose a B0.5 V type. Both classifications agree with previous determinations (e.g. Bagnuolo et al. 2001).

5. Orbital solution

We fitted an orbital solution to our RV measurements using the FOTEL code (Hadrava, 2004), with the initial values taken from Ferrero (2016). During the fitting process, lower weight was assigned to individual data that accumulate in a short phase range (e.g., $\phi \sim 0.25$). Most of the parameters in our solution are in accordance with calculations by previous authors. The results are shown in Table 1 and Fig. 2.

Table 1: Orbital parameters obtained by fitting our RVs, measured in He I $\lambda\lambda$5015 and 5875.

Parameter	Value	+/−
P [days]	29.1350	0.0002
T_0 [HJD]	2455608.11	0.01
e	0.713	0.003
ω [°]	126.3	1.4
γ_1 [km s^{-1}]	33	1
γ_2 [km s^{-1}]	21	1
K_1 [km s^{-1}]	105.3	0.1
K_2 [km s^{-1}]	195.7	0.2
$a_1 \sin i$ [$R_\odot$]	42.2	0.2
$a_2 \sin i$ [$R_\odot$]	78.6	0.3
$M_1 \sin^3 i$ [$M_\odot$]	18.2	0.2
$M_2 \sin^3 i$ [$M_\odot$]	9.8	0.2
q	0.538	0.007
RMS [km s^{-1}]	2.0	

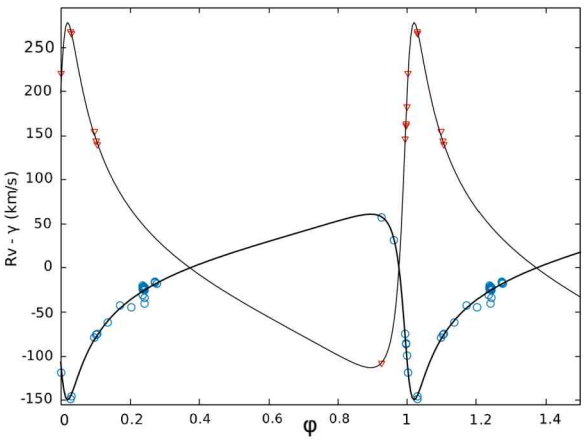

Figure 2: Radial velocity curves of both components in ι Ori Aa (blue points: primary; red: secondary).

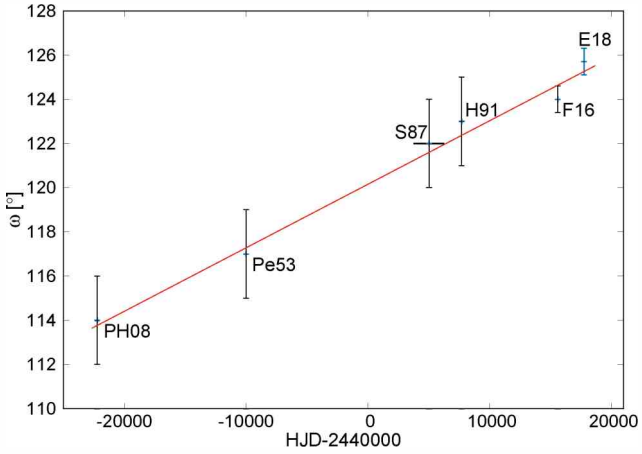

Figure 3: Secular variation of the periastron longitude in ι Ori Aa. PH09: data adjusted by Plaskett & Harper (1909); Pe53: Pearce (1953); S87: Stickland et al. (1987); H91: Hilditch et al. (1991); F16: Ferrero (2016), E18: determined in this work. Horizontal bars: time span of RVs data. Red line: linear regression.

Table 2: Apsidal motion rate measurements by other authors.

Author	$\dot{\omega}$ [° day^{-1}]	±
Stickland et al, (1987)	0.00041	0.00003
Marchenko et al, (2000)	0.00049	0.00003
Ferrero (2016)	0.00037	0.00012

6. Analysis of apsidal motion

We compared our new orbital solution with the already published ones. The major disagreement among orbital parameters is in the longitude of the periastron. When present and previous studies are plotted together, it is clear that there is a linear trend in the longitude of the periastron against time. By computing a linear regression to these data, we obtained a value for the apsidal motion rate $\dot{\omega} = 0.00029 \pm 0.00003$ ° day^{-1} (see Fig. 3). Our result alongside previous calculated values (see Table 2) leaves little room for doubt regarding the existence of the apsidal motion.

7. Summary and future work

We measured RVsfor the binary system ι Ori Aa, obtained a new orbital solution and were able to disentangle the spectra of its components, which allowed us to spectrally classify it. We confirmed the existence of apsidal motion and calculated its rate.

The next stage of this work consists in the determination of the fundamental parameters and photospheric abundances of the two components of the binary system ι Ori Aa, as well as of AE Aur and μ Col. This will be done using IACOB–GBAT tool developed by Simón-Díaz et al. (2011) and will require to refine the separated spectra using more available data.

Acknowledgements: JEB thanks the Facultad de Ciencias Astronómicas y Geofísicas, UNLP, for their financial support. Special thanks to P. Hadrava for providing the FOTEL code. S. S.-D. acknowledges financial support from the Spanish MINECO and the Gobierno de Canarias.

References

Bagnuolo Jr. W.G., et al., 2001, ApJ, 554, 362
Ferrero G., 2016, *Estudio de la variación de la línea de las ápsides en sistemas binarios masivos*, Ph.D. thesis, Univ. Nac. de La Plata
Gies D.R., Bolton C.T., 1986, ApJS, 61, 419
González J.F., Levato H., 2006, A&A, 448, 283
Gualandris A., Portegies Zwart S., Eggleton P.P., 2004, MNRAS, 350, 615
Hadrava P., 2004, Publications of the Astronomical Institute of the Czechoslovak Academy of Sciences, 92, 1
Hilditch R.W., et al., 1991, The Observatory, 111, 14
Marchenko S.V., et al., 2000, MNRAS, 317, 333
Miczaika G.R., 1951, ZA, 29, 305
Pablo H., et al., 2017, MNRAS, 467, 2494
Pearce J.A., 1953, AJ, 58, 223
Plaskett J.S., Harper W.E., 1909, ApJ, 30, 373
Raskin G., Van Winckel H., Davignon G., 2004, A.F.M. Moorwood, M. Iye (Eds.), *Ground-based Instrumentation for Astronomy, Proc. SPIE* , vol. 5492, 322–330
Simón-Díaz S., et al., 2011, *Journal of Physics Conference Series, Journal of Physics Conference Series*, vol. 328, 012021
Simón-Díaz S., et al., 2015, A.J. Cenarro, F. Figueras, C. Hernández-Monteagudo, J. Trujillo Bueno, L. Valdivielso (Eds.), *Highlights of Spanish Astrophysics VIII*, 576–581
Sota A., et al., 2011, ApJS, 193, 24
Stickland D.J., et al., 1987, A&A, 184, 185
Walborn N.R., Fitzpatrick E.L., 1990, PASP, 102, 379

Equilibrio químico en un gas de hidrógeno magnetizado

M. Vera Rueda[1,2] & R. Rohrmann[1]

[1] *Instituto de Ciencias Astronómicas, de la Tierra y del Espacio, CONICET–UNSJ, Argentina*
[2] *Facultad de Ciencias Exactas, Físicas y Naturales, UNSJ, Argentina*

Contacto / vera.gmatias@gmail.com

Resumen / Se estudian los equilibrios de ionización y disociación del hidrógeno en condiciones típicas de enanas blancas magnéticas. La poblaciones se obtienen por minimización de la energía libre de Helmholtz total del gas, que incluye las contribuciones de electrones libres y de varias especies atómicas y moleculares (H, H^+, H^-, H_2, H_2^+). Se toman en cuenta los efectos del campo magnético sobre los modos de energía traslacionales e internos de todas las partículas. La evaluación de la función de partición vibro–rotacional de moléculas incluye promediaciones sobre distintas orientaciones del campo. El modelo permite evaluar las poblaciones de las distintas especies para valores arbitrarios de temperatura, densidad del gas e intensidad del campo magnético (hasta 10^9 G).

Abstract / We study the equilibrium of the ionization and dissociation of hydrogen in typical conditions of magnetic white dwarfs. Populations are obtained by the total Helmholtz free energy minimization of the gas, which includes contributions of free electrons and different atomic and molecular species (H, H^+, H^-, H_2, H_2^+). We take into account the effects of the magnetic field over traslational and internal energy modes of all the particles. The evaluation of the vibro-rotational partition function for molecules, includes an averaging over different field orientations. This model allows to evaluate populations of the different species for arbitrary values of temperature, gas density and magnetic field intensity (up to 10^9 G).

Keywords / white dwarfs — stars: atmospheres — magnetic fields

1. Introducción

Hoy en día, se sabe que una fracción significativa de enanas blancas posee campos magnéticos intensos (B), con magnitudes de hasta 10^9 G (García-Berro et al., 2016), o $\beta \approx 0.5$ ($\beta = B/B_0$, con $B_0 = 2.35 \times 10^9$ G). En tales condiciones, varias propiedades de la materia se ven modificadas respecto del caso $B = 0$ (Potekhin et al., 1999). Entonces, resulta de especial interés el cálculo de poblaciones en atmósferas propias de enanas blancas magnéticas (MWD, por sus siglas en inglés), para luego resolver el transporte de radiación. En este trabajo se considera una atmósfera hidrogénica constituida por H, H^+, H^-, H_2, H_2^+, y electrones libres. Las poblaciones de tales especies se calculan resolviendo las reacciones: $H \leftrightarrow H^+ + e^-$, $H_2 \leftrightarrow 2H$, $H^- \leftrightarrow H + e^-$, $H_2^+ \leftrightarrow H + H^+$. Estas evaluaciones tienen en cuenta *i)* el acople magnético entre los estados internos y traslacionales de los átomos, *ii)* los cambios inducidos por B en las energías internas y en los modos vibro–rotacionales de las moléculas, *iii)* los efectos del campo magnético sobre ecuaciones tipo Saha.

2. Acople magnético

En presencia de un campo magnético externo, aparece un acoplamiento entre los estados internos del átomo y el movimiento de su centro de masa (Vincke & Baye, 1988). En tal caso, su movimiento puede ser descripto por el pseudomomento $\boldsymbol{K} = \boldsymbol{p}_e + \boldsymbol{p}_p + e\,B\,(\boldsymbol{r}_e - \boldsymbol{r}_p)$, donde $\boldsymbol{p}_i$ es el momento de la partícula i (e^- o p^+), y $\boldsymbol{r}_i$ su posición. Con esto, el hamiltoniano del sistema puede descomponerse en la suma de una parte traslacional, otra que corresponde a los estados internos del átomo, y una tercera asociada al acoplamiento entre el movimiento del centro de masa y los movimientos internos.

Luego, bajo ciertas condiciones (Vincke & Baye, 1988), el término de acople puede considerarse como una perturbación, y las energías pueden expresarse:

$$E(\beta, \boldsymbol{K}) = E_I(\beta) + \frac{K_\parallel^2}{2M} + \frac{K_\perp^2}{2M_E(\beta, K_\perp^2)}, \qquad (1)$$

siendo E_I la energía interna del átomo, $K_\parallel$ y $K_\perp$ las componentes del pseudomomento paralela y perpendicular al campo, M la masa total del átomo y M_E una masa efectiva que depende del estado, de la intensidad del campo, y de $K_\perp$. La contribución de $K_\perp$ se vuelve crucial, de manera que, cuando esta es distinta de cero, las energías de enlace toman la forma:

$$E_B(\beta, K_\perp) = k\,E_B(\beta) - F(m, \beta) + \frac{K_\perp^2}{2M_E(\beta, K_\perp^2)}, \qquad (2)$$

con k una constante, $E_B(\beta)$ la energía interna del átomo con protones en reposo, F una corrección de la energía interna y, el último término, una corrección continua. El panel (a) de la Fig. 1 muestra cómo se ven afectadas las energías para algunos estados del átomo, donde $E_B(\beta)$ se calculó con el código H2DB (Schimeczek & Wunner, 2014) , y usando el ajuste para M_E de Potekhin (1998), y la relación $K_\perp^2/2M_E \approx \frac{1}{2} M_E \langle v \rangle^2$ (Vincke & Baye, 1988).

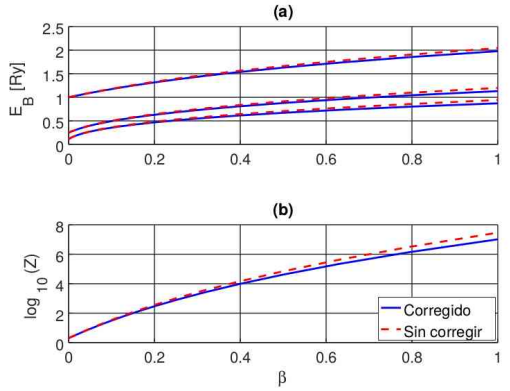

Figura 1: Niveles de energía del hidrógeno (a) y función de partición (b) en función de β, para un núcleo fijo de masa infinita (línea roja de trazos) y para el átomo corregido por acople magnético (línea azul continua).

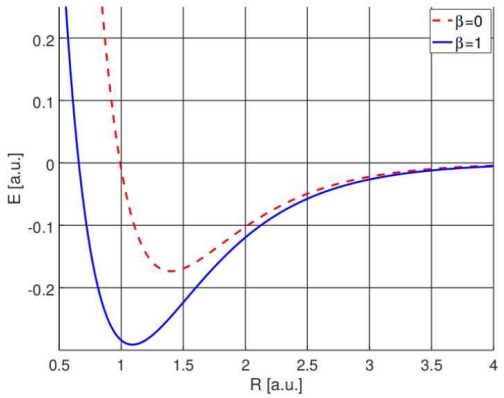

Figura 2: Curvas de energía potencial de H_2 en ausencia de campo magnético (línea roja de trazos), y con campo magnético de intensidad $\beta = 1$ (línea azul continua).

Para el cálculo de la función de partición se tomó como base la aproximación de Pavlov & Meszaros (1993),

$$Z = (2\,\pi\,m\,k\,T)\sum_i \frac{M_{E,i}}{M} exp\,(-E_B(\beta, K_\perp)/kT)\,, \quad (3)$$

donde los factores $M_{E,i}/M \approx 1$ para campos típicos de MWDs. En el panel (b) de la Fig. 1 se puede observar el efecto de esta corrección sobre Z para una temperatura de 10 000 K.

3. Espectro de energías moleculares

El hamiltoniano de una molécula diatómica contempla también la energía cinética de los núcleos, de manera que la energía total del átomo puede expresarse:

$$E = E_n^{\rm el} + E_{\rm rot}^{\rm nucl} + E_{\rm vib}^{\rm nucl}, \quad (4)$$

donde $E_n^{\rm el}$ es la energía de la molécula rígida en el n-ésimo estado electrónico, $E_{\rm rot}^{\rm nucl}$ la energía rotacional del núcleo, y $E_{\rm vib}^{\rm nucl}$ su energía vibracional.

3.1. Espectros rotacionales

El espectro de energías de una molécula diatómica está dado por:

$$F(J) = \frac{E(J)}{hc} = B_e\,J\,(J+1), \quad (5)$$

donde J es el número cuántico rotacional, y B_e una constante de rotación que depende de la distancia internuclear, R_e, y cuyo valor se calculó en función de β a partir de los datos provistos por Detmer et al. (1997) y Schmelcher et al. (2000) para H_2, y por Guan et al. (2003) y Medel Cobaxin et al. (2015) para H_2^+.

3.2. Espectros vibracionales

Para una molécula diatómica, el espectro de energías vibracionales corregido por anarmonicidad se puede escribir (Hollas, 2004):

$$G(\nu) = \frac{E(\nu)}{hc} \approx \omega_e\left(\nu+\frac{1}{2}\right) - \omega_e\chi_e\left(\nu+\frac{1}{2}\right)^2, \quad (6)$$

siendo ν el número cuántico vibracional, ω_e el número de onda armónico, y χ_e una constante de anarmonicidad. Los valores de estas constantes están tabulados para campos nulos. En presencia de B, las curvas de energía se ven afectadas tal y como lo muestra la Fig. 2, donde el pozo de potencial se ha hecho más profundo y se ha desplazado hacia R menores.

El cálculo de ω_e se realizó con datos de Detmer et al. (1997) para H_2, y de Medel Cobaxin et al. (2015) para H_2^+, integrando para distintos β y θ (ángulo entre el campo y el eje molecular), y χ_e se calculó con $E_D \approx hc\omega_e^2/4\omega_e\chi_e$ (Demtröder, 2006), donde E_D es la energía de disociación.

3.3. Función de partición

Asumiendo modos dinámicos independientes (Tatum, 1966), la función de partición puede escribirse:

$$Z = Z_{\rm rot}Z_{\rm vib}Z_{\rm el}, \quad (7)$$

donde $Z_{\rm rot}$ es la componente rotacional , $Z_{\rm vib}$ la vibracional, y Z_e la parte electrónica. En el caso de Z_{rot}, se utilizó una aproximación para altas temperaturas (Herzberg, 1950), y se incluyó la constante rotacional corregida por distorsión centrífuga $B_\nu = B_e - \alpha_\epsilon(\nu+\frac{1}{2})$, donde α_e es una constante de interacción vibro–rotacional conocida a campo cero, y cuya variación con β se supuso proporcional a B_e.

La componente vibracional de Z se calculó según el esquema 6:

$$Z_{\rm vib} = \sum_{\nu=0}^{\nu_{\rm max}} \exp\left\{-\frac{hc}{kT}\left[\omega_e\nu' - \omega_e\chi_e\nu'^2\right]\right\} \quad (8)$$

tal que $\nu' = (\nu+1/2)$, y ν_{max} es el mayor entero menor o igual a $\omega_e/2\omega_e\chi_e$.

Finalmente, $Z_{\rm el}$ se calculó según:

$$Z_{el} = \sum \widetilde{\omega}_e\,\exp\left(-\frac{T_e}{kT}\right), \quad (9)$$

donde $\widetilde{\omega}_e = (2-\delta_{0,\Lambda})\,(2S+1)$ es el peso estadístico (Tatum, 1966), y T_e la energía electrónica del estado (en cm^{-1}). Las energías electrónicas en función de β

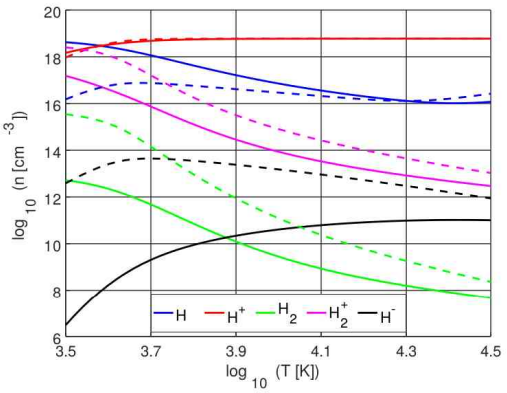

Figura 3: Variación de la densidad en función de T para distintas especies, con $\rho = 10^{-5}$ g cm^{-3}, cuando el campo es nulo (líneas continuas) y para $\beta = 0.1$ (líneas de trazos).

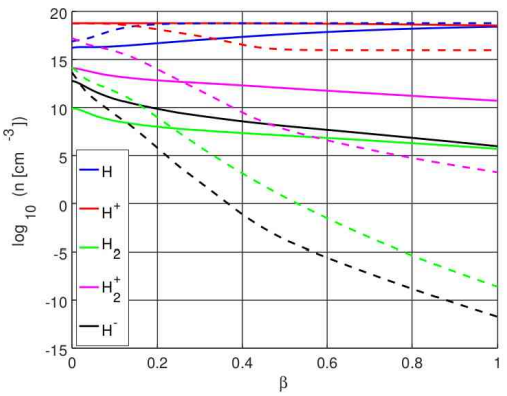

Figura 4: Curvas poblacionales en función de β para distintas especies, con $\rho = 10^{-5}$ g cm^{-3}, $T = 5\,000$ K (líneas continuas), y $T = 15\,000$ K (líneas de trazos).

se obtuvieron de los trabajos de Detmer et al. (1997) y Schmelcher et al. (2000) para H_2, y de Guan et al. (2003) y Medel Cobaxin et al. (2015) para H_2^+.

4. Balance químico

El equilibrio de ionización de un gas formado por átomos, electrones y protones, está dado por:

$$\mu_0 + \mu_1 + \mu_e = 0, \tag{10}$$

donde μ_0, μ_1 y μ_e son los potenciales químicos de los átomos neutros, de los protones y de los electrones respectivamente. Luego, considerando que $\mu = (\partial F/\partial N)_{VT}$, donde F es la energía de Helmholtz, y suponiendo que ésta tiene la forma típica de un gas ideal, la expresión anterior conduce a (Gnedin et al., 1974):

$$\frac{n_1 n_e}{n_0} = \frac{Z_1}{Z_0}\left(\frac{m_e kT}{2\pi\hbar^2}\right)^{3/2} \frac{\hbar\omega_B}{kT} coth\left(\frac{\hbar\omega_B}{2kT}\right), \tag{11}$$

siendo n_e, n_i $(i = 0, 1)$ las densidades numéricas de las partículas, ω_B la frecuencia ciclotrón, m_e y m_i las masas, y Z_i las funciones de partición. Además, en el caso de las moléculas, el balance viene dado por la ecuación de disociación:

$$\frac{n_{H^o}^2}{n_{H_2^o}} = \frac{Z_{H^o}^2}{Z_{H_2^o}}\left(\frac{MkT}{2\pi\hbar}\right)^{3/2} exp\left(-\frac{E_D}{kT}\right), \tag{12}$$

con M la masa reducida, y E_D la energía de disociación. Con estas expresiones del balance, bajo las condiciones de electroneutralidad y conservación de la masa, se calculó iterativamente la densidad de cada especie. Algunos resultados se pueden ver en las Figs. 3 y 4.

5. Resultados

Los campos magnéticos intensos son capaces de modificar significativamente las condiciones de la materia y la radiación. Tales campos, introducen un cambio importante en el esquema de energías atómicas y moleculares, ya sea por modificaciones en la estructura interna de las partículas como por afecciones en sus movimientos. A gran escala, los campos intensos producen un cambio en las densidades poblacionales. En las Figs. 3 y 4 se observa que B tiende a reducir la tasa de ionización de los átomos; este comportamiento es más suave a mayor T. Además, produce una disminución de la velocidad a la que decae la densidad de hidrógeno molecular; de esta forma, a campo cero, la abundancia de moléculas es inversamente proporcional a la temperatura; pero, a campos intensos, esta relación de invierte. El efecto producido por el campo sobre H^-, es reducir su densidad en proporción a la magnitud de B, pero cambiando su comportamiento con T, pasando de decrecer a crecer rápidamente con ella para B más intensos. También se puede observar que, a excepción de H^+ y de H^-, las otras especies decaen con la temperatura. El átomo neutro es la única especie cuya densidad crece con la magnitud del campo; las otras, presentan caídas que se vuelven más suaves cuanto más alta es la temperatura.

Referencias

Demtröder W., 2006, *Atoms, Molecules and Photons*

Detmer T., et al., 1997, PhRvA, 56, 1825

García-Berro E., Kilic M., Kepler S.O., 2016, International Journal of Modern Physics D, 25, 1630005

Gnedin I.N., Pavlov G.G., Tsygan A.I., 1974, Zhurnal Eksperimentalnoi i Teoreticheskoi Fiziki, 66, 421

Guan X., Li B., Taylor K.T., 2003, Journal of Physics B Atomic Molecular Physics, 36, 3569

Herzberg G., 1950, *Molecular Spectra and Molecular Structure: Spectra of Diatomic Molecules*

Hollas M., 2004, *Modern Spectroscopy*

Medel Cobaxin H., et al., 2015, Journal of Physics B Atomic Molecular Physics, 48, 045101

Pavlov G.G., Meszaros P., 1993, ApJ, 416, 752

Potekhin A.Y., 1998, Journal of Physics B Atomic Molecular Physics, 31, 49

Potekhin A.Y., et al., 1999, Contributions to Plasma Physics, 39, 101

Schimeczek C., Wunner G., 2014, Computer Physics Communications, 185, 614

Schmelcher P., Detmer T., Cederbaum L.S., 2000, PhRvA, 61, 043411

Tatum J.B., 1966, Publications of the Dominion Astrophysical Observatory Victoria, 13, 1

Vincke M., Baye D., 1988, Journal of Physics B Atomic Molecular Physics, 21, 2407

Searching for chromospheric activity cycles in 1111 FGK-type stars from the HARPS GTO planet search program

M. Flores[1,2], M. Jaque Arancibia[3], C. Saffe[1,2], A. Buccino[4,5] & P. Miquelarena[2]

[1] *Instituto de Ciencias Astronómicas, de la Tierra y del Espacio, CONICET–UNSJ, Argentina*
[2] *Departamento de Astronomía y Geofísica, UNSJ, Argentina*
[3] *Departamento de Física y Astronomía, Universidad de La Serena, La Serena, Chile*
[4] *Departamento de Física, Facultad de Ciencias Exactas y Naturales, UBA, Argentina*
[5] *Instituto de Astronomía y Física del Espacio, CONICET–UBA, Argentina*

Contact / matiasflorestrivigno@conicet.gov.ar

Resumen / El monitoreo de muchas estrellas con ciclos magnéticos podría ayudar a un mejor entendimiento de la dependencia de estos con las propiedades estelares y el lugar ocupado por el Sol en este contexto. Hoy en día, existen muchos interrogantes relacionados con el ciclo solar (por ejemplo, la amplitud, forma y las fluctuaciones en la longitud del ciclo), los cuales podrían ser tratados si se incrementara el número de ciclos de actividad detectados en estrellas análogas-solares y gemelas-solares. En este trabajo, realizamos una búsqueda sistemática de ciclos de actividad cromosféricos en una muestra de 1111 estrellas FGK pertenecientes al programa de búsqueda de planetas HARPS GTO. Como resultado, pudimos analizar detalladamente la actividad cromosférica para 600 de estos objetos. Para este fin, calculamos el índice de Mount Wilson para cada objeto y luego las series temporales correspondientes fueron individualmente analizadas mediante el periodograma de Lomb-Scargle generalizado.

Abstract / The monitoring of many stars with magnetic cycles could help for a better understanding of their dependence with the stellar properties and the place occupied by the Sun in this context. Up to now, there are many questions related with the solar cycle (for example, amplitude, shape and length cycle fluctuations), which could be addressed if the number of stellar activity cycles detected in solar-analogues and solar-twin stars were increased. In this work, we performed a systematic search for chromospheric activity cycles in a sample of 1111 FGK stars belonging to the HARPS GTO planet search program. As a result, we were able to analyse in detail the chromospheric activity for 600 of these objects. To this end, we calculate the Mount Wilson index for each object and then the corresponding temporal series were individually analysed by using the generalised Lomb-Scargle periodogram.

Keywords / stars: solar-type — activity — chromospheres

1. Introducción

Wilson (1978) showed for the first time that, as the solar case, long-term chromospheric variations in the Ca II H&K lines can be found in other stars. This was followed by several studies (Vaughan et al., 1978; Duncan et al., 1991; Baliunas et al., 1995; Henry et al., 1996; Baliunas et al., 1998). Another important pioneer research was carry out by Baliunas et al. (1995), who grouped a sample of 111 FGK-type stars into three classes according to their variability type (i.e. cyclic, erratic and flat stars). These activity studies have important implications on different fields. In particular, studying a range of stars with physical characteristics similar to the Sun (solar-analogues and solar-twins) across a range of ages and other parameters could be very useful to place its ∼11 yr cycle in context (e.g. Hall et al., 2007, 2009).

The Sun monitoring reveals that its 11 yr activity cycle varies in amplitude, shape and length (e.g. Charbonneau, 2010; Hathaway, 2010). However, the origin of these fluctuations is not clear yet.

In order to address these open questions, it would be suitable the monitoring of many stars similar to our Sun. In this way, we could answer if these cycle fluctuations are common in other stars and also we could explore their possible source. Frequently, new activity cycles are reported in literature (e.g. Metcalfe et al., 2010; Buccino et al., 2014; Egeland et al., 2015; Flores et al., 2017; Egeland, 2017). However, only a relatively low percentage of these stars are in fact solar-analogues or solar-twins stars (e.g. Hall et al., 2007; Egeland et al., 2015; Flores et al., 2016, 2018). For this reason, we have an ongoing programme that currently monitors the stellar activity in a sample with these types of stars. We mainly use the extensive database of the High Accuracy Radial velocity Planet Searcher (HARPS) spectra, which are occasionally complemented with CASLEO observations. In particular, we have been working with a sample of 1111 FGK stars observed in the context of the HARPS GTO (Guaranteed Time Observations) programs. Both the quality and the quantity of the available spectra, allow us to carry out detailed activity studies (e.g. Flores et al., 2016, 2017, 2018).

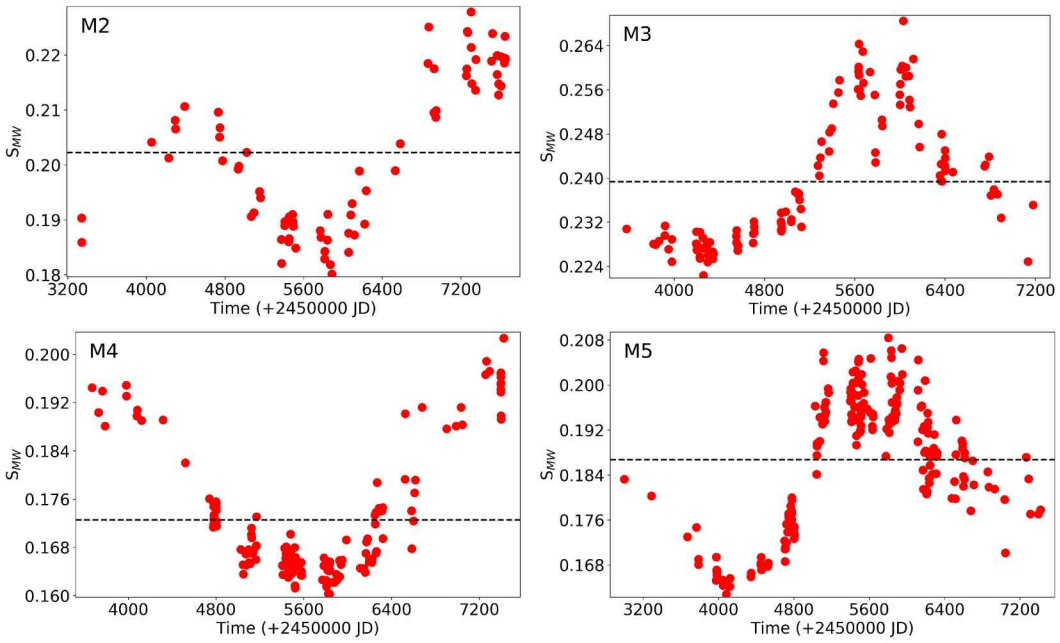

Figure 1: Time series of S_{MW} index for some stars with clear cyclic behaviour. Dashed lines indicate the $\langle S_{MW} \rangle$.

2. Observations and data reduction

The spectra of the 1111 FGK-type stars used here were downloaded from the European Southern Observatory (ESO) archive* (Mayor et al., 2003). They were acquired with the HARPS spectrograph (R∼115000), attached to the La Silla 3.6 m (ESO) telescope, and are part of the HARPS GTO programs: HARPS-1 (Mayor et al., 2003); HARPS-2 (Lo Curto et al., 2010) and HARPS-4 (Santos et al., 2011). These data have been automatically processed by the HARPS pipeline**, and cover a spectral range between 3782—6913 Å. After discarding those spectra with a low signal-to-noise ratio (∼S/N < 100), we normalised and cleaned from cosmic rays and telluric features using IRAF*** routines.

In order to measure the standard Mount Wilson index S_{MW}, first we integrated the flux in two windows centred at the cores of the Ca II H&K lines (3968.47 Å and 3933.66 Å, respectively), weighted with triangular profiles of a 1.09 Å full width at half-maximum (FWHM), and computed the ratio of these fluxes to the mean continuum flux, integrated in two passbands of 20 Å width centred at 3891 and 4001 Å. Then, we used the calibration procedure of Lovis et al. (2011) to derive the S_{MW} indexes from HARPS spectra (see Flores et al., 2017).

*`http://archive.eso.org/wdb/wdb/adp/phase3_spectral/form?phase3_collection=HARPS`

**`http://www.eso.org/sci/facilities/lasilla/instruments/harps/overview.html`

***IRAF is distributed by the National Optical Astronomical Observatories, which is operated by the Association of Universities for Research in Astronomy, Inc., under a cooperative agreement with the National Science Foundation.

3. Results

Previous to computing the S_{MW} index for the whole sample of 1111 FGK stars, we excluded those stars with less than ten spectra****. As a result, we obtained 600 stars (out of 1111, corresponding to 54 % of the sample) available to analyse. Then, in order to study the long-term chromospheric activity for these 600 FGK stars, we computed the generalised Lomb-Scargle (GLS) periodogram and the false-alarm probability (FAP) of the periods, following Zechmeister & Kürster (2009). For the detection of reliable periodicities, we use a cut-off in FAP of 0.1 per cent (0.001). As a result, we detected clear chromospheric activity cycles in 30 stars (out of 600, corresponding to 5 % of the sample). Some of these chromospheric activity cycles have already been published by our group (Flores et al., 2016, 2017, 2018). The 570 remaining objects of the sample were classified as erratic ($(\sigma/ < S_{MW} >) > 2$ %) or flat ($(\sigma/ < S_{MW} >) < 1.5$ %), following the Baliunas et al. (1995) criteria. In addition, a high percentage of stars remains, at the moment, as unclassified.

Due to space constraints, in Fig. 1 we only show the time series corresponding to four (out of 30) of the objects with clear cyclic behaviour, these four stars have a resulting FAP $< 10^{-15}$. Both the periods and the mean Mount Wilson activity indexes ($\langle S_{MW} \rangle$) are shown in Table 1.

Fourteen of the cyclic stars found here are G-type stars, which allow us to compare their cycle properties directly with the solar one. For example, it can be observed that the star M2 seems to show an activity cycle with variable amplitude, which is also showed by the solar cycle.

****As previously mentioned, the S/N of the selected spectra must be greater than or equal to 100.

Table 1: Cycle length and mean activity levels corresponding to the stars of Fig. 1 and Fig. 2.

Ref.#	HIP	Cycle (days)	$\langle S_{MW} \rangle$
M1	27435	3755±200	0.173±0.001
M2	42291	3316±650	0.202±0.002
M3	90656	3274±700	0.239±0.002
M4	57172	4170±870	0.172±0.001
M5	86765	3401±820	0.186±0.003

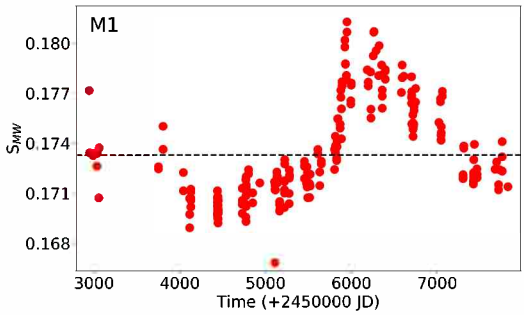

Figure 2: Time series of S_{MW} index for the star HIP 27435. The dashed line indicates the $\langle S_{MW} \rangle$.

Another object of interest within these fourteen G-type stars, is showed in the Fig. 2. Here, we present a long-term activity cycle of 10.2 yr (see the corresponding GLS periodogram of Fig. 3) found in a solar-analogue star (e.g. Delgado Mena et al., 2014). This cycle has not yet been reported in literature. In addition to the similarity between this activity cycle with the solar one, their mean activity levels are also very similar to each other $\log(R'_{HK})$=-4.94 vs. $\log(R'_{HK})$=-4.94/-4.91, according to the solar values derived by Hall et al. (2007) and Mamajek & Hillenbrand (2008). These similar patterns indicate that this solar-analogue star would be a good candidate, if we want to explore several solar cycle properties.

4. Conclusions and future work

The HARPS database has also proven to be a good tool for the search of chromospheric activity cycles. The quantity and quality of spectra available have allowed us to detect new activity cycles in several stars, in particular, in solar-analogues and solar-twins (see Flores et al., 2016, 2017, 2018).

Our mail goal is to study these new activity cycles in order to compare them with the solar cycle properties. In this same direction, those stars with signatures of flat activity which could be in a Maunder Minimum state†, are also important if we want to know a little more about the solar cycle and its properties.

Both the search of activity cycles and the characterisation of the types of variability in this sample of 600 objects, are affected by the large number of stars that remains, at the moment, as unclassified. In this case, we are referring to stars with few observations, those with high FAP's in their temporal series, stars with very noisy temporal series or not very dense and also stars with a limited sampling. The statistical, when possible, will be improved with CASLEO observations.

†The period between 1645 and 1715 during which solar activity was greatly reduced (e.g. Eddy, 1976).

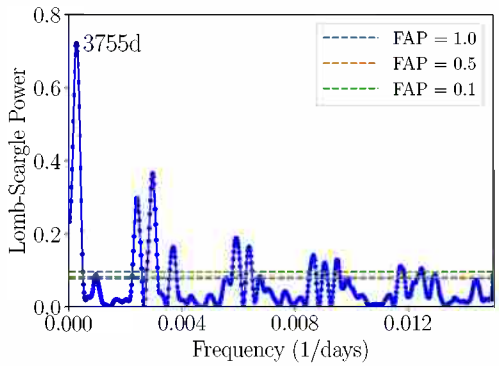

Figure 3: GLS periodogram for the Mount Wilson indexes data of the star M1. Horizontal dashed lines correspond to a FAP of 0.1, 0.5 and 1 (per cent), respectively.

We are now working with the solar-analogue star M1, which has an activity cycle and a mean activity level very similar to the solar values. Beside the variation detected in the Ca II H&K lines, M1 also shows other spectral lines with signs of appreciable variations (e.g. H_α and Fe II). It is an interesting finding because these lines might be used, for instance, to detect a possible activity cycle in those surveys that do not include the classical Ca II H&K lines in their spectra. These results will be promptly published.

References

Baliunas S. L., et al., 1995, ApJ, 438, 269
Baliunas S. L., et al., 1998, in Cool Stars, Stellar Systems, and the Sun. pp 154, 153
Buccino A. P., et al., 2014, ApJL, 781, L9
Charbonneau P., 2010, Living Reviews in Solar Physics, 7, 3
Delgado Mena E., et al., 2014, A&A, 562, A92
Duncan D. K., et al., 1991, ApJS, 76, 383
Eddy J. A., 1976, Science, 192, 1189
Egeland R., et al., 2015, ApJ, 812, 12
Egeland R., 2017, PhD thesis, Montana State University, Bozeman, Montana, USA
Flores M., et al., 2016, A&A, 589, A135
Flores M. G., et al., 2017, MNRAS, 464, 4299
Flores M., et al., 2018, MNRAS, 476, 2751
Hall J. C., Lockwood G. W., Skiff B. A., 2007, AJ, 133, 862
Hall J. C., et al., 2009, AJ, 138, 312
Hathaway D. H., 2010, Living Reviews in Solar Physics, 7, 1
Henry T. J., et al., 1996, AJ, 111
Lo Curto G., et al., 2010, A&A, 512, A48
Lovis C., et al., 2011, ArXiv e-prints
Mamajek E. E., Hillenbrand L. A., 2008, ApJ, 687, 1264
Mayor M., et al., 2003, The Messenger, 114, 20
Metcalfe T. S., et al., 2010, ApJL, 723, L213
Santos N. C., et al., 2011, A&A, 526, A112
Vaughan A. H., Preston G. W., Wilson O. C., 1978, PASP, 90, 267
Wilson O. C., 1978, ApJ, 226, 379
Zechmeister M., Kürster M., 2009, A&A, 496, 577

Estudio del estado evolutivo del sistema binario que contiene al pulsar de milisegundos PSR J1227−4853

J. González[1], M. Echeveste[1], M.A. De Vito[1,2] & O.G. Benvenuto[1,2,3]

[1] *Facultad de Ciencias Astronómicas y Geofísicas, UNLP, Argentina*
[2] *Instituto de Astrofísica de La Plata, CONICET–UNLP, Argentina*
[3] *Comisión de Investigaciones Científicas de la Provincia de Buenos Aires, Argentina*

Contacto / juliang1555@gmail.com

Resumen / El pulsar PSR J1227−4853 pertenece a un sistema binario que recientemente ha realizado una transición, pasando del estado de Sistema Binario de Baja Masa en Rayos X, en el que se observaba al sistema como fuente de rayos X, al estado de pulsar, en el que se observa al pulsar de milisegundos.
Este objeto es uno de los tres sistemas binarios eclipsantes conocidos que han realizado esta clase de transición. Todos ellos son miembros de la familia *redback*.
Utilizando nuestro código de evolución binaria, hemos hallado las características de un sistema binario interactuante que podría ser un posible progenitor del sistema que contiene a PSR J1227−4853.

Abstract / The pulsar PSR J1227−4853 belongs to a binary system which recently had made a transition from the Low Mass X-Ray Binary state, in which we observe the system as an X ray source, to a pulsar state, where we can see the millisecond pulsar.
This object is one of the three know eclipsing binary systems that have made this kind of transitions. All of them are members to the redback family.
Using our binary evolutionary code, we have found the characteristics of a close binary system that could be a possible progenitor of the system harboring PSR J1227−4853.

Keywords / binaries (including multiple): close — Stars: evolution — pulsars: individual PSR J1227−4853

1. Introducción

El pulsar PSR J1227−4853 se encuentra en un sistema binario que hasta hace poco tiempo se mostraba como una fuente de rayos X. En el año 2015, Roy et al. (2015) observaron un decaimiento en la emisión en rayos X, y detectaron la presencia del pulsar. Podemos entender este cambio en el marco de la evolución de sistemas binarios que presentan transferencia de masa entre sus componentes, conocidos como Sistemas Binarios Interactuantes (SBI). En este caso, el sistema binario está compuesto por una estrella de neutrones (EN) y una compañera que le provee del material que acreta a través del desborde de su lóbulo de Roche. Este material además lleva consigo momento angular, que acelera a la EN, propiciando así el rejuvenecimiento del pulsar. Este proceso se conoce como "reciclado del pulsar" (Alpar et al., 1982).

Cuando el material provisto por esta compañera alcanza la superficie de la EN, el sistema se muestra como una intensa fuente de rayos X. Este estado es el de "emisión en rayos X". Si por algún motivo (que no discutiremos en este trabajo) cesa la acreción por parte de la EN, decae la luminosidad en altas energías y se puede detectar al pulsar en emisión de radio.Este es el "estado de pulsar".

Actualmente se conocen tres sistemas que han cambiado de estado, pasando de estado de emisión en rayos X al de pulsar, o inversamente: PSR J1023+0038, conocido como el "eslabón perdido" ya que fue el primero de estos objetos en el que se detectó esta transición, confirmando la teoría de reciclado de pulsares en SBI; PSR J1824−2452I, perteneciente al cúmulo globular NGC 6626 (M28); PSR J1227−4853, que es el objeto de estudio en este trabajo. Esto nos indicaría que el proceso de reciclado no es continuo, como se desprendía desde el modelo de evolución binaria estándar, sino que ocurre en ciclos.

Los tres sistemas que han realizado estas transiciones pertenecen a la familia *redback*. Estas binarias están compuestas por una EN receptora y una compañera donante que aún quema hidrógeno en su núcleo, con masas características $M_2 \sim 0.5\ M_\odot$ (Roberts, 2013). Al igual que sus parientes, las *black widows*, presentan períodos orbitales (P) menores que 1 día.La diferencia más notable entre ambas familias radica en las masas características de las compañeras del pulsar. En las *black widows* son un orden de magnitud menor que en el caso de las *redback* ($M_2 \sim 0.05\ M_\odot$), y son objetos que se encuentran en estado de degeneración. Además, han sufrido una importante etapa de ablación por parte del viento del pulsar, responsable de la bajísima masa de su compañera (ver Sección 2.). El primer objeto de la familia *black widow*, B 1957+20, fue hallado por Fruchter et al. (1988) en el año 1988.

La transición más reciente en este grupo fue observada en PSR J1227−4853, yendo del estado de emisor de rayos X al estado de pulsar (Roy et al., 2015).

Tabla 1: Parámetros observados para el sistema binario que contiene a PSR J1227−4853.

Parámetro	Valor
P	0.288 d
q	0.194
M_2 (mínima)	0.211 $M_\odot$

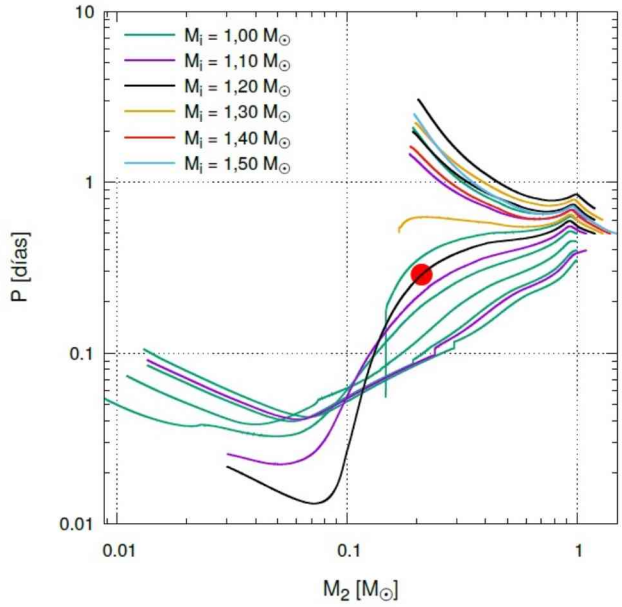

Figura 1: Plano $M_2 - P$ para algunos de los cálculos evolutivos realizados en la búsqueda de un sistema binario que reproduzca el estado actual de PSR J1227−4853. El punto rojo representa dicho estado.

Combinando la amplitud de la velocidad radial proyectada para el pulsar, $K_1 = 50.622619464(1)$ km s^{-1}, con la amplitud de la velocidad radial proyectada de la compañera, $K_2 = 261(5)$ km s^{-1} (de Martino et al., 2014), los autores restringen el valor del cociente de masas $q = M_2/M_P = 0.194(3)$. La función de masas para este sistema es $f = 0.00386973\ M_\odot$. Tomando la inclinación propuesta por de Martino et al. (2014), $i \lesssim 73°$, la masa de la compañera se encuentra en el rango $0.167 - 0.462\ M_\odot$, mientras que para el pulsar el rango es $0.86 - 2.38\ M_\odot$. El valor del período orbital del sistema es $P = 0.288$ d, y el pulsar tiene un período de rotación $P_P = 1.686$ ms.

Los datos observacionales característicos para este sistema, se presentan en la Tabla 1. El valor de la masa mínima se calcula considerando una inclinación de 90° y una masa para la EN de 1.35 $M_\odot$.

2. Evaporación e Irradiación

La evaporación por el viento del pulsar produce una tasa de pérdida de masa extra del sistema, fundamental en el modelado de sistemas del tipo *black widow* (Stevens et al., 1992).

La irradiación sobre la estrella donante es producto de la luminosidad de acreción que libera la EN cuando cae sobre ella el material cedido por su compañera. Esto modifica la evolución de esta componente, y del sistema binario. Es importante considerar este efecto en el cálculo evolutivo de sistemas tipo *redback* (Hameury & Ritter, 1997). Los resultados más importantes que se obtienen cuando se considera la irradiación en los cálculos evolutivos son, por un lado, el estado de casi desborde del lóbulo de Roche de la estrella donante. Esto es observado en sistemas pertenecientes a la familia *redback*, en los que la estrella donante ocupa una importante fracción de su lóbulo de Roche. Por otro lado, y vinculado con este estado, los episodios de transferencia de masa cíclica, en lugar de un único y prolongado evento, como se encuentra en el modelo estándar de evolución binaria.

3. Búsqueda del progenitor

Utilizando nuestro código de evolución binaria (Benvenuto & De Vito, 2003) en el que consideramos los efectos de la irradiación de la EN sobre su compañera (Benvenuto et al., 2014) realizamos una serie de cálculos evolutivos hasta encontrar los parámetros iniciales correspondientes a un posible progenitor del sistema que mejor ajusten a los datos actuales.

En la Fig. 1 mostramos los recorridos evolutivos en el plano $M_2 - P$. Este plano es de fundamental importancia en los pulsares de milisegundo que se encuentran en sistemas binarios ya que allí se ubican, en regiones bien identificadas, las compañeras de estos objetos. Las enanas blancas de helio de baja masa, enanas blancas de carbono/oxígeno, las compañeras no degeneradas de la familia *redback* y objetos de masa muy baja en estado de degeneración en la familia *black widow* se ubican en zonas relativamente bien determinadas en este plano (ver, por ejemplo, Benvenuto et al. 2014).

Nuestra grilla consistió en un grupo de estrellas donantes con masas iniciales entre 1.00 y 1.50 $M_\odot$ y meta-

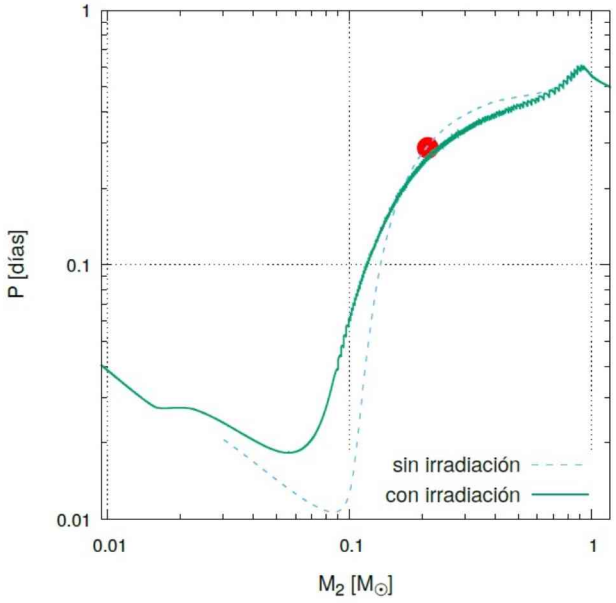

Figura 2: Plano $M_2 - P$ para los cálculos con y sin irradiación.

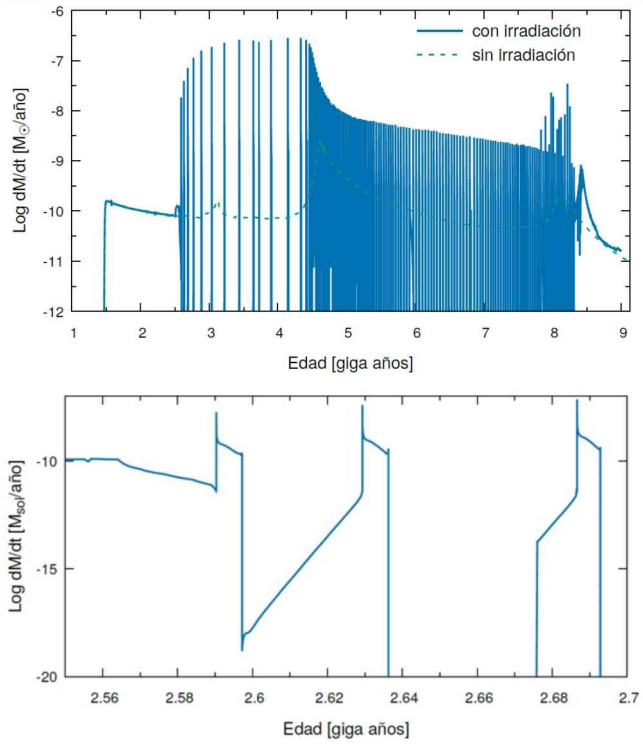

Figura 3: Panel superior: tasa de transferencia de masa en función de la edad para los cálculos con y sin irradiación. Panel inferior: ampliación de una región del panel superior.

licidad solar; los períodos orbitales iniciales se eligieron entre 0.25 y 0.75 días; la EN se consideró con una masa canónica como valor inicial. Como puede observarse en la Fig. 1, el mejor ajuste se obtuvo para un sistema masa inicial de la estrella donante de 1.20 $M_\odot$ y período orbital inicial de 0.5 d.

En las Figs. 2 y 3 puede observarse el recorrido evolutivo en el plano $M_2 - P$ y la transferencia de masa cíclica, respectivamente, cuando se considera la irradiación en el cálculo que nos provee al mejor candidato para describir el estado actual de este sistema.

4. Conclusiones y trabajo a futuro

Hemos encontrado los parámetros iniciales que caracterizan a un posible progenitor para el sistema binario que contiene a PSR J1227−4853, considerado en este trabajo. Los cálculos realizados indican que el sistema evolucionará hacia la región del plano $M_2 - P$ ocupada por la familia de las *black widows*.

La incorporación de la irradiación no modifica sustancialmente el camino evolutivo, sin embargo la modificación que esta introduce en la tasa de transferencia de masa resulta necesaria (aunque no suficiente) para explicar la transición que presentó este sistema desde un estado de emisor de rayos X a un estado de pulsar.

Si bien considerar la irradiación hace de nuestros modelos aproximaciones más realistas, y la transferencia de masa cíclica que resulta de ellos constituye una descripción más apropiada para los objetos de la familia *redback*, no alcanzan para describir las transiciones que van de estado de emisión en rayos X al de pulsar, o inversamente. Las observaciones muestran que estas transiciones ocurren en escalas de tiempo del orden de meses, mientras que los ciclos de transferencia de masa son de miles de años.

Consideramos que estos episodios de transiciones están vinculados a fenómenos de corta escala en el disco de acreción que rodea a la EN. Esperamos, en un futuro cercano, dedicarnos a estudiar el disco de acreción que rodea a la EN en *redbacks*.

Referencias

Alpar M.A., et al., 1982, Nature, 300, 728
Benvenuto O.G., De Vito M.A., 2003, MNRAS, 342, 50
Benvenuto O.G., De Vito M.A., Horvath J.E., 2014, ApJL, 786, L7
de Martino D., et al., 2014, MNRAS, 444, 3004
Fruchter A.S., Stinebring D.R., Taylor J.H., 1988, Nature, 333, 237
Hameury J.M., Ritter H., 1997, A&AS, 123, 273
Roberts M.S.E., 2013, J. van Leeuwen (Ed.), *Neutron Stars and Pulsars: Challenges and Opportunities after 80 years*, *IAU Symposium*, vol. 291, 127–132
Roy J., et al., 2015, ApJL, 800, L12
Stevens I.R., Rees M.J., Podsiadlowski P., 1992, MNRAS, 254, 19P

Formación de sistemas binarios ultracompactos

M. Echeveste[1], J. González[1], O.G. Benvenuto[1,2,3] & M.A. De Vito[1,2]

[1] *Facultad de Ciencias Astronómicas y Geofísicas, UNLP, Argentina*
[2] *Instituto de Astrofísica de La Plata, CONICET–UNLP, Argentina*
[3] *Comisión de Investigaciones Científicas de la Provincia de Buenos Aires, Argentina*

Contacto / maite.echeveste@gmail.com

Resumen / Estudiamos desde un punto de vista teórico los sistemas binarios ultracompactos (UCXBs) en el marco de los sistemas binarios interactuantes. Empleando nuestro código de evolución binaria investigamos la formación de los UCXBs explorando el espacio de parámetros del problema (período orbital y masa inicial de la estrella donante) con el objeto de hallar la región que da lugar a su formación. Tuvimos en cuenta el efecto de evaporación originada por el viento del púlsar y la irradiación mutua, efectos importantes a tener en cuenta en sistemas donde ambas componentes se encuentran muy próximas y que han sido ignorados en otros trabajos.

Abstract / We study from a theoretical point of view the ultracompact binary systems (UCXBs) in the framework of interacting binary systems. Using our binary evolution code we investigate the formation of UCXBs by exploring the parameter space of the problem (orbital period and initial mass of the donor star) in order to find the region that gives rise to its formation. We took into account the evaporation effect caused by the pulsar wind and mutual irradiation. These are important effects to be taken into account in systems where both components are very close and that have been ignored in other papers.

Keywords / binaries (including multiple): close — stars: evolution

1. Introducción

Los sistemas binarios ultracompactos que emiten en rayos X (UCXBs, por sus siglas en inglés) son el resultado de la evolución de sistemas binarios en los que se han dado episodios de transferencia de masa. Son un caso particular de los sistemas binarios de baja masa con emisión en rayos X (LMXB, por sus siglas en inglés), en donde el período orbital alcanza un valor $P \leq 1$ h, la luminosidad en rayos X, $L_X \geq 10^{36}$ erg s^{-1} y tienen su magnitud absoluta disminuida respecto a los LMXB, ya que la mayor parte del flujo en el óptico proviene de la emisión del disco de acreción y este es menor en los UCXBs (Nelemans & Jonker, 2010).

Se cree que en algunos sistemas binarios que constan de una estrella de neutrones (EN) y otra estrella donante normal en una órbita con período muy corto, la donante alcanza el estado de enana blanca (EB) de helio. Como consecuencia de la pérdida de momento angular por efecto de la radiación gravitatoria, la órbita se vuelve cada vez más cerrada y eventualmente la EB llena su lóbulo de Roche. En este estado el sistema sufre un proceso de transferencia de masa tardío, formando un UCXB. Los UCXBs resultan interesantes por diversos motivos (Lombardi et al., 2006):

- Dominan el brillo en rayos X duros de galaxias elípticas.
- Para entender la estructura y evolución estelar de objetos de baja masa degenerados y casi-degenerados.
- Están relacionados con la formación de púlsares reciclados (púlsares de milisegundos).
- Serían los progenitores de púlsares binarios con compañeras de muy baja masa en cúmulos globulares.
- Son fuentes ideales para el *Laser Interferometer Space Antenna* (LISA).

Vale la pena mencionar que en la base de datos de púlsares ATNF* es posible encontrar varios sistemas binarios que cuentan con períodos suficientemente cortos como para que evolucionen al estado de UCXB en una escala de tiempo menor que la edad del Universo.

2. Marco teórico

Los LMXBs son descriptos por el modelo estándar (Podsiadlowski et al., 2002) como sistemas en los que la estrella donante pierde materia debido al desborde de su lóbulo de Roche. Una fracción de esta materia es acretada por la EN que en este momento actúa como un emisor de rayos X. Büning & Ritter (2004) mostraron que es necesario considerar en los modelos esta irradiación, que al ser recibida por la estrella donante, hace que el proceso de transferencia de masa ocurra en forma de pulsos. De esa manera, modelos más realistas muestran que el sistema binario debería observarse como un LMXB durante el período de transferencia de masa y como un púlsar y un objeto que lo acompaña durante el siguiente período en que la transferencia cesa (Benvenuto et al., 2014). En este trabajo consideramos la irradiación con el objeto de aportar a la comprensión de su efecto sobre los sistemas que estudiamos. Por otra parte, consideramos el efecto de evaporación de la estrella donante debido al viento del púlsar. Este fenómeno produce una tasa extra de

*`http://www.atnf.csiro.au`

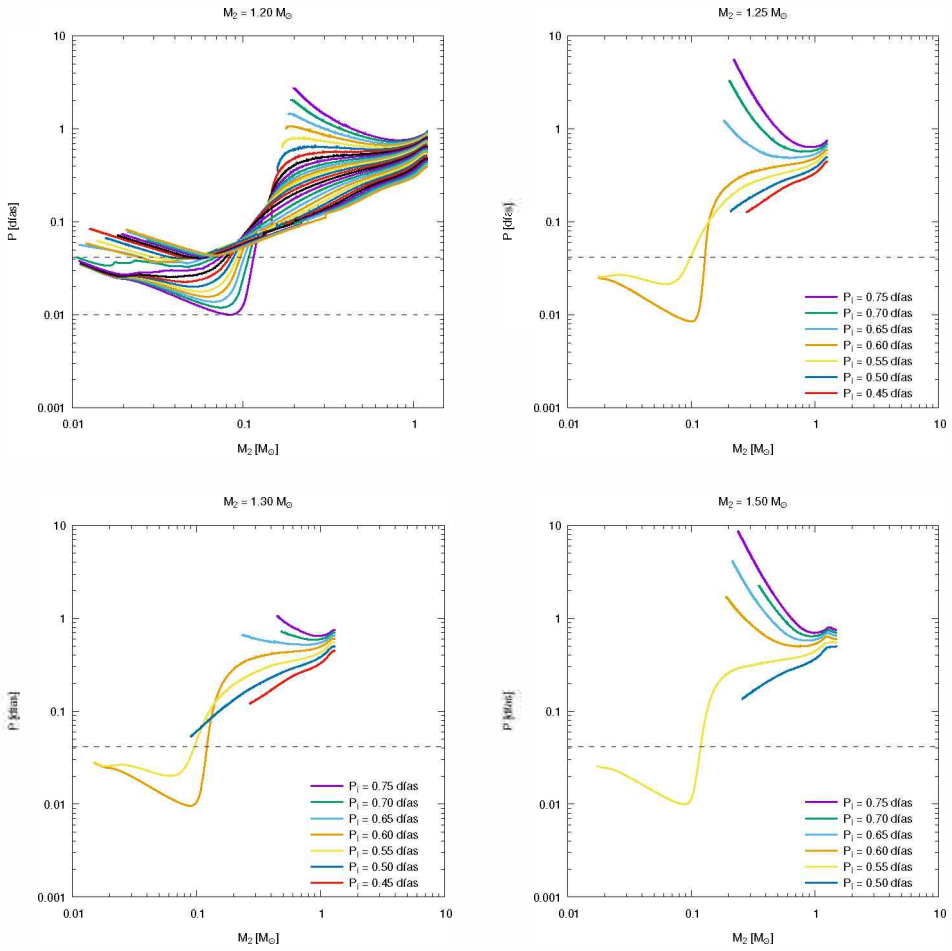

Figura 1: Relación masa de la estrella donante vs Período orbital para diferentes valores de la masa inicial de la estrella donante. Las líneas punteadas corresponden a $P = 1$ h y a $P = 14.4$ min.

pérdida de masa del sistema en estadíos avanzados en que ambas estrellas se encuentran muy próximas entre sí. Como consecuencia, el período orbital del sistema es mayor y la masa de la estrella donante es más chica (en concordancia con las observaciones) que lo predicho por los modelos que no consideran este efecto.

3. Los cálculos

Utilizando nuestro programa de evolución binaria (Benvenuto & De Vito, 2003) calculamos una serie de recorridos evolutivos utilizando distintos valores para la masa inicial de la estrella donante ($M_{2,i} = 1.20, 1.25, 1.30, 1.40$ y $1.50 M_\odot$) y del período orbital inicial (P_i). Para el caso de $M_{2,i} = 1.20$ realizamos una exploración muy detallada variando P_i desde 0.42 hasta 0.94 d, con un paso de 0.02 d. Para $M_{2,i} = 1.40$ y $1.50 M_\odot$ utilizamos valores de P_i desde 0.50 hasta 0.75 d, con un paso de 0.05 d y para $M_{2,i} = 1.25$ y $1.30 M_\odot$ usamos P_i desde 0.45 hasta 0.75 d con un paso de 0.05 d. Encontramos que los sistemas que evolucionan a UCXB son:

- $M_{2,i} = 1.20 M_\odot$, $P_i = 0.60$, 0.62, 0.64, 0.66, 0.68, 0.70, 0.72, 0.74, y 0.76 d;
- $M_{2,i} = 1.25 M_\odot$, $P_i = 0.55$, y 0.60 d;
- $M_{2,i} = 1.30 M_\odot$, $P_i = 0.55$, y 0.60 d;
- $M_{2,i} = 1.40 M_\odot$, $P_i = 0.55$ d;
- $M_{2,i} = 1.50 M_\odot$, $P_i = 0.55$ d.

En la Fig. 1 se muestran los caminos evolutivos en el plano *masa de la estrella donante* (M_2) vs. *período orbital del sistema* (P). Cada gráfico corresponde a un valor distinto para $M_{2,i}$, como se indica en la parte superior. Las distintas curvas representan los recorridos correspondientes a diferentes valores de P_i. En el caso en que $M_{2,i} = 1.20$ M$_\odot$, se puede ver que en los sistemas convergentes la masa de la estrella donante alcanza valores extremadamente pequeños. En los casos de las configuraciones que alcanzan el estado de UCXB, M_2 llega a ser entre $\simeq 0.075$ y 0.042 M$_\odot$ en el momento en que se alcanza el mínimo valor de P.

Para los valores de $M_{2,i} = 1.25$, 1.30 y 1.50 M$_\odot$, todos los caminos evolutivos con $P_i = 0.65$, 0.70 y 0.75 d divergen. Por otro lado, en los cuatro casos, los sistemas con P_i de 0.55 d terminan en configuraciones ultracompactas, llegando a tener un P mínimo de $\simeq 0.01$ d (14.4 min) para el caso de $M_{2,i} = 1.50$ M$_\odot$ y un P mínimo aún menor para 1.25 M$_\odot$ y 1.30 M$_\odot$. La diferencia más notable entre estas tres Figuras es que para las dos

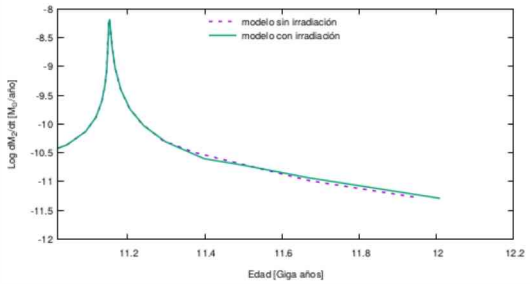

Figura 2: Variación de la tasa de transferencia de masa para los UCXBs con $M_{2,i} = 1.20$ M$_\odot$ y $P_i = 0.70$ días para el modelo irradiado y no irradiado.

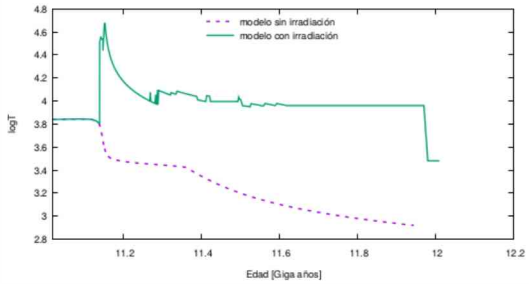

Figura 3: Edad vs Logaritmo de la temperatura efectiva de la estrella donante en el punto enfrentado a la EN para el UCXB con $M_{2,i} = 1.20$ M$_\odot$ y $P_i = 0.70$ d en el modelo irradiado y no irradiado.

masas iniciales menores, el valor de $P = 0.60$ d conlleva a UCXB mientras que para $M_{2,i} = 1.50$ M$_\odot$ el sistema se vuelve divergente.

Por otro lado, y debido a la complejidad numérica que implica considerar el efecto de irradiación, estudiamos este efecto solo sobre uno de los sistemas que evolucionaron a UCXB, el correspondiente a $M_{2,i} = 1.20 M_\odot$ y $P_i = 0.70$ d. El efecto fue considerado a partir de que el sistema alcanza $P = 1$ h, ya que antes de esto la irradiación no cambia cualitativamente su evolución. En la Fig. 2 se grafica el *logaritmo de la tasa de transferencia de masa* en función de la *Edad* del sistema para dos sistemas con los parámetros iniciales mencionados, en el que uno de los dos está afectado por la irradiación y el otro no. Como puede verse, ambas curvas son iguales, por lo que podemos concluir que en este caso el efecto de irradiación no modifica de manera apreciable la transferencia de masa.

Sin embargo, este efecto produce un cambio en la temperatura de la estrella donante en el punto enfrentado a la EN, como puede verse en la Fig. 3. El aumento abrupto en la temperatura que sufre la estrella modelada teniendo en cuenta el efecto de irradiación ocurre en el mismo momento en que se produce el pico en el segundo episodio de transferencia de masa, por lo que evidentemente estos dos hechos están relacionados.

Además, comparamos nuestros resultados con datos observacionales de UCXBs listados en Heinke et al. (2013). Analizando los recorridos evolutivos de algunos de los sistemas con $M_{2,i} = 1.20 M_\odot$ que evolucionan a UCXB en función de P (en el rango de 10 a 60 min) y del logaritmo de la tasa de transferencia de masa, se puede ver (Fig. 4) que cuando se superponen las curvas calculadas con las observaciones, estas se encuentran cerca de los recorridos computados.

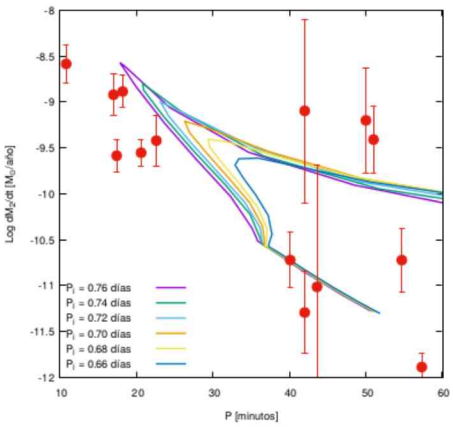

Figura 4: UCXBs con $M_{2,i} = 1.20$ M$_\odot$ y P_i entre 0.76 y 0.66 d en el plano P vs Logaritmo de la transferencia de masa. Las observaciones y sus correspondientes errores están representados mediante puntos rojos y barras de error.

4. Conclusiones

Hemos estudiado la formación de los UCXBs empleando el código de evolución binaria (Benvenuto & De Vito, 2003) y considerando además el efecto de evaporación. Realizando una exploración del período orbital inicial, P_i, y de la masa inicial de la estrella donante, $M_{2,i}$, hemos encontrado que nuestros modelos predicen que el rango de períodos iniciales para los que se alcanza la configuración que corresponde a los UCXBs es extremadamente delgado tal como fue hallado por otros autores (Istrate et al., 2014). Esto puede ser interpretado como una muestra de que algún proceso importante ha sido omitido en los modelos. Planeamos en un futuro cercano estudiar la posibilidad de que el intervalo de períodos iniciales sea más amplio en el caso de considerar interacciones dinámicas con un tercer objeto que pasa cerca y perturba el sistema. Por otro lado, estudiamos el efecto de irradiación sobre uno de los sistemas que evoluciona a UCXB a partir de que alcanza $P = 1$ h. No encontramos cambios apreciables en las fases de transferencia de masa aunque sí una gran diferencia en la temperatura de la estrella donante en el punto que está enfrentado a la estrella de neutrones.

Referencias

Benvenuto O.G., De Vito M.A., 2003, MNRAS, 342, 50
Benvenuto O.G., De Vito M.A., Horvath J.E., 2014, ApJL, 786, L7
Büning A., Ritter H., 2004, A&A, 423, 281
Heinke C.O., et al., 2013, ApJ, 768, 184
Istrate A.G., Tauris T.M., Langer N., 2014, A&A, 571, A45
Lombardi Jr. J.C., et al., 2006, ApJ, 640, 441
Nelemans G., Jonker P.G., 2010, NewAR, 54, 87
Podsiadlowski P., Rappaport S., Pfahl E.D., 2002, ApJ, 565, 1107

Spectropolarimetry of SN 2010jl

J. Quirola-Vásquez[1,2], F.E. Bauer[1,2,3], A. Clocchiatti[1,2], P. Zelaya[1] & D. Farías[1]

[1] *Instituto de Astrofísica, Pontificia Universidad Católica de Chile, Santiago, Chile*
[2] *Millennium Institute of Astrophysics, Santiago, Chile*
[3] *Space Science Institute, Boulder, Colorado, USA*

Contact / jquirola@astro.puc.cl

Resumen / La SN 2010jl es una de las supernovas tipo IIn más brillantes jamás detectadas en todas las bandas de energía, debido a una fuerte interacción con el medio circunestelar. Con una distancia de $\sim$ 40 Mpc y una magnitud absoluta de $M_{\rm peak} \approx -20.5$, la SN 2010jl es uno de los objetos mejor estudiados del tipo IIn desde ondas de radio hasta Rayos-X. Estudiamos posibles asimetrías en la SN 2010jl analizando datos de espectropolarimetría óptica de alta S/N obtenidos por el instrumento VLT FORS2-PMOS en +44, +93 y +542 días después de su aparente explosión. Encontramos simetrías axiales en el material eyectado analizando la polarización del continuo, así como asimetrías en las regiones de formación de las líneas más intensas.

Abstract / SN 2010jl is one of the brightest SNe type IIn ever detected in all energy bands, due to a strong circumstellar medium interaction. With a distance of $\sim$ 40 Mpc and absolute magnitude of $M_{\rm peak} \approx -20.5$, SN2010jl is one of the best-studied examples of the IIn class from Radio to X-rays bands to date. We study potential asymmetries in SN 2010jl by analyzing high S/N optical linear spectropolarimetry data obtained by VLT FORS2-PMOS instrument at +44, +93 and +542 days after the apparent SN explosion. We found axial symmetries in the ejecta analyzing the polarization of the continuum, as well as asymmetries in the line forming regions of the most intense emission lines.

Keywords / supernovae: general — supernovae: individual (SN 2010jl)

1. Introduction

Core-collapse supernovae (CCSNe) are produced by the explosion of massive stars ($M > 8$ M$_\odot$; Woosley et al., 2002) releasing a huge amount of material which enriches the interstellar medium with heavy elements. Particularly, supernovae (SNe) type IIn are a subclass of CCSNe (less than 10 % of the total number of CCSNe; Eldridge et al., 2013) which present narrow or intermediate width Hydrogen and Helium emission lines in their optical spectra (Schlegel, 1990; Filippenko, 1997). Overall, SNe type IIn are associated with the interaction of fast-moving SN ejecta and slower-moving dense circumstellar medium (CSM, $n \gtrsim 10^{6-8}\,{\rm cm}^{-3}$; Chevalier & Fransson, 1994; Chugai, 1997; Bauer et al., 2008). The CSM was created by stellar winds and mass-loss episodes during previous evolutionary phases of the progenitor star. Moreover, SNe type IIn are characterized by intense, composite-profile emission lines and lack of broad P-Cygni absorption and high X-ray/Radio emission (Schlegel, 1990; Patat et al., 2011; Bauer et al., 2011).

The majority of extragalactic SNe are too distant to resolve their geometry with currently available, or even planned, telescope facilities (Reilly et al., 2017). Spectropolarimetry is a powerful tool to constrain the 3D geometry of unresolved extragalactic SNe, which are critical to understanding the nature of the explosion. There is substantial evidence that suggests CCSNe are not spherically symmetric; the best example is the resolved asymmetric structure of SN 1987A (Fransson et al., 2013; Frank et al., 2016), which has been observed in many different energy bands. Other CCSNe, without the same spatial resolution, show evidence of asphericity using X-rays or spectropolarimetry techniques.

SN 2010jl was discovered by Newton & Puckett (2010) on 2010 November 3, and subsequently was classified as a type IIn on November 5 by Benetti et al. (2010). SN 2010jl is located at α=09^{h}42^{m}53^s.337, δ=+09°29′42.″13 (J2000, Chandra et al., 2015) in the host galaxy UGC 5189A at a distance of 40 Mpc (z=0.0107). Using archival data, the explosion date was established around 15–25 days before I-band maximum, i.e. 2010 September 29–October 9 (Chandra et al., 2015). In this document, we analyze the spectropolarimetry of SN 2010jl at three different epochs. Spectropolarimetric observations were acquired with the FOcal Reducer and low dispersion Spectrograph (FORS2), in its dual-beam spectropolarimeter PMOS mode. The observational epochs correspond to days +44 (E1), +93 (E2), and +542 (E3) after the SN explosion. We adopted October 1, 2010, as the likely explosion date.

2. Polarization analysis

The electromagnetic polarization is characterized by the Stokes parameters I, Q, U and V (Chandrasekhar, 1960; Wang & Wheeler, 2008). The degree of linear ($V = 0$) polarization is defined as the quadratic sum of the Stokes parameters Q and U, P=$\sqrt{Q^2+U^2}$. On the other hand, the polarization angle on the sky is given by

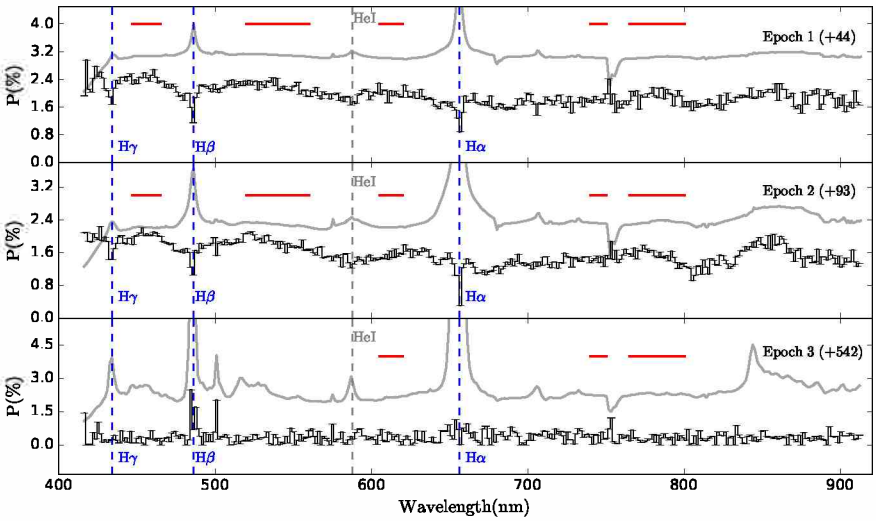

Figure 1: Spectropolarimetric data were taken by VLT FORS2-PMOS instrument at E1, E2, and E3 epochs. The degree of polarization (*black* error lines), uncorrected by the interstellar polarization (ISP), as a function of wavelength is presented with the data binned to 15 Å. The *grey* lines are the spectra at each epoch.

θ=0.5 arctan(U/Q) taking into account the quadrants in the Q–U plane (Mauerhan et al., 2014). In Fig. 1 we can see the degree of polarization P (uncorrected by interstellar polarization, ISP) for three different epochs as a function of the wavelength.

We derived the contribution by the interstellar medium (ISM) to the observed polarization. The most important physical process that contributes to the intrinsic polarization is electron scattering. Computing the interstellar polarization is non-trivial, and depends on the assumption that specific wavelength regions of the spectra must be intrinsically unpolarized (Reilly et al., 2016). We considered that the polarization of narrow Hα lines comes from the CSM via recombination; thus, the non-zero polarization of the narrow components of Hα must come only from ISM, where the average ISP obtained from the three epochs is $P_{\rm ISP,ave}$=0.52±0.01 %. We used this value of ISP to correct the data.

2.1. Continuum polarization

After defining the contribution from the ISP, we analyzed the polarization of the continuum. This was determined by taking the inverse error-weighted average of Stokes parameters Q and U in the wavelength regions defined by the lack of emission lines (see *horizontal, red* lines in Fig. 1). As the spectrum of SN 2010jl evolves with time, including the continuum's regions, the degrees of polarization of the continuum are $P_{\rm con,1}$=1.80±0.01 %, $P_{\rm con,2}$=1.41±0.01 % and $P_{\rm con,3}$=0.39±0.01 % for E1, E2 and E3, respectively. The polarization degree at E1 is similar to the obtained by Patat et al. (2011), $P_{\rm con}$ ∼1.9(%), acquired four days after E1. Furthermore, the polarization angles for the continuum are $\theta_{\rm con,1}$∼ 135.8°, $\theta_{\rm con,2}$ ∼137.6° and $\theta_{\rm con,3}$∼19.3° for E1, E2 and E3, respectively. Such a large degree of polarization suggests that the photosphere of the SN may have significant departures from axisymmetry.

2.2. Intrinsic line polarization

Fig. 2 shows the dependence of the degree and angle of polarization concerning the velocity of the emission lines at different epochs. We analyzed the temporal evolution of the intrinsic polarization of the emission lines at E1, E2 and E3. To determine the intrinsic polarization of the lines, we consider that the observed polarization ($P_{\rm obs}$) is a contribution of the continuum polarization ($P_{\rm con}$) and the line polarization ($P_{\rm Line}$) as (Reilly et al., 2016, 2017): $P_{\rm obs}$=($P_{\rm con}F_{\rm con}$+$P_{\rm Line}F_{\rm Line}$)/$F_{\rm obs}$, where $F_{\rm line}$ and $F_{\rm con}$ are the line and continuum fluxes, respectively. These values were measured from the data, where we obtained that the value $P_{\rm line}$ changes according to the observed polarization. The Balmer lines show similarities at E1 and E2, with the line cores being strongly depolarized. These narrow lines likely arise from recombination of Hydrogen in a distant, presumably largely isotropic stellar wind. The same behavior is presented in other emission lines such as He I λ5876. Meanwhile at E3, the intrinsic polarization is essentially constant for Hα and Hγ; additionally the polarization of Hβ increases sharply. This later feature suggests that beyond day 540 the spatial origin of Hβ is different respect to the other Balmer lines.

The intrinsic polarization of H$_\alpha$ is P$_{\rm line}$=0.69±0.2 % over the three epochs. We see a similar trend for He I λ5876, with an intrinsic polarization of $P_{\rm line}$=0.45±0.47(%). On the other hand, the intrinsic polarization of Hγ falls with time from $P_{\rm line}$=1.47±0.36 % to 0.34±0.14 %, while the polarization of Hβ is steady during the first two epochs $P_{\rm line}$=0.46±0.35 %, but increases to 1.58±0.28 % at E3. The polarization angles of Hγ and He I λ5876, as well as the very high-velocity portions of Hα and Hβ,

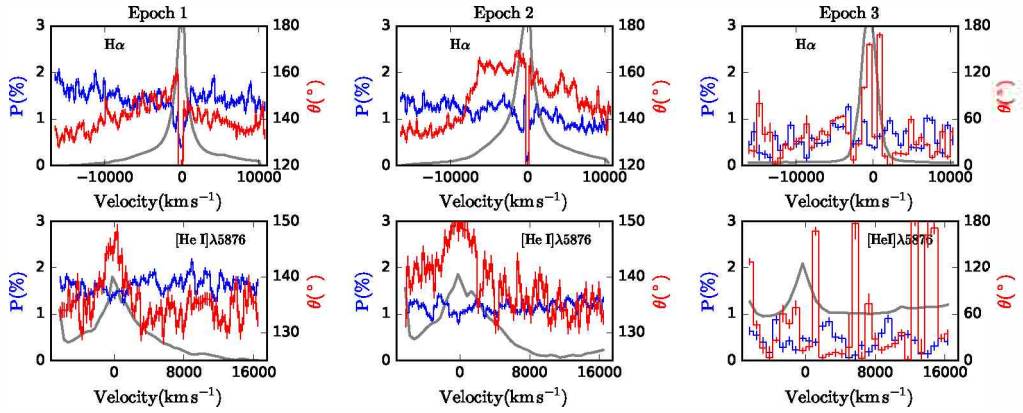

Figure 2: Angle (*red* solid line) and degree (*blue* solid line) of polarization in the velocity space for the most intense emission lines (*grey* solid line) for three epochs, E1 (*left* panels), E2 (*center* panels), and E3 (*right* panels).

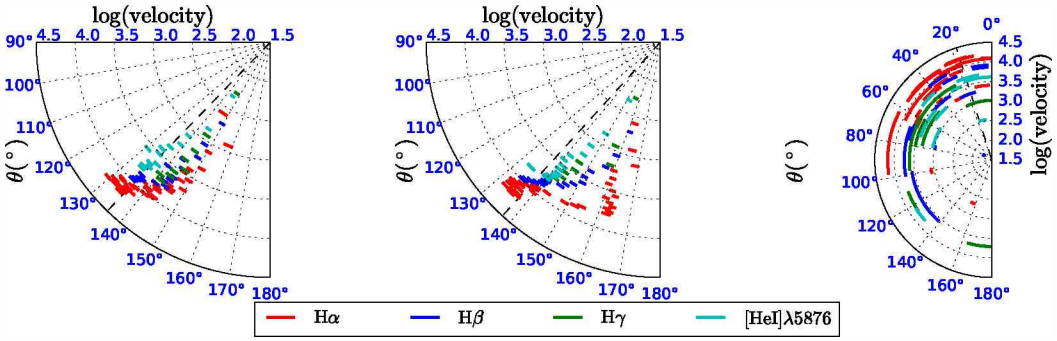

Figure 3: Polar diagram of SN 2010jl at epochs E1, E2, and E3 from *left* to *right*, respectively. The diagrams show the polarization angle as a logarithmic function of the velocity (km s^{-1}; increasing radially) of the blue portion of the lines. The polarization angles across the line profiles for Balmer lines and HeIλ5876 are plotted as colors, while the continuum polarization angle is denoted by the *black* dashed line.

are reasonably well-aligned with continuum angle during E1 and E2, and possibly E3 (see Fig. 3). Intriguingly, the moderate velocity portions of all lines, during E1 and E2, are associated with higher angles. At E3, the high-velocity portions of the polarized lines appear to be spread over a large range of angles, which may point to a higher degree of asymmetry in the inner layers of the SN.

3. Conclusions

SN 2010jl is one of the brightest SNe type IIn ever detected in all energy bands, due to a strong CSM interaction. With a distance of ~ 40 Mpc, it is an excellent object to use spectropolarimetry to understand its asymmetries and geometry. According to our analysis, the ejecta itself may show asymmetries at different epochs, as implied by the rotation of the continuum polarization angle by $\sim$110° between E1/E2 to E3. Furthermore, the emission lines present hints of asymmetries either by the CSM or the SN itself.

Acknowledgements: We acknowledge support from: CONICYT through Programa de Capital Humano Avanzado, folio #21180886 (JQ-V) Basal AFB-170002 (JQ-V, FEB, AC), and FONDECYT Regular 1141218 (JQ-V, FEB); the Ministry of Economy, Development, and Tourism's Millennium Science Initiative through grant IC120009, awarded to The Millennium Institute of Astrophysics, MAS (JQ-V, FEB, AC).

References

Bauer F.E., et al., 2008, ApJ, 688, 1210-1234
Bauer F.E., et al., 2011, Proceedings of the International Astronomical Union, 7, 325
Benetti S., et al., 2010, Central Bureau Electronic Telegrams, 2536, 1
Chandra P., et al., 2015, ApJ, 810, 32
Chandrasekhar S., 1960, *Radiative transfer*, Dover
Chevalier R.A., Fransson C., 1994, ApJ, 420, 268
Chugai N.N., 1997, Ap&SS, 252, 225
Eldridge J.J., et al., 2013, MNRAS, 436, 774
Filippenko A.V., 1997, ARA&A, 35, 309
Frank K.A., et al., 2016, ApJ, 829, 40
Fransson C., et al., 2013, AJ, 768, 88
Mauerhan J., et al., 2014, MNRAS, 442, 1166
Newton J., Puckett T., 2010, Central Bureau Electronic Telegrams, 2532, 1
Patat F., et al., 2011, A&A, 527, L6
Reilly E., et al., 2016, MNRAS, 457, 288
Reilly E., et al., 2017, MNRAS, 470, 1491
Schlegel E.M., 1990, MNRAS, 244, 269
Wang L., Wheeler J.C., 2008, ARA&A, 46, 433
Woosley S.E., Heger A., Weaver T.A., 2002, Reviews of Modern Physics, 74, 1015

Accretion disks in symbiotic stars

G.J.M. Luna[1]

[1] *Instituto de Astronomía y Física del Espacio, CONICET–UBA, Argentina*

Contact / gjmluna@iafe.uba.ar

Resumen / En general, el mecanismo de acreción en sistemas simbióticos, donde una gigante roja transfiere materia a su compañera enana blanca, es difícil de observar y existen más posibilidades de hacerlo en aquellos sistemas donde no hay quema nuclear cuasiestable de material en la superficie de la enana blanca. Utilizando datos en altas energías, que permiten observar las regiones más internas del proceso de acreción, hemos estudiado dos eventos sin precedentes en dos sistemas simbióticos, RT Cru y T CrB, con masas de objeto compacto similares, pero con diferentes períodos orbitales lo que implica diferentes mecanismos de acreción.
Durante los últimos 20 años, se observaron dos aumentos de brillo en el óptico en RT Cru, separados por aproximadamente 4000 días y con una amplitud de ΔV$\sim$1.5 mag. Aunque similar a erupciones tipo *dwarf-nova*, el comportamiento en rayos X duros no se condice con lo observado en prototipos de la clase *dwarf-novae*. Alternativamente, estos eventos podrían explicarse si la tasa de acreción aumenta a medida que la enana blanca orbita dentro del viento de la gigante roja, con un período orbital de $\sim$4000 días.
En T CrB hemos observado un incremento en la tasa de acreción, el cual ha cambiado dramáticamente la estructura de la parte más interna del disco. Datos en óptico, UV y rayos X sugieren que el aumento de brillo en óptico que se registró en 2014 junto con la abrupta disminución del brillo en rayos X duros y la aparición de una componente *soft* en rayos X, indican que este evento, debido a una inestabilidad en el disco de acreción, podría ser similar a otro evento observado 8 años antes de la explosión termonuclear de 1946.

Abstract / The nature of accretion in symbiotic binaries, in which the red giant transfers material to a white dwarf (WD) companion, has been difficult to uncover. The accretion flows in a symbiotic binary are most clearly observable, however, when there is no quasi-steady shell burning on the WD to hide them. Through observations in the high energy regime, which provide a view of the innermost accretion structures, we have studied two unprecedented events in two systems, RT Cru and T CrB, which host similar massive white dwarf but have very different orbital periods with correspondingly different accretion mechanism.
In the past 20 years, RT Cru has experienced two similar optical brightening events, separated by $\sim$4000 days and with amplitudes of ΔV$\sim$1.5 mag, reminiscent of dwarf-novae-type outbursts, but the hard X-ray behavior does not correspond to that observed in well-known dwarf nova. An alternative explanation for the brightening events could be that they are due to an enhancement of the accretion rate as the WD travels through the red giant wind in a wide orbit, with a period of about $\sim$4000 days.
We have witnessed a change in the accretion rate for the first time in the symbiotic recurrent nova T CrB. Optical, UV and high energy data indicate that during an optical brightening event that started in early 2014 (ΔV$\approx$1.5), the hard X-ray emission has almost vanished and the X-ray spectrum became much softer and a bright, new, blackbody-like component appeared. We suggest that the optical brightening event, that could be a similar event to that observed about 8 years before the most recent thermonuclear outburst in 1946 is due to a disk instability.

Keywords / binaries: symbiotic — accretion, accretion disks — stars: individual (RT Cru, T CrB)

1. Introducción

White dwarf symbiotic stars are binary systems composed of an accreting white dwarf, a mass-lossing red giant and a nebulae that surrounds the system. The accretion mechanism/s in symbiotic stars is believed to be mostly due to some form of wind accretion, with a few exceptions where there is evidence of Roche-lobe overflow. A few symbiotic stars have X-ray emission sometimes hard and bright enough to be detected with the Neil Gehrels *Swift Observatory* Burst Alert Telescope (BAT). The hard X-ray spectrum is most likely due to a hot, highly absorbed, optically thin thermal plasma from the accretion disk boundary layer. Given the large size of the accretion disk, it should be prone to instabilities (Duschl, 1986). In fact, variability is virtually a hallmark of symbiotic stars. Large amplitude novae-type outburst are detected in those few symbiotic stars that belong to the recurrent novae class, where the sudden brightening is due to a thermonuclear runaway on the WD surface (see e.g. O'Brien et al., 2006, and references therein). Somewhat smaller outburst, known as classical symbiotic outburst, are also common and their origin is still a matter of debate (see e.g. Sokoloski et al., 2006; Kato et al., 2012). Outbursts with even smaller amplitude are observed in most symbiotic stars, likely due to instabilities in the accretion disks.

Here we present the observations of two symbiotic binary systems, RT Cru and T CrB, each one representing a case of the two accretion mechanisms. In both systems we have detected significant changes in their hard X-ray flux as observed with the *Swift*/BAT, which, to-

gether with changes in their X-rays/UV/optical fluxes, can be explained as due to a change in the accretion rate through the accretion disk. However, the overall behavior of both systems is fundamentally different. In T CrB we observed that in early 2014, an optical brightening with ΔV$\sim$1 mag started and was referred as a "super-active" state by Munari et al. (2016). The light curve from the AAVSO indicates that the maximum brightness was reached around 4–5 April 2016 (see Figure 1 in Luna et al., 2018a). Almost in tune with the optical brightness increase, the *Swift*/BAT 14–50 keV flux declined from $\sim$4 mCrab to $\sim$2 mCrab, and then exhibited a sudden drop to 0 (within 1 sigma) until now. The 0.3–10 keV X-ray flux has decreased significantly and the UV flux increased by at least a factor of 40 over the quiescent value. A deep *XMM–Newton* observation taken well into the super-active state revealed a complex spectrum (Fig. 1) that can be divided into three energy ranges. Above 3 keV, there is a highly absorbed thermal component, likely the same δ-type component seen in T CrB in its normal state (Kennea et al., 2009; Luna et al., 2013). Below $\sim$0.7 keV, the spectra are dominated by a soft, unabsorbed component. A blackbody provide an good description of this region. Photons are also detected in the intermediate energy range (0.7–3 keV). All components are absorbed by interstellar absorption and local, partial covering absorption that blocks 99.7 % of the emission. The softest X-ray spectrum consists of blackbody-like emission (with $T_{\rm bb}$=4$\times$10^5 K) from a region smaller than the surface of the WD, with a spherical surface area of 4.2$\times$10^7 km^2 (in the case of a WD with 1.2 M$_\odot$ and $R_{\rm WD}$=5$\times$10^8 cm, this represents approximately 13 % of the surface of the WD). The hard (0.6$<E<$10 keV) spectra were consistent with a multi-temperature, cooling flow, with maximum temperature $kT_{\rm max}$=12.9 keV.

In RT Cru we observed that the optical light curve shows two similar brightening events separated by $\sim$4,000 days. In contrast with T CrB, during the second event, *Swift* detected an increase in the BAT hard X-ray flux of at least a factor of two Luna et al. (see Figure 1 in 2018b). Interestingly, the hardness ratio within the BAT band remained fairly constant. During bright states, such as those seen during 2001 and 2012, lines from the Balmer series, He I λ5875, He II λ4686, [O III] λ5007 and other highly ionized species are strong, with a moderately bright continuum dominating at longer wavelengths. In turn, during faint optical states, Hα and other lines were very faint or absent in the spectra, with the red giant continuum prevailing toward longer wavelengths (see Figure 4 in Luna et al., 2018b). Our *NuSTAR* observations taken during a low-optical state allowed us to detect for the first time in a symbiotic system, a clear signature of reflection in the hard X-ray spectrum, with an amplitude of 0.77$\pm$0.21. This detection allows us to accurately determine the plasma shock temperature with a value of $kT_{\rm max}$=53$\pm$4 keV, which in the case of strong shock conditions and optically thin boundary layer, can be translated into a WD mass of 1.25$\pm$0.02 M$_\odot$.

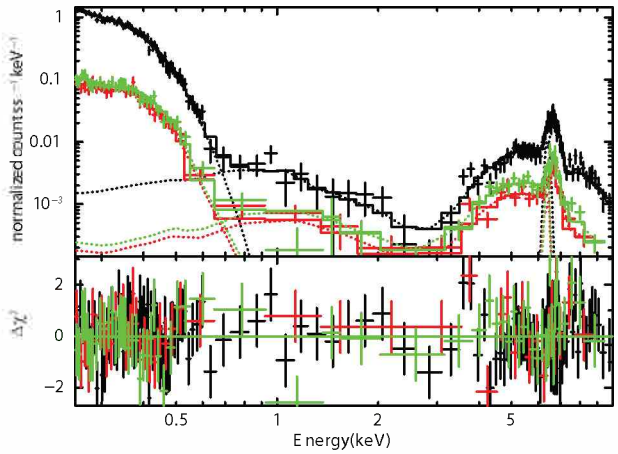

Figure 1: *XMM*-Newton *pn* (black), MOS1 (red), and MOS2 (green) X-ray spectra of T CrB data with the best spectral model (solid line) and the contribution of each model's component (dotted lines). The model consists of a blackbody plus an optically thin cooling-flow and a Gaussian profile centered at the Fe Kα energy of 6.4 keV. The fit residuals in units of χ^2_ν are shown in the bottom panel.

2. Consequences of changing $\dot{M}$

A major question for accreting WDs, particularly in those accreting at rates around 10^{-9} $M_\odot$ yr^{-1}, is the structure of the boundary layer. At lower $\dot{M}$, the boundary layer should remain optically thin to its own radiation and emit entirely in the hard X-rays regime, with temperatures of a few 10^8 K. At high $\dot{M}$, the boundary layer is expected to become optically thick, and begin radiating with temperatures of less than 10^6 K, in the extreme UV/soft X-rays. The threshold where the boundary layer becomes optically thin or thick has been modeled in some cases. Narayan & Popham (1993) concluded that when $\dot{M}$=3.16$\times$10^{-10} $M_\odot$ yr^{-1}, the boundary layer would be hot and a source of hard X-rays, with a transition to this regime starting at $\dot{M}$ $\sim$10^{-10} $M_\odot$ yr^{-1}. In their study of optically thick solutions for the boundary layer in cataclysmic variables, Popham & Narayan (1995) derived $\dot{M}$ values for the transition for different values of M$_{WD}$, Ω and the viscosity parameter α. By assuming that the transition would occur at τ_*=1, the authors found that in a non-rotating WD, the transition accretion rate at τ_*=1, $\dot{M}(\tau_*=1)_{tr}$, would occur at rates greater than about 7.5$\times$10^{-7} $M_\odot$ yr^{-1}. A slightly smaller optical depth, τ_*=0.8 yielded $\dot{M}(\tau_*=0.8)_{tr}$=4.6$\times$10^{-8} $M_\odot$ yr^{-1}. Suleimanov et al. (2014) found that these thresholds might be overestimated due an underestimation of the Rosseland opacity which can be off by two orders of magnitude.

We suggest that the optical brightening event observed in T CrB, which could be similar to that observed about 8 years before the most recent thermonuclear outburst in 1946, is due to a disk instability. The changes observed in optical, UV and X-rays demonstrate that after early 2014, the rate of mass transfer onto the WD, $\dot{M}$ increased and the boundary layer became predominantly optically thick. We modeled the X-ray spectrum

with all components absorbed by interstellar absorption and local, partial covering absorption that blocks 99.7 % of the X-rays. The soft X-ray spectrum is modeled with a blackbody-like emission. The hard spectrum was modeled with a multi-temperature, cooling flow. In fact, at a distance of about 800 pc (as recently determined with *GAIA*), the blackbody-emitting region has a luminosity of $6.68{\times}10^{35}$ ergs s^{-1}. Assuming an standard accretion disk where half of the accretion luminosity is radiated in the boundary layer, we found that the accretion rate feeding the optically thick portion of the boundary layer was about $6.6{\times}10^{-8}$ M$_{\odot}$ yr^{-1}. The luminosity of the optically thin portion of the boundary layer, from the cooling flow spectral model in the 0.3-50 keV, was $4.7{\times}10^{32}$ ergs s^{-1}. These accretion rates are consistent with the expected theoretical values where the boundary layer is optically thick/thin to its own radiation (Patterson & Raymond, 1985; Narayan & Popham, 1993; Popham & Narayan, 1995).

The multiwavelength behavior in RT Cru is different from disk instability, dwarf-novae type outbursts, which have a rapid rise to maximum, the time-lapse of which is determined by the distance between the region in the accretion disk where the instability has started and the boundary layer. In RT Cru, it took approximately 2000 days from optical minimum to maximum, but a similar delay was not observed between optical and hard X-rays. The prototypical dwarf nova SS Cyg (Wheatley et al., 2003) exhibits a hardening of the X-ray spectrum during optically faint phases, which can be explained if the accretion rate is low and the optical depth of the boundary layer is small. During outburst, the X-ray spectrum softens due to the increase of the accretion rate, similarly to what we have observed in T CrB. Such softening of the X-ray emission is not observed during the optical brightening in RT Cru. The constancy of the hardness ratio observed with BAT indicates that the temperature of the hard X-ray emitting plasma has not changed during the optical brightening. The optical brightening around JD 2451870 and the re-brightening approximately 4 000 days later could, nevertheless, have been due to disk instabilities such as those behind dwarf novae-type outbursts, if the accretion rate did not change enough to greatly increase the optical depth of the boundary layer. Our simultaneous *Swift* XRT and UVOT observations suggest that the boundary layer has remained optically thin throughout the optical brightening and thus the derived accretion rate of $\approx 4.1{\times}10^{-9}$ $M_{\odot}$ yr^{-1} is still below the optically thick/thin threshold.

In Fig. 2 we show the phase-folded AAVSO+ASAS light curve with a period of 3 992 d (best period found through phase-dispersion minimization) and we include an auxiliary color scale for the observation to clearly highlight the time of phase coincidence. The fact that not only the maximum but also the fading rate after it seem to repeat, suggest that there could be a periodicity.

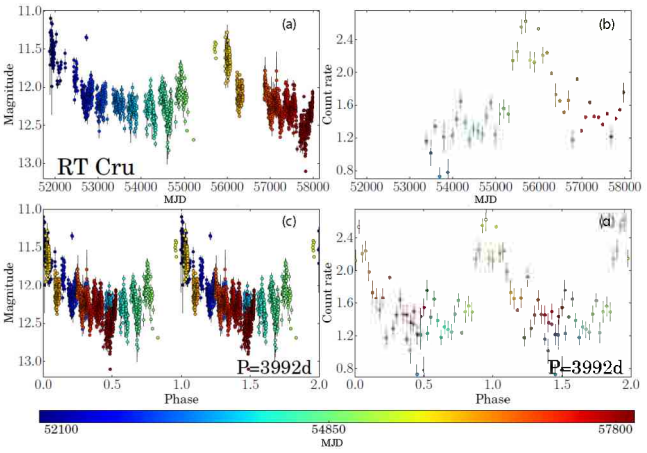

Figure 2: *(a)*: AAVSO+ASAS V magnitude light curve. *(b)*: *Swift*/BAT light curve in 10^{-4} count s^{-1}, with 100 d bin size. *(c)* AAVSO+ASAS V-magnitude light curve folded at a period of 3 992 d. *(d) Swift*/BAT light curve at a period of 3 992 d. We include an auxiliary color scale to clearly highlight the time of phase coincidence. The observations cover a single cycle, which is not enough to obtain a secure determination of its likelihood. However, the fact that the maximum and the fading rate seem to repeat, suggests that the periodicity could be real.

Until more data are available, this is only speculative. If this is indeed a periodic behavior, it could be a long orbital period and in such a case, the optical and high-energy brightening could be explained if the accretion rate onto the WD increases when it "travels" through the densest part of the red giant's wind.

Acknowledgements: I thanks the SOCHIAS-AAA organizers for their help to attend the meeting.

References

Duschl W.J., 1986, A&A, 163, 56
Kato M., Mikołajewska J., Hachisu I., 2012, ApJ, 750, 5
Kennea J.A., et al., 2009, ApJ, 701, 1992
Luna G.J.M., et al., 2013, A&A, 559, A6
Luna G.J.M., et al., 2018a, A&A, 619, A61
Luna G.J.M., et al., 2018b, A&A, 616, A53
Munari U., Dallaporta S., Cherini G., 2016, NewA, 47, 7
Narayan R., Popham R., 1993, Nature, 362, 820
O'Brien T.J., et al., 2006, Nature, 442, 279
Patterson J., Raymond J.C., 1985, ApJ, 292, 535
Popham R., Narayan R., 1995, ApJ, 442, 337
Sokoloski J.L., et al., 2006, ApJ, 636, 1002
Sulcimanov V., et al., 2014, A&A, 571, A55
Wheatley P.J., Mauche C.W., Mattei J.A., 2003, MNRAS, 345, 49

Asteroseismic analysis of subdwarf B variable stars of KIC 10001893 and EPIC 220641886

M. Uzundag[1], M. Vučković[1], R. Silvotti[2], A. Baran[3] & R.H. Østensen[4]

[1] *Instituto de Física y Astronomía, Facultad de Ciencias, Universidad de Valparaíso, Valparaíso, Chile*
[2] *INAF-Osservatorio Astronomico di Torino, Pino Torinese, Italy*
[3] *Uniwersytet Pedagogiczny, Obserwatorium na Suhorze, Poland*
[4] *Department of Physics, Astronomy, and Materials Science, Missouri State University, USA*

Contact / murat.uzundag@postgrado.uv.cl

Resumen / KIC 10001893 y EPIC 220641886 son estrellas subenanas B pulsantes de tipo V1093 Her. Las mismas han sido observadas por *Kepler* en las misiones nominal y K2, respectivamente. A partir de la amplitud espectral de las estrellas, se puede decir que la mayoría de las frecuencias de sus pulsos se encuentran en modo g. De las frecuencias detectadas, 248 pertenecen al dominio de modo g y 15 dentro del rango de modo p, mostrando la naturaleza híbrida de ambas estrellas. Para identificar el grado de los modos hemos utilizado la herramienta sísmica *asymptotic period spacing*. En nuestro análisis, no hemos podido detectar multipletes rotacionales en ninguna de las dos estrellas, lo cual podría indicar que se encuentran en dirección polar. A la estrella KIC 10001893 le hemos asignado modos dipolares y cuadrupolares, mientras que a la estrella EPIC 220641886 le hemos asignado modos que van desde $l = 1$ hasta $l = 12$, exceptuando los modos $l = 3$ y $l = 11$, que no han sido observados.

Abstract / KIC 10001893 and EPIC 220641886 are V1093 Her type pulsating subdwarf-B stars, which were observed by the *Kepler* spacecraft during nominal and K2 mission respectively. The amplitude spectrum of both stars show similar characteristics that the majority of the pulsation frequencies lay in the gravity g-mode domain. While the g-mode region contains 248 frequencies, the p-mode region contains just 15, altogether indicating the hybrid nature of both stars. We used one of the seismic tools, asymptotic period spacing effectively to identify the modal degree of the majority of the modes. We could not find rotational multiplets for both stars which is likely due to pole-on orientation. We assigned dipole and quadrupole modes for KIC 10001893, while for EPIC 220641886 we defined modal degrees ranging from $l = 1$ to $l = 12$, apart from $l = 3$ and $l = 11$ modes, which are not seen.

Keywords / subdwarfs — stars: oscillations (including pulsations)

1. Introduction

Hot subdwarf stars of spectral class B (sdB) are core helium-burning stars, found both in the disk and halo of our Galaxy. The observed properties locate them in the extreme horizontal branch (EHB) part of the HR diagram. Their effective temperatures range from 20 000 to 40 000 K and surface gravities range from 5.0 $\leq \log g \leq$ 6.2 (in cgs units). They are compact objects with radii typically on the order of 0.2 $R_\odot$ and masses confined to about 0.47 $M_\odot$. These stars have experienced extreme mass-loss at the end of the red giant branch phase, in which nearly entire hydrogen envelope is lost, leaving a helium burning core with a very thin inert hydrogen-rich envelope ($M_{\rm env} < 0.01$ $M_\odot$) unable to ascend the asymptotic giant branch. After depletion of helium in the core, they will become subdwarf O (sdO) stars burning helium in a shell surrounding a C/O core and, eventually, they will end their lives as DAO white dwarfs (Heber, 2016). SdB stars are found to pulsate with short period p-modes known as V361 Hya stars and long period g-modes known as V1093 Her stars. Theoretically, Charpinet et al. (1996) explained excitation mechanism for V361 Hya stars as low-order acoustic modes, while Fontaine et al. (2003) explained the excitation mechanism for V1093 Her stars as high-order g-modes. The short period pulsators have frequencies higher than 2000 μHz, while the long period pulsators have frequencies usually below than 1000 μHz, which makes them quite hard to detect from the ground. The V361 Hya stars are found between 28 000 K and 35 000 K with higher surface gravity $\log g$ and V1093 Her pulsators are somewhat cooler with temperatures ranging from 24 000 K to 30 000 K and lower *logg*. There exist also sdB stars that display both kinds of pulsation modes and referred to as hybrid pulsators (Baran et al., 2005). Their nature as hybrid pulsators, gives an invaluable opportunity to understand both the core and the envelope behavior of the stars. Understanding the interior structure of a pulsator heavily depends on the identification of the pulsation modes; which can be achieved by the analyses of precise photometric data using asteroseismological tools. High-precision *Kepler* photometry allowed us to detect many frequencies that we had never obtained previously. Non-radial pulsations are described by spherical harmonics as radial nodes, surface nodes and azimuthal orders n, l, m respectively. The detection of the frequencies with high resolution is a key point to apply asteroseismological methods such as rotational multiplets and asymptotic period spacing to identify the spherical harmonics. In

this paper, we present our analysis of two pulsationally rich long period hybrid sdB stars KIC 10001893 and EPIC 220641886. KIC 10001893 was studied extensively by Baran et al. (2011); Silvotti et al. (2014); Uzundag et al. (2017). The star was observed during the nominal mission of *Kepler* and it yields millions of data points which allow us to characterize pulsation properties of the star. EPIC 220641886 (=HD 4539) is a well known, bright (V = 10.24 mag), sdB star for which g-mode pulsations have been suspected but not confirmed (Schoenaers & Lynas-Gray, 2007). From observations made by the *Kepler* spacecraft during K2 mission, which after failure of the second wheel of *Kepler*, the duty of the mission changed slightly and this makes the data much shorter in comparison with the normal mission of the spacecraft.

Here, using the *Kepler* data, we provide a detailed analysis of KIC 10001893 and EPIC 220641886. Firstly, we have calculated Fourier spectra of the stars. Then, using asteroseismological tools such as asymptotic period spacing and rotational multiplets, we have identified the pulsational modes of both stars. After identification of the pulsational modes, we constructed the échelle diagrams.

2. Methods

After we got all available data from the "Barbara A. Mikulski Archive for Space Telescopes" (MAST)*, we started to extract light curves of the objects. We used short-cadence (SC) data allowing for covering the frequency range up to 8495 μHz, and assuring both p- and g-modes regions are covered. Then, in order to identify pulsation frequencies of the targets, we used Fourier technique to calculate the amplitude spectrum of both stars Fig. 1.

2.1. Rotational multiplets

In the presence of stellar rotation, non-radial modes of degree l split into $2\,l+1$ components differing in azimuthal (m) number. In the case of slow rotation, the frequency splitting can be derived from the following equation:

$$\nu_{n,l,m} = \nu_{n,l,0} + \Delta\nu_{n,l,m} = \nu_{n,l,0} + m\frac{1 - C_{n,l}}{P_{\rm rot}} \qquad (1)$$

where $\Delta\nu_{n,l,m}$ is a rotational splitting, $\mathrm{P_{rot}}$ is a star's rotation period and $C_{n,l}$ is the Ledoux constant (Ledoux, 1951). The method is quite useful both for identification of the pulsation modes and for determining the rotation period of the surface and the core. However, we could not use this method for any of the two stars. The method is strongly dependent of both the inclination of the star and on the frequency resolution. If the stars are pole-on oriented, there is no way to see azimuthal orders on surface of the star and therefore their amplitude spectra. Another dependence is frequency resolution to apply the method, in fact, the frequency resolution is enough for KIC 10001893, the star does not show any tendency amongst frequencies concerning splitting value so it is quite possible that the star is either pole-on oriented or rather slow rotator. However, it is harder to evaluate the amplitude spectra of EPIC 220641886 due to shorter length of the data and thus lower resolution.

*archive.stsci.edu

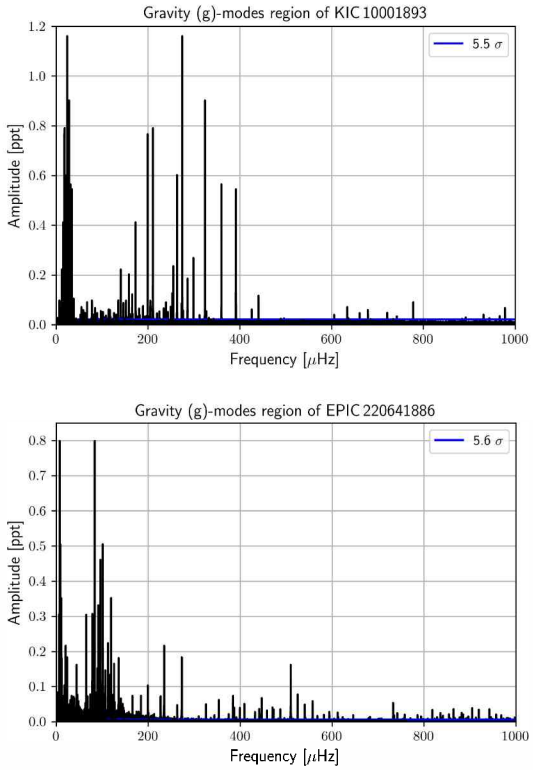

Figure 1: Amplitude spectra of KIC 10001893 and EPIC 220641886, the figures only cover gravity mode regions of the targets.

2.2. Asymptotic period spacing

In order to identify the pulsation modes in the g-mode region, we used asymptotic period spacing. In the asymptotic limit ($n >> l$), consecutive radial overtones are evenly spaced in period Charpinet et al. (2000). For given n and l values, periods of consecutive overtones can be derived from the following equation,

$$\Pi_{l,n} = \frac{\Pi_0}{\sqrt{l(l+1)}}n + \epsilon, \qquad (2)$$

where $\Pi_{l,n}$ is the period spacing, Π_0 and ϵ are constants.

3. Results

We found 110 oscillation frequencies for KIC 10001893 and 153 frequencies for EPIC 220641886. We defined the threshold as 5.4 and 5.6 sigma, respectively, to make sure the signals are produced by the stars intrinsically. The sigma is calculated based on median value of whole range of Fourier spectra. Then, it has been multiply by 5.4 for normal mission of *Kepler* (KIC 10001893) and 5.6 for K2 mission (EPIC 220641886).

3.1. KIC 10001893

The frequency resolution equals 0.0162 μHz as defined by $\Delta f = 1.5/\mathrm{T}$, where T is the time coverage of the data. We identified 110 oscillation frequencies including p- and g-modes region. After identification of the frequencies, we have started to search for pulsational modes using asymptotic period spacing. We identified 50 modal degrees among the g-modes, which is more than 49% of the modes. Out of those 50 modes, 32 are dipole modes and 18 are quadrupole modes. Additionally, we calculated échelle diagrams for $l=1$ and 2 and the diagram for dipole modes shows a common feature of a horizontal shift that called as a hook feature (for detail Baran & Winans, 2012; Uzundag et al., 2017).

3.2. EPIC 220641886

We have analysed K2 observations of one of the brightest known sdBs, confirming the previous report by Schoenaers & Lynas-Gray (2007) that EPIC 220641886 is a V1093 Her-type pulsator. We identify more than 150 pulsation frequencies (144 g-modes, 9 p-modes). Although the frequency resolution is 11 times worse than nominal *Kepler* mission, the amplitude spectra of the star displays quite rich content in terms of g-modes. We have identified 10 sequences between $l=1$ and $l=12$, excluding $l=3$ and $l=11$ which are not seen, likely due to cancellation effects. Since the period spacing changes with l (gets lower with increasing l), the identification of the modes seems quite robust, at least up to $l=6$. It is obvious that cancellation effects are important for high-l modes (Dziembowski, 1977), we are able to see them in EPIC 220641886 is simply due to the fact that this star is particularly bright. In addition to that the modes are visible in the échelle diagrams for $1 \leq l \leq 12$ (Silvotti, Uzundag, et al. 2019, in prep). Here, we present the échelle diagrams for dipole and quadrupole modes Fig. 2.

4. Conclusion

We have shown our analyses of two long period subdwarf B pulsating stars. Both objects show quite rich contents in terms of g-modes, which are sensitive to the core properties of the stars. In total, we identified 248 g-modes, 15 p-modes in both stars. Both stars are hybrid which can be an important feature to constrain both the core and the envelope parameters. Thanks to uninterrupted observations, the seismic tools are becoming quite useful for pulsating sdB stars, specifically, asymptotic period spacing. Using asymptotic relations, we have identified sequences of near-consecutive modes for degrees $(1 \leq l \leq 2)$ for KIC 10001893, $(1 \leq l \leq 12)$ for EPIC 220641886 which will be crucial to make future asteroseismic modeling of both stars.

Acknowledgements: MU gratefully acknowledge financial support from organizing committee. The authors would like to thank Mariana B. Sánchez for translation on the abstract. ASB gratefully acknowledges financial support from the Polish National Science Center under projects No. UMO-2017/26/E/ST9/00703 and UMO-2017/25/B/ST9/02218.

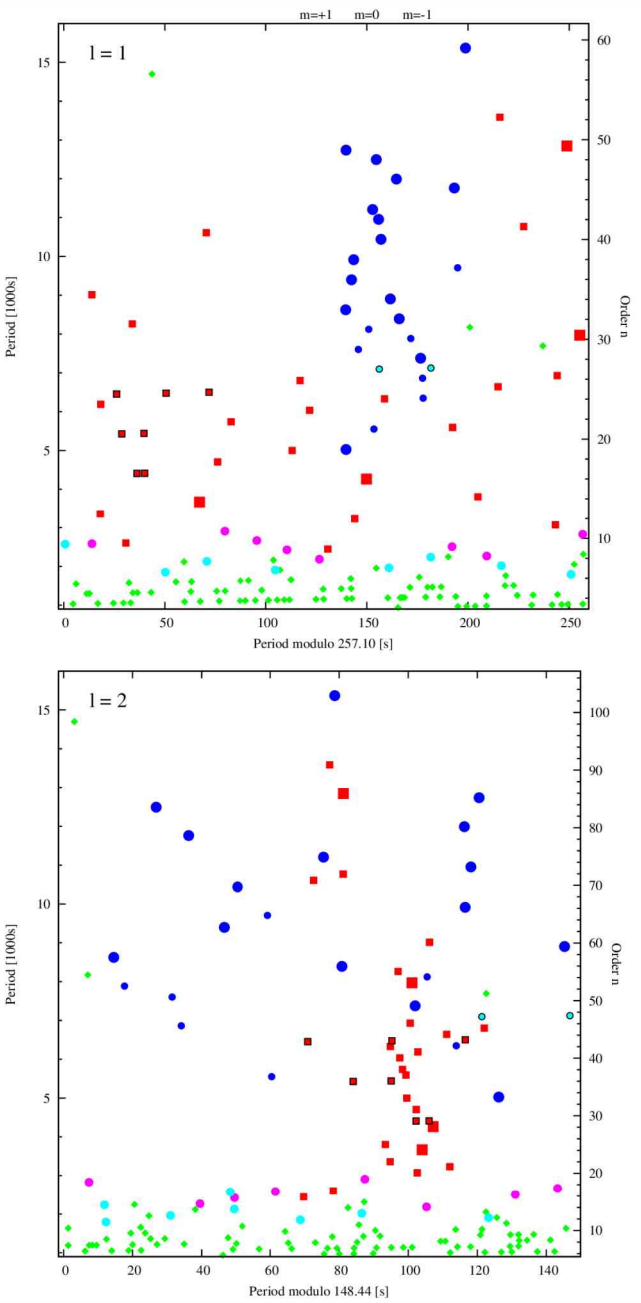

Figure 2: Échelle diagrams of EPIC 220641886 for dipole and quadrupole modes.

References

Baran A., et al., 2005, MNRAS, 360, 737
Baran A.S., Winans A., 2012, AcA, 62, 343
Baran A.S., et al., 2011, MNRAS, 414, 2871
Charpinet S., et al., 1996, ApJL, 471, L103
Charpinet S., et al., 2000, ApJS, 131, 223
Dziembowski W., 1977, AcA, 27, 203
Fontaine G., et al., 2003, ApJ, 597, 518
Heber U., 2016, PASP, 128, 082001
Ledoux P., 1951, ApJ, 114, 373
Schoenaers C., Lynas-Gray A.E., 2007, Communications in Asteroseismology, 151, 67
Silvotti R., et al., 2014, A&A, 570, A130
Uzundag M., et al., 2017, MNRAS, 472, 700

The Lithium content of Globular Clusters

L. Monaco[1]

[1] *Departamento de Ciencias Fisicas, Universidad Andres Bello, Santiago, Chile*

Contact / lorenzo.monaco@unab.cl

Resumen / El litio es uno de los pocos elementos producidos durante la breve fase de la nucleosíntesis cosmológica, unos minutos después del big bang. Por lo tanto, el estudio de su abundancia en estrellas viejas y pobres en metales revela detalles de las condiciones físicas del universo en esta fase temprana. Describiré cómo el estudio de la abundancia de litio en cúmulos globulares proporciona información sobre sus proceso de formación y el valor cosmológico.

Abstract / Lithium is one of the few elements produced during the brief phase of cosmological nucleosynthesis, a few minutes after the big-bang. Therefore, the study of its abundance in old, metal-poor stars reveals details of the physical conditions of the universe in this early phase. I will describe how the study of the lithium abundance in globular clusters provide information about both their formation process and the cosmological value.

Keywords / stars: abundances — stars: atmospheres — primordial nucleosynthesis — globular clusters: general

1. Introduction: the cosmic lithium problem

According to standard cosmology, only a few light elements (H, D, ^{3}He, ^{4}He and traces of ^{7}Li) were produced in appreciable amount during a brief phase of nucleosynthesis (standard big-bang nucleosynthesis, SBBN) which took place a few minutes after the big-bang (Coc et al., 2014). It is from this simple chemical composition, that the first stars (population III) formed a few hundreds of million years afterwards and, soon after, started enriching the interstellar medium (ISM, Bromm & Larson, 2004).

In their seminal papers, Spite & Spite (1982b,a) showed that warm, un-evolved halo stars present the same lithium abundance, within the measurement errors, over a wide range of temperatures and metallicities. The interstellar medium from which these, presumably old, stars formed should not have had time to be enriched in lithium by galactic sources (Romano et al., 1999; Prantzos, 2012; Molaro et al., 2016) and the constant lithium abundance (A(Li)*) measured in their atmospheres (the so called "Spite plateau") was suggested to reflect the cosmic production occurred during the SBBN phase. In fact, since the production of elements during SBBN is determined by the baryon to photon ratio (the η parameter), a cosmological parameter not constrained by first principles, the lithium level at the Spite plateau was used as a tool to determine the η parameter.

However, when η was measured from the cosmic microwave background data of the *WMAP* first and the *Plank* satellites later (Hinshaw et al., 2013; Planck Collaboration et al., 2014), it became possible to predict the amount of lithium produced during the SBBN. This resulted to be three times in excess to the value of the Spite plateau (A(Li)=2.69±0.03 against A(Li)=2.2±0.1 dex, Coc et al., 2014). This discrepancy is usually referred to as the cosmic lithium problem.

*A(Li)=$\log\frac{n(Li)}{n(H)}+12.0$.

2. Searching for a solution

Once the existence of a discrepancy between the lithium abundance at the plateau and the SBBN predictions was acknowledged, the community started to look for a solution to this riddle. To further complicate the observational scenario, a "meltdown" of the Spite plateau was evidenced at metallicities [Fe/H]<-2.8 dex (Bonifacio et al., 2007; Aoki et al., 2009; Sbordone et al., 2010; Bonifacio et al., 2018), where an increase in the scatter, no longer compatible with the measurement errors, together with a lower mean abundance, was observed.

It is worth mentioning that no discrepancy emerged between the prediction and observations, for the elements produced during the SBBN other than lithium (Coc et al., 2014). Therefore, any proposed solution should be able to reconcile the lithium discrepancy, while preserving the agreement achieved for the other elements. At the same time, it should be able to account for a plateau having a dispersion in abundance compatible with the measurement errors and flat over a wide range in temperature ($T_{eff} > 5900$ K) and metallicity (-2.8 to -2 dex, Spite et al., 2012). It should also account for the meltdown of the plateau at [Fe/H]<-2.8 dex.

Solutions to the cosmic lithium problem have been searched for following different routes, either requiring modification to the SBBN theory, investigating the cross section of the nuclear reactions involved, or considering stellar processes which may affect the lithium abundance measured in the stellar atmospheres. We refer the reader to the reviews on the subject by Spite et al. (2012) and Iocco (2012) summarizing both the observational and theoretical aspects of the problem.

Particular interest into solutions outside the stan-

dard cosmological model was triggered by the claim of the detection of a significant amount of ^{6}Li in a sample of metal-poor stars by Asplund et al. (2006). SBBN does not, in fact, produce this isotope in any appreciable amount. On the other hand, the production of ^{6}Li is an outcome of many theories outside the standard model (Iocco, 2012). The abundance of ^{6}Li is measured as an asymmetry in the red wing of the lithium resonance doublet at 6707.8 Å. Such an asymmetry may, however, also be the signature of convective motions in the stellar atmospheres, as readily noticed (Cayrel et al., 2007). Indeed, it seems now well established from state of the art analysis, that the great majority of the claimed ^{6}Li detections were, in fact, due this affect (Steffen et al., 2012; Lind et al., 2013).

3. Stellar solutions

If we accept the SBBN predictions, we may search for solutions to the cosmic lithium problem related to the stellar astrophysics theory.

Diffusion may deplete the lithium content in the stellar atmosphere from its original value. In fact, being heavier than hydrogen, lithium is susceptible to sink into the stellar atmospheres (Michaud et al., 1984). The constant lithium observed at the Spite plateau, suggested that diffusion was inefficient in the atmospheres of metal-poor stars. Furthermore, the lithium depletion in the stellar atmosphere of a metal-poor dwarf is temperature/mass dependent as a consequence of the different extension of the convective envelope (Salaris & Weiss, 2001). Therefore, the inclusion of diffusion in the stellar models is unable to simultaneously reduce the lithium abundance while at the same time produce a plateau similar to the observed one (but see Bressan et al., 2013; Fu et al., 2015).

Richard et al. (2005) tried to remedy the situation including some turbulent mixing phenomenon in their models, beside diffusion, which could be activated at some specific temperature and could bring material, more or less efficiently, down to regions at temperatures $T>2.5\times10^6$ K, where ^{7}Li is readily destroyed. This way, they were able to produce a plateau at a value compatible with observations, starting from the SBBN lithium abundance accepted at that time.

Piau et al. (2006), on a different approach, searched for a solution in the local conditions of formation of the Milky Way halo. They proposed that a first generation of massive population III stars might have efficiently depleted in lithium the material from which population II halo stars observed at the Spite plateau formed. A fraction between one third to one half of the halo material should have been processed in order to obtain a $\sim$0.3 dex depletion in the lithium abundance. An additional, in situ depletion was needed, though, to reconcile the observed value with the cosmological predictions. Prantzos (2007), however, noticed that the enrichment of the ISM caused by these Pop III stars would have led to a metallicity larger than observed in extremely metal poor stars.

We notice that lithium depletion may occur already during the pre-main sequence phase, when temperatures high enough to destroy lithium may be reached in the stellar core, and when the convective envelope extends down to these regions. Standard models indicate this should be significant for masses lower than $\sim$0.7 $M_\odot$ only (Salaris & Weiss, 2001). Fu et al. (2015), on the contrary, proposed a model in which lithium is totally destroyed during the pre-MS phase for masses as high as 0.8 $M_\odot$, and then restored in the stellar atmosphere through a phase of late accretion from the ISM. They were able to reproduce a plateau compatible with the observations.

From the observational point of view, Nissen & Schuster (2012) were able to put into evidence a dependence of the lithium abundance with metallicity and stellar mass. Their sample, however, comprises stars at [Fe/H]$\geq$-1.6 dex only. Meléndez et al. (2010) also showed a similar dependence of the lithium depletion with stellar mass on a sample of stars extended down to [Fe/H]=-3.5 dex. These latter authors found the trend of depletion with mass to be similar to the predictions of Richard et al. (2005) models.

4. Information from globular clusters

Globular clusters (GCs) are among the oldest objects known in the Galaxy (Marín-Franch et al., 2009). They are, thus, precious cosmological probes and witnesses of the early epochs of formation of the Galaxy. For a long time they have been considered the prototype of simple stellar populations and have been a key testbed of the stellar evolution theory (Renzini & Fusi Pecci, 1988). This peculiar combination of properties has made GCs interesting tools to investigate the cosmic lithium problem.

Korn et al. (2006) used high resolution, high signal-to-noise spectra to measure the abundances of main sequence (MS), sub-giant branch (SGB) and red giant branch (RGB) stars in the GC NGC 6397. They detected variations in the abundances of Li, Fe, Ca and Ti, as a function of the evolutionary phase compatible with Richard et al. (2005) models. This lead to suggest those models to provide a "probable" solution to the cosmic lithium problem. It should be noticed, though, that Richard et al. (2005) do not identify the physical origin of the turbulent mixing phenomenon they introduce in their models and the temperature at which this is activated is determined by the comparison with the observations only.

González Hernández et al. (2009), investigated two groups MS and SGB stars at the same temperature in NGC 6397. They found the equivalent widths of the lithium resonance doublet to be stronger among SGB than in MS stars confirming, thus, that the primitive Li abundance was alterer by diffusion. On the other hand, the very same model used by Korn et al. (2006) was unable to simultaneously reproduce the abundance trends with temperature observed among SGB and MS stars.

Richard et al. (2005) models were further employed to study the behavior of the abundance with the evolutionary phase in M30 and NGC 6752. Different values of

the temperature parameter at which the additional turbulent mixing phenomenon is activated may be required in different clusters (Mucciarelli et al., 2011; Nordlander et al., 2012; Gruyters et al., 2014, 2016). These observations and models recover an original lithium abundance $\sim 0.1-0.2$ dex lower with respect to SBBN predictions, although with errors of the order of ± 0.1 dex.

Interestingly, the lithium abundance measured among MS stars in GCs, with the exception of 47 Tuc, was found at the same level of halos stars, i.e. A(Li)$\simeq$2.2 dex (Dobrovolskas et al., 2014). This includes ω Centauri (Monaco et al., 2010), commonly considered as the remnant of a dwarf galaxy accreted by the Milky Way (see Ibata et al., 2019, and references therein). Indeed, the need of high resolution, high signal-to-noise spectroscopy of un-evolved stars, has largely limited, until recently, the investigation of the cosmic lithium problem to Milky Way stars, with the only exception of ω Cen. In fact, even in the closest galaxy, the Sagittarius dwarf spheroidal (Sgr dSph, Ibata et al., 1994), MS stars are too faint to be observed with the current instrumentation on 8-10 m class telescopes. Howk et al. (2012) managed to measure the lithium abundance in the ISM of the Small Magellanic Cloud (SMC). This has the advantage of not being affected by the phenomena at play in the atmosphere of dwarf stars. These authors measured a lithium level compatible with the SBBN predictions. However, at the SMC metallicity ([Fe/H]>-1), contamination from galactic sources should already be affecting the observed abundances. This is particularly evident when comparing the A(Li) in the SMC with the trend with metallicity of galactic stars (Howk et al., 2012). Therefore, one has to conclude that either the measured value is larger than the primordial one, due to the enrichment by galactic sources, or that this latter should have been very limited in the SMC.

5. Pristine abundances from RGB stars

When a star evolves from the MS to the SGB and RGB, the deepening of the convective envelope bring to the surface material which was exposed to high temperatures and is, hence, depleted in lithium. This dilution causes an overall decrease of the surface lithium abundance. An additional decrease in A(Li) occur when the star cross the RGB-bump luminosity level, where an additional extra-mixing episode is known to take place (Gratton et al., 2004).

Mucciarelli et al. (2012) showed that RGB stars which have already completed the dilution, and evolving still below the luminosity of the RGB-bump (lower RGB stars, LRGB), can be used to infer their initial surface abundance. The amount of dilution is, in fact, reliably predicted by standard stellar models and LRGB stars lie at a plateau that resembles the (dwarf) Spite plateau but at a lower level (A(Li)$\simeq$1.0 dex, Mucciarelli et al., 2012). Furthermore, the resulting A(Li) level of LRGB stars is largely independent of the details of the diffusion processes affecting the surface abundance in dwarf stars. Therefore, the use of LRGB stars has the double advantage of removing one of the main uncertainties about the physical processes in the stellar atmospheres, while at the same time allowing for the use of brighter stars and, thus, reaching further distances. The lower temperatures of LRGB with respect to MS stars also helps at obtaining stronger lines, while dealing with surface Li levels over 1 dex lower than in MS.

Indeed, the use of LRGB stars has allowed Mucciarelli et al. (2014), to measure the lithium abundance of M54, a massive GC lying within the nucleus of the Sgr dSph galaxy (Monaco et al., 2005; Bellazzini et al., 2008). By averaging the spectra of 51 LRGB stars, Mucciarelli et al. (2014) were able to measure A(Li)$_{LRGB}$=0.93$\pm$0.11 dex, corresponding to a initial abundance in the range A(Li)=2.29-2.35 dex, hence again significantly lower than SBBN predictions. The results obtained for ω Cen and M54 indicate, thus, that the cosmic lithium problem is not limited to the Milky Way, but it is common to other, admittedly close, (dwarf) galaxies.

6. Lithium and the formation of globular clusters

GCs revealed to be more complex than thought, hosting multiple stellar populations (MPs) characterized by variations in the content of their light elements (C, N, O, Na, Mg, Al). Most GCs hosts at least two stellar populations: one usually termed "first generation" (FG) presenting a chemical composition similar to typical halos stars, and an additional "second" (SG) or polluted generation, presenting trends in their chemical patterns which can be explained by processing by the CNO cycle and other high temperature hydrogen burning chains, namely the NeNa and MgAl cycles. When these patterns were identified in low-mass main sequence stars, it was realized that they are a birthmark (Gratton et al., 2001). However, the identity of the polluters which contaminated the ISM from which the second stellar generation formed is still matter of an intensive and lively debate. A completely satisfactory and accepted model for the GC formation is still lacking and we refer the reader to the recent review by Bastian & Lardo (2018) for a description of the current state of affairs.

One of the most notable features marking the presence of MPs in GCs is the Na-O anti-correlation (Carretta et al., 2009b,a), with FG stars presenting an enhancement in oxygen, typical of the [α/Fe] enhancement of halo stars, and about solar [Na/Fe] abundance ratios, while SG stars have enhanced [Na/Fe] and lower [O/Fe] abundance ratios. Since the NeNa cycle likely responsible for the Na-O anti-correlation is activated at temperatures significantly larger than required to destroy lithium, one may expect anti-correlations between both Na-O and Na-Li. However, some polluter may have a significant lithium yield acting in the opposite direction. Therefore, the study of the lithium content of GCs, may hold crucial information about the polluters of the ISM from which SG stars formed and, hence, into the formation process of GCs.

Among the main candidates as polluters, fast rotating massive stars (FRMS, Decressin et al., 2007) do not produce lithium, while asymptotic giant branch

(AGB) and super-AGB (∼6.5—8 $M_{\odot}$) stars may produce significant amount of lithium through the Cameron & Fowler (1971) mechanism during hot bottom burning (D'Antona et al., 2012). Pollution from AGB stars, would tend to generate a Na-O correlation, rather than an anti-correlation. For this reason models considering AGB stars as polluters also include some level of dilution of the AGB ejecta with the pristine gas of the cluster (D'Ercole et al., 2010).

Indeed, Li correlations and anti-correlations with light elements were detected in a few GCs and not detected in others (Pasquini et al., 2005; Lind et al., 2009; Shen et al., 2010; Monaco et al., 2012; Dobrovolskas et al., 2014; D'Orazi et al., 2014, 2015; Mucciarelli et al., 2018). Modeling has been attempted in some cases without, however, succeeding at univocally identifying the polluters responsible for the observed Li-Na patterns (D'Antona et al., 2012), although indications in favor of the AGB scenario were also found (D'Antona et al., 2019).

Monaco et al. (2012) identified a dwarf star in M4 (#37934) presenting a lithium content compatible with the cosmological value. While it is possible that this star, at odds with the others, was able to preserve the primordial abundance of lithium, the fact that it is a SG star rather suggests that its high lithium content is the result of pollutions. In D'Antona et al. (2012) models, a limited number of stars may form from the pure ejecta of super-AGB stars, before dilution with the pristine gas. These stars may present A(Li) similar or even larger than observed in #37934, depending on the mass of the polluter super-AGB. Stars formed from the pure ejecta of super-AGB stars would also present enrichment in He and Na. This latter at a level significantly higher than observed in #37934. No other chemical peculiarities were identified in this star, other than its high lithium abundance (Spite et al., 2016). A lithium rich MS star was also identified in NGC 6397 at a level significantly higher even than the meteoritic abundance (A(Li)≃4.03 dex, Koch et al., 2011) again supporting the pollution scenario. At variance with the M4 case, this star belongs to the FG and no radial velocity variations greater than 0.95 $km\,s^{-1}$ were detected over 8 years (Pasquini et al., 2014). Li et al. (2018) also identified MS and SGB metal-poor field stars having A(Li)>4 dex, suggesting that a pollution mechanism may be at work already among MS stars and not necessarily related to the environment, at odds to what the M4 and NGC 6397 cases might have indicated. Notice that, similarly to the case of #37934 in M4, also the Li-rich dwarfs in NGC 6397 and among metal-poor field stars do not present any other chemical anomaly other than in their Li abundance (Pasquini et al., 2014; Li et al., 2018), a situation which resembles that of Li-rich giants observed in the field (Castilho et al., 2000; Ruchti et al., 2011).

Mucciarelli et al. (2018) used again LRGB stars to study the lithium content in the various stellar populations (of different metallicity) of ω Cen. They found well defined Al-Li and Na-Li anti-correlations. This latter more extended than usually seen in other clusters. While most of the stars present a lithium abundance similar to that of field LRGB stars, a significant number of Li-depleted (upper limits or measures lower than A(Li)=0.8 dex) stars were found at all metallicities. All of them are SG stars. FRMS may be a viable polluters for the ISM from which these stars were born. On the other hand, both FG and SG stars having normal lithium abundance are present in ω Cen. The normal lithium content in SG, Na enhanced stars, suggest a polluter which had a significant lithium yield, like super-AGB stars. Hence, different kind of stars may have polluted the ISM from which SG stars formed (see also D'Orazi et al., 2015; Carretta et al., 2018). Notice that upper limits only could be measured at [Fe/H]>-1.3 dex.

Mucciarelli et al. (2019) detected two Li-rich stars in ω Cen, having A(Li)=1.65 and 2.40, to be compared with the normal halo value of A(Li)≃1.0 dex. It should be noted that, unless they resulted from mass-transfer form a companion (Casey et al., 2019), these A(Li) are to be corrected for the dilution process the stars went through and correspond to original lithium abundances over one dex larger. The most Li-rich of these stars, #25664, belong to the dominant metal-poor ω Cen population and presents a Na content larger than the rest of the distribution, namely [Na/Fe]=+0.87 dex. This is similar to what predicted for stars formed by the pure ejecta of super-AGB stars by the D'Antona et al. (2012) models. Together with its large original lithium abundance, this makes this stars a strong candidate of this, so far, theoretical type of stars.

Notice that Li-rich stars were detected in GCs in the MS, SGB and RGB, both above and below the RGB-bump level (see Kirby et al., 2016; Gruyters et al., 2016, and references therein).

7. Conclusions

A discrepancy emerged between the constant lithium abundance measured in warm metal-poor halo dwarf stars (A(Li)≃2.2±0.1 dex, the Spite plateau level) and the predictions of SBBN coupled with the baryon to photon ratio measured by the *WMAP* and *Plack* satellites (A(Li)≃2.69±0.03 dex, Coc et al., 2014). The origin of this cosmic lithium problem is still an unsolved riddle. Various mechanisms were proposed as possible solutions, but no consensus has been reached yet on none of them (see Spite et al., 2012; Iocco, 2012; Fu et al., 2015, and references therein).

GCs, being old and close to simple stellar populations, played an important role in this controversy. GCs observations put into evidence the effects of diffusion in the stellar atmosphere of MS stars (González Hernández et al., 2009). However, modeling the diffusion process and possible additional phenomena still represent a mayor uncertainty when trying to recover the primordial lithium level.

LRGB stars allow to recover the pristine lithium abundance, being only marginally influenced by the details of the diffusion processes affecting the atmospheres of MS stars. Field metal-poor LRGB stars imply a pristine lithium abundance significantly lower than SBBN predictions (Mucciarelli et al., 2012). LRGB allowed to infer the formation lithium abundance of stars in M54, a

GC belonging to the Sgr dSph (Mucciarelli et al., 2014). This and the measures in ω Cen (Monaco et al., 2010) are both compatible with the Spite plateau level, indicating that the cosmic lithium problem exists also in other galaxies.

The formation process of GCs is also a matter of debate. GCs host multiple populations, but the nature of the polluters of the ISM from which SG stars are formed is unclear. Different polluters may or may not have a significant lithium yield. Lithium is a fragile element destroyed at relatively low temperatures ($T>2.5\times10^6$ K) while significantly hotter temperatures are required to generate the observed abundance patterns. In this respect, the study of the lithium content in GCs is a precious tool to understand the nature of the polluters which gave rise to SG stars. Observations seem to support the idea that different polluters may be simultaneously at play (D'Orazi et al., 2015; Carretta et al., 2018; Mucciarelli et al., 2018).

The Li-Na-rich LRGB star recently discovered in ω Cen (Mucciarelli et al., 2019) may be the first detection of a star formed by the pure ejecta of super-AGB stars before dilution with the residual pristine gas in the cluster (D'Antona et al., 2012).

Lithium rich MS stars were detected in GCs (Koch et al., 2011; Monaco et al., 2012) and field metal-poor stars (Li et al., 2018). The mechanism(s) producing such enrichment are yet to be isolated (see, e.g., Pasquini et al., 2014).

Acknowledgements: I wish to thank the organizers for the opportunity to present this contribution and for the lively, pleasant and interesting meeting we attended. I also acknowledge support from "Proyecto Interno" of the Universidad Andres Bello.

References

Aoki W., et al., 2009, ApJ, 698, 1803
Asplund M., et al., 2006, ApJ, 644, 229
Bastian N., Lardo C., 2018, ARA&A, 56, 83
Bellazzini M., et al., 2008, AJ, 136, 1147
Bonifacio P., et al., 2007, A&A, 462, 851
Bonifacio P., et al., 2018, A&A, 612, A65
Bressan A., et al., 2013, *European Physical Journal Web of Conferences*, *European Physical Journal Web of Conferences*, vol. 43, 03001
Bromm V., Larson R.B., 2004, ARA&A, 42, 79
Cameron A.G.W., Fowler W.A., 1971, ApJ, 164, 111
Carretta E., et al., 2009a, A&A, 505, 117
Carretta E., et al., 2009b, A&A, 505, 139
Carretta E., et al., 2018, A&A, 615, A17
Casey A.R., et al., 2019, arXiv e-prints
Castilho B.V., et al., 2000, A&A, 364, 674
Cayrel R., et al., 2007, A&A, 473, L37
Coc A., Uzan J.P., Vangioni E., 2014, JCAP, 10, 050
D'Antona F., et al., 2012, MNRAS, 426, 1710
D'Antona F., et al., 2019, ApJL, 871, L19
Decressin T., et al., 2007, A&A, 464, 1029
D'Ercole A., et al., 2010, MNRAS, 407, 854
Dobrovolskas V., et al., 2014, A&A, 565, A121
D'Orazi V., et al., 2014, ApJ, 791, 39
D'Orazi V., et al., 2015, MNRAS, 449, 4038
Fu X., et al., 2015, MNRAS, 452, 3256
González Hernández J.I., et al., 2009, A&A, 505, L13
Gratton R., Sneden C., Carretta E., 2004, ARA&A, 42, 385
Gratton R.G., et al., 2001, A&A, 369, 87
Gruyters P., Nordlander T., Korn A.J., 2014, A&A, 567, A72
Gruyters P., et al., 2016, A&A, 589, A61
Hinshaw G., et al., 2013, ApJS, 208, 19
Howk J.C., et al., 2012, Nature, 489, 121
Ibata R., et al., 2019, arXiv e-prints
Ibata R.A., Gilmore G., Irwin M.J., 1994, Nature, 370, 194
Iocco F., 2012, Memorie della Societa Astronomica Italiana Supplementi, 22, 19
Kirby E.N., et al., 2016, ApJ, 819, 135
Koch A., Lind K., Rich R.M., 2011, ApJL, 738, L29
Korn A.J., et al., 2006, Nature, 442, 657
Li H., et al., 2018, ApJL, 852, L31
Lind K., et al., 2009, A&A, 503, 545
Lind K., et al., 2013, A&A, 554, A96
Marín-Franch A., et al., 2009, ApJ, 694, 1498
Meléndez J., et al., 2010, A&A, 515, L3
Michaud G., Fontaine G., Beaudet G., 1984, ApJ, 282, 206
Molaro P., et al., 2016, MNRAS, 463, L117
Monaco L., et al., 2005, MNRAS, 356, 1396
Monaco L., et al., 2010, A&A, 519, L3
Monaco L., et al., 2012, A&A, 539, A157
Mucciarelli A., Salaris M., Bonifacio P., 2012, MNRAS, 419, 2195
Mucciarelli A., et al., 2011, MNRAS, 412, 81
Mucciarelli A., et al., 2014, MNRAS, 444, 1812
Mucciarelli A., et al., 2018, A&A, 618, A134
Mucciarelli A., et al., 2019, A&A, 623, A55
Nissen P.E., Schuster W.J., 2012, A&A, 543, A28
Nordlander T., et al., 2012, ApJ, 753, 48
Pasquini L., et al., 2005, A&A, 441, 549
Pasquini L., et al., 2014, A&A, 563, A3
Piau L., et al., 2006, ApJ, 653, 300
Planck Collaboration, et al., 2014, A&A, 571, A16
Prantzos N., 2007, SSRv, 130, 27
Prantzos N., 2012, A&A, 542, A67
Renzini A., Fusi Pecci F., 1988, ARA&A, 26, 199
Richard O., Michaud G., Richer J., 2005, ApJ, 619, 538
Romano D., et al., 1999, A&A, 352, 117
Ruchti G.R., et al., 2011, ApJ, 743, 107
Salaris M., Weiss A., 2001, A&A, 376, 955
Sbordone L., et al., 2010, A&A, 522, A26
Shen Z.X., et al., 2010, A&A, 524, L2
Spite F., Spite M., 1982a, A&A, 115, 357
Spite M., Spite F., 1982b, Nature, 297, 483
Spite M., Spite F., Bonifacio P., 2012, Memorie della Societa Astronomica Italiana Supplementi, 22, 9
Spite M., et al., 2016, A&A, 594, A79
Steffen M., et al., 2012, Memorie della Societa Astronomica Italiana Supplementi, 22, 152

The formation of compact ellipticals through the merger of globular clusters

F. Urrutia Zapata[1], M. Fellhauer[1], A.G. Alarcón Jara[1] , D. Matus Carrillo[1] & C.A. Aravena[1]

[1] *Departamento de Astronomía, Universidad de Concepcion, Concepción, Chile*

Contact / feurrutia@udec.cl

Resumen / Las galaxias elípticas compactas se han identificado muy recientemente. Sus características principales son un gran brillo superficial en el centro y un gran grado de compacticidad. La galaxia prototipo de este nuevo tipo de galaxia es M32, un satélite de la galaxia Andrómeda. Mediante simulaciones numéricas, tratamos de formar galaxias elípticas compactas usando un escenario de formación llamado "fusión de cúmulos globulares", que consiste en la fusión de docenas y hasta más de cien cúmulos globulares en una distribución observada en el Universo llamada Cluster Complex. Se ha demostrado que, para objetos de masa menor a $10^9 M_\odot$, como Faint Fuzzies y galaxias ultra compactas, este escenario de formación reproduce muy bien los parámetros observacionales. Nuestras simulaciones también reproducen muy bien todas las propiedades de galaxias compactas elípticas y por lo tanto abren un nuevo canal de formación para explicar la existencia de este tipo de galaxias.

Abstract / Compact elliptical galaxies (cE) have been identified as such very recently. Their principal characteristics are a high surface brightness in the center and a high level of compactness. The prototype galaxy for this type of galaxies is M32, a satellite of Andromeda galaxy. Using numerical simulations, we try to form a cE in the context of a formation scenario called "Merging star cluster scenario", which consists in the merger of dozen or even more than hundred globular clusters in a distribution observed in the Universe called Cluster Complex. It has been shown that for objects with less mass than a cE ($10^9 M_\odot$), like Faint Fuzzies and Ultra compact dwarf galaxies, the merging star cluster scenario reproduces very well their observational parameters. Our simulations also reproduce very well all probed properties of cE galaxies and therefore open up a new formation channel to explain the existence of this types of galaxies.

Keywords / galaxies: formation — evolution — dwarf — star clusters — Methods: numerical

1. Introduction

Compact elliptical galaxies (cE) have very special characteristics. They possess a high stellar density compared to dwarf ellipticals of the same size (Faber, 1973), and a very small effective radius (R_{eff}) considering the mass of these types of galaxies ($\approx 10^9$ $M_\odot$). The archetype for this type of galaxies is the 32nd object in the Catalog of Messier. M32 is a satellite of Andromeda (M31), it has an effective surface brightness in the bulge of 18.23 R-mag arcsec^{-2} (Graham, 2002), an R_{eff} of the bulge of 27" ($\sim$ 100 pc), and a velocity dispersion of 76 ± 10 km s^{-1} (van der Marel et al., 1998).

The standard theories about their formation sees these objects as galaxies. They could either be stripped and truncated remnants of nucleated larger objects (Faber, 1973) or they could be the natural extension of the class of elliptical galaxies (Wirth & Gallagher, 1984; Kormendy et al., 2009). Huxor et al. (2011) found two cEs, which show evidence of formation resulting from the ongoing tidal stripping of more massive progenitors, but later Huxor et al. (2013) reported the first isolated cE. Furthermore, their dark matter content is still under debate.

We try to form cE galaxies using a different formation scenario called "Merging Star Cluster Scenario". In this scenario, the cEs form from merging Young Massive Clusters (YMCs) inside a cluster complex (CC). CCs are found in starbursting galaxies like the Antennae, Whirlpool or Tadpole. In small confined regions of several hundred parsecs, dozens or even hundreds of YMCs form. These regions are found within these galaxies and also in the long tidal tails of interacting galaxies.

Previous studies (Fellhauer & Kroupa, 2002a,b) have shown that the YMCs inside of those CCs merge and build a larger, more massive object like extended star clusters or ultra-compact dwarf galaxies (UCDs). These objects can have masses up to 10^8 $M_\odot$.

In this project we extend this formation scenario to even higher masses of order 10^9 $M_\odot$, as may be found in more gas-rich, stronger starbursts in the early Universe. These more massive CCs could have been progenitors of cEs, opening up a formation channel for them.

2. Setup

We use the particle-mesh code SUPERBOX (Fellhauer et al., 2000) to model the evolution of massive CCs with a total mass of 10^9 $M_\odot$ distributed into $N_0 = 64$ or 128 equal mass SCs (regarding their mass rather UCDs). Each SC/UCD is modeled as a Plummer sphere with Plummer radius R_{sc} = 4, 10 or 20 pc using 100,000 particles.

The SCs are placed inside a CC, following a Plummer

Table 1: Parameters varied in the 162 simulations.The distance to the center of the galaxy of the CC (R_{gal}), the Plummer radius of the SCs/UCDs (R_{sc}), the Plummer radius of the CC (R_{cc}) and the initial number of "UCDs" in the CC (N_0).

R_{gal} [kpc]	R_{sc} [pc]	R_{cc} [pc]	N_0
20	4	50	64
60	10	100	128
100	20	200	

distribution with scale-radius R_{cc} = 50, 100 or 200 pc at different distances to the host galaxy R_{gal} = 20, 60 or 100 kpc.

All these values are based on real observational data collected for these types of stellar systems.

We perform in total 162 simulations. We simulate each combination of the parameters shown in Tab. 1 using three different random seeds for the positions and velocities of the SCs inside the CC.

3. Results

In all simulations, the merger process leads to a stable object which we are analyzing after 10 Gyr of simulation time.

We determine the number of constituents N_{merger}, which have merged into the final object and measure the final bound mass of this object M_{merger}. To obtain the effective radius R_{eff} of our object we fit a Sersic profile (Sérsic, 1963) to the surface density. We determine the central surface brightness by producing a 2D pixel-map of the surface densities of our object, searching for the pixel with the highest value and converting this value into magnitudes per arcsec^2 using a generic mass-to-light ratio (M/L) of unity. The ellipticity of our object is taken from the routine ELLIPSE in IRAF. As input we use the 2D pixel map we already produced from our simulation results. We use the ellipticity of the nearest isophote to a generic distance of 100 pc. Finally, we use all particles in the central pixel to calculate the central velocity dispersion of our object.

We do not see any significant difference between the results obtained if we distribute the mass of the CC into 64 objects or 128. With this we do agree with previous studies (e.g. Brüns et al., 2009). The histogram in the left panel of Fig. 1 shows the number of simulations in which a certain fraction of SCs/UCDs merge, ending up in the final object. The green and blue bars represent simulations with 64 and 128 constituents, respectively. It is clearly visible that in almost all simulations the majority of objects merge and build the final cE. Furthermore, we do not see any strong influence of the distance to the host galaxy.

One might expect differences in this merging behavior: the less filled the CC is with SCs the lower should be the number of merged SCs. We see this trend in our simulations as well. The few simulations that have a low N_{merger} value are mainly the simulations with R_{sc} = 4 pc and R_{cc} = 100 or 200 pc.

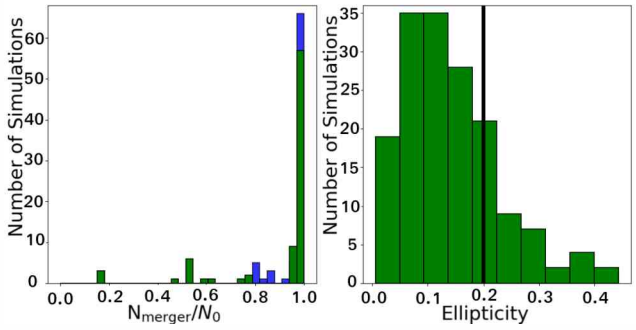

Figure 1: Left panel: Number of simulations vs. N_{merger} (total number of simulations is 162). Right panel: Histogram of the ellipticity of the final merger objects. The black line at $\epsilon = 0.2$ denotes the commonly adopted value for cE galaxies. Most simulations exhibit objects with ϵ values below or equal to 0.2, i.e. resemble the shape of most cE galaxies observed.).

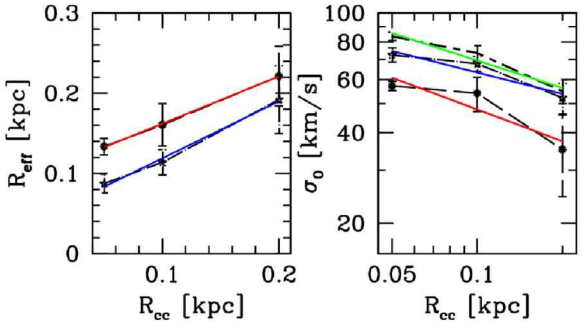

Figure 2: Left panel: R_{eff} as function of the distribution size R_{cc}. The upper curve is from R_{sc} = 4 pc simulations and for the lower curve both R_{sc}-values of 10 and 20 pc are used. A linear fit is shown in red and blue. Right panel: σ_0 as function of R_{cc}. Bottom line (red) is for R_{sc} = 4 pc, middle line (blue) for R_{sc} = 10 pc and top line (green) for R_{sc} = 20 pc. The fitting lines shown in color are power-laws.

In the literature, it is usually considered that cE have no significant ellipticity (e.g. Chilingarian et al., 2007). The ellipticity of M32 is about E2 which means that the smaller axis is about 20% shorter than its larger axis. The exact ellipticity of M32 is 0.17 (Kent, 1987). The ellipticity of the final object is not related to any of our simulation parameters (R_{gal}, R_{sc} and R_{cc}). In the right panel of Fig. 1 one can see that almost all the simulations have ellipticity in the range of cEs, i.e. $\epsilon = 0.2$ or less.

If we analyze the R_{eff} of our merger object we see no significant difference between R_{sc} = 10 pc and 20 pc, i.e. as long as we build our merger object out of extended constituents, their size does not influence the scale radius of the final object. Only if concentrated initial SCs are used, then we may see a slower merging process (see Fellhauer et al., 2002, for a more detailed explanation) and a more extended final object.

The left panel of Fig. 2 shows only two different lines as we choose to bin the simulations with R_{sc} = 10 and 20 pc here (top line shows R_{sc} = 4 pc results, bottom line R_{sc} = 10 and 20 pc). A very clear linear trend is

visible, with a increasing size of the distribution, we see a larger final object. We fit a line to the results and obtain a slope of 0.59 ± 0.01 for $R_{sc} = 4$ pc, shown as the red line, and 0.71 ± 0.06 for the other results (blue line). As we focus more on simulations with extended initial objects, we can state the following relation as a rule of thumb: $R_{eff} \approx 0.7 \cdot R_{cc}$.

In the right panel of Fig. 2, we show the dependency of σ_0 on R_{cc}. We see a straightforward trend, which is expected taking the previous results into account. As the final mass of our cEs is approximately the same, the velocity dispersion should depend on the size of the object only, i.e. more concentrated, smaller objects should exhibit larger velocity dispersion. Exactly this is visible in our results. Smaller constituents lead to a slower merging and more extended objects and therefore exhibit lower velocity dispersions, i.e. R_{sc} and σ_0 are correlated. On the contrary, larger distributions lead to larger objects and henceforth to small velocity dispersions, the two quantities (R_{cc} and σ_0) are anti-correlated. The fitting lines shown in the right panel of Fig. 2 are power laws. We obtain the following exponents for the decrease: -0.4 ± 0.2, -0.24 ± 0.08 and -0.30 ± 0.07 for the different choices of $R_{sc} = 20$, 10 and 4 pc, respectively. As we have found an almost linear dependency of R_{eff} on R_{cc}, we would expect from simple stellar dynamical arguments (Virial equilibrium) that $\sigma \sim R_{cc}^{-0.5}$. We see this relation only holds if we start our CC with large enough constituents, i.e. UCD-like objects.

4. Discussion and conclusions

Every simulation performed in this study leads to a final bound object in which the majority of SC have merged. We analyzed the resulting object and are determined its shape, mass, effective radius, central surface brightness and central velocity dispersion. These values are compared with observational values of compact ellipticals found in the literature. The main result of this study is that indeed it is possible to obtain a cE galaxy in the merging star cluster scenario, matching all the above mentioned observables. We established the following relations: The effective radius of the final object is inversely proportional to the size of the SCs used, and linearly proportional to the size of the CC used. As a rule-of-thumb we give $R_{eff} = 0.7 R_{cc}$. With our studied parameter range, the obtained effective radii are between 90 and 260 pc, which marks the range of cE galaxies.

The range of ellipticity ϵ is between 0.05 and 0.32, with almost all simulations having ellipticities in the range of cEs ($\epsilon \leq 0.2$). We always obtain central surface brightnesses which are matching the values of cEs (not shown in this article). The merger objects exhibit velocity dispersions in the range of about 50 to 80 $\mathrm{km\,s^{-1}}$, thereby matching the observational values.

There is one thing which our simple stellar dynamical models cannot reproduce. Observing M32, Monachesi et al. (2012) found two different stellar populations. Our simulations do not treat metallicities, and gas is not included. Our equal-mass particles are representations of the phase-space and not actual stars. We would speculate that when forming a CC that massive, the expelled gas seen e.g., as H-alpha bubbles around the CCs in the Antennae (e.g. Whitmore et al., 1999), stays bound to the forming merger object and is able to fall back in, forming at least a second generation of stars.

In Alarcón Jara et al. (2018) we have shown that the results, regarding shapes and kinematics, and our conclusions do not change when adopting a star formation history into similar models. So, we are confident that in our scenario an included star formation history would also show no major differences.

The merging star cluster scenario is not the only way to produce a cE galaxy. Other models for the formation of cEs are the tidal stripping and truncation scenario (Faber, 1973) either with an elliptical galaxy with a dense core as origin (e.g. Faber, 1973) or the bulge of a partially stripped disc galaxy (e.g. Bekki et al., 2001); or that cEs could also have an intrinsic origin and are the natural extension of the class of elliptical galaxies to smaller sizes and lower luminosities (Wirth & Gallagher, 1984; Kormendy et al., 2009).

Therefore, our scenario opens up a novel possible formation channel to explain the existence of cE galaxies.

Acknowledgements: FU, MF, AA, CA and DM acknowledge support through Fondecyt regular No. 1180291 and Chilean BASAL Centro de Excelencia en Astrofśica y Tecnologás Afines (CATA) grant AFB-170002. MF acknowledges support through PII20150171 and Quimal 170001.

References

Alarcón Jara A.G., et al., 2018, MNRAS, 473, 5015
Bekki K., et al., 2001, ApJL, 557, L39
Brüns R.C., Kroupa P., Fellhauer M., 2009, ApJ, 702, 1268
Chilingarian I., et al., 2007, A&A, 466, L21
Faber S.M., 1973, ApJ, 179, 423
Fellhauer M., Kroupa P., 2002a, MNRAS, 330, 642
Fellhauer M., Kroupa P., 2002b, AJ, 124, 2006
Fellhauer M., et al., 2000, NewA, 5, 305
Fellhauer M., et al., 2002, Celest. Mech. Dyn. Astron., 82, 113
Graham A.W., 2002, ApJL, 568, L13
Huxor A.P., Phillipps S., Price J., 2013, MNRAS, 430, 1956
Huxor A.P., et al., 2011, MNRAS, 414, 3557
Kent S.M., 1987, AJ, 94, 306
Kormendy J., et al., 2009, ApJS, 182, 216
Monachesi A., et al., 2012, ApJ, 745, 97
Sérsic J.L., 1963, BAAA, 6, 41
van der Marel R.P., et al., 1998, ApJ, 493, 613
Whitmore B.C., et al., 1999, AJ, 118, 1551
Wirth A., Gallagher III J.S., 1984, ApJ, 282, 85

Dynamo effect in the double periodic variable DQ Velorum

R.I. San Martín-Pérez[1], D.R.G. Schleicher[1], R.E. Mennickent[1] & J.A. Rosales[1]

[1] *Departamento de Astronomía, Facultad de Ciencias Físicas y Matemáticas, Universidad de Concepción, Concepción, Chile*

Contact / rubensanmartinp@gmail.com

Resumen / DQ Velorum es una variable de doble período galáctica que consiste de un sistema binario semi-separado con una estrella acretora de tipo espectral B y una estrella donadora de tipo espectral A, además de un disco de acreción en la estrella acretora. El sistema presenta un período orbital de 6.08337 días y un período largo de 189 días cuyo origen sigue en debate. En este trabajo estudiamos la posibilidad de que este período sea producto de una dínamo magnético, estudiando la evolución completa del sistema. Nuestro modelo ajusta de muy buena manera el estado actual del sistema y puede ser usado para describir la evolucion de DQ Velorum. Además, el modelo predice un incremento en el número de dínamo en la estrella donor en épocas de alta transferencia de masa y una razón de los períodos largo y orbital muy cercana a la que se observa en el sistema.

Abstract / DQ Velorum is a galactic double periodic variable (DPV), this system is a semi-detached binary comprised of a B-type gainer and an A-type donor star plus an extended accretion disc around the gainer. The system presents an orbital period of 6.08337 days and a long period of 189 days whose origin is still under debate. Here we studied the possibility that this period may be driven by a magnetic dynamo while investigating the entire evolution of the system. Our model matches in a very good way the current state of the system and it can potentially be used to describe the evolution of DQ Velorum. It also predicts an increase of the dynamo number of the donor during epochs of high mass transfer in this system, and a theoretical long to orbital period ratio that is very close to the observed one at the present system age.

Keywords / stars: activity — low-mass — rotation — binaries: close — dynamo

1. Introduction

An important class of close interacting binaries are the so-called Algol-type variables. Such systems consist of semi-detached binaries with intermediate mass components. In these systems the less massive star (donor) is more evolved than the most massive star (gainer) and the mass ratio indicates that some processes may have occurred in order to explain the high mass of the main sequence companion star. In particular mass transfer, as originally explained by Crawford (1955) and confirmed by Kippenhahn & Weigert (1967); van Rensbergen et al. (2011) and de Mink et al. (2014) through numerical calculations. The apparent mass paradox between binary components can be well understood if the donor star was once the most massive star in the system, it evolved faster than its companion starting a fast process of mass exchange through Roche lobe overflows (RLOF) onto its companion (Eggleton & Kisseleva-Eggleton, 2006).

One of the most important features in the Algol-type binaries is the presence of long cycles. The presence of these cycles is known since a long time (e.g. Lorenzi (1980a,b); Guinan (1989)). Nevertheless, the interpretation and origin of such a cycles are still under debate.

We aim to give an explanation on the origin of this cycle. We focused our study on a sub-class of the Algol classification which are the double periodic variable (DPV) binary systems, which consist of semi-detached interacting binary systems with intermediate mass components that were found by Mennickent et al. (2003), presenting the main characteristics of the Algol systems.

This report is based on the DPV system DQ Velorum, a binary system that was fully studied by Barría et al. (2013a,b, 2014) which presents the following stellar parameters: $M_d = 2.2 \pm 0.2$ $M_\odot$, $M_g = 7.3 \pm 0.3$ $M_\odot$, $R_d = 8.4 \pm 0.2$ $R_\odot$, $R_g = 3.6 \pm 0.2$ $R_\odot$, $L_d = 2.66 \pm 0.036$ $L_\odot$, $L_g = 3.14 \pm 0.16$ $L_\odot$, $P_{orb} = 6.08337 \pm 0.00013$ days and a long period of $P_{long} = 189$ days. Here we explored the magnetic dynamo cycle as a potential origin of the long period. For this purpose we studied the entire evolution of this systems using the binary evolution models proposed by van Rensbergen et al. (2008, 2011). For the dynamo we used the relation proposed by Soon et al. (1993) and Baliunas et al. (1996) that relates the rotational velocity, activity period and the dynamo number via $D = \alpha \Delta\Omega d^3/\eta^2$. Here α is a measure of helicity, $\Delta\Omega$ is the large-scale differential rotation, d is the characteristic length scale of convection and η the turbulent magnetic diffusivity in the star.

2. Methods

In order to study how the dynamo number D and the ratio of the long to orbital period changes as the system is evolving, we are fitting our system to the van Rensbergen binary evolution models (van Rensbergen et al., 2008, 2011). These models were developed in

order to study the evolution of close binaries, including both conservative and non-conservative scenarios, by solving the stellar structure equations using the *Brussels* binary evolutionary code (for a detailed description of the code see De Loore & Doom (1992)). The code was modified in order to include convective mixing, radius corrections and nuclear physics, following Prantzos et al. (1986). Also, following De Loore & De Greve (1992) a moderate convective core overshooting is applied. Mass loss by stellar winds and period changes due to angular momentum loss are also included in this model. Initial conditions were established by using an unevolved system with a B-type primary at birth from the 9th catalog of spectroscopic binaries (Pourbaix et al., 2004), distinguishing between late B-type [2.5, 7] $M_{\odot}$ and early B-type [7, 16.7] $M_{\odot}$ primaries. We inspected all the 561 conservative and non-conservative evolutionary tracks that are available at the Center Doneés Stellaires (CDS) looking for the model that describes the best our system. A multi-parametric χ^2 minimization was performed in order to find the best match, this test is given by (Mennickent et al., 2012):

$$\chi^2_{i,j} = \left(\frac{1}{N}\right) \sum_k w_k \left[\frac{(S_{i,j,k} - O_k)}{O_k}\right]^2, \quad (1)$$

where N is the number of observations (7), $S_{i,j,k}$ is the synthetic model where i indicates the model, j the time t_j and k the stellar or orbital parameter, O_k are the observed stellar parameters. To perform our test, we are fitting the mass, radii and luminosities of both stars in the system and also the orbital period of the binary. $w_k = \sqrt{O_k/\epsilon O_k}$ is the statistical weight of the parameter O_k and ϵO_k is the error associated to the parameter O_k. The model with the minimum χ^2 corresponds to the model that describes best the evolution of the system. After we found the best model for our system, we are following the relation between the long period P_{long} and the orbital period P_{orb} given by (Soon et al., 1993; Baliunas et al., 1996)

$$P_{long} = D^{\gamma} P_{rot}, \quad (2)$$

where D is the dynamo number and γ is a power law index, with values usually between 1/3 and 5/6 (Saar & Brandenburg, 1999; Dubé & Charbonneau, 2013). In order to calculate the dynamo number D we follow the dynamo model by Schleicher & Mennickent (2017), they proposed that the long period is related to the orbital period following the relation

$$P_{long} = P_{orb} \left(11.5 \left(\frac{2\sqrt{2}}{15}\right)^{1/3} \frac{\mathrm{R}_{\odot}}{\mathrm{km\,s^{-1}\,yr}}\right)^{-2\gamma} \times \left(\frac{L_2^{2/3} R_2^{2/3}}{M_2^{2/3}} \left(\frac{l_m}{H_p}\right)^{-4/3} \left(\frac{P_{kep}}{\epsilon_H R_2}\right)^2\right)^{-\gamma}, \quad (3)$$

where l_m is the mixing length, H_p is the pressure scale height and P_{kep} is the Keplerian orbital period of a test particle on the surface of the donor star. They found a good fit with $\gamma \sim 0.31 \pm 0.05$. More recently, Navarrete et al. (2018) and Völschow et al. (2018) showed that a magnetic dynamo can explain the modulation periods which are produced by changes in the quadrupole moment of the star in post common envelope (PCE) binaries. The latter shows that the model is potentially feasible in systems where the evolutionary process is different in comparison with the DPV systems.

2.1. Model fitting

We applied the χ^2 minimization test to the parameters listed in Table 1. We found that, the model that describes best the system corresponds to the same non-conservative and with slow mass transfer rate under synchronous rotation model reported by Barría et al. (2014). The latter also presents the following ratios between observations and model predictions: $M_{d,obs}/M_{d,model} = 0.94$, $M_{g,obs}/M_{g,model} = 1.007$, $R_{d,obs}/R_{d,model} = 0.97$, $R_{g,obs}/R_{g,model} = 0.99$, $L_{d,obs}/L_{d,model} = 1.11$, $L_{g,obs}/L_{g,model} = 0.93$ and $P_{orb,obs}/P_{orb,model} = 0.99$ at a stellar age of $\sim 68 \pm 0.5$ Myr. This means that the model can describe in a very good way the evolution of the system. The top panel in Fig. 1 presents the evolutionary track of both components of the system, there, the path with circles denotes the evolution of the gainer star. We also indicate the observational and predicted state of the gainer (black dot with and without error bars, respectively). The path with triangles corresponds the evolution of the donor star, also it is plotted the observational state of the donor (red triangle with error bars) and the prediction of the model for the donor (red triangle without error bars). The prediction of the current state of each component of the system, almost overlaps with the current observational state of the binary.

2.2. Evolution of the dynamo number and long-to-orbital period ratio

Once the fit is done both dynamo number D and ratio of long to orbital period were calculated using Eq. 3. As seen in Fig. 1 middle, the dynamo number D follows an almost constant evolution during the first 55 Myr, after this, the dynamo number grows dramatically fast, which will possibly produce a strong magnetic activity and the stars begins an active mass transfer phase. This situation lasts for a very short time (~ 1 to ~ 2 kyr) and right after the dynamo peak, it starts to decrease until the star becomes magnetically inactive at a stellar age of ~ 77 Myr. The ratio of long to orbital period also grows as fast as the dynamo number, this means that both periods (long and orbital) are almost constant during the first 55 Myr. After this interval of constant evolution both periods grow very rapidly, producing a star with a longer magnetic cycle and with a longer orbital period as seen in the bottom panel of Fig. 1.

3. Conclusions

We have found that DQ Velorum is an old system with a small mass transfer rate as reported by Barría et al. (2014). The system is well described by the models proposed by van Rensbergen et al. (2008, 2011), so it seems

Table 1: Observational stellar parameters for DQ Velorum. Taken from Barría et al. (2013b); Mennickent et al. (2016)

Parameter	Value
M_d [$M_\odot$]	2.2 ± 0.2
M_g [$M_\odot$]	7.3 ± 0.3
R_d [$R_\odot$]	8.4 ± 0.2
R_g [$R_\odot$]	3.6 ± 0.2
L_d [$L_\odot$]	2.66 ± 0.036
L_g [$L_\odot$]	3.14 ± 0.16
P_{orb} [days]	6.08337 ± 0.00013

feasible to use them as a potential description for the system evolution. We studied the evolution of the dynamo number D, finding that after an almost constant evolution of this parameter the star becomes strongly active in a short period due to the short orbital period of the system starting a rapid mass transfer phase. The latter also applies to other stellar parameters like radius, mass and luminosity. This strongly active phase of the star lasts for a very short time (~ 1 to ~ 2 kyr) and is followed by a magnetic activity decrease until the star becomes magnetically inactive, with no mass exchange between both stars.

Acknowledgements: D.R.G.S. and R.I.S.M.P. thank for funding through Fondecyt regular (project code 1161247) and the "Concurso Proyectos Internacionales de Investigación, Convocatoria 2015" (project code PII20150171). R.E.M. and D.R.G.S. acknowledge FONDECYT 1190621. D.R.G.S. and R.E.M. thank for funding through BASAL Centro de Astrofísica y Tecnologías Afines (CATA) PFB-06/2007.

References

Baliunas S.L., et al., 1996, ApJ, 460, 848
Barría D., et al., 2013a, A&A, 552, A63
Barría D., et al., 2013b, Central European Astrophysical Bulletin, 37, 217
Barría D., et al., 2014, A&A, 567, A140
Crawford J.A., 1955, ApJ, 121, 71
De Loore C., De Greve J.P., 1992, A&AS, 94, 453
De Loore C.W.H., Doom C., 1992, Science, 258, 1506
de Mink S.E., et al., 2014, ApJ, 782, 7
Dubé C., Charbonneau P., 2013, ApJ, 775, 69
Eggleton P.P., Kisseleva-Eggleton L., 2006, Ap&SS, 304, 75
Guinan E.F., 1989, SSRv, 50, 35
Kippenhahn R., Weigert A., 1967, ZA, 65, 251
Lorenzi L., 1980a, A&A, 85, 342
Lorenzi L., 1980b, A&AS, 40, 271
Mennickent R.E., Otero S., Kołaczkowski Z., 2016, MNRAS, 455, 1728
Mennickent R.E., et al., 2003, A&A, 399, L47
Mennickent R.E., et al., 2012, MNRAS, 421, 862
Navarrete F.H., et al., 2018, A&A, 615, A81
Pourbaix D., et al., 2004, A&A, 424, 727
Prantzos N., et al., 1986, ApJ, 304, 695
Saar S.H., Brandenburg A., 1999, ApJ, 524, 295
Schleicher D.R.G., Mennickent R.E., 2017, A&A, 602, A109
Soon W.H., Baliunas S.L., Zhang Q., 1993, ApJL, 414, L33
van Rensbergen W., et al., 2008, A&A, 487, 1129
van Rensbergen W., et al., 2011, A&A, 528, A16
Völschow M., et al., 2018, ArXiv e-prints

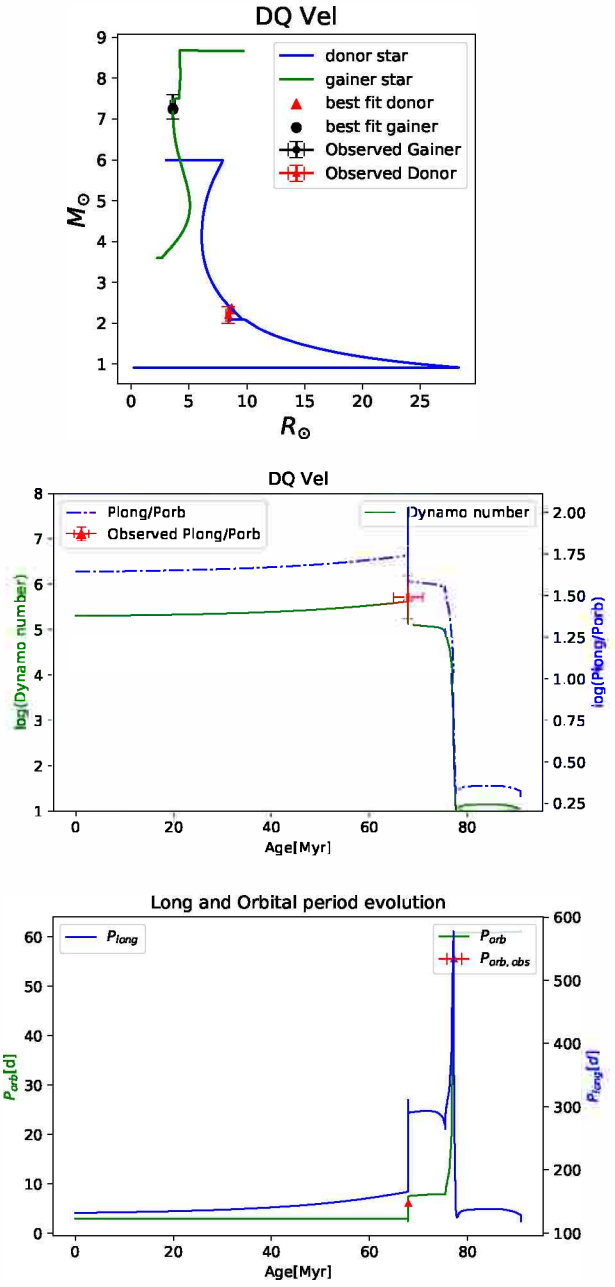

Figure 1: Top: The best model for DQ Velorum. We show the evolution of the gainer (circles), its observed (black dots with errors) and predicted (red triangles) parameters. The path with triangles shows the evolution of the donor, the observed (red triangle with error bars) and predicted parameters (red triangle without error bars). Middle: The dynamo number (solid line) and the ratio of long to orbital period (dashed line). We also plot the observed ratio of long to orbital period (triangle with error bars) with a value of $\log(P_{long}/P_{orb}) = 1.492$, the same value reported by Schleicher & Mennickent (2017). Bottom: Evolution of the orbital (path with asterisks) and long (path with triangles) periods, along with the observed value of the orbital period (marked with an error-bar triangle in log scale).

Open cluster candidates in the VVVX area: VVVX CL 076 and CL 077

J. Borissova[1,2], V.D. Ivanov[3], P. Lucas[4], R. Kurtev[1,2], J. Alonso-Garcia[5], S. Ramírez Alegría[5], D. Minniti[6,2], N. Medina[1,2] & A.-N. Chené[7]

[1] *Instituto de Física y Astronomía, Universidad de Valparaíso, Chile*
[2] *Millennium Institute of Astrophysics, Santiago, Chile*
[3] *European Southern Observatory, Garching bei München, Germany*
[4] *Centre for Astrophysics, University of Hertfordshire, UK*
[5] *Unidad de Astronomía, Facultad de Ciencias Básicas, Universidad de Antofagasta, Chile*
[6] *Departamento de Física, Facultad de Ciencias Exactas, Universidad Andrés Bello, Santiago, Chile*
[7] *Gemini Observatory, Northern Operations Center, Hilo, USA*

Contact / jura.borissova@uv.cl

Resumen / Se reportan algunos parámetros básicos de dos cúmulos estelares, VVVX CL 076 y CL 077, recientemente descubiertos en el área del disco galácico, cubierta por el relevamiento público del ESO "VISTA Variables in the Via Lactea eXtended (VVVX)". El análisis preliminar muestra que ambos cúmulos son jóvenes y relativamente cercanos al Sol.

Abstract / We are reporting some basic parameters of two newly discovered clusters, VVVX CL 076 and CL 077, recently discovered in the galactic disk area covered by the VISTA Variables in the Via Lactea eXtended (VVVX) ESO Public Survey. The preliminary analysis shows that both clusters are young and relatively close to the Sun.

Keywords / Galaxy: open clusters and associations — Galaxy: disk — infrared: stars

1. Introduction

Young star clusters are sites of recent star formation and early evolution in the Milky Way and are often only visible at the infrared wavelengths, being highly obscured by gas and dust. The VISTA Variables in the Via Lactea eXtended (VVVX) ESO Public Survey is a near-infrared photometric sky survey that covers nearly 1700 square degrees towards the Galactic disk and bulge. It offers an excellent opportunity to search for new, undiscovered star clusters in our Galaxy. Recently, Borissova et al. (2018) reported a list of 120 new star cluster candidates found by visual inspection of 40 % of the disk area covered by VVVX. In this paper, we present the near infrared photometry and Gaia DR2 proper motions and distance estimates for VVVX CL 076 and VVVX CL 077.

Fig. 1 shows the composite JHK_S color images of the target clusters. The equatorial coordinates of CL 076 are $\alpha(2000) = 273.3545°$, $\delta(2000) = -18.0921°$ and CL 077 is centered around $\alpha(2000) = 273.3960°$, $\delta(2000) = -18.0966°$. Both clusters are projected very close to the Galactic plane at galactic latitudes −0.10 and −0.14 deg respectively.

2. Analysis

To construct the color-magnitude diagrams, we performed PSF photometry of a 2.5 × 2.5 arcmin area surrounding the selected candidate in the J, H, and K_S bands. We used the DoPHOT photometric routine following Alonso-García et al. (2017). The instrumental magnitudes were transformed to the standard system. This procedure is described in detail by Alonso-García et al. (2017), Borissova et al. (2011) and Borissova et al. (2014).

The most probable cluster members are selected by statistical decontamination procedure and Gaia DR2 proper motion diagrams. To separate the field stars from probable cluster members we used the iterative field-star decontamination algorithm, which divides the magnitude and color ranges into a grid of cells. In each cell, it estimates the expected number density of cluster stars by subtracting the respective field-star number density and, summing over all cells, it obtains a total number of member stars. The most probable cluster members obtained in this manner are cross-matched with Gaia DR2 catalog (Gaia Collaboration et al., 2018), the proper motion vector diagrams μ_δ vs. $\mu_\alpha \cos\delta$ are created and the stars with obviously different proper motion are rejected (Fig. 2, upper panel). The lower panel of Fig. 2 shows the color-magnitude diagrams for VVVX CL 076 and VVVX CL 077. Following Zasowski et al. (2013), we then fit the Padova theoretical isochrones with solar metallicity (Bressan et al., 2012). The best fit for VVVX CL 076 gives an age of 32 Myr, while VVVX CL 077 is most probably 10 Myr old. The confidence intervals are ±3 and ±2 Myr, respectively. We used the Gaia RD2 parallaxes as initial values for the distances, while the mean reddening is determined by the interactive process of the fitting. The reddening val-

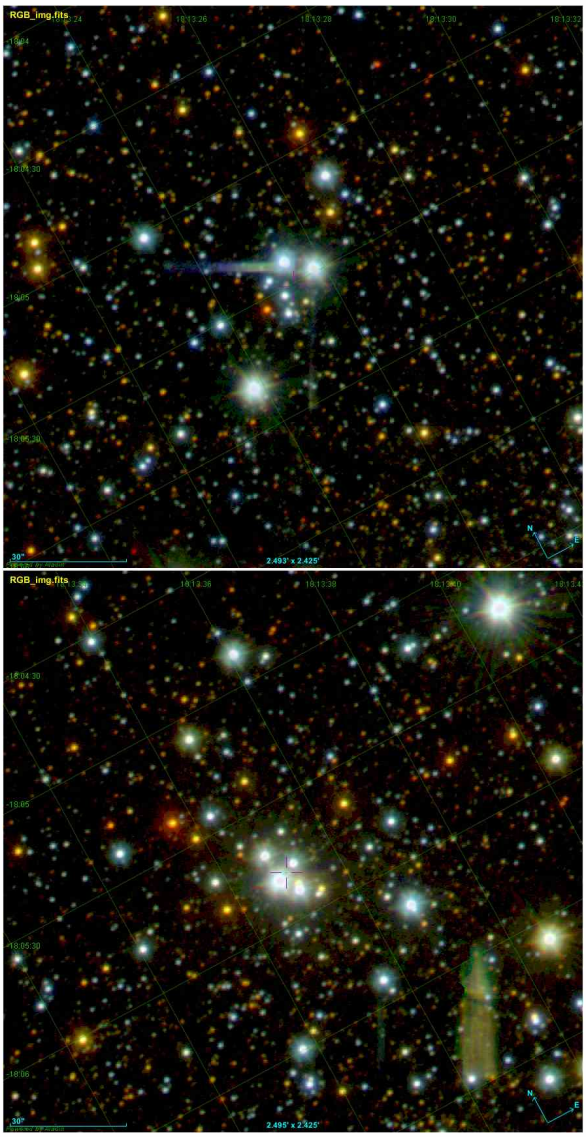

Figure 1: VVVX JHK_S composite color images of CL 076 (upper panel) and CL 077 (lower panel). The field of view is 5×5 arcmin. The North and East vectors are drawn on each image.

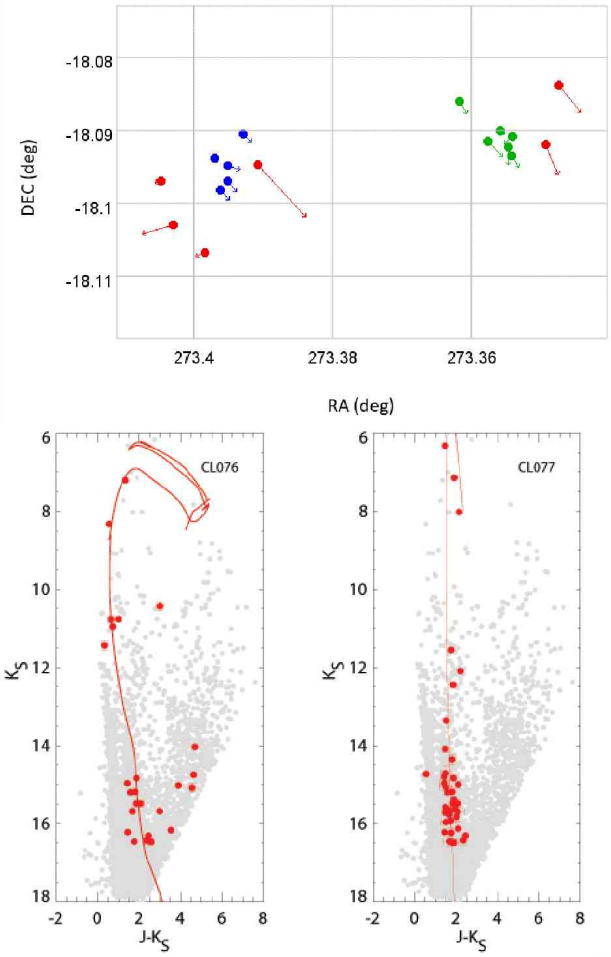

Figure 2: Upper panel: The VVVX CL 076 and CL 077 proper motion diagrams with sky vectors overplotted. Blue and green circles are most probable CL 076 and CL 077 members, respectively, while the red circles stand for field stars. The proper motion vectors are scaled by factor of 2 for better visibility. Lower panel: The VVVX CL 076 and CL 077 K_S vs $(J - K_S)$ diagram with most probable cluster members (red large circles) overplotted. The solid red lines are best fit solar isochrones of 32 and 10 Myr, respectively, taken from the Padova database.

ues are $E(J-K_S) = 1.6\pm0.2$ and $E(J-K_S) = 1.7\pm0.2$, for CL 076 and CL 077, respectively. The errors represent uncertainty of the fitting procedure with quadratically added errors from photometry and transformation to the standard system. The Gaia DR2 mean reddening, as reported in Borissova et al. (2018) is determined as $E(BP-RP) = 1.4\pm0.3$ and $E(BP-RP) = 1.6\pm0.1$, thus the differential reddening is possible, but dipper photometry and/or spectra of individual cluster members are necessary to estimate it.

We used the Gaia DR2 (Bailer-Jones et al., 2018) distance estimates. The histogram of distance distribution of all stars within 1 arcmin radius of each cluster is shown in Fig. 3. As can be seen, most of the stars are centered around 3 kpc. If we select only most probable cluster members, CL 076 is placed around 1.6 kpc, while CL 077 stands at 1.8 kpc. The associated errors are around 1 kpc, thus such obtained distances should be taken with caution.

The cluster radii were measured by eye on the VVVX K_S combined tiles and are estimated in Borissova et al. (2018) as $17'$ and $53'$. This method was preferred over automated algorithms, because of the small number of the most probable cluster members. The area around cluster candidates is smoothed and the density contours are over-plotted with the lower limit of the contour equal to the density of comparison field.

Since these clusters are projected very close to each other, have similar distances and proper motions, one can speculate that this is a binary system, formed by triggering on the same molecular cloud. More data are necessary to confirm (or reject) this hypothesis.

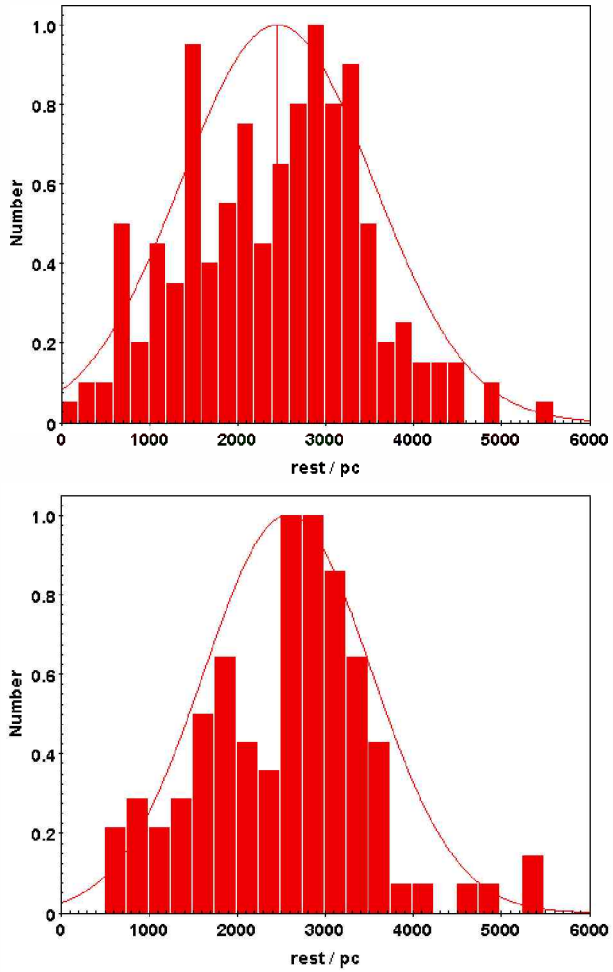

Figure 3: The histograms of distance distribution of CL 076 and CL 077. The solid lines are Gaussian distributions of the whole sample.

3. Summary

The newly discovered clusters projected in the VVVX disk area are analyzed using VVVX near infrared photometry and Gaia DR2 proper motion and distance estimates. The preliminary results show that both clusters are moderately reddened with $E(J-K_S) = 1.6 \pm 0.2$ and $E(J-K_S) = 1.7 \pm 0.2$. They are relatively nearby: with distances 1.6 and 1.8 kpc from the Sun, and young: with ages of 32 Myr and 10 Myr, for CL 076 and CL 077, respectively.

Acknowledgements: We gratefully acknowledge data from the ESO Public Survey program ID 198.B-2004 taken with the VISTA telescope, and products from the Cambridge Astronomical Survey Unit (CASU). This work has made use of data from the European Space Agency (ESA) mission *Gaia* (`https://www.cosmos.esa.int/gaia`), processed by the *Gaia* Data Processing and Analysis Consortium (DPAC, `https://www.cosmos.esa.int/web/gaia/dpac/consortium`). Support is provided by the Ministry for the Economy, Development and Tourism, Programa Iniciativa Cientica Milenio grant IC120009, awarded to the Millennium Institute of Astrophysics (MAS). ANC's work is supported by the Gemini Observatory. SRA thanks the support by the FONDECYT Iniciación project No. 11171025 and the CONICYT + PAI "Concurso Nacional Inserción de Capital Humano Avanzado en la Academia 2017" project PAI 79170089. J.A-G. also acknowledges support by FONDECYT Iniciación 11150916. MH acknowledges support by the BASAL Center for Astrophysics and Associated Technologies (CATA) through grant PFB-06. We are grateful to anonymous referee for very useful comments, which significantly improve the manuscript.

References

Alonso-García J., et al., 2017, ApJL, 849, L13
Bailer-Jones C.A.L., et al., 2018, AJ, 156, 58
Borissova J., et al., 2011, A&A, 532, A131
Borissova J., et al., 2014, A&A, 569, A24
Borissova J., et al., 2018, MNRAS, 481, 3902
Bressan A., et al., 2012, MNRAS, 427, 127
Gaia Collaboration, et al., 2018, A&A, 616, A1
Zasowski G., et al., 2013, AJ, 146, 64

Truncated γ-exponential models for multi-mass systems

Y.J. Gomez-Leyton[1] & L. Velazquez[1]

[1] *Universidad Católica del Norte, Antofagasta, Chile*

Contact / ygomez@ucn.cl

Resumen / Los modelos γ-exponenciales se propusieron previamente como un intento fenomenológico para caracterizar las propiedades de los sistemas estelares durante la evolución cuasi estacionaria bajo la incidencia de la evaporación: por ejemplo, cúmulos globulares. Estos modelos representan una familia paramétrica de distribuciones que unifican perfiles con núcleos isotérmicos y halos politrópicos, proporcionando así una generalización adecuada para varios modelos disponibles en la literatura. Comenzamos nuestra discusión revisando algunos resultados sobre el caso de sistemas de una sola masa. En particular, enfatizamos que estos modelos predicen la existencia de un nuevo tipo de fenómeno colectivo: el *colapso gravitacional asintótico*. Esta inestabilidad gravitacional difiere del *colapso gravotérmico normal* (por ejemplo, el asociado con el modelo isotérmico) porque su aparición requiere que el sistema libere una cantidad infinita de energía. Posteriormente analizamos cómo la presencia de un espectro de masas modifica la termodinámica de estos modelos, en particular, la aparición de fenómenos colectivos. Si bien la descripción teórica concierne a cualquier sistema de múltiples masas, nuestro estudio computacional aborda el caso más simple: el sistema de dos componentes. Este análisis permite una comprensión importante sobre la termodinámica de los sistemas estelares bajo la incidencia simultánea de la evaporación y los efectos de segregación de masa. Para los modelos actuales, el incremento de los efectos de segregación de masa no afecta la interrupción de la evaporación del sistema, pero favorece la aparición del colapso gravitacional, por ejemplo: tiende a reducir el intervalo de estabilidad de la energía al aumentar el límite inferior de energía crítica para la aparición de este fenómeno. Los casos extremos aparecen bajo ciertas condiciones, donde el colapso gravotérmico cambia su carácter de asintótico a normal.

Abstract / The γ-exponential models were previously proposed as a phenomenological attempt to characterize the properties of stellar systems with a quasi-stationary evolution under the incidence evaporation: e.g.: globular clusters. They represent a parametric family of distributions that unify profiles with isothermal cores and polytropic haloes, thus providing a suitable generalization for several models available in the literature. We start our discussion revisiting some results concerning the case of single-mass systems. In particular, we emphasized that these models predict the existence of a new type of collective phenomenon: the *asymptotic gravothermal collapse*. This gravitational instability differs from the *normal gravothermal collapse* (e.g.: the one associated with isothermal model) because its occurrence requires that the system releases an infinite amount of energy. Afterwards, we analyze how the presence of a mass spectrum modifies the thermodynamics of these models, in particular, the occurrence of collective phenomena. Although the theoretical description concerns to any multi-mass system, our computational study addresses the simplest case: the bi-component system. This analysis allows a major understanding about the thermodynamics of stellar systems under the simultaneous incidence of the evaporation and the mass-segregation effects. For the present models, the growth of mass-segregation effects does not affect the system evaporation disruption but favors the occurrence of gravothermal collapse, e.g.: it tends to reduce the energy interval of stability by increasing the lower bound critical energy for the occurrence of this phenomenon. Extreme cases appear under certain conditions, where gravothermal collapse changes its character from asymptotic to normal.

Keywords / cosmology: dark matter — galaxies: statistics — methods: numerical — methods: statistical

1. Truncated γ-exponential models

Let us consider a system composed of several species of identical particles, and let us denote by m_i and N_i the mass and number of particles of i-th specie. Considering $N = \sum_i N_i$ the total number of particles, one can introduce relative abundance $c_i = N_i/N$ and the average mass $m = \sum_i m_i N_i/N$. The average mass m can be employed to introduce the mass fraction ν_i for the i-th specie $\nu_i = m_i/m$. Accordingly, the mass fraction ν_i and the relative abundances c_i satisfy the normalization conditions, $\sum_i \nu_i c_i = 1$ and $\sum_i c_i = 1$. The one-body quasi-stationary distribution function (DF) of the i-th specie $f_\gamma^{(i)}(q,p|\beta) = A_i E\left\{\beta\left[\varepsilon_c^{(i)} - \varepsilon_i(q,p)\right];\gamma\right\}$, where β is the inverse temperature parameter and (q,p) are the canonical variables of the phase space, position and moment, respectively. The DF is based on simple thermo-statistical models (Gunn & Griffin, 1979; Meylan & Heggie, 1997; Zocchi et al., 2012), where $E(x;\gamma)$ is the truncated γ-exponential function that we have proposed (Gomez-Leyton & Velazquez, 2014) which considers a continuous deformation of the ordinary exponential function, given by:

$$E(x;\gamma) = \Theta(x) \sum_{k=0}^{\infty} \frac{x^{\gamma+k}}{\Gamma(\gamma+1+k)}, \qquad (1)$$

whose introduction is based on fractional calculus (Miller & Ross, 1993), with $\Theta(x)$ and $\Gamma(x)$ being the Heaviside step and Gamma function, respectively. This proposed parametric family of models generalizes other models that include evaporations, such as Woolley models (Woolley, 1954) when $\gamma = 0$, King models (King, 1966a,b) for $\gamma = 1$ and Wilson models (Wilson, 1975) for $\gamma = 2$. A subset of polytropic models (Chandrasekhar, 1960) is obtained in the high energy limit, including the known model of (Plummer, 1911).

We have introduced here the individual mechanical energy for particles of the i-th specie

$$\varepsilon_i(q,p) = \frac{1}{2m_i}p^2 + m_i\phi(q) \tag{2}$$

(Binney & Tremaine, 1987) where the constant A_i must satisfy the normalization condition

$$\int f_\gamma^{(i)}(q,p|\beta)\; d^3q\, d^3p = 1. \tag{3}$$

The escape energy for the i-th specie $\varepsilon_c^{(i)} = m_i\phi_c$ is determined by its mass $m_i = \nu_i m$ and the tidal potential $\phi_c = -GM/R_t$, where M is the total mass of the system, and R_t the called tidal radius. This last quantity is assumed to be the same for all species because it is determined from the external gravitational influence of other systems. Introducing the dimensionless potential $\Phi(q) = \beta m[\phi_c - \phi(q)]$. The mathematical problem of this investigation is to solve the following second-order non-linear differential Poisson equation in terms of the dimensionless potential $\Phi(\xi)$ and assuming spherical symmetry:

$$\frac{1}{\xi^2}\frac{d}{d\xi}\left[\xi^2\frac{d}{d\xi}\Phi(\xi)\right] = -4\pi\eta\sum_i \frac{\nu_i c_i}{Z_i}E\left[\nu_i\Phi(\xi);\gamma+\frac{3}{2}\right] \tag{4}$$

where $\xi = r/R_t$ is the dimensionless radius, $\eta = \beta GMm/R_t$ is the inverse dimensionless temperature and

$$Z_i = \int E\left[\nu_i\Phi(q);\gamma+\frac{3}{2}\right]\; d^3q/R_t^3 \tag{5}$$

is the partition function in terms of the tidal radius R_t. This problem can be numerically integrated by demanding the following conditions at the origin of the system, $\Phi(0) = \Phi_0$ and $\partial\Phi(0)/\partial\xi = 0$, and considering the boundary conditions $\xi = 1$, $\Phi(1) = 0$ and $\partial\Phi(1)/\partial\xi = -\eta$. Suitable values for partition functions $Z = Z_i$ and dimensionless inverse temperature η are required to perform the numerical integration of differential equation. Since these quantities are unknown, one needs to implement a scheme of successive iterations to obtain their values by self-consistence (Velazquez et al., 2009).

2. Results for the bi-component system

The mass spectrum of the bi-component system is defined from two parameters: the relative mass abundance of the first component $p = M_1/(M_1+M_2)$ and the mass ratio parameter $\theta = m_1/m_2$ of individual masses (m_1, m_2). According to the results shown in Fig. 1, the presence of a mass-spectrum and the incidence of evaporation are important realistic factors for understanding the thermodynamics of stellar systems. The incidence of evaporation manifests as a truncation of quasi-stationary distribution functions with isothermal cores; which also leads to the truncation of spatial distributions at the called *tidal radius*, as well as the existence of an upper bound for energy of quasi-stationary solutions where stellar systems undergo the evaporation disruption (Gomez-Leyton & Velazquez, 2014). Moreover, under a major incidence of evaporation, the system increases its stability against gravothermal collapse, which is translated into the existence of quasi-stationary configurations with lower energies, and cores more dense and hotter. However, the most significant consequence of evaporation is the distinction between the normal gravothermal collapse, where quasi-stationary configuration with minimal energy exhibits finite values for its energy, temperature and density, and the asymptotic gravothermal collapse, where the corresponding values of such a configuration turn infinite when deformation parameter γ of the present models falls inside a certain interval $\gamma_c < \gamma \leq \gamma_m = 7/2$, whose lower bound γ_c depends on the mass spectrum.

On the other hand, a direct consequence of mass spectrum is the existence of mass-segregation effects, that is, the tendency of heavier members of a gravitationally bound system to concentrate toward the center, while lighter members are displaced to the outer regions. By itself, mass-segregation phenomenon introduces important quantitative and qualitative modifications in most of thermodynamic dependencies. The most important of all them is the growth of the critical energy associated with the occurrence of gravothermal collapse, which implies that mass-segregation favors the occurrence of the gravothermal collapse. Under certain conditions, the presence of a mass spectrum can even modify the nature of gravothermal collapse from asymptotic to normal. Our computational study of the bi-component system evidences that the effects of evaporation and mass-segregation on the thermodynamics of the present stellar models follow opposite tendencies or exhibit opposite consequences, which enable us to talk about a certain competition among evaporation and mass-segregation effects.

Acknowledgements: Authors thank the partial financial support of VRIDT-UCN research programme, and CONICYT ACT1204, FONDECYT REGULAR 1170834 and CONICYT grant 22140036 (Chilean agencies). The authors thank Professor A. Zarate to allow us the access to computational facilities of Research Group on Science Materials and Nanotechnology-UCN.

References

Binney J., Tremaine S., 1987, *Galactic dynamics*, Princeton University Press, Princeton, NJ

Chandrasekhar S., 1960, *Principles of stellar dynamics*, Dover, New York

Gomez-Leyton Y.J., Velazquez L., 2014, J. Stat. Mech.: Theory Exp., 4, 04006

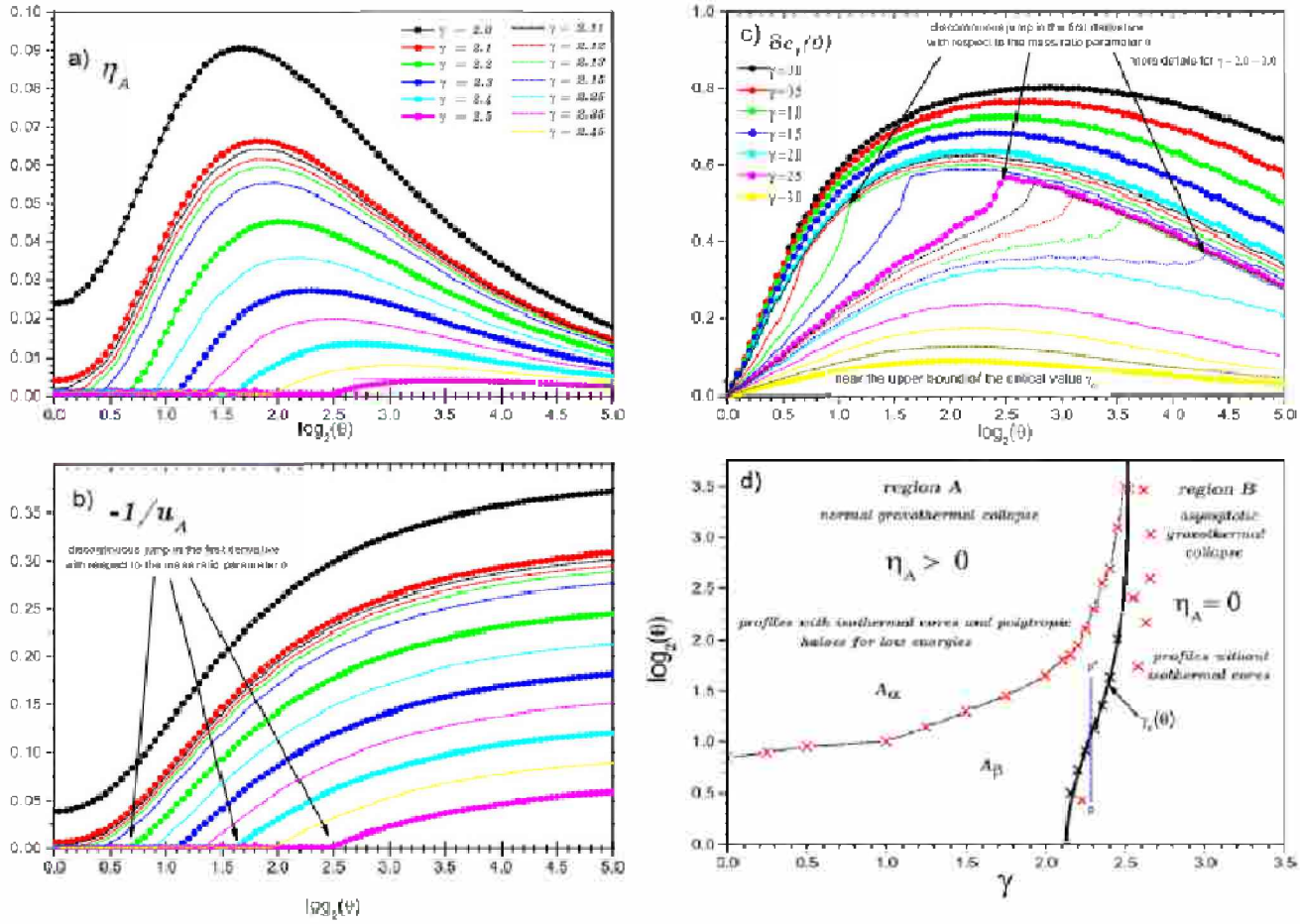

Figure 1: Panel a) and b) Dependencies of the dimensionless inverse temperature $\eta = \beta GMm/R_t$ and the negative of the inverse dimensionless energy $-1/u$ evaluated at the critical points of gravothermal collapses vs. the mass ratio parameter $\theta = m_1/m_2$. The calculations were performed with relative mass abundance of the first component fixed at the value $p = M_1/(M_1 + M_2) = 0.25$ and some values of deformation parameter γ near the critical value $\gamma_c \simeq 2.13$ (single-mass case) in order to show the influence of the mass spectrum on the character of gravothermal collapse. In particular, the qualitative changes observed for dependencies with $\gamma = 2.5$ between the values $k = 2$ and 3, which are associated with the suppression of divergence of the dimensionless energy at the gravothermal collapse u_A (minimum energy that the system can reach), actually occurs when $k = \log_2(\theta) \simeq 2.5$.
Panel c) the central value of deviation of local relative abundance of the heavy specie $\delta c_1(0)$ vs. the mass ratio parameter $\theta = m_1/m_2$ at the point of gravothermal collapse for different values of deformation parameter γ, we have highlighted more details for $\gamma = 2.0 - 3.0$ with a step of 0.1 and near of the upper bound of the critical value γ_c with a step of 0.02 since $2.52 - 2.58$.
Panel d) Phase diagram in the semi-plane $(\gamma, \log_2\theta)$ with different qualitative behaviors of the order parameter η_A (the dimensionless inverse temperature $\eta = \beta GM^2/R_t$ evaluated at the critical point u_A of gravothermal collapse) for the bi-component system with relative mass abundance of the heavy component fixed at the value $p = M_1/(M_1 + M_2) = 0.25$. This scheme summarizes the nature of gravothermal collapse under the incidence of evaporation effects and the presence of a mass spectrum. Crosses are points estimated from our computational study, which were employed to conform this scheme. The dash-dot segment $p - p'$ (blue) represents a change of mass ratio parameter $\theta = m_1/m_2$ that keeps fixed the deformation parameter γ. If this segment crosses the boundary between the regions A and B [the curve $\gamma_c(\theta)$], one can observe the discontinuous jump in the first derivative of some observables with respect to the mass ratio parameter θ.

Gunn J.E., Griffin R.F., 1979, AJ, 84, 752
King I.R., 1966a, AJ, 71, 64
King I.R., 1966b, AJ, 71, 276
Meylan G., Heggie D.C., 1997, A&A Rv, 8, 1
Miller K., Ross B., 1993, *An Introduction to the Fractional Calculus and Fractional Differential Equations*, Wiley
Plummer H.C., 1911, MNRAS, 71, 460
Velazquez L., García S.G., Guzmán F., 2009, PhRvE, 79, 011120
Wilson C.P., 1975, AJ, 80, 175
Woolley R.V.D.R., 1954, MNRAS, 114, 191
Zocchi A., Bertin G., Varri A.L., 2012, A&A, 539, A65

G4CS: GeMS/GSAOI Galactic Globular Cluster Survey

B.W. Miller[1], T.H. Puzia[2], S. Monty[3], E.R. Carrasco[1], M. Simunovic[4] & the G4CS team

[1] *Gemini Observatory, La Serena, Chile*
[2] *Pontificia Universidad Católica de Chile, Santiago, Chile*
[3] *University of Victoria, Victoria, Canada*
[4] *Gemini Observatory, Hilo, USA*

Contact / bmiller@gemini.edu

Resumen / Presentamos los primeros resultados del proyecto GeMS/GSAOI *Galactic Globular Cluster Survey* (G4CS) en los cúmulos globulares (CGs) NGC 3201 y NGC 2298. Usando el instrumento *Gemini South Adaptive Optics Imager* (GSAOI) en combinación con el *Gemini Multi-conjugate adaptive optics System* (GeMS) en el telescopio Gemini-Sur de 8.1 metros, hemos obtenido observaciones profundas de aquellos CGs en el infrarrojo-cercano, detectando sus poblaciones estelares hasta una magnitud $K_s = 21$ Vega mag. La fotometría de *Point spread function* (PSF) fue realizada usando una PSF con variabilidad espacial de manera de corregir variaciones de la óptica adaptativa dentro del campo de visión. Los catálogos fotométricos resultantes en el infrarrojo-cercano fueron expandidos con fotometría óptica y ultra-violeta del *Hubble Space Telescope*. Aplicamos luego una selección basada en movimientos propios y correcciones al enrojecimiento diferencial para usar la diferencia característica en color-luminosidad entre la textitlower main sequence knee (MSK) y la *main sequence turnoff* (MSTO) para determinar las edades. Mediante las combinaciones de filtros K_s vs. F606W$-K_s$ y F336W vs. F336W$-K_s$ obtenemos los diagnósticos más precisos y las usamos para determinar las edades de las poblaciones estelares, las distancias y valores de enrojecimiento para ambos CGs. Hacemos un ajuste para tres conjuntos de modelos de isócronas usando un método de pseudo-χ^2. Utilizando un promedio ponderado de los resultados del ajuste se calculan las edades absolutas de 12.2 ± 0.5 Gyr y 13.2 ± 0.4 Gyr para NGC 3201 y NGC 2298, respectivamente. Los parámetros obtenidos están en buena concordancia con determinaciones recientes de las edades de estos CGs, y nuestros resultados se encuentran entre los más estadísticamente robustos. Esto demuestra el poder de GeMS/GSAOI como una herramienta para la exploración de las características de CGs y de sus poblaciones estelares constituyentes.

Abstract / We present the first results from the GeMS/GSAOI Galactic Globular Cluster Survey (G4CS) of the Milky Way globular clusters (GCs) NGC 3201 and NGC 2298. Using the Gemini South Adaptive Optics Imager (GSAOI) behind the Gemini Multi-conjugate adaptive optics System (GeMS) on the 8.1-meter Gemini South telescope, we have collected deep near-IR observations of the clusters, resolving their stellar populations down to $K_s = 21$ Vega mag. Point spread function (PSF) photometry was performed utilizing a spatially variable PSF to overcome adaptive optics (AO) correction variations across the field of view. The resulting near-IR photometric catalogs were augmented with optical and near-ultraviolet photometry from the *Hubble Space Telescope*. We apply proper motion cleaning and differential reddening corrections before utilizing the characteristic color-luminosity difference between the lower main sequence knee (MSK) and main sequence turnoff (MSTO) to determine the ages. We find that the K_s vs. F606W$-K_s$ and F336W vs. F336W$-K_s$ filter combinations provide the most diagnostic power and we use them to derive the stellar population ages, distances and reddening values for both clusters. We fit three sets of isochrone models to the two color combinations using a pseudo-χ^2 approach. A weighted average of the results gives best-fit absolute ages of 12.2 ± 0.5 Gyr and 13.2 ± 0.4 Gyr for NGC 3201 and NGC 2298, respectively. Our derived parameters are in good agreement with recent age determinations of the two clusters, with our constraints on the ages ranking among the most statistically robust. These findings demonstrate the power of GeMS/GSAOI as a tool for the exploration of both cluster characteristics and their constituent stellar populations.

Keywords / globular clusters: individual (NGC 2298, NGC 3201) — galaxies: star clusters: general — infrared: stars — methods: data analysis

1. Introduction

Globular clusters are near simple-stellar populations (SSPs) so that deep color-magnitude diagrams (CMDs) in conjunction with accurate metallicity measurements can yield accurate age determinations. Therefore, globular clusters can be used to study star formation and chemical enrichment processes as well as provide important clues to the formation of the Galaxy. The GeMS/GSAOI Galactic Globular Cluster Survey (G4CS) is a homogeneous, deep near-IR study of Milky Way globular clusters within 23 kpc with the GeMS multi-conjugate adaptive optics system (Rigaut et al., 2014) and GSAOI imager on the Gemini South 8.1-meter telescope. The targets were selected from the samples of recent surveys using HST (Sarajedini et al., 2007; Piotto et al., 2015) so that photometry is available from the near-UV to the near-IR. This provides cover-

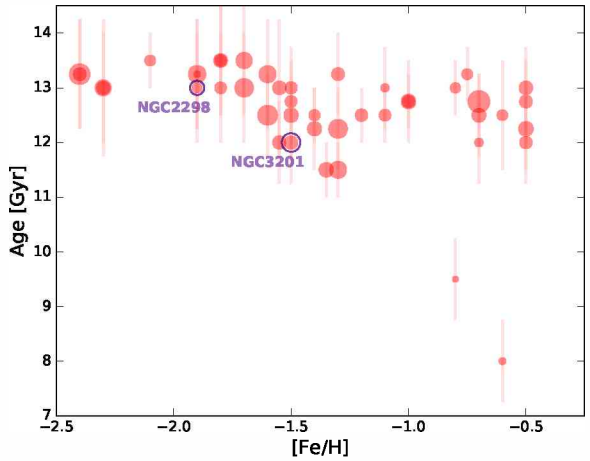

Figure 1: The age-metallicity relationship for the G4CS sample using data from Dotter et al. (2010). The two GCs from this study are circled and labeled. The symbol size scales with the V-band integrated luminosity; larger corresponds to brighter. The sample covers the transition region between the flat and steep age-metallicity relations Marín-Franch et al. (2009) that the survey aims to resolve (Monty et al. (2018), ©AAS. Reproduced with permission.)

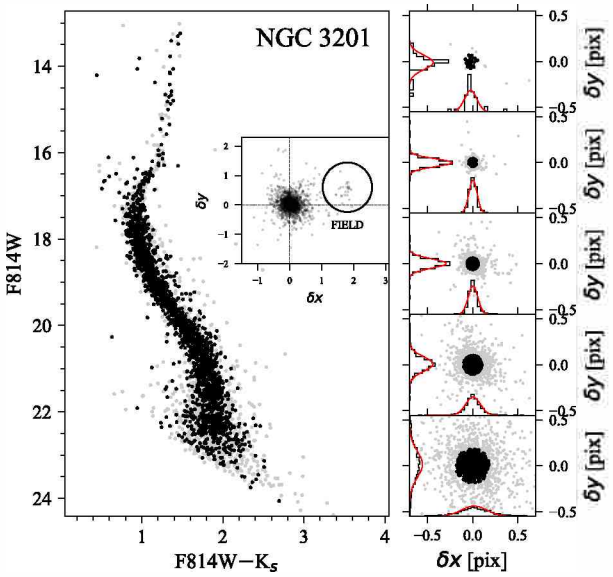

Figure 2: CMDs of cluster members (black points) and non-members (grey points) for NGC 3201. The vector point diagrams are shown for five magnitude bins. The black lines in each sub-panel show the density histograms for horizontally and vertically binned data. The red lines show Gaussian probability density function fits. The cleaned CMD shows clear evidence for the main-sequence knee. (Monty et al. (2018), ©AAS. Reproduced with permission.)

age over a broad range of age, metallicity, and mass (see Fig. 1). The goals of the survey are to investigate the morphology of near-IR CMDs at low stellar mass, compare those with stellar models, derive ages with accuracies of about 1 Gyr, and quantify the binary and blue-straggler populations. This contribution presents the results from the first two clusters observed for the survey, NGC 2298 and NGC 3201 (Monty et al., 2018).

2. Observations and Analysis

The GeMS/GSAOI J, H, and K_s observations were carried out in January and February 2014. Nine, 30-second exposures were obtained in each filter, though some had to be rejected due to poor image quality. Mean image quality was about $0.12''$ for the NGC 3201 dataset and $0.08''$ for that of NGC 2298. The data were reduced and stacked using the THELI software (Schirmer, 2013).

Point-spread function (PSF) photometry was done on the stacked images using DAOPHOT-IV/ALLSTAR (Stetson, 1994) using a cubically-varying PSF. A temporary misalignment, now corrected, in the laser guide star wavefront sensor resulted in larger than normal image distortions over the field. This resulted in higher than normal photometric errors. We rejected photometry with an error more than 1-σ above the mean error as a function of magnitude to ensure that the photometry used in the remainder of the analysis is reliable. The photometry was calibrated by bootstrapping to the 2MASS system using either FLAMINGOS-2 (Gemini South) or Hawk-I (ESO VLT) imaging of the same fields. Finally, the photometry was corrected for differential reddening and cleaned using relative proper-motion measurements by comparing the GSAOI data with previous HST imaging (Fig. 2).

Table 1: Distances, reddenings, and ages from DSED isochrone fits

Name	Distance [kpc]	E_{B-V} [mag]	Age [Gyr]
NGC 3201	5.1 ± 0.1	0.25 ± 0.01	12.2 ± 0.5
NGC 2298	10.6 ± 0.2	0.20 ± 0.01	13.2 ± 0.4

3. Results

Experiments with different filter combinations showed that two combinations — K_s vs. F606W$-K_s$ and F336W vs. F336W$-K_s$ — provided the most diagnostic power. We then fit these CMDs to isochrones from three stellar evolutionary models: Dartmouth (DSED; Dotter et al. (2008)), Victoria-Regina (VR; VandenBerg et al. (2014)), and A Bag of Stellar Tracks and Isochrones (BaSTI; Pietrinferni et al. (2004)). After fixing the metallicities and [α/Fe] ratios to literature values, we then fit main-sequence ridgelines (created from a running-average of stars near the main sequence) to the isochrones using a pseudo-χ^2 fitting method to determine distances, mean reddenings, and ages and their uncertainties. The fits were weighted to give emphasis to the main-sequence turnoff and the main-sequence saddle (inflection point were the main sequence starts to turn down, see Fig. 3)

The results of fitting three models gave very consistent results. The most self-consistent results were obtained with the DSED isochrones and those given in Table 1.

There is good agreement between these values and previous results from the literature. Fig. 4 is a violin

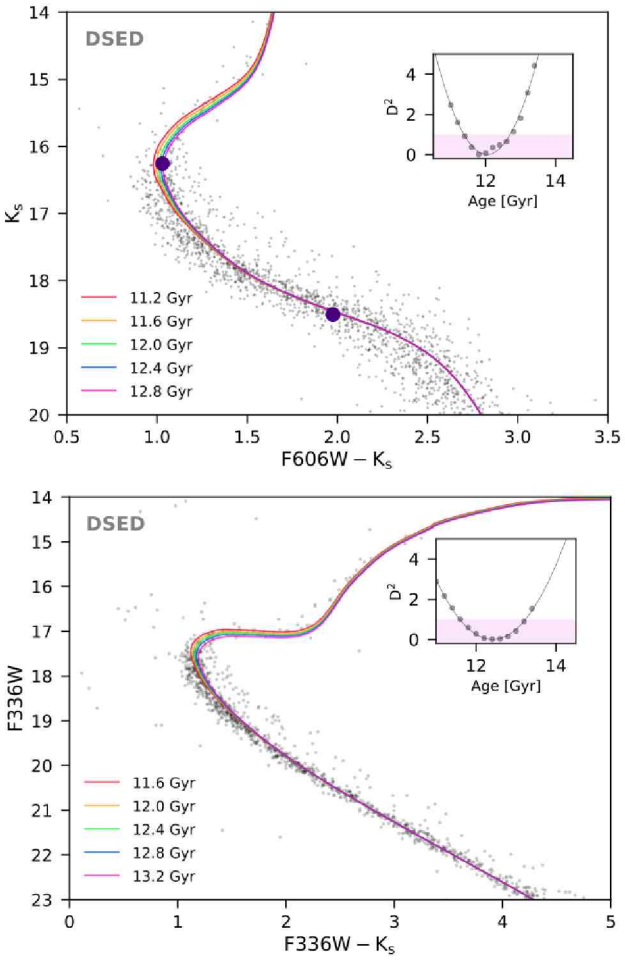

Figure 3: Example of the pseudo-χ^2 minimization process for NGC 3201 with the DSED isochrones with fixed [Fe/H]=−1.59, [α/Fe]=+0.2 and an age range of 10.0–14.0 Gyr. The fits are anchored to the main-sequence turnoff and the main-sequence saddle point (dots in top panel). D^2 is the effective χ^2 statistic defined by Equation 2 of Monty et al. (2018). ©AAS. Reproduced with permission.

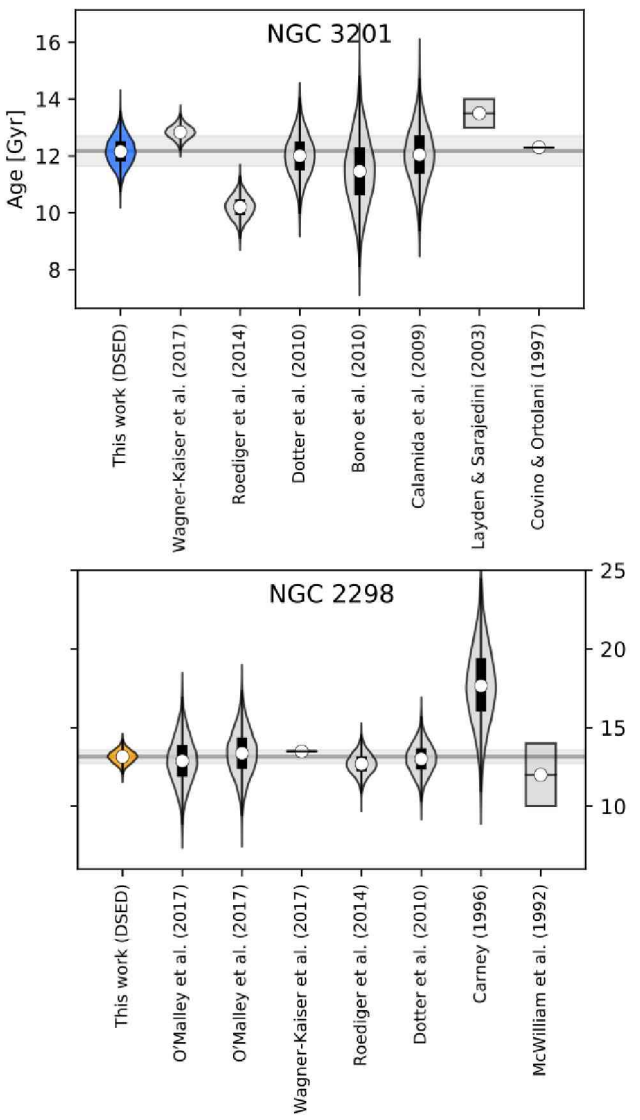

Figure 4: Violin plot comparisons of our ages with literature values. The horizontal lines and surrounding light-shaded regions represent the weighted mean and error of the mean from the DSED isochrones only (the same as the 'This work' violin). Vertical boxes indicate published ranges, while horizontal bars without vertical spread indicate values for which no uncertainties were not given. Thick black vertical bars inside the violins indicate the $\pm1\sigma$ uncertainty ranges, while the violins represent the Gaussian distributions. (Monty et al. (2018), ©AAS. Reproduced with permission.)

plot comparing our DSED ages with recent results from the literature. Our results tend to be within $\pm1\sigma$ of the literature values but with smaller uncertainties, in general. This shows the power of combining UV+optical HST and near-IR GeMS/GSAOI observations to determine accurate ages for Milky Way globular clusters. More G4CS observations are in hand and will give new insight into the stellar populations in globular clusters and the history of the Galaxy.

Acknouledgements: This research is based on observations obtained at the Gemini Observatory, which is operated by the Association of Universities for Research in Astronomy, Inc., under a cooperative agreement with the NSF on behalf of the Gemini partnership: the National Science Foundation (United States), the National Research Council (Canada), CONICYT (Chile), Ministério da Ciência, Tecnologia e Inovação (Brazil) and Ministerio de Ciencia, Tecnología e Innovación Productiva (Argentina).

References

Dotter A., et al., 2008, ApJS, 178, 89
Dotter A., et al., 2010, ApJ, 708, 698
Marín-Franch A., et al., 2009, ApJ, 694, 1498
Monty S., et al., 2018, ApJ, 865, 160
Pietrinferni A., et al., 2004, ApJ, 612, 168
Piotto G., et al., 2015, AJ, 149, 91
Rigaut F., et al., 2014, MNRAS, 437, 2361
Sarajedini A., et al., 2007, AJ, 133, 1658
Schirmer M., 2013, ApJS, 209, 21
Stetson P.B., 1994, PASP, 106, 250
VandenBerg D.A., et al., 2014, ApJ, 794, 72

Study of star clusters in the Small Magellanic Cloud from Ca II triplet spectroscopy

L.V. Gramajo[1,2], M.C. Parisi[1,2], D. Geisler[3,4], J.J. Clariá[1,2] & S. Vásquez[5]

[1] *Observatorio Astronómico de Córdoba, UNC, Argentina*
[2] *Consejo Nacional de Investigaciones Científicas y Técnicas, Argentina*
[3] *Universidad de Concepción, Concepción, Chile*
[4] *Universidad de La Serena, La Serena, Chile*
[5] *Museo Interactivo Mirador, Chile*

Contact / luciana.gramajo@gmail.com

Resumen / Presentamos resultados obtenidos a partir de espectros en el infrarrojo cercano de estrellas gigantes rojas de dos cúmulos estelares de edad intermedia pertenecientes a la Nube Menor de Magallanes (NmM): NGC 411 y NGC 419. Los espectros, obtenidos utilizando el instrumento FORS2 del VLT (Paranal, Chile), están centrados en la región del triplete del Ca II (∼ 8600 Å). Usando estas líneas de absorción, medimos las velocidades radiales medias de los cúmulos con un error de ∼3 km s^{-1}. También medimos anchos equivalentes, a partir de los cuales derivamos las metalicidades medias de los cúmulos con un error de 0.05 dex. Por otro lado, con el objetivo de examinar las propiedades químicas globales de la NmM en la región interna de la galaxia, analizamos los resultados derivados para estos dos cúmulos estelares conjuntamente con los obtenidos para otros veinte cúmulos, previamente estudiados por nuestro grupo, también observados con el VLT y analizados con las mismas técnicas que en el presente trabajo.

Abstract / We present results obtained from near-infrared spectra of red giant stars of two intermediate-age star clusters belonging to the Small Magellanic Cloud (SMC): NGC 411 and NGC 419. The spectra, obtained using the FORS2 instrument on the VLT (Paranal, Chile), are centered in the Ca II triplet region (∼8600 Å). Using these absorption lines, we measure cluster mean radial velocities with an error of ∼3 km s^{-1}. We also measure equivalent widths from which we derive cluster mean metallicities with an error of 0.05 dex. In addition, with the aim of examining the global chemical properties of the SMC in the inner part of the galaxy, we analyze the results derived for these two star clusters together with those obtained for another twenty clusters previously observed by our group with the VLT and studied by applying the same technique.

Keywords / galaxies: star clusters — Magellanic Clouds — stars: abundances

1. Introduction

A significant aspect to analyze in the context of the chemical evolution of the Small Magellanic Cloud (SMC) is the possible existence of a metallicity gradient. A metallicity variation with distance from the center of the SMC has been investigated not only for clusters (Parisi et al. 2009, 2015, hereafter P09, P15; Dias et al. 2014, 2016) but also for field stars (Parisi et al. 2010, 2016, hereafter P10, P16; Dobbie et al. 2014; Choudhury et al. 2018). There is agreement among the different authors about the clear existence of a field star metallicity gradient in the internal region of the SMC. However, the existence of a cluster metallicity gradient cannot be ensured and substantial differences have been found between the chemical behavior of the clusters and field stars (P15, P16). In particular, in a series of papers (P09, P10, P15, P16), a sample of 29 SMC clusters (20 of them in the internal SMC region) and their surrounding fields were analyzed.

The radial velocities (RVs) and metallicities of the observed stars allow us to discriminate possible physical cluster members from field stars (see Section 4. for more details).

In the present work, we performed similar spectroscopic analyses for two SMC stellar clusters, namely: NGC 411 ($\alpha = 1^h\ 7^m\ 56^s$ and δ = -71° 65′ 5″) and NGC 419 ($\alpha = 1^h\ 8^m\ 18^s$ and δ = -72° 53′ 3″). These clusters are aged 1.2 ± 0.2 Gyr and between 1.2 and 1.6 Gyr, respectively (Alves & Sarajedini, 1999; Glatt et al., 2008). We show in Fig. 1 their positions in the galaxy, as well as the location of an additional sample of SMC clusters also studied with the Ca II triplet (CaT) technique.

2. Spectroscopic observations

Using the FORS2 instrument on the Very Large Telescope (VLT, Chile), we obtained spectra for 61 red giant stars of these two clusters and of their surrounding fields. Color-magnitude diagrams were built from aperture photometry of the pre-images in the V and I bands. Spectra have a dispersion of 0.85 Å px^{-1} and cover a range of ∼1600 Å centered in ∼8600 Å, the region of the CaT lines. We used the pipeline (v. 3.9.5) provided by the VLT to perform the reduction of the spectra.

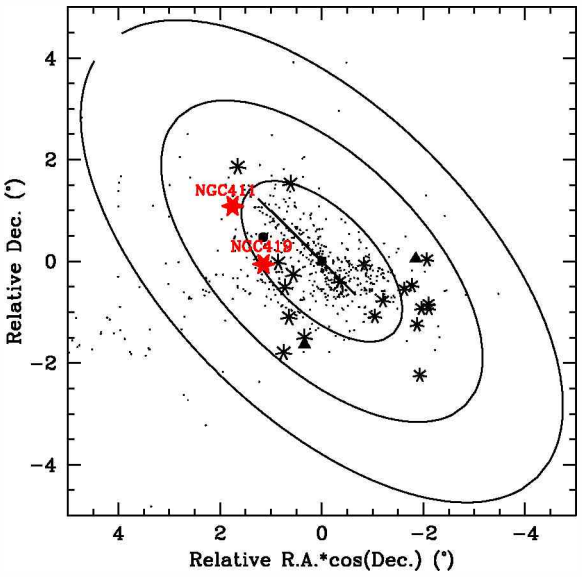

Figure 1: Spatial distribution of SMC clusters having CaT metallicites, located in the inner part of the galaxy ($a < 4°$). Clusters studied by P09 and P15 are plotted with asterisks, while those examined by G18 are identified with triangles. The black circle represents cluster NGC 416 taken from Da Costa & Hatzidimitriou (1998). The two clusters here studied are shown with red stars. The center and the bar of the galaxy are represented by a square and a solid line, respectively. The ellipses have semi-major axes a of 2°, 4° and 6°, respectively. Clusters from the catalog of Bica et al. (2008) are plotted in black dots.

3. Radial velocities and metallicities

We performed cross-correlations between the observed spectra and those of 30 template spectra obtained by Cole et al. (2004), in order to measure RVs of our program stars. For that purpose, we used the IRAF task FXCOR (Tonry & Davis, 1979), which also calculates heliocentric velocities from the observed ones. For each target, we adopted as the heliocentric RV the average of each cross-correlation result, which has a typical error of ∼7.5 km s^{-1}. This error is the sum in quadrature between the standard deviation of the cross-correlations (6 km s^{-1}) and the error introduced by the correction for the star centering in the slit (4.5 km s^{-1}). Metallicities were determined according to the procedure described by Grocholski et al. (2006), P09 and P15, using the sum of the equivalent widths of the three CaT lines and the calibration of Cole et al. (2004).

4. Membership selection

To discriminate cluster members from field stars, we followed a procedure based on the combination of the apparent cluster radius with the RVs and metallicities of the observed stars (P09, P15). We built the corresponding radial stellar density profiles (P09) from which we estimated the cluster radii. The behavior of the RVs and the metallicities as a function of the distance to the center of NGC 411 are shown in Figs. 2 and 3,

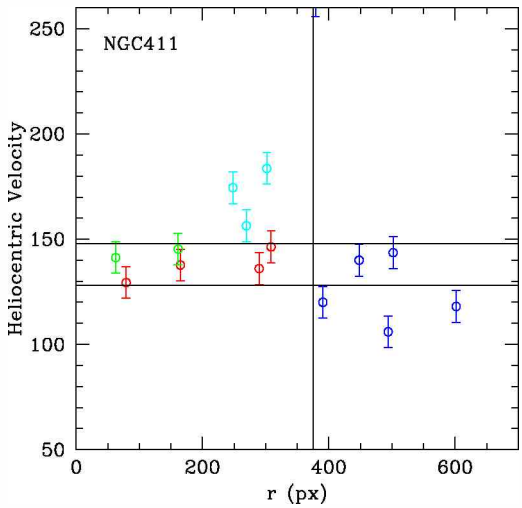

Figure 2: RV vs. distance from the center (r) of NGC 411. The vertical line indicates the adopted cluster radius. The horizontal lines represent our velocity cuts (±10 km s^{-1}). Color code: nonmembers outside the cluster radius (blue circles), nonmembers eliminated because of discrepant RV or metallicity (teal and green circles, respectively), and final cluster members (red circles).

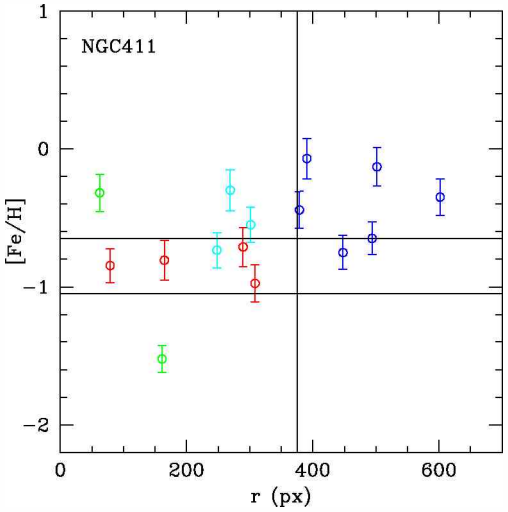

Figure 3: Metallicity vs. distance from the center (r) of NGC 411. The vertical line indicates the adopted cluster radius. The horizontal lines represent the metallicity cuts (± 0.20 dex). The color code is the same as in Fig. 2.

respectively. We discarded as cluster members stars with distances to the cluster center larger than the cluster's radius (marked with a vertical line in both figures) and having RVs and metallicities outside of the adopted cuts. Color code of symbols in Figs. 2 and 3 are explained in the captions. The RV cuts (± 10 km s^{-1}, horizontal lines in Fig. 2) were calculated considering the sum in quadrature between the intrinsic cluster velocity dispersion (5 km s^{-1}, Pryor & Meylan, 1993) and our final adopted error in the RV measurements (7.5 km s^{-1}). The metallicity cuts (±0.2 dex, horizon-

tal lines in Fig. 3) are the rounded up values of our typical metallicity error (0.14 dex). Finally, we calculated cluster mean RVs and metallicites from stars that turned out to be cluster members. We followed the same procedure for the cluster NGC 419. We obtained mean RVs of 137.4±3.1 km s^{-1} and 172.9±3.0 km s^{-1} for NGC 411 and NGC 419, respectively. The mean metallicity values found are [Fe/H] = −0.83±0.05 and [Fe/H] = −0.65±0.05 for NGC 411 and NGC 419, respectively. The quoted RVs and metallicity errors correspond to the standard error of the mean. On the other hand, the metallicities of the stars discarded as cluster members allowed us to estimate the mean metallicity of the surrounding stellar fields: [Fe/H] = -0.68 ± 0.10 and [Fe/H] = -0.82 ± 0.04 for NGC 411 and NGC 419, respectively. Our cluster metallicities exhibit an excellent agreement with the values obtained by previous authors: NGC 411: -0.84 ± 0.03 (Da Costa & Hatzidimitriou, 1998) and ~ -0.8 (Kayser et al., 2009); NGC 419: −0.7-−0.6 (Kayser et al., 2009).

5. Inner metallicity gradient: preliminary results

Fig. 4 shows the metallicities as a function of the semi-major axis a for clusters and field stars, represented with black symbols. In the mentioned papers, an elliptical system was adopted in which the corresponding semi-major axis a is used instead of the projected distance to the Galactic center (see P09 for more details). In Fig. 4 we also plot with triangles the CaT metallicity of the clusters L11 and NGC 339, and their surrounding fields, which we studied in Gramajo et al. (2018, G18). We also include the cluster NGC 416 (black circle). Among the many interesting conclusions that can be drawn from this figure, we highlight the fact that in the inner region, field stars present a small metallicity dispersion, in contrast with the large dispersion found for the star clusters. Such a difference is not observed in the outer part of the SMC ($a > 4°$), where both populations present similar metallicity behavior (P16). On the other hand, while field stars exhibit a negative metallicity gradient in the inner regions of the SMC, in excellent agreement with the results found by Dobbie et al. (2014) and Choudhury et al. (2018), clusters do not clearly show a statistically significant metallicity gradient due to their extremely large metallicity dispersion. In fact, it is interesting to note that clusters appear to be distributed in two groups, above and below the sequence followed by the field stars. This result could be reflecting a possible difference in the chemical evolution of clusters and field stars (P16). The positions of NGC 411 and NGC 419 and of their surrounding fields are represented in Fig. 4 by red stars, respectively. As can be seen, they reinforce what was raised by P16. Dias et al. (2016, D16) suggest splitting the star cluster samples according to their positions in the SMC: main body, wing/bridge, counter-bridge, and west halo. Each of these groups would follow a tidal characteristic which is a consequence of the interaction of the SMC with the Large Magellanic Cloud and of both galaxies with the Milky Way. D16 argued in favor of the existence of a

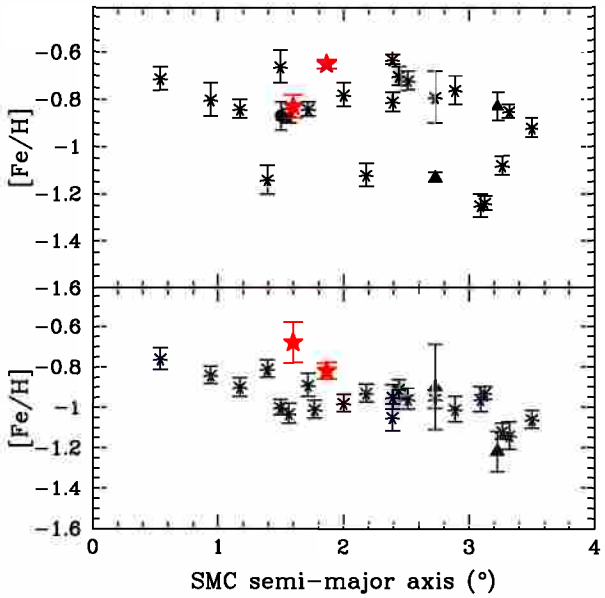

Figure 4: *Upper panel:* Mean metalllicity vs. semi-major axis a for the SMC clusters. Symbols are the same as in Figure 1. *Bottom panel:* Mean metalllicity vs. semi-major axis a for field stars from P10 and P16 (asterisks), G18 (triangles) and the present study (stars).

metallicity gradient in the west halo. However, their photometric metallicities do not have the precision required in order to be conclusive. Our sample is not large enough to significantly test the split proposed by D16. Nevertheless, it represents an interesting idea to explore. To do that, a larger spectroscopically studied cluster and field samples are needed. We have created a trinational project involving Chile (PI: B. Dias), Brazil (PI: L. Kerber) and Argentina (PI: C. Parisi) to obtain spectroscopic data of the SMC, with the aim of analyzing the chemical properties of the SMC with a larger cluster sample with very precise CaT metallicities.

References

Alves D.R., Sarajedini A., 1999, ApJ, 511, 225
Bica E., et al., 2008, MNRAS, 389, 678
Choudhury S., et al., 2018, MNRAS, 475, 4279
Cole A.A., et al., 2004, MNRAS, 347, 367
Da Costa G.S., Hatzidimitriou D., 1998, AJ, 115, 1934
Dias B., et al., 2014, A&A, 561, A106
Dias B., et al., 2016, A&A, 591, A11
Dobbie P.D., et al., 2014, MNRAS, 442, 1663
Glatt K., et al., 2008, AJ, 136, 1703
Gramajo L.V., et al., 2018, BAAA, 60, 249 (G18)
Grocholski A.J., et al., 2006, AJ, 132, 1630
Kayser A., et al., 2009, *The Age-Metallicity Relation of the SMC*, 157
Parisi M.C., et al., 2009, AJ, 138, 517 (P09)
Parisi M.C., et al., 2010, AJ, 139, 1168 (P10)
Parisi M.C., et al., 2015, AJ, 149, 154 (P15)
Parisi M.C., et al., 2016, AJ, 152, 58
Pryor C., Meylan G., 1993, S.G. Djorgovski, G. Meylan (Eds.), *"Structure and Dynamics of Globular Clusters"*, *ASP Conference Series*, vol. 50, 357
Tonry J., Davis M., 1979, AJ, 84, 1511

Radial trends in Galactic globular clusters and their possible origin

V. Kravtsov[1,2]

[1] *Sternberg Astronomical Institute, Lomonosov Moscow State University, Moscow, Russia*
[2] *Instituto de Astronomía y Ciencias Planetarias de Atacama, Universidad de Atacama, Copiapó, Chile*

Contact / vkravtsov1958@gmail.com

Resumen / El tiempo de relajación al radio de semimasa de los cúmulos globulares (CGs) de nuestra Galaxia está típicamente dentro de unos pocos Ga (10^9 años). Entonces se espera que la mayoría de los CGs estén bastante bien relajados, tomando en cuenta su edad alrededor de 12–13 Ga. O sea, cualquier segregación radial inicial entre estrellas de la misma masa inicial en la secuencia principal (SP), particularmente entre los progenitores de las actuales estrellas pertenecientes a las ramas de subgigantes y gigantes rojas (RSG, RGR, por sus siglas en inglés), ya debería desaparecer. Sin embargo, se han acumulado pruebas que contradicen esta expectativa. La paradoja se podría resolver tomando en cuenta el efecto de colisiones estelares que ocurren en los núcleos densos de CGs. La tasa de colisiones es particularmente elevada mientras los núcleos están colapsando. Esta formación de nuevas estrellas hace que las partes centrales sean no relajadas. Llama la atención que los rezagados azules de colisión observados actualmente en CGs sean mucho menos numerosos que sus homólogos de menor masa acumulados en la SP durante el tiempo de vida de los CGs. El efecto de este proceso seria que las estrellas de la misma luminosidad en las SP/RSG/RGB no serán de la misma masa sino de un rango no despreciable.

Abstract / The relaxation time at the half-mass radius of Galactic globular clusters (GGCs) is typically within a few Gyr. Hence, the majority of GGCs are expected to be well relaxed systems, given their age is around 12-13 Gyr. So any initial radial segregation between stars of the same initial mass on the main sequence (MS), in particular, the progenitors of the present day sub-giant and red-giant branch (SGB, RGB) stars should already have dissipated. However, a body of evidence contradicting to these expectations has been accumulated to date. The paradox could be solved by taking into account the effect of stellar collisions. They occur at particularly high rate in collapsing nuclei of GGCs and seem to be mainly responsible for unrelaxed central regions and the radial segregation observed. We draw attention that actually observed collisional blue stragglers should be less numerous than their lower-mass counterparts formed and accumulated at and below the present day MS turnoff. The effect of this is that MS/SGB/RGB stars of a given luminosity are not of the same mass but fall in a range of mass.

Keywords / globular clusters: general — Hertzsprung–Russell and C–M diagrams — stars: low-mass

1. Introduction

There is strong evidence that stellar populations in Galactic globular clusters (GGCs) exhibit dissimilarities in comparison with stellar populations in Galactic open clusters and in the field. The key one is that anti-correlations between abundances of some chemical elements, in particular, O-Na anti-correlation, are not observed among field and Galactic open cluster stars. The apparent manifestations of multiple stellar populations are not obviously observed (at least in statistical sense) in open clusters, too. Therefore, we should search for those factors which could be responsible for (or the main contributors to) these dissimilarities. An interesting unexplored possibility is assumed to be stellar collisions which do occur in the densest part of GGCs but are of much lower probability or improbable at all in other environments, i.e. in open clusters and in the field.

2. Radial segregation in globular clusters

One of the intriguing and controversial issues of multiple stellar populations in GGCs is whether there is any significant difference in radial distribution of the sub-populations in their parent globular clusters. Probably, Norris & Freeman (1979) were first who reported on the difference in the radial distribution of red giant branch (RGB) stars with different CN strength in a GGC, namely in 47 Tuc. Radial color variations were later recovered in GGCs in the sense that the clusters were found to be bluer, in addition to the strengthening of Balmer absorption lines, towards the cluster centers. These effects were summarized and discussed by Djorgovski & Piotto (1993). It has been found that most of these GCs are post-core-collapse objects and the gradient typically extends to at least a few tens of arcsec in radius and even up to ∼100 arcsec or further. Carretta et al. (2009) statistically achieved generalized conclusion about different spatial distributions of the spectroscopically distinguished components of stellar populations in a sample of 15 GGCs. Radial segregation between the

sub-samples of both SGB and RGG stars with different UV-based photometric characteristics was found in a number of GGCs (Kravtsov et al., 2010a,b, 2011; Lardo et al., 2011). HST photometry in the central parts of two metal-rich GGCs, NGC 6388 and NGC 6441, revealed (Bellini et al., 2013) a probable difference in the radial distribution of two distinct stellar sub-populations in each of the clusters. Larsen et al. (2015) found a radial trend of the ratio of primordial to nitrogen-enhanced giants in the GGC M15, which changes its sign at the radial distance near the half-light radius. Similarly, Lim et al. (2016) found more centrally concentrated CN-weak red giants compared to the CN-strong ones, in the GGCs NGC 362 and NGC 6723. Recently, Dalessandro et al. (2018) reported that first-generation stars in the GC M80 are significantly more centrally concentrated than extreme second-generation stars out to ∼2.5 half-light radius from the cluster center. It is important that these radial effects were revealed not only among SGB and RGB stars, but also among MS turnoff (MSTO) stars in 47 Tuc (Kučinskas et al., 2014).

An important point here is that the proposed scenarios of the origin of sub-populations in GGCs proceed from observational fact that the sub-populations are old and nearly coeval within a few 10^8 yr. This implies very unlikely radial segregation between the sub-populations in the majority of GGCs for the following reason. Galactic GGCs are about 12-13 Gyr old while their relaxation time at the half-mass radius is typically within a few Gyr (Harris, 1996). Therefore, the majority of GGCs have to be well relaxed systems. This implies that any initial or very old radial segregation between stars of the same or slightly different mass on the main sequence (MS) should already have dissipated. A portion of these primordial MS stars were, in particular, the progenitors of the present day SGB and RGB stars. This means that stars actually located on these branches at the same luminosity level are expected to exhibit no radial segregation between them. However, a body of evidence contradicting to the latter expectation has been accumulated to date and demonstrated above.

One can assume that the observed radial effects are due to fairly different mass among SGB/RGB/MSTO stars or/and unrelaxed effects caused by recently occurred processes in the innermost parts of GGCs. We (Kravtsov, 2017) recently already suggested that a radial trend of the mass of RGB stars might mimic the iron abundance trend in NGC 3201 we found earlier (Kravtsov, 2013) in this and some other GGCs. Here in developing these assumptions we consider the process that could mainly be responsible for the radial trends/segregation.

3. Lower-mass counterparts of collisional blue stragglers

Collision of MS stars is thought to be the most efficient mechanism, alternative to mass transfer in binary systems, of blue straggler (BS) formation in the densest parts of GGCs. In agreement with these expectations, collisional BSs (CBSs) were isolated in GGCs (Ferraro et al., 2009; Dalessandro et al., 2013). However, the impact of stellar collisions should not be reduced to this particular outcome of the formation of CBSs. It should be considered in more general context, since stellar collisions are a mechanism inducing fictive star formation in GGCs and leading to the formation and accumulation, during 12–13 Gyr, of populations of newly formed MS stars, lower-mass counterparts of CBSs. They should be much more numerous than the observed CBSs because of longer lifetime and higher rate of their formation as compared to CBSs.

Mass transfer in binary systems, where it is allowed between MS stars among their various possible combinations, forms new modified MS stars, the majority of which are mass-transfer BS (MTBSs) located above the MSTO (Stępień & Kiraga, 2015). Their lower-mass counterparts formed simultaneously with MTBSs are less numerous and fall in narrower mass range than lower-mass counterparts of CBSs, but they are added to the population of latter MS stars in the upper MS and thereby increase the total population of modified MS stars below the MSTO and the proportion modified-to-primordial (Mod/Prim) MS stars. This proportion is increased with increasing GC age. We note here that the main "reservoir" of MS stars, potential targets of collision, is at M < 0.45 $M_\odot$. The portion of MS stars in this mass range depends on initial mass function of GGCs, but the number of primordial MS stars in this mass range is roughly ten times the number of MS stars with mass 0.45 $M_\odot$ < M < 0.85 $M_\odot$. Therefore, the rate of stellar collisions in the mass range M < 0.45 $M_\odot$ with formation of lower-mass counterparts of BSs can be many times as high as that in the mass range 0.45 $M_\odot$ < M < 0.85 $M_\odot$ (Davies, 2016) that results in the formation of CBSs.

Some important sequences of the formation and accumulation of lower-mass counterparts of BSs in the present day GGCs are as follows:

First, it is obvious that the MS, in general, and its upper part, in particular, should consist of stars of different mass at a given luminosity in contrast to a lower-density (or/and much younger) population of MS stars. The range of mass near the present day MSTO may be as large as $\Delta M \sim 0.10$ $M_\odot$. Stellar models show that, for example, a star of the mass 0.8 $M_\odot$ and [Fe/H]≈ −1.3, formed 2 Gyr ago from two collided primordial MS stars of the mass 0.4 $M_\odot$ each one, would be now fainter, by nearly 1.0 mag. in the V band, than its primordial counterpart of the same mass, which is approaching to the present day MSTO.

Second, very important point is that the new MS stars formed by collision are expected to have modified superficial CNO abundance as compared with that of primordial MS stars (Glebbeek et al., 2008).

Third, primordial stars of mass M and lower-mass counterparts of BSs of the mass(es) $M + \Delta M$ (because of higher hydrogen abundance in their nuclei) will evolve from the MS to a given luminosity on the RGB on the same timescale. That is the RGB should also harbor stars of a range of mass at a given luminosity, ΔM being larger on the RGB than on the MS due to contribution of evolved BSs themselves.

The relative number of lower-mass counterparts of CBSs formed and accumulated even in the oldest open clusters is expected to be much smaller than in globular clusters. Indeed, stellar density (i.e., concentration), one of the key parameters defining the probability of collisions in stellar aggregates, is several orders of magnitude higher in (the centers of) globular than open clusters. A more detailed comparative analysis of the impact of other important parameters (such as the relative number of binary stars, the velocity dispersion of stars, etc.) on the occurrence of collisions in both types of star clusters is the subject of a separate publication.

Acknowledgements: We are grateful to the organizers of the meeting for the opportunity to give the talk and to the referee for useful comments.

References

Bellini A., et al., 2013, ApJ, 765, 32
Carretta E., et al., 2009, A&A, 505, 117
Dalessandro E., et al., 2013, ApJ, 778, 135
Dalessandro E., et al., 2018, ApJ, 859, 15
Davies M.B., 2016, MmSAI, 87, 479
Djorgovski S., Piotto G., 1993, S.G. Djorgovski, G. Meylan (Eds.), *Structure and Dynamics of Globular Clusters*, *Astronomical Society of the Pacific Conference Series*, vol. 50, 203
Ferraro F.R., et al., 2009, Nature, 462, 1028
Glebbeek E., Pols O.R., Hurley J.R., 2008, A&A, 488, 1007
Harris W.E., 1996, AJ, 112, 1487
Kravtsov V., 2013, A&A, 554, L6
Kravtsov V., et al., 2010a, A&A, 512, L6
Kravtsov V., et al., 2010b, A&A, 516, A23
Kravtsov V., et al., 2011, A&A, 527, L9
Kravtsov V.V., 2017, AJ, 154, 79
Kučinskas A., Dobrovolskas V., Bonifacio P., 2014, A&A, 568, L4
Lardo C., et al., 2011, A&A, 525, A114
Larsen S.S., et al., 2015, ApJ, 804, 71
Lim D., et al., 2016, ApJ, 832, 99
Norris J., Freeman K.C., 1979, ApJL, 230, L179
Stępień K., Kiraga M., 2015, A&A, 577, A117

A Bolometric study of the Stripped–Envelope SN 2010jr

J. Pineda G.[1] & F. Olivares E.[2,1]

[1] *Departamento de Astrnomía, Universidad de Chile, Santiago, Chile*
[2] *Millennium Institute of Astrophysics, Santiago, Chile*

Contact / japineda@das.uchile.cl

Resumen / Las supernovas (SN) de envoltura removida provienen del colapso gravitatorio de estrellas masivas que han perdido su envoltura de hidrógeno y/o helio. Con el estudio de sus curvas de luz podemos restringir los parámetros físicos de la explosión y las propiedades de la estrella progenitora. Esta investigación utiliza la fotometría de la SN 2010jr en el ultravioleta, óptico, e infrarrojo para construir y ajustar las curvas de luz de cada filtro a través del método de procesos gaussianos. Luego, para cada época calculamos la distribución de energía espectral, la cual ajustamos e integramos en frecuencia para obtener finalmente la curva pseudo-bolométrica en el rango de longitudes de onda observado. La curva pseudo-bolométrica nos permitirá calcular el tiempo de explosión y estimar parámetros fundamentales de la SN tales como la masa de níquel sintetizado en la explosión, la energía cinética y la masa total eyectada.

Abstract / Stripped-Envelope supernovae come from the core collapse of massive stars that have lost their Hydrogen and/or Helium envelopes. Studying their light curves (LCs) we can constrain the physical parameters of the explosion and their progenitor properties. This research used the photometry of SN 2010jr in the ultraviolet (UV), optical and near-infrared (NIR) to construct and fit the LCs of each filter through the Gaussian Process (GP) method. Then, for each epoch we calculate the Spectral Energy Distribution, which we fit and integrate in frequency to finally obtain the pseudo-bolometric LC in the observed wavelength range. The pseudo-bolometric LC will enable us to calculate the explosion time of the SN and constrain fundamental parameters like nickel mass synthesized in the explosion, the kinetic energy and the total ejected mass.

Keywords / Supernovae: individual: SN 2010jr — methods: data analysis

1. Introduction

The process related with the end of the life in massive stars ($> 8M_{\odot}$) is called a core-collapse supernova explosion. In these events the SN brightness increases suddenly and can sometimes even outshine its own host galaxy. We classify a SN as a type II when Hydrogen lines are present in the spectra (Filippenko, 1997). If there are no Hydrogen lines, the SN is a type I. In addition, type I are divided into the presence (Ia) or lack (Ib and Ic) of the Si II line. We can also differentiate between Ib and Ic using the He I line.

The Stripped-Envelope supernovae (SESNe) comprise the types Ib, Ic and IIb. These SNe are characterized by a three-phase pattern in the shape of their LCs. These trace the different processes in the SN evolution: the shock breakout (SBO), the cooling phase and thermalization. The SBO is rarely detected because it occurs immediately after core-collapse and last only a few hours (e.g. Bersten et al. 2018). The next phase is sometimes observed at a couple of days after explosion (Bufano et al., 2014). It is characterized by an early LC decline produced by the adiabatic cooling following the SBO passage through the envelope. Finally, we have the third peak that is due to thermalization of γ rays from the decay of the ^{56}Ni synthesized in the explosion (Gangopadhyay et al. 2018). By constructing a bolometric LC we can determine the physical parameters of the explosion such as total ejected mass, nickel mass and kinetic energy. We can also infer further properties of the SN progenitor such as the pre-explosion radius by modelling the cooling phase.

2. Observations and data

Our study object is the type IIb SESN 2010jr discovered in Nov 12.09 UT, 2010, at 16.2 mag. The data set consists of (1) photometry in the *g',r',i',z',J,H,K* filters from GROND (Gamma-ray Burst Optical/Near-infrared Detector) mounted at the 2.2-m MPG telescope at La Silla Observatory (Greiner et al., 2008) and (2) photometry in the *V,B,U,UVm1,UVw1,UVw2* filters from the UV/Optical telescope (UVOT) at the Neil Gehrels *Swift* Observatory (Gehrels et al., 2004).

A representative LC sample is presented in Fig. 1. The LCs show two stages: the early optical and UV emission by the cooling phase, which is dominated by the energy deposited by the shock wave and the brightening to a broad maximum due to the decay of radioactive material synthesized during the explosion.

3. Analysis

3.1. UV, optical and NIR LCs through GP

One of our work aims is implement the GP prediction to accurately describe the LC behavior in between the observed data points. In Fig. 2, we use the GP framework

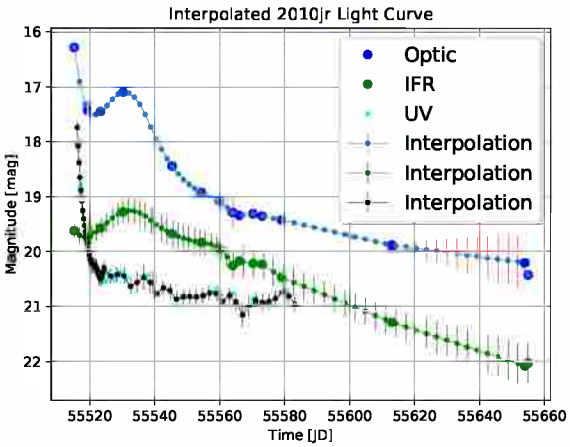

Figure 1: The LCs of SN 2010jr (magnitude against MJD) in *g,H,UVw2*, representative of each wavelength range (optical, NIR and UV). We arbitrarily offset the LC in magnitude for aesthetic purposes. The interpolation corresponds to a combined quadratic fit for the early phase around maximum and a linear fit for the late phase of the radioactive tail.

GPy* and the python library GEORGE (Ambikasaran et al. 2015) to interpolate the data. The GP is a regression method that generate predictions alongside with error bars and it is based on the Gaussian distribution for which we used the Rational Quadratic Kernel prediction from the result of testing many kernels:

$$K(x_i, x_j) = K\left(1 + \frac{(x_i - x_j)^2}{2al^2}\right)^{-a}, \quad (1)$$

where l is the length-scale and determines the wiggles in the function, K is the output variance related with the mean average distance from the function and a is the scale parameter related with the function smoothness.

We compared the GP results (Fig. 2) with those from Fig. 1. The prediction in between points is better using GP than the polynomial interpolation, because in the latter we are forcing linear and quadratic behavior. We also evidenced that large errors are due to lack of data in a given range (e.g. at late times in the UV filters; bottom panel, Fig. 2). For this reason we need data in several filters. On the other hand, for both methods we can see the LC starting with a bright magnitude, reaching the main peak, and then decreasing over the time, which is consistent with the post SN explosion process.

3.2. SEDs and pseudo-bolometric LCs

After GP modelling all the LCs in the UV, optical and NIR bands, we built the pseudo-bolometric LC. First, we proceed to integrate the SEDs frequency range. For this purpose, we converted magnitudes into flux at the central wavelength filter and obtained the SEDs shown in Fig. 3. To obtain the SED, it is necessary to (1) correct the magnitudes for Galactic foreground extinction, (2) use the heliocentric redshift to correct the central wavelengths of the filters, and (3) correct the magnitudes for host-galaxy extinction (taken from Bufano et al. 2014). Finally, The total flux is converted into luminosity using the distance**.

The Fig. 3 shows the expected behavior of the SN

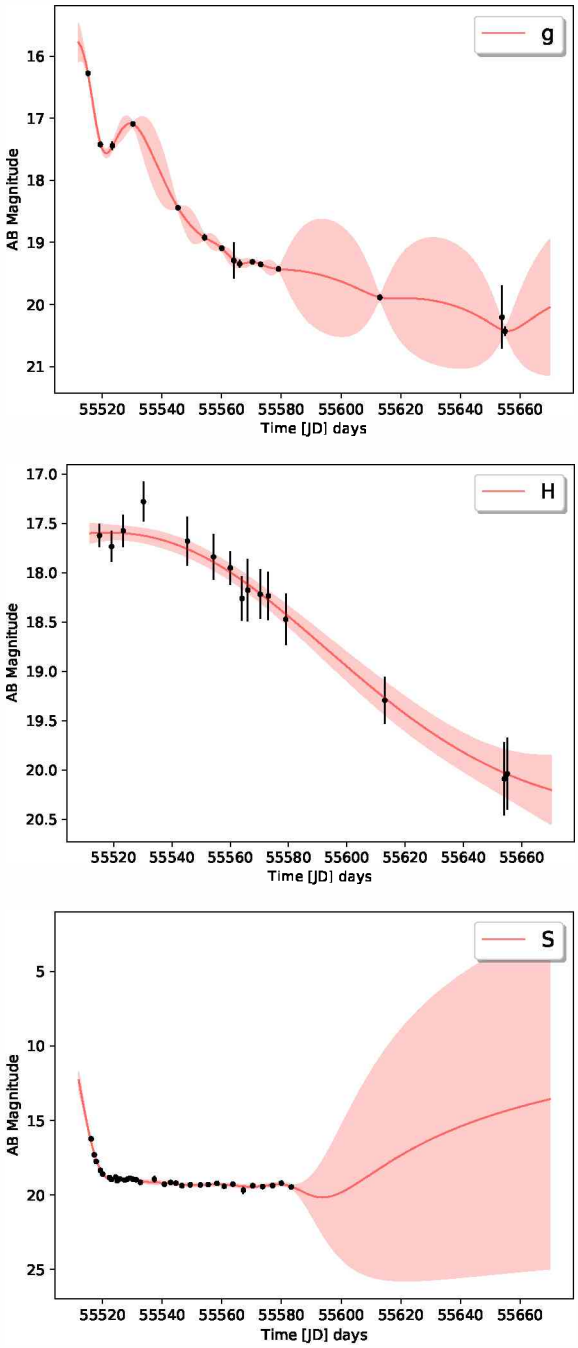

Figure 2: AB magnitude against MJD time: LCs, using GP to interpolate. Representative LCs for optical g band (top), NIR H band (middle) and UV *UVw2* band (bottom) are shown. While the red line is the best fit, the pink areas depict the uncertainty of the modelling.

*GPy: A Gaussian process framework in python. `http://github.com/SheffieldML/GPy`

**`http://ned.ipac.caltech.edu`

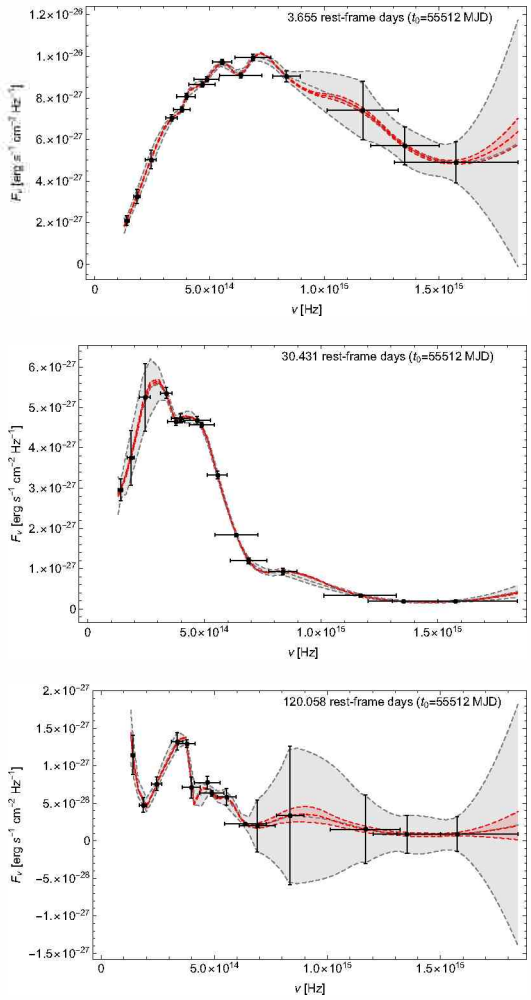

Figure 3: Representative SEDs of SN 2010jr at three different rest-frame times: before maximum (top), after maximum (middle) and at the radioactive tail (bottom). Each SED covers the UV, optical and NIR. The red line is the data interpolation and the gray region is the corresponding error.

SED. At the early times we observe a peak at higher frequencies (top panel), which is then cooling towards lower frequencies as the SN expands (middle). The late-time SED (bottom) is probing the nebular regime during the radioactive tail, thus no clear black-body maximum is observed. The interpolation was obtained with a polynomial fitting (quadratic and linear) and using a Simpson's rule to integrate between the data points. Currently we are improving our kernel for the SED interpolation implementing the GP method.

Finally, from the bolometric LC in Fig. 4 we can determine the main parameters of the SN explosion such as total ejected mass, kinetic energy and synthesized ^{56}Ni mass, using the Morozova et al. 2015 models in the pseudo-bolometric LCs. Moreover, the early behavior of the bolometric LC shows the cooling phase. From this interesting feature of SN 2010jr we can derive the radius of the progenitor prior to explosion.

4. Summary and discussion

Multi-wavelength photometry of SN 2010jr has been interpolated through GP of each LC that together cover

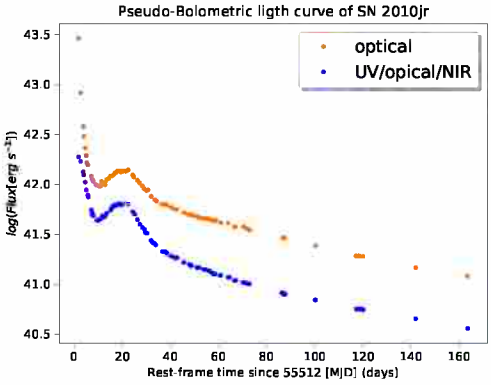

Figure 4: Pseudo-bolometric LCs of SN 2010jr in two wavelength ranges: optical (orange) and UV/optical/NIR (blue).

the range $0.170 - 2.1\mu m$, including *Swift*/UVOT and GROND data. We concluded that the best covariance matrix for the LCs interpolation is the Rational-Quadratic-Kernel, because it give us an accurate fitting for the intervals in which we have no data.

SEDs composed by 14 photometric data points have been interpolated and integrated over wavelength. We will implement the GP method for the SED interpolation by replacing the use of the Simpson's rule for integration over wavelength.

We constructed optical and UV/optical/NIR pseudo-bolometric LCs with the purpose of studying the physical parameters of the explosion and the progenitor-star properties prior to explosion. The ^{56}Ni is related with the peak brightness and the shape of the LC is determined by both the explosion kinetic energy and the total ejected mass. We are currently working on a model to determine accurately rise times for a sample of SESNe to constrain the physical parameters using the pseudo-bolometric LC and different properties of the SN such as the progenitor types which still remains an open question in the field.

Acknowledgements: J.P. thanks support from the Chilean Astronomical Society (SOCHIAS), the Argentine Association of Astronomy (AAA) and Departamento de Astronomía, Universidad de Chile. Support for F.O.E. is provided by the Ministry of Economy, Development and Tourism's Millennium Science Initiative through grant IC120009, awarded to the Millennium Institute of Astrophysics (MAS), and by the FONDECYT grant nr. 11170953.

References

Ambikasaran S., et al., 2015, IEEE TPAMI, 38, 252
Bersten M.C., et al., 2018, Nature, 554, 497
Bufano F., et al., 2014, MNRAS, 439, 1807
Filippenko A.V., 1997, ARA&A, 35, 309
Gangopadhyay A., et al., 2018, BSRSL, 87, 351
Gehrels N., et al., 2004, ApJ, 611, 1005
Greiner J., et al., 2008, PASP, 120, 405
Morozova V., et al., 2015, ApJ, 814, 63

Studying star-forming processes towards G29.862–0.044

M.B. Areal[1], S. Paron[1], M.E. Ortega[1] & C. Fariña[2]

[1] *Instituto de Astronomía y Física del Espacio, CONICET-UBA, Argentina*
[2] *Isaac Newton Group of Telescopes, La Palma, España and Instituto de Astrofísica de Canarias, La Laguna, España*

Contact / mbareal@iafe.uba.ar

Resumen / Presentamos un estudio multiespectral hacia el objeto estelar joven (YSO, por su sigla en inglés) G29.862–0.044 (en adelante G29), localizado en la región de formación estelar G29.96–0.02, y ubicado a una distancia de aproximadamente 6.5 kpc. Para estudiar el medio interestelar circundante a G29 se utilizaron datos de líneas moleculares (resolución angular de 15″) obtenidos de la base de datos del Telescopio James Clerk Maxwell. Se caracterizó la nube molecular en la que se encuentra embebido el YSO y se determinaron parámetros físicos del *outflow* molecular relacionado. Adicionalmente se analizaron datos del infrarrojo cercano (resolución espacial del orden de 0.5″) obtenidos con el instrumento NIRI en Gemini Norte con el fin de observar más detalladamente el ambiente circumestelar de G29. La emisión en la banda Ks hacia G29 presenta una morfología en forma de cono que apunta hacia el outflow molecular rojo. El objetivo de este trabajo es obtener un panorama lo más completo posible del YSO, de los procesos que generan la formación estelar, y del medio interestelar circundante. Estudios como este son de relevancia porque contribuyen a una comprensión integral de la formación de estrellas.

Abstract / We present a multi-wavelength study towards the young stellar object (YSO) G29.862–0.044 (hereafter G29), which is embedded in the massive star-forming region G29.96–0.02, located at a distance of about 6.5 kpc. The surrounding interstellar medium of G29 is studied using molecular lines data (angular resolution about 15 ″) obtained from the databases of the James Clerk Maxwell Telescope. The physical conditions of G29 molecular outflows and the clump where the YSO is embedded are characterized. Near-IR data is also analyzed (spatial resolution of about 0.5 ″) obtained with NIRI at Gemini North to have a detailed view of the circumstellar ambient of G29. The Ks emission towards G29 exhibits a cone-like feature pointing to the red molecular outflow. The aim of this work is to obtain a complete picture of this YSO, the related star-forming processes, and the interstellar medium around it. Studies like this are important because they contribute to a comprehensive understanding of star formation.

Keywords / ISM: clouds — jets and outflows — molecules

1. Introduction

Young stellar objects (YSOs) are usually found embedded in dense molecular clumps, environments with plenty of molecular gas and interstellar dust. The region G29.9–0.02 (see Fig. 1), located at the distance of 6.2 kpc, is very active in massive star formation. Figure 1 is a three-colour image displaying the Spitzer-IRAC 8 μm emission in red, the Herschel-PACS 70 μm emission in green, and in blue, the radio continuum emission at 20 cm as extracted from the New GPS of the Multi-Array Galactic Plane Imaging Survey (MAGPIS). The emissions were selected to highlight the borders of the photodissociation regions (PDRs) (displayed in the 8 μm emission), the distribution of the ionized gas (shown with the 20 cm emission) and the warm dust (70 μm emission). In a previous work we studied the ^{13}CO/C^{18}O abundance ratio throughout the whole region, in relation with these sources and with star-forming processes (Paron, Areal & Ortega, 2018). In the present work we focus on studying the southern massive YSO, cataloged as the Red MSX source G029.862–0.044 (hereafter G29).

2. Data

In order to perform a multispectral study of G29, we used public data (^{12}CO, ^{13}CO and C^{18}O J=3–2), and dedicated observations (near-IR data).

The data of the CO isotopes were obtained from public databases generated with observations of the 15-m James Clerck Maxwell Telescope. The ^{12}CO J=3–2 data belong to the COHRS survey (Dempsey et al., 2013), while the data of the other CO isotopes belong to the CHIMPS survey (Rigby et al., 2016).

The near-IR observations were carried out with the Near InfraRed Imager and Spectrometer (NIRI; Hodapp et al. 2003) at the Gemini-North 8.2-m telescope, on July 2017 in queue mode (Band-1 Program GN-2017B-Q25). NIRI was used with the f/6 camera that provides a plate scale of 0.″117 pix^{-1} and a field of view of 120″ × 120″. The seeing of the Ks image presented here is about 0.″4.

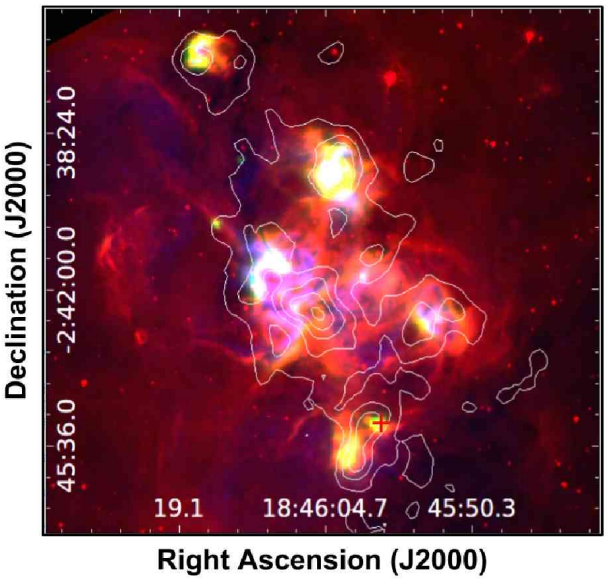

Figure 1: Three-colour image towards G29.96–0.02 displaying the Spitzer-IRAC 8 μm emission in red, the Herschel-PACS 70 μm emission in green, and the radio continuum emission at 20 cm, as extracted from the MAGPIS, in blue. Contours of the $C^{18}O$ J=3–2 line integrated between 96 and 106 km s^{-1} with levels of 5, 11, 16, 22 and 27 K km s^{-1} are included. The YSO position is indicated with the red cross.

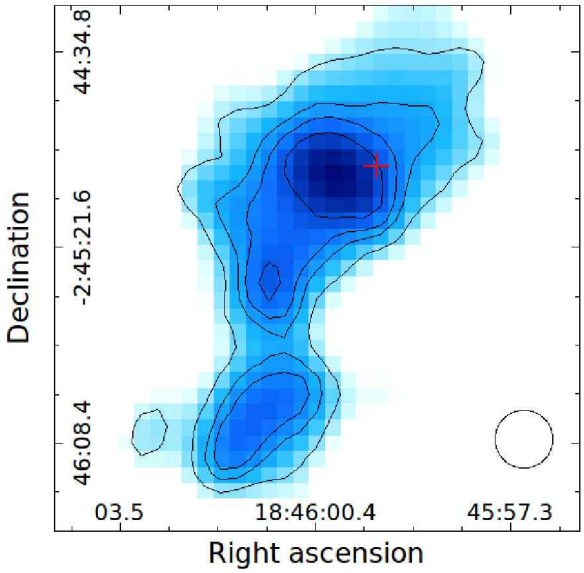

Figure 2: $C^{18}O$ J=3–2 emission integrated between 96 and 106 km s^{-1}. The contour levels are 3, 5, 9 and 13 K km s^{-1}. The YSO position is indicated with the red cross and the beam is represented by the circle.

3. Results

3.1. Molecular cloud

To characterize the molecular cloud in which the YSO is embedded we used the $C^{18}O$ J=3–2 emission, because it is an optically thin tracer of the molecular gas. The $C^{18}O$ emission integrated between 96 and 106 km s^{-1} is presented in Fig. 2 showing the morphology of the molecular cloud associated with G29.

Assuming local thermodynamic equilibrium and using its typical formulae, the mass of the cloud was obtained. The H_2 column density, $N(H_2)$, was calculated from the $C^{18}O$ column density and the conversion factor $X^{18} \sim 1.7 \times 10^{-7}$ (Wilson, 1999). The estimated mass is $M \sim 1 \times 10^4$ $M_\odot$.

3.2. Molecular outflow

The YSOs at the earliest stages of formation are characterized by the presence of molecular outflows. We used the ^{12}CO J=3–2 data to find the molecular outflows related to G29. We identified the presence of a red molecular outflow, but the blue molecular outflow could not be distinguished. This can be due to the presence of a dense concentration of cold dust southwards the YSO, AGAL G029.852–00.059 from Urquhart et al. (2014), that could hide the blue molecular outflow. Also the molecular gas related to the cold dust feature may confuse the observation of the gas associated with the blue outflow. This result is in agreement with that of Li et al. (2016), who studied the outflowing activity of G29 using the ^{12}CO J=1–0 line.

The ^{12}CO emission integrated between 108 and 113 km s^{-1} is presented in Fig. 3, which shows the morphology of the molecular outflow. We estimated the outflow physical parameters from the ^{12}CO emission, obtaining a mass of M_{red} 82 $M_\odot$ and an energy $E_{kred} \sim 2 \times 10^{46}$ erg. These are typical values of massive molecular outflows according to Maud et al. (2015).

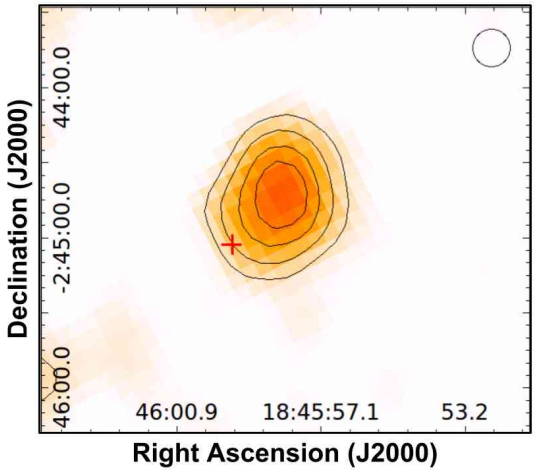

Figure 3: ^{12}CO J=3–2 emission integrated between 108 and 113 km s^{-1}. The contour levels are 7, 11, 14 and 18 K km s^{-1}. The YSO position is indicated with the red cross and the beam is represented by the circle.

3.3. Cicumstellar ambient

With the aim of studying in more detail the YSO and its surroundings we performed near-infrared observations using NIRI at Gemini North. The J, H and Ks broad bands, and some narrow bands such as molecular hy-

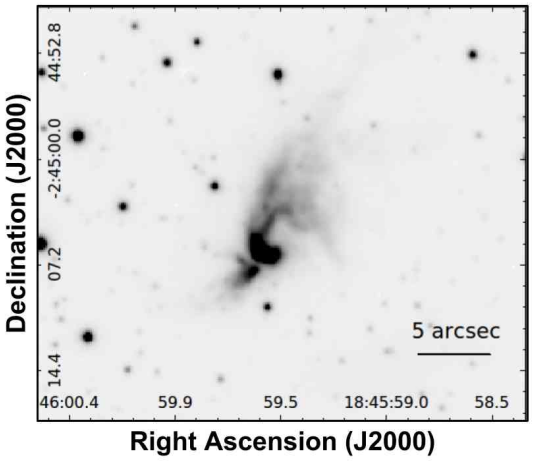

Figure 4: Ks emission obtained with NIRI-Gemini.

drogen lines, among others, were observed. In this work we present only the Ks emission (see Fig. 4).

The Ks emission towards G29, exhibits a cone-like feature pointing to the northwest in direction to the red molecular outflow. It can be seen that there are two arc-like features inside the cone-like structure, which is very similar to what was found towards massive young stellar objects characterized by the presence of precessing jets (Weigelt et al., 2006; Paron et al., 2013, 2016). Also in Fig. 4 it is observed a smaller structure towards the southwest, which may be generated by a jet extending to the opposite direction.

As proposed in previous works (see for example Weigelt et al. 2006), the near-IR emission at the Ks band towards this kind of objects likely arises from a cavity cleared in the circumstellar material by the action of a jet, and may be due to a combination of different emitting processes: radiation from the central protostar that is reflected at the inner walls of the cavity, emission from warm dust, and emission of some lines that these bands contain. Further investigation is needed in order to determine such processes. We are currently analyzing in detail the near-IR data set (the JHKs broad-bands and specially the emission lines observed with the narrow-bands), which will provide valuable information about the origin and physical processes taking place in this intriguing structure.

Acknowledgements. This work was partially supported by grants awarded by ANPCYT and UBA (UBACyT) from Argentina. M.B.A. specially thanks the financial support received to assist to the Second Binational Meeting AAA-SOCHIAS.

References

Dempsey J.T., Thomas H.S., Currie M.J., 2013, ApJS, 209, 8
Hodapp K.W., et al., 2003, PASP, 115, 1388
Li F.C., et al., 2016, AJ, 152, 92
Maud L.T., et al., 2015, MNRAS, 453, 645
Paron S., Areal M.B., Ortega M.E., 2018, A&A, 617, A14
Paron S., Fariña C., Ortega M.E., 2013, A&A, 559, L2
Paron S., Fariña C., Ortega M.E., 2016, A&A, 593, A132
Rigby A.J., et al., 2016, MNRAS, 456, 2885
Urquhart J.S., et al., 2014, A&A, 568, A41
Weigelt G., et al., 2006, A&A, 447, 655
Wilson T.L., 1999, Reports on Progress in Physics, 62, 143

Synthetic observations of H_2D^+ towards high-mass starless cores

J. Zamponi[1], D.R.G. Schleicher[1], S. Bovino[1], A. Giannetti[2], G. Sabatini[1,2,3] & S. Ferrada[1]

[1] *Departamento de Astronomía, Universidad de Concepción, Concepción, Chile*
[2] *Istituto di Radioastronomia - INAF - Italian ARC, Bologna, Italy*
[3] *Dipartimento di Fisica e Astronomia, Università degli Studi di Bologna, Bologna, Italy*

Contact / jzamponi@udec.cl

Resumen / Las estrellas masivas jóvenes residen comúnmente en cúmulos moleculares densos y masivos, y son conocidas por estar altamente oscurecidas y distantes. Durante su proceso de formación, la deuteración es considerada como un buen indicador de la etapa de formación en la que se encuentra un objeto. Observaciones adecuadas de regiones con emisión de deuterio son cruciales, aunque difíciles de realizar. En este trabajo se realizó un estudio para detectar la transición o-H_2D^+(1_{10}-1_{11}) en moléculas deuteradas, utilizando una fuente sintética e intentando identificar cuán diferente es la información obtenida por un interferómetro o un telescopio de disco simple. Con objeto de analizar la detectabilidad de esta transición, procesamos la simulación magneto-hidrodinámica de una nube colapsante haciendo uso del código de transferencia radiativa POLARIS. Utilizando los mapas de intensidad resultantes, realizamos observaciones sintéticas de tipo interferométricas (*ALMA*) y de disco simple (*APEX*) de una nube en varios estados evolutivos, siempre usando modelos realistas. Finalmente, derivamos densidades de columna para comparar nuestras simulaciones con observaciones anteriormente realizadas. Las densidades de columna obtenidas para el o-H_2D^+ concuerdan con valores reportados en la literatura, en el rango de 10^{10-11} cm^{-2} y 10^{12-13} cm^{-2} en mediciones interferométricas y de disco simple.

Abstract / Young massive stars are usually found embedded in dense and massive molecular clumps, and are known for being highly obscured and distant. During their formation process, deuteration is regarded as a potentially good indicator of the formation stage. Therefore, proper observations of such deuterated molecules are crucial, but still, hard to perform. In this work, we test the observability of the transition o-H_2D^+(1_{10}-1_{11}), using a synthetic source, to understand how the physical characteristics are reflected in observations through interferometers and single-dish telescopes. In order to perform such tests, we post-processed a magneto-hydrodynamic simulation of a collapsing magnetized core using the radiative transfer code POLARIS. Using the resulting intensity distributions as input, we performed single-dish (*APEX*) and interferometric (*ALMA*) synthetic observations at different evolutionary times, always mimicking realistic configurations. Finally, column densities were derived to compare our simulations with real observations previously performed. Our derivations for o-H_2D^+ are in agreement with values reported in the literature, in the range of 10^{10-11} cm^{-2} and 10^{12-13} cm^{-2} for single-dish and interferometric measurements, respectively.

Keywords / ISM: molecules — stars: massive — stars: formation — radio lines: ISM

1. Introduction

Massive star formation takes place in the densest part of molecular clouds, which are characterized by low gas temperatures (T_g <20 K), high column densities ($N_g \sim 10^{23-25}$ cm^{-2}) and a large degree of CO-depletion. In the earlier stages, due to the latter process, further chemical reactions become much more efficient, such as the formation of deuterated molecules. This process is called *deuterium fractionation* (D_{frac}) and explains the increased ratio of a deuterated isotopologue column density and its hydrogenated version.

The reactions that lead to deuteration are the following:

$$H_3^+ + HD \rightleftharpoons H_2D^+ + H_2 + 230 \text{ K}, \quad (1)$$
$$H_2D^+ + HD \rightleftharpoons D_2H^+ + H_2 + 180 \text{ K}, \quad (2)$$
$$D_2H^+ + HD \rightleftharpoons D_3^+ + H_2 + 230 \text{ K}, \quad (3)$$

where H_2D^+ and D_2H^+ are the first two deuterated ions created. H_2D^+, in particular, has been suggested to be a reliable chemical clock for star forming regions, due to its sensitivity to environmental conditions (e.g. Caselli et al. (2003); Brünken et al. (2014)).

Observations of several high-mass clumps have shown that deuteration increases over time as the collapse of the molecular clump proceeds, reaching a maximum point right before the formation of a protostellar object (Fontani et al., 2011). At this stage, the radiation from the stellar object will lead to an increase of temperatures, with subsequent evaporation of CO, and an eventual decrease of the deuteration fraction.

In this work we traced the abundance of o-H_2D^+, by performing synthetic observations towards simulated massive starless cores, and compared the results with available observations.

Fig. 1 shows a schematic view of the workflow followed in this work, from the acquisition of the source,

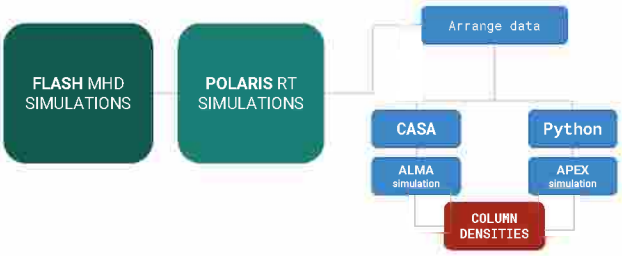

Figure 1: Flowchart of the pipeline workflow.

Table 1: Initial parameters of the selected core. The collapse is isothermal, at T=15 K.

Run	Radius [pc]	Mass [$M_\odot$]	$t_{\rm ff}$ [kyr]	$\alpha_{\rm vir}$	$\mathcal{M}$
Hmu10M2	0.1	60	67	0.48	2

to the derived, observatory-dependent column densities.

2. Synthetic source

As synthetic source we used the simulated collapsing molecular cores from Körtgen et al. (2017).

These cores are turbulent and magnetized ($B \sim 70\mu$ G), 60 $M_\odot$ in mass, and 0.1 pc in radius. The main parameters of the cores are listed in Table 1. A snapshot of their gas surface density distribution after 32.1 kyr of evolution is shown in the left panel of Fig. 2.

3. Radiative Transfer

We employed the POLArized RadIation Simulator (POLARIS) radiative transfer code (Reissl et al., 2016) to simulate the resulting intensity distributions of several quantities included in the cloud simulation, such as, temperature, dust, gas and magnetic field distribution. POLARIS makes use of a Monte Carlo approach to trace the path of light rays before reaching the synthetic detector. This method significantly reduces the numerical noise as well as the runtime compared to previous methods (Haworth et al., 2018). To map the deuterated molecule distributions, the Line Radiative Transfer (LRT) simulation mode of POLARIS was used for the o-H_2D^+ transition (1_{10}-1_{11}), assuming local thermodynamical equilibrium (LTE) conditions. We analyzed 11 evolutionary stages of the core up to 1 $t_{\rm ff}$, placing it at a distance of 1.4 kpc, based on the distance to a similar source already observed (Pillai et al., 2012). The resulting intensity distribution of a POLARIS simulation is shown in the second panel of Fig. 2.

4. Synthetic observations

To make observations as realistic as possible, we post-processed the ideal synthetic maps from POLARIS, in order to take into account instrument-related effects.

4.1. Single-dish observations

For the single-dish case, new tasks were written to solve each step involved in the creation of realistic cubes. We do not attempt to make statements regarding the Atacama Pathfinder Experiment (*APEX*) real throughput and/or performance, therefore, we refer to the modeled observations to as *APEX*-like observations. We developed a Python module that allows to perform common tasks on data cubes and single images, such as the convolution with a point spread function (PSF), conversion between intensities, fluxes and brightness temperatures and the addition of noise. We first convolved the ideal images with the beam of the telescope, represented by the PSF, here assumed to be Gaussian. The beam resolution was 16.8" at 372.4 GHz (Δv=0.03 km s^{-1}). Then we added normally-distributed noise to the images. In order to increase the peak signal-to-noise ratio (SNR), the spectra were binned up to 0.5 km s^{-1}, resulting in a noise level ($T_{\rm rms}$) of 0.02 K. Such a setup returns detections at a 5σ confidence level, for an integration of 1.8 hr. The values were computed using the *APEX* Observing Time Calculator. See the rightmost panel in Fig. 2 for a 16.8" single-pointing synthetic observation.

4.2. Interferometric observations

For the interferometric observations, we used the Common Astronomy Software Applications (CASA). CASA has been designed for the Atacama Large Milimiter-submiliter Array (*ALMA*) and the Very Large Array (*VLA*) data analysis, and provides also a simulation mode. As with the single-dish data, we used the POLARIS outcome as the input model and then generated the measurement set by calling the SIMOBSERVE task. SIMOBSERVE simulates an actual observation by creating a visibility set. We used a synthesized beam of 0.55" for o-H_2D^+, reached by the Cycle 6 C43-3 array configuration in band 7. In this case, we set the *ALMA* spectral resolution one order of magnitude wider than *APEX* (0.3 km s^{-1}), in order to improve the sensitivity. The noise level was set at 6 mJy for an integration time of 40 min, obtained with the *ALMA* Sensitivity Calculator. We imaged the data by deconvolving the visibilities using the CLEAN algorithm. The cleaning step was performed by the SIMANALYZE task. The outcome of an *ALMA* simulation is shown in the third panel of Fig. 2.

5. Results & Conclusions

5.1. Column densities

Column densities of o-H_2D^+ were obtained as in Vastel et al. (2006), via

$$N(X) = \frac{8\pi\nu^3}{c^3}\frac{Q(T_{\rm ex})}{g_u A_{ul}}\frac{e^{E_u/T_{\rm ex}}}{e^{h\nu/kT_{\rm ex}}-1}\int \tau dv, \qquad (4)$$

where u and l refer to the upper and lower energy level of each transition, respectively. All of the parameters required here are retrieved from the Leiden Atomic and Molecular Database (LAMDA) (Schöier et al., 2005), and summarized in Table 2. The partition function (Q)

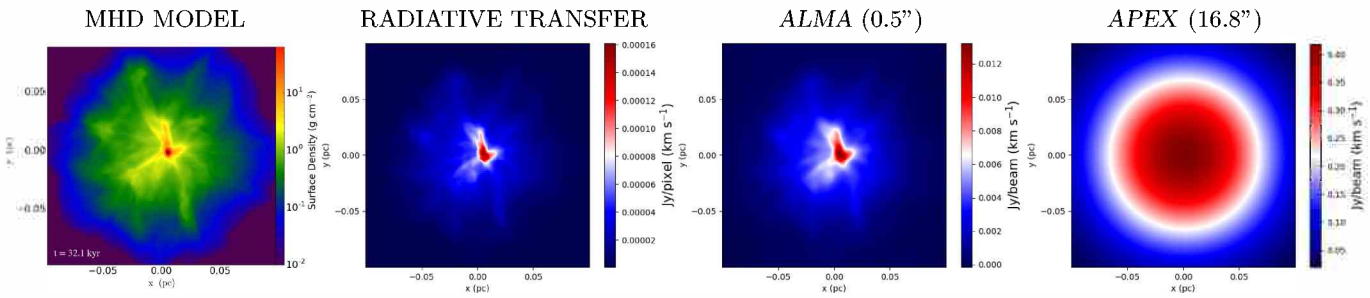

Figure 2: *Left to right:* Gas surface density distribution of the clump used as synthetic source at 32.1 kyr; o-H_2D^+ emission taken as the output of the POLARIS radiative transfer simulation; *ALMA* synthetic observation of the clump at 0.5" resolution and *APEX* synthetic observation at 16.8" resolution.

Table 2: LAMDA parameters for the o-H_2D^+(1_{10}-1_{11}) transition. The statistical weight g_{ul} is 9 and T_{ex} 15 K.

Transition	ν [GHz]	A_{ul} [s^{-1}]	E_{ul} [K]	Q[T_{ex}]
o-H_2D^+(1_{10}-1_{11})	372.421	$1.08{\cdot}10^{-4}$	17.87	1.122

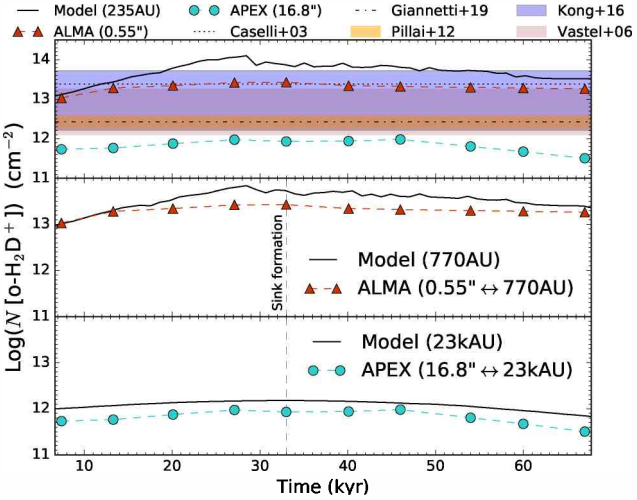

Figure 3: *Top panel:* Column densities derived from the model (solid line) along with interferometric (green pentagons) and single-dish (blue hexagons) observations. Colored areas and horizontal dashed lines represent ranges of values observed onto similar sources; *central and bottom panels:* Comparison of the information loss between *ALMA* (middle) and *APEX* (bottom) by averaging the model in the region of each beam.

was recreated by a cubic spline interpolation of the available values in the Cologne Database for Molecular Spectroscopy* (CDMS). Under the LTE assumption, the excitation temperature (T_{ex}) is assumed to match T_{gas}.

In this work we performed synthetic observations of a collapsing molecular magnetized core at different angular resolutions, attempting to understand the main differences of observing with an interferometer or a single-dish. In the upper panel of Fig. 3 we show the column densities derived from the model (solid black curve) at 235 AU (highest resolution element in the simulation), from *ALMA* at 0.55" and from *APEX* at 16.8", respectively. Column densities at each time were averaged over the highest resolution element. It can be observed that the retrieved column densities decrease by 10 (*ALMA*) and 10^2 (*APEX*) from the model, because, when centered on the peak emission, the inclusion of lower surrounding values is more significant for wider beams, then, decreasing the mean for low resolutions. Therefore, we expect *APEX* estimations to be lower than those retrieved by *ALMA*. Colored regions in Fig. 3 as well as semi-dashed and dotted lines represent observed column densities reported in the literature, obtained via single-dish observations (*APEX*, *JCMT* and *CSO*) toward low-mass sources.

As a measurement of the information loss, middle and bottom panels of Fig 3 present the ratio between both resolutions and the model averaged over the area corresponding to each beam. The highest ratios in interferometric observations (middle panel) are up to $10^{0.5}$. For single-dish observations (bottom panel) the highest ratios are around $10^{0.3}$. Such ratio decrease for wider beams because the model curve smooths due to the inclusion of surrounding lower values into the average.

Acknowledgements: JZ and DRGS thank for funding via Fondecyt regular 1161247. DRGS and SB also thank for funding via Conicyt Programa de Astronomia Fondo Quimal 2017 QUIMAL170001 and BASAL Centro de Astrofísica y Tecnologías Afines (CATA) PFB-06/2007. SB thanks for funding through Fondecyt Iniciacion 11170268. SB and JZ also thanks for funding through the DFG priority program "The Physics of the Interstellar Medium" (project BO 4113/1-2). The simulations were performed with resources provided by the *Kultrun Astronomy Hybrid Cluster* at the Department of Astronomy, Universidad de Concepción. We also thank Robi Banerjee, Bastian Körtgen, Stefan Reissl and Sebastian Wolf for important contributions to the presented study.

References

Brünken S., et al., 2014, Nature, 516, 219
Caselli P., et al., 2003, A&A, 403, L37
Fontani F., et al., 2011, A&A, 529, L7
Haworth T.J., et al., 2018, NewAR, 82, 1
Körtgen B., et al., 2017, MNRAS, 469, 2602
Pillai T., et al., 2012, ApJ, 751, 135
Reissl S., Wolf S., Brauer R., 2016, A&A, 593, A87
Schöier F., et al., 2005, A&A, 432, 369
Vastel C., et al., 2006, ApJ, 645, 1198

*http://www.astro.uni-koeln.de/cdms

Molecular Clouds resolved with ALMA ^{12}CO J=1-0 and J=2-1 observations towards the Magellanic Bridge

M.T. Valdivia[1], M. Muñoz[1], M. Rubio[1] & H. Saldaño[2]

[1] *Departamento de Astronomía, Universidad de Chile, Santiago, Chile*
[2] *Observatorio Astronómico de Córdoba, UNC, Argentina*

Contact / maria.valdivia@ug.uchile.cl

Resumen / Presentamos los resultados de observaciones de ^{12}CO $J = 1 - 0$ y $J = 2 - 1$, hechas con el interferómetro ALMA para las regiones B y C del Puente de Magallanes. La resolución de los datos provenientes de ALMA nos permite resolver nubes moleculares: la región B consta de al menos 5 nubes, con radios equivalentes que varían de 2 a 4.5 pc; la región C está compuesta de 7 nubes con radios equivalentes entre 0.5 y 2.5 pc. Todas estas nubes moleculares tienen perfiles de velocidad muy angostos ($\Delta v = 0.7 - 1.8$ km s^{-1}), indicando la presencia de gas frío. Las razones de línea son todas cercanas a 1 (varían entre 0.8 a 1.4), lo que es consistente con nubes densas y ópticamente gruesas. Estas fuentes siguen las mismas tendencias en sus propiedades físicas que otras nubes de baja metalicidad en el Grupo Local, incluyendo las Nubes de Magallanes.

Abstract / We present the results of the ALMA ^{12}CO $J = 1 - 0$ and $J = 2 - 1$ observations done in regions B and C of the Magellanic Bridge. The resolution of ALMA data allows us to identify individual molecular clouds: region B is resolved into at least 5 clouds with radii spanning from 2 to 4.5 pc and region C consists of 7 clouds with radii from 0.5 to 2.5 pc. All of these have narrow velocity line widths ($\Delta v = 0.7 - 1.8$ km s^{-1}), which indicate very cold and quiescent gas. We also found that the line ratios are all close to 1 (ranging from 0.8 to 1.4) consistent with optically thick and dense clouds. These sources follow the same tendencies in their physical properties than other dwarf galaxies of the Local Group, including the SMC and LMC.

Keywords / ISM: clouds — ISM: molecules — Magellanic Clouds

1. Introduction

The Magellanic Bridge was first recognized by Hindman et al. (1963), through 21 cm observations of HI. With an extension between 15 to 21 kpc wide, it is thought that it was caused by a close interaction between the Large Magellanic Cloud (LMC) and the Small Magellanic Cloud (SMC) around 200 Myrs ago (Gardiner et al., 1994). It is the closest tidally interacting system, at around 60 kpc from the Sun (Harries et al., 2003), and it has a metallicity of $Z_\odot/5 - Z_\odot/10$ (Lehner et al., 2008). The first detection of a carbon monoxide (CO) bright source in the Bridge was made by Muller et al. (2003), using measurements of the ^{12}CO $J = 1 - 0$ rotational transition. Based on this and coincidences of HI and 100 μm emission, Mizuno et al. (2006) found seven more sources using the NANTEN telescope. These have narrow velocity profiles (linewidths smaller than 2 km s^{-1}), low integrated CO brightnesses (10 to 140 mK km s^{-1}) and are associated with young stellar objects (Chen et al., 2014).

In this work, we focus on the sources labeled as Magellanic Bridge B and C (MagBridgeB and MagBridgeC). Individual clouds can be resolved due to the enhanced resolution of the line emission data obtained with the Atacama Large Millimeter/Submillimeter Array (ALMA) interferometer. We compare the molecular clouds in this metal-poor region with others found in metal-poor galaxies of the Local Group and in the Milky Way, using for this purpose the virial mass vs. CO luminosity and the relation known as Larson's law, which relates velocity dispersion and size ($\sigma_v \propto S^\alpha$) (Larson, 1981).

2. Data

Observations for the ^{12}CO $J = 1-0$ and $J = 2-1$ were carried out by the ALMA telescope during Cycle 3: the $J = 1 - 0$ line cube was carried out in band 3 using the main array 12m antennas, with a rest frequency of 115.2 GHz, and the $J = 2-1$ line cube, in band 6 using the Atacama Compact Array (ACA) 7 m antennas at a rest frequency of 230.8 GHz.

The reduction and cleaning of the data was done using Common Astronomy Software Applications (CASA). The properties of the cubes are in Table 1. Also, the line cubes were integrated through the velocity axis between 140 and 149 km s^{-1} for MagBridgeB and 175 and 182 km s^{-1} for MagBridgeC. The rms of this integration is also in Table 1.

The clouds were identified using the following procedure over the $J = 1 - 0$ data: the rms of the integrated image was taken, and using a contour map set at 3σ over the image, the area covered by each cloud was determined. Then, using the line cube and the contours, we obtained the mean spectra of each source with CASA, which we used to estimate the center, peak temperature, and FWHM of each cloud. This procedure does

Table 1: Properties of the images, given by region and emission line. The rms is calculated for the integrated images.

	MagBridgeB		MagBridgeC	
Line	1-0	2-1	1-0	2-1
Beam major [″]	3.3	6.9	3.6	6.6
Beam minor [″]	2.5	6.0	3.3	5.7
Δv [km s^{-1}]	0.5	0.16	0.5	0.5
rms [Jy beam^{-1} km s^{-1}]	0.11	1.23	0.23	1.26

not recognize clouds that have a different structure in the velocity axis, but only separates clouds if they can be spatially resolved.

To compare the emission of both rotational transitions, first we convolved the $J = 1-0$ integrated image and line cube to the same resolution of the corresponding $J = 2-1$ map for each source (B and C). Afterwards, we obtained the 3σ contours for the $2-1$ transition image and used those contours to obtain a mean spectra of each source, for each rotational transition.

3. Results

3.1. Detection of molecular clouds

In the ^{12}CO(1-0) ALMA cubes, we detected 5 molecular features for source B (labeled from 1 to 5) and 7 for source C (labeled from 1 to 7), all with signal-to-noise over 10. The integrated moment map, with the identified regions, is in Fig. 1 for MagBridgeB and C. Almost all are separated by at least one beam size, except for regions 4 and 5 of MagBridgeC: their angular distance (around 3″) is slightly less than the semi-major axis size of the beam area, so after convolution with the CO(2-1) beam, they are considered to be the same region.

From a comparison between the molecular features observed in the $J = 1-0$ transition with those observed in the $J = 2-1$ line, it can be appreciated that they coincide spatially and in velocity range.

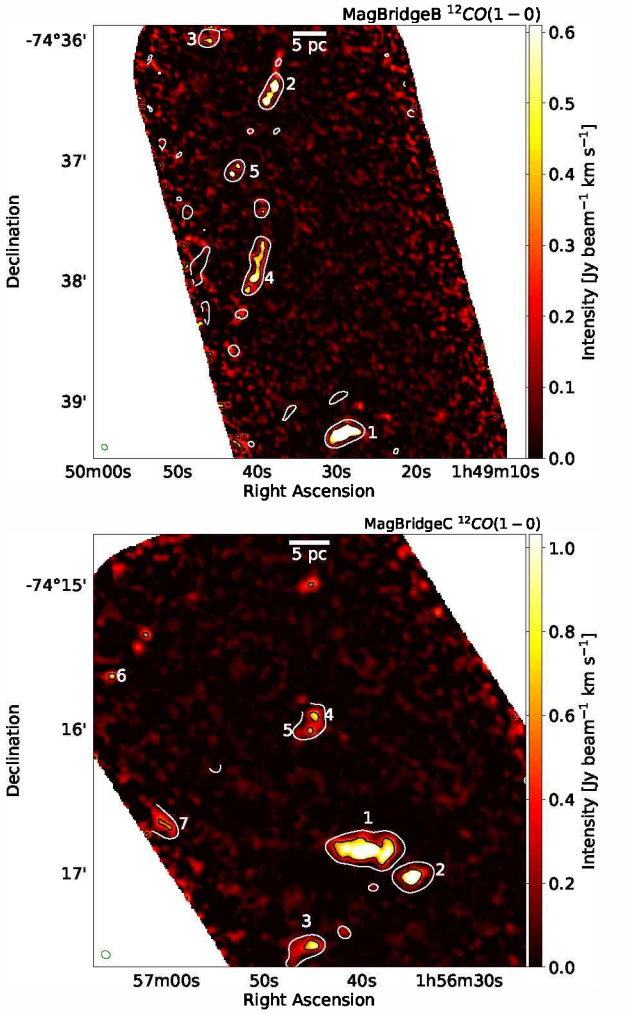

Figure 1: $J = 1-0$ integrated moment maps for MagBridgeB and C. Black contours are 3σ level for $J = 1-0$ integrated moment map and green ellipses on the bottom left corners are the beam sizes. The identified clouds are labeled with white numbers. White contours correspond to 3σ level for $J = 2-1$ integrated moment map. Top: MagBridgeB. Bottom: MagBridgeC.

3.2. Physical properties of the molecular clouds

We have derived the radii, luminosities and virial and H_2 masses for each of the clouds based on the $J = 1-0$ line cube. The radii R_{eq} are calculated approximating each source as a spherical cloud and obtaining the projected area (πR_{eq}^2). For this, we assume that the Magellanic Bridge is at a similar distance from us as the SMC (63 kpc away, Harries et al. 2003). The virial mass M_{vir} was calculated using equation 3 of MacLaren et al. (1988): we used a value of $k_2 = 190$ for a density distribution of $\rho(r) \propto r^{-1}$. The CO luminosity L_{CO} was calculated in K km s^{-1} pc^2 using:

$$L_{CO} = 2453 S_{CO}\Delta V D_L^2 \quad (1)$$

where $S_{CO}\Delta V$ is the integrated flux density in Jy km s^{-1} and D_L is the luminosity distance in Mpc (Bolatto et al., 2013). Only for comparison, we calculate the H_2 mass (molecular mass) M_{mol} using the galactic H_2 mass to CO luminosity factor $\alpha_{CO} = 4.3$ M$_\odot$ (K km s^{-1} pc^2)$^{-1}$, which assumes a CO-to-H_2 conversion factor X_{CO} of 1×10^{20} cm^{-2} (K km s^{-1})$^{-1}$.

The ranges for each of these parameters for the whole sample is in Table 2. The narrow CO emission ($\Delta v \lesssim$ 2 km s^{-1}) indicates very cold and (probably) inactive gas. There is a tendency for the virial mass to be at least 5 times greater than the molecular mass, calculated using the galactic value. This implies that the CO-to-H_2 conversion factor in this region needs to be higher, in agreement with the suggestion that the conversion factor increases with decreasing metallicity (Bolatto et al., 2013).

We compare our data with other metal-poor molecular clouds (Rubio et al., 2015) and galactic plane clouds, which have a power law exponent α of 0.5 for Larson's law and 0.81 for mass vs. luminosity (Solomon et al., 1987). We plot data from Bolatto et al. (2008), Wong et al. (2011), Rubio et al. (2015) and Schruba et al. (2017)

Table 2: Ranges for the physical parameters calculated for the clouds using CO(1-0) data. R_{eq} and Δv are taken directly from the data, whereas the mass, luminosity and line ratios are derived.

Cloud	Δv	R_{eq}	M_{vir}	L_{CO}	M_{mol}	$R_{\frac{CO(2-1)}{CO(1-0)}}$
	[km s^{-1}]	[pc]	[$M_\odot$]	[K km s^{-1} pc^2]	[$M_\odot$]	
B	0.3 - 0.8	1.9 - 4.5	349 - 2578	3.7 - 106.0	16 - 456	0.82 - 1.36
C	0.3 - 0.7	0.5 - 2.5	91 - 984	3.9 - 137.7	17 - 592	0.86 - 1.96

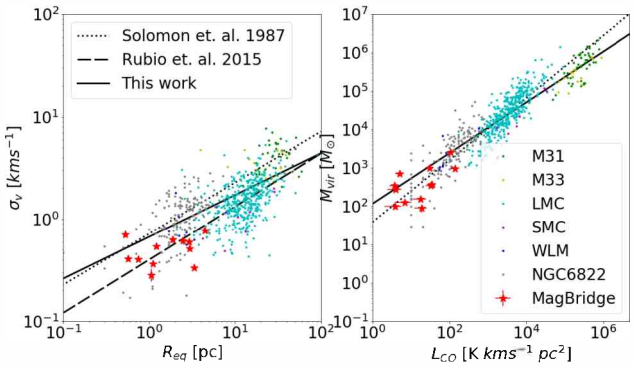

Figure 2: Correlations of molecular clouds in dwarf galaxies within the Local Group. Red stars correspond to the data in this work. Dotted lines mark the relations for the Milky Way molecular clouds. The dashed line corresponds to the relation for dwarf galaxies (Rubio et al., 2015) excluding the MagBridge (this work) and NGC 6822 (Schruba et al., 2017). The solid line is a fit to all points (this work). Left: R_{eq} vs. σ_v. Right: L_{CO} vs. M_{vir}.

for dwarf galaxies, which are shown in Fig. 2. Our work complements the small size and low-luminosity edge of these relations and in general, our data correlate with other metal-poor clouds. Using Maximum Likelihood and Markov Chain Monte Carlo (MCMC), we fit the best line that correlates them all. A power law fit gave us an exponential index of 0.41 for Larson's law, similar to the indexes (0.5 and 0.52) found by Solomon et al. (1987) and Rubio et al. (2015) respectively, and of 0.66 for virial mass vs. luminosity, lower than the index for galactic plane clouds. This indicates that the clouds found are close to virial equilibrium and the differences in the power laws can be a result of lower metallicity.

3.3. Line Ratios

We define the line ratio as the ratio between the peak temperature of the spectra, in Kelvin, for both transitions:

$$R_{\frac{CO(2-1)}{CO(1-0)}} = T_{CO(J=2-1)}/T_{CO(J=1-0)} \quad (2)$$

A ratio close to 1 in Eq. 2 is consistent with optically thick clouds (Eckart et al., 1990).

In both regions studied, most of the clouds have line ratios close to 1, as seen in Table 2. The coldest clouds in each region have the smallest ratios (cloud 4 in MagBridgeB and cloud 3 in MagBridgeC). At the same time, those with the greatest ratio (cloud 1 in MagBridgeB and cloud 4 in MagBridgeC) are probably the hottest. Also, there are no line ratio gradients within the clouds, which show that there are no important temperature gradients within them.

4. Conclusions

We study two regions of the Magellanic Bridge where, due to the enhanced ALMA resolution, two previous CO detections could be resolved into 12 individual molecular clouds. In general, the clouds have equivalent radii smaller than 5 pc, narrow velocity profiles consistent with cold and quiescent gas and line ratios consistent with optically thick gas. These clouds are smaller than other recently reported ones in metal-poor dwarf galaxies and follow the same trends in size vs. velocity dispersion and mass vs. luminosity. These relations suggest that these clouds are in an approximate virial equilibrium. Other relations (like velocity dispersion vs. virial mass and column density vs. luminosity) will be studied as future work.

Acknowledgements: We would like to thank the editor of the BAAA R. Gamen and the anonymous referee for their useful comments that helped to improve this article. M.T.V. wishes to acknowledge support from CONICYT-PFCHA/ Magister Nacional/2018 - 22180279 and support from SOCIIAS grant through ALMA/CONICYT project #31160034. M.R. wishes to acknowledge support from ENLACE-FONDECYT project ENL22/18, Universidad de Chile, FONDECYT grant no.1140839 and partial support through project BASAL PFB-06. This research made use of APLpy, an open-source plotting package for Python (Robitaille and Bressert, 2012). This paper makes use of the following ALMA data: ADS/JAO.ALMA#2015.1.01013.S.

References

Bolatto A. D., et al., 2008, ApJ, 686, 948
Bolatto A. D., Wolfire M., Leroy A. K., 2013, ARA&A, 51, 207
Chen C. H. R., et al., 2014, ApJ, 785, 162
Eckart A., et al., 1990, ApJ, 348, 434
Gardiner L. T., Sawa T., Fujimoto M., 1994, MNRAS, 266, 567
Harries T. J., Hilditch R. W., Howarth I. D., 2003, MNRAS, 339, 157
Hindman J. V., Kerr F. J., McGee R. X., 1963, Australian Journal of Physics, 16, 570
Larson R. B., 1981, MNRAS, 194, 809
Lehner N., et al., 2008, ApJ, 678, 219
MacLaren I., Richardson K. M., Wolfendale A. W., 1988, ApJ, 333, 821
Mizuno N., et al., 2006, ApJ, 643, L107
Muller E., et al., 2003, MNRAS, 339, 105
Rubio M., et al., 2015, Nature, 525, 218
Schruba A., et al., 2017, ApJ, 835, 278
Solomon P. M., et al., 1987, ApJ, 319, 730
Wong T., et al., 2011, ApJS, 197, 16

The Stellar Population, 3D structure, and kinematics of the Galactic bulge

M. Zoccali[1,2]

[1] *Instituto de Astrofísica, Pontificia Universidad Católica de Chile, Santiago, Chile*
[2] *Millennium Institute of Astrophysics, Santiago, Chile*

Contact / mzoccali@astro.puc.cl

Resumen / Nuestro entendimiento de la estructura y la población estelar del bulbo Galáctico ha mejorado significativamente en los últimos ∼5 años, gracias a mapeos fotométricos en el infrarrojo como el VISTA Variables in the Vía Láctea (VVV Minniti et al., 2010) junto a campañas masivas de observación espectroscópicas como ARGOS, Gaia ESO, GIBS y APOGEE. Presento aquí una versión muy resumida y simplificada, proveniente de una charla invitada dirigida a colegas chilenos y argentinos que trabajan en distintas áreas de la astrofísica. Este trabajo, lejos de representar una revisión completa de la literatura, se propone guiar al lector hacia las interpretaciones que actualmente logran el máximo consenso en la comunidad. La reciente conferencia sobre "The Galactic bulge at the crossroads" organizada en Pucón, Chile, en diciembre 2018 me ha ayudado mucho en obtener esa visión global. Este artículo, entonces, es recomendado para alumnos jóvenes o colegas de otras áreas. Para una visión más completa se recomienda el artículo de Barbuy et al. (2018), o la edición 2016 de *Publication of the Astronomical Society of Australia*, que incluye una sección especial dedicada a artículos de revisión sobre el bulbo Galáctico.

Abstract / Our understanding of the structure and stellar population of the Galactic bulge has improved significantly in the last ∼5 years or so, thanks to large near infrared photometric surveys such as the VISTA Variables in the Vía Láctea (VVV Minniti et al., 2010) coupled to massive spectroscopic campaigns such as ARGOS, Gaia ESO, GIBS and APOGEE. I provide here a summarized and simplified overview, proceeding from an invited review talk delivered to Chilean and Argentinian colleagues from many different fields of astrophysics. The present short paper, far from providing an extensive review of the literature, is meant to point the reader towards the interpretations that currently obtain the widest consensus in the community. The recent conference on "The Galactic bulge at the crossroad", held in Pucón, Chile, in December 2018 greatly helped me draw this global picture. This paper is therefore recommended for young students and/or outsiders to this topic. For a complete review, I refer the readers to Barbuy et al. (2018), and to the 2016 issue of the Publication of the Astronomical Society of Australia, including a special section dedicated to review papers on Galactic bulge.

Keywords / stars: abundances — Galaxy: bulge — Galaxy: stellar content

1. Introduction

The Milky Way galaxy includes three main stellar components, in order of decreasing mass: the disk, the bulge and the halo. It should be noted that the word "bulge" here indicates whatever its included within a radius of ∼2.5 kpc (by some authors up to 3.5 kpc) from the Galactic center, independent from its shape. Bulge and halo are the oldest ones, according to our understanding, with the halo being possible older than the bulge. The disk, with its $\sim 6\times10^{10}$ $M_\odot$ is between 3 and 4 times more massive than the bulge, and about 100 times more massive than the halo. It is, however, a relatively younger component that has formed stars from ∼ 10 Gyr ago down to the present time. For this reason, in order to understand how did the Milky Way form, as a whole, the bulge plays a crucial role, being at the same time massive and old. In other words, it is the first massive stellar component to be set in place.

It is also the only galaxy bulge that can be resolved into individual stars down to the faintest ones, and for which detailed chemical abundances can be obtained through high resolution spectra at least for its giants. It might be used, therefore, as a bridge to try and solve the tension currently present between the formation scenarios proposed to explain local bulges, and the interpretation of the observations of star forming bulges at high redshift.

Specifically, following the review paper by Kormendy & Kennicutt (2004), local bulges have been morphologically classified into *classical* and *pseudo*-bulges. The first ones, more spheroidal and massive with respect to the disk, are interpreted as formed via violent dissipationless merging of primordial subunits. *Pseudo*-bulges instead, including bars and smaller structures with kinematical signatures similar to small disks, are interpreted as the natural product of the dynamical evolution of disks, as the instabilities induced by spiral arms drive stars towards the center, arranging most of them in elongated orbits supporting bars. Theoretical simulations (Debattista et al., 2017; Tissera et al., 2018; Fragkoudi et al., 2018) prove that both scenarios can occur, and would form central bulges with several properties com-

patible with the observed ones. Both scenarios, however, assume that most of the stars currently in the bulge have been formed elsewhere, either in external subunits or in the disk, and have been driven to their current position on a second time, by some independent mechanism.

The two scenarios mentioned above are probably two extremes, with reality being some combination of both phenomena. Both of them, however, as well as any combination of them, contrast with observations of star forming galaxies at redshift ∼2, corresponding to ∼10 Gyr ago, when the bulk of bulge stars must have formed. Studies of these infant galaxies at several wavelengths (e.g., Tadaki et al., 2017) show that they are undergoing a starburst phase at their center, i.e., stars are forming, very efficiently, already at their final position in the bulge. Similar conclusions are reached by e.g. Immeli et al. (2004); Carollo et al. (2007); Elmegreen et al. (2008); Genzel et al. (2008); Bournaud et al. (2009)

2. The three dimensional structure of the Galactic bulge

Fig. 1 shows an artistic image of the Milky Way, as seen from the Northern Galactic Hemisphere, released from NASA in 2017 and reflecting the latest result from the infrared Spitzer satellite. It can be seen that the central region contains a bar. This was first suggested by de Vaucouleurs (1964), as a possible cause for the non-circular motions of the gas in the inner Galaxy, and later confirmed by Blitz & Spergel (1991), as a way to explain the asymmetries in the near infrared light profile of the bulge. Since then, at least a few dozen independent studies have confirmed the existence of a bar at the center of the Milky Way and have determined its main parameters, most often by using core Helium burning stars in the red clump (RC), as distance indicators. Among them, I believe that the most accurate are the ones derived by Wegg & Gerhard (2013) and Simion et al. (2017) from VVV data. They perform a thorough modeling of the most homogeneous, deep and complete photometric data currently available for the bulge. Wegg & Gerhard (2013), in particular, derive an axis ratio of (10:6.3:2.6), exponential scalelengths (0.70:0.44:0.18) kpc and inclination angle with respect to the Sun-Galactic center direction of 27°. They also model the appearance of a boxy/peanut (B/P) structure in the outer bulge, starting from ∼400 pc from the Galactic plane, whose existence was first discovered by McWilliam & Zoccali (2010) and Nataf et al. (2010). The latter B/P structure, sometime referred as the *X-shape*, has also been seen directly in the bulge maps obtained from the WISE satellite as processed by Ness & Lang (2016).

Much before discovering the existence of a B/P structure in our own Galaxy, such features had been seen in nearby galaxies, and their nature and origin was well understood. Once bars are formed, they often undergo dynamical instabilities that produce bending, up or down the plane, of the most elongated orbits, turning them into *bananas*, or *smiles* and *frawns*. This process,

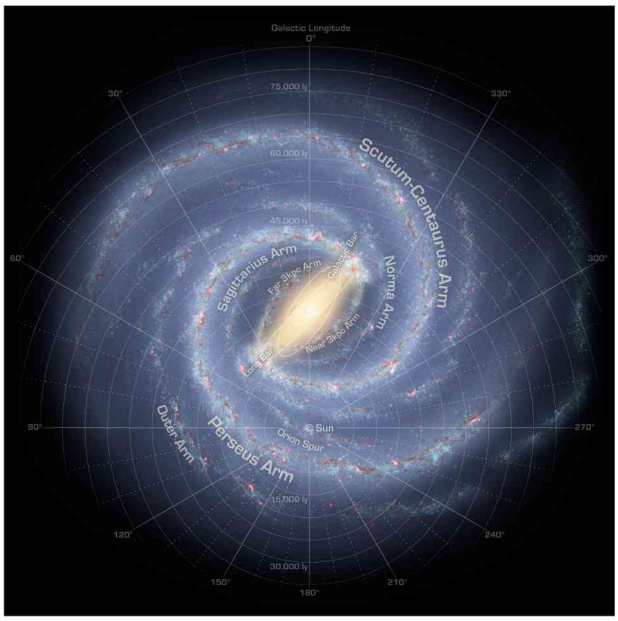

Figure 1: The most accurate artistic image of the Milky Way, reflecting the results from the GLIMPSE survey, on the Spitzer Telescope. The central region includes a prominent bar, with two major arms (Scutum-Centaurus and Perseus) attached to its ends. Another two minor arms are located between the major ones. Image credit: NASA/JPL-Caltech/R. Hurt (SSC/Caltech).

also called buckling, thickens the bar bringing stars away from the plane, while the *smiles* and *frawns* orbits sustain the B/P, or X-shape (Patsis et al., 2002; Athanassoula, 2005). The observational evidence pointing to the existence of a B/P structure in the Milky Way is the fact that the bulge RC magnitude changes smoothly across the bulge area, as the line of sight crosses the near or the far side of the bar, and the RC becomes double in a few specific directions, where the line of sight crosses two arms of the X-shape. Alternative explanations for the change in the magnitude of the RC have been proposed by Lee et al. (2015); Joo et al. (2017), invoking the presence of two populations of stars in the bulge, with different helium abundance, hence different RC magnitude. One of the two, and only occasionally both, prevails in different lines of sights with a complicate fine-tuning of their spatial distribution.

Dynamical models following the secular evolution of galactic bars predicts that only the central part of the bar thickens due to bending and buckling instabilities, leaving a thin, longer bar in the outer part. This structure has been identified in the Milky Way by different authors, starting from Hammersley et al. (1994, 2000), later followed by, e.g., Benjamin et al. (2005); López-Corredoira et al. (2007); Cabrera-Lavers et al. (2007, 2008). It was long debated whether the long bar was a different structure, formed independently from the main bar, or part of the same one. The fact that the inclination angle of the long bar seemed to be different from the one of the main bar added confusion and disagreement to the matter. The debate seems finally settled after Wegg et al. (2015), who were able to fit a combination of

data from UKIDSS, VVV, 2MASS and GLIMPSE with a single model, shown in Fig. 2, including the main bar, the B/P and the long bar. The similarity between the best fit model in Fig. 2 and the output of the dynamical models of bar evolution shown by Athanassoula et al. (2015, their Fig. 4) is a strong argument in favor of a single process giving rise to the bar, the B/P and the thin long bar in our Galaxy.

The central $\pm 1^\circ$ from the Galactic center have always been challenging both to the observations, due to high stellar density and foreground obscuration, and to any attempt at fitting the same bar model reproducing the bar far from the center. Alard (2001) first proposed that the large residuals obtained in the attempt to deproject 2MASS star counts could be explained by the existence of an inner bar, a separate component with a different inclination angle. Many other studies have confirmed the existence of a change in the bar inclination angle in the innermost $\sim 1^\circ$, including Rodriguez-Fernandez & Combes (2008); Nishiyama et al. (2005); Gonzalez et al. (2011). Gerhard & Martinez-Valpuesta (2012) demonstrated that the observed change in angle could also be explained by a central axisymmetric structure, rather than an inner bar. Recent observational evidences support this latter hypothesis, as the inner region of the Galaxy, roughly included within a radius of $\sim$150 pc, shows a high stellar density peak that seems roundish both in the plane of the sky (Valenti et al., 2016) and in the Galactic plane (Zoccali & Valenti, 2016). We will come back on the peculiarities of the innermost region of the bulge when discussing the stellar kinematics, in Sect. 5. below. For a more complete review about the bulge 3D structure, the reader should refer to Zoccali & Valenti (2016).

3. The bulge stellar mass and density distribution

The distribution of RC stars in the plane of the sky, as measured from VVV catalogs corrected for completeness and interstellar extinction was used by Valenti et al. (2016) to derive the stellar density profile of the bulge. Their map shows the known asymmetries, signature of the bar, but also the central high density peak mentioned above. The same authors derived an empirical conversion factor between the number of RC stars and the total stellar mass. The latter was measured by integrating the empirical initial mass function (IMF) by Zoccali et al. (2000); Zoccali et al. (2003) within a small field observed with *HST*. This factor allowed to transform the projected density of RC stars per square degrees into total stellar mass, hence derive both a mass profile and a total stellar mass for the Galactic bulge, resulting into 2×10^{10} M$_\odot$.

An alternative, more conventional way to measure the total mass of a system is the matching of the stellar three dimensional (3D) density profile and kinematics within a self consistent dynamical model. This has been done recently by Portail et al. (2015, 2017) who concluded that the total mass within a volume of ($\pm 2.2 \times \pm 1.4 \times \pm 1.2$ kpc) is $1.84 \pm 0.07 \times 10^{10}$ M$_\odot$. This

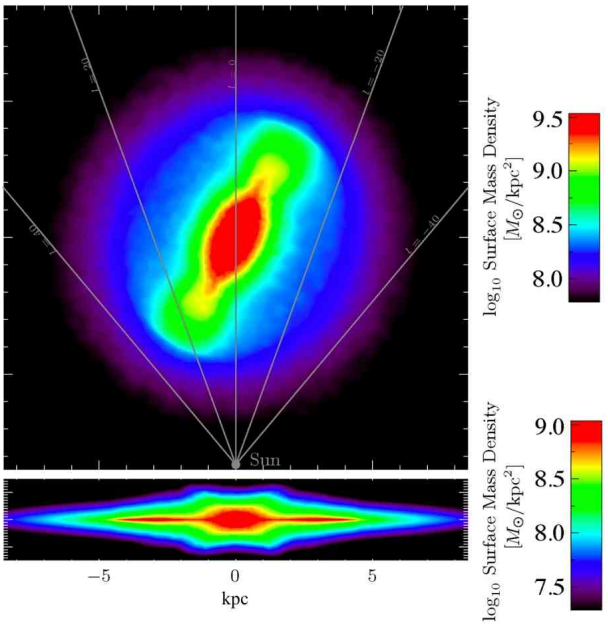

Figure 2: Best fitting model reproducing the Galactic bar (central oval in red) with its B/P structure sticking out at large distances from the plane, clearly visible in green in the lower panel. Also shown is the long bar, as a thin structure (in red) extending to large longitudes. Adapted from Wegg et al. (2015).

obviously includes the dark matter component, while the stellar part is estimated to be between 1.25 and 1.6×10^{10} M$_\odot$.

The apparent inconsistency between these two results is most likely due to the fact that Valenti et al. (2016) estimates the mass of all the stellar population along the line of sight contributing to the observed RC, in the region of the sky comprised within $-10^\circ < l < 10^\circ$ and $-10^\circ < b < 10^\circ$. Portail et al. (2015), on the contrary, define a box with axis proportional to the main bar axis, that corresponds to a smaller volume of space.

In any case, the current accuracy in the determination of the bulge stellar mass allows us to establish beyond any doubt that the Galactic bulge is a massive stellar component of the Milky Way, making up about 1/4 of the total stellar mass. In addition, regardless of the absolute calibration of the total mass, the projected stellar density and mass *profiles*, which only depend on the variation of the number of RC stars across the sky, are both robust determinations, given that the VVV photometry is mostly complete at the magnitude of the RC. These will be used further below in order to characterize the shape of the two metallicity components of the Galactic bulge.

4. Two metallicity components in the Galactic bulge

The metallicity distribution function (MDF) of bulge stars was first measured by McWilliam & Rich (1994), in the low reddening Baade's Window, at (l, b)=$(1, -4)$.

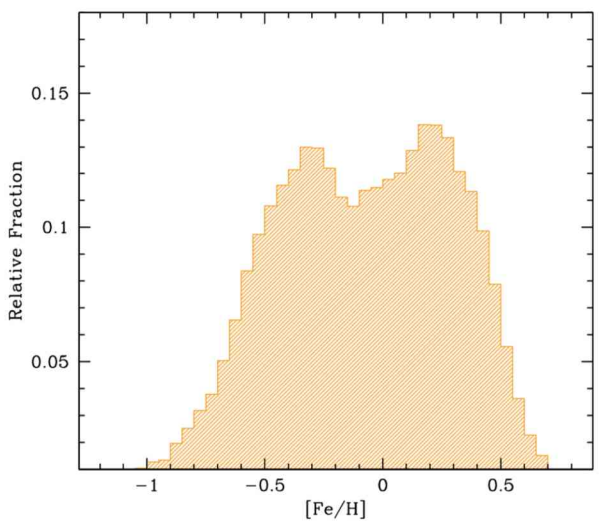

Figure 3: Metallicity distribution function of all the stars measured within the GIBS survey (Zoccali et al., 2017). The existence of a bi-modality is very evident, with the metal poor component centered at [Fe/H]=−0.4 dex and the metal rich one centered at [Fe/H]=+0.3 dex.

They concluded that most bulge stars had roughly solar metallicity, with a sharp decline at super solar metallicity and a longer tail towards the metal poor regime. For almost two decades this MDF was assumed to be representative of all the stars in the bulge, with a mean metallicity gradient hard to quantify but qualitatively close to a decrease by about 0.6 dex per kpc, towards higher latitudes (e.g. Zoccali et al., 2008).

Recent wide area spectroscopic surveys allowed us to map the MDF in several line of sights across the bulge area (Ness et al., 2013a; Rojas-Arriagada et al., 2014, 2017; Zoccali et al., 2017). The results proved that the sub-solar metallicity tail seen by McWilliam & Rich (1994) was in fact a second component. Indeed, when measured with increased statistics and precision, the bulge MDF is everywhere bimodal, with a metal-poor peak at [Fe/H]~ -0.4 dex and a metal rich one at [Fe/H]$\sim +0.3$ dex (Fig. 3). The position of the two peaks does not change across the bulge area, but their relative importance does change significantly, with metal rich stars largely dominating at intermediate latitudes ($\sim$70 % of the total at $b = -3.5^\circ$ and metal poor ones dominating in the outer part ($\sim$70 % at $b = -8.5^\circ$). At latitude closer to the Galactic plane, the relative importance of the metal poor component increases again (Schultheis et al., 2015; Zoccali et al., 2017; Feldmeier-Krause et al., 2017) though its relative contribution is somewhat poorly quantified, due to the difficulties to measure a large number of stars at high spectral resolution in the innermost, high extinction regions of the Galaxy.

The two metallicity components seem to have different properties also in space distribution and kinematics. By analyzing the luminosity function of the target RC stars belonging to each component Ness et al. (2012); Rojas-Arriagada et al. (2014) demonstrated that the metal poor stars do not show the split RC identified in the metal rich ones at $|l| < 2^\circ$, $|b| < 5^\circ$, and interpreted as the observational signature of the B/P structure. On a further analysis by Rojas-Arriagada et al. (2017), the magnitude of the metal poor RC stars turned out to be constant with longitude, at fixed latitudes, contrary to the behavior of metal rich stars, brighter at positive longitudes, where the line of sight crosses the near side of the Galactic bar. These results, then, point towards the bar being made only by metal rich stars, while metal poor ones are found at the same mean distance across all longitudes, therefore tracing a more axisymmetric structure.

Independent confirmation of the same result came from Zoccali et al. (2017). While their RC target box was too small to analyse the luminosity function, they coupled the metal-poor/metal-rich fraction given by the MDF in each of 26 fields with the projected total stellar density in Valenti et al. (2016). This allowed them to derive two separate density maps, tracing each of the two metallicity components individually. The projected distribution of metal rich stars is a well defined rectangular box, as expected for a bar seen edge-on, while the distribution of metal poor stars is roundish, consistent with the projection in the sky of an axisymmetric structure such as a spheroid. Integration of both density maps over the whole bulge area yields a relative contribution to the bulge total mass close to 50 % for each of the two components (Zoccali et al., 2018).

While it is reasonably established that the bulge hosts two components with different shape, metallicity distribution, element ratio, and —as discussed below— kinematics, it is not clear whether they formed via a completely different process, or via the same one, at work under different conditions. While there is only one mechanism currently known to produce galaxy bars, the final shape (axis ratio) of the bars strongly depends on the radial velocity dispersion of the initial disk (Debattista et al., 2017; Fragkoudi et al., 2018). Specifically, a disk with large velocity dispersion along the radial direction such as a hypothetical primordial disk in the Milky Way, would give rise to a much less pronounced bar, compatible with the *spheroidal* distribution observed for metal poor stars. Obviously, such axisymmetric structure could also be a *classical bulge* resulting from the violent accretion of galactic fragments at early times. Models have not yet been able to identify observational features able to discriminate between the two scenarios.

For a more complete review about the bulge metallicity distribution the reader should refer to Ness & Freeman (2016), while a highly recommended review more specific on the bulge chemical composition and evolution can be found in McWilliam (2016).

4.1. ...or three?

One of the main products of both the OGLE III (Soszyński et al., 2011) and the VVV survey has been the identification and characterization of a large number of RR Lyrae (RRL) variable stars in the Galactic bulge. These variables are clean tracers of the oldest stellar population (> 10 Gyr) and, because they obey a

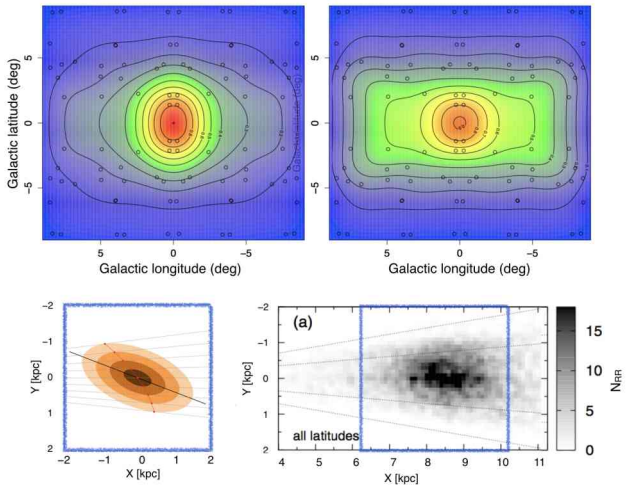

Figure 4: Top: projected stellar density maps, in the plane of the sky, for the metal poor (left) and the metal rich (right) components of the Galactic bulge, from GIBS (Zoccali et al., 2017). Bottom: density of RR Lyrae projected on the Galactic plane. The optical data from the OGLE survey (left, from Pietrukowicz et al., 2015) show an elongated structure very similar to the Galactic bar, while the combination of OGLE with VVV near infrared data (right, from Dékány et al., 2013) show a roundish structure, with no trace of elongation in the direction of the bar major axis.

tight Period-Luminosity relation, each of them yields a precise measure of its distance. It is therefore straightforward, at least in principle, to deproject their stellar density in the sky into a 3D density distribution.

In practice, two groups have attempted to do so using the OGLE III optical data (Pietrukowicz et al., 2015) or their combination with VVV near infrared data (Dékány et al., 2013), respectively, with contrasting results. While the former authors find that RRL variables trace a bar only slightly less elongated than the main bar traced by RC stars, the latter find a rather spheroidal component (Fig. 4). A similar result was obtained by Gran et al. (2016) using only near infrared VVV data for newly identified RRL stars in the outer bulge. The discrepancy is most likely due to the choice of the extinction law, as interstellar reddening is invariably tight to the determination of distances, and it obviously affects different photometric bands in a different way. Although the distance to each individual RRL is of course much more precise than the distance to each individual RC star, the number of RRL in the bulge is several orders of magnitudes lower than the number of RC stars, and therefore small systematics that might vary with longitudes end up having a large effect on the final results. In particular, the amount of foreground dust in the bulge direction is slightly larger at negative longitudes than it is at positive ones, at least close to latitude $b = -3°$ that is where the density of RRL is largest. Outside this region the RRL are intrinsically less abundant, as the whole stellar density declines, while inside this region the OGLE III survey has mapped only the region close to the bulge projected minor axis ($l \sim 0$).

Other independent indications, however, suggest that RRL trace a different component from RC stars, and they come from the kinematics. Indeed, Kunder et al. (2016) measured the radial velocity of ∼1000 RRL in the bulge, deriving a flat rotation curve and a radial velocity dispersion larger than that of RC stars (see Sec. 5.). This would be an argument in favor of a spheroidal distribution of RRL, as spheroids are supported by velocity dispersions, while bars are supported by rotation.

Although the space distribution and 3D kinematics of RRL remains to confirmed, if one temporarily accepts the result that RRL trace a spheroidal component with little or no rotation, a natural question would be: *do RRL trace the same spheroidal component as metal poor RC stars, or are they part of a third one?*. While I believe that this question is still open, a few considerations might be of help. First, the metallicity distribution of RRL, though very broad, peaks at [Fe/H]=−1.0 dex, while metal poor RC stars have their metallicity peak at [Fe/H]=−0.4 dex. However it is also expected that RRL, in order to pulsate, need to fall on the instability strip, while burning He in their core. That is, they spend their horizontal branch phase at a bluer color than RC stars. Given that metallicity is the *first parameter* determining the color of an old star, while on the horizontal branch, it is perfectly possible that RRL represent the most metal poor tail of the metal poor bulge component. Second, a strong argument in favor of RRL tracing the same component as metal poor RC stars would be represented by the evidence of metal poor RC stars also showing no sign of rotation and a higher velocity dispersion. This will be discussed in the next section.

5. Kinematics

Recent spectroscopic surveys mapping the radial velocity of stars in the Galactic bulge at different longitudes, such as the Bulge Radial Velocity Assay (BRAVA Rich et al., 2007; Howard et al., 2009; Kunder et al., 2012), the Abundances and Radial Velocity Galactic Origins Survey (ARGOS Freeman et al., 2013; Ness et al., 2013b,a), the Giraffe Inner Bulge Survey (GIBS Zoccali et al., 2014, 2017), the Gaia-ESO Survey (GES Gilmore et al., 2012; Rojas-Arriagada et al., 2014, 2017), and the Apache Point Observatory Galactic Evolution Experiment (APOGEE Majewski et al., 2017; Ness & Freeman, 2016) all agree that the bulge shows a high degree of "cylindrical rotation". This means that the radial velocity curve (radial velocity as a function of longitude) is largely independent on latitude, with the rotation speed only slightly increasing closer to the plane (Fig. 5). In particular, Shen et al. (2010) showed that the a pure-disk model galaxy correctly reproduces the observed velocities, as the small increase of the rotation speed towards the Galactic plane is consistent with projection effects.

At the same time, the radial velocity dispersion goes from $\sigma \approx 80$ km/s at latitudes b=−8° to $\sigma \approx 140$ km s^{-1} at b=−1°. The latter value represent, in fact, a high-sigma peak only visible within the inner ∼2° of the Galaxy (i.e., within a radius of ∼240 pc). This peak,

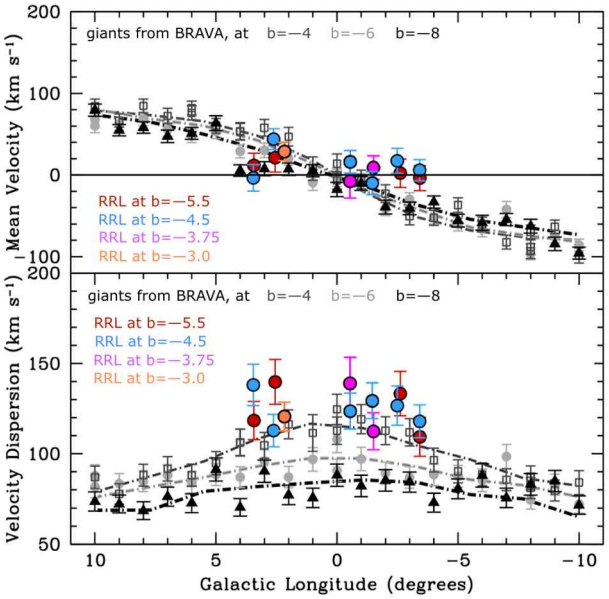

Figure 5: Comparison between the radial velocity profile (top) and the velocity dispersion profile (bottom) for bulge giants measured within the BRAVA survey, shown with black/grey symbols, and for RR Lyrae observed by Kunder et al. (2016), shown with colored symbols. It is clear that RR Lyrae have a flat rotation (top), and a higher velocity dispersion (bottom) compared to other giants. Adapted from Kunder et al. (2016).

mapped by Valenti et al. (2018), spatially coincides with the region where a change in the bar pivot angle had been detected by Alard (2001); Nishiyama et al. (2005); Gonzalez et al. (2011), who interpreted it as evidence for the presence of an inner bar. Later on, Zoccali & Valenti (2016) showed that the data are more consistent with the presence of a central, axisymmetric concentration of stars. It is worth noticing that no model has been shown to reproduce the central peak in velocity dispersion, yet.

As discussed in Sect. 4., spectroscopic surveys with enough resolution to derive stellar metallicities allowed us to identify two stellar components in the bulge, with different mean [Fe/H]. It was quickly evident that the metal rich and metal poor components had, at least, different velocity dispersion trend across the bulge area. Specifically, metal poor stars have higher sigma ($\sim$80 km s^{-1}) than the metal rich ones ($\sim$60 km s^{-1}) in the outer bulge, whereas in the inner few degrees they have lower sigma ($\sim$120 km s^{-1}) compared to the metal rich ones ($\sim$140 km s^{-1}). The global sigma is, of course, close to the metal poor one in the outer bulge, where the metal poor component dominates, and closer to the metal rich one in the inner bulge, where the metal rich dominates. As a word of caution, it should be kept in mind that the two metallicity components have some overlap at intermediate metallicities, therefore some cross-contamination certainly affects the determination of the kinematics of each component individually.

Concerning the rotation velocity pattern, Clarkson et al. (2018) used a combination of broad band filters available on *HST* to distinguish between metal poor and metal rich stars (Renzini et al., 2018), and the magnitude difference between main sequence stars and a mean fiducial line as a proxy for distances. They then used the distribution of proper motions in longitude to demonstrate that metal poor stars rotate significantly slower than metal rich stars. This is consistent with the other evidences that metal poor stars follow a spheroidal distribution, although it would be desirable to confirm this result by means of radial velocities at different longitudes.

Interestingly, Kunder et al. (2016) demonstrated that a sample of $\sim$1000 RR Lyrae variables observed at different longitudes show a high velocity dispersion and a flat rotation curve (see Fig. 5). What still needs to be verified is whether RR Lyrae, tracing the oldest component of the Galactic bulge, belong to the metal poor component described above, or they trace a third, older and more metal poor component. Unfortunately their MDF is not useful to demonstrate whether RR Lyrae and metal poor RC stars belong to the same component, as it is expected that only the most metal poor tail of a population with the MDF of metal poor stars would cross the instability strip, and therefore pulsate, when burning He in their core. The kinematics would be much more informative, but at the moment it is available for a relatively small sample of RR Lyrae and metal poor stars, which makes the results not conclusive yet.

For a more complete review about the bulge kinematics, and its correlation with metallicity, the reader should refer to Babusiaux (2016).

6. The ages of stars in the Galactic bulge

A fundamental information about the origin of the Galactic bulge obviously comes from the age distribution of its stars. While it seems now well established that the age of the bulk of bulge stars is close to 10 Gyr (Ortolani et al., 1995; Zoccali et al., 2003; Valenti et al., 2013; Clarkson et al., 2008; Surot et al., 2019), the actual age distribution, and in particular the size and age of a possible younger population is still strongly debated. The intrinsic difficulty in measuring the age distribution of bulge stars is due to the fact that foreground disk main sequence stars strongly contaminate the bulge turnoff region of the CMD. Decontamination has been attempted both with a statistical approach, using a disk control field, and kinematically, using the fact that the proper motion distribution of foreground disk stars overlaps only partially with that of bulge stars. All the attempts at deriving the age distribution from the shape of the decontaminated turnoff region yielded a population mostly old, with the only exception of Bernard et al. (2018) who find that 10% of bulge stars are younger than 5 Gyr. Independent measurements of the age distribution of bulge stars have been made, in the last 10 years, by Bensby et al. (2017, and references therein). They measured stellar surface parameters (T_{eff} and log g) of individual stars, by means of high resolution spectra obtained while the targets were microlensed (hence significantly brightened) by some unseen foreground object. These parameters, together with the metallicity,

allowed them to place the stars in the theoretical HR diagram, and thus derive their age by comparison with stellar isochrones. The result is that 38% of the sample stars are younger than 8 Gyr, with most of them having super solar metallicity. This percentage represents a factor of 3-4 discrepancy with Clarkson et al. (2008). A recent study by Renzini et al. (2018) uses a combination of *HST* filters to generate metallicity sensitive indices, and therefore separate bulge stars (decontaminated from disk stars by means of proper motions) into metal poor and metal rich ones. The authors found no difference in the magnitude distribution of turnoff stars of both sample. The debate is still open!

7. Summary and Outlook

In the last ∼5 years or so, consensus has been reached that the Galactic bulge is a massive ($1.5-2\times10^{10}M_{\odot}$) component of the Milky Way, including two separate populations. One of them, making up a little more than a half of the total mass, has super solar metallicity, is arranged in a bar that flares up into a peanut, or X-shape, in its outskirt, plus a thin component extended out to ∼4.5 Kpc, confined in the plane. The shape of this component and its kinematics, all indicate a clear disk origin. Another component, with mean metallicity [Fe/H]=−0.4 dex, has a shape very close to a spheroid, higher dispersion and little or no rotation. Its origin is not clear, it might be the result of a violent merging phase, before the bar, or it might also come from an older, hotter disk.

Some of the most significant open problems are the following:

i) Do the RR Lyrae variable trace the same spheroidal component as the metal poor stars? Or do they trace a third, old and metal poor component? Answer to this question will certainly come from the high resolution spectroscopy for tens of thousands of stars enabled by the forthcoming near infrared fibre spectrograph MOONS (Cirasuolo et al., 2014). It will be available at the VLT around 2021, and, among other studies focused on the innermost bulge regions (i.e., the nuclear bulge) it will allow to derive kinematics and metallicities for a large sample of metal poor red clump stars and RR Lyrae.

ii) Is the metal rich component significantly younger than the metal poor one? Addressing this question is harder in my opinion. It requires large statistics, precise (relative) proper motions and metallicities for a large sample of bulge turnoff stars. The first two are already available from *HST* and will certainly improve with the advent of JWHST. The second might have to wait for the 30m class telescopes, and perhaps some more time until multi-object spectrographs will be available on them.

iii) What is the structure and the stellar population of the Nuclear bulge, i.e., the region within $|b|<1^{\circ}$ and $|l|<3^{\circ}$. This will most likely be addressed by the high spatial resolution imagers of the JWST and/or the ELTs, together with efficient, near infrared spectrographs such as MOONS.

Acknowledgements: I am grateful to the organizers of the Second Binational Meeting AAA-SOCHIAS for the invitation to deliver the present review talk. I also acknowledge support from the Ministry for the Economy, Development, and Tourism's Programa Iniciativa Científica Milenio through grant IC120009, awarded to Millenium Institute of Astrophysics (MAS), the BASAL CATA Center for Astrophysics and Associated Technologies through grant PFB-06, and from FONDECYT Regular 1150345.

References

Alard C., 2001, A&A, 379, L44
Athanassoula E., 2005, MNRAS, 358, 1477
Athanassoula E., et al., 2015, MNRAS, 454, 3843
Babusiaux C., 2016, PASA, 33, e026
Barbuy B., Chiappini C., Gerhard O., 2018, ARA&A, 56, 223
Benjamin R.A., et al., 2005, ApJL, 630, L149
Bensby T., et al., 2017, A&A, 605, A89
Bernard E.J., et al., 2018, MNRAS, 477, 3507
Blitz L., Spergel D.N., 1991, ApJ, 379, 631
Bournaud F., Elmegreen B.G., Martig M., 2009, ApJL, 707, L1
Cabrera-Lavers A., et al., 2007, A&A, 465, 825
Cabrera-Lavers A., et al., 2008, A&A, 491, 781
Carollo C.M., et al., 2007, ApJ, 658, 960
Cirasuolo M., et al., 2014, *Ground-based and Airborne Instrumentation for Astronomy V*, *Proc. SPIE*, vol. 9147, 91470N
Clarkson W., et al., 2008, ApJ, 684, 1110
Clarkson W.I., et al., 2018, ApJ, 858, 46
de Vaucouleurs G., 1964, F.J. Kerr (Ed.), *The Galaxy and the Magellanic Clouds*, *IAU Symposium*, vol. 20, 195
Debattista V.P., et al., 2017, MNRAS, 469, 1587
Dékány I., et al., 2013, ApJL, 776, L19
Elmegreen B.G., Bournaud F., Elmegreen D.M., 2008, ApJ, 688, 67
Feldmeier-Krause A., et al., 2017, MNRAS, 464, 194
Fragkoudi F., et al., 2018, A&A, 616, A180
Freeman K., et al., 2013, MNRAS, 428, 3660
Genzel R., et al., 2008, ApJ, 687, 59
Gerhard O., Martinez-Valpuesta I., 2012, ApJL, 744, L8
Gilmore G., et al., 2012, The Messenger, 147, 25
Gonzalez O.A., et al., 2011, A&A, 534, L14
Gran F., et al., 2016, A&A, 591, A145
Hammersley P.L., et al., 1994, MNRAS, 269, 753
Hammersley P.L., et al., 2000, MNRAS, 317, L45
Howard C.D., et al., 2009, ApJL, 702, L153
Immeli A., et al., 2004, A&A, 413, 547
Joo S.J., Lee Y.W., Chung C., 2017, ApJ, 840, 98
Kormendy J., Kennicutt Jr. R.C., 2004, ARA&A, 42, 603
Kunder A., et al., 2012, AJ, 143, 57
Kunder A., et al., 2016, ApJL, 821, L25
Lee Y.W., Joo S.J., Chung C., 2015, MNRAS, 453, 3906
López-Corredoira M., et al., 2007, AJ, 133, 154
Majewski S.R., et al., 2017, AJ, 154, 94
McWilliam A., 2016, PASA, 33, e040
McWilliam A., Rich R.M., 1994, ApJS, 91, 749
McWilliam A., Zoccali M., 2010, ApJ, 724, 1491
Minniti D., et al., 2010, NewA, 15, 433
Nataf D.M., et al., 2010, ApJL, 721, L28
Ness M., Freeman K., 2016, PASA, 33, e022
Ness M., Lang D., 2016, AJ, 152, 14
Ness M., et al., 2012, ApJ, 756, 22
Ness M., et al., 2013a, MNRAS, 430, 836
Ness M., et al., 2013b, MNRAS, 432, 2092
Nishiyama S., et al., 2005, ApJL, 621, L105
Ortolani S., et al., 1995, Nature, 377, 701

Patsis P.A., Skokos C., Athanassoula E., 2002, MNRAS, 337, 578
Pietrukowicz P., et al., 2015, ApJ, 811, 113
Portail M., et al., 2015, MNRAS, 448, 713
Portail M., et al., 2017, MNRAS, 470, 1233
Renzini A., et al., 2018, ApJ, 863, 16
Rich R.M., et al., 2007, ApJL, 658, L29
Rodriguez-Fernandez N.J., Combes F., 2008, A&A, 489, 115
Rojas-Arriagada A., et al., 2014, A&A, 569, A103
Rojas-Arriagada A., et al., 2017, A&A, 601, A140
Schultheis M., et al., 2015, A&A, 584, A45
Shen J., et al., 2010, ApJL, 720, L72
Simion I.T., et al., 2017, MNRAS, 471, 4323
Soszyński I., et al., 2011, AcA, 61, 1
Surot F., et al., 2019, arXiv e-prints
Tadaki K.i., et al., 2017, ApJ, 834, 135
Tissera P.B., et al., 2018, MNRAS, 473, 1656
Valenti E., et al., 2013, A&A, 559, A98
Valenti E., et al., 2016, A&A, 587, L6
Valenti E., et al., 2018, A&A, 616, A83
Wegg C., Gerhard O., 2013, MNRAS, 435, 1874
Wegg C., Gerhard O., Portail M., 2015, MNRAS, 450, 4050
Zoccali M., Valenti E., 2016, PASA, 33, e025
Zoccali M., Valenti E., Gonzalez O.A., 2018, A&A, 618, A147
Zoccali M., et al., 2000, ApJ, 530, 418
Zoccali M., et al., 2003, A&A, 399, 931
Zoccali M., et al., 2008, A&A, 486, 177
Zoccali M., et al., 2014, A&A, 562, A66
Zoccali M., et al., 2017, A&A, 599, A12

Chemodynamical tracers for the formation of dSph. Leo I vs Simulations

A.G. Alarcón Jara[1], M. Fellhauer[1], J.D. Simon[2] & A. del Pino[3]

[1] *Universidad de Concepción, Concepción, Chile*
[2] *Observatories of the Carnegie Institution for Science, Pasadena, CA, USA*
[3] *Space Telescope Science Institute, Baltimore, MD, USA*

Contact / alexralarconj@udec.cl

Resumen / Presentamos un análisis de la cinemática interna de la galaxia esferoidal enana Leo I usando BEACON a fin de encontrar patrones químicos-cinemáticos entre estrellas de distintas poblaciones estelares, empleando sus metalicidades y velocidades a lo largo de la linea de visión. Comparamos nuestros resultados con los diferentes escenarios propuestos para la formación de galaxias esferoidales enanas, especificamente el modelo de disolución de cumulos de estrellas y su principal predicción.

Abstract / We present an analysis of the internal kinematics of the Leo I dwarf spheroidal galaxy using BEACON to find chemo-kinematic patterns among stars of different stellar populations, using their metallicity and velocity along the line of sight. We compare our results with the different scenarios proposed for the formation of dwarf spheroidal galaxies, specifically the dissolving star cluster model and its main prediction.

Keywords / galaxies: dwarf — kinematics and dynamics — Local Group — structure

1. Introduction

Dwarf spheroidal galaxies (dSph) are the most common type of galaxies in the Universe, however, due to their low luminosity, their study has been very difficult. These systems have stellar masses of $10^5 - 10^7$ $M_\odot$, but their velocity dispersions of $\sim$10 km s^{-1} out to large radii imply dynamical masses 2 orders of magnitude larger (e.g. Simon & Geha, 2007; Koch et al., 2009; Kleyna et al., 2002, 2003; Muñoz et al., 2005, 2006; Simon & Geha, 2007; Walker et al., 2007). They are therefore thought to be the most dark matter dominated objects known in the Universe (e.g. Mateo, 1998; Walker et al., 2009).

In the standard hierarchical galaxy formation models, larger galaxies are formed from smaller objects like dwarf galaxies through major and/or minor mergers (Kauffmann et al., 1993; Cole et al., 1994). Thus, it is important to study these galaxies to understand the formation and evolution of normal sized galaxies.

There are different models that could explain the origin of dSph galaxies considering different mechanisms. Gnedin et al. (1999) and Mayer et al. (2007) proposed that dSph galaxies were formed from dwarf disc satellites of a larger galaxy, then their gas was removed by ram-pressure and additional tidal stirring changed their form.

D'Onghia et al. (2009) proposed that dSph galaxies were formed by encounters between two dwarf disc galaxies and resonant stripping destroyed the form of the galaxies, leaving the DM halo intact.

According to the dissolving star cluster scenario proposed by Assmann et al. (2013a,b); Alarcón Jara et al. (2018), a dSph galaxy is formed by the fusion and dissolution of several star clusters, formed within a DM halo. In order to corroborate those formation models it is necessary to understand the details of the star formation histories and the kinematics of dSphs. dSphs galaxies have been generally considered to be pressure-supported systems with little or no rotation. On the other hand, significant rotation signatures have been reported for some dSph galaxies in the literature (Battaglia et al. (2008); Lewis et al. (2007); Fraternali et al. (2009)). However, these works are based on V_{LOS} measurements of only a few tens of RGB stars in each galaxy, which may not be enough to derive conclusive results. Large spectroscopic data sets are needed to understand the internal kinematics of dSph galaxies. Recent work by del Pino et al. (2017) shows that the spherical shape of the Fornax dSph could be due to the superposition of many different stellar components with distinct kinematics, differentiated by their chemical composition. The main prediction of the dissolving star cluster model, is that stars formed in the same star cluster follow similar orbits while they dissolve. This motivates us to search for streaming motions or circular orbits of stars with similar chemical compositions (since they were formed in the same molecular gas cloud) in galaxies where large spectroscopic data sets are available.

2. Method: BEACON

Acquisition of large spectroscopic samples and proper motions of dwarf galaxies will allow us to disentangle the internal kinematic of dwarf galaxies. BEACON is a new software tool developed by del Pino et al. (2017). The code is optimized to find groups of stars with similar

chemo-kinematic properties in resolved stellar systems. Its development was motivated by the results of del Pino et al. (2015), which show that the Fornax dSph galaxy contains different stellar populations with different angular momentum. This prediction was corroborated using BEACON, see del Pino et al. (2017).
The code has been optimized for joining together groups of stars with similar positions, velocities and metallicities, then if the number of stars in the group is bigger than a minimum cluster size (MCS), the code classifies them as a one side stream (OSS). If at the opposite side of the center of mass exists another stream with similar chemical composition, but with opposite velocity, then the two groups are classified as a both side stream (BSS).

3. Results

3.1. BEACON & simulated data

In the thrashing scenario of a dwarf disc galaxy, one would expect to see some left-over/coherent rotation signal in the kinematics of the stars. But, most of the dwarf spheroidal galaxies do not show signals of rotation, and if they do, this signal is very weak. In the dissolving star cluster model proposed by Assmann et al. (2013a), stars sustain orbits similar to the ones held by their dissolved cluster. We would expect to see many "rotation" signals in randomly oriented directions.
In the left panels of Fig. 1 we present simulated examples of different streams formed by dissolved star clusters. According to this model, for a young star cluster which is not entirely dispersed within the dark matter halo, we shall see a one side stream like is seen in the first panel. Additionally, depending on the orbit of the star cluster within the dark matter halo, we shall see different rotating patterns as in the second and third panels, where the majority of the stars follow circular orbits. We apply BEACON to these streams and the results are shown in the right panels of Fig. 1. BEACON is able to detect one-side streams and both side streams, but it has problems detecting the stars close to the center, as they have lower velocities and positions out of the standard deviation of the recovered sample.

In a simulation we can give a certain metallicity to each star according to the age of the star cluster where it was formed: the older, the more metal-poor. We use data from a simulation in which we form 8 star clusters using a constant star formation history during 10 Gyr, this means that we formed one star cluster every 1.25 Gyr. For simplicity, the metallicities are given using a linear age to metallicity ratio. To mimic the data, we choose randomly 1000 stars of the simulation and we add the typical error values found in our Leo I catalog, ($\pm$ 2.5 km s^{-1} for the velocity and $\pm$ 0.2 Fe H^{-1} for the metallicity). Applying BEACON to this sample with the optimal parameters, we can recover approximately 70% of the stars from the same star cluster correctly.

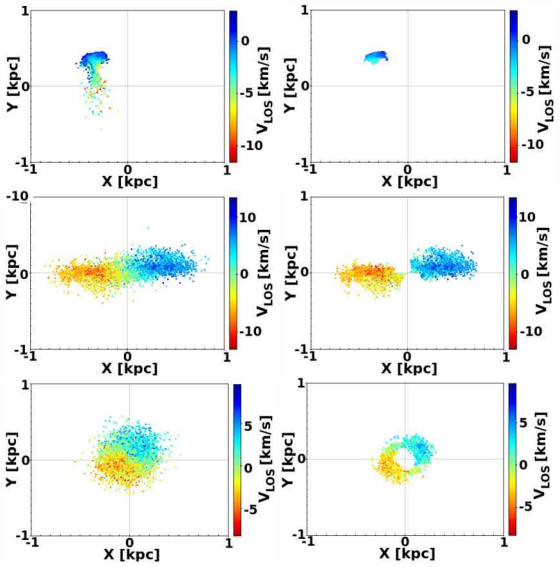

Figure 1: Dissolved star clusters in simulations. Left panels show the different kinds of streams that simulations of the dissolving star cluster model reproduce, and the right panels show the particles that BEACON is able to recover from those streams. We can see that BEACON is able to recover one side streams (first panel) and both side streams (second and third panels), but the stars in the center are more difficult to recover using this code.

3.2. BEACON in real data of Leo I

Leo I, a satellite of the Milky Way, is one of best candidates to test formation models because it is orbiting at 250 $\pm$ 20 kpc (Karachentsev & Kashibadze, 2006) from the Milky Way, so it has not recent tidal interactions with the Galaxy, it also formed stars at a relatively constant rate until ~1 Gyr ago (Weisz et al., 2014). We use data from Leo I obtained from the Keck/DEIMOS instrument by Sohn et al. (2007); Kirby et al. (2010) and new data acquired with Magellan/IMACS in March 2018. We applied BEACON to the 943 stars combining these three samples.

We found 230 stars classified in 10 different rotating stream candidates that share similar metallicities. An example of one of these streams is given in Fig. 2, where we see a clear signal of rotation. We calculate the angular momentum and then normalize it by the number of stars in each group, representing the angular momentum per unit of stellar mass. Those 10 different streams show different angular momentum directions (Fig. 3 left panel) distributed randomly in the galaxy. This result is in favor of the dissolving star cluster scenario shown in Fig. 3 right panel.

4. Discussion and conclusions

Motivated by the predictions of the dissolving star cluster model we investigate the presence of stream motions using BEACON, to find chemo-kinematic patterns in stars of Leo I. We find multiple rotating populations in Leo I, similar to the results obtained for Fornax by del Pino et al. (2017). This could indicate that the overall

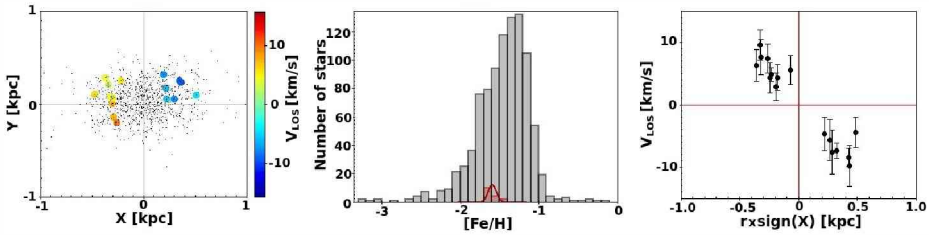

Figure 2: Example of a group of stars recovered by BEACON: The left panel shows the distribution of the stars in the galaxy with black dots, stars that are part of the same stream are coloured according to their velocity. Middle panel shows a histogram with the metallicity distribution from the stars of our sample, and in red the metallicity of the stars from the stream. The right panel shows the velocities of the stream versus the distance from the center.

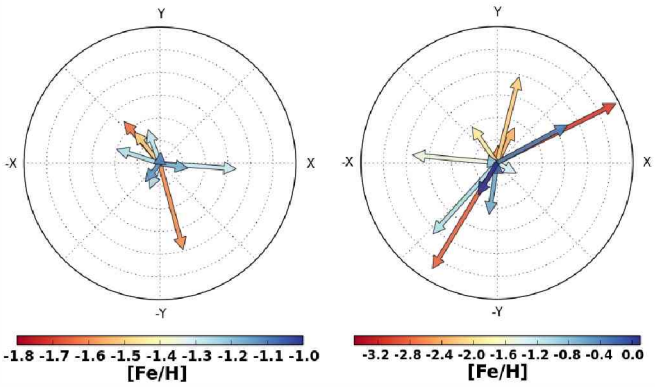

Figure 3: Angular momentum per unit of stellar mass for different streams: The left panel shows the different angular momentum patterns recovered by BEACON in the sample of 943 stars from Leo I according to their Fe to H ratio. Circles have radius from 0 to 3 $\times 10^{3}$ pc ^{2} s^{-1} with step of 0.5 $\times 10^{3}$ pc^{2} s^{-1} for each dotted concentric circle. The right panel shows the angular momentum for a simulation of the dissolving star cluster model with 16 star clusters dissolved. It is clear that there is no net rotation signal, in agreement with the predictions of the dissolving star cluster model.

structure of dSph galaxies is due to the superposition of different stellar populations with different orbits.
In the context of the dissolving star cluster model, these chemo-kinematic patterns are one of the main predictions and arise naturally with the model. However, the patterns found in Leo I and Fornax can be explained with other models assuming rotating progenitors as well. For example, the tidal stirring model explains the formation of dSphs as interactions between a dwarf disc galaxy and a Milky Way size galaxy. These interactions could be responsible for reshaping a disc galaxy into a dSph (Mayer et al., 2007). Simulations show that after a significant time, the final object conserves some signatures of this process and could have remnant rotation around the minor axis. In Leo I, the specific angular momentum of the stream candidates is randomly distributed around the galaxy as is predicted by the dissolving star cluster model.

Another option to explain this pattern implies that the evolution of dSph galaxies could involve several mergers between two or more galaxies. Two disc galaxies collide and as a result they could form a dSph. This idea has been studied before and shows that some of the orbits of the progenitors could remain after the collision and that some stars could still be on their initial orbits after the merging, presenting angular momentum vectors in different directions (Amorisco & Evans, 2012). As the formation process of dSph galaxies is still unclear, it is necessary to apply BEACON to other dSphs with large and high quality data, when available, in order to search for chemo-dynamical substructures in those systems and obtain a better understanding of the origin of dSphs.

Acknowledgements: AA acknowledges funding from Carnegie Observatories through their Carnegie-Chile Fellowship and Fondecyt Regular No. 1180291. MF acknowledges funding through the Concurso Proyectos internatcionales de Investigación, Convocatoria 2015 (project code PII20150171), BASAL Centro de Astrofísica y Tecnologías Afines (CATA) AFB-170002 and Fondecyt regular No. 1180291.

References

Alarcón Jara A.G., et al., 2018, MNRAS, 473, 5015
Amorisco N.C., Evans N.W., 2012, ApJL, 756, L2
Assmann P., et al., 2013a, MNRAS, 432, 274
Assmann P., et al., 2013b, MNRAS, 435, 2391
Battaglia G., et al., 2008, ApJL, 681, L13
Cole S., et al., 1994, MNRAS, 271, 781
del Pino A., et al., 2015, MNRAS, 454, 3996
del Pino A., et al., 2017, MNRAS, 465, 3708
D'Onghia E., et al., 2009, Nature, 460, 605
Fraternali F., et al., 2009, A&A, 499, 121
Gnedin O.Y., et al., 1999, ApJ, 514, 109
Karachentsev I.D., Kashibadze O.G., 2006, Astrophysics, 49, 3
Kauffmann G., White S.D.M., Guiderdoni B., 1993, MNRAS, 264, 201
Kirby E.N., et al., 2010, ApJS, 191, 352
Kleyna J., et al., 2002, MNRAS, 330, 792
Kleyna J.T., et al., 2003, ApJL, 589, L59
Koch A., et al., 2009, ApJ, 690, 453
Lewis G.F., et al., 2007, MNRAS, 375, 1364
Mateo M.L., 1998, ARA&A, 36, 435
Mayer L., et al., 2007, Nature, 445, 738
Muñoz R.R., et al., 2005, ApJL, 631, L137
Muñoz R.R., et al., 2006, ApJ, 649, 201
Simon J.D., Geha M., 2007, ApJ, 670, 313
Sohn S.T., et al., 2007, ApJ, 663, 960
Walker M.G., et al., 2007, ApJL, 667, L53
Walker M.G., et al., 2009, ApJ, 704, 1274
Weisz D.R., et al., 2014, ApJ, 789, 147

Stirring up a embedded star cluster with a moving gas filament

D. Matus Carrillo[1], M. Fellhauer[1] & A. Stutz[1,2]

[1] *Departmento de Astronomía, Facultad de Ciencias Físicas y Matemáticas, Universidad de Concepción, Concepción, Chile*
[2] *Max-Planck-Institute for Astronomy, Heidelberg, Germany*

Contact / dimatus@udec.cl

Resumen / Realizamos simulaciones para probar los efectos de un filamento de gas en movimiento sobre un cúmulo estelar joven (i.e. el modelo *Slignshot*). Modelamos un *Orion Nebula Cluster* como una esfera de Plummer, y el Filamento con Forma de Integral como un potencial cilíndrico, donde su posición viene dada por una función sinusoidal. Observamos que en un filamento estático, un cúmulo inicialmente esférico evoluciona de forma natural hacia una distribución elongada de estrellas. Para un filamento en movimiento, observamos distintos remanentes y los clasificamos en 4 categorías. Cúmulos "saludables", donde casi todas las estrellas permanecen dentro del filamento y del cúmulo; cúmulos "destruidos" son el caso opuesto, casi sin estrellas en el filamento o cerca del centro de densidad del cúmulo; cúmulos "ejectados", donde una fracción mayor de estrellas permanecen unidas al cúmulo, pero casi ninguna se mantiene dentro del filamento; y cúmulos de "transición", donde aproximadamente el mismo número de partículas es eyectado del cúmulo y del filamento. Un cúmulo con las características de *Orion Nebula Cluster* podría permanecer dentro del filamento o ser eyectado, pero no será destruido.

Abstract / We perform simulations to test the effects of a moving gas filament on a young star cluster (i.e. the "Slingshot" Model). We model Orion Nebula Cluster-like clusters as Plummer spheres and the Integral Shaped Filament gas as a cylindrical potential. We observe that in a static filament, an initially spherical cluster evolves naturally into an elongated distribution of stars. For sinusoidal moving filaments, we observe different remnants, and classify them into 4 categories. "Healthy" clusters, where almost all the stars stay inside the filament and the cluster; "destroyed" clusters are the opposite case, with almost no particles in the filament or near the centre of density of the clusters; "ejected" clusters, where a large fraction of stars are close to the centre of density of the stars , but almost none of them in the filament; and "transition" clusters, where roughly the same number of particles are ejected from the cluster and from the filament. A cluster similar to an Orion Nebula Cluster might stay inside the filament or be ejected, but it will not be destroyed.

Keywords / methods: numerical — Galaxy: open clusters and associations: individual: ONC

1. Introduction

The Orion nebula is the nearest site of massive star formation. One of its predominant features is the Integral Shaped Filament (ISF, Bally et al., 1987), a filament of gas in where the Orion Nebula Cluster (ONC, Hillenbrand & Hartmann, 1998) is forming.

Observations of the protostars in the ONC show that they are distributed in different ways in space: protostars are located right on top of the ridgeline of the filament, meanwhile pre-main-sequence stars are symmetrically distributed around the filament (Stutz & Gould, 2016; Kainulainen et al., 2017; Stutz, 2018). A similar behavior is observed for the radial velocity of the stars, where protostars have radial velocities close to the velocity of the gas, with a low velocity dispersion, and the pre-main-sequence stars have a larger velocity dispersion of the order or larger than the velocity of the gas (Stutz & Gould, 2016).

To explain these observations, Stutz & Gould (2016) proposed a scenario where the gas of the ISF oscillates. The protostars are formed from this gas and move with the oscillating filament. Once they accrete enough mass, they are ejected from their birthplace and start moving with the transverse velocity of the oscillation at the moment of decoupling. Stutz & Gould (2016) named this scenario "the Slingshot".

To test this hypothesis, Boekholt et al. (2017) showed that an initially narrow distribution of stars can be dynamically heated to produce a broad distribution with a net relative velocity when the filament oscillates with a certain amplitude and period. Moreover, Gaia data of the protostars plus the radial velocities of the gas confirm that the gas of the ISF moves like a standing wave (Stutz et al., 2018).

In this work we continue the exploration of the Slingshot via simulations, this time replacing the string of stars with spherical star clusters of different masses.

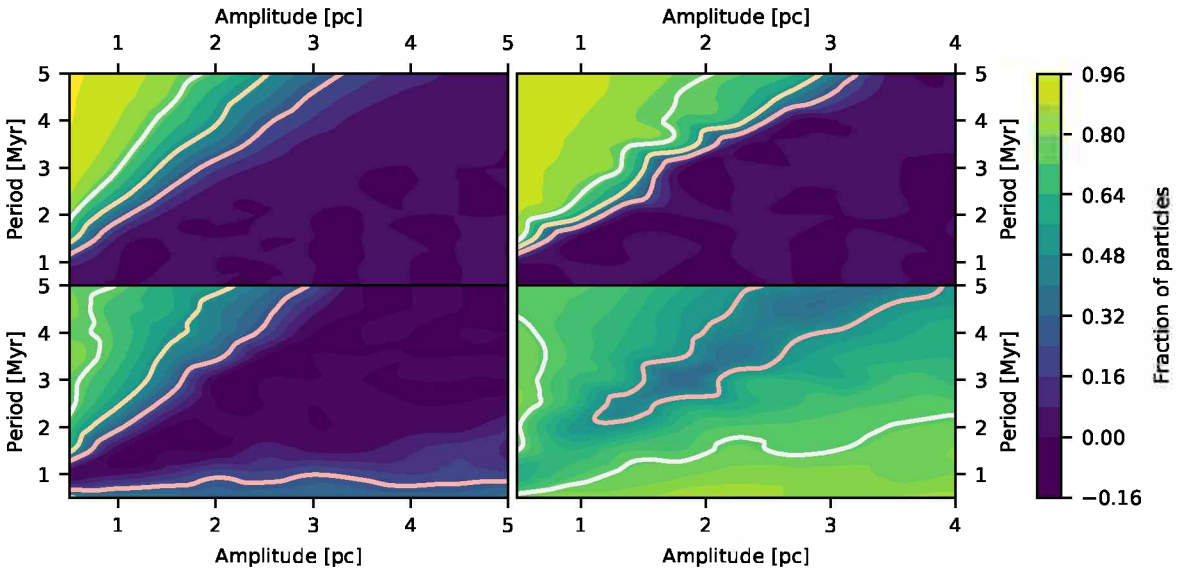

Figure 1: Fraction of particles inside the filament (top) and inside the cluster (bottom) after one oscillation for a cluster with $R_{\rm pl} = 0.1$ pc, $M_{\rm pl} = 250$ M$_\odot$ (left) and $R_{\rm pl} = 0.1$ pc, $M_{\rm pl} = 1000$ M$_\odot$ (right). The contours indicate 75%, 50% and 25% of the initial number of particles. Notice that the number of particles inside the filament drops drastically after it reaches $\sim 50\%$ for the more massive cluster, but decreases smoothly for the less massive cluster.

2. Method

2.1. The gas filament

To study the effect of the ISF on a young star cluster, we build a cylindrical potential as in Boekholt et al. (2017), using the observed line density of the gas at the position of the ONC (Stutz, 2018) as a constraint to obtain the relevant parameters of the model in the region of interest.

The ISF likely moves due to the interplay of gravitational and magnetic forces (Stutz & Gould, 2016; Schleicher & Stutz, 2018), but in this work we assume that the gas potential is moving along the x-axis like an harmonic oscillator:

$$x(t) = A \sin\left(\frac{2\pi}{P} t\right), \qquad (1)$$

where A is the amplitude of the oscillation and P is the period.

2.2. The star cluster

We use a cluster of equal-mass point particles to represent the ONC. The particles are distributed following a Plummer profile (Plummer, 1911) and located inside the cylindrical potential.

The presence of an external potential means that there is an extra component to the net force that acts on the particles, but due to the symmetry of the filament, that extra acceleration can be non-zero only in the x-y plane. Therefore, a standard Plummer sphere will collapse due to the extra mass of the filament along those axes. We avoid that initial contraction by increasing the x-y velocity of the particles so that the cylindrical Lagrangian radii of the cluster inside the filament remains roughly constant.

2.3. The code

The system of particles is evolved using the PH4 N-body code (McMillan et al., 2012). To account for the gas filament, we implement the background potential using AMUSE (Pelupessy et al., 2013). We couple this potential with the N-body solver using the BRIDGE (Fujii et al., 2007) method, in which the velocities of the stars are periodically updated using the acceleration due to the filament.

3. Results

Due to the cylindrical symmetry of the potential used to represent the filament, the embedded clusters tend to elongate along the z axis. Particles moving throughout the length of the gas filament, will do so following corkscrew orbits around the center of the potential.

We determine the state of the cluster by counting the stars inside the filament, measured as the number of stars that never move beyond $5R_{\rm pl}$ from the centre of the filament. Inside the cluster, we define the evolution in a similar fashion using the centre of density of the particle system instead.

If the filament moves slowly, a large fraction of particles stays inside the filament and the cluster. As the amplitude of the oscillation increases, or the period decreases, a larger fraction of stars are ejected from the system, up to the moment where no stars are inside the filament (Fig. 1, top left) or close to the centre of density of the stars (Fig. 1, bottom left). If the filament moves too quickly, it will not spend enough time inside the cluster to perturb the particles and a large fraction

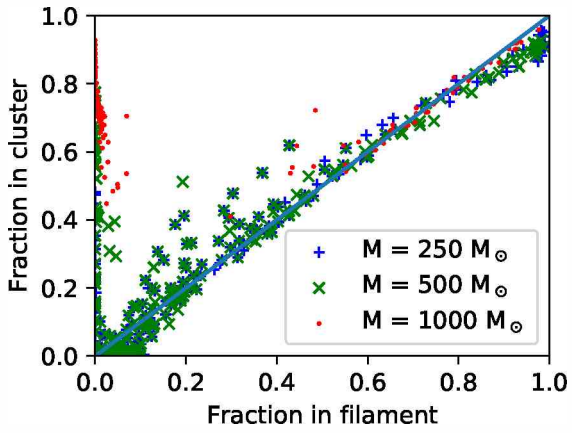

Figure 2: Fractions of particles inside cluster and filament for models with $R = 0.1$ pc after one full oscillation. The blue line is a reference for a 1:1 ratio.

of stars (but not all of them, so we can still identify an over-density of particles) will be ejected from the cluster.

A more massive cluster will have a similar behavior. However, being more tightly bound, it will not be destroyed (Fig. 1, bottom right). The fraction of particles in the filament will have a sharper transition from the high values characteristic of the slow filaments to the empty filament state (Fig. 1, top right).

Fig. 2 shows the fraction of stars inside the filament, versus the fraction of stars inside the cluster, for clusters with $R_{\rm pl} = 0.1$ pc. This shows us a sequence of remnants after one full oscillation of the filament that can be cataloged into 4 groups:

- Slow filaments (i.e. large period and/or small amplitudes) will keep a large number of particles inside the cluster and filament, and in this case, it behaves like a cluster inside a static filament. Some stars are ejected from these "healthy" clusters, since the filament is still injecting energy into the cluster.
- Some combinations of period and amplitude will produce remnants that are completely destroyed, where only a small (< 20 %) fraction of stars will stay inside the filament and move with it.
- A high fraction of stars in the cluster, but almost none in the filament is observed when the cluster is ejected from the filament. There is negligible mass loss when the cluster is outside the filament.
- The last kind of objects are those where the same number of particles are ejected from the filament and cluster. Most of the mass loss happens between the beginning of the simulation and by the time the filament reaches its maximum amplitude. After that, there are small losses each time the filament reaches the maximum distance from the origin.

Not all the models will produce remnants in every category. As can be seen in Fig. 2, none of the clusters with $M_{\rm pl} = 1000$ M$_\odot$ are destroyed. Moreover there is a gap where none of the cluster remnants end with < 40 % of the particles inside the filament, with the exception of the ejected clusters. This means that the cluster can stay inside the filament or it can be ejected after losing less than half of its mass, but it is not destroyed by the filament.

4. Conclusions

We present results of the first simulations of the effects of an oscillating cylindrical potential in the early evolution of a young star cluster. We explore the space of oscillation parameters with star clusters of different densities and masses.

We find 3 possible evolution trends:

- Small, low-mass clusters stay bound and move with the filament, if the filament is moving slowly.
- Fast-moving filaments can eject and destroy star clusters
- Large, high-mass clusters stay bound and the filament just moves through, pumping energy into the cluster.

The fate of the cluster in an oscillating potential is decided quickly. By the time the filament reaches its maximum amplitude, any star that manages to stay inside the cluster or the gas filament will likely stay there for the rest of the simulation time. A cluster like the ONC might be ejected or stay inside the filament, but these simulations suggest that it will endure the stirring by the filament and it will not be destroyed.

The physics behind the origin of the sharp transition, shown in Figure 1 (top right panel) is still under investigation, but we believe that it might be related to the mass ratio between the cluster and the gas filament.

Acknowledgements: DM gratefully acknowledges support from the Chilean BASAL Centro de Excelencia en Astrofísica y Tecnologías Afines (CATA) grant AFB-170002 and Fondecyt regular No. 1180291. MF acknowledges support through Fondecyt regular 1180291, Basal AFB-170002 and PII20150171. AS acknowledges funding through Fondecyt Regular (project code 1180350), "Concurso Proyectos Internacionales de Investigación" (project code PII20150171), and Chilean Centro de Excelencia en Astrofísica y Tecnologías Afines (CATA) BASAL grant AFB-170002.

References

Bally J., et al., 1987, ApJL, 312, L45
Boekholt T.C.N., et al., 2017, MNRAS, 471, 3590
Fujii M., et al., 2007, PASJ, 59, 1095
Hillenbrand L.A., Hartmann L.W., 1998, ApJ, 492, 540
Kainulainen J., et al., 2017, A&A, 600, A141
McMillan S., et al., 2012, R. Capuzzo-Dolcetta, M. Limongi, A. Tornambè (Eds.), *Advances in Computational Astrophysics: Methods, Tools, and Outcome*, *Astronomical Society of the Pacific Conference Series*, vol. 453, 129
Pelupessy F.I., et al., 2013, A&A, 557, A84
Plummer H.C., 1911, MNRAS, 71, 460
Schleicher D.R.G., Stutz A., 2018, MNRAS, 475, 121
Stutz A.M., 2018, MNRAS, 473, 4890
Stutz A.M., Gonzalez-Lobos V.I., Gould A., 2018, ArXiv e-prints
Stutz A.M., Gould A., 2016, A&A, 590, A2

Expected abundance patterns from the first generation of stars

C. Olave[1], D.R.G. Schleicher[1], V.B. Díaz[1] & P. FFibla[1]

[1] *Departamento de Astronomía, Facultad de Ciencias Físicas y Matemáticas, Universidad de Concepción, Concepción, Chile*

Contact / colave@udec.cl

Resumen / Se cree que las primeras estrellas en el Universo (Población III) fueron responsables de sintetizar los primeros elementos pesados, creando por lo tanto las condiciones químicas sobre las que la segunda generación de estrellas se formó. Uno de los objetivos de las investigaciones actuales es restringir de mejor manera la función de masa inicial de las estrellas de población III, utilizando los patrones de abundancia de estrellas extremedamente pobres en metales. Esencial para modelar su influencia en la historia cósmica. Aquí presentamos un conjunto de predicciones para las razones de abundancia de carbono y europio, suponiendo diferentes tipos de función de masa inicial, parametrizada mediante el índice α, masa máxima y masa mínima. Discutiremos brevemente el espacio de parámetros consistente con datos de las estrellas extremadamente pobres en metales conocidas hasta ahora.

Abstract / The first stars in the Universe (Population III) are thought to be responsible for synthesizing the first heavy elements, thereby creating the chemical conditions from which the second generation of stars has formed. One of the aims of current investigations is to better constrain the Initial Mass Function of Population III stars from the observed abundance patterns of extremely metal poor stars, which is essential to model their influence on cosmic history. We present a set of predictions for the abundance ratios of carbon and europium yields, assuming different types of initial mass function, parametrized by the index α, and the upper and lower mass cutoff. We will briefly discuss the parameter space that is consistent with the extremely metal poor stars known so far.

Keywords / nuclear reactions, nucleosynthesis, abundances — stars: early-type

1. Introduction

Population III, or Pop. III, stars are the first generation of stars, believed to have formed around 380 Myr after the Big Bang (WMAP and Planck).

These stars were responsible for synthesizing the first heavy elements and giving way to the origin of complex structures by acting as the initial source of the reionization of the Universe. At the end of their lives, massive stars exploded as supernovae ejecting all their material into the intergalactic medium, setting the chemical conditions where the second generation of stars was formed.

Depending on their masses, stars can have different fates, which translates into several ways of chemically affect the environment (Heger & Woosley, 2002). 10-35 $M_\odot$, non-rotating stars finishes its life as type II supernova; in the range of $100 - 250$ $M_\odot$ the star is partially or completely disrupted due to pair-antipair instability, ejecting all the material inside the core. In this scenario, stars with ≤ 150 $M_\odot$ go into a state of pulsational pair-instability, where it is not clear if they spread any metal or not; stars with masses around 35-100 $M_\odot$ and higher than 250 $M_\odot$ are predicted to die as a black hole and yield no nucleosynthesis products to the interstellar medium.

To understand how this stellar population enriched the Universe it is crucial to better constrain their initial mass function, therefore modeling their impact on cosmic history. Nevertheless, direct observations of these stars are still elusive, which has led to believe that the first stars are very massive, thus they are not expected to live for a long time. A second interesting possibility is that Pop. III stars consist of low-mass objects, and thus they may still remain in the present Universe masked by older stellar population.

Studies in the field of elemental abundances of extremely metal-poor (EMP) stars can help to constrain the evolution of Pop. III stars, as they are believed to carry the nucleosynthetic signature of the first stars. In particular, studies of elements with $Z > 26$, are important to understand the processes that form them (s-/r-process) and when they began to occur.

Extensive observations of metal-poor stars have enabled us to classify them according to distinctive features, such as their carbon abundance. Some of them have been found to exhibit an enriched carbon abundance, [C/Fe] $> +0.7$, commonly known as carbon enhanced metal-poor stars (hereafter, CEMP stars). The latter also consist of further sub-classes, depending on the enrichment presented of both s- and/or r-process elements (CEMP-s, CEMP-r and CEMP-s/r), or if the stars have a typical solar abundance of neutron capture elements (CEMP-no; [Ba/Fe] 0.0) (originally defined by Beers & Christlieb (2005)). Observational data have suggested that CEMP-no stars to arise from an intrinsic process, linking them as direct descendants to the first stars (Norris et al. (2013) for a summary of the evidence on this claim). One of the possible origins proposed is

the 'mixing and fall-back' model, in which a first generation star explodes as supernova without the sufficient energy to expelled all the synthesize material in its core, therefore only external layers, rich in lighter elements, are released while heavy material is captured and falls back onto the neutron star or black hole.

Here we calculate [Eu/Fe] and [C/Fe] ratios, focusing on the initial mass function (IMF) prescriptions that could in principle explain the abundances imprinted in the most metal-poor stars we currently know.

2. Methodology

We employ the following formula to describe the IMF:

$$\phi(M) = \phi_0 M^{-1+\alpha}. \quad (1)$$

We explore four values for the index α, this is $\alpha = 3$ (Salpeter-IMF), $\alpha = 2$, $\alpha = 1$ and $\alpha = 0$ (logarithmically flat IMF). The equation is normalized as,

$$\int_{M_{low}}^{M_{up}} M\phi(M)dM = c, \quad (2)$$

where M_{low} and M_{up} represent the low-mass and high-mass cutoffs, respectively. The low-mass limit was varied from 5 to 20 $M_\odot$ and the maximum mass from 25 to 300 $M_\odot$.

Three different sets of stellar yields are adopted: The work of Nomoto et al. (2006) gives information for primordial stars between 13-40 $M_\odot$. Heger & Woosley (2002) is very elaborated for stars between 140-260 $M_\odot$, that lead to pair-instability supernovae for different masses of the helium cores, while Karlsson et al. (2013) covers the rest of the mass range.

In the case of Eu, we test two models considering the contribution of different progenitor masses for the SNe, with constant Eu yields over the whole selected mass range. Stellar yields in massive low-metallicity stars were taken from Cescutti et al. (2006), who consider production for stars between 10-25 $M_\odot$ as the progenitors of this element (MEu1). In addition, we adopt yields from the work of Argast et al. (2004) in order to see the variations in the expected abundance patterns of n-capture elements, when considering the metal production of lower mass core-collapse SNe (i.e., 8-10 M⊙) combined with r-process yields from core-collapse SNe in the range of 20-25 $M_\odot$ (MEu2).

The total yield for element X is given as:

$$X_{tot} = \sum_i N_i X_i. \quad (3)$$

Here X_i is the yields for a single star in the i-th mass interval, in units of solar masses, and N_i is the number of stars in the i-th mass range.

We note that all above interpretations assume single, non-rotating stars. The effects of rotation in zero-metallicity stars will not be addressed here, however, we point out the importance of including it in further models for comparison, as it may change significantly the results (Stacy et al., 2011). We adopt the typical definitions of elemental abundances and ratios. The absolute abundance is determined as the number of atoms of element X per 10^{12} hydrogen atoms, $A(X) = \log_{10}(N_X/N_H) + 12.0$. The logarithmic abundance ratio relative to the solar ratio for element X and Y is defined as $[X/Y] = \log_{10}(N_X/N_Y)_\star - \log_{10}(N_X/N_Y)_\odot$. We use solar abundances from Asplund et al. (2009).

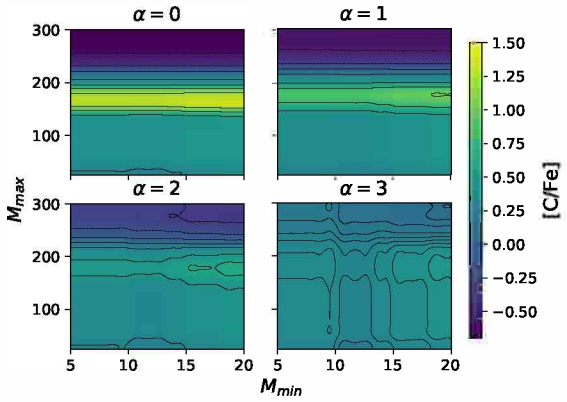

Figure 1: [C/Fe] for different prescriptions of the IMF. The x-axis represent M_{min} and y-axis M_{max}. The contour lines indicate zones of an enhanced [C/Fe]. Notice that [C/Fe] is very sensitive to the upper mass limit for a flatter IMF (i.e., $\alpha = 0$), where it also reaches both of its extreme values.

3. Results

3.1. Carbon

Abundances of carbon and oxygen have been suggested to be the key elements to distinguish between different star formation modes, as carbon and oxygen are indeed the most efficient coolants in case of metal-enriched clouds (Bromm & Loeb, 2003; Omukai et al., 2005).

In Fig. 1, we present several values for the relative abundances of carbon. The results are obtained with four different IMF models. Notice that [C/Fe] is overall super-solar, however, it drops drastically if we consider extreme values for the upper mass cutoff in a flat IMF (top left panel of Fig. 1). The window to reproduce CEMP stars carbon abundances is reached mostly at low values of α.

3.2. Europium

Europium is a heavy, neutron-capture element and peculiar for the reason that it is produced almost entirely by the r-process (roughly 95% of solar europium has been produced via the r-process, Mashonkina et al., 2003). In spite of the fact that Eu lines are weak, thus very often it is possible to derive only upper limits, this element is important to distinguish between r-process scenarios, due to its insensitivity to other production sites.

Fig. 2 present [Eu/Fe] abundance ratios for several IMFs. The contour lines denotes zones of enrichment. Notice that in this model, europium production is limited to a very narrow range of masses (10-25 M⊙), making [Eu/Fe] vary widely between the chosen mass limits.

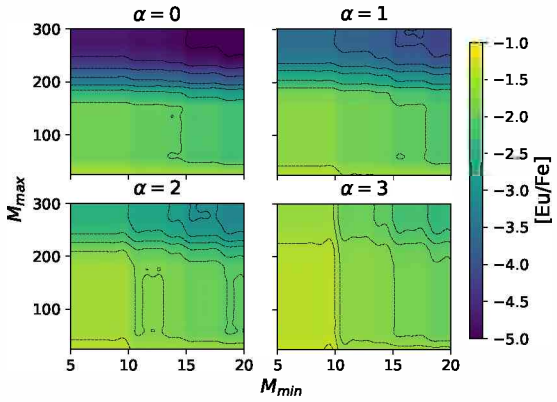

Figure 2: MEu1: [Eu/Fe] predicted by adopting the four different IMFs. The x-axis represent M_{min} and the y-axis M_{max}. Contour lines indicate zones of over-density.

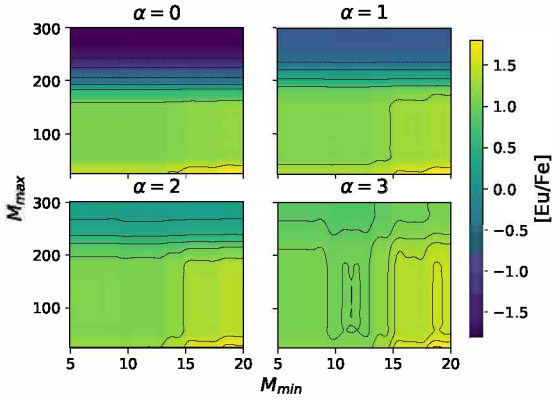

Figure 3: MEu2: [Eu/Fe] for different prescriptions of the IMF, considering stars of 8-10 $M_\odot$ and 20-25 $M_\odot$.

This is also visible when observing the extreme cases, where [Eu/Fe] has a difference of almost 4 orders of magnitude. On the other hand, when the Pop. III IMF is extended down to lower masses, we obtain a window of enhanced ratios, which covers more area in the case of a Salpeter-like choice for the index α. Based on the selection of masses proposed by Argast et al. (2004), the order of [Eu/Fe] increases significantly as shown in Fig. 3, with a strong dependence on the minimum mass.

3.3. Abundance ratios by CEMP-no stars

In the following analysis, we compare the results obtained by our different models to the observed abundance ratios of some of the extremely-metal poor stars we currently now. Our sample data has been extracted from the available literature, in particular Yoon et al. (2016) and references therein. In total we use 87 CEMP-no stars with [Fe/H] -2.5 and at least an upper limit for [Eu/Fe] 1.0. Claimed binary systems are not considered here to avoid mixing on different paths of formation.

Roughly 70 % of the data presents [C/Fe] between 0.7 and 1.3. The median of the entire sample is [C/Fe]= 0.99. In the case of europium, as Eu lines get very weak at [Fe/H] -3, Eu detections are mostly constrained only by upper limits. The median of the sample is 0.21, which falls in the range of the model considering low (8-10 $M_\odot$) and high-mass (20-25 $M_\odot$) core-collapse SNe. Combining these constraints we can mark an upper limit for the M_{max} of roughly 200 $M_\odot$, while the lower mass cutoff is not well restricted in our models. However, our results discard Pop. III stars as objects of several hundreds of solar masses. The index of the IMF, on the other hand, is satisfied for both cases with $\alpha = 1 - 2$.

4. Discussion

If the chemical abundances we observe in extremely metal-poor stars can be reconciled with the yields of Pop. III stars, it can allow to constrain the masses that the first generation of stars should have had in the past and the form of the initial mass function (Iwamoto et al., 2005).

Past studies have focused on recreating the abundance ratios found in EMP stars, considering a single or a few prescriptions for the IMF. Here we vary the IMF in order to understand how this choice affects subsequent stellar evolution. We were able to reproduce abundances consistent with CEMP-no metal-poor stars found in the Universe, which are believed to born directly out of the gas of first-generation stars. Model MEu1 fell slightly short on the [Eu/Fe] ratio, even for some extreme cases, favoring the presence of only less-massive stars. On the contrary, MEu2 fits better the observed abundances for the CEMP-no stars. Nevertheless, further models have to be done taking into account elements as nitrogen, oxygen or barium, in order to place a stricter restriction on the form of the IMF of the first stars.

Acknowledgements: CO, DRGS, VBD and FF thank for funding via CONICYT PIA ACT172033 and the 'Concurso Proyectos Internacionales de Investigación, Convocatoria 2015' (project code PII20150171). CO and DRGS also thank BASAL Centro de Astrofísica y Tecnologías Afines (CATA) PFB-06/2007. DRGS acknowledges funding through CONICYT project Basal AFB-170002. FF and VBD thank for funding through Fondecyt regular (project code 1161247). VBD thanks to Conicyt for financial support on her master studies (CONICYT-PFCHA/MagísterNacional/2017-22171293).

References

Argast D., et al., 2004, A&A, 416, 997
Asplund M., et al., 2009, ARA&A, 47, 481
Beers T.C., Christlieb N., 2005, ARA&A, 43, 531
Bromm V., Loeb A., 2003, Nature, 425, 812
Cescutti G., et al., 2006, A&A, 448, 557
Heger A., Woosley S.E., 2002, ApJ, 567, 532
Iwamoto N., et al., 2005, Science, 309, 451
Karlsson T., Bromm V., Bland-Hawthorn J., 2013, Reviews of Modern Physics, 85, 809
Mashonkina L., et al., 2003, A&A, 397, 275
Nomoto K., et al., 2006, Nuclear Physics A, 777, 424
Norris J.E., et al., 2013, ApJ, 762, 28
Omukai K., et al., 2005, ApJ, 626, 627
Stacy A., Bromm V., Loeb A., 2011, MNRAS, 413, 543
Yoon J., et al., 2016, ApJ, 833, 20

Formation of massive black hole seeds in the early Universe: Runaway stellar collisions in the first star clusters

B. Reinoso[1], D.R.G. Schleicher[1], M. Fellhauer[1], R.S. Klessen[2,3], T.C.N. Boekholt[4], M.Z.C. Vergara[1] & P.J. Alister Seguel[1]

[1] *Departamento de Astronomía, Facultad Ciencias Físicas y Matemáticas, Universidad de Concepción, Concepción, Chile*
[2] *Universität Heidelberg, Zentrum für Astronomie, Institut für Theoretische Astrophysik, Heidelberg, Germany*
[3] *Universität Heidelberg, Interdisziplinäres Zentrum für Wissenschaftliches Rechnen, Heidelberg, Germany*
[4] *CIDMA, Departamento de Física, Universidade de Aveiro, Aveiro, Portugal*

Contact / breinoso@udec.cl

Resumen / La presencia de agujeros negros supermasivos cuando el Universo tenía solo mil millones de años de edad, presenta un gran desafío para los modelos actuales de formación y crecimiento de agujeros negros, dado el corto tiempo que se impone para reunir 10^9 $M_\odot$ en un solo objeto compacto. En este trabajo presentamos un mecanismo de formación de agujeros negros de masa intermedia (10^3 $M_\odot$) que consiste en repetidas fusiones entre estrellas de población III.1 en los primeros cúmulos estelares densos formados en el Universo.

Abstract / The presence of supermassive black hole seeds when the Universe was only one billion years old, presents a big challenge to the actual models for the formation and growth of black holes, due to the short time imposed to gather 10^9 $M_\odot$ in a single compact object. In this work, we present a mechanism for the formation of intermediate mass black holes (10^3 $M_\odot$), which consists in repeated mergers between population III.1 stars in the first dense star clusters formed in the Universe.

Keywords / stars: Population III — cosmology: dark ages, reionization, first stars — galaxies: star clusters: general

1. Introduction

Stellar collisions and mergers have been invoked to explain the formation of massive stars (Bonnell et al., 1998; Clarke & Bonnell, 2008) and quantitative studies suggest that in present-day star clusters the fraction of stars that participate in this process is about $0.1 - 1\%$(Baumgardt & Klessen, 2011). While in the present-day Universe this mechanism does not produce very massive products given the small amount of physical collisions, the conditions predicted for the early Universe are much more favorable. Computational hydrodynamics simulations have found evidence for fragmentation during the collapse of the clouds at densities of 10^9 cm^{-3} or higher (e.g., Smith et al., 2012; Latif et al., 2013), especially if dust is present early on (e.g., Klessen et al., 2012; Bovino et al., 2016). These densities can lead to the formation of compact stellar systems with a half mass radius of $r_h = 0.1$ pc or even less.

The high temperature due to the low metallicity of the primordial gas contributes to the high accretion rates of $\sim 10^{-3} - 10^{-1}$ $M_\odot$ yr^{-1} found in numerical simulations (Abel et al., 2002; Yoshida et al., 2006). Some first stellar evolution models by Stahler et al. (1986) or Omukai & Palla (2003) suggest that these stars can become as large as 300 $R_\odot$, and that this can be enhanced in the presence of variable accretion rates (Smith et al., 2012). The most extreme cases with accretion rates of ~ 0.1 $M_\odot$ yr^{-1} have produced the largest stars, potentially reaching more than 1000 $R_\odot$ for a 100 $M_\odot$ star (Schleicher et al., 2013; Haemmerlé et al., 2017).

Due to these considerations, it is natural to think that stellar mergers between population III (Pop. III) stars could play an important role in the formation of very massive objects and black hole seeds in the early Universe. Indeed, this process was mentioned as an important pathway in Rees (1984), and taken into account in models by Devecchi et al. (2012) and Boekholt et al. (2018). Furthermore, N-body simulations using initial conditions given by the output of cosmological simulations have yield black holes with masses as large as 10^3 $M_\odot$ (Lupi et al., 2014; Katz et al., 2015; Sakurai et al., 2017).

We present a systematic investigation to understand the process of repeated mergers in the first star clusters of the Universe and how the final object depends on the number of stars and their radii. We describe our setup in Sec. 2., we present our results in Sec. 3. and give a final summary in Sec. 4..

2. Setup

We performed a total of 280 N-body simulations of isolated, gas free star clusters modeled with a single stellar population, without including an IMF but using equal mass and equal radii stars. The simulations

were performed using a modified version of NBODY6 * (Aarseth, 2000).

2.1. Star clusters

We employ a simplified model of the first star clusters of the Universe, modeling these systems as a Plummer distribution(Plummer, 1911) with a total mass of $M_{\rm cluster} = 10^4$ M$_\odot$ and a half mass radius of $r_{\rm h} = 0.1$ pc. The clusters are initially virialized, and our parameter space is formed by combinations of the number of stars that we varied as $N = 100, 500, 1000, 5000$ and the stellar radius that we varied as $R_{\rm star} = 20, 50, 100, 200, 500, 1000, 5000$ R$_\odot$. The clusters are formed by equal mass stars with $M_{\rm star} = M_{\rm cluster}/N$. No mass loss is included in our calculations. We decided to stop the simulations at 3 Myr given that at this point the merger process has stopped in all the clusters.

2.2. Stellar mergers

Stellar mergers are automatically activated in NBODY6 when using the stellar evolution package based on the work by Hurley et al. (2000), however, these routines do not cover the metallicity range of the Pop. III stars. For this reason, we had to deactivate these routines and instead specify explicitly the radius of the stars and the radius of the merger product. A physical collision occur when the separation d of two stars becomes equal or smaller to the sum of their radius ($d \leq R_1 + R_2$). In this case the two stars are replaced by a new star in the center of mass of the previous configuration. We assume no mass loss during the merger, therefore $M_{\rm new} = M_1 + M_2$, then we calculate the radius by requiring that the density remains constant, that is, $R_{\rm new} = R_1 \left((M_1 + M_2)/M_1\right)^{1/3}$. We assume that the new star quickly settles into a new equilibrium configuration in which the density is the same of an unperturbed star of the same mass. This is consistent with previous calculations by e.g. Haemmerlé et al. (2017).

3. Results

3.1. Evolution of the clusters

In the presence of mergers, before a core-collapse (Heggie, 1979) occurs during the evolution of the clusters, there are several physical collisions that yield stars more massive than the average, and these mergers occurs at distances not larger than the half-mass radius. This is specially important for clusters containing a larger number of stars, i.e. $N = 1000$ and $N = 5000$, in which there are several mergers that do not involve the most massive object at first, but these products sink to the center, contributing finally to the mass enhancement of the most massive object, which eventually encompasses around 10% of the total mass of the cluster. We find that the total fraction of collisions in a cluster, i.e. the total number of mergers divided by the initial number of stars, $f_{\rm coll} = N_{\rm col}/N$, depends mainly on the stellar radius, ranging from $0.01 - 0.02\%$ for 20 R$_\odot$ stars, to 0.08% for 200 R$_\odot$ stars. The total number of mergers depend on the number of stars, therefore, so does the mass enhancement of the most massive object. Thus, the most promising case for producing massive black holes is when the number of stars in the cluster is large, however, as we will see later, not large enough so that the onset of the mass growth is not delayed too much. The latter is important if we consider a time-limit given by the lifetime of the stars that could explode as a supernova and destroy the cluster, halting the process of mergers.

3.2. Modelling the runaway growth

The runaway growth is the process of repeated mergers involving the same object, which grows very rapidly in mass and becomes the most massive object. We want to find an expression that allow us to estimate the mass of the most massive object before the death of the massive stars in the cluster. To do this, we reconstruct the merger history of the most massive star, i.e. the amount of mergers experienced by the most massive object in a given time interval during the simulation. We then fit to this data the following function,

$$N_{\rm col} = A \int_0^t \exp\left(-\frac{(t - t_{\rm delay})^2}{2t^2_{\rm duration}}\right) dt. \quad (1)$$

The function in Eq. 1 depends on three parameters: $t_{\rm delay}$, which is the time-delay until the runaway growth begins; $t_{\rm duration}$, which is the duration of the runaway growth; and A, a normalization factor related to the total number of mergers. The number of mergers as a function of time experienced by the most massive object in each of our simulations is fitted, using as a fitting model the Eq. 1, so we can understand how the three parameters of that function depend on the number of stars N and the radius of the stars $R_{\rm star}$.

We find that $t_{\rm delay}$ increases with the number of stars because the onset of the runaway growth is related to the half-mass relaxation time-scale which in turn increases with the number of stars, but at the same time, $t_{\rm delay}$ decreases with the stellar radius given that the onset of mergers begins earlier with larger stars. We also find that, as expected, the normalization factor A related to the total number of mergers increases with both N and $R_{\rm star}$. We did not find a clear relation between $t_{\rm duration}$ and the stellar radius, we just find an increase in the duration time with the number of stars. These relations are described in Eqs. 2, 3 and 4. In these equations $\log(x)$ refers to a base 10 logarithm of x.

*Webpage NBODY6: `https://www.ast.cam.ac.uk/~sverre/web/pages/nbody.htm`

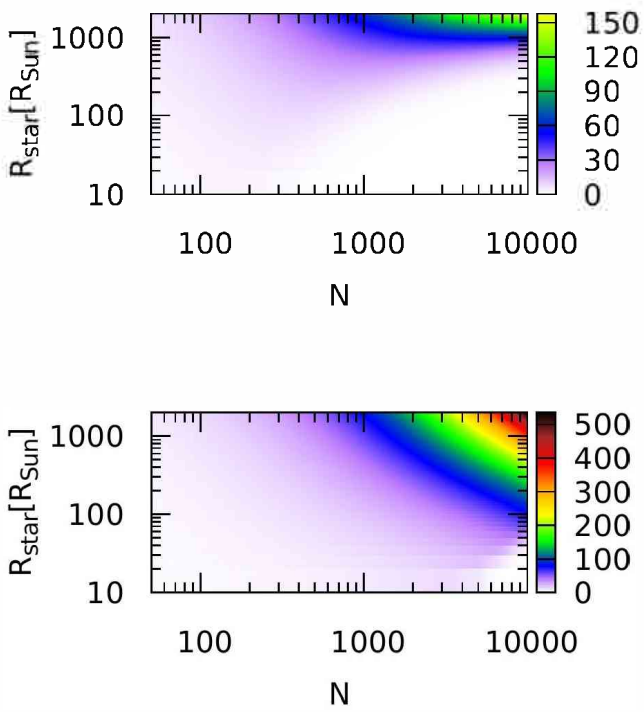

Figure 1: Total number of mergers with the most massive object after 1 Myr (upper panel) and after 10 Myr (bottom panel) in color scale (right axis) depending on the initial number of stars of the cluster (x-axis) and the stellar radius in $R_\odot$ (y-axis). The most promising scenario for forming black holes is favoured for a large number of stars if the time is enough (bottom panel) and if the radius of the stars is large, as expected.

$$\log(A) = \left[0.16\log\left(\frac{R_{\rm star}}{R_\odot}\right) - 0.05\right]\log(N) + 0.06\log\left(\frac{R_{\rm star}}{R_\odot}\right) - 1.43, \quad (2)$$

$$\log\left(\frac{t_{\rm delay}}{t_{\rm cros}}\right) = \left[1.09 - 0.21\log\left(\frac{R_{\rm star}}{R_\odot}\right)\right]\log(N) + 0.30\log\left(\frac{R_{\rm star}}{R_\odot}\right) - 0.79, \quad (3)$$

$$\log\left(\frac{t_{\rm duration}}{t_{\rm cros}}\right) = 0.34\log N + 0.34. \quad (4)$$

With these equations we can then find the number of mergers for a broad combination of N and $R_{\rm star}$ as presented in Fig.1 (Reinoso et al., 2018) where we calculated the number of mergers up to 1 Myr (top panel) and up to 10 Myr (bottom panel) by integrating Eq. 1 for different combinations of N and $R_{\rm star}$, and a time limit of 1 and 10 Myr (See Fig. 1).

4. Summary

We performed a total of 280 N-body simulations of isolated, gas free and virialized star clusters formed by Pop. III stars. We found that these systems evolve towards the phase of core-collapse and quickly the merger process takes place, being faster for clusters with less stars but producing more massive objects in clusters with a larger number of stars. If we set a time-limit to this process given by the life-time of the Pop. III stars, that we consider somewhat in between 1 and 10 Myr, then the most plausible case for producing massive black hole seeds is for clusters containing stars with radius larger or equal to 100 $R_\odot$ in which we can expect a minimum enhancement of 15 times the initial mass of the stars and up to 100 times if the time-limit is 10 Myr and the cluster contains 10 000 stars with 100 $R_\odot$.

Acknowledgements: BR thanks personal funding by SOCHIAS. DRGS and BR acknowledge funding through Fondecyt regular No. 1161247, MF through Fondecyt regular No. 1180291. BR has financial support through CONICYT-PFCHA/MagisterNacional/2017-22171385. DRGS and MF acknowledge funding through PII20150171 and BASAL (CATA) AFB-170002. DRGS and BR are grateful for funding through ALMA-Conicyt 31160001, Quimal 170001 and Anillo ACT172033. RSK acknowledges financial support from the DFG via SFB 881 and SPP 1573 and from ERC Advanced Grant 339177. TB acknowledges support through grants: SFRH/BPD/122325/2016, UID/MAT/04106/2013 and from ENGAGE SKA, POCI-01-0145-FEDER-022217

References

Aarseth S.J., 2000, V.G. Gurzadyan, R. Ruffini (Eds.), *The Chaotic Universe*, 286–287
Abel T., Bryan G.L., Norman M.L., 2002, Science, 295, 93
Baumgardt H., Klessen R.S., 2011, MNRAS, 413, 1810
Boekholt T.C.N., et al., 2018, MNRAS, 476, 366
Bonnell I.A., Bate M.R., Zinnecker H., 1998, MNRAS, 298, 93
Bovino S., et al., 2016, ApJ, 832, 154
Clarke C.J., Bonnell I.A., 2008, MNRAS, 388, 1171
Devecchi B., et al., 2012, MNRAS, 421, 1465
Haemmerlé L., et al., 2017, ArXiv e-prints
Heggie D.C., 1979, MNRAS, 188, 525
Hurley J.R., Pols O.R., Tout C.A., 2000, MNRAS, 315, 543
Katz H., Sijacki D., Haehnelt M.G., 2015, MNRAS, 451, 2352
Klessen R.S., Glover S.C.O., Clark P.C., 2012, MNRAS, 421, 3217
Latif M.A., et al., 2013, MNRAS, 436, 2989
Lupi A., et al., 2014, MNRAS, 442, 3616
Omukai K., Palla F., 2003, ApJ, 589, 677
Plummer H.C., 1911, MNRAS, 71, 460
Rees M.J., 1984, ARA&A, 22, 471
Reinoso B., et al., 2018, A&A, 614, A14
Sakurai Y., et al., 2017, MNRAS, 472, 1677
Schleicher D.R.G., et al., 2013, New Journal of Physics, 15, 023017
Smith R.J., et al., 2012, MNRAS, 424, 457
Stahler S.W., Palla F., Salpeter E.E., 1986, ApJ, 302, 590
Yoshida N., et al., 2006, ApJ, 652, 6

Siblings, friends and acquaintances: Testing the galaxy association methods

J.P. Caso[1,2] & C.A. Vega-Martínez[1,2]

[1] *Facultad de Ciencias Astronómicas y Geofísicas, UNLP, and Instituto de Astrofísica de La Plata (CONICET–UNLP), La Plata, Argentina*
[2] *Consejo Nacional de Investigaciones Científicas y Técnicas, Argentina*

Contact / jpcaso@fcaglp.unlp.edu.ar (JPC); cnvega@fcaglp.unlp.edu.ar (CVM)

Resumen / Se presentan resultados preliminares tendientes a comprobar la exactitud de los métodos de asociación aplicados a *surveys* de galaxias, en busca de establecer sus limitaciones y determinar posibles alternativas para mejorar sus resultados. Nos enfocamos en el método de *friends-of-friends*, llevando a cabo el análisis en la simulación cosmológica de materia oscura MDPL2, del proyecto *Multidark*. Los resultados apuntan a una elevada fracción de contaminantes, en particular para halos masivos en ambientes de alta densidad. Cotas en los parámetros de asociación y la aplicación de test de subestructura pueden mitigar el número de falsos positivos.

Abstract / We present preliminary results to test the accuracy of association methods applied to galaxy surveys, in order to constraint their limitations and develop possible alternatives to improve them. We focused in the friends-of-friends (FoF) method, carrying on the analysis on the dark matter cosmological simulation MDPL2, from the Multidark project. Results point to a large fraction of contaminants from the application of the FoF method, particularly for massive haloes in high density environments. Thresholds in the association parameters and the subsequent use of tests for substructures can mitigate the occurance of fake positives.

Keywords / galaxies: statistics — distances and redshifts — clusters: general

1. Introduction

An accurate classification of the environments where galaxies belong is a key point to understand its role in galaxy evolution. Several efforts have been made to classify galaxies as probable cluster/group members, mainly by friends-of-friends (FoF) methods, but the limitations of observational astronomy might result in false positives and/or lost members. The aim of this ongoing project is to take advantage of a large sample of galaxy halos extracted from a high resolution cosmological dark matter simulation to model the available data of observational surveys and test the methods. Here we focus in the FoF method.

2. The sample

In order to achieve this goal we analyzed the MDPL2 public simulation, part of the Multidark project (Klypin et al., 2016). This simulation consists in a cubic volume of 1 h^{-1}Gpc of size, considering 3840^3 dark matter particles with mass of 1.51×10^9 $h^{-1}\mathrm{M}_\odot$. The dark matter halos of the simulation were detected using the ROCKSTAR halo finder, which catalogs are also publicly available. For this project we use the list of halos found at the snapshot corresponding to the local Universe ($z = 0$). We selected halos with masses above 10^{11} $\mathrm{M}_\odot$, and divided the simulation in cubic samples with 100 h^{-1}Mpc sides, in order to obtain samples with similar sizes than observational surveys of the nearby universe. We included an overlapped envelope of width 10 h^{-1}Mpc to avoid biases at the edges of the samples. We force each halo of the simulation to act as host of a unique galaxy. Therefore, the main halos become hosts of the central galaxies of each system, and the satellite halos are the hosts of the satellite galaxies.

We assigned to each halo a luminosity in the K band by using a simple halo occupation distribution method (HOD Vale & Ostriker, 2006), which estimates the luminosities in a non parametric way. By taking this approach, the magnitudes are obtained from the combination of the halo mass function of the simulation samples with the K luminosity function measured by Kochanek et al. (2001). In order to add uncertainties to radial velocities (V_R), we analysed V_R measurements from the 2MASS Redshift Survey (Huchra et al., 2012) to derive typical uncertainties in V_R (eV_R). Hence, we added randomly generated eV_R, assuming Gaussian distributions dependent on the K magnitude.

We applied the FoF algorithm supported on V_R and projected distances (D_p), following Crook et al. (2007). The latter value, was calculated from the angular separation and the distance in the line-of-sight estimated from the average V_R for each pair of galaxies. In order to select the thresholds for both linking parameters, we run the FoF algorithm in a subsample of the data and determine the percentage of accuracy for main haloes and satellite haloes separately. This analysis showed that setting the thresholds in $D_{\mathrm{p,max}} = 525$ kpc and $\Delta_{\mathrm{V,max}} = 1000$ km s^{-1} are commitment values to ob-

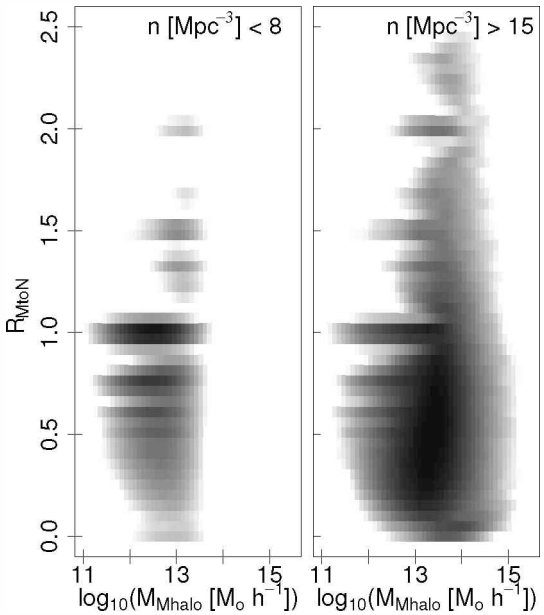

Figure 1: Distribution of ratios between real satellites and haloes associated by the method (R_{MN}) for main haloes as a function of their virial masses, for two different ranges of environmental densities.

tain a high accuracy for main and satellite haloes.

3. Results

Fig. 1 presents the distribution of ratios between the number of real satellites and haloes associated by the method (R_{MtoN}) for main haloes as a function of their virial masses. We focused on main haloes with at least two satellites, assuming this as a simplistic definition of galaxy groups. The sample was split in equally populated ranges of environmental density, calculated as the number of haloes lying in a surrounding sphere of 1.75 Mpc h^{-1}. The left panel corresponds to haloes in sparse environments, with numerical densities $n < 8$. The right panel is an analogue for denser environments, typical of clusters of galaxies ($n > 15$). The grey scale ranges from the maximum of the distribution and a hundredth of it . The fraction of main haloes around $R_{MtoN} = 1$ decreases with environmental density, representing 40% and 7%, respectively. This is due to high environmental densities favor the occurrence of "fake positives", with 62% of the main haloes presenting $R_{MtoN} < 1$ in the right panel.

The occurrence of fake positives in the association method can produce changes in the velocity dispersions for a main halo (i.e., "group/cluster of galaxies"), with respect to that obtained from their real members. To study this effect, Fig. 2 shows the distribution of the change in velocity dispersion ($\Delta\sigma_{V_R}$) when fake positives are considered. We split the sample in three bins, depending on the value of R_{MtoN}, main haloes largely contaminated ($R_{MtoN} < 0.33$, solid curves), moderately contaminated ($0.33 < R_{MtoN} < 0.66$, dashed curves) and less contaminated ($0.66 < R_{MtoN} < 1$), dotted curves). As expected, in these latter cases $\Delta\sigma_{V_R}$ com-

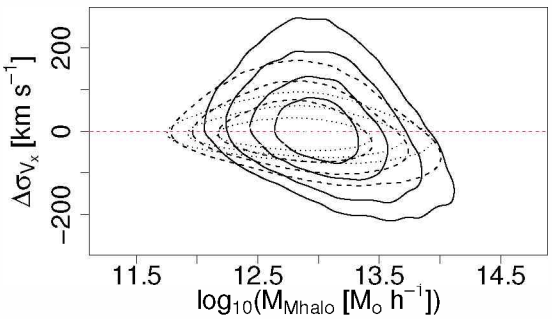

Figure 2: Distribution of the change in velocity dispersion ($\Delta\sigma_{V_R}$) for main haloes when fake positives are considered. The line types differentiate between main haloes largely contaminated ($R_{MtoN} < 0.33$, solid curves), moderately contaminated ($0.33 < R_{MtoN} < 0.66$, dashed curves) and less contaminated ($0.66 < R_{MtoN} < 1$), dotted curves).

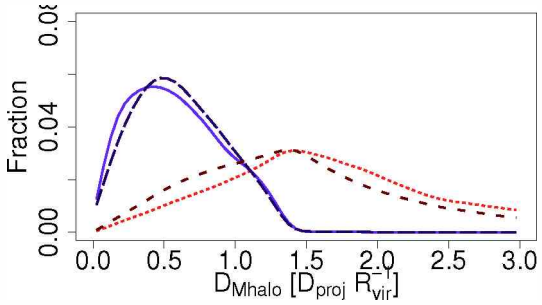

Figure 3: Distribution of projected distances to the main halo (D_{Mhalo}) in terms of the virial radius, for real satellites and fake positives in two different mass ranges. Main haloes with virial mass of $1-5\times10^{12}$ h^{-1}M$_\odot$ are represented with solid and dotted curves, respectively. Main haloes ranging $3-20\times10^{13}h^{-1}$M$_\odot$ are shown with long-dashed and dashed curves, respectively.

prise a more restricted range of values. For largely contaminated main haloes, the distribution of $\Delta\sigma_{V_R}$ is significantly asymmetric, with main haloes more massive than few times 10^{13} h^{-1}M$_\odot$ preferring a decrease in σ_{V_R}.

We also analyzed the distribution of projected distances to the main halo (D_{Mhalo}) in terms of the virial radius (Fig 3), particularly for main haloes in the virial mass ranges of $1-5\times10^{12}$ h^{-1}M$_\odot$ and $3-20\times10^{13}$ h^{-1}M$_\odot$. These ranges correspond to the estimated masses for the Local Group (Carlesi et al., 2017) and nearby clusters of galaxies like Fornax (Drinkwater et al., 2001), respectively. The projected distributions for real satellites (solid and long-dashed curves, respectively) and fake positives (dotted and dashed curves, respectively) were plotted separately. In both cases the distribution of real satellites vanished at ≈ 1.5 R_{vir}, coincidentally with the typical maximum for the distribution of fake positives. These latter distributions are more extended, which might be partially solved by applying an upper limit in projected distance to the association method.

From Fig. 3 we can infer that constraints on the projected distances might be useful to reduce the number of fake positives. In order to do this, we selected as up-

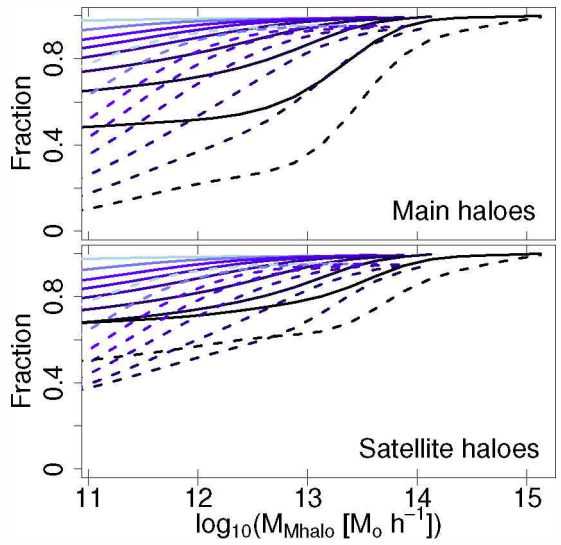

Figure 4: Fraction of accurately classified haloes, as a function of their virial masses. The gradient in the colour curves gets darker for environments with increasing numerical density. The original fractions are plotted with dashed curves, while results from the run with constraints correspond to solid curves.

per limit the 95th percentile of the projected distance from the main haloes centre to their farthest satellite $D_{Mh,max}$. An equivalent upper limit can be set up for the radial velocity differences between the main haloes and their satellites. We repeated the halo association algorithm in our data sample but considering these new constraints. Although a considerable fraction of fake positives survive, results show an improvement with respect to the previous implementation. To understand the impact of considering theses constraints, the Fig. 4 shows the fraction of accurately classified main haloes (upper panel) and satellites only (lower panel), as a function of their virial masses. The gradient in the colour curves gets darker for environments with increasing numerical density. The original fractions are plotted with dashed curves, while results from the run with constraints correspond to solid curves. In general, the accuracy in the association tends to increases with virial mass, but it decreases with environmental density in both main and satellite halos. The inclusion of the new constraints increases the fraction in all the cases. The worst reported values increases from ≈ 0.1 to ≈ 0.5 for main haloes, and from ≈ 0.4 to ≈ 0.7 for satellites.

In order to analyze options to improve the accuracy of haloes association, we selected from the simulation main haloes in dense environments with more than ten satellites and virial masses from $\approx 10^{13}$ to $\approx 10^{14}$ $M_{\odot}$, which correspond to the mass range of nearby clusters of galaxies like Fornax and Virgo. From this sample, we selected those presenting at least five fake positives corresponding to the same main halo, representing low-mass groups wrongly classified by the method as satellites of a more massive system. When running the substructure test from Colless & Dunn (1996), in approximately 30 per cent of them, the presence of substructure cannot be rule out at the 0.1 confidence level, and the proportion increases to nearly 50 per cent for the 0.2 confidence level. A control sample was chosen from the main haloes in similar environments and mass range, but presenting a fraction of real members to fake positives from 0.9 to 1.1. From these, in 1 % of the cases the presence of substructure cannot be rule out at the 0.1 confidence level. Hence, despite the percolation algorithm results in an overpopulation of satellites for massive haloes, subsequent analysis might improve the results.

4. Summary

We use the MDPL2 dark matter simulation to reproduce observational results from FoF analysis of observational surveys of galaxies. We summarize the preliminary results in the following.

- The fraction of contaminants in groups/clusters of galaxies can be large, particularly for massive haloes in high density environments.
- These contaminants can lead to uncertain observational parameters, like radial velocity dispersions and radial projected distributions.
- The use of constraints in the algorithm mitigates the occurrence of the fake positives, but it remains in a large percentage in high density environments.
- Subsequent analysis for substructure could help to detect some cases.

Acknowledgements: This research was funded with grants from Consejo Nacional de Investigaciones Científicas y Técnicas de la República Argentina (PIP 112-201101-00393), Agencia Nacional de Promoción Científica y Tecnológica (PICT-2013-0317), and Universidad Nacional de La Plata (UNLP 11-G150), Argentina.

References

Carlesi E., et al., 2017, MNRAS, 465, 4886
Colless M., Dunn A.M., 1996, ApJ, 458, 435
Crook A.C., et al., 2007, ApJ, 655, 790
Drinkwater M.J., Gregg M.D., Colless M., 2001, ApJ, 548, L139
Huchra J.P., et al., 2012, ApJS, 199, 26
Klypin A., et al., 2016, MNRAS, 457, 4340–4359
Kochanek C.S., et al., 2001, ApJ, 560, 566–579
Vale A., Ostriker J.P., 2006, MNRAS, 371, 1173

What do globular clusters tell us about isolated ellipticals? The case of NGC 6411

J.P. Caso[1,2], L.P. Bassino[1,2], T. Richtler[3] & R. Salinas[4]

[1] *Facultad de Ciencias Astronómicas y Geofísicas, UNLP, and Instituto de Astrofísica de La Plata (CONICET–UNLP), La Plata, Argentina*
[2] *Consejo Nacional de Investigaciones Científicas y Técnicas, Argentina*
[3] *Departamento de Astronomía, Universidad de Concepción, Concepción, Chile*
[4] *Gemini Observatory, La Serena, Chile*

Contact / jpcaso@fcaglp.unlp.edu.ar (JPC); lbassino@fcaglp.unlp.edu.ar (LB); tom@astro-udec.cl (TR); rsalinas@gemini.edu (RS)

Resumen / Esta contribución resume el estudio fotométrico de la galaxia elíptica aislada NGC 6411 y su sistema de cúmulos globulares (CGs). Nuestros resultados indican que la galaxia presenta un sistema de CGs pobre, con evidencias de bimodalidad en su distribución de color y una extensión aproximada de 65 kpc. Se ha detectado un exceso de CGs brillantes, fuertemente concentrados hacia la galaxia y de colores intermedios, lo cual podría indicar que NGC 6411 ha experimentado una fusión de edad intermedia.

Abstract / This contribution summarizes a photometric study of the isolated elliptical NGC 6411 and its globular cluster (GC) system. The results point to a poor GC system, with evidence of bimodality and an extension of about 65 kpc. An excess of bright GCs with intermediate colours and strongly concentrated towards the galaxy has been found, suggesting that NGC 6411 experienced an intermediate-age merger.

Keywords / galaxies: elliptical and lenticular, cD – evolution – star clusters: individual: NGC 6411

1. Introduction

Merging processes are thought to be the main source of mass accretion since $z \approx 2$ (e.g. van Dokkum et al., 2010). Due to the extremely low density environment they inhabit, isolated ellipticals (iEs) might have experienced less mergers, evolving more quietly. Both observational and numerical studies indicate that they have experienced a larger proportion of late mergers than Es in clusters, presenting bluer colours and lighter dark matter haloes (e.g. Niemi et al., 2010; Lacerna et al., 2016; Richtler et al., 2015). Hence, their study may reveal important clues about the evolution of galaxies. Globular clusters (GCs) formed under environmental conditions achieved during massive star formation episodes (Kruijssen, 2014), driven by galaxy mergers and interactions. This fact implies a direct connection between the formation of GC systems (GCS) and the evolution of their host galaxies.

We present preliminary results of the study of the GCS of the iE NGC 6411. It is a moderately bright galaxy with an estimated distance of 40 Mpc based on surface-brightness fluctuations (SBF Blakeslee et al., 2001). It hosted a Ia supernova (SN 1999da Filippenko, 1999), and spectroscopic analysis reveals that the luminosity in its inner region is dominated by a young and metal-rich population (González Delgado et al., 2015).

2. Observations and data reduction

The data set consists of a field observed with the GMOS camera at Gemini North (programme GN-2015A-Q-70, PI: L.P. Bassino), containing the galaxy, plus science verification observations (programme GN-2001B-SV-67) from the Gemini Observatory Archive (hereafter, CompF). The GMOS field of view is $\approx 5.5 \times 5.5$ arcmin^2. Both programmes were observed in g', r' and i' filters with similar exposure times.

The data reduction was carried out with the tasks from the GEMINI-GMOS package, within IRAF. Afterwards, the galaxy light of NGC 6411 was subtracted in order to improve point source detection. Because GCs usually present effective radii smaller than $R_{\rm eff} = 10$ pc (Brüns & Kroupa, 2012), they should be detected as point sources at the distance of NGC 6411. Hence, the software SExtractor (Bertin & Arnouts, 1996) was used to generate a source catalog of point sources. Then, PSF photometry was carried out with the DAOPHOT package within IRAF.

In order to calculate the photometric completeness, we added in the three filters 20000 artificial stars. We obtained completeness curves for different galactocentric radii, which were used in the analysis (for futher details, see Bassino & Caso, 2017).

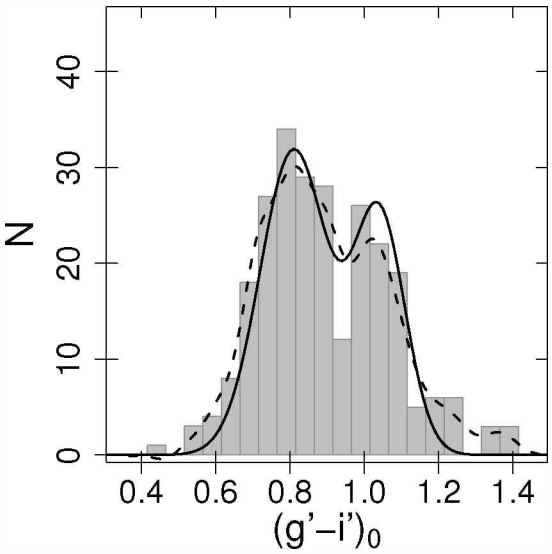

Figure 1: Background corrected colour distribution for GC candidates brighter than $i'_0 = 25.5$ mag. The dashed curve corresponds to a smoothed distribution obtained with a Gaussian kernel. The solid curve represents the fit result.

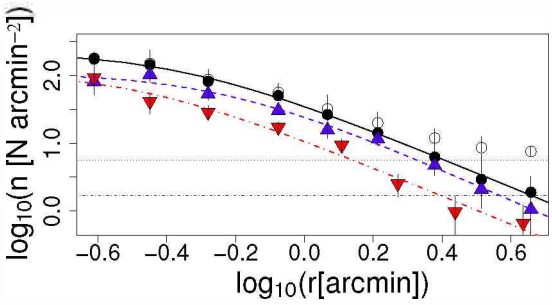

Figure 2: The filled symbols show the background corrected radial distribution for the entire sample (black circles), blue GCs (upwards triangles) and red ones (downwards triangles). The dashed-dotted horizontal line corresponds to the 30% of the contamination level.

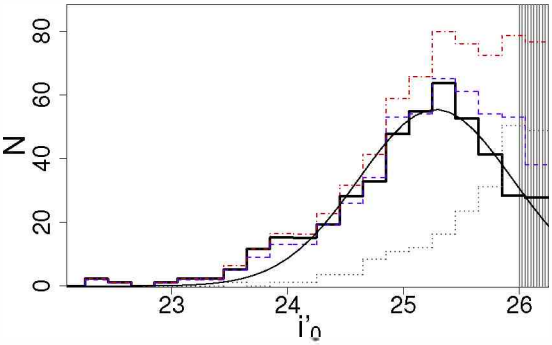

Figure 3: Raw (blue dashed histogram), completeness corrected (dashed-dotted red histogram) and background and completeness corrected (black solid histogram). The grey dotted histogram is the completeness corrected LF for the CompF field. The vertical lines indicate the luminosity range avoided due to completeness drop.

3. Results

The histogram in Fig. 1 corresponds to the background corrected colour distribution for all GC candidates brighter than $i'_0 = 25.5$ mag. The dashed curve indicates the smoothed distribution obtained with a Gaussian kernel. In order to determine whether the GCS colour distribution is better represented by two Gaussians instead of one, we used the Gaussian Mixture Method algorithm (GMM, Muratov & Gnedin, 2010). We statistically subtracted the contamination contribution from the GC candidates, repeating the process 25 times. In all cases GMM indicated a negative kurtosis and DD larger than 2, pointing to a bimodal distribution. The solid curve in the figure corresponds to the mean parameters for the sum of two Gaussians. From these results, we adopted $(g' - i')_0 = 0.95$ as the limit between blue and red GCs.

Open circles in Fig. 2 show the radial distribution for GC candidates brighter than $i'_0 = 26$, corrected for completeness. The dotted horizontal line indicates the contamination level. Filled symbols show the radial distributions corrected by completeness and contamination for all the GCs brighter than $i'_0 = 26$ (circles), blue GCs (upwards triangles) and red ones (downwards triangles). We fitted modified Hubble profiles to each radial distribution, indicated with a solid curve for the entire population, and dashed and dashed-dotted ones for the blue and red subpopulations, respectively. The dashed-dotted horizontal line corresponds to 30% of the contamination level, a value used in several studies to determine the GCS extension (e.g. Caso et al., 2017). We obtain ≈ 5 arcmin, i.e. ≈ 65 kpc.

The GC luminosity function (GCLF) of early-type galaxies can be represented by a Gaussian distribution with a turn-over magnitude (TOM) in the V-band of $M_{V,TOM} \approx -7.4$ mag (e.g. Jordán et al., 2007). Fig. 3 shows the GCLF of NGC 6411 in terms of the i' magnitude. The blue dashed histogram shows the raw GCLF, and the dashed-dotted red histogram is the completeness corrected GCLF. The grey dotted histogram is the completeness corrected LF for the CompF field, and the black solid histogram corresponds to the background and completeness corrected GCLF.

The solid curve is a Gaussian fitted to this latter histogram, resulting $i'_{0,TOM} \approx 25.3$. From Eqs. 1 and 2 of Bassino & Caso (2017), and the mean colour for the GC candidates, $(g' - i')_0 \approx 0.9$, the absolute magnitude of the TOM in the i'-band results $M_{i',TOM} \approx -8$ mag. Then, the distance modulus for NGC 6411 is $m - M \approx 33.3$ mag, in agreement with measurements of Blakeslee et al. (2001) from SBF and the fundamental plane. The numerical integration of the Gaussian indicates that the GCs brighter than $i'_0 = 26$ mag correspond to $\approx 85\%$ of the entire population. From this value and the integration of the Hubble modified profile fitted to the radial distribution, the total population of GCs results in ≈ 700 members.

An excess of GCs brighter than $i'_0 = 24$ mag can be seen in the GCLF. As we might be missing some bright objects with a strict photometric χ^2-selection, we relax these limits in the three filters. This results in an enlarged sample of GC candidates brighter than $i'_0 = 24$ mag, with marginal changes for the fainter ones (≈ 5

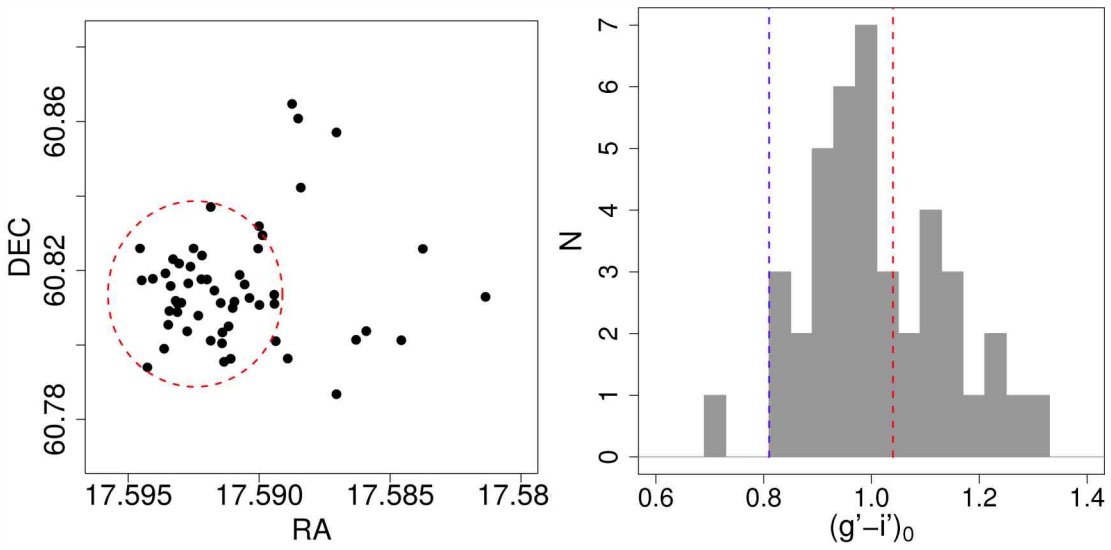

Figure 4: **Left panel:** projected spatial distribution for GC candidates brighter than $i'_0 = 24$ mag. The red dashed circle is centered in the galaxy and its radius is 1.5 arcmin. North is up, East to the left. **Right panel:** colour distribution for GC candidates brighter than $i'_0 = 24$ mag. The vertical lines correspond to the colour peaks for blue and red GCs from Fig. 1.

per cent). We visually inspect the brightness profile and residuals of these bright candidates, but no evidence of saturation or deficient subtraction was found.

The left panel of Fig. 4 shows the projected spatial distribution for the GC candidates brighter than $i'_0 = 24$ mag. The ≈ 76 per cent of these objects are located at galactocentric distances smaller than 1.5 arcmin. This proportion is larger than those corresponding to blue and red GCs fainter than $i'_0 = 24$ mag, at 95% confidence level. A Kolmogorov-Smirnov test (Kolmogorov, 1933) also points to different projected distributions for faint and bright GC candidates. The right panel of Fig. 4 shows the colour distribution for the bright GCs with galactocentric distances up to 1.5 arcmin. The vertical lines indicate the colour peaks for blue and red GC candidates from Fig. 1. The majority of the bright GCs present intermediate colours, around $(g' - i')_0 = 0.95$. From Bressan et al. (2012) SSP models, the bright GCs colours cannot simultaneously match the ages and metallicities derived by González Delgado et al. (2015) for the galaxy. We considered that the starburst that formed these bright GCs was driven by an older event.

4. Summary

- The galaxy does not present evidence of recent merger events, like tidal structures, after subtracting a smoothed surface brightness component.
- The total population of the GCS results in ≈ 700 members, implying a poor GCS, as usually found in low density enviroments.
- The TOM of the GCLF is in agreement with SBF studies, and the colour distribution resembles those found in typical bright Es, with old GCS.
- We detect an excess of bright GCs, strongly concentrated towards the galaxy. Their colours are mainly intermediate between those of blue and red GCs and do not agree with ages derived by the spectroscopic studies, pointing to an older event.

Acknowledgements: This research was funded with grants from Consejo Nacional de Investigaciones Científicas y Técnicas de la República Argentina (PIP 112-201101-00393), Agencia Nacional de Promoción Científica y Tecnológica (PICT-2013-0317), and Universidad Nacional de La Plata (UNLP 11-G150), Argentina. TR acknowledges support from CONICYT project Basal AFB-170002.

References

Bassino L.P., Caso J.P., 2017, MNRAS, 466, 4259
Bertin E., Arnouts S., 1996, A&AS, 117, 393
Blakeslee J.P., et al., 2001, MNRAS, 327, 1004
Bressan A., et al., 2012, MNRAS, 427, 127
Brüns R.C., Kroupa P., 2012, A&A, 547, A65
Caso J.P., Bassino L.P., Gómez M., 2017, MNRAS, 470, 3227
Filippenko A.V., 1999, IAU Circ, 7219
González Delgado R.M., et al., 2015, A&A, 581, A103
Jordán A., et al., 2007, ApJs, 171, 101
Kolmogorov A., 1933, Giornale dell'Istituto Italiano degli Attuari, 4, 83
Kruijssen J.M.D., 2014, Classical and Quantum Gravity, 31, 244006
Lacerna I., et al., 2016, A&A, 588, A79
Muratov A.L., Gnedin O.Y., 2010, ApJ, 718, 1266
Niemi S.M., et al., 2010, MNRAS, 405, 477
Richtler T., et al., 2015, A&A, 574, A21
van Dokkum P.G., et al., 2010, ApJ, 709, 1018

Distribución de galaxias en vacíos cósmicos

I.G. Alfaro[1], A.N. Ruiz[1,2] & D. García Lambas[1,2]

[1] *Instituto de Astronomía Teórica y Experimental, CONICET–UNC, Argentina*
[2] *Observatorio Astronómico de Córdoba, UNC, Argentina*

Contacto / geralfa_93@hotmail.com.ar

Resumen / En este trabajo se estudia la función de correlación bipuntual de galaxias dentro de las grandes regiones subdensas de la estructura en gran escala del Universo, a las cuales denominamos *voids*. Los datos utilizados corresponden a un catálogo sintético derivado de utilizar el modelo semi-analítico de Guo et al. en la simulación numérica Millennium. Los resultados obtenidos muestran que el pasaje entre el espacio real y el espacio de redshift tiene un efecto mucho menor en las correlaciones medidas en la distribución de galaxias dentro de los voids, que en las obtenidas para el catálogo completo. Esto implica que las primeras se encuentran menos afectadas por las distorsiones que provocan las velocidades peculiares de las galaxias.
Para disminuir aun más la diferencia entre las correlaciones, se construyó un perfil de velocidad radial media en función de la distancia al centro del void, y se lo restó a las velocidades peculiares de las galaxias que pueblan las regiones subdensas. El método de corrección alcanza su máxima efectividad entre 0.6 y 6 h^{-1}Mpc, dónde la diferencia en las correlaciones disminuyen hasta 50 %.

Abstract / The aim of this work is to study the two point galaxy-galaxy correlation function inside the largest subdense regions of the large-scale structure of the Universe, known as voids. We use a synthetic catalog, derived from the semi-analytic model of Guo et al. in the Millnnium Simulation. The results we obtained show that the differences between real and redshift space correlation functions, are much smaller for galaxies inside voids than for galaxies with the same luminosity but located elsewhere. This implies that galaxies inside cosmic voids are clearly less affected by distortions due to peculiar velocities.
In order to reduce even more the differences between both correlations, we compute a radial velocity profile of the expansion of voids. This profile was used to subtract from the peculiar velocity of galaxies the component related with the expansion of the void itself. We show that this correction has its maximum effectiveness at scales between 0.6 and 6 h^{-1}Mpc, where the difference in the real and redshift space correlation functions decreases up to 50 %

Keywords / cosmology: large-scale structure of universe — methods: statistical — galaxies: statistics

1. Introducción

Los catálogos observacionales constituyen una herramienta fundamental para el desarrollo de la astronomía en gran escala, sin embargo, en la actualidad no contamos con una medición precisa de las velocidades peculiares de las galaxias. Esto dificulta desafectar los mismos de las distorsiones propias del *espacio de redshfit* (Peebles, 1980), y acceder a la distribución real de los objetos (espacio real). Es por esto que, para estudiar la distribución que siguen las galaxias dentro de las grandes regiones subdensas del Universo, a las que denominamos *voids*, optamos por utilizar un catálogo de galaxias sintéticas, que nos permite alternar entre el espacio real y el espacio de redshift. Los datos empleados en este trabajo se obtuvieron de utilizar el modelo semi-analítico de Guo et al. (2011) en la simulación numérica Millennium (Springel et al., 2005).

A partir de estos datos elaboramos dos catálogos de galaxias sintéticas: uno correspondiente a la distribución real que tienen estos objetos (espacio real), y el otro, a la distribución distorsionada que describen las galaxias para un observador situado en $Z \to -\infty$ (espacio de redshift). Ambos catálogos solo consideran objetos con magnitudes $M_r \leq -17$ y cuentan con 6 150 491 galaxias.

2. Funciones de correlación en el espacio real y el espacio de redshift

Con el objetivo de diferenciar las propiedades de la distribución de galaxias en el espacio de redshift respecto a las del espacio real, medimos la función de correlación bipuntual de galaxias en ambos catálogos, utilizando el estimador de Davis & Peebles (1983), dado por:

$$\hat{\xi}_{DP}(r) = \frac{N_{rd}}{N}\frac{DD(r)}{DR(r)} - 1. \quad (1)$$

El estimador requiere un conjunto de puntos aleatorios con distribución uniforme e igual función de selección que la muestra de objetos, siendo N el número de objetos de la muestra, N_{rd} el número de puntos aleatorios, $DD(r)$ $(DR(r))$ la cantidad de pares galaxia-galaxia (galaxia-punto aleatorio) separados por una distancia en un dado intervalo centrado en r.

Las funciones de correlación obtenidas para los dos catálogos pueden observarse en la Fig. 1, la línea azul corresponde a las distribución de galaxias en el espacio

real, y la roja a la del espacio de redshift. A ambos resultados se les ajustó, mediante el método de cuadrados mínimos, una ley de potencias de la forma $(r/r_0)^{-\gamma}$, representadas con una línea punteada negra (espacio real) y una verde (espacio de redshift). Los valores obtenidos para r_0 y γ se muestran en la leyenda de la figura.

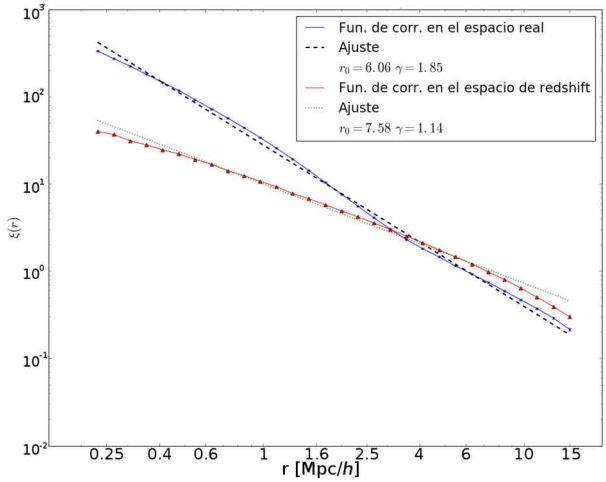

Figura 1: Funciones de correlación de galaxias (líneas continuas) en todo el espacio real (azul) y todo el espacio de redshift (rojo). Las líneas punteadas muestran la ley de potencias que mejor ajusta $\xi(r)$, sus parámetros son $r_0 = 6.06 \pm 0.21$ y $\gamma = 1.85 \pm 0.03$ en el espacio real (línea de puntos gruesos negra),y $r_0 = 7.58 \pm 0.32$ y $\gamma = 1.14 \pm 0.02$ en el de redshift (línea de puntos finos verde).

Los resultados muestran una gran diferencia entre las distribuciones de galaxias en los espacios real y de redshift, debido a las distorsiones que producen las velocidades peculiares en este último. Al pasar al espacio de redshift, los pares de galaxias cercanos disminuyen, los pares perdidos se recuperan en distancias mayores haciendo que las funciones se crucen.

Si bien no existe una única definición para los voids, todas coinciden en que son regiones extremadamente subdensas donde la interacción entre galaxias resulta mucho menos probable que en las regiones de mayor densidad. Esto implica que las distorsiones que producen las velocidades peculiares son menores dentro de estos ambientes, lo que debería reflejarse en sus funciones de correlación. Para identificar los voids, utilizamos en ambos espacios el método descrito en el trabajo de Ruiz et al. (2015), el cual define a los voids como regiones esféricas, donde el parámetro de densidad integrado es menor a -0.9. Los voids se identificaron utilizando galaxias brillantes ($M_r < -20.6$), para luego identificar las galaxias débiles ($-20.6 \leq M_r \leq -17$) en su interior. Encontramos 2018 voids en el espacio real y 2027 en el de redshift, en ambos casos los radios varían entre 7.5 y 26.5 h^{-1}Mpc.

Una vez identificados los voids y las galaxias que los pueblan, calculamos la función de correlación en su interior. Para ello fue necesario construir distribuciones esféricas uniformes de puntos aleatorios con los mismos centros y radios que los voids identificados. Como estamos interesados en estudiar la distribución de galaxias dentro de los voids, los pares $DD(r)$ y $DR(r)$ solo consideran objetos dentro de un mismo void. Los resultados obtenidos en ambos espacios pueden verse en la Fig. 2 junto con sus correspondientes ajustes.

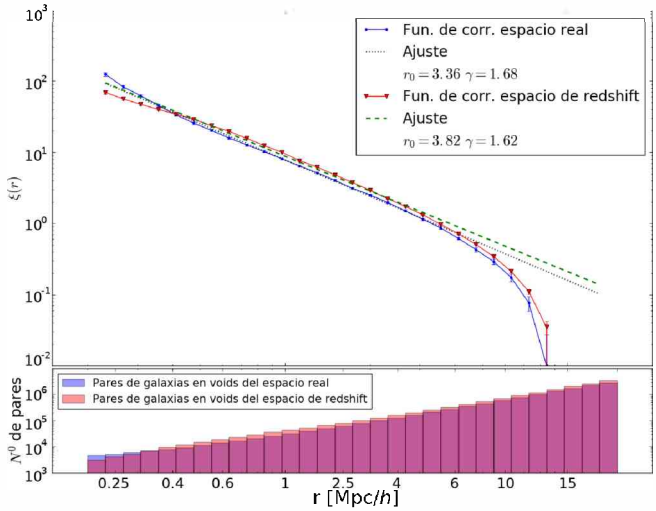

Figura 2: Arriba: Funciones de correlación (líneas continuas) medidas para galaxias dentro de los voids en el espacio real (azul) y de redshift (rojo). Las líneas punteadas muestran la ley de potencias que mejor ajusta $\xi(r)$, sus parámetros son $r_0 = 3.36 \pm 0.03$ y $\gamma = 1.68 \pm 0.01$ en el espacio real (línea de puntos gruesos negra),y $r_0 = 3.82 \pm 0.08$ y $\gamma = 1.62 \pm 0.03$ en el de redshift (línea de trazos finos verde). Abajo: Histogramas de pares de galaxias separados por una distancia r, en el espacio real (azul) y en el espacio de redshift (rojo).

Vemos que las diferencias entre las funciones de correlación de un espacio y otro disminuyen considerablemente comparadas con las de la distribución completa de galaxias, lo que muestra que en estas regiones el efecto de las velocidades peculiares es menor.

3. Corrección por outflow

La dinámica interna de un void se caracteriza por el desplazamiento de las galaxias que habitan su interior hacia las paredes del mismo (Paz et al., 2013), a este efecto lo denominamos *outflow*, y fue nuestro principal motivador para buscar establecer un perfil de velocidad radial media en función de la distancia al centro del void. Para calcularlo separamos los voids por tamaños, en cada muestra tomamos el radio del void más chico y lo dividimos en 30 intervalos iguales, luego descontamos de cada galaxia la velocidad de desplazamiento del void que habita (Ceccarelli et al., 2016), calculamos su velocidad radial y con ellas la velocidad radial media de cada intervalo. La información de todas las muestras puede verse en la Fig. 3, dónde los colores representan a que muestras de voids corresponden los datos.

El perfil medio de la velocidad radial en función de la distancia al centro del void se obtuvo usando los datos de todas las muestras. Tomamos intervalos de 1 h^{-1}Mpc de

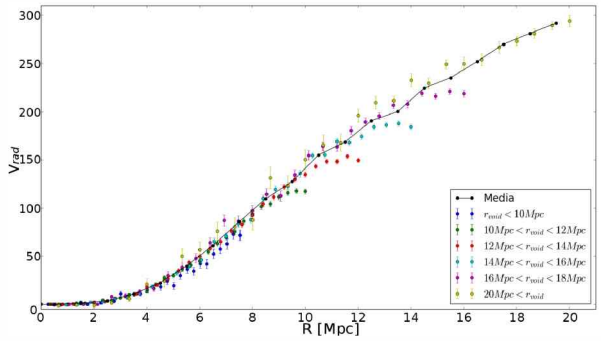

Figura 3: Velocidades radiales medidas en función de la distancia al centro del void, los distintos colores indican a que muestra de galaxias en voids corresponden. Los puntos y la línea negra muestran el perfil de velocidad radial media de las galaxias en el interior de los voids, construido usando la información de todas las muestras.

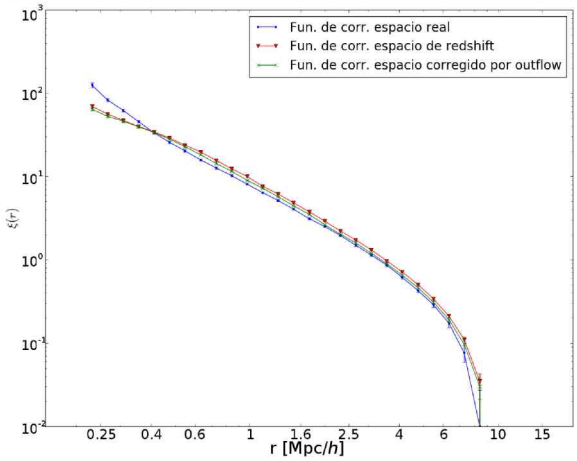

Figura 4: Funciones de correlación medida dentro de los voids del espacio real (línea azul), el espacio de redshift (línea roja) y el espacio corregido por outflow (línea verde).

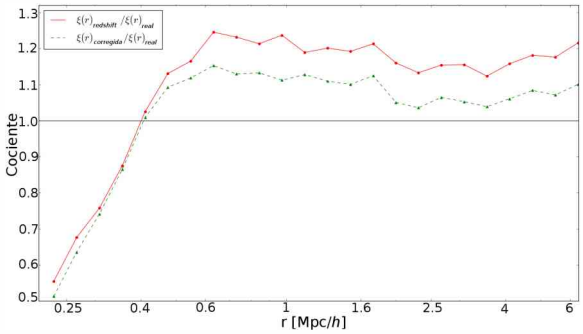

Figura 5: Cociente entre las funciones de correlación. La línea roja muestra el cociente entre la función de correlación medida dentro de voids del espacio de redshift y del espacio real, mientras que la línea verde muestra el cociente entre la función de correlación medidas dentro de voids del espacio corregido por outflow y del espacio real.

ancho y calculamos el valor medio de todos los puntos que caen dentro (puntos negros en la Fig. 3). Si bien no ajustamos una forma funcional al perfil, el mismo se obtiene interpolando los puntos negros.

Utilizando el perfil de velocidad radial es posible asignar a cada galaxia dentro de los voids del espacio de redshift una velocidad radial producto del *outflow* y utilizarla para modificar la posición de los objetos, teniendo en cuenta que solo la componente a lo largo de la línea de la visual se ve afectada por las velocidades peculiares. A esta nueva distribución de galaxias la denominamos *espacio corregido por outflow*.

El cálculo de la función de correlación en este nuevo espacio se hizo exactamente igual que dentro de los voids del espacio real y de redshift, con la diferencia que, al corregir solamente la dirección a lo largo de la línea de la visual, los voids en el espacio corregido por outflow toman forma elipsoidal, por lo que las distribuciones de puntos aleatorios tienen esta misma geometría. La correlación medida para el espacio corregido por outflow puede verse en la Fig. 4 (línea verde), junto con la obtenida dentro de los voids del espacio real (línea azul) y el espacio de redshift (línea roja). Para visibilizar mejor el efecto de la corrección, la Fig. 5 muestra con una línea roja el cociente entre la función de correlación del espacio de redshift y la del espacio real, y con una línea verde el cociente entre la correlación del espacio corregido por outflow y la del espacio real.

4. Conclusiones

Los resultados de las funciones de correlación medidas en todo el espacio real y todo el espacio de redshift muestran que la distribución de galaxias varía considerablemente entre uno y otro. Las distorsiones causadas por las velocidades peculiares desarman los pares de galaxias cercanos, los cuales se recuperan recién en escalas más grandes. Sin embargo, las diferencias entre las correlaciones disminuyen ampliamente cuando consideramos solo las galaxias que pueblan los voids.

Mediante un perfil de velocidad radial para el flujo coherente de objetos desde el interior del void hacia sus paredes, modificamos las posiciones de las galaxias dentro de los voids, disminuyendo aun más las diferencias entre las correlaciones. Este método de corrección alcanza su máxima efectividad entre $0,6h^{-1}$Mpc y $6h^{-1}$Mpc, donde las diferencias disminuyen hasta 50 %, aunque resulta inútil para recuperar los pares cercanos de galaxias, dado que las velocidades peculiares entre estos son producidas por la atracción gravitatoria que se ejercen, y no por un efecto de mayor escala, como es el *outflow*.

Referencias

Ceccarelli L., et al., 2016, MNRAS, 461, 4013
Davis M., Peebles P.J.E., 1983, ApJ, 267, 465
Guo Q., et al., 2011, MNRAS, 413, 101
Paz D., et al., 2013, MNRAS, 436, 3480
Peebles P.J.E., 1980, *The large-scale structure of the universe*
Ruiz A.N., et al., 2015, MNRAS, 448, 1471
Springel V., et al., 2005, Nature, 435, 629

Impact of radiation backgrounds on the formation of massive black holes

V.B. Díaz[1], D.R.G. Schleicher[1], S. Bovino[1], P. FFibla[1], R. Riaz[1], S. Vanaverbeke[2] & C. Olave[1]

[1] *Departamento de Astronomía, Facultad de Ciencias Físicas y Matemáticas, Universidad de Concepción, Concepción, Chile*

[2] *Centre for mathematical Plasma-Astrophysics, Department of Mathematics, KU Leuven, Heverlee, Belgium*

Contact / vdiazd@udec.cl

Resumen / La existencia de agujeros negros supermasivos de mil millones de masas solares a muy alto corrimiento al rojo, nos ha motivado a estudiar como estos objetos tan masivos se forman durante los primeros miles de millones de años después del Big Bang. Un modelo prometedor que se ha propuesto es el colapso directo de nubes de gas protogalácticas. Este escenario requiere altas tasas de acreción para crear rápidamente objetos masivos y la inhibición del enfriamiento que causa H_2 I, el cuál es importante en el proceso de fragmentación. Estudios recientes mostraron que, si usamos un fondo radiativo fuerte, el hidrógeno molecular se destruye, favoreciendo las altas tasas de acreción y por lo tanto formando objetos de muy alta masa. En este trabajo estudiamos el impacto de campos de radiación UV en una nube de gas primordial, usando el código *GRADSPH-KROME* para investigar el proceso de fragmentación en escalas de unidades astronómicas y por lo tanto la formación de los primeros agujeros negros supermasivos. Encontramos que para suprimir la formación de H_2 I es necesario un valor de J_{21} muy alto ($\sim 10^5$). Como se mostró en un trabajo previo, tales fondos de radiación fuertes son muy raros, por lo que el colapso directo es dificil de conseguir. Por lo tanto, este método dificilmente podría explicar la formación de los primeros agujeros negros supermasivos.

Abstract / The presence of supermassive black holes (SMBHs) of a few billion solar masses at very high redshift, has motivated us to study how these massive objects formed during the first billion years after the Big Bang. A promising model that has been proposed to explain this, is the direct collapse of protogalactic gas clouds. In this scenario, very high accretion rates are needed to form massive objects early on, and the suppression of H_2 I cooling is important in regulating the fragmentation. Recent studies have shown that if we use a strong radiation background, the hydrogen molecules are destroyed, favoring the high accretion rates and therefore producing objects of very high mass. In this work, we study the impact of UV radiation fields in a primordial gas cloud using the recently coupled code *GRADSPH-KROME* for the modeling of gravitational collapse, including primordial chemistry to explore the fragmentation in AU scales and hence the formation of thr first SMBHs. We found that, to suppress the formation of H_2 I, a very high value of J_{21} is required ($\sim 10^5$). As shown in a previous work, such strong radiation backgrounds are very rare, so that the direct collapse may be difficult to achieve. Therefore, this method could hardly explain the formation of the first SMBHs.

Keywords / black hole physics — cosmology: theory — early Universe — stars: formation — hydrodynamics

1. Introduction

More than 100 supermassive black holes (SMBHs) with masses of about 10^9 $M_\odot$ at very high redshift ($z \geq 6$) have been discovered in the last years through several surveys (Gallerani et al., 2017; Schleicher, 2018). The highest-redshift quasar observed are at $z = 7.54$ with a mass of 8×10^8 $M_\odot$ (Bañados et al., 2018), and another one at $z = 7.085$ with a mass of 2×10^9 $M_\odot$ (Mortlock et al., 2011). The formation of the first structures is not yet understood, and the formation of the first SMBHs is still an open question in cosmology. Among the models that have been proposed to explain the formation of SMBHs in the early universe, the direct collapse of protogalactic gas clouds (Loeb & Rasio, 1994; Bromm & Loeb, 2003; Shlosman et al., 2016) is a very promising scenario as it provides the most massive black holes seeds ($M \sim 10^5$ $M_\odot$), which can then grow at relatively moderate accretion rates to form SMBHs.

The formation of direct collapse black holes (DCBHs) requires an efficient accretion rate of gas to the central object ($\dot{M} \approx 1$ $M_\odot$ yr^{-1}), and the suppression of fragmentation of the cloud (Schleicher et al., 2013; Hosokawa et al., 2013). These conditions can be achieved if the gas collapses isothermally at a temperature of $T \approx 10^4$ K (Omukai et al., 2008). Such a collapse is possible if the gas has zero metallicity and the main cooling mechanism in the early universe (H_2 I cooling) is suppressed, due to an intense radiation background (Bromm & Loeb, 2003; Visbal et al., 2014).

In order to study the cooling process of the gas cloud, we need to include the chemical reactions involved in the formation (via gas-phase reactions) of H_2 I:

$$H + e^- \rightarrow H^- + \gamma, \quad (1)$$

$$H + H^- \rightarrow H_2 + e^-. \quad (2)$$

Once the first generation of stars (Pop III) are formed, they will irradiate the intergalactic medium

(IGM) with a UV flux and pollute it with metals, through supernova explosions, leading to the formation of the second generation of stars (Pop II). The UV flux produced by these stellar populations, can destroy H_2 I through the Solomon process (Eq. 3) and photo-detach electrons from H^- (Eq. 4).

$$H_2 + \gamma_{LW} \rightarrow H + H, \quad (3)$$

$$H^- + \gamma_{0.76} \rightarrow H + e^-. \quad (4)$$

Thus, massive primordial haloes of $10^7 - 10^8$ $M_\odot$ that formed in the early universe and irradiated by nearby star-forming regions of Pop II and Pop III at $z = 15-20$, are the most plausible cradles for DCBH formation. The available flux from star-forming regions is measured in units of J_{21}, with $J_{21} = 1$ corresponding to a flux of 10^{-21} erg cm^{-2} s^{-1} Hz^{-1} sr^{-1} at the Lyman limit. We assume for simplicity that the shape of the spectrum corresponds to that of a blackbody.

In a recent study, Latif et al. (2015) performed three-dimensional (3D) cosmological simulations to determine the critical UV flux $J_{21}^{\rm crit}$ above which H_2 I cooling is suppressed in protogalactic gas clouds of $10^7 - 10^8$ $M_\odot$, including the impact of X-ray ionization and realistic Pop II spectra. They found that $J_{21}^{\rm crit}$ for realistic Pop II spectra, is a few times 10^4 and weakly depends on the adopted radiation spectra in the range between $T_{\rm rad} = 2 \times 10^4 - 10^5$ K, and that the impact of X-ray ionization is negligible. These results suggest that DCBHs could be rarer than previously thought.

2. Computational Methods

In this work, we performed our simulations with the coupling of the Smoothed Particle Hydrodynamics (SPH) code *GRADSPH*[⋆] (Vanaverbeke et al., 2009) with the chemistry package *KROME*[⋆⋆] (Grassi et al., 2014). This combined code, called *GRADSPH-KROME*, allows us to include the chemistry and cooling in hydrodynamical simulations of the star forming gas. The code was previously employed by Riaz et al. (2018c) to explore the fragmentation process for the formation of binary systems. Here we explore the chemical conditions in the presence of different UV fluxes, to determine the flux that is required for an atomic collapse.

2.1. GRADSPH

GRADSPH is a parallel SPH code combined with a tree code gravity (TCG) method for evolving 3D self-gravitating, astrophysical fluids. It uses the standard M4-kernel or a cubic spline kernel with a compact support that contains particles within a smoothing sphere of size $2h_i$ (Price & Monaghan, 2007). This smoothing length is determined by $h_i = \eta (m_i/\rho_i)^{1/3}$, where η is a dimensionless parameter which determines the size of the smoothing length of the SPH particle given its mass and density. It is important to know that the mass contained within the smoothing sphere of each particle should be held constant. Also, *GRADSPH* implemented a second-order PEC (predict-evaluate-correct) scheme combined with an individual particle time stepping method, to solve the system of ordinary differential equations that updates the positions and velocities of the particles. The work presented in Riaz et al. (2018a) and Riaz et al. (2018b) are examples of simulations with *GRADSPH*.

2.2. Chemistry, cooling and UV background

The *KROME* package allows us to model chemical network in numerical simulations. In this work, we prepare a chemical network based on the network react_xrays provided by *KROME*, with the chemical reactions presented in Glover (2015a) and Glover (2015b), giving a total of 35 chemical reactions with 9 different chemical species (e^-, H^-, H I, H II, He I, He II, He III, H_2 I, H_2 II). The initial mass fraction of these chemical species are: $f_{\rm H} = 0.75$, $f_{\rm H_e} = 0.24899$, $f_{\rm H_2} = 10^{-3}$, $f_{\rm H} = 8.2 \times 10^{-4}$, $f_{\rm e^-} = 4.4 \times 10^{-8}$, while for the other species is set to zero.

2.3. Setup

Our spherical primordial gas cloud is modeled as a distribution of 507 443 SPH particles, with an initial temperature of 10^4 K. This cloud has a total mass of $M_{cloud} = 6.4 \times 10^6$ $M_\odot$, a radius of $R_{cloud} = 80.4$ pc and an initial density of $\rho_{cloud} = 2.0 \times 10^{-22}$ g cm^{-3}. Additionally, the gas is in solid body rotation with an angular velocity of $\omega = 2.3 \times 10^{-15}$ rad s^{-1}, and is turbulent with a Mach number $\mathcal{M} = 1.0$.

3. Results

Fig. 1 shows the thermal and species profiles for different strengths of the UV flux. We can see that, for the weaker value of J_{21}, the cooling due to H_2 I becomes effective, thus, the gas initialized with a temperature of 10^4 K, cools down to about 10^3 K. For $J_{21} = 10^4$ we can see that the H_2 I formation remains suppressed until a density of 10^{-20} g cm^{-3}, which illustrates the presence of two gas phases at the same density, similar to Fig. 3 in Latif et al. (2014). For the higher value of J_{21} we see that the gas is in an atomic state in which H_2 I remains suppressed, due to the high radiation, and it remains in a hot phase following the theoretical expectations. Nevertheless, the value of $J_{21}^{\rm crit}$ that we found is very high, in the range of $10^4 - 10^5$. Also, the right panel of Fig. 1 shows the evolution of H_2 I, H II and e^-. As they act as catalysts, we see that for the weaker values of J_{21}, the amount of e^- and H II is the same after the reaction and recombination have taken place, and their number densities are depleted due to the formation of H_2 I. For $J_{21} = 10^5$ the H II and e^- number densities increase and become constant, because the formation of H_2 I remains inhibited.

[⋆] `http://www.swmath.org/software/1046`

[⋆⋆] `http://www.kromepackage.org`

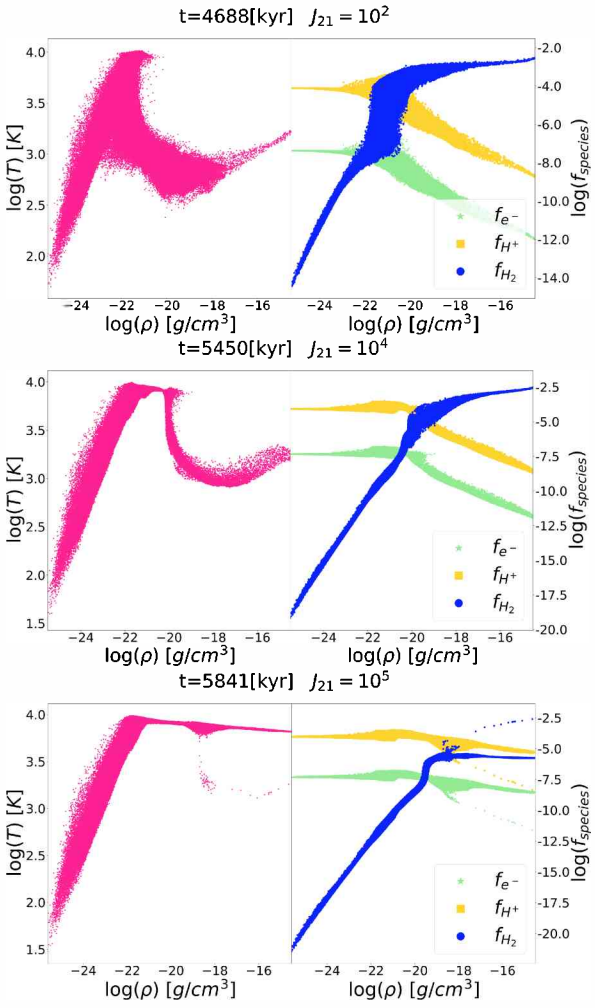

Figure 1: Thermal and species profiles (H_2 I in blue dots, H II in yellow squares and e^- in green stars) for different strengths of UV flux. Upper panel is for $J_{21} = 10^2$ middle panel for $J_{21} = 10^4$ and bottom panel for $J_{21} = 10^5$.

4. Conclusions and Outlook

To form a supermassive star or a massive black hole seed, we need high accretion rates, as shown in Schleicher et al. (2013) and Hosokawa et al. (2013), these high accretion rates requires large sound speeds and therefore a hot gas. For such a hot gas to remain atomic, we found a very high value of J_{21} is required, in the range of $10^4 - 10^5$. As shown in Dijkstra et al. (2014), these high values occur very rarely. This is because, in order to obtain the necessary high values of J_{21} for the DCBHs formation sites, we have to consider very nearby star-forming galaxies. The later includes galactic winds, that will produced metal enrichment suppressing the predicted DCBHs formation sites. Also, Dijkstra et al. (2014) estimated the DCBH number density (n_{DCBH}) finding at $z = 10$ that $n_{DCBH} \sim 10^{-3}$ cMpc^{-3} for $J_{21} = 30$, and $n_{DCBH} \sim 10^{-10} - 10^{-5}$ cMpc^{-3} for $J_{21} = 300$. Sugimura et al. (2014) re-estimate this value but for $J_{21} = 1400$, finding that $n_{DCBH} \sim 10^{-10} - 10^{-7}$ cMpc^{-3} at $z = 10$. We can see that n_{DCBH} decreases if we increase the value of J_{21} so, with our values of J_{21}, n_{DCBH} will be much lower. For comparison, the observed high redshift SMBH number density is $n_{SMBH} \sim 10^{-9}$ cMpc^{-3} at $z \sim 6$, thus we conclude that black hole formation via direct collapse is efficiently suppressed and could hardly explain all the observed quasars at high redshift. This is because the formation of DCBHs requires $n_{DCBH} \gg n_{SMBH}$ to provide a viable mechanism for SMBHs. However, we can consider alternative pathways to form SMBHs, such as collisions in primordial star clusters (Reinoso et al., 2018; Boekholt et al., 2018), among others (for additional formation channels see Latif & Ferrara, 2016 and Woods et al., 2018).

Acknowledgements: This research was partially supported by the supercomputing infrastructure of the NLHPC (ECM-02), also the authors acknowledge the Kultrun Astronomy Hybrid Cluster (projects Conicyt Programa de Astronomia FondoQuimal QUIMAL170001, Conicyt PIA ACT172033, and Fondecyt Iniciacion 11170268) for providing HPC resources that have contributed to the research results reported in this paper. VBD thanks to Conicyt for financial support on her master studies (CONICYT-PFCHA/MagísterNacional/2017-22171293). DRGS, SB, FF, CO, RR and VBD thank for funding via CONICYT PIA ACT172033. FF and VBD thank for funding through Fondecyt regular (project code 1161247). RR, CO, FF and DRGS thank for funding through the 'Concurso Proyectos Internacionales de Investigación, Convocatoria 2015' (project code PII20150171). DRGS and SB acknowledge funding through CONICYT project Basal AFB-170002.

References

Bañados E., et al., 2018, Nature, 553, 473
Boekholt T.C.N., et al., 2018, MNRAS, 476, 366
Bromm V., Loeb A., 2003, ApJ, 596, 34
Dijkstra M., Ferrara A., Mesinger A., 2014, MNRAS, 442, 2036
Gallerani S., et al., 2017, PASA, 34, e022
Glover S.C.O., 2015a, MNRAS, 451, 2082
Glover S.C.O., 2015b, MNRAS, 453, 2901
Grassi T., et al., 2014, MNRAS, 439, 2386
Hosokawa T., et al., 2013, ApJ, 778, 178
Latif M.A., Ferrara A., 2016, PASA, 33, e051
Latif M.A., et al., 2014, MNRAS, 443, 1979
Latif M.A., et al., 2015, MNRAS, 446, 3163
Loeb A., Rasio F.A., 1994, ApJ, 432, 52
Mortlock D.J., et al., 2011, Nature, 474, 616
Omukai K., Schneider R., Haiman Z., 2008, ApJ, 686, 801
Price D.J., Monaghan J.J., 2007, MNRAS, 374, 1347
Reinoso B., et al., 2018, A&A, 614, A14
Riaz R., Vanaverbeke S., Schleicher D.R.G., 2018a, A&A, 614, A53
Riaz R., Vanaverbeke S., Schleicher D.R.G., 2018b, MNRAS, 478, 5460
Riaz R., et al., 2018c, MNRAS, 479, 667
Schleicher D.R.G., 2018, ArXiv e-prints
Schleicher D.R.G., et al., 2013, A&A, 558, A59
Shlosman I., et al., 2016, MNRAS, 456, 500
Sugimura K., Omukai K., Inoue A.K., 2014, MNRAS, 445, 544
Vanaverbeke S., et al., 2009, Comput. Phys. Commun., 180, 1164
Visbal E., Haiman Z., Bryan G.L., 2014, MNRAS, 442, L100
Woods T.E., et al., 2018, arXiv e-prints, arXiv:1810.12310

AGN rate in cosmic filaments

N. Perez[1], V. Mesa[3], D. Galdeano[1,2], G. Coldwell[1,2], S. Alonso[1,2] & F. Duplancic[1,2]

[1] *Departamento de Astronomía y Geofísica, Facultad de Ciencias Exactas, Físicas y Naturales, UNSJ, Argentina*
[2] *Consejo Nacional de Investigaciones Científicas y Técnicas, Argentina*
[3] *Instituto Argentino de Nivología, Glaciología y Ciencias Ambientales, CONICET, Argentina*

Contact / noeliarocioperez@hotmail.com

Resumen / Filamentos, cúmulos, láminas y vacíos son las estructuras fundamentales de la red cósmica. Las galaxias en filamentos representan aproximadamente la mitad de la masa bariónica en el universo. Diferentes propiedades de las galaxias están correlacionadas con su ubicación dentro de la estructura filamentaria. En particular, la presencia de galaxias AGN requiere condiciones particulares del entorno. Los resultados sobre la dependencia de la tasa de AGN con respecto a la proximidad y a las propiedades filamentarias son presentados en este trabajo.

Abstract / Filaments, clusters, sheets and voids are the building blocks of the cosmic web and galaxies in filaments representing approximately half of the baryon mass in the universe. Different properties of galaxies are correlated with their location within the filamentary structures. In particular, the presence of AGN galaxies requires particular environmental conditions. The results on the dependence of the AGN rate with respect to the proximity and filament properties are shown in this work.

Keywords / galaxies: active — large-scale structure of the universe

1. Introduction

The baryonic matter in the Universe is arranged into dense compact clusters, elongated filaments, weak two-dimensional sheets and huge voids. The galaxy maps, given by the 3D distributions of galaxies, are visually dominated by filaments since they are the most outstanding structures of the cosmic web. Filaments are traced by galaxies and groups. Usually, all structural features are connected by filaments (Tempel et al., 2014).

Galaxy properties are dependent on the density environment (Dressler, 1980). Nevertheless, AGNs do not seem to follow the standard morphology-density relation and they are known to inhabit low density environment avoiding the galaxy cluster center (Montero-Dorta et al., 2009; Padilla et al., 2010; Coldwell et al., 2014). Instead, the AGNs tend to be located in regions where the probability of galaxy interactions is higher (Coldwell et al., 2014, 2017, 2018). Although Yang et al. (2018) analyzed the dependence of the black-hole growth with the environment considering filaments, the occurrence of AGNs in filamentary structures has not been yet explored in detail. The study of the fraction of AGN and the dependence of their properties with that from filament parameters will contribute to the understanding of the relation between these active objects and larger structures.

2. Data

For this study we used the catalog of filaments, obtained from the SDSS (DR8, Tempel et al., 2014). This catalog provides several properties such as filament length, luminosity calculated with galaxies within 0.5 and 1 h^{-1} Mpc from the filament axis (Lum 0.5 and Lum 1, respectively), number of galaxies closer than 0.5 and 1 h^{-1} Mpc from the filament axis (N 0.5 and N 1, respectively), etc. Besides, the information of the filament galaxy member is available.

The AGN catalog was built from the SDSS (DR8) galaxy catalog (Aihara et al., 2011), (York et al., 2000), in the redshift range $0.04 < z < 0.1$, by using the Kewley et al. (2001) selection criteria. The lower limit prevents that small, fixed-size apertures affects galaxy properties as derived by the fiber spectra, and the upper limit corresponds to the luminosity completeness limit for the SDSS sample. In addition, the AGN sample was split in Seyfert and LINER subsamples with the Kewley et al. (2006) including only galaxies with S/N > 2 for all the lines employed in the diagnostic diagrams used to discriminate Seyfert 2 from star-forming and LINER galaxies. In this work, both type of active objects are studied separately by considering the recent discussion referred to the LINER galaxies belonging to the AGN population (See Coldwell et al., 2017, for extra detials). With these conditions we obtained a sample composed of 5600 LINER and 5123 Seyfert galaxies.

3. Analysis

To study the AGN rate in cosmic filaments we cross-correlated the AGN sample with the galaxies associated to filaments longer than 5 h^{-1} Mpc. We found that 3087 Seyfert and 3796 LINER galaxies, representing the 60 % and 68 % respectively, are associated to filaments. Furthermore, we calculated the dependence of these fractions with different parameters representing the characteristics of filaments. The results shown in Table 1

indicate that the percentage of LINER galaxies associated to filaments is slightly higher than that for Seyfert ones, independently of their proximity to the nearest filament axis. However the percentages of both AGN samples are almost identical with respect to other filament parameters such as length, luminosities Lum 0.5 and Lum 1 given by the sum of the luminosities of observed galaxies that are closer to the filament axis than 0.5 and 1 $Mpch^{-1}$, respectively, and N 0.5 and N 1 given by the number of galaxies in the filament that are closer than 0.5 and 1 $Mpch^{-1}$, respectively.

On the other hand, we studied the relation between the AGN properties, $M_g - M_r$ colors and stellar age indicator given by the $D_n(4000)$ parameter (Balogh et al., 1999), and the distance to the filaments by considering the difference detected in Table 1 with respect to this parameter. Then, we estimated the fraction of Seyfert and LINER redder older than the mean of the whole galaxy sample, given by $M_g - M_r > 0.76$ and $D_n(4000) > 1.53$, respectively.

In order to understand the behavior of the active objects we used control samples, following the works of Coldwell et al. (2014, 2017, 2018), Vera et al. (2016) and Alonso et al. (2018) to compare the results with respect to galaxies belonging to filaments, without nuclear activity. Every control sample was built by matching the redshift, luminosity, color and stellar age with respect to the corresponding target sample as can be observed in Fig. 1. All the uncertainties were derived with a bootstrap re-sampling technique (Barrow et al., 1984). The results are presented in Figs. 2 and 3.

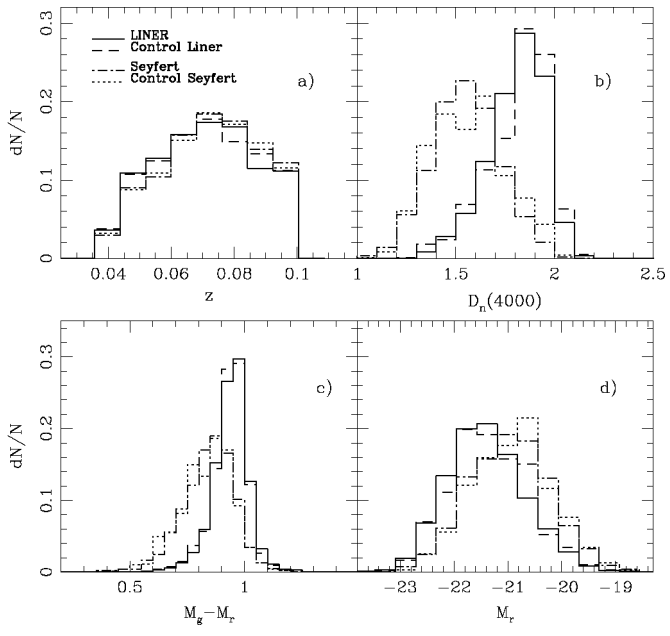

Figure 1: Normalized distributions of a) redshift, b) stellar age, c) galaxy colors and d) luminosity for LINER (solid line), Seyferts (dot-dashed line), and their respective control LINER (dashed) and control Seyfert (dotted) samples.

4. Results

- The percentages of LINER galaxies associated to filaments longer than 5 h^{-1} Mpc is slightly higher than that for Seyfert galaxies. This effect is noticeable in the fraction with respect to the distance from the filament axis, LINERs show an excess of 5% with respect to Seyfert galaxies. However, by using other filament parameters, such as filament length, luminosity and number of galaxies to generate subsamples, the percentage of Seyferts and LINERs remain similar. It is important to notice that the fractions corresponding to both control samples were included in Table 1, showing no significant difference with their respective target samples.
- The fractions of old, given by ($D_n(4000) > 1.53$), galaxies for AGN and control samples do not show a significant difference. In addition, the increasing fraction of old galaxies at smaller distances from the filaments is consistent with that expected for the morphology-density relation.
- In the case of galaxy color, both LINER and Seyfert samples show a different behavior with respect to their respective control samples. While the fractions of red AGN, (M_g–$M_r > 0.76$), is almost independent from the distance to the filaments, the control samples present a lack of red galaxies at higher distances in agreement with the color-density relation.
- The galaxy color is the more sensitive parameter to detect difference in the samples. In upcoming studies this will be used to perform more detailed analysis, aimed to shed light on the physical processes involved in the results related to the fraction of AGN in filamentary structures.

References

Aihara H., et al., 2011, ApJS, 195, 26
Alonso S., et al., 2018, A&A, 618, A149
Balogh M.L., et al., 1999, ApJ, 527, 54
Barrow J.D., Bhavsar S.P., Sonoda D.H., 1984, MNRAS, 210, 19P
Coldwell G.V., et al., 2014, MNRAS, 437, 1199
Coldwell G.V., et al., 2017, MNRAS, 467, 3338
Coldwell G.V., et al., 2018, MNRAS, 476, 2457
Dressler A., 1980, ApJ, 236, 351
Kewley L.J., et al., 2001, ApJ, 556, 121
Kewley L.J., et al., 2006, MNRAS, 372, 961
Montero-Dorta A.D., et al., 2009, MNRAS, 392, 125
Padilla N., Lambas D.G., González R., 2010, MNRAS, 409, 936
Tempel E., et al., 2014, MNRAS, 438, 3465
Vera M., Alonso S., Coldwell G., 2016, A&A, 595, A63
Yang G., et al., 2018, MNRAS, 480, 1022
York D.G., Adelman J., et al. A., 2000, AJ, 120, 1579

Characteristics of filaments	LINER [%]	Control LINER [%]	Seyfert [%]	Control Seyfert [%]
Distance from the nearest filament axis $< 0.5\ h^{-1}\ Mpc$	39.28±1.65	37.29±1.13	33.27±1.64	32.56±1.15
Distance from the nearest filament axis $< 1\ h^{-1}\ Mpc$	50.08±1.95	49.67±1.56	42.92±1.95	43.91±1.42
Distance from the nearest filament axis $< 2\ h^{-1}\ Mpc$	68.39±2.46	69.07±1.75	60.09±2.48	62.10±1.81
Galaxies in filaments 1σ longer than the mean	15.31±0.88	15.96±0.65	16.49±1.03	16.24±0.73
Galaxies in filaments with Lum0.5 1σ brighter than the mean	14.41±0.85	14.28±0.64	13.96±0.92	13.85±0.66
Galaxies in filaments with Lum1 1σ brighter than the mean	16.49±0.93	13.24±0.57	12.93±0.88	12.82±0.62
Galaxies in filaments with N0.5 1σ greater than the mean	13.20±0.80	13.59±0.58	14.67±0.95	13.56±0.65
Galaxies in filaments with N1 1σ greater than the mean	12.64±0.78	12.66±0.60	12.80±0.87	11.91±0.60

Table 1: Percentages of AGN and control galaxies associated to filaments longer than $5\ h^{-1}\ Mpc$.

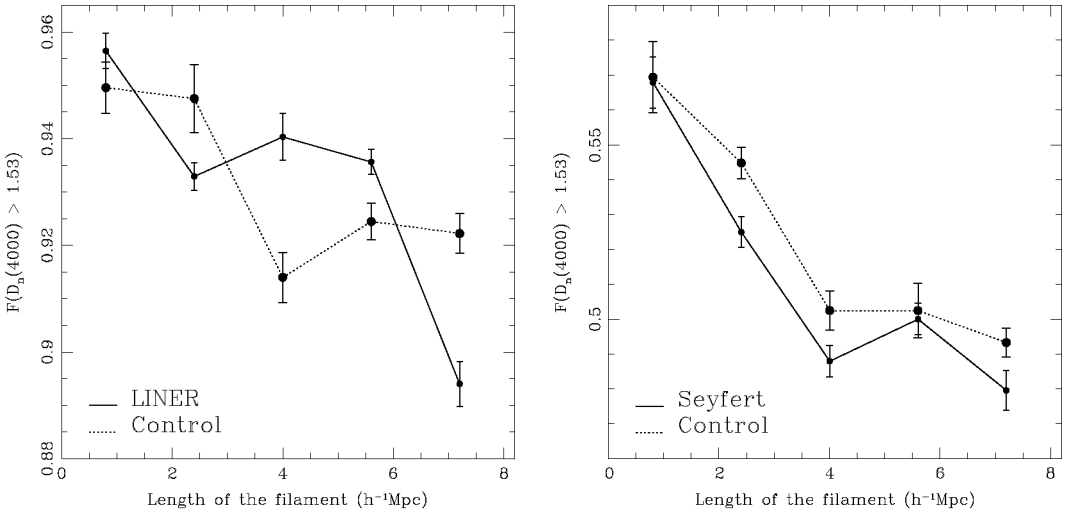

Figure 2: Fraction of old ($D_n(4000) > 1.53$) galaxies as a function of distance to the filament in $h^{-1}\ Mpc$, for LINERs (left) and Seyferts (right).

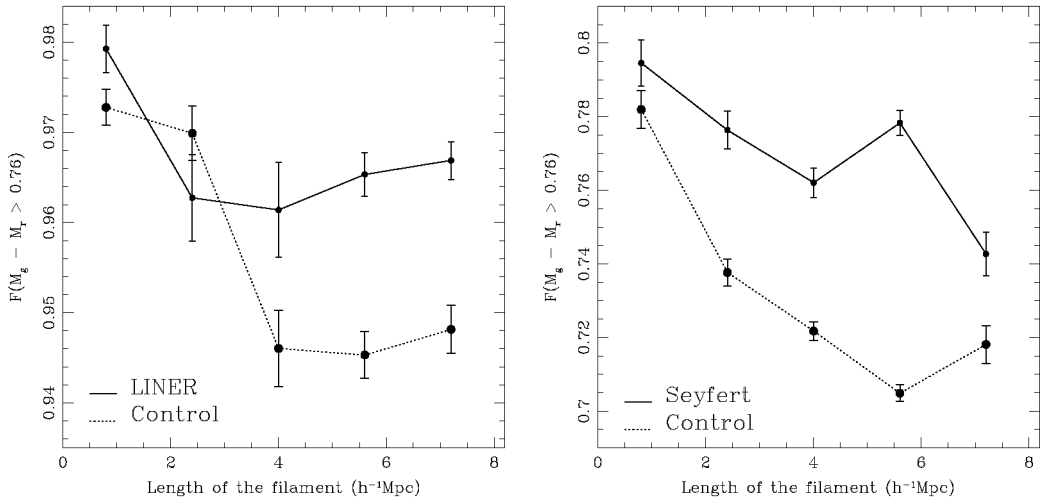

Figure 3: Fraction of red (M_g–$M_r > 0.76$) galaxies as a function of the distance to the filament in $h^{-1}\ Mpc$, for LINERs (left) and Seyferts (right).

Analysis of Lick Indices in early-type galaxies in the Virgo cluster

M.C. Scalia[1,2], A. Smith Castelli[1,2] & F. Faifer[1,2]

[1] *Instituto de Astrofísica de La Plata, CONICET–UNLP, Argentina*
[2] *Facultad de Ciencias Astronómicas y geofísicas, UNLP, Argentina*

Contact / mcscalia@fcaglp.unlp.edu.ar

Resumen / Los procesos involucrados en la formación y evolución de galaxias de tipo temprano están poco entendidos. El análisis de datos espectroscópicos homogéneos de una muestra de galaxias cercanas podría proporcionar pistas sobre dichos procesos, a través de la información relacionada con sus edades y contenido químico. En este trabajo presentamos un análisis preliminar del comportamiento de los índices de Lick en una muestra de 148 galaxias de tipo temprano, ubicadas en el Cúmulo de Virgo. Utilizamos datos espectroscópicos obtenidos del *Sloan Digital Sky Survey* (SDSS) DR14. A partir de este análisis, buscamos obtener edades e información química de estas galaxias que nos ayuden a trazar su trayectoria evolutiva. Este trabajo forma parte de la etapa inicial de la Tesis Doctoral de María Cecilia Scalia, desarrollada en la Facultad de Ciencias Astronómicas y Geofísicas de la Universidad Nacional de La Plata (Argentina)

Abstract / The processes involved in the formation and evolution of early-type galaxies are poorly understood. The analysis of homogeneous spectroscopic data of a sample of nearby galaxies might provide clues about such processes, via the information related to their ages and chemical content. In this work, we present a preliminary analysis of Lick Indices of a sample of 148 early-type galaxies located in the Virgo Cluster. We use spectroscopic data obtained from the Sloan Digital Sky Survey (SDSS) DR14. From this analysis we aim at obtaining age and chemical information of these galaxies that help us to trace their evolutionary path. This work is part of the ongoing doctoral studies of María Cecilia Scalia, developed at Facultad de Ciencias Astronómicas y Geofísicas of Universidad Nacional de La Plata (Argentina)

Keywords / Galaxies: abundances, Galaxies: clusters: individual: Virgo, Galaxies: elliptical and lenticular, cD

1. Introduction

The Virgo Cluster is the largest and extremely rich cluster in the neighborhood of the Local Group (Binggeli et al., 1985; Kim et al., 2014). For this reason, it offers a good opportunity to inquire into diverse properties. Early-type galaxies are good tracers of the design of the structures of the clusters and follow a color-magnitude relation (CMR) in which giant galaxies are redder than dwarfs (Bower et al., 1992; Smith Castelli et al., 2013; Roediger et al., 2017). Because of these characteristics, the exploration of age and chemical composition proves useful to find clues about the processes involved in the formation and evolution of this kind of galaxies. We will explore the behavior of Lick indices in a sample of early-type galaxies of the Virgo Cluster. Our aim is to determine if these indices can help to trace the age and chemical properties of the different substructures within this cluster.

2. The Virgo cluster

Following the works of Binggeli et al. (1987), hereafter B87, Davies et al. (2014), hereafter D14, review the current knowledge about Virgo sub-structures (see Fig. 1):

- *Sub-cluster A:* galaxies in this area are around but not exactly centered on NGC 4486 and have radial velocities of about 1300 km s^{-1}. B87 describes it as a rich sub-cluster in early-type galaxies and located at ∼17 Mpc (Gavazzi et al., 1999).
- *Sub-cluster B:* galaxies in this region are not exactly centered on M49, have radial velocities of about 1000 km s^{-1} and they are at ∼23 Mpc (Gavazzi et al., 1999). B87 describes this sub-cluster as rich in late-type galaxies and place it as falling into sub-cluster A from behind. D14 found no difference in the morphological mix of both sub-clusters.
- *W cloud:* galaxies here have a greater velocity (∼2200 km s^{-1}) than the sub-clusters. B87 states that W cloud is more distant than the sub-clusters and it is falling into them.
- *M cloud:* galaxies in this region are similar in distance and kinematic to those in the W cloud.
- *Southern extension:* it appears as a filamentary structure at the south of the cluster. Galaxies in this area are at about the same mean distance as the sub-clusters A and B, and B87 states that they are falling into these sub-clusters.

The W and M clouds are dominated by late-type galaxies, whereas the Southern extension lacks these galaxies (Kim et al., 2014) .

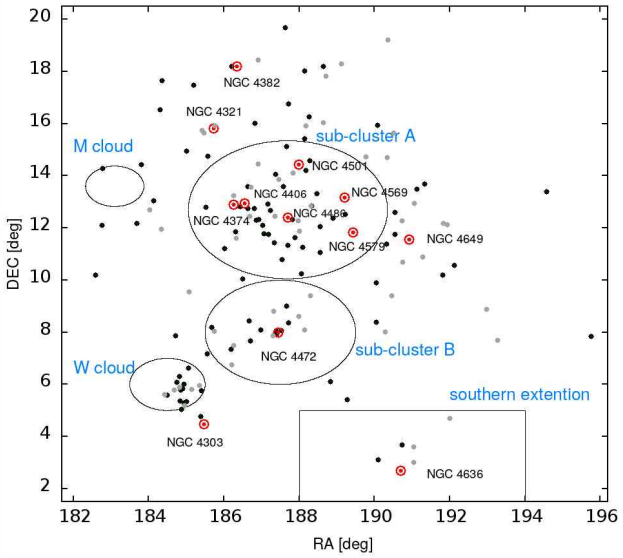

Figure 1: The projected spacial distribution of our sample. The black dots shows galaxies with S/N>20 and gray dots, those with 10<S/N<20. As a reference, we also add the brightest galaxies of Virgo (red dots). Black solid lines delineate the sub-structures identified in Virgo (B87).

3. The sample

The sample is composed of 125 early-type galaxies of the Virgo Cluster Catalogue (VCC, Binggeli et al., 1985) and 23 of the Extended Virgo Cluster Catalog (EVCC, Kim et al., 2014) that were not previously included in the VCC. They were selected because their spectra, obtained from the SDSS DR14, do not show perceptible emission lines and display a median signal-to-noise ratio S/N >10 (per Å). The spectrograph of SDSS uses optical fibers with a diameter of 3". Each fiber covers an equivalent physical region of ∼0.26 kpc diameter, considering the distance of 16.5 Mpc to the Virgo Cluster (Mei et al., 2007). This is the very central region of the galaxies.

4. The Lick indices

The Lick system (Worthey et al., 1994; Worthey & Ottaviani, 1997) defines absorption-line indices that can be used to derive the age and metallicity of stellar systems from low resolution spectra (∼9 Å), by comparing these indices with single stellar population models. In this work, these 25 indices were calculated using the LICK_EW code which is provided as part of the EZ_AGES package (Graves & Schiavon, 2008). The routine calculates errors of the indices following the equations given by Cardiel et al. (1998), and using the error spectra given by SDSS. The strength of absorption features in the spectra is measured in a bandpass centered on the feature of interest, flanked to the blue and red wavelengths by "pseudo-continuum" bandpasses. The average flux (in wavelength and magnitude units) is found for the flanking pseudo-continua, and a straight line is drawn between the centers of the pseudo-continua. The index is measured by integrating the ratio of the feature/continuum flux over the feature bandpass. We have calibrated these indices onto the commonly used Lick/IDS system, following the measurements obtained by Carson & Nichol (2010). In the near future, we will compare the values of the indices with those obtained from Simple Stellar Population (SSP) models. However, as a first step, it is interesting to explore their own intrinsic errors, if they trace structures within Virgo and if they can help to set, for example, the color scatter within the color-magnitude relation.

5. Results and future work

We compared the relative error of Lick indices with the S/N ratio in the spectroscopic data. Fig. 2 shows the sample of 148 galaxies with two indices: Hβ and Mgb. This is an important step before comparing the indices with models, to check how errors of absorption features translate into uncertainties in the derived mean age and metallicity of an old stellar population. The projected spacial distribution of our sample can be seen in Fig. 3, where the color is coded according to the index values, and shows the total variation of each index within the sample. There, triangles indicate galaxies with spectra with S/N<20. It can be seen how both indices seem to trace some of the sub-structures of the Virgo Cluster like, for example, the W cloud. The CMR defined by our sample is shown in Fig. 4. As a reference, we also show the Virgo sample of Chen et al. (2010) with black points. Colored points describe how Hβ and Mgb vary along the CMR. From this work in progress, we aim at obtaining the age, metallicity and α-enhancement ratio of these galaxies, which will help us trace their evolutionary path. To determine this parameters, we will compare several observed Lick indices with simple stellar populations models, that have a variable [α/Fe] abundance ratio (Thomas et al., 2003).

Acknowledgements: We thank both the LOC and SOC for their hard work and for making possible, by means of financial support, the participation to this meeting of many young researchers and students. We also thank the institutions that support our work: CONICET and UNLP (Argentina), the language office of FCAG, and the editors and referees of the BAAA.

References

Binggeli B., Sandage A., Tammann G., 1985, AJ, 90, 1681
Binggeli B., Tammann G.A., Sandage A., 1987, AJ, 94, 251
Bower R., Lucey J., Ellis R., 1992, MNRAS, 254, 601
Cardiel N., et al., 1998, A&AS, 127, 597
Carson D.P., Nichol R.C., 2010, MNRAS, 408, 213
Chen C.W., et al., 2010, ApJS, 191, 1
Davies J.I., et al., 2014, MNRAS, 438, 1922
Gavazzi G., et al., 1999, MNRAS, 304, 595
Graves G.J., Schiavon R.P., 2008, ApJS, 177, 446
Kim S., et al., 2014, ApJS, 215, 22
Mei S., et al., 2007, The Astrophysical journal, 655, 144
Roediger J.C., et al., 2017, ApJ, 836, 120
Smith Castelli A.V., et al., 2013, ApJ, 772, 68
Thomas D., Maraston C., Bender, 2003, MNRAS, 339, 897
Worthey G., Ottaviani D.L., 1997, ApJS, 111, 377
Worthey G., et al., 1994, ApJS, 94, 687

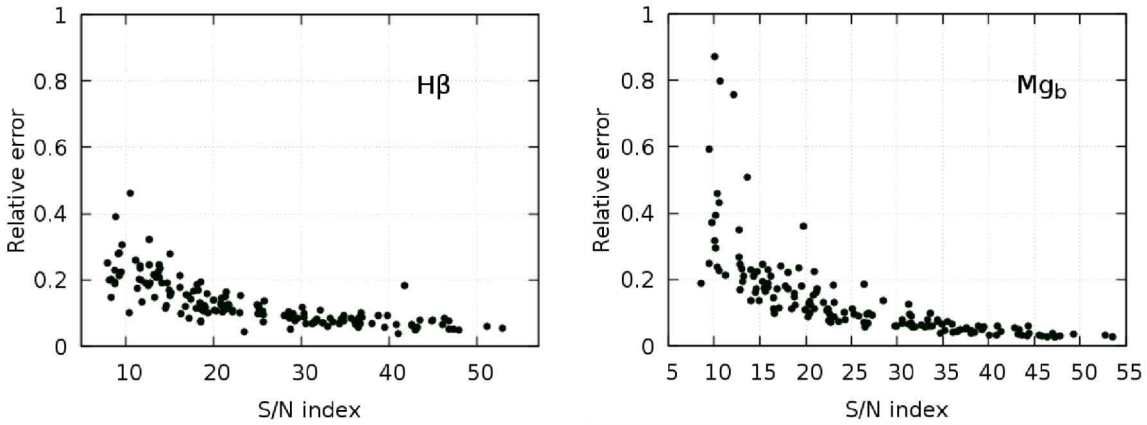

Figure 2: The relative error of Lick indices compared with the S/N ratio in the spectroscopic data of our sample.

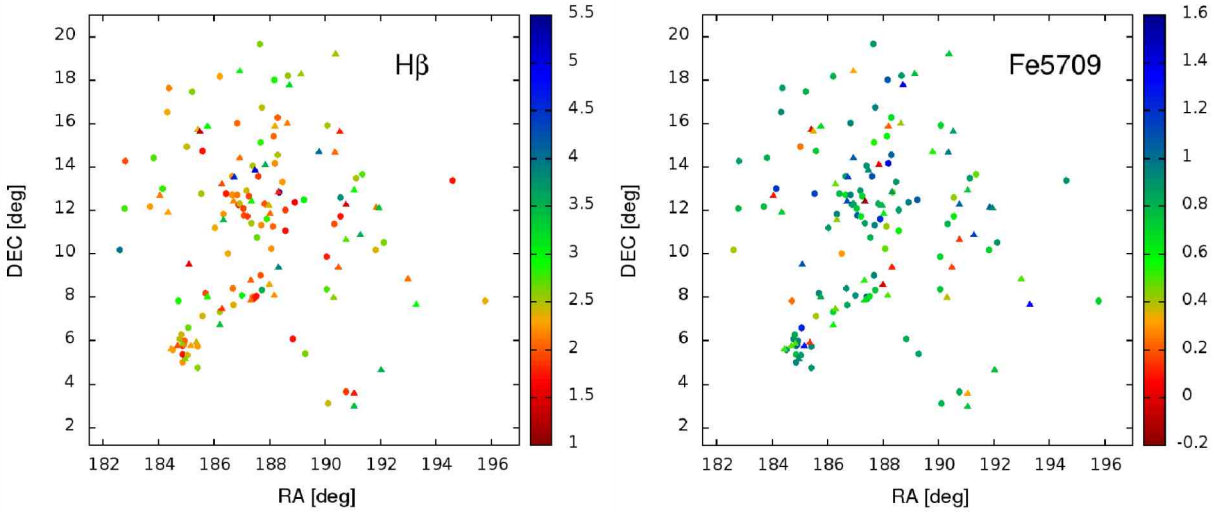

Figure 3: Projected spacial distribution of our sample, color coded according to the values of the Hβ and Mgb indices. The triangles indicate galaxies with spectra with S/N<20.

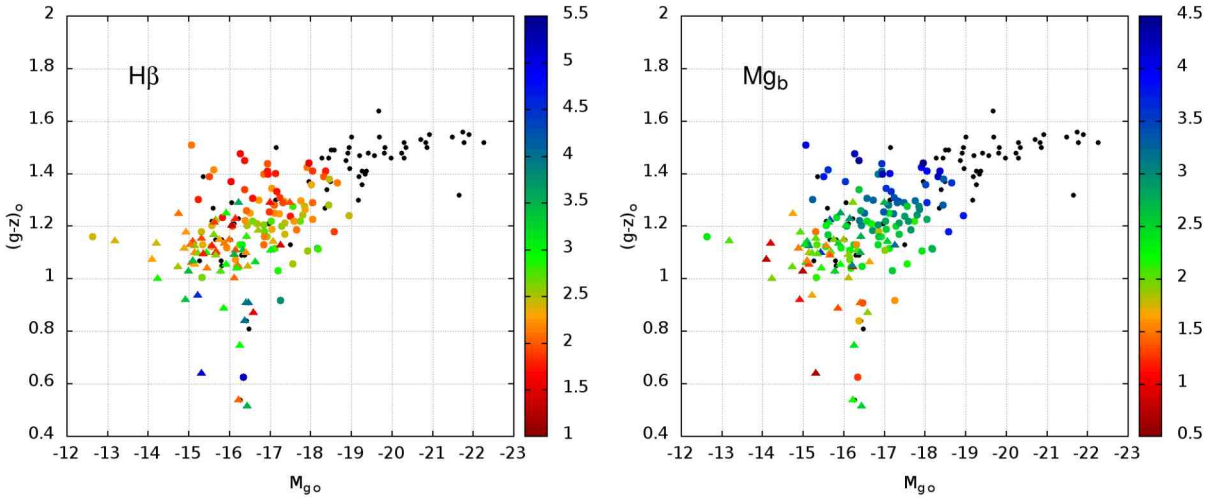

Figure 4: The color-magnitude relation (CMR) defined by our sample and the sample of Chen et al. (2010) (black points). Colored points show how Hβ and Mgb vary along the CMR. Triangles indicate galaxies with spectra that have S/N<20.

Wide-field study of a heavily populated globular cluster system: the case of NGC 1172

A.I. Ennis[1,2], L.P. Bassino[1,2], M. Gómez[3] & J.P. Caso[1,2]

[1] *Facultad de Ciencias Astronómicas y Geofísicas, UNLP, Argentina*
[2] *Instituto de Astrofísica de La Plata, CONICET–UNLP, Argentina*
[3] *Departamento de Ciencias Físicas, Universidad Andrés Bello, Santiago, Chile.*

Contact / ennis.ana@gmail.com

Resumen / Se presentan los resultados preliminares del estudio fotométrico de campo amplio del sistema de cúmulos globulares (SCG) de la galaxia elíptica de campo NGC 1172, realizado a partir de imágenes obtenidas con GMOS en Gemini Sur en los filtros g', r' e i'. El objetivo del trabajo es caracterizar el SCG de la galaxia para revelar indicios sobre su formación y evolución.

Abstract / Preliminary results of the photometric wide-field study of the globular cluster system (GCS) of the field elliptical galaxy NGC 1172 are presented. The images used were obtained with GMOS in Gemini South in the filters g', r' and i'. The aim of this work is to characterize the GCS of the host galaxy in order to find clues about its formation and evolution.

Keywords / galaxies: star clusters: general — galaxies: elliptical and lenticular, cD — galaxies: evolution

1. Introduction

Elliptical galaxies are thought to have accreted most of their material through minor mergers since z $\sim$ 2 (van Dokkum et al., 2010). This implies that elliptical galaxies in dense environments have undergone different growth mechanisms than the few ones found in low-density habitats (Richtler et al., 2015). Because of this, elliptical galaxies in groups are an interesting subject of study, since they provide a suitable scenario for examining evolutionary processes in action (Bassino & Caso, 2017). Massive early-type galaxies (ETGs) usually present rich globular cluster systems (GCS), where clues about their evolutionary history can be found since they are good tracers of the star formation history (e.g. Pota et al., 2015; Caso et al., 2019) and also, of the gravitational interactions that a galaxy might experience (e.g. Escudero et al., 2015). Accretion processes or mergers may leave traces in the shape of disruptions in the GCS' spatial distribution, or even in the presence of younger populations when the interaction causes a star formation event (e.g. Caso et al., 2015; Bassino & Caso, 2017).

One of the most studied characteristics of GCSs both in the Milky Way and in other galaxies, is the bimodality usually found in their colour distribution. Though this separation could be an effect of an age gap, spectroscopic studies have shown the biggest difference between these two subpopulations lies in their metal content (Brodie et al., 2012). Despite globular clusters (GCs) being all metal poor, the "blue" subpopulation shows a significantly lower value of metallicity than the "red" one. Recent studies have found in some ETGs a third subpopulation of GCs with intermediate colours (Sesto et al., 2018). These clusters are probably young, possibly created due to a merger that involved enough gas to trigger star formation.

NGC 1172 is an elliptical galaxy that presents no bright companions within a 30′ radius, though it has been suggested it could be a member of the NGC 1209 group (Sandage, 1978). Previous photometric studies of its GCS performed with ACS/WFC images (Cho et al., 2012) found a rich population of clusters, with a specific frequency of $S_N \sim 9$, which is significantly high for a galaxy of this magnitude (Harris et al., 2013). In this work, we perform a wide field photometric study of the GCS in order to cover its full extension, and look for evidences of interactions in its properties.

2. Observations and Photometry

2.1. Processing

Figure 1 shows the observed fields. The CCD images for the central field and the two adjacent ones were obtained in programmes GS-2016B-Q-37 (PI: Caso) and GS-2017B-Q-38 (PI: Caso), respectively. All fields were observed in the g', r' and i' filters with a 2×2 binning, resulting in a scale of 0.146 arcsecpixel^{-1}. From the Gemini Observatory Archive (GOA*), calibration images were obtained in order to carry out bias and flat-field corrections using Gemini routines within IRAF. The images of each filter are slightly dithered so that the combination of them removes bad pixels and cosmic rays, as well as the gaps between CCDs.

*http://archive.gemini.edu/

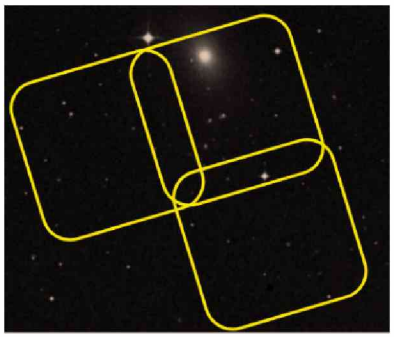

Figure 1: SDSS image with the observed fields, both central and adjacent, marked with yellow lines.

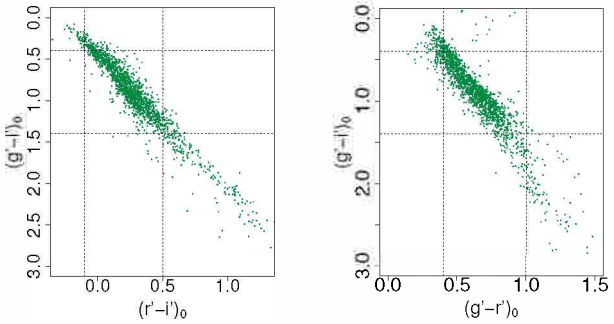

Figure 2: Colour-colour diagrams for all SExtractor point-like sources. Dashed lines show the limits used for the selection.

2.2. Source Selection

We used SExtractor (Bertin & Arnouts, 1996) to identify sources in the three fields, combining the selection obtained using the *gaussian* and *mexhat* filters to ensure the highest possible level of completeness. The selection criteria to obtain a catalog of point-like sources was CLASS STAR > 0.5. The final photometry was performed using a PSF fitting for which we used the task ALLSTAR, which gives for each object a goodness fit. These were used to refine the selection.

2.3. Photometric Calibration

The photometry was transformed to the standard system following the guidelines described in the Gemini observatory website**. We used observations of the E2-A standard star field (Smith et al., 2002) taken in the same programmes. In addition to this, a correction for galactic extinction was also applied, using the absorption coefficients provided by Schlafly & Finkbeiner (2011).

2.4. GC selection

Once the calibrated and corrected magnitudes for all point-sources were obtained, a selection was made using the colour criteria that is typical of GC populations (Faifer et al., 2011). In Fig. 2 the dashed lines show the chosen limits, $0.4 < (g' - i')_0 < 1.4$, $0.4 < (g' - r')_0 < 1$ and $-0.1 < (r' - i')_0 < 0.5$. In Fig. 3, we present the colour-magnitude diagram with no magnitude limits established yet, since the completeness test is currently being carried out. With this selection, we obtain a total of ~ 1300 GCs. For a more accurate estimation and considering the usual depth reached in GMOS images for this filter, we considered a limit in magnitude of $i'_0 = 25$, which leaves us with ~ 500 candidates.

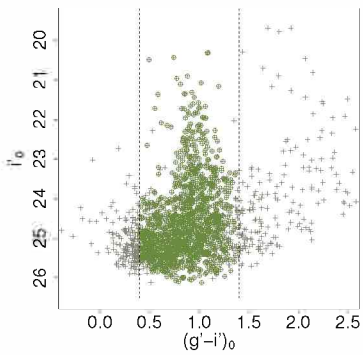

Figure 3: Colour magnitude diagram where grey crosses represent all SExtractor point-like sources, and green circles represent those that fulfill the colour criteria.

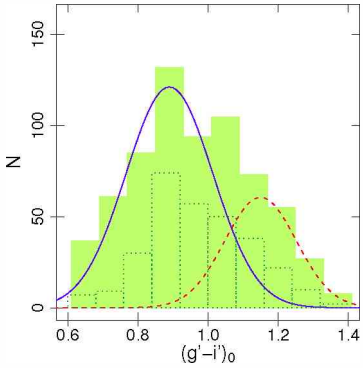

Figure 4: Colour distribution for candidate GCs with $i'_0 < 25$ (green histogram). The superimposed empty histogram shows the distribution for the central field only. Blue and red lines show Gaussian fits with the typical mean colours for the "blue" and "red" subpopulations.

3. Results

3.1. Colour distribution

Fig. 4 shows the colour distribution for all the candidate GCs with $i'_0 < 25$. As mentioned before, in GCSs this distribution is expected to show a clear bimodality. Though in this case two peaks at the usual colours are found, $(g'_0 - i'_0) \sim 0.85$ and $(g'_0 - i'_0) \sim 1.15$, there is also a significant over density at around $(g'_0 - i'_0) \sim 1.05$. Even if we subtract the GCs present in the adjacent fields, it can be seen that the central one also shows this apparent third subpopulation which does not fall into neither the "red" nor the "blue" ones. Though further analysis is required to confirm this, the fact that we find GCs that do not belong to neither of the classic subpopulations, could mean that we are in the presence of a younger

**https://www.gemini.edu/

subpopulation, possibly born from a starburst event as a consequence of a merger or accretion process.

3.2. Radial distribution

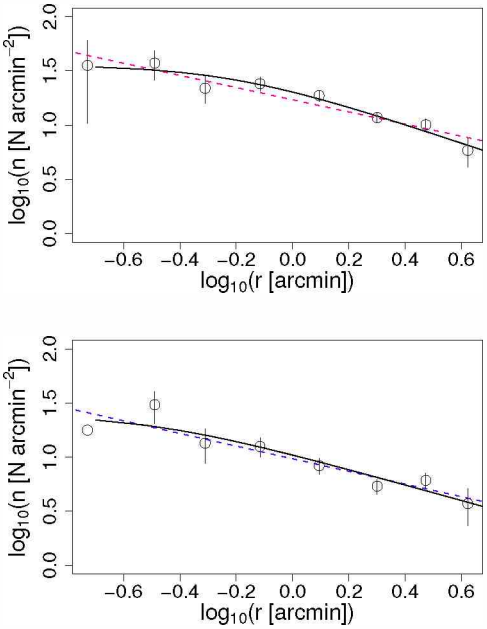

Figure 5: Radial distribution for candidate GCs with $i'_0 < 25$ in the central field (top panel) and for the blue subpopulation in the central field (lower panel). The open circles represent the corresponding histogram points. In both cases, dotted lines represent a power law fit, and solid lines, a Hubble-Reynolds law fit.

In Fig. 5 we show the radial distribution for those GCs situated in the central field, and for the blue subpopulation in particular. In order to consider the effect that can be seen in the regions closer to the galactic centre, where both the saturation in the image and the physical effect of stronger tidal forces cause a decrease in the amount of GCs, a Hubble-Reynolds law was fitted (Dirsch et al., 2003). The results point to an apparent agreement between the complete sample and the blue subpopulation (GCs with $(g' - i')_0 < 0.95$), though further analysis is currently being performed over this field and the adjacent ones.

3.3. Effective radii distribution

In Fig. 6 we show the effective radii distribution for candidate GCs, as obtained from the analysis performed on the ACS/WFC images. The values for the radii were obtained with ISHAPE (Larsen, 1999). The peak of the distribution is $0.026''$, which corresponds to ~ 3 pc for a distance of 21 Mpc (Tonry et al., 2001). This value is in agreement with results for the Virgo cluster from Jordán et al. (2005).

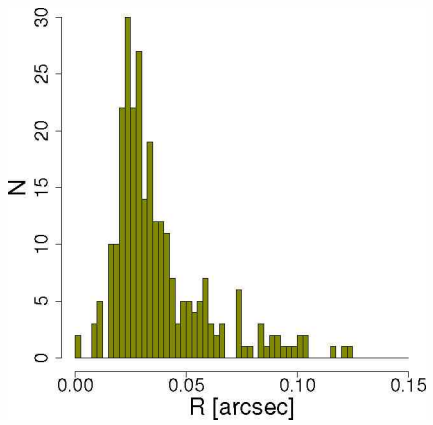

Figure 6: Effective radii distribution for candidate GCs from our ACS/WFC photometry.

Acknowledgements: This work was funded with grants from Consejo Nacional de Investigaciones Científicas y Técnicas de la República Argentina, Agencia Nacional de Promoción Científica y Tecnológica, and Universidad Nacional de La Plata, Argentina. Based on observations obtained at the Gemini Observatory (GS-2013B-Q-37), which is operated by the Association of Universities for Research in Astronomy, Inc., under a cooperative agreement with the NSF on behalf of the Gemini partnership: the National Science Foundation (United States), the National Research Council (Canada), CONICYT (Chile), the Australian Research Council (Australia), Ministério da Ciência, Tecnologia e Inovação (Brazil) and Ministerio de Ciencia, Tecnología e Innovación Productiva (Argentina). This research has made use of the NASA/IPAC Extragalactic Database (NED) which is operated by the Jet Propulsion Laboratory, California Institute of Technology, under contract with the National Aeronautics and Space Administration. This research has made use of the SIMBAD database, operated at CDS, Strasbourg, France.

References

Bassino L.P., Caso J.P., 2017, MNRAS, 466, 4259
Bertin E., Arnouts S., 1996, A&AS, 117, 393
Brodie J.P., et al., 2012, ApJ, 759, L33
Caso J.P., Bassino L.P., Gómez M., 2015, MNRAS, 453, 4421
Caso J.P., et al., 2019, MNRAS, 483, 4371
Cho J., et al., 2012, MNRAS, 422, 3591
Dirsch B., Richtler T., Bassino L.P., 2003, A&A, 408, 929
Escudero C.G., et al., 2015, MNRAS, 449, 612
Faifer F.R., et al., 2011, MNRAS, 416, 155
Harris W.E., Harris G.L.H., Alessi M., 2013, ApJ, 772, 82
Jordán A., et al., 2005, ApJ, 634, 1002
Larsen S.S., 1999, A&AS, 139, 393
Pota V., et al., 2015, MNRAS, 450, 1962
Richtler T., et al., 2015, A&A, 574, A21
Sandage A., 1978, AJ, 83, 904
Schlafly E.F., Finkbeiner D.P., 2011, ApJ, 737, 103
Sesto L.A., et al., 2018, MNRAS, 479, 478
Smith J.A., et al., 2002, AJ, 123, 2121
Tonry J.L., et al., 2001, ApJ, 546, 681
van Dokkum P.G., et al., 2010, ApJ, 709, 1018

Chemodynamics in Blue Compact Dwarf galaxies: II Zw 33 and Mrk 600

F. Campuzano-Castro[1,2], G.F. Hägele[1,2], G. Bosch[1,2], V. Firpo[3], M. Cardaci[1,2], D. Muthukrishna[4] & N. Morrell[5]

[1] *Instituto de Astrofísica de La Plata, CONICET–UNLP, Argentina*
[2] *Facultad de Ciencias Astronómicas y Geofísicas, UNLP, Argentina*
[3] *Gemini Observatory, La Serena, Chile*
[4] *University of Cambridge, Cambridge, United Kingdom*
[5] *Las Campanas Observatory, Carnegie Observatories, La Serena, Chile*

Contact / fedecampu@gmail.com

Resumen / Realizamos un estudio cinemático de cinco regiones de formación estelar pertenecientes a dos galaxias enanas compactas azules: II Zw 33 and Mrk 600, utilizando datos espectroscópicos de alta resolución obtenidos con el espectrógrafo MIKE del telescopio Clay. Los espectros presentan líneas de emisión con perfiles muy complejos revelando multiples componentes Gaussianas. Con el propósito de analizar la cinemática de estas regiones de formación estelar, desarrollamos un programa en Python, basado en el paquete de minimización de mínimos cuadrados no lineal y ajuste de curvas (*LMFit*), y utilizamos un método estadístico, para analizar la bondad de la inclusión de una nueva componente gaussiana en el modelo. Se estimaron las propiedades físicas del gas (densidades y temperaturas electrónicas), abundancias químicas iónicas y totales de diversas especies atómicas y el grado de ionización en cada región de formación estelar.

Abstract / We performed a kinematic study of five star-formation regions belonging to two Blue Compact Dwarf galaxies: II Zw 33 and Mrk 600, using high resolution spectroscopic data obtained with the MIKE spectrograph mounted at the Clay telescope. The spectra present very complex emission-line profiles showing multiple Gaussian components. In order to analyze the kinematics of these star-forming regions we developed a Python code, based on the Non-Linear Least-Square Minimization and Curve-Fitting (*LMFit*) package, and used a statistical method, to analyze the goodness of the inclusion of a new Gaussian in the model. We estimated the physical conditions (electron densities and temperatures), ionic and total chemical abundances of several atomic species and the ionization degree on each star-forming region.

Keywords / HII regions — galaxies: kinematics, abundance — galaxies: dwarf, individual (IIZw33, Mrk600)

1. Introduction

Blue Compact Dwarf galaxies (BCDs) are objects with luminosities dominated by, at least, one intense star forming knot. Their blue color is due to the UV radiation from young and massive stars (Sargent & Searle, 1970). Distinguished by the presence of active star formation, these objects do not show large amounts of dust or heavy elements (see Hunter & Hoffman, 1999 and Cairós et al., 2001). BCDs are gas-rich objects with mass fractions of HI usually larger than 30 % of the total mass, and present a very similar appearance to the giant HII regions detected in massive galaxies (Sargent & Searle, 1970; Terlevich et al., 1991).

BCDs are considered excellent laboratories to study star formation in low metallicity environments, showing chemical abundances in the range of 1/3 to 1/50 $Z_{\odot}$ (see Kunth & Östlin, 2000).

II Zw 33 and Mrk 600, are BCDs (catalogued by Gil de Paz et al., 2003) with multiple star forming regions (see Fig. 1). In the next sections, we will present the observations and preliminary results of the multiple components analysis.

2. Observations

Five knots with high Hα emission (three in II Zw 33 and two in Mrk 600) were observed using high resolution spectra with the Echelle double arm spectrograph MIKE, mounted at the Clay 6.5-m Telescope (LCO). No binning was applied to the 2k×4k CCD detector, and the effective slit used for II ZW 33 and Mrk 600 was 0.7" and 1" wide, resulting in a spectral resolution of about 8 and 11 km s^{-1}, respectively. The spectral range covered by the observations was from λ3300 Å to λ9300 Å, guaranteeing the simultaneous measurement of the nebular emission lines from [O II]$\lambda\lambda$3726 Å, 3729 Å to [S III]λ9069 Å at both ends of spectrum.

The data were reduced using *IRAF* in the usual manner and following the details described in Firpo et al. (2005).

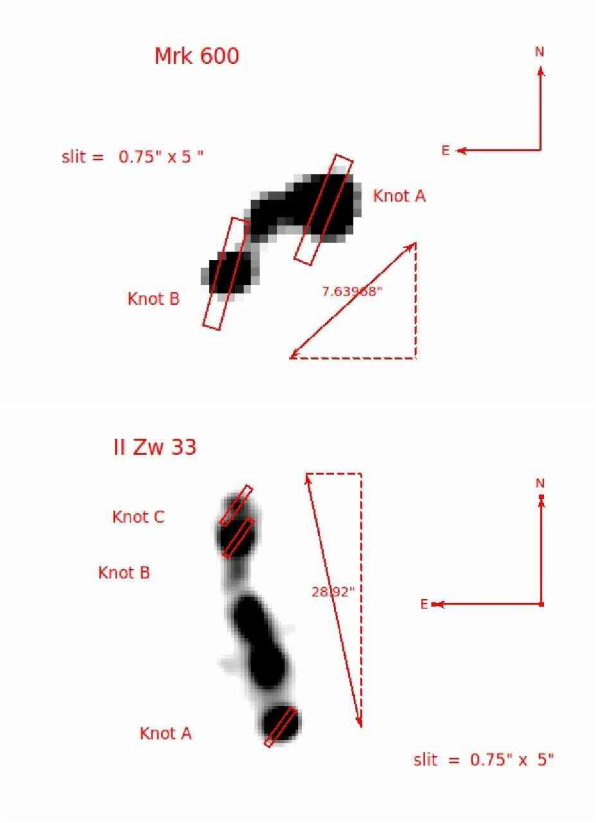

Figure 1: Hα images taken from NED (`https://ned.ipac.caltech.edu/`) with the used slits overimposed

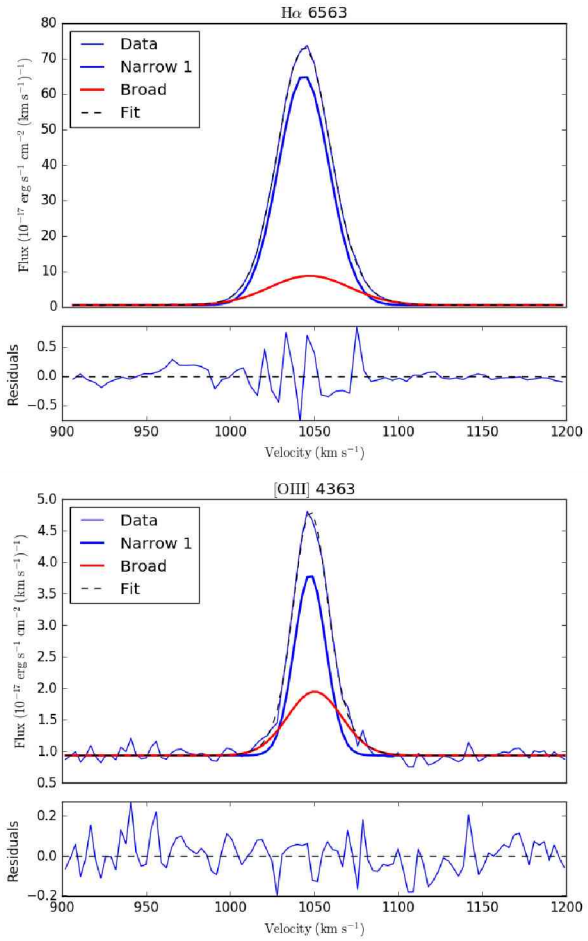

Figure 2: Multi Gaussian fit to the Hα (upper panel) and the [O III]λ4363 Å (lower panel) auroral emission-line for the knot B of Mrk 600. We over imposed the narrow and broad kinematic components in blue and red, respectively.

3. Results and discussion

We performed a multiple-Gaussian-components fit to the emission lines in the spectra. To do that we used our own Python code based on *LMFit* function, which provides a high-level interface for non-linear optimization and curve fitting in Python. We used different models combining a linear function (to fit the local continuum) and Gaussian functions (to fit the multiple kinematic components). The parameters to fit are the slope and intercept for the linear function and the velocity, velocity dispersion and amplitude, for the Gaussians.

We used the Akaike indicator to evaluate the statistical relevance of adding a new Gaussian component to the model following Bosch et al. (in preparation). When the addition of such component produces a change in the Akaike Information Criterion ($|\Delta AIC|$) lower than 10 (see Jun-Jie et al., 2016, for details on this criterion), the new component was considered as non statistically significant.

We followed the same methodology as in Hägele et al. (2012) to study the physical conditions estimated for each kinematic component. We assumed a two ionization zone scheme on which the different ions originate (see Garnett, 1992). Depending on their ionization degree:

- High ionization zone: [O III], [Ne III], [Ar IV], He II.
- Low ionization zone: HI, [S II], [O II], [O I], [Ar III], [N II].

The strongest emission-line is the [O III]λ5007 Å for the high ionization, and Hα for the low ionization zone.

For each knot we were able to measure more than twenty emission-lines including some weak auroral emission-lines sensitive to temperature, which are about 1 or 2 % of the [O III]λ5007 Å flux for this kind of objects. In Fig. 2 we show two examples of the fitting performed for the Hα and the [O III]λ4363 Å auroral emission lines, corresponding to the knot B of Mrk 600. Using this kinematic information, we were able to perform a chemodynamic study for the star forming knots, by applying the direct method developed by Hägele et al. (2006, 2008, 2012).

We employed the reddening-corrected, emission-line fluxes to estimate the electron densities (from the [O II]λ3729 Å/λ3726 Å and [S II]λ6717 Å/λ6731 Å emission-line ratios) and different electron temperature.

The ionic and total chemical abundances of different species are derived using the strong emission lines present in our spectra, and the adequate electron temperature estimated using (when possible) the direct method, or empirical or theoretical relations. The results for Mrk 600 are in agreement with those

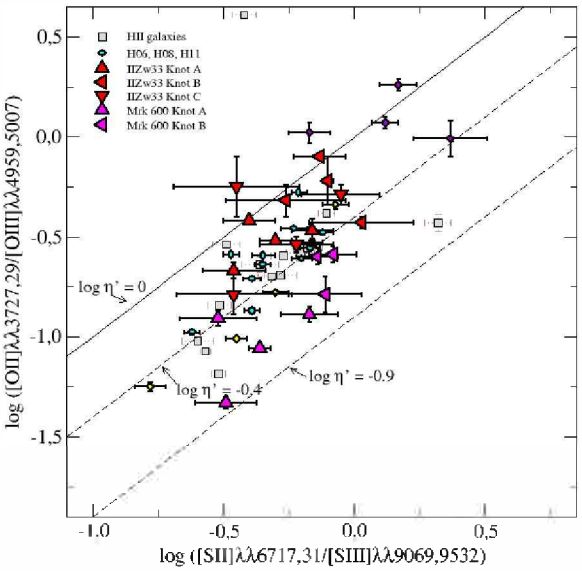

Figure 3: log([O II]/[O III]) vs. log([S II]/[S III]), the η' softness diagram, for the different knots II Zw 33 and Mrk 600 (filled red and violet triangles, respectively), the objects studied in H06, H08 and H11 (turquoise circles), and H II galaxies from the literature as described in H08 (open squares). The diagonals in this diagram correspond to constant values of η'.

estimated by Lagos et al. (2018). With the aim to study the nature of the ionizing sources for the different kinematic components we performed BPT diagnostic diagrams(Baldwin et al. (1981)). In particular we used the [O III]λ5007 Å/Hβ vs.[N II]λ6584/Hα and [O III]λ5007/Hβ vs.[S II]λ(6717+6731) Å/Hα, finding that all the objects and all kinematic components show behaviors compatible with the presence of a star-forming region as the main ionizing source.

We were able to perform an analysis of the ionization structure for the different kinematic components of each star forming knot using the "softness parameter" η (= $(O^+/O^{2+})/(S^+/S^{2+})$), which is intrinsically related to the shape of the ionizing continuum and depends only slightly on the geometry (Vilchez & Pagel, 1988). We were also able to use the pure observational counterpart parameter η'.

$$\eta' = \frac{[\mathrm{O\,II}]\lambda\lambda 3726,29\ \text{Å}/[\mathrm{O\,III}]\lambda\lambda 4959,5007\ \text{Å}}{[\mathrm{S\,II}]\lambda\lambda 6717,31\ \text{Å}/[\mathrm{S\,III}]\lambda\lambda 9069,9532\ \text{Å}}.$$

We found different ionization structures for these two galaxies. All the kinematic components of the knots belonging to II Zw 33 are located in a region with lower effective temperatures of the ionizing radiation field, in the η and η' (see Fig. 3) diagrams, than those estimated for the regions belonging to the Mrk 600.

4. Summary

We performed the kinematic decomposition of the emission-line profiles using a Python code developed by us, which is based on the *LMFit* package. We use the Akaike Information Criterion to evaluate the goodness of adding a new Gaussian to the line-profile model. Here we present preliminary results of the first study performed for II Zw 33 and Mrk 600 BCD galaxies.

Acknowledgements: Federico Campuzano Castro wants to thank the organizers of the meeting.

References

Baldwin J.A., Phillips M., Terlevich R., 1981, A&A, 93, 5
Cairós L.M., et al., 2001, ApJS, 136, 393
Firpo V., Bosch G., Morrell N., 2005, MNRAS, 356, 1357
Garnett D.R., 1992, AJ, 103, 1330
Gil de Paz A., Madore B.F., Pevunova O., 2003, VizieR Online Data Catalog, 214, 70029
Hägele G.F., et al., 2006, MNRAS, 372, 293
Hägele G.F., et al., 2008, MNRAS, 383, 209
Hägele G.F., et al., 2012, MNRAS, 422, 3475
Hunter D.A., Hoffman L., 1999, AJ, 117, 2789
Jun-Jie W., Xue-Feng W., Fulvio M., 2016, A&AS, 90, 285
Kunth D., Östlin G., 2000, ApJS, 10, 1
Lagos P., et al., 2018, MNRAS, 477, 492
Sargent W.L.W., Searle L., 1970, ApJL, 162, L155
Terlevich R., et al., 1991, ApJL, 91, 285
Vilchez J.M., Pagel B.E.J., 1988, MNRAS, 231, 257

A formation scenario for faint and ultra-faint dwarf spheroidal galaxies

C.A. Aravena[1], M. Fellhauer[1], F. Urrutia Zapata[1] & A.G Alarcón Jara[1]

[1] *Departamento de Astronomía, Universidad de Concepción, Chile*

Contact / cataaravena@udec.cl

Resumen / Las galaxias enanas esferoidales débiles y ultradébiles representan una nueva población de galaxias enanas esferoidales clásicas, con propiedades físicas muy similares. Corresponden a los sistemas del Universo local más dominados por materia oscura, con magnitudes absolutas entre $-7 < M_v < -1.5$, masa estelar del orden de $10^2 M_\odot < M_\star < 10^5 M_\odot$, además de ser las galaxias enanas con más baja metalicidad en el Grupo Local ([Fe/[H] $\lesssim -2.5$). Son extremadamente valiosas para el entendimiento de la formación de estructuras en el Universo y una importante prueba de la formación de galaxias a escalas más pequeñas. Desarrollamos simulaciones numéricas usando nuestros modelos de formación de galaxias enanas esferoidales clásicas previos, para estudiar un nuevo modelos de formación de galaxias enanas esferoidales débiles y ultradébiles con un potencial de fondo, que imita un halo de materia oscura. Las estrellas se encuentran inicialmente en equilibrio virial, distribuidas en una región de formación estelar filamentaria con una distribución fractal al interior de un halo analítico, formando el componente luminoso que hoy observamos. Seguimos su evolución por un periodo de 5 000 millones de años.

Abstract / Faint and ultra-faint dwarf spheroidal galaxies represent a new population of dwarf spheroidal galaxies with very similar physical properties. They are the most dark matter dominated systems in the local Universe with absolute magnitudes between $-7 < M_v < -1.5$, a stellar mass range of $10^2 M_\odot < M_\star < 10^5 M_\odot$ and they are the most metal-poor ([Fe/[H] $\lesssim -2.5$) dwarfs in the Local Group. They are extremely valuable for our understanding of structure formation in the Universe and useful probes of galaxy formation on smallest scales. We perform numerical simulations using our previous formation models of classical dwarf spheroidal galaxies to study a star formation scenario for faint and ultra-faint dwarf spheroidal galaxies with a strong background potential mimicking the dark matter halo. Our stars are initially in virial equilibrium and placed in a filamentary stellar distribution, a fractal distribution within an analytical halo, building the faint luminous components that we observe. We follow their evolution for 5 Gyr.

Keywords / methods: numerical — galaxies: dwarf — galaxies: formation — galaxies: star formation — galaxies: kinematics and dynamics

1. Introduction

The dwarf spheroidal galaxies (dSph) around the Milky Way offer a unique opportunity to investigate galaxy formation and evolution by studying the photometric properties of the resolved stellar populations (Okamoto et al., 2012). Since 2005, the Sloan Digital Sky Survey (SDSS) and similar surveys have discovered a large number of new dwarf galaxies orbiting around the Milky Way. A new population of dwarf galaxies in the Local Group (LG), known as ultra-faint dwarfs (UFDs), appears to be an extension of the classical dSphs with very similar physical properties.

UFDs galaxies do not contain any gas at the present time and their stars are very iron-poor, with ages $\gtrsim 10 - 12$ Gyr, so they are the most metal poor population in the LG, and maybe galaxies where star formation ended in the earliest epoch of the Universe (Tollerud et al., 2011; Vincenzo et al., 2014). These systems can have luminosities smaller than $\sim 1\,000\ L_\odot$, and are $\sim 10 - 1\,000$ times fainter that the classical dSph or even most of the Galactic globular clusters. They are the most dark matter (DM) dominated systems, do not show recent star formation activity and have a high mass-to-light ratio > 100.

They are located close to the Milky Way, mostly within its virial radius. They show different morphologies and most of the dwarfs are elongated, demonstrating that they are not spherically symmetric systems and probably do not have an isotropic velocity dispersion. Several dwarfs also appear irregular, opening up the possibility that their structure has been significantly affected by the tidal field of the Milky Way.

The origin of UFDs is a matter of ongoing debate. Several solutions have been suggested so far for resolving the crisis. It is common for galaxy formation models to alleviate the missing satellite problem by truncating the star formation in dark matter halos below some nominal mass threshold, sometimes termed the "filtering mass". With this threshold tuned to match the observations, there are several models that attempt to explain the origin of dSph galaxies by considering different mechanisms. Some of them are based on the tidal and ram-pressure stripping model (Mayer et al., 2007). The model proposed by D'Onghia et al. (2009) considers a mechanism known as resonant stripping and can be used to explain the formation of isolated dSph galax-

ies. There is another model that explains the formation of dwarf galaxies based on energy and momentum conservation when gas-rich galaxies interact, in which the dSph galaxies are in fact DM free tidal dwarf galaxies (Metz et al., 2007), and there are models which consider dwarf galaxies in isolation, but they usually take only a smooth gas distribution into account and focus on higher masses for the dwarfs (Assmann et al., 2013b; Alarcón Jara et al., 2018).

Models that explain the origin of dSph galaxies in isolation with high resolution are proposed by Assmann et al. (2013a). Their fiducial model tested a possible scenario for formation of dSph galaxies using the particle mesh code SUPERBOX, where they performed numerical simulations of isolated galaxies, but distributed the newly formed stars into dissolving star clusters (SCs) within the DM halo. The model is based on the assumption that the stars form in hierarchical structures, i.e. SCs. The star formation events range from slowly forming stars in small clusters and associations to intense starbursts, in gas-rich environments, typically producing a few hundred young SCs, within a region of just a few hundred parsec.

Assmann's models proposed that the dynamical evolution of these SCs, that is, their dissolution due to the gas expulsion, may explain the formation of classical dSph galaxies, including all their irregularities in the stellar kinematic distribution as well as surviving SCs around them. The SCs form with low star formation efficiency (SFE) and, thus, are designed to dissolve inside the DM halo to form luminous component of the dSph galaxy.

Alarcón Jara et al. (2018) present a dissolving SCs scenario adding different star formation histories (SFHs) to the models, as an extension of the work of Assmann et al. (2013a), placing SCs into the simulations at different moments in time. The SCs form with low SFE and thus, are designed to dissolve inside the DM halo to form the luminous component of the dSph galaxy.

Alarcón Jara et al. (2018) show this formation scenario works even with different SFHs, DM halo profiles and SFEs to dissolve the SCs. They not only reproduce the observational data that we have today, also provide observers with predictions for future observations.

We perform numerical simulations using the Astrophysical Multipurpose Software Environment (AMUSE), to study a star formation scenario for faint and ultra-faint dwarfs spheroidal galaxies based on the dissolving star clusters models. We study a formation scenario in which stars are initially placed in a fractal distribution inside the centre of the DM halo, building the faint luminous component that we observe.

2. Method and initial conditions

The stars are initially placed in a fractal distribution. We use the method introduced by Goodwin & Whitworth (2004) to generate a initial sub-structured distributions. This method defines a cube of size $N_{\rm div} = 2$ in which the fractal is created. Starting in the centre of the cube with a first-generation parent which is divided in $N_{\rm div}^3$ sub-cubes. Each sub-cube, called child can turn into a parent for the next generation with a probability of $N_{\rm div}^{\rm D-3}$, where D is the fractal distribution. Specifically for us, we choose a value of $N_{\rm div}^3 = 8$ and a fractal dimension of D = 1.6. An example of this is shown in (Fig. 1, top left panel). The process is repeated until the number of children reaches a larger number than the number of particles. The velocities of the children are inherent from the parents including a random component that decreases with each new generation (Domínguez et al., 2017; Goodwin & Whitworth, 2004).

For our simulations of Segue 1 we consider 700 particles in virial equilibrium with equal mass ($\rm M_\star = 0.5\,M_\odot$) i.e. a total luminous mass of $\rm M = 350\,M_\odot$. We assume a physical size $\rm r_{fractal}$ of the system of 10, 30 and 50 pc.

We consider an analytic background potential. For this set of simulations we use a Plummer potential (Plummer, 1911):

$$\rho(r) = \frac{3\rm M_{Pl}^3}{4\pi \rm R_{Pl}} \left(1 + \frac{r^2}{\rm R_{Pl}^2}\right)^{-\frac{5}{2}} \quad (1)$$

with $\rm M_{Pl}$ and $\rm R_{Pl}$ the Plummer mass and Plummer radius respectively. For Segue 1, we have an effective radius $\rm R_{eff} = 30$ pc and within that $\rm R_{eff}$ the measured mass in DM is $\rm M_{halo}(r_h) = 6 \times 10^5\ M_\odot$. Our DM halo has a default scale-length of $\rm R_{Pl} = 1$ kpc. To obtain the measured dynamical mass within $\rm r_h$ we choose a Plummer mass of $\rm M_{Pl} = 2.15 \times 10^{10}\ M_\odot$.

3. Results

We follow the evolution of the initial fractal distribution within an analytical halo for 5 Gyr. We choose three different values for $\rm r_{fractal}$, namely, 10, 30 and 50 pc and perform for each value three different random realisations.

In Fig. 1 we show an example of the initial conditions and the time evolution of our distribution of stars. The initial radius $\rm r_{fractal}$ in the shown example is 50 pc. We note that even after 5 Gyr of evolution, the galaxy is still evolving and we recognise that the distribution of stars form a luminous object that resembles an UFD galaxy.

Fig. 2 shows the time-evolution of the Lagrangian radii (10, 20,..., 90% of the total mass) for the same distribution of stars as shown in Fig. 1. We see that 5 Gyr are not enough for the Lagrangian radii to stay constant.

To determine the effective radius, we would have to fit single Sérsic profiles to our simulation data, but for the kind of distribution of stars we obtain after 5 Gyr of evolution (see Fig. 1) we have to consider the Lagrangian radii at 50 % of the total mass have to instead. In Fig. 3 we show the half-mass radius against the initial size of the fractal. As the scale-length of a dSph usually should be smaller than the half-mass radius, we see that for our choice of DM halo we need fractal distribution of 50 pc or more.

What is very clearly visible is, that our formation scenario produces objects that have the distorted shapes of UFD intrinsically, without the need of an external influence.

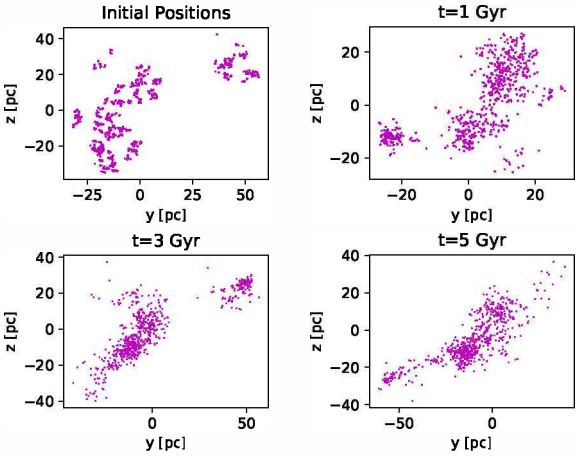

Figure 1: Example of the evolution of the distribution of stars from t=0 to t=5 Gyr. Top left panel: Initial distribution of stars at t=0 from a turbulent gas cloud for Segue I. The filamentary stellar formation region is form for 700 particles with equal mass i.e. a total luminous mass of M=350 $M_\odot$. The purple points represent the stars ($M_\star$=0.5 $M_\odot$) in virial equilibrium, with a fractal distribution of D = 1.6 in a radius of $r_{fractal}$ = 50 pc. Top right: Distribution of stars after 1 Gyr of evolution. Bottom right: Distribution of stars after 3 Gyr of evolution. Bottom left: Final state of the distribution of stars after 5 Gyr.

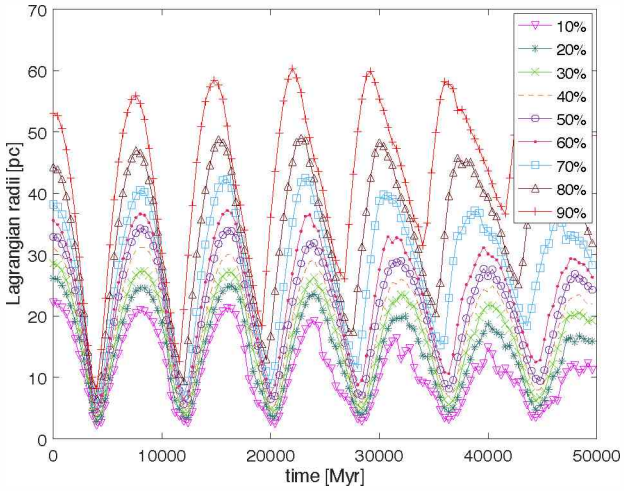

Figure 2: Lagrangian radii of our initial model with a fractal radius of $r_{fractal}$ = 50 pc. The plot shows the Lagrangian radii between 10 % to 90 % of the total mass. We concluded that 5 Gyr are not enough for radii stay constant.

4. Conclusions

In this paper we tested a possible formation scenario, originally proposed by Assmann et al. (2013a,b) for the formation of UFD galaxies with numerical simulations using AMUSE and the direct N-body integrator ph4. In our simulations we considered the evolution of different fractal distributions of 700 particles within an analytical halo with a Plummer distribution. From the Lagrangian radii we observe that even after 5 Gyr of evolution the galaxy is still evolving (see Fig. 2).

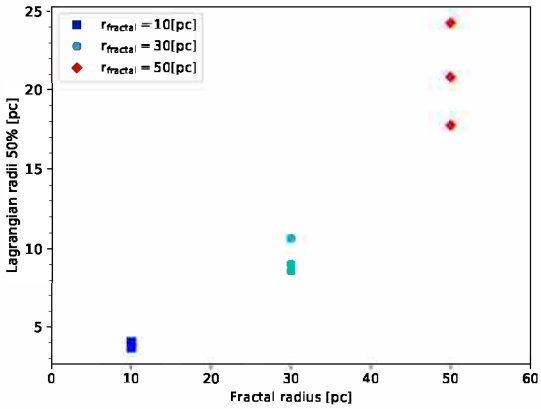

Figure 3: Lagrangian radii at 50 % after 5 Gyr of evolution as a function of the fractal radius of the distribution of stars. Blue squares represent the Lagrangian radii at 50 % as a function of their fractal radius of 10 pc. Cyan circles represent the relation between the Lagrangian radii at 50 % of the total mass with a fractal radius of 30 pc and the red diamonds represent the Lagrangian radii for a fractal radius of 50 pc.

We conclude that due to the initial fractal distributions the kind of distribution of stars we obtain after 5 Gyr of evolution is still complex to study the effective radius of the galaxy, so is necessary follow their evolution for the next 5 Gyr.

On the other hand, our results show that the variation in the fractal radius of the initial distributions of stars can produce, in some cases, results far away from the observational data that we have today, making necessary study the impact on the variation of the Plummer radius for the analytical halo as well.

Our main result is that our final object forms a luminous object that resembles a UFD galaxy like Segue 1, patchy distribution of stars observed ellipticities and effective radii velocity dispersion.

Acknowledgements: CA, FUZ and AAJ acknowledge funding through Fondecyt Regular No. 1180291 and the Chilean BASAL Centro de Excelencia en Astrofisica y Tecnologias Afines (CATA) grant PFB-06/2007. MF acknowledges support through Fondecyt regular 1180291, Basal AFB-170002 and PII20150171.

References

Alarcón Jara A.G., et al., 2018, MNRAS, 473, 5015
Assmann P., et al., 2013a, MNRAS, 432, 274
Assmann P., et al., 2013b, MNRAS, 435, 2391
Domínguez R., et al., 2017, MNRAS, 472, 465
D'Onghia E., et al., 2009, Nature, 460, 605
Goodwin S.P., Whitworth A.P., 2004, A&A, 413, 929
Mayer L., et al., 2007, Nature, 445, 738
Metz M., Kroupa P., Jerjen H., 2007, MNRAS, 374, 1125
Okamoto S., et al., 2012, ApJ, 744, 96
Plummer H.C., 1911, MNRAS, 71, 460
Tollerud E.J., et al., 2011, ApJ, 726, 108
Vincenzo F., et al., 2014, MNRAS, 441, 2815

Stellar populations in bulges The isolated galaxies

L. Morelli[1], L. Costantin[2], E.M. Corsini[2], E. Dalla Bontà[2], L. Coccato[3], J. Méndez-Abreu[4] & A. Pizzella[2]

[1] *Instituto de Astronomía y Ciencias Planetarias Universidad de Atacama, Copiapó, Chile*
[2] *Dipartimento di Fisica e Astronomia "G. Galilei", Università di Padova, Italy*
[3] *European Southern Observatory, Garching, Germany*
[4] *Instituto Astrofísico de Canarias, La Laguna, Spain*

Contact / lorenzo.morelli@uda.cl

Resumen / En una reciente serie de artículos se han presentado los resultados de la investigación sobre la población estelar y sus gradientes en las regiones de la galaxias donde la luz esta dominada por el bulbo.
En la presentación oral se han mostrado los resultados de estos trabajos y los últimos avances del proyecto, mostrando las propriedades de la población estelar en el bulbo de galaxias en ambiente aislado.

Abstract / In a recent series of papers we presented the results of the investigation on the stellar populations and their gradients of the bulge dominated region.
The results of these works have been presented in the talk along with the last progresses in this projects, showing the properties of the stellar populations in the bulge dominated regions of galaxies in isolated environment.

Keywords / galaxies: abundances — galaxies: bulges — galaxies: formation — galaxies: kinematics and dynamics — galaxies: spiral — galaxies: stellar content

1. Introducción

Most of the stars in the local universe reside in the bulges of disk galaxies. Their morphological classification is based on the relative prominence of the spheroidal and disk components and their structures reflects the different formation processes. Thus, it follows that understanding how bulges assembled is a crucial step in understanding galaxy formation.

Dissipative collapse (e.g., Gilmore & Wyse, 1998), major and minor merging events (e.g., Cole et al., 2000), and redistribution of disk material due to the presence of a bar or environmental effects (e.g., Kormendy & Kennicutt, 2004) drives to the variety of properties observed in bulges. Theoretical models give strong constraints on the resulting galaxy that need to be tested with observations. In particular, an invaluable piece of information to understand the processes of formation and evolution of galaxies is imprinted in their stellar populations (e.g., Seidel et al., 2015; McDermid et al., 2015; Corsini et al., 2018) and even more in their radial gradients (e.g., Gorgas et al., 2007; Morelli et al., 2008; González Delgado et al., 2014; Morelli et al., 2015b) since different formation scenarios predict different radial trends of age, metallicity, and alpha/Fe enhancement.

To take on this challenge we have started a campaign to investigate the stellar populations of bulges of galaxies residing in dense environments to compare their nature with the nature of bulges in isolated galaxies.

In Morelli et al. (2008, 2012, 2015a) the central value and radial gradient of age, metallicity, and [α/Fe] enhancement has been measured for a large number of high-surface brightness (HSB) and low-surface brightness (LSB) galaxies. The only common feature for these bulges (independently from their morphological type and environment) is the negative metallicity gradient along the galaxy radius. All these characteristics are supporting scenarios like violent relaxation due to a merging event, or dissipative collapse in monolithic scenario and discourage secular evolution. However, secular evolution could still be the main responsible for the formation of galaxies with small bulges (Costantin et al., 2017, 2018). The variety of the results testifies the complexity of the topic and could be due to the continuous interactions between the cluster galaxies and their dense environment (Corsini et al., 2017).

2. Isolated bulges

A way to make the observational picture simpler is studying the bulges of isolated galaxies, for which the interactions with the surrounding environment or with other galaxies are likely to be negligible (Hirschmann et al., 2013).

In Morelli et al. (2016) we analysed the stellar populations of the bulges of a carefully selected sample of HSB isolated disk galaxies to be compared with the complementary samples of bulges in HSB cluster galaxies and giant LSB galaxies. In Fig. 1 we reported the comparison of morphological type, central velocity disper-

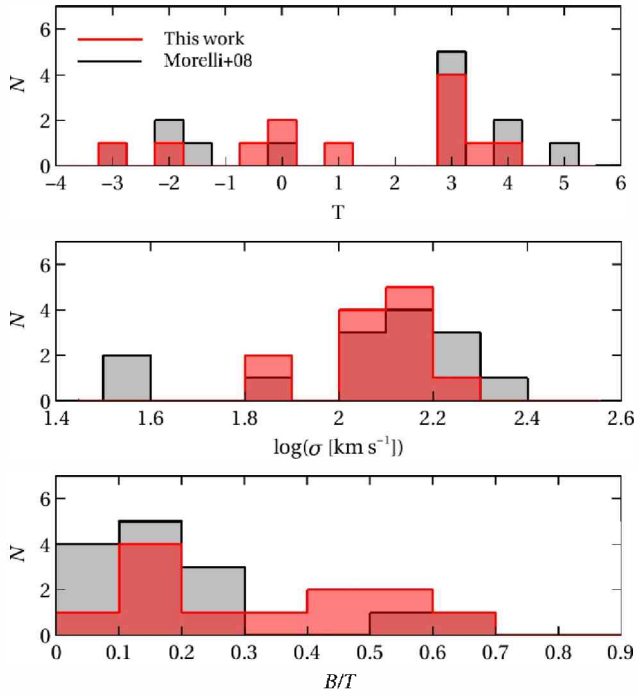

Figure 1: Distribution of the morphological type (upper panel), central velocity dispersion (middle panel), and B/D ratio (lower panel) for the sample galaxies (red histograms). The distribution of the same quantities for the group and cluster galaxies studied by Morelli et al. (2008) is plotted for a comparison (grey histograms).

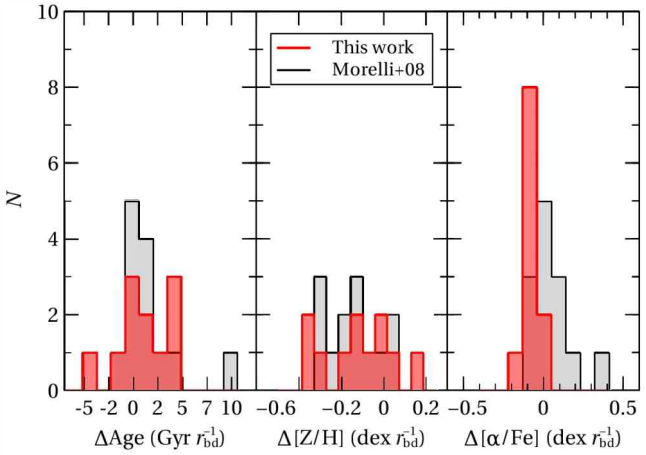

Figure 2: Distribution of the gradients of mean age (left-hand panel), total metallicity (central panel), and total α/Fe enhancement (right-hand panel) for the sample bulges (red histograms). The distribution of the same quantities for the bulges of group and cluster galaxies studied by Morelli et al. (2008) is plotted for a comparison (grey histograms).

sion, and B/D ratio between the two sample.

In order to measure the stellar populations gradients in the bulge we had to derive the relative importance of disc, bulge and bar along the radius. Their structural parameters were derived from the sky and mask-subtracted i-band images by applying the Galaxy Surface Photometry Two-Dimensional Decomposition (GASP2D) algorithm (Méndez-Abreu et al., 2008, 2014). Following the photometric decomposition we defined $r_{\rm bd}$, the radius where the surface brightness contribution of the bulge component is equal to the contribution from the other components.

The gradients of age, metallicity and α-enhancement were derived as the difference between the value derived at radius $r_{\rm bd}$, and the central value obtained within $0.1r_{\rm e}$. We confirm the negative radial trend in metallicity also for the isolated galaxy, but the main result is the negative gradient for the [α/Fe] enhancement (Fig. 2).

3. Conclusions

We analysed the surface-brightness distribution, stellar kinematics, and stellar population properties of a sample of isolated galaxies selected from the Catalogue of Isolated Galaxies (Karachentseva, 1973), to constrain the dominant mechanism of the assembly of their bulges. We give particular attention to the stellar populations gradient along the radius of the galaxy.

All the sample bulges show a negative gradient for the α/Fe enhancement. This is a prediction of the dissipative collapse model for bulge formation and it has never been observed before. We suggest that the gradients imprinted during the inside-out formation process are preserved in the bulges of isolated galaxies, which suffered a limited number of interactions and mergers, whereas the gradients are cancelled in the bulges of group and cluster galaxies as a consequence of phenomena driven by environment.

Acknowledgements: This investigation was based on observations obtained at the ESO Telescopes at the La Silla Paranal Observatory under programmes 76.B-0375, and 80.B-00754. This work was partially supported by Padua University through grants 60A02-5857/13, 60A02-5833/14, 60A02-4434/15, and CPDA133894. LM acknowledges financial support from Padua University grant CPS0204. JMA acknowledges support from the European Research Council Starting Grant SEDmorph (P.I. V. Wild).

References

Cole S., et al., 2000, MNRAS, 319, 168
Corsini E.M., et al., 2017, MNRAS, 466, 974
Corsini E.M., et al., 2018, A&A, 618, A172
Costantin L., et al., 2017, A&A, 601, A84
Costantin L., et al., 2018, MNRAS, 481, 3623
Gilmore G., Wyse R.F.G., 1998, AJ, 116, 748
González Delgado R.M., et al., 2014, A&A, 562, A47
Gorgas J., Jablonka P., Goudfrooij P., 2007, A&A, 474, 1081
Hirschmann M., et al., 2013, MNRAS, 433, 1479
Karachentseva V.E., 1973, Soobshch. Spets. Astrofiz. Obs., 8, 3
Kormendy J., Kennicutt R.C., 2004, ARA&A, 42, 603
McDermid R.M., et al., 2015, MNRAS, 448, 3484
Méndez-Abreu J., et al., 2008, A&A, 478, 353
Méndez-Abreu J., et al., 2014, A&A, 572, A25
Morelli L., et al., 2008, MNRAS, 389, 341
Morelli L., et al., 2012, MNRAS, 423, 962
Morelli L., et al., 2015a, Astron. Nachr., 336, 208
Morelli L., et al., 2015b, MNRAS, 452, 1128
Morelli L., et al., 2016, MNRAS, 463, 4396
Seidel M.K., et al., 2015, MNRAS, 451, 936

Origin of high ionization lines in active galactic nuclei

Y. Diaz[1,2] & A. Rodríguez-Ardila[3,4]

[1] *Instituto Nacional de Pesquisas Espaciais/MCTI, São Jose dos Campos, SP, Brazil*
[2] *Instituto de Física y Astronomía, Facultad de Ciencias, Universidad de Valparaíso, Valparaíso, Chile*
[3] *Laboratorio Nacional de Astrofísica/MCTI, Itajubá, MG. Brazil*
[4] *Instituto de Astrofísica de Canarias, La Laguna, Tenerife, Spain*

Contact / yaherlyn.diaz@postgrado.uv.cl

Resumen / Presentamos evidencias de que la fotoionización por radiación de la fuente central no puede explicar la emisión de líneas coronales observadas en los núcleos galácticos activos (AGN, por sus siglas en inglés). Encontramos que la emisión coronal en los objetos estudiados se extiende a distancias de hasta 150–200 pc y es coespacial con el *jet* de radio. Los modelos de fotoionización de CLOUDY muestran que la fotoionización no es el único mecanismo físico responsable de la emisión de líneas coronales. Otros procesos como los choques son necesarios para explicar la emisión del gas de alta ionización. En general, nuestro trabajo destaca la necesidad de observaciones IFU con alta resolución angular, para comprender, con mayor precisión, los procesos físicos que ocurren en los parsecs centrales de las AGNs.

Abstract / We present strong evidence that the photoionization by radiation from the central engine cannot explain the emission of Coronal lines observed in Active Galactic Nuclei (AGN). We found that the coronal emission in the studied objects is extended to distances of up to 150–200 pc and co-spatial with the radio jet. Photoionization models of CLOUDY show that photoionization is not the only physical mechanism responsible for the emission of coronal lines. Another processes such as shocks are necessary to explain the emission of the high ionization gas. Overall, our work highlights the need of high angular IFU observations to understand, more accurately, the physical processes associated to the central few parsecs in AGNs.

Keywords / galaxies: nuclei — galaxies: kinematics and dynamics — techniques: spectroscopic

1. Introduction

Active galactic nuclei (AGNs) present, in their spectra, lines of high ionization or coronal lines (CLs). Due to the potential necessary for its production (>100 eV), the CLs trace a part of the ionizing continuum which is not always directly accessible from observations due to galactic absorption. It is known that CLs are generally emitted in compact regions near the central source, but the physical conditions of the gas and the mechanisms associated with its production are under discussion.

In this work we analyze the most internal parsecs of a sample of four nearby active galaxies with prominent coronal emission to study the physical mechanisms responsible for the production of CLs. For this purpose, observations of high angular resolution ($\sim$ 0.1" px^{-1}) collected with integral field spectroscopy and adaptive optics (AO) allowed the study of the spatial distribution of the high ionization gas and model the reasons [Si VI]/Brγ, [S IX]/Paβ, [Ca VIII]/Brγ and [S VIII]/Paβ using CLOUDY. The width, shape of the profiles, and position of the centroid lines are additional diagnostics used to determine the contribution of energy processes such as outflows and shocks between the jets and the Narrow Line Region (NLR) gas.

2. Observations

- Four nearby active galaxies with prominent coronal emission: NGC 1068, NGC 1386, NGC 4151 and ESO 428-G014
- Observations with AO using NIFS/Gemini and SINFONI/VLT
- High-quality spectroscopic data spatially resolved at smaller scales of 0.15" px^{-1}, that translate to a angular scale of $\sim$ 15"px^{-1}.

For this work, we use galaxies with multiwavelength data, because this allows a more complete analysis of the physics associated to the gas. In addition, we select objects with evidence of the presence of outflows and extended coronal emission.

3. Morphology and extension of the Coronal line Region

Visual inspection of Fig. 1 shows that the region emitting [Si VI]λ1.963μm and Brγ for ESO 428-G14 is highly inhomogeneous and elongated along the NE-SW direction. The gas morphology is extended, reaching up to 195 pc to the SE and 110 pc to the NW. It forms a bright spot at NW that can be associated with an helical–shape. These are best seen in the Brγ image. This gas distribution is also reported by May et al. (2018).

Fig. 2 shows the flux map of the AGN NGC 1386. The morphology of the high ionization emitting gas

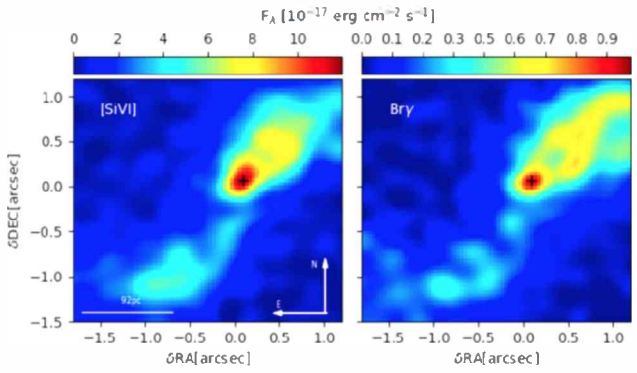

Figure 1: Flux distribution maps of [Si VI]λ1.962μm and Brγ for ESO 428-G14. The color bar indicates the values of integrated flux in units of 10^{-17} erg cm^{-2} s^{-1}. The orientation and spatial scale are the same for all panels.

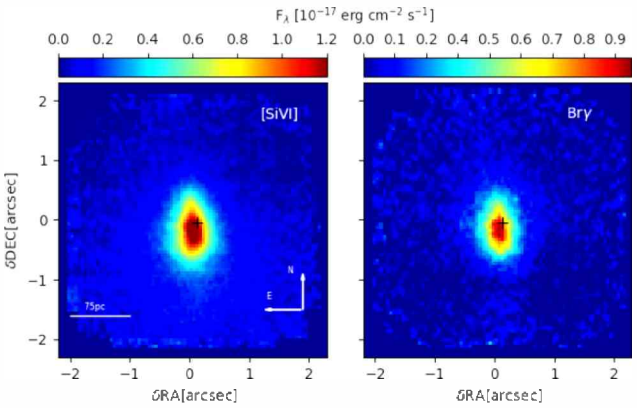

Figure 2: The same as Fig. 1 for NGC 1386.

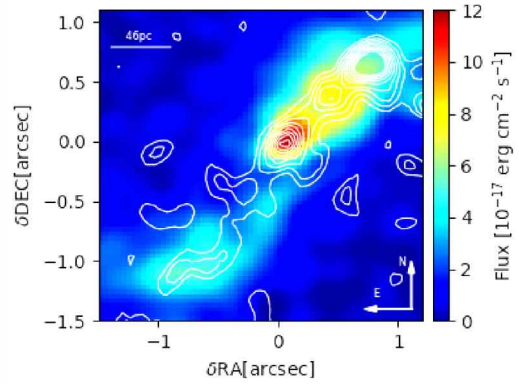

Figure 3: Flux distribution map of [Si VI]λ1.963μm overlaid with the VLA 2 cm radio emission for ESO 428-G14.

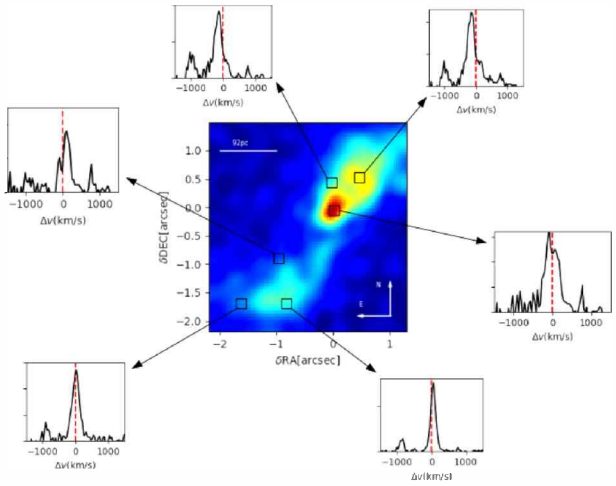

Figure 4: [Si VI] emission-line profiles for ESO 428-G14. The spectra were extracted from different spatial regions of $\sim$0.25$\times$0.25 arcsec^2. [Si VI] emission displays a very intricate profile, with multiple components and strong variations in their form and width from region to region.

[Si VI]λ1.963μm displays one prominent region of emission. It is characterized by a blob of $\sim$1" in radius, centered at the AGN and slightly elongated in the NS direction. The brightest region of this component is highly elongated in the NS direction, with a size of $\sim$1.2"$\times$0.6". This morphology was already observed by Rodríguez-Ardila et al. (2017). The morphology of Brγ emission is similar to the distribution observed for the high ionization line but with a shorter extension in the NS direction (0.5"$\times$0.5").

In Fig. 3, we overlapped the 2 cm radio map from VLA (Falcke et al., 1998) to the [Si VI] emissions and we found that the coronal gas is distributed along a PA very close to that of the radio jet, forming multiple filaments and knots of emission. This feature suggests a strong association between [Si VI] and the radio-jet: the jet plays a fundamental role in the morphology of the Coronal Line region (CLR) gas in ESO 428-G14. We defined the AGN location as the position where the K-band continuum emission (2.2 μm) peaks, which coincides with the maximum intensity of the [Si VI] emission. Also, X-ray observations obtained with *Chandra* show a PA similar to that of [Si VI] for this galaxy (May et al., 2018).

The CLs of ESO 4028-G14 display very intricate profiles, with multiple components and strong variations in their form and width from region to region. As an example, Fig. 4 shows the [Si VI] line profiles of spectra extracted from different spatial regions $\sim$0.2"$\times$0.2".

4. Kinematics of the CLs

As can be seen in Fig. 5 and Fig. 6, [Si VI] is significantly broader than Brγ. Moreover, high-velocity clouds are observed at distances of up to $\sim$100 pc from the center and coincident with regions of strong radio emission, suggesting outflowing gas, probably due to interaction of the radio-jet with the interstellar medium.

5. Photoionization models

We investigate if photoionization by the central source alone is able to sustain highly ionized clouds at the distances detected in ESO 428-G14. To this aim, we run grids of photoionization models with CLOUDY Ferland et al. (version C17.01; 2017). The input parameters are

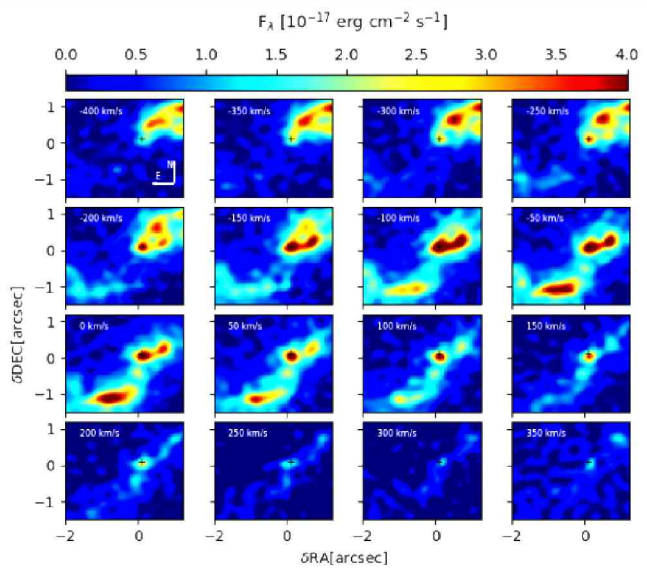

Figure 5: Channel maps derived for Brγ for ESO428-G14. A velocity bin of 50km s^{-1} is used to slice the data-cube. The color bar indicates the values of integrated flux in units of 10^{-17} erg cm^{-2} s^{-1}.

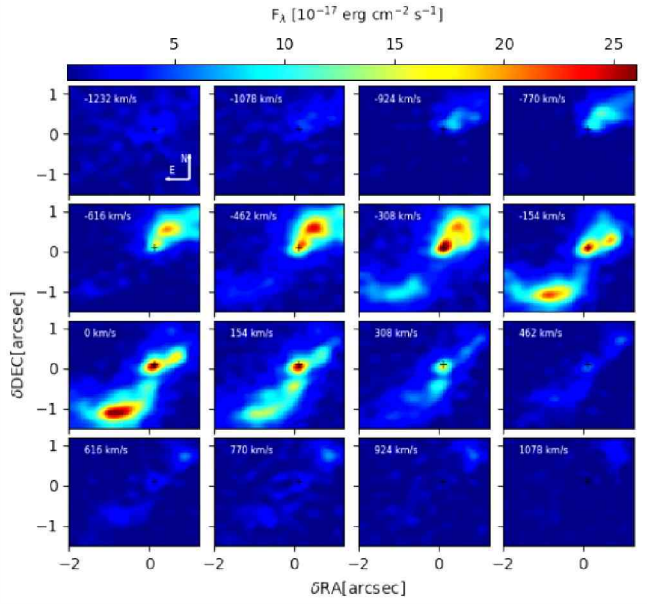

Figure 6: Channel maps derived for [Si VI] 1.963 μm for ESO428-G14. A velocity bin of 154kms^{-1} is used to slice the data-cube. The color bar indicates the values of integrated flux in units of 10^{-17} erg cm^{-2} s^{-1}.

the gas density, the distance of the clouds to the nucleus, the spectral energy distribution of the ionizing radiation ("Table AGN" command, similar to that deduced by Mathews & Ferland (1987), solar abundances and clouds with no dust. We used the total AGN luminosity (2×10^{42} erg s^{-1}).

The observed line ratios and the photoionization models are presented in Fig. 7. The extended gas distribution cannot be reproduced by photoionization by

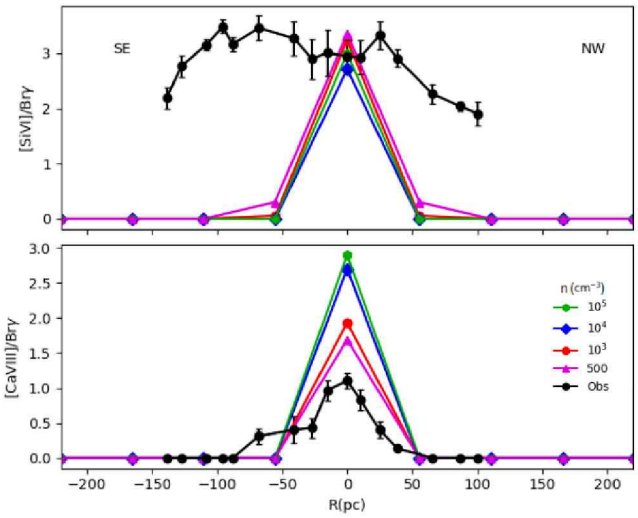

Figure 7: Predicted emission lines ratios [Si VI]/Brγ (upper panel) and [Ca VIII]/Brγ (bottom panel) for clouds with different densities (10^3 cm^3 red, 10^4 cm^3 blue, 10^3 cm^5 green and 500 cm^3 purple) for ESO 428-G14. The full circles are the observed line ratios.

the central source. Also, in May et al. (2018) we tested the scenario where the AGN luminosity is higher to explore the possibility of any potential AGN variability, and the result is the same. Also this previous scenario is observed for the whole sample. A combination of photoionization by the central source and shock excitation is necessary to explain the extended emission.

6. Conclusions

- For [Si VI] and Brγ in NGC 1386 the light distribution is compact and clearly resolved.
- For ESO 428-G14, [Si VI] is emitted by gas with a wide range of velocities, both positives and negatives, reaching values as high as $\sim$1000 km s^{-1} and ~ -1000 km s^{-1}. The gas in the central regions ($\sim$0.5 arcsec) is more turbulent, emitting at practically at all the displayed velocity range.
- Photoionization by radiation from the central engine is not able to explain the extended emission of high ionization gas. Another physical mechanism (such shocks) must be also considered to explain its large extended high–ionization region.

Acknowledgements: Diaz Y. thanks to CAPES and CONICYT PIA ACT172033 and A. Rodríguez-Ardila to CNPq.

References

Falcke H., Wilson A.S., Simpson C., 1998, ApJ, 502, 199
Ferland G.J., et al., 2017, RMxAA, 53, 385
Mathews W.G., Ferland G.J., 1987, ApJ, 323, 456
May D., et al., 2018, MNRAS, 481, L105
Rodríguez-Ardila A., et al., 2017, MNRAS, 470, 2845

Diez años de observaciones desde radio hasta rayos gamma del blazar Markarian 501

A. Pichel[1] & A.C. Rovero[1]

[1] *Instituto de Astronomía y Física del Espacio, CONICET–UBA, Argentina*

Contacto / anapichel@iafe.uba.ar

Resumen / El blazar Mrk 501 es observado constantemente desde su descubrimiento en muy altas energías en 1996. En este trabajo presentamos las observaciones tomadas de los últimos diez años (2008–18) que incluyen instrumentos de radio, óptico, rayos X y rayos gamma. A partir de las curvas de luz, buscamos períodos de alta y baja actividad, para estudiar la variabilidad y las correlaciones entre las diferentes bandas de energía. A partir de esos resultados, se quiere conseguir una manera de predecir los *flares* de muy alta energía y determinar para las observaciones si hay un origen común para diferentes períodos de actividad en las distintas bandas. Encontramos una correlación moderada para los rayos X y los rayos gamma.

Abstract / The blazar Mrk 501 is constantly observed since the discovery at very high energies in 1996. We present, in this work, the observations taken from the last ten years (2008–18) including radio, optical, X-ray and gamma-ray instruments. From the light curves, we look for periods of high and low activity, to study the variability and correlations between the different energy bands. From these results, we want to get a way to predict very high energy flares and determine for the observations if there is a common origin for different periods of activity in the different bands. We found a moderate correlation between gamma-ray and X-ray.

Keywords / galaxies: active — BL Lacertae objects: individual: Mrk 501

1. Introducción

Los blazares forman parte de los núcleos activos de galaxias (AGN, por sus siglas en inglés), en donde los jets apuntan hacia la línea de visual del observador. Presentan una alta luminosidad y tienen emisiones rápidas de forma irregular, en espacios temporales cortos, del orden minutos a horas, hasta meses. Esta variabilidad está posiblemente asociada con regiones de emisión compactas cercanas a la base del jet y del agujero negro. La caracterización de esta variabilidad presenta un desafío para los observatorios actuales, ya que requiere un monitoreo constante durante meses en todo el espectro electromagnético. Por otro lado, la variabilidad de los blazares puede tomarse como una herramienta ya que a partir de las observaciones multifrecuencia simultáneas o cuasi contemporáneas, durante *flares*, se podrían romper degeneraciones entre los distintos modelos de emisión (e.g. Krawczynski et al. 2001).

Markarian 501 es un blazar cercano ($z = 0.034$) tipo *high-frequency-peaked* (HBL), y fue detectado por primera vez a muy altas energías por el telescopio Whipple en 1996 (Quinn et al., 1996). En los años subsiguientes, Mrk 501 fue observado regularmente en varias bandas de energía, presentando bajo estado de actividad. En particular, durante 1997, fue detectado un *flare* excepcionalmente fuerte con niveles de flujo máximos de hasta 10 veces el flujo de la Nebulosa del Cangrejo, que fue detectado a muy altas energías y en rayos X (Aharonian et al., 1999). Varios *flares* han sido observados en el transcurso de estos 20 años (e.g. Albert et al. 2007; Aliu et al. 2016) aunque ninguno de tal magnitud como el de 1997. En los últimos años se ha cambiado el enfoque y se realizaron varias campañas de 4-5 meses de duración (Aleksić et al., 2015; Ahnen et al., 2017), independientemente de la actividad de la fuente, para poder estudiar los estados de baja y alta actividad. En este trabajo nos concentramos en el estudio de la variabilidad de períodos largos de meses/años, buscando correlaciones entre los distintos instrumentos. Las observaciones utilizadas en este trabajo fueron obtenidas de base de datos públicas, salvo las de *Fermi-LAT* y *Swift-XRT* que fueron analizadas por los autores.

2. Curvas de luz

2.1. Variabilidad

Mrk 501 es monitoreado frecuentemente en todo el espectro electromagnético, con observaciones que van desde todos los días, cada varios días o semanas, dependiendo del nivel de intensidad de la fuente y la dedicación que tenga disponible el instrumento. En la Fig. 1 se pueden observar los resultados para el monitoreo durante 2008–2018, desde radio hasta rayos gamma. Como primera prueba para encontrar variabilidad, se realizó un ajuste con una función constante para todas las bandas de energía. Se encontraron pocos datos de archivo del VLBA en 15 GHz, con la fuente variable en esos años, con un pico en su actividad alrededor del período 1 (p1: MJD 54940–54960), y un mínimo de actividad alrededor del período 2 (p2: MJD 55860–56000).

En la banda V del óptico, se observó que la fuente se mantuvo estable durante el período MJD 54500–56500,

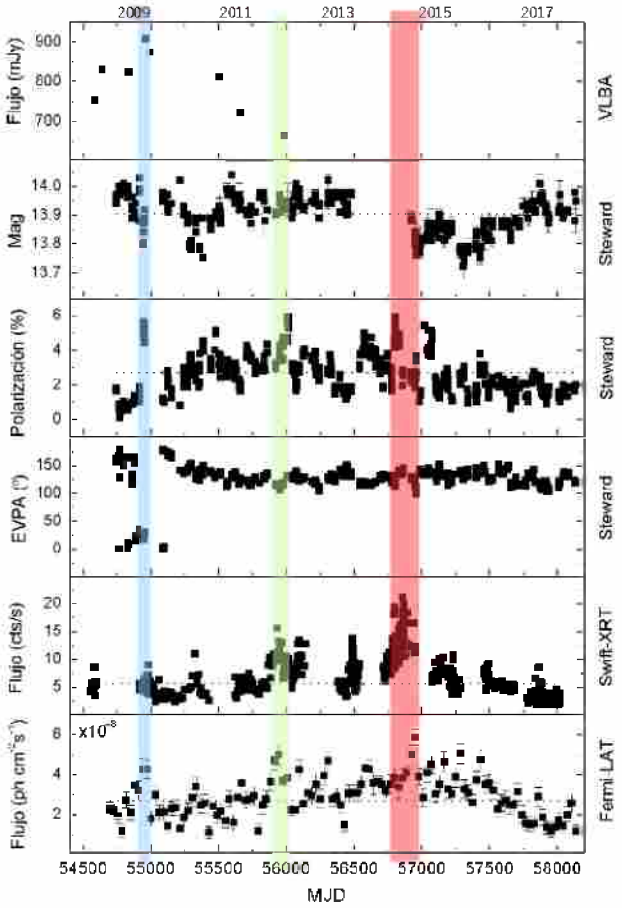

Figura 1: Curvas de luz para Mrk 501. *Primero (desde panel superior):* VLBA a 15 GHz. *Segundo:* Banda V medida en el Observatorio Steward. *Tercero:* Polarización óptica medida en el Observatorio Steward. *Cuarto:* $EVPA$ medido en el Observatorio Steward. *Quinto:* Cuentas obtenidas en la banda 0.3–10 keV tomadas con *Swift-XRT*. *Sexto:* Flujo obtenido en la banda de los rayos gamma de alta energía con *Fermi-LAT*. Los distintos períodos de alta activada están marcados en colores, siendo el período de 1 en azul, el período 2 en verde y el período 3 en rojo.

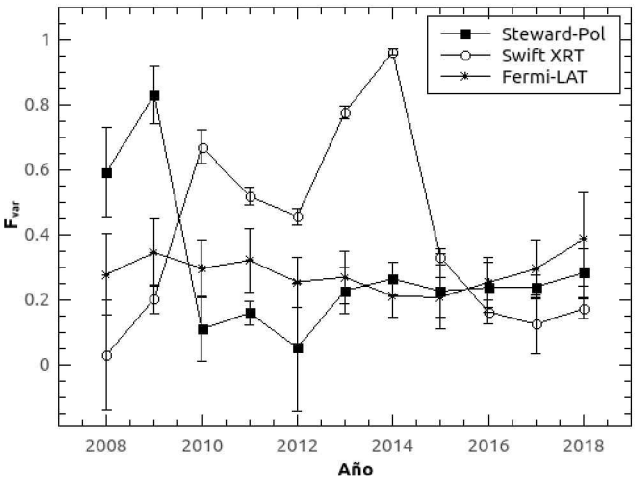

Figura 2: $F_{\rm var}$ para rayos gamma con *Fermi-LAT*, rayos X obtenidos para *Swift-XRT* y la polarización lineal en el óptico medido en el Observatorio Steward.

con picos de mayor actividad, del ∼10 % con respecto al promedio (13 900±0.005 mag). En el segundo período (MJD 56900–58300) hubo una disminución en la intensidad durante la primera parte, para luego aumentar hasta llegar al valor promedio. El grado de polarización lineal en el óptico presentó variaciones diarias, sobre todo en el 2008–09 con variaciones del 30–40 %, con un mínimo en 54750–54850, llegando a un máximo para abril–mayo de 2009 (p1). Esta variabilidad también puede apreciarse en la Fig. 2. Para el ángulo de polarización del vector eléctrico ($EVPA$) se obtuvo un promedio de 125.7±2.6 °, manteniéndose estable a lo largo de los 10 años de estudio, pero con la particularidad que durante los períodos 54829–59, 54886–55080 y 55091–94 tuvo una rotación abrupta, disminuyendo su valor de ∼120 ° a valores entre 5 y 30 °. Justo en el último período (p1) la fuente presentó un $flare$ a muy altas energías observado con VERITAS (Aliu et al., 2016). Luego se observó un incremento en el EVPA llegando a un máximo de ∼175 durante los días 55122–54. En la banda de los rayos X, Mrk 501 se mostró variable con picos en la actividad entre 3 a 5 veces la emisión a baja actividad (4.88±0.03 cuentas s $^{-1}$). Esta variabilidad también puede verse a lo largo de los años en la Fig. 2, con mayor variabilidad entre 2010–14. En la banda de los rayos gamma, la fuente se mantuvo estable, con pequeños $flares$. Durante el p2 la fuente presentó un estado de actividad alto en rayos X, con el triple de intensidad que el *baseline*. Este aumento también puede observarse en rayos gamma y en la polarización, mientras que en radio se obtuvo un mínimo de intensidad.

Durante el período 3 (p3: MJD 56750—5700), Mrk 501 estuvo en un alto estado de actividad en rayos X, con una intensidad máxima 4.3 veces mayor que la emisión promedio en los 10 años estudiados. Cabe destacar que la polarización lineal tuvo un aumento del doble que la emisión promedio unos diás antes que el $flare$ en rayos X. Unos días después del $flare$, hubo un aumento en la intensidad en rayos gamma, que se mantuvo en un estado de alta actividad durante varios meses. Dentro de ese período hubo otro $flare$, detectado a muy altas energías por H.E.S.S. (Cologna et al., 2017) sin detectar la contraparte en rayos X, gamma o en el óptico.

Una correlación de la variabilidad en las diferentes longitudes de onda puede dar indicaciones sobre los procesos que intervienen en los mecanismos de emisión. A lo largo de estos años, se han observado correlaciones entre los flujos en rayos X y rayos gamma (e.g. Horan et al. 2009). También hay casos donde no se encontró esa correlación a partir de observaciones simultáneas en rayos X y rayos gamma (e.g. Krawczynski et al. 2004). A su vez, en otras observaciones se han encontrado correlaciones entre la polarización óptica y rayos gamma sin correlacionar con rayos X (Aliu et al., 2016). Con el fin de ir más allá en la cuantificación de la variabi-

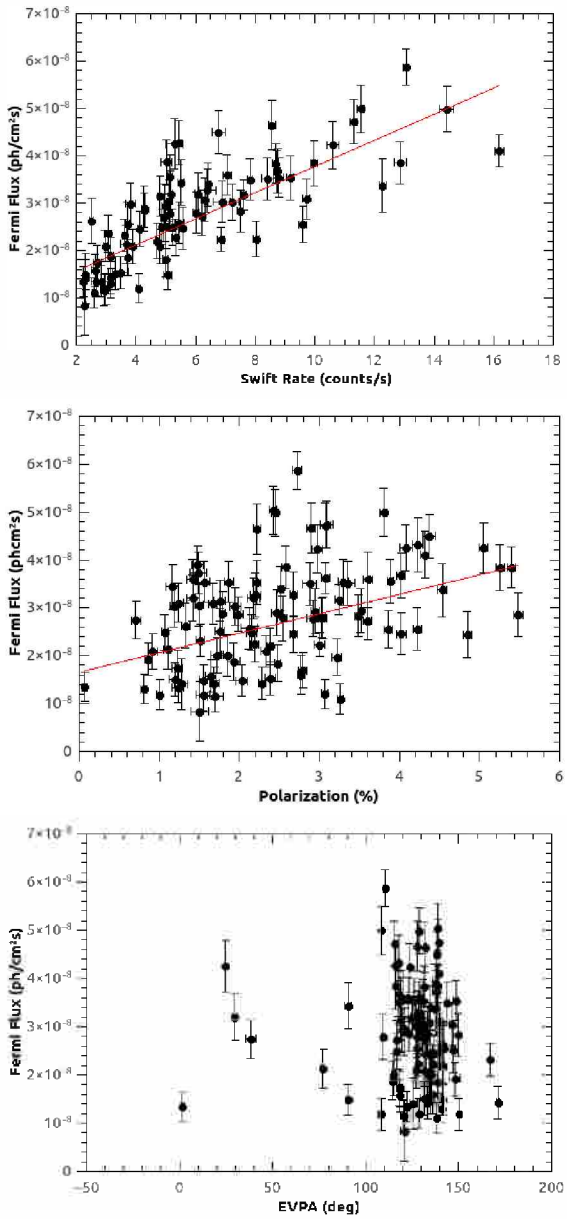

Figura 3: Flujos promediados mensualmente de *Fermi-LAT* vs. *Swift-XRT* (*panel superior*); vs. el grado lineal de polarización óptica con promedios mensuales (*medio*); y vs. el ángulo del vector eléctrico de polarización con promedios mensuales (*panel inferior*).

lidad del flujo presente en las curvas de luz, se obtuvo la variabilidad en la amplitud fraccional, F_{var} (Zhang et al., 2005) para todos los instrumentos involucrados y para los distintos años considerados en este trabajo, utilizando la siguiente expresión:

$$F_{\rm var} = \sqrt{(S^2 - \sigma^2)/F^2}, \quad (1)$$

donde F es el flujo promedio, S es la desviación estándar y σ el error cuadrático medio. $F_{\rm var}$ es utilizada principalmente para medir la variabilidad de un conjunto de observaciones en donde no se mantiene constante el intervalo de tiempo (e.g. Edelson et al. 2002). Si presenta un valor cercano a cero indica que no hubo variabilidad significativa, y un valor cercano a uno indica variabilidad. En la Fig. 2 se observa los resultados de la $F_{\rm var}$ calculada para rayos gamma, rayos X y la polarización lineal para cada año de observación. Se observa que la fuente presentó variabilidad moderada para rayos gamma, y una alta variabilidad, por ejemplo 2008–09, para la polarización óptica, y 2010–14 para rayos X, con un pico máximo en el *flare* detectado en el 2014.

2.2. Correlaciones

Se estudió para los años de observación si hubo una correlación entre los flujos de rayos gamma, rayos X y la polarización en el óptico, utilizando un ajuste lineal entre ambos. Una correlación fuerte entre dos bandas de energía se asocia con un origen en común de ambas poblaciones de fotones. Se puede apreciar en la Fig. 3, una modesta correlación (r=0.7) entre los rayos X y los rayos gamma, mientras que no se observa ninguna tendencia entre rayos gamma con la polarización óptica (r=0.2) y el $EVPA$. Se puede observar que el *flare* detectado en el período 1, detectado por VERITAS, corresponde a los 4 puntos donde el $EVPA$ es muy pequeño, del orden de 0–30 °, que no se correlaciona con la actividad de *Fermi-LAT*.

3. Discusión

Markarian 501 es un blazar constantemente monitoreado en todos los rangos de energía. Este blazar tuvo estados de alta y baja actividad desde el 2008 al 2018, exhibiendo varios períodos de unos meses de alta actividad en rayos X y rayos gamma (p2: MJD 55860–56000; p3: MJD 56800–57000), con varios *flares* detectados a muy altas energías con VERITAS y H.E.S.S. Estudiando la correlación con datos promediados mensualmente, se obtuvo una correlación moderada para la emisión de rayos X y rayos gamma. Este comportamiento no se encontró para otras longitudes de onda. El monitoreo constante diario o cada varios días es importante y necesario para detectar *flares* rápidos y estados de alta actividad, y así poder explicar su origen, como se producen y alguna manera para poder predecirlos.

Agradecimientos: Este trabajo ha sido parcialmente financiado por subsidios otorgados por CONICET y por ANPCyT.

Referencias

Aharonian F.A., et al., 1999, A&A, 349, 11
Ahnen M.L., et al., 2017, A&A, 603, A31
Albert J., et al., 2007, ApJL, 666, L17
Aleksić J., et al., 2015, A&A, 573, A50
Aliu E., et al., 2016, A&A, 594, A76
Cologna G., et al., 2017, *6th International Symposium on High Energy Gamma-Ray Astronomy, American Institute of Physics Conference Series*, vol. 1792, 050019
Edelson R., et al., 2002, ApJ, 568, 610
Horan D., et al., 2009, ApJ, 695, 596
Krawczynski H., et al., 2001, ApJ, 559, 187
Krawczynski H., et al., 2004, ApJ, 601, 151
Quinn J., et al., 1996, ApJL, 456, L83
Zhang Y.H., et al., 2005, ApJ, 629, 686

Role of gas fragmentation in the formation of supermassive black hole seeds

M. Suazo[1], J. Prieto[1] & A. Escala[1]

[1] *Departamento de Astronomía, Universidad de Chile, Santiago, Chile.*

Contact / matias.suazo@ug.uchile.cl

Resumen / Observaciones de cuásares en etapas tempranas del universo muestran que estas estructuras ya albergaban agujeros negros supermasivos de hasta 10^9 $M_\odot$. Radiación de fondo UV parece ser clave en la formación de semillas masivas de agujeros negros, ya que su presencia calienta el ambiente, y suprime refrigerantes moleculares permitiendo la formación de una estructura masiva. En este trabajo presentamos simulaciones cosmológicas realizadas con el código hidrodinámico RAMSES con el fin de estudiar la formación de semillas en diferentes escenarios. Nuestros resultados muestran que la radiación UV no es un único factor determinista en la formación de semillas masivas, la dinámica también parece ser importante. Esto, porque la dinámica es capaz de cambiar las condiciones de formación de semillas.

Abstract / High redshift quasars observations show that they already hosted supermassive black holes with masses up to 10^9 $M_\odot$. The UV background intensity seems to be a key parameter in the formation of massive seeds, since its presence heats the environment and suppresses molecular coolants, allowing the formation of a massive structure. Several cosmological simulations performed with the hydrodynamical code RAMSES are presented in this work to study the formation of seeds in different scenarios. Our results show that UV radiation does not determine the feasibility of forming massive seeds as a unique parameter, since other factors like gas dynamics may alter the formation of such objects.

Keywords / methods: numerical — quasars: supermassive black holes

1. Introduction

Quasars are intriguing astrophysical objects. They are primordial galaxies powered by supermassive black holes (SMBHs) in their centers. Observations of $z > 6$ quasars (Bañados et al., 2018) show that these objects already hosted SMBHs with masses up to 10^9 $M_\odot$ when the universe was ∼0.7 Gyr old. The formation of such massive objects is still a puzzle. Various mechanisms to form these structures have been proposed. For further reading, see Volonteri (2010) and Latif & Ferrara (2016).

Of all scenarios, direct collapse black hole (DCBH) model has been shown to be efficient in forming massive seeds. It consists of the immediate collapse of a gas cloud into a seed of 10^4 - 10^6 $M_\odot$. In this model, the seed would ultimately collapse into a black hole keeping most of its mass. The seeds need to accrete at rates ≥ 0.1 $M_\odot$ yr^{-1} (Schleicher et al., 2013; Sakurai et al., 2015). However, this scenario demands strict conditions. A very massive halo is indeed necessary to have the gas reservoir to form a massive seed and also to ensure high gas temperature (∼8000 K) to allow atomic cooling to operate. An intense UV background is also required in order to dissociate molecular hydrogen: an efficient coolant in this epoch. This radiation has been typically justified by setting a star forming galaxy in the surrounding of the possible DCBH. In comparison to molecular and metal cooling, atomic cooling is characterized by acting more smoothly in the temperature ranges involving DCBH conditions, permitting an isothermal collapse that does not produce fragments (Latif et al., 2013b, 2014).

Though the DCBH model may explain the formation of massive seeds, there are still some obstacles that gas needs to overcome. One obstacle arises when gas is photo-evaporated, in which case a dense core is prevented to be formed. Ionization also impedes the formation of a central structure, since it leads to an increase in the electron fraction, which is one of H_2 catalysts (Johnson et al., 2014). Another obstacle corresponds to the tidal interaction that the neighborhood may be exerting against the pristine halo, that could disrupt it, avoiding the formation of a massive central object (Chon et al., 2016).

The purpose of this work is to study the feasibility of forming massive black hole seeds in halos where fragmentation is allowed.

2. Methodology

We performed a set of three simulations in box sizes of 1 h^{-1}Mpc in comoving units using the adaptive mesh refinement hydrodynamical cosmological code RAMSES (Teyssier, 2002). Initial conditions were created using the MUSIC code (Hahn & Abel, 2011). We got a maximum resolution of 10^{-2} pc in proper units. The cosmology used is the one given by the Planck Collaboration et al. (2016) that sets $\Omega_b = 0.3089$, $\Omega_\Lambda = 0.6911$, $\sigma_8 = 0.8159$, $n_s = 0.9967$, $H_0 = 67.74$ km s^{-1}Mpc^{-1}. We used 32 cells per Jeans length as the minimum rea-

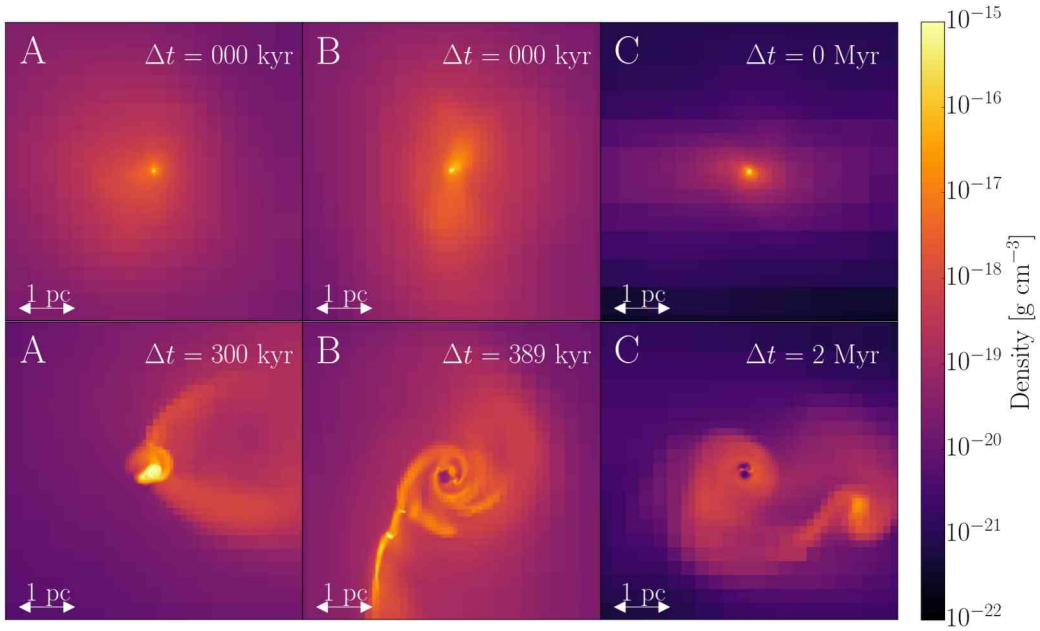

Figure 1: Density projection for all re-simulated halos irradiated by a uniform UV background. Halos A and B are under the effect of $J_{21} = 10000$, while C is irradiated by a UV background of $J_{21} = 10$. In all cases 5 pc are projected, and Δt is the time relative at which the first sink particle is formed in the re-run respectively.

sonable value suggested by Latif et al. (2013a) to resolve turbulences. No scheme for radiative transfer is included.

2.1. Chemical model

The thermal and chemical evolution of the gas were solved employing the publicly available package KROME (Grassi et al., 2014). We used a primordial chemistry network made up of the following species: H, H^+, H^-, He, He^+, He^{++}, e^-, H_2, H_2^+. We assumed a uniform isotropic UV background of various intensities that would come from a star forming neighborhood. The spectra of those regions are black-bodies with $T_{\rm eff} = 2 \times 10^4$ K, which is in the range that mimics realistic spectra (Latif et al., 2015).

2.2. Sink particles

The gravitational collapse of dense regions is a phenomenon quite recurrent in astrophysical simulations, therefore, a huge dynamical range is required. However, computational resources are not always sufficient to resolve the small scales. As a consequence, some numerical artifacts have arisen, one of them being the so-called sink particles.

Sink particles are particles that approximate the scales that are not resolved by the collapse of a region into a single point. A modified algorithm to the one presented in the RAMSES code (Bleuler & Teyssier, 2014) was used to create sink particles. It considers: the cell from which the sink particle will form has to be in the highest level of refinement, also the mass of such cell has to be larger than its Jeans mass.

Table 1: Virial mass, spin parameter and number of particles in the low resolution DM-only simulated halos.

Halo	Virial Mass [$M_\odot$]	Spin parameter	$n_{\rm part}$
A	9.68×10^7	0.016	1612
B	2.68×10^8	0.038	4471
C	4.90×10^7	0.022	821

3. Results

We performed 3D simulations to study the effect of gas fragmentation in the formation of primordial SMBH seeds in three different halos. We started from only Dark Matter (DM) low resolution simulations initialized at $z = 99$ in 1 comoving h^{-1} cMpc box sizes, in order to re-simulate some of them. Halo masses were required to be higher than $\sim 5 \times 10^7$ $M_\odot$ to guarantee the virial temperature to be in the atomic cooling regime (> 8000 K), in which gas is mainly cooled down due to electronic transitions in the hydrogen atom. We identified dark matter halos using the HOP clump finder (Eisenstein & Hut, 1998).

Three halos were selected to be re-simulated, some of their properties are shown in Table 1, which includes virial mass, bullock spin parameter (Bullock et al., 2001), and number of particles. Halos A and B were

re-simulated including a strong uniform UV background with a $J_{21} = 10000$ value, while halo C was re-simulated including a weak uniform UV background with a $J_{21} = 10$ value. J_{21} stands for 10^{-21} erg s^{-1} Hz^{-1} cm^{-2} str^{-1}.

In Fig. 1 we show density projections for our re-simulated halos under the presence of a uniform UV background according to the values mentioned in the paragraph above. In all these cases 5 pc are projected, and Δt refers to the time relative at which the first sink particle is formed in each run respectively. The first sink particle in halo A is formed at $z = 11.28$ (400.1 Myr), in halo B it is formed at $z = 10.80$ (425 Myr), and in halo C it is at $z = 11.03$ (412.5 Myr).

Halo A is shown in the leftmost column, B is represented in the middle column, and C is pictured in the rightmost column. Top row represents the state of the central 5 pc at the time the first sink particle is formed in each simulation, while the bottom row represents an evolved stage of the same region. Δt values chosen in this row were based on portraying changes in the structure, also to reveal the differences in the timescales to see them. In halos A and B projections are performed along the axis at which the structure is perpendicular. In halo C several structures are formed, so the projection was made along the z-axis arbitrarily. Projections are centered in the position of the first sink particle created.

Halo A initially starts as a central, dense spherical structure with a single sink particle in its center (not shown). As the simulation advances, the central structure acquires some asymmetries, but they do not affect its growing, fragmentation is not seen either. Just one sink particle is formed and it reaches 8.8 $\times 10^4$ M$_\odot$ at the end of the run. On the other hand, halo B behaves in a different way, it begins as a central dense object with a single sink particle in the center in the similar fashion to A, however it soon fragments forming a spiral-like structure as time goes on, from which new sink particles are formed. After a sink particle merging episode, the most massive sink particle ends up with 5.5 $\times 10^4$ M$_\odot$. In both halos 5 pc represent the extent of all structures formed. Finally, in halo C there is a similar behavior to the other cases: a central, dense structure is observed, and evolves into a spiral-like structure from which new sink particles are created. However, in Fig. 2 we can see a 100 pc region encompassing all features in this halo at the end of the run. Unlike the others, fragmentation happens at a larger scale, forming various cored regions. The most massive sink particles ends up with 1.6 $\times 10^4$ M$_\odot$ at the end of the run after three merger episodes.

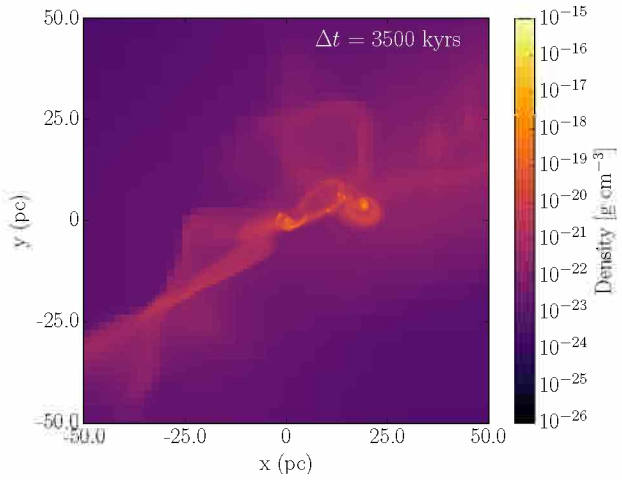

Figure 2: Density projection at 100 pc for halo C at the end of this run.

4. Conclusion

We got very different outcomes for our variety of halos. Halo A can be seen as the *traditional* DCBH scenario, since it forms a very dense, central object, whose central sink particle reaches a mass close to 10^5 M$_\odot$. Halo B is very similar to the DCBH in terms of the timescale and the final mass observed, however, it is the outcome of fragmentation and merger episodes. Simulations A and B have in common the same intensity value in the UV background. Despite of this, we find that the UV background is not the only parameter determining the behavior of the structure formed, since the history of the dark matter halo is different for everyone and matters. In halo C fragmentation also occurs, but unlike halo B, the scales where this process happen are larger, observed from 5 pc up to 100 pc. Unlike halos A and B, timescales for halo C are larger for one order of magnitude. Though the most massive sink particle in halo C is the lightest compared to the other halos, it is still very massive, and it can still grow through new merger episodes.

Acknowledgements: We received partial support from Center of Excellence in Astrophysics and Associated Technologies (PFB 06). We acknowledge partial support from FONDECYT through grant 1181663. The Geryon cluster at the Centro de Astro-Ingenieria UC was extensively used for the calculations performed in this work. BASAL CATA PFB-06, the Anillo ACT-86, FONDEQUIP AIC-57, and QUIMAL 130008 provided funding for several improvements to the Geryon cluster. Powered@NLHPC: This research was partially supported by the supercomputing infrastructure of the NLHPC (ECM-02).

References

Bañados E., et al., 2018, Nature, 553, 473
Bleuler A., Teyssier R., 2014, MNRAS, 445, 4015
Bullock J.S., et al., 2001, ApJ, 555, 240
Chon S., et al., 2016, ApJ, 832, 134
Eisenstein D.J., Hut P., 1998, ApJ, 498, 137
Grassi T., et al., 2014, MNRAS, 439, 2386
Hahn O., Abel T., 2011, MNRAS, 415, 2101
Johnson J.L., et al., 2014, MNRAS, 445, 686
Latif M.A., Ferrara A., 2016, PASA, 33, e051
Latif M.A., et al., 2013a, MNRAS, 430, 588
Latif M.A., et al., 2013b, MNRAS, 436, 2989
Latif M.A., et al., 2014, ApJ, 792, 78
Latif M.A., et al., 2015, MNRAS, 446, 3163
Planck Collaboration, et al., 2016, A&A, 594, A13
Sakurai Y., et al., 2015, MNRAS, 452, 755
Schleicher D.R.G., et al., 2013, A&A, 558, A59
Teyssier R., 2002, A&A, 385, 337
Volonteri M., 2010, A&A Rv, 18, 279

Galaxias de bajo brillo superficial: ¿análogas a los satélites de Andrómeda en Pegasus I?

N. González[1,2], A. Smith Castelli[1,2], F. Faifer[1,2], C. Escudero[1,2] & S.A. Cellone[1,3]

[1] *Facultad de Ciencias Astronómicas y Geofísicas, UNLP, Argentina.*
[2] *Instituto de Astrofísica de La Plata, CONICET–UNLP, Argentina*
[3] *Complejo Astronómico El Leoncito, CONICET–UNLP–UNC–UNSJ, Argentina*

Contacto / ngonzalez@fcaglp.unlp.edu.ar

Resumen / Presentamos los resultados preliminares de un estudio donde parece existir un efecto de sesgo en las distribuciones de tamaño de las galaxias de bajo brillo superficial (LSB) detectadas en diferentes entornos, en el sentido de que los grupos/cúmulos más distantes carecen de objetos de radio efectivo pequeños, mientras que los sistemas grandes no se encuentran en el Grupo Local y los entornos cercanos. Si bien puede haber una escasez real de galaxias LSB grandes en entornos de baja densidad como el Grupo Local, la no detección de sistemas pequeños (y débiles) a grandes distancias es claramente un efecto de selección. Como ejemplo, las galaxias LSB con tamaños similares a las de los satélites de Andrómeda en el Grupo Local, ciertamente se perderán en una identificación visual a la distancia de Pegasus I.

Abstract / We show the preliminary results of a study where there seems to be a bias effect in the size distributions of the detected low-surface brightness (LSB) galaxies in different environments. In this sense, more distant groups/clusters would lack small effective radius objects, while large systems would not found in the Local Group and nearby environments. While there may be an actual shortage of large LSB galaxies in low-density environments like the Local Group, the non-detection of small (and faint) systems at large distances is clearly a selection effect. As an example, LSB galaxies with similar sizes to those of the satellites of Andromeda in the Local Group, will be certainly missed in a visual identification at the distance of Pegasus I.

Keywords / Galaxies: dwarf — galaxies: photometry — galaxies: groups: (Pegasus I)

1. Introducción

En el trabajo de González et al. (2018) se plantea una posible correlación entre la distancia de los cúmulos/grupos que albergarían galaxias de bajo brillo superficial (LSB) y sus radios efectivos. Esta correlación parece indicar que las galaxias LSB poseen un tamaño real más grande a mayores distancias. En cambio, sus tamaños aparentes resultan más pequeños a distancia lejanas. Este efecto podría deberse solamente a las limitaciones que resultan de observar estos tipos de objetos de bajo brillo superficial. Esto es, las LSB pequeñas observadas a grandes distancias podrían confundirse con objetos de fondo, mientras que aquellas galaxias LSB cercanas podrían no detectarse debido a sus tamaños angulares extremadamente grandes. Sin embargo, la probabilidad de encontrar galaxias LSB grandes en un volumen pequeño alrededor del Grupo Local resultaría baja. Recientemente, Müller et al. (2018) encontraron posibles galaxias ultra difusas (UDGs) extremadamente grandes en el grupo de Leo-I (D $\sim$ 10.7 Mpc). De confirmarse su pertenencia en este grupo, estos objetos pasarán a ser las UDGs más cercanas.

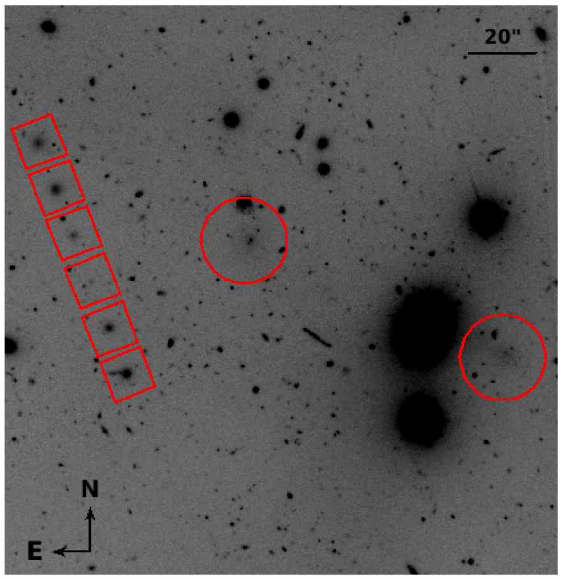

Figura 1: Mosaico de 2.85 × 2.85 arcmin en el filtro g' en el cual se muestra dos de las galaxias LSB detectadas en Pegasus I (círculos) reportadas en González et al. (2018). Superpuesto en este mosaico, a modo de comparación se muestra la apariencia que tendrían las dSphs de Andrómeda llevadas a la distancia de Pegasus I (cuadrados).

2. Selección de las candidatas a LSB

Con respecto a la posible presencia de un sesgo en la detección de galaxias LSB, nos preguntamos cuántos

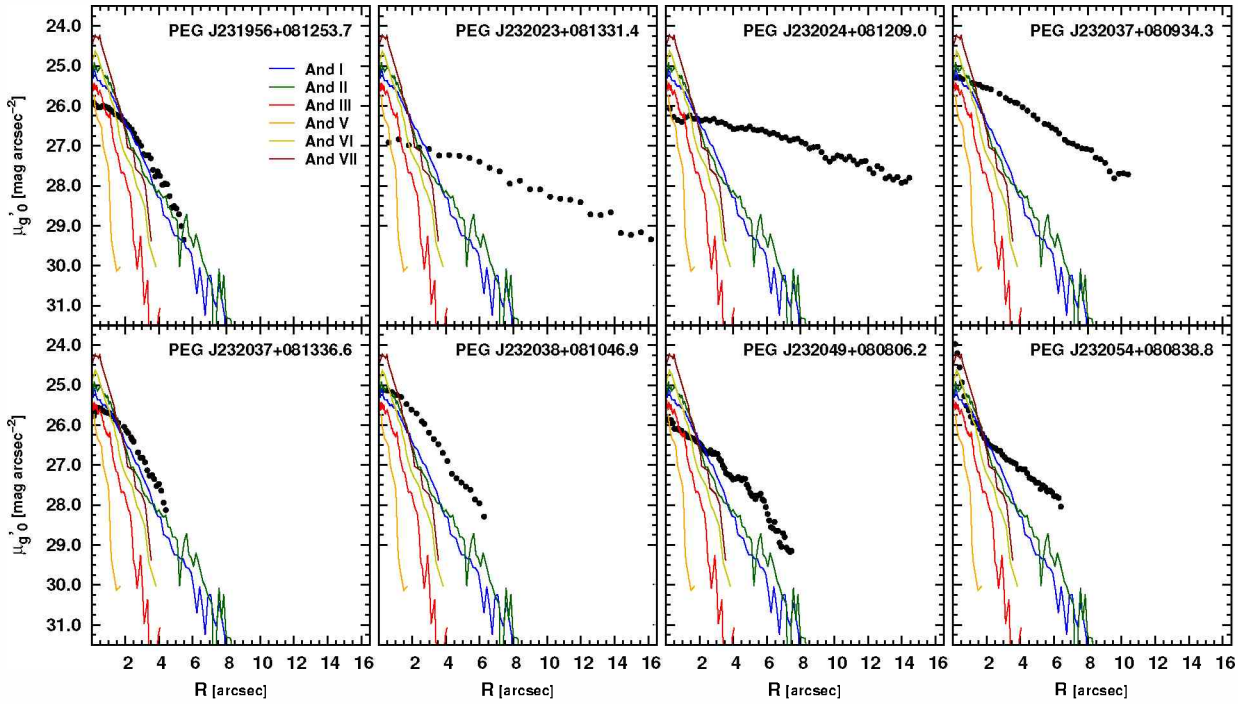

Figura 2: Comparación entre los perfiles de brillo g' de las galaxias LSB detectadas en Pegasus I (círculos negros) reportadas en González et al. (2018) y las seis galaxias dSph satélites de Andrómeda (Caldwell et al., 1992; Caldwell, 1999). Los perfiles de brillo en la banda V de las galaxias satélites de Andrómeda fueron transformados a la banda g' a través de las relaciones presentadas por Fukugita et al. (1995), y se escalearon a la distancia de Pegasus I.

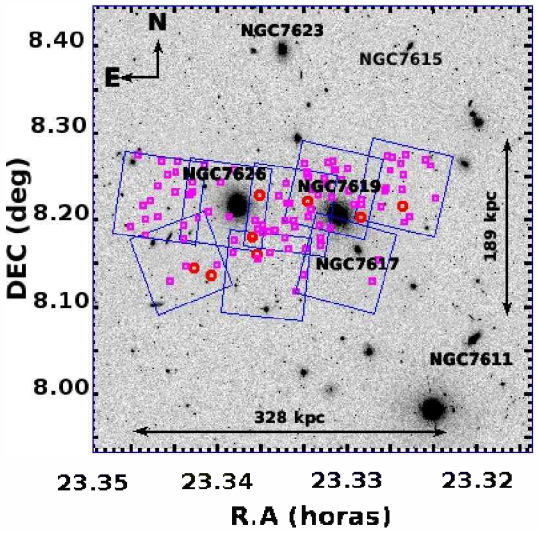

Figura 3: Mosaico de 30.5×30.5 arcmin en el filtro r' de SDSS DR12 mostrando la región central del grupo de Pegasus I. Los marcos azules corresponden a los campos de GEMINI-GMOS utilizados en este trabajo ($\sim$ 5.5 arcmin de lado). Los círculos rojos indican la ubicación de las candidatas LSB (González et al., 2018). Los cuadrados violetas indican la ubicación de galaxias candidatas cuya morfología resultan similares a las galaxias satélites observadas en Andrómeda.

objetos similares a los satélites dSph de Andrómeda ($D \sim 0.784$ Mpc) aparecerían a la distancia de Pegasus I ($D \sim 50$ Mpc). En la Fig. 1 mostramos los modelos de seis de estás galaxias obtenidas de los perfiles de brillo reportados por Caldwell et al. (1992) y Caldwell (1999), sobrepuesto en uno de los campos GEMINI-GMOS en Pegasus I.

Adicionalmente, comparamos los perfiles de brillo superficial de las galaxias LSB con los de los satélites de Andrómeda escalados a la distancia de Pegasus I (ver Fig. 2). Se puede ver que las dSphs de Andrómeda muestran tamaños entre $2 < r_{\rm tot} < 8$ arcsec y brillos superficiales centrales entre $24.5 < \mu_{0,g'} < 26$ mag arcsec^{-2}. Su brillo superficial central es bastante bajo, pero aún más brillante que los de las galaxias LSB detectadas en Pegasus I. Sin embargo, en comparación, sus tamaños aparentes resultan más pequeños.

En este contexto, la pregunta que surge es, ¿Cuántas LSB de tipo temprano se podrían perder en la inspección visual porque son muy pequeñas y fáciles de confundir con los objetos de fondo? Para buscar estos objetos decidimos utilizar el software SExtractor (Bertin & Arnouts, 1996) adoptando los siguientes criterios:

CLASS_STAR $\leqslant 0.2$,
FLAGS $\leqslant 2$,
Elipticidad $\leqslant 0.2$,
$2 < r_{\rm tot} < 8$ arcsec,
$24.5 \lesssim \mu_{0_{(g',r',i')}} \lesssim 26$ mag arcsec^{-2},
$0 \lesssim g' - i' \lesssim 1.3$,
y $0 \lesssim g' - r' \lesssim 1.2$

Se adoptaron estos rangos de colores considerando los valores mostrados para las galaxias LSB de tipo temprano en la sección 5.1 de González et al. (2018).

3. Datos fotométricos

Este trabajo está basado en ocho campos profundos tomados en los filtros g', r' e i' (Fukugita et al., 1996), empleando la cámara GMOS de Gemini Norte*. Estas imágenes cubren el entorno cercano a las dos galaxias dominantes de Pegasus I: NGC 7626 y NCG 7619, y se utilizaron para obtener la selección preliminar de noventa galaxias candidatas cuya morfología resultan similares a las galaxias satélites de Andrómeda. La Fig. 3 muestra la orientación de los diferentes campos analizados y la ubicación de estos objetos. Por su parte, en la Fig. 4, se muestran las imágenes de cuatro de estás candidatas en los filtros g' e i'.

Dado que las galaxias LSB con tamaños similares a las de los satélites de Andrómeda serán difíciles de detectar en una inspección visual a la distancia de Pegasus I, la identificación de las mismas se realizó utilizando SExtractor en las imágenes GEMINI-GMOS. Para ello, utilizando las tareas ELLIPSE y BMODEL de IRAF, se procedió a modelar las distribuciones de brillo superficial de las galaxias elípticas NGC 7626 y NGC 7619 y sus respectivos halos, incluyendo varios objetos extendidos. Luego, se restaron dichos modelos con el fin de poder identificar y medir las candidatas a galaxias LSB (para más detalles, remitimos al lector a la sección 3 de González et al. (2018)). Posteriormente realizamos la fotometría con SExtractor utilizando el criterio de selección mencionado en la Sec. 2., el cual permitió identificar noventa objetos con características similares a los satélites de Andrómeda a la distancia de Pegasus I.

4. Resultados preliminares y trabajo a futuro

En este trabajo se realizó la detección de objetos similares a las galaxias satélites dSph de Andrómeda en el grupo Pegasus I. Como resultado, se detectaron en el grupo noventa objetos con estas características. El primer paso, será realizar una revisión detallada de estos objetos, y analizar si los mismos presentan algún tipo de subestructura y/o posible formación estelar, ya que no es esperable que estas características estén presentes en galaxias de tipo temprano. Para ello, se comenzará inspeccionando las imágenes de cada objeto en los filtros g' e i'. Como ejemplo, en la Fig. 4, se muestran en los paneles superiores dos objetos que son potencialmente candidatos a ser galaxias similares a las satélites de Andrómeda. En contraparte, en los paneles inferiores se muestran dos objetos que podrían ser descartados de la primera selección por mostrar un cierta subestructura.

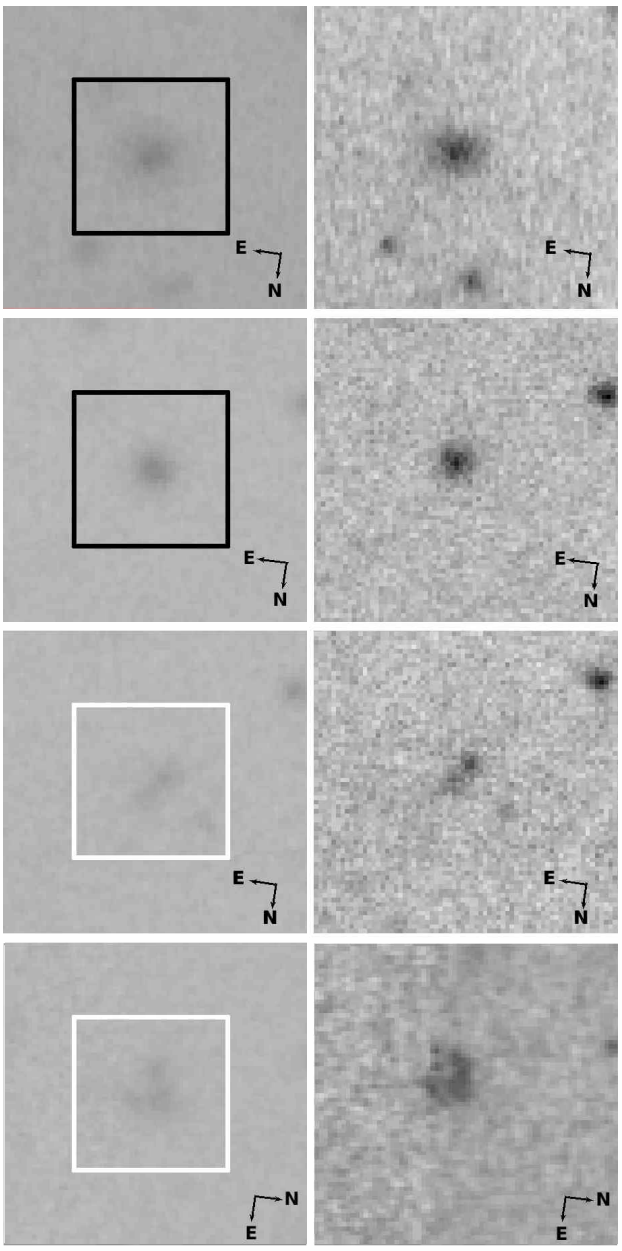

Figura 4: En los paneles izquierdos se muestran las imágenes de 10×10 arcsec en el filtro g' de cuatro de los objetos encontrados en la primera búsqueda con características similares a los satélites de Andrómeda a la distancia de Pegasus I. En los paneles derechos se muestran sus respectivas imágenes en el filtro i'. En ambos filtros se considero los mismos niveles de despliegue. Los cuadros negros señalan los objetos potencialmente candidatos, los cuadros blancos indican los objetos que podrían ser descartados.

Referencias

Bertin E., Arnouts S., 1996, A&AS, 117, 393
Caldwell N., 1999, AJ, 118, 1230
Caldwell N., et al., 1992, AJ, 103, 840
Fukugita M., Shimasaku K., Ichikawa T., 1995, PASP, 107, 945
Fukugita M., et al., 1996, AJ, 111, 1748
González N.M., et al., 2018, A&A, 620, A166
Müller O., Jerjen H., Binggeli B., 2018, A&A, 615, A105

*Programas GN-2008B-Q-14, PI: F. Faifer; GN-2012A-Q-55, PI: A. Smith Castelli; GN-2012B-Q-69, PI: F. Faifer; GN-2014A-Q-70, PI: F. Faifer; GN-2014B-Q-17, PI: N. González; GN-2015B-Q-13, PI: N. González.

Correlations for cosmology from the homogenization of GRB-associated supernova observations

F. Olivares E.[1,2]

[1] *Millennium Institute of Astrophysics, Santiago, Chile*
[2] *Departamento de Astrnomía, Universidad de Chile, Santiago, Chile*

Contact / f.olivares.e@gmail.com

Resumen / Las explosiones de rayos gamma (GRBs) de larga duración han sido encontradas en asociación a supernovas (SNs) desde el emblemático caso de GRB 980425/SN 1998bw. Un GRB puede ser detectado hasta $z \sim 9$ y sus SNs hasta $z \approx 1$. Correlaciones entre sus observables podrían ser útiles, por ejemplo para estimar luminosidades intrínsecas, si no fuese por la gran diversidad en sus observaciones. A partir de una muestra de > 30 SNs asociadas a GRBs, seleccioné aquéllas con observaciones en al menos dos filtros. Desarrollé un método para calcular el brillo intrínseco de la SN de manera más exacta. Usando parámetros del GRB y de la SN misma, evalué diferentes correlaciones. Encontré que usar la energía espectral máxima del GRB y el ancho de la curva de luz de la SN resulta prometedor para estandarizar la luminosidad de las GRB–SNs. Demostré que con las GRB-SNs se pueden determinar distancias con una precisión de ∼11 %–15 %. Estos resultados ofrecen nuevas oportunidades para explotar las GRB–SNs con el fin de sondear la expansión del Universo.

Abstract / Long γ-ray bursts (GRBs) have been found in association with supernovae (SNe) since the emblematic case of the GRB 980425/SN 1998bw. The GRB emission can be detected up to $z \sim 9$ and their SN counterpart has been observed up to $z \approx 1$. Correlations between GRB–SN observables could be useful, e.g. in determining extragalactic distances and intrinsic luminosities, if it was not for the large diversity of GRB–SN observations. With a sample of > 30 GRB-associated SNe from the literature, I selected those having observations in at least two filters. I developed a novel methodology to derive an accurate rest-frame SN brightness. Using parameters of the GRB emission and the SN itself, I evaluated different correlations. I found that using the GRB peak spectral energy and the SN light-curve width proves promising to standardize the SN luminosity. I demonstrated that GRB–SNe can determine distances with ∼11 %–15 % precision. These results unfold new opportunities to exploit GRB–SNe to probe the cosmic expansion of the Universe.

Keywords / supernovae: general — gamma-ray bursts: general — cosmology: observations

1. Introduction

The core collapse of some rapidly-rotating massive stars ($\gtrsim 15\,M_\odot$; Smartt 2009) leads to the formation of a relativistic jet that produces a γ-ray burst (GRB). The central engine powering the jet through accretion is either a black hole or a neutron star. Then a broad-lined type Ic SN follows expelling the remainder envelope at high velocities. These GRB-associated SN are more energetic than normal type Ic SNe peaking at about $M_V = -20$ mag and expanding as fast as $40\,000\,\mathrm{km\,s^{-1}}$ (Klose et al. 2019). GRB-SNe are detected up to $z \sim 1$, therefore there has been a growing interest at turning them into distance indicators Cano, 2014; Cano et al., 2014. Moreover, future all-sky surveys, e.g. LSST, will find hundreds of orphan GRB afterglows. Thus it is necessary to develop a robust methodology to standardize the luminosity of the associated SNe. So far, studies have included only handful of events in sample analyses. Here, I present an analysis on 20 GRB-SN events, I describe the first steps towards a reliable homogenization method to attenuate the diversity of GRB-SN observations, and I show the results of evaluating correlations using rest-frame GRB and SN parameters.

2. Data & Method

The GRB and SN data were acquired from several literature sources*. The GRB data consisted of z-corrected E_{peak} measurements, while the SN data included the maximum brightness and light-curve (LC) width. The GRB quantity corresponds to an average E_{peak} over the whole duration of the γ-ray emission. The SN quantities were characterized following the approach by Zeh et al. (2004), where k and s are the luminosity ratio and stretch factor with respect to SN 1998bw. From a complete sample of > 30 events, I selected a sub-sample of 20 events for which SN observations are available in

*Galama et al. (1998); Nakamura et al. (2001); Patat et al. (2001); Christensen et al. (2004); Mazzali et al. (2003, 2006); Sakamoto et al. (2005); Watson et al. (2004); Sazonov et al. (2004); Ulanov et al. (2005); Kann et al. (2006, 2019); Ferrero et al. (2006); Campana et al. (2006); Kaneko et al. (2007); Vreeswijk et al. (2008); Golenetskii et al. (2008); Richardson (2009); Nomoto et al. (2010); Tanvir et al. (2010); Thöne et al. (2011); Starling et al. (2011); Fan et al. (2011); Cano et al. (2011, 2014); Schady et al. (2012); Melandri et al. (2012); Olivares E. et al. (2012, 2015); Gendre et al. (2013); Cucchiara & Perley (2013); Schulze et al. (2013, 2014); Klose et al. (2013, 2019); and a few more circulars.

at least two filters. Estimations of $A_{V,\mathrm{host}}$ were usually obtained from the GRB afterglow SED (e.g. Olivares E. et al. 2015) and have been taken into account to compute the final k_λ values, where λ is the filter central wavelength in the rest frame.

When plotting the k_λ-SEDs in the top panel of Fig. 1, the considerable diversity in spectral shape is immediately evident. This is mainly attributed to the different photosphere temperatures at peak luminosity. The method to apply K corrections consisted in using the relative SEDs to compute new k values for a given band at rest-frame wavelengths. This band was chosen to maximize the number of events with SED coverage. Flux differences in the spectral lines compared to SN 1998bw affecting k_λ interpolation are considered negligible in a narrow λ band, therefore a low-order polynomial interpolation of the relative SEDs was sufficient. The rest-frame λ band in which the SED coverage overlaps for different GRB-SNe is shown in grey in the bottom panel of Fig. 1. To avoid extrapolation, the narrower blue and green λ bands are defined covering $(\lambda_{1\mathrm{b}}, \lambda_{2\mathrm{b}}) = (427, 467)\,\mathrm{nm}$ and $(\lambda_{1\mathrm{g}}, \lambda_{2\mathrm{g}}) = (495, 559)\,\mathrm{nm}$, respectively. Thus, rest-frame k values are defined as $k_{\mathrm{blue}} = (1/\Delta\lambda_{\mathrm{blue}}) \int_{\lambda_{1\mathrm{b}}}^{\lambda_{2\mathrm{b}}} k_{\mathrm{i}}(\lambda)\, d\lambda$ and $k_{\mathrm{green}} = (1/\Delta\lambda_{\mathrm{green}}) \int_{\lambda_{1\mathrm{g}}}^{\lambda_{2\mathrm{g}}} k_{\mathrm{i}}(\lambda)\, d\lambda$, where $\Delta\lambda_{\mathrm{blue}} = \lambda_{2\mathrm{b}} - \lambda_{1\mathrm{b}}$, $\Delta\lambda_{\mathrm{green}} = \lambda_{2\mathrm{g}} - \lambda_{1\mathrm{g}}$, and $k_{\mathrm{i}}(\lambda)$ is the interpolation function between the available k_λ values. Analogously, I defined the rest-frame stretch factors s_{blue} and s_{green}. Uncertainties have been computed through MC simulations for k and s values in both bands.

3. Results

With custom rest-frame k and s values at hand, I explored the parameter space. The SN 1998bw data have been excluded from the analysis because of: (1) its low-luminosity GRB; (2) its massive host galaxy; (3) the undetected GRB afterglow, which prevented an accurate extinction estimation; (4) its small luminosity uncertainty, which hampers a reliable calculation of correlation dispersions. Although SN 1998bw was nearby and often used as a template, its outlier nature has extensively discussed (e.g. Woosley & Bloom, 2006).

3.1. Luminosity vs. Stretch

Initially explored by Zeh et al. (2004), the k-s plane is derived solely from SN LCs. Although when investigating the k-s plane in the blue band I found no significant correlation, for the green band (Fig. 2) I recovered a trend similar to what has been previously reported by Cano (2014). A different analysis of the k values yields an almost identical trend (solid line in Fig. 2; Klose et al. 2019). The correlation analysis for the 14 events in the green band resulted in a reduced k dispersion of $\sigma_k = 0.29$ (originally $\sigma_k = 0.37$).

3.2. SN Luminosity vs. GRB E_{peak}

This parameter plane was initially explored by Li (2008) using three GRB-SNe and the X-ray flash (XRF) SN

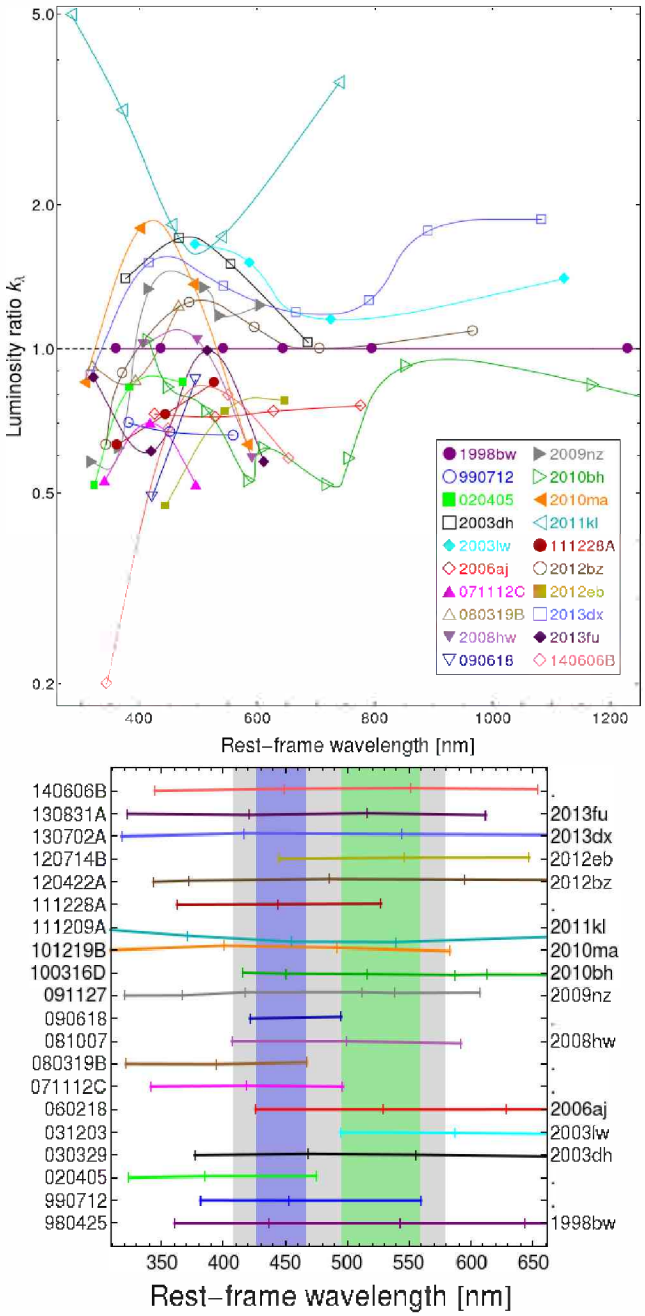

Figure 1: *(Top)* GRB-SN SEDs relative to SN 1998bw in the rest frame. Each event is represented by a different color and symbol. *(Bottom)* Vertically-separated relative SEDs of our GRB-SN sample. The blue and green regions are the λ bands that avoid extrapolation for 17 and 15 events, respectively.

2008D. Since we are aiming at homogenizing and reducing diversity, in this research I treated XRFs as a different kind of event compared to GRB-SNe and left XRF-SNe out of the sample. Again, when investigating this plane for k_{blue} I found a scatter plot. However, the correlation analysis of the 9 events in the green band resulted in a reduced k dispersion of $\sigma_k = 0.22$ (originally $\sigma_k = 0.36$) as shown in Fig. 3. The relation previously reported by Li (2008) was recovered doubling the sample size of GRB–SNe and leaving out XRF–SNe.

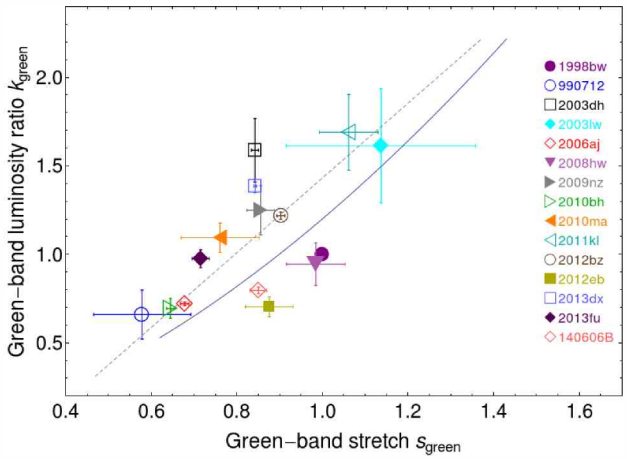

Figure 2: Luminosity ratios vs. stretch factors in the green band for 15 events. The dashed line is a weighted linear regression. The solid line corresponds to the power-law fit from Klose et al. (2019).

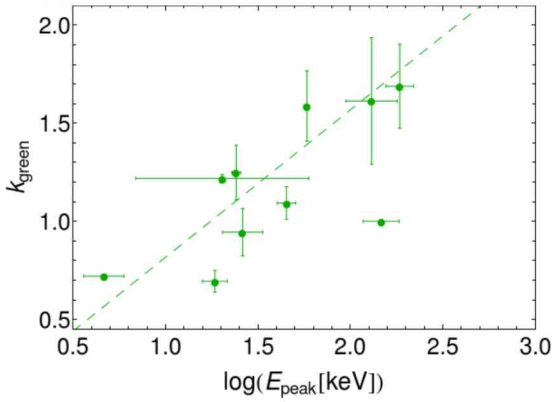

Figure 3: Peak spectral energy vs. luminosity ratios in the green band for 10 events. The dashed line is a weighted linear regression.

4. Discussion & Conclusions

So far the largest sample of >30 GRB–SNe was analyzed in search for correlations. A subset of 20 events complied with the requirements of the methodology (see §2. for details). I computed rest-frame luminosity ratios k and stretch factors s for the SN sample. The relation between luminosity and stretch is recovered with a dispersion of $\sigma_k = 0.29$, which translates into a precision in distance of 15 %.

The GRB $E_{\rm peak}$ from the γ-ray spectrum integrated over the whole event duration was corrected for the redshift of each event. It is worth noticing that estimating a characteristic $E_{\rm peak}$ for GRBs is not trivial. The average $E_{\rm peak}$ depends on the duration and variability of the γ-ray emission. Plus, there are also biases involving the estimation of $E_{\rm peak}$ from the time-integrated γ-ray spectrum and the used instrumentation. Regardless, using 9 GRB–SNe I recover the relation between the SN luminosity and $E_{\rm peak}$ previously investigated by Li (2008) with 4 events without having to include any XRF–SNe. The luminosity dispersion of $\sigma_k = 0.22$ translates into a distance dispersion of just 11 %.

When using blue-band SN parameters no significant relations were found probably due to the larger sampled by the blue band, the inclusion of peculiar events such as GRB 090618, and the diversity induced by metal absorption lines at bluer wavelength.

Although the additional dispersion in the Hubble diagram due to z was not taken into account, it is worth to highlight the reduced dispersion achieved by both investigated correlations. While the dispersion in the k-s green-band plane was reduced by 22 %, the dispersion in the k-$E_{\rm peak}$ green-band plane was reduced by 39 %, making GRB-associated SNe in promising distance indicators up to redshifts of about 0.7. It is worthy to mention that the sample size will have to be increased to allow for better statistical constraints.

Acknowledgements: Support was provided by the Ministry of Economy, Development, and Tourism's Millennium Science Initiative through grant IC120009, awarded to The Millennium Institute of Astrophysics, MAS, and FONDECYT grant 11170953.

References

Campana S., et al., 2006, Nature, 442, 1008
Cano Z., 2014, ApJ, 794, 121
Cano Z., et al., 2011, MNRAS, 413, 669
Cano Z., et al., 2014, A&A, 568, A19
Christensen L., et al., 2004, A&A, 413, 121
Cucchiara A., Perley D., 2013, GCN Circ., 15144, 1
Fan Y.Z., et al., 2011, ApJ, 726, 32
Ferrero P., et al., 2006, A&A, 457, 857
Galama T.J., et al., 1998, Nature, 395, 670
Gendre B., et al., 2013, ApJ, 766, 30
Golenetskii S., et al., 2008, GCN Circ., 7482, 1
Kaneko Y., et al., 2007, ApJ, 654, 385
Kann D.A., Klose S., Zeh A., 2006, ApJ, 641, 993
Kann D.A., et al., 2019, A&A in press, arXiv:1606.06791, arXiv:1606.06791
Klose S., et al., 2013, CBET, 3677, 1
Klose S., et al., 2019, A&A, 622, A138
Li L.X., 2008, MNRAS, 388, 603
Mazzali P.A., et al., 2003, ApJL, 599, L95
Mazzali P.A., et al., 2006, ApJ, 645, 1323
Melandri A., et al., 2012, A&A, 547, A82
Nakamura T., et al., 2001, ApJ, 550, 991
Nomoto K., et al., 2010, NewAR, 54, 191
Olivares E. F., et al., 2012, A&A, 539, A76
Olivares E. F., et al., 2015, A&A, 577, A44
Patat F., et al., 2001, ApJ, 555, 900
Richardson D., 2009, AJ, 137, 347
Sakamoto T., et al., 2005, ApJ, 629, 311
Sazonov S.Y., et al., 2004, Nature, 430, 646
Schady P., et al., 2012, A&A, 537, A15
Schulze S., et al., 2013, CBET, 3587, 1
Schulze S., et al., 2014, A&A, 566, A102
Smartt S.J., 2009, ARA&A, 47, 63
Starling R.L.C., et al., 2011, MNRAS, 411, 2792
Tanvir N.R., et al., 2010, ApJ, 725, 625
Thöne C.C., et al., 2011, Nature, 480, 72
Ulanov M.V., et al., 2005, NCimC GSPC, 28, 351
Vreeswijk P.M., et al., 2008, GCN Circ., 7444, 1
Watson D., et al., 2004, ApJL, 605, L101
Woosley S.E., Bloom J.S., 2006, ARA&A, 44, 507
Zeh A., Klose S., Hartmann D.H., 2004, ApJ, 609, 952

Exploring the star formation histories of galaxies in different environments from MaNGA spectra

M. Argudo-Fernández[1,2], M. Boquien[2], F. Yuan[3], S. Shen[3], J. Yin[3] & R. Chang[3]

[1] *Centro de Astronomía, Universidad de Antofagasta, Chile*
[2] *Chinese Academy of Sciences, South America Center for Astronomy, China–Chile Joint Center for Astronomy, Santiago, Chile*
[3] *Shanghai Astronomical Observatory, Chinese Academy of Sciences, Shanghai, China*

Contact / maria.argudo@uantof.cl

Resumen / La historia de formación estelar (SFH) de las galaxias nos permite investigar cuándo las galaxias formaron sus estrellas y ensamblaron su masa. Podemos restringir la SFH con un alto nivel de precisión de las galaxias con poblaciones estelares resueltas, ya que somos capaces de discriminar entre las estrellas de diferentes edades del espectro que emiten. MaNGA (*Mapping Nearby Galaxies at APO*) proporcionará espectroscopía resuelta para casi 10 000 galaxias en el universo local. Los principales objetivos de MaNGA son comprender el "ciclo de vida" de las galaxias actuales a partir de pistas impresas de su nacimiento y ensamblaje a través de su crecimiento continuo y de la formación y fusión de galaxias, hasta su muerte por extinción en los últimos tiempos. En este programa de investigación pretendemos utilizar datos MaNGA para restringir el SFH de las galaxias cercanas e investigar cómo se formaron y evolucionaron. Sin embargo, aún no está clara la importancia relativa de la evolución secular (naturaleza) sobre la crianza, y la separación de los efectos de la evolución impulsada por la interacción en las propiedades de galaxias observadas no es trivial. Nuestro equipo cuenta con expertos en el campo de la formación y evolución de galaxias, el entorno de galaxias, el modelado espectral de galaxias y los modelos de evolución química de galaxias, con experiencia en el trabajo conjunto. En esta contribución presentamos un programa de investigación entre China y Chile en el que usamos datos de MaNGA para restringir la SFH en galaxias cercanas que se encuentran en diferentes entornos para investigar cómo se formaron y cómo evolucionan. En particular, mostramos los resultados de nuestra metodología aplicada a una muestra de galaxias aisladas y a una fusión de galaxias.

Abstract / The star formation history (SFH) of galaxies allow us to investigate when galaxies formed their stars and assembled their mass. We can constrain the SFH with high level of precision from galaxies with resolved stellar populations, since we are able to discriminate between stars of different ages from the spectrum they emit. MaNGA (Mapping Nearby Galaxies at APO) will provide resolved spectroscopy for nearly 10 000 galaxies in the local Universe. MaNGA's key goals are to understand the "life cycle" of present day galaxies from imprinted clues of their birth and assembly through their ongoing growth via star formation and merging, to their death from quenching at late times. However, the relative importance of secular evolution (nature) over nurture is not yet clear, and separating the effects of interaction-driven evolution in the observed galaxy properties is not trivial. We present here the current state of a China–Chile collaboration program where we use MaNGA data to constrain the SFH of nearby galaxies in different environments to investigate how they form and evolve. In particular, we show the results of our methodology applied to a sample of isolated galaxies and a galaxy merger.

Keywords / galaxies: general — galaxies: formation — galaxies: evolution

1. Introduction

The electromagnetic emission of galaxies is our main window into their formation and their evolution. Young stellar populations dominate the UV-optical energy budget of galaxies. As they evolve and die they produce dust and inject vast amounts of metals in the interstellar medium, which have a direct impact on the formation of new stars, shielding and cooling molecular clouds, but also reddening and dimming the UV-to-near-infrared spectrum. In case of intense feedback from young, massive stars, star formation can even be quenched altogether, affecting the shape and appearance of galaxies. At the same time, galaxy can be red and dim simply because they are not forming stars anymore. In other words, the electromagnetic spectrum of galaxies encodes the past and current physical processes that have driven their evolution across cosmic times.

In this endeavour, spectral and photometric models are outstanding tools for measuring the physical properties of galaxies. Yet, they both have their own strengths and weaknesses. Spectra allow us to detect the presence of an AGN and access to the physical conditions of the ionised gas and of the stellar populations through emission and absorption lines and spectral indices. This yields, for instance, estimates of the extinction of the ionised gas, of the metallicity (both of the ionised gas and the stars), and constraints on the stellar forming regions (SFR) on very short (Halpha, ∼10 Myr) and very long (D4000, ∼1 Gyr) timescales. However spectra

are limited to a relatively narrow range in wavelengths and thus are only sensitive to a fraction of the baryonic components of galaxies. Conversely, photometric observations from the UV to the far-IR allow us to also probe young stellar populations that dominate the UV and the dust that reprocesses short wavelength radiation into the IR. Combined together, such a broad wavelength coverage provides us with the leverage we need to constrain the attenuation curve of the stellar continuum, the UV-based and IR-based SFR, and the stellar mass of galaxies. In other words, spectral and photometric data provide us with complementary and synergistic constraints on the physical properties of galaxies.

Regarding spectroscopic data, Integral Field Spectroscopy (IFS) provides us with a 3-dimensional view of galaxies (one spectral, two spatial) that encodes the processes driving their evolution, allowing us to go far beyond either the broadly used approaches of spatially-resolved photometry and spatially-unresolved spectroscopy. MaNGA (Mapping Nearby Galaxies at APO, Bundy et al., 2015) is an IFS survey designed to investigate an unprecedented sample of 10 000 nearby galaxies across a range of masses and spatial resolutions. The last MaNGA release, corresponding to the fifteenth data release of the SDSS (SDSS-DR15; Aguado et al., 2019), provides 4824 datacubes for 4621 unique galaxies. The MaNGA legacy dataset will be used to address a broad range of open questions in galaxy formation, including: 1. the nature of present-day galaxy growth via merging and gas accretion, 2. the processes responsible for terminating star formation in galaxies, and 3. the broad formation history of galaxy sub-components, including the disk, bulge, and dark matter halo.

We are carrying out a self-consistent spectro-photometric modelling of MaNGA galaxies using the CIGALE code. CIGALE (Code Investigating GALaxy Emission, Boquien et al., 2018) is a state-of-the-art self-consistent SED modelling code from the far-ultraviolet to the radio domain, including the contributions from stellar populations of all ages, thermal and non-thermal gas emission, dust (both in absorption and emission; the energy absorbed by the dust in the UV-to-near-IR domain is re-emitted self-consistently in the mid- and far-IR), and optionally an active nucleus. To estimate the physical properties of the modelled targets, it is based on a Bayesian-like analysis method. Even if CIGALE normally only handles broadband data, as a pathfinder work for this project we have developed an experimental version that fits spectra, with excellent results.

Following this methodology and using MaNGA 3-D maps, we will measure their physical properties (SFH, mass, metallicity, ionised gas and stellar continuum extinctions, etc.) with unprecedented precision and accuracy combining IFS data from MaNGA with multi-wavelength SED modelling from the UV to the IR. We therefore will provide new constraints on the assembly of galaxies across cosmic times.

Because processes governing the evolution of galaxies can be strongly intertwined, in this research program we collaborate to address these issues putting our own tools and expertise in common, from fundamental spectral modelling to the interpretation of the results of these models to understand the effect of the environment on the evolution of galaxies. In particular, we show here the recent results of two projects developed in the framework of this collaboration: 1. the SFH of spiral isolated galaxies, and 2. the SFH of a galaxy merger. In the case of the study of the galaxy merger, we use both, photometry and spectra SED fitting to constraint the SFH. We tested the spectra SED fitting technique that we are developing for isolated galaxies on the study of the merging galaxy. In the future, the results will be used to effectively incorporate the combined SED modelling in state-of-the-art self-consistent modelling codes.

2. SFH of spiral isolated galaxies

From models, it is predicted that disks grow from inner to outer parts of galaxies, the so-called inside-out model of galaxy formation. This means that first stars form in the centre and later in the outer regions. As a consequence, we expect to observe gradients in stellar age and metallicity as a function of galaxy radii. At the same time, galaxies can evolve secularly (nature) or through the effect of their large-scale environments (nurture). To understand the fundamental physical processes at play within galaxies, it is important to separate nature from nurture. To this effect isolated galaxies and the power of IFS MaNGA data are the key ingredients to reach this goal.

How exactly do galaxies build their disk when they grow in isolation, unaffected by external influences? We aim at characterising the SFH of isolated galaxies, under the assumption of the inside-out scenario, and to compare with chemical evolution models.

The sample of isolated galaxies used in this study is selected from the SDSS-based catalogue of Isolated Galaxies (SIG Argudo-Fernández et al., 2015), which is composed of 3702 galaxies. We found 176 SIG galaxies in the last data release of MaNGA. Of them, we selected the 60 galaxies that we have classified as almost face-on spirals. We expect to double the number of SIG galaxies by the end of the survey. We divide each galaxy in radial bins of 3 arcsec (the spatial resolution of MaNGA is 2.5 arcsec). We use CIGALE to fit the stacked spectra in each radial bin to get the parameters of the SFH. An example of the spectral fitting in shown in the left panel of Fig. 1.

The right panel of Fig. 1 shows the parameters of the SFH according to the results with CIGALE (age, timescale τ, stellar metallicity [Z/H], and dust attenuation A_V). We find that, in general, the age and τ gradients of spiral SIG galaxies are in agreement in the inside-out disk growth. However, the stellar metallicity ([Z/H]) and dust attenuation (A_V) gradients show more diverse results, which indicate that the evolution of the disk is more complex than expected (Argudo-Fernández et al. in prep.).

3. Dust attenuation and SFH of merging galaxy MRK 848

Simulations show that the interaction of two galaxies in a pair can cause the gas inflow, triggering star-bursts

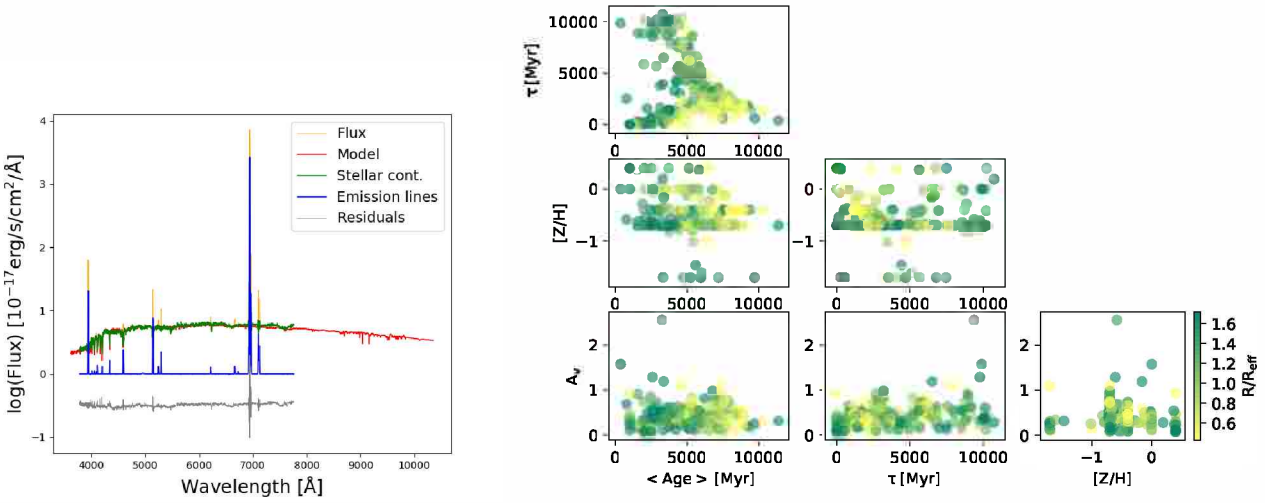

Figure 1: Preliminary results of the analysis of the SFH in the selected sample of SIG galaxies (Argudo-Fernández et al. in prep.). Left panel: Example of the result of the spectral fitting technique. The observed MaNGA spectra, with stellar continuum (without emission lines) and fitted emission lines by the MaNGA Data Analisys Pipeline (Westfall et al., 2019), best fit model using CIGALE, and residuals are coloured according to the legend. Right panel: Bayesian-like estimation of SFH's parameters. Results are coloured as a function of the effective radius, from yellow to green from inner to outer radial bins.

in the central regions of galaxies. While numerous observations have found that there is enhancement of star formation in galaxy pairs, the enhancement may depend on the local environment. Also, the spatial extent of the enhanced star formation in pairs is still not clear.

The UV and IR data are usually used to constrain the star formation rate and dust attenuation for mergers, which are tracers of the evolutionary stage of the systems. However, spatially resolved studies of galaxy mergers are restricted to very close galaxies, especially due to the lack spatial resolution in IR data. In Yuan et al. (2018), we show how the use of UV-to-IR broadband SED, in combination with MaNGA IFS, provide unique opportunity to study the star formation histories and dust attenuation at the tail and core parts of the merging galaxy Mrk 848. We use CIGALE to perform the photometric SED fitting, and CIGALE and PPXF (i.e., parametric and non-parametric methods) to perform the spectral SED fitting. This is a pilot study for the future application in a sample of MaNGA mergers (in progress).

We find that dust derived from full spectra fitting is systematically lower than from UV to IR SED fitting (see Fig. 9 in Yuan et al. (2018)). Additionally, using both photometry and spectroscopy SED modelling, we found a starburst younger than 100 Myr in core region, consistent with the scenario where the interaction-induced gas in-flow enhances the star formation in the centre of galaxies.

Acknowledgements: We thank all the members of the Local and Scientific Organizing Committees for the opportunity to present the our collaboration project, and for their active participation that allowed us to carry out a successful meeting. Participants are also thanked for contributing to this conference having been enriched with many valuable works and lively discussions. This work was supported by CONICYT Astronomy Program CAS-CONICYT project No. CAS17002. This work is sponsored by the Chinese Academy of Sciences (CAS), through a grant to the CAS South America Center for Astronomy (CASSACA) in Santiago, Chile. Funding for the Sloan Digital Sky Survey IV has been provided by the Alfred P. Sloan Foundation, the U.S. Department of Energy Office of Science, and the Participating Institutions. SDSS acknowledges support and resources from the Center for High-Performance Computing at the University of Utah. The SDSS web site is www.sdss.org.

References

Aguado D.S., et al., 2019, ApJS, 240, 23
Argudo-Fernández M., et al., 2015, A&A, 578, A110
Boquien M., et al., 2018, ArXiv e-prints
Bundy K., et al., 2015, ApJ, 798, 7
Westfall K.B., et al., 2019, arXiv e-prints
Yuan F.T., et al., 2018, A&A, 613, A13

Revealing the role of environmental and mass quenching with SAG

S.A. Cora[1,2], T. Hough[1], C.A. Vega-Martínez[1] & A.A. Orsi[3]

[1] *Instituto de Astrofísica de La Plata, CONICET–UNLP, Argentina*
[2] *Facultad de Ciencias Astronómicas y Geofísicas, UNLP, Argentina*
[3] *Centro de Estudios de Física del Cosmos de Aragón, Teruel, Spain*

Contact / sacora@fcaglp.unlp.edu.ar

Resumen / Estudiamos la relevancia de procesos que dependen de la masa estelar o de la densidad del ambiente en la supresión de la formación estelar (SF, por sus siglas en inglés) de galaxias satélites pasivas a $z = 0$. Analizamos un catálogo de galaxias generado mediante la combinación del modelo semi-analítico SAG con la simulación MultiDark MDPL2. Encontramos que $M_\star \approx 10^{10.5}\,\mathrm{M}_\odot$ es la escala de masa estelar donde los procesos de supresión que dependen de la masa se vuelven importantes. Los procesos de ambiente dominan la supresión de SF de las satélites de baja masa ($M_\star \lesssim 10^{10.1}\,\mathrm{M}_\odot$). Las galaxias de alta masa tienen más probabilidad de experimentar un cese de su SF mientras son centrales, y aquéllas que permanecen activas luego de que se convierten en satélites son principalmente afectadas por procesos dependientes de la masa. El proceso completo de supresión de la SF es bien descrito por un escenario de retardo-luego-atenuación. Durante la primera fase, la tasa de formación estelar de las satélites disminuye de manera similar a la de las galaxias centrales en un tiempo que varía desde $\approx 3\,\mathrm{Gyr}$ a $\approx 1\,\mathrm{Gyr}$ para satélites de baja masa ($M_\star \approx 10^{10}\,\mathrm{M}_\odot$) y alta masa ($M_\star \approx 10^{11}\,\mathrm{M}_\odot$), respectivamente. Durante la segunda etapa, las tasas de enfriamiento del gas y, en consecuencia, de la SF disminuyen más abruptamente hasta que la satélite se vuelve pasiva. Esto ocurre en $\approx 1\,\mathrm{Gyr}$ independientemente de la masa estelar.

Abstract / We study the relevance of mass and environmental quenching to the star formation (SF) history of $z = 0$ passive satellite galaxies by analysing a galaxy catalogue generated from the combination of the semi-analytic model of galaxy formation SAG and the MultiDark simulation MDPL2. We find $M_\star \approx 10^{10.5}\,\mathrm{M}_\odot$ to be the stellar mass scale where mass quenching becomes important. Environmental processes dominate the SF quenching of low-mass satellite galaxies ($M_\star \lesssim 10^{10.1}\,\mathrm{M}_\odot$). High-mass galaxies are more likely to quench as centrals, and those that remain active after first infall are mainly affected by mass quenching. The whole quenching process is well described by a delay-then-fade quenching scenario. During the first phase of this two-stage process, the star formation rate of satellites declines as they were centrals in a delay time that ranges from $\approx 3\,\mathrm{Gyr}$ to $\approx 1\,\mathrm{Gyr}$ for low-mass ($M_\star \approx 10^{10}\,\mathrm{M}_\odot$) and high-mass ($M_\star \approx 10^{11}\,\mathrm{M}_\odot$) satellites, respectively. During the second stage, the gas cooling rate and, consequently, the star formation rate decay more abruptly until the satellite becomes passive. The time span of this fading phase is $\approx 1\,\mathrm{Gyr}$, largely independent of stellar mass.

Keywords / galaxies: clusters: general — galaxies: evolution — methods: numerical

1. Introduction

Passive galaxies are characterised by low levels of star formation (SF). The fractions of passive galaxies present strong correlations with stellar mass, environmental density (given either by local density or halo mass) and halo-centric radius, both locally (Wetzel et al., 2012) and at high redshift (Peng et al., 2010; Muzzin et al., 2012; Lin et al., 2014; Jian et al., 2017; Kawinwanichakij et al., 2017). Both central galaxies (those residing at the centres of their host dark matter haloes) and satellite galaxies (those orbiting in the group potential) are more likely to be quenched as their stellar masses increase. This dependence is stronger for the former and is produced by mass quenching (e.g. Peng et al., 2010; Henriques et al., 2017), which refers to self-regulating processes that contribute towards suppressing the SF and depend on stellar mass, such as feedback from active galactic nuclei (AGN) (e.g. Fabian, 2012; Beckmann et al., 2017) and stellar feedback (e.g. Hopkins et al., 2014; Chan et al., 2018). For a given stellar mass, the fraction of passive satellites increases with increasing halo mass as a result of the larger effect of environment-dependent physical processes like ram pressure stripping (RPS, Gunn & Gott, 1972), tidal stripping (TS, Merritt, 1983), and turbulent viscous stripping (Nulsen, 1982), i.e. environmental quenching.

The aim of this work is to contribute to our understanding of the relative role of mass and environmental quenching in $z = 0$ passive satellites. We use the latest version of our semi-analytic model of galaxy formation SAG (acronym for Semi-Analytic Galaxies; Cora et al., 2018, hereafter Paper I). The results obtained from the analysis of the galaxy population generated by this model regarding the current topic are exhaustively analysed in Cora et al. (2019, hereafter Paper II).

2. Model of galaxy formation

We use an hybrid model of galaxy formation that combines our semi-analytic model of galaxy formation SAG with the cosmological dark matter (DM) MULTIDARK simulation MDPL2, which is part of the COSMOSIM database*. This simulation follows the evolution of 3840^3 particles within a box of side-length $1\,h^{-1}\,\mathrm{Gpc}$, with a mass resolution $m_\mathrm{p} = 1.5 \times 10^9\,h^{-1}\,\mathrm{M}_\odot$ per DM particle (Klypin et al., 2016). It is consistent with a flat ΛCDM model characterised by Planck cosmological parameters: $\Omega_\mathrm{m} = 0.307$, $\Omega_\Lambda = 0.693$, $\Omega_\mathrm{B} = 0.048$, $n_\mathrm{s} = 0.96$ and $H_0 = 100\ h^{-1}$ km s^{-1} Mpc^{-1}, where $h = 0.678$ (Planck Collaboration et al., 2014). DM haloes have been identified with the ROCKSTAR halo finder (Behroozi et al., 2013a), and merger trees were constructed with CONSISTENTTREES (Behroozi et al., 2013b). SAG assigns one galaxy to each new detected halo in the simulation. Thus, each system of haloes contains a central galaxy associated to the main host halo. DM structures contained within them are subhaloes which host satellite galaxies. When subhaloes are no longer detected because of numerical resolution effects, the satellites are called orphans and their orbits are integrated taking into account mass loss by TS and dynamical friction effects.

SAG includes physical processes that affect the baryonic components. A hot gas halo is formed when the gas is shock-heated as it falls into the potential well of the DM halo. The radiative cooling of hot gas allows the formation of a rotationally supported disc from which quiescent SF takes place. The number of supernovae (SNe) of type Ia and II are estimated from the initial mass function (IMF) assumed; we adopt the Chabrier IMF (Chabrier, 2003). The energetic and chemical SN feedback contributes towards regulating the amount of stars formed and determining the metallicity of all baryonic components. Starbursts triggered by disc instabilities and/or galaxy mergers allow the formation of a stellar bulge and the growth of a central supermasive black hole (BH). Gas accretion onto BHs produces AGN feedback that reduces gas cooling in large (sub)haloes, preventing them from forming stars at late times. When the galaxy becomes a satellite, its hot gas halo is gradually removed by a robust model of environmental effects through the action of RPS and TS. These processes can also strip the cold gas disc when it is not longer shielded by the hot gas halo. The physical processes implemented in SAG are characterised by efficiencies and parameters that are tuned by using the Particle Swarm Optimization Technique (PSO, Ruiz et al., 2015) in order to satisfy a set of observational constraints.

3. Role of mass and environmental quenching in passive satellites

We classify a satellite as passive when its specific star formation rate (sSFR), defined as the ratio between its star formation rate (SFR) and its stellar mass, is lower that a certain threshold, i.e. $\mathrm{sSFR} < 10^{-10.7}\,\mathrm{yr}^{-1}$, following Brown et al. (2017). The predictions of MDPL2 regarding the fraction of currently passive satellites as a function of stellar mass, halo mass and halo-centric distance (see figs. 11 and 12 of Paper I) are in agreement with those inferred from observations (Wetzel et al., 2012). We extend this analysis considering the dependence of these fractions on the time of first infall z_infall, defined as the moment in which the galaxy becomes a satellite for the first time.

Fig. 1 presents the dependence on z_infall of the fraction of $z = 0$ passive satellites that are quenched at time of first infall, fq_infall. All satellites within main host haloes of present-day mass $\log(M_\mathrm{halo}[\mathrm{M}_\odot]) \geq 12.3$ are considered. They are grouped according to their local stellar mass (different lines). Low-mass satellites ($M_\star \lesssim 10^{10.1}\,\mathrm{M}_\odot$) have null or very small values of fq_infall regardless of z_infall, which indicates that they have not suffered mass quenching while being centrals. Self-regulating processes such as AGN feedback or disc instabilities do not quench the SF of these satellites neither prior to nor after infall because of their low stellar mass. Low-mass satellites are mainly affected by environmental processes which act for longer on galaxies that have been accreted earlier. Therefore, the fractions of $z = 0$ passive satellites, fq_z0, are larger for galaxies with higher z_infall (see figure 1 of Paper II).

High-mass galaxies ($M_\star \gtrsim 10^{10.5}\,\mathrm{M}_\odot$) are more likely to be quenched as centrals as arises from the higher values of fq_infall for more massive galaxies, at fixed z_infall (Fig. 1). Moreover, for a given stellar mass range, fq_infall is larger for galaxies that have been accreted at later times (lower z_infall). This is explained by the combination of the stellar mass growth of a galaxy prior to infall and the time elapsed under the action of mass quenching processes while being central. After infall, the SF quenching of high-mass satellites continues to be dominated by mass quenching processes.

These results allow us to conclude that environmental processes dominate the SF quenching of low-mass satellites, and that $M_\star \approx 10^{10.5}\,\mathrm{M}_\odot$ is the mass scale where mass quenching becomes important. This picture is consistent with the results of previous works (van den Bosch et al. 2008, Peng et al. 2010, W13, Lin et al. 2014, Kawinwanichakij et al. 2017, Cochrane & Best 2018).

4. Delay-then-fade quenching scenario

The evolution of the sSFR of $z = 0$ passive satellites that were star-forming at infall indicates that their SF quenching process consists of two stages. During the first one, the rates of gas cooling experience a reduction of ≈ 50 percent with respect of their values at infall ($\approx 30 - 40\,\mathrm{M}_\odot\,\mathrm{yr}^{-1}$). These values allow the satellites to sustain high levels of SF so that their SFR declines gradually as if they were centrals (delay phase). During the second stage, the gas cooling rates and, consequently, the SFR decline faster until the satellites become passive (fading phase). The cooling rates reach values as low as $\approx 5\,\mathrm{M}_\odot\,\mathrm{yr}^{-1}$ by the time the satellites are quenched, which shows that the halt of cold gas supply is not a necessary condition for the onset of the SF

*https://www.cosmosim.org

quenching as assumed in the strangulation quenching scenario (Peng et al., 2015).

The origin of the decrease of the gas cooling rates depends on the stellar mass. In low-mass satellites, this decrease occurs because of the gradual removal of the hot gas halo through RPS; the fraction of the hot gas with respect to the total baryonic component of the satellites is reduced to $f_{\rm hot} \approx 0.5$ by the time they become passive. On the other hand, high-mass satellites keep a larger fraction of their hot gas reservoir by that time ($f_{\rm hot} \gtrsim 0.7$), and the cooling rates are reduced as a consequence of AGN feedback. Without an efficient replenishment through gas cooling, the cold gas disc is gradually depleted mainly by SF and/or removal through SN feedback. RPS of the cold gas does not play any role in the fading of SF. It only acts on a small fraction of satellites ($\approx 5-15$ percent) that have lost their protective hot gas halo before being quenched. This process may also contribute towards reducing even more the cold gas fraction after SF quenching.

The length of time of the delay and fading phases ($t_{\rm q,delay}$ and $t_{\rm q,fade}$, respectively) are comprised within the quenching time $t_{\rm q}$, which characterises the whole quenching process. The latter is estimated as the period of time elapsed since the galaxy is accreted and the moment in which it becomes passive. Median values of $t_{\rm q}$ are smaller for more massive galaxies: $t_{\rm q} \approx 4-5\,$Gyr for $M_\star \approx 10^{10}\,{\rm M}_\odot$ and $\approx 2\,$Gyr for $M_\star \approx 10^{11}\,{\rm M}_\odot$, consistent with results from Wetzel et al. (2013). The time span of the delay and fading phases are obtained by considering the physically motivated cooling-rate based criterion, i.e. we define $t_{\rm q,fade}$ as the period of time elapsed since the gas cooling rate is reduced to half the value it has at infall until the satellite becomes passive. We find median values of $t_{\rm q,fade} \approx 1\,$Gyr, regardless of stellar mass. Therefore, median values of the delay time range from $t_{\rm q,delay} \approx 3\,$Gyr for low-mass satellites ($M_\star \lesssim 10^{10}\,{\rm M}_\odot$) to $\approx 1\,$Gyr for high-mass ones ($M_\star \approx 10^{11}\,{\rm M}_\odot$). The comparison of the length of time of the two phases for a given stellar mass shows that our model is only consistent with the delay-then-rapid quenching scenario proposed by Wetzel et al. (2013) for low-mass satellites. This scenario does not represent the situation of high-mass satellites whose delay and fading phases have similar lengths of time. Hence, we propose a *delay-then-fade* quenching scenario to fairly describe all the possible situations.

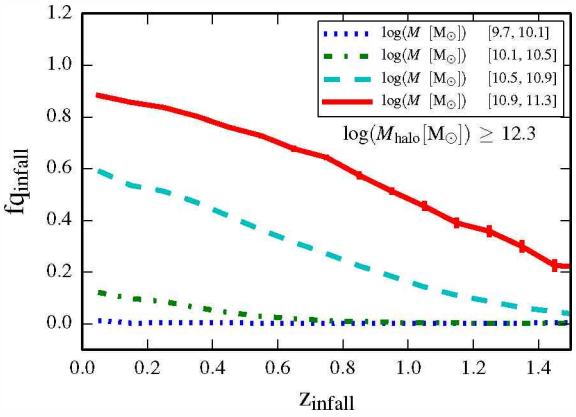

Figure 1: Fraction of $z = 0$ passive satellites that are quenched at first infall, $fq_{\rm infall}$, as a function of the redshift at infall, $z_{\rm infall}$. All satellites within main host haloes of present-day mass $\log(M_{\rm halo}[{\rm M}_\odot]) \geq 12.3$ are included. They are grouped according to their $z = 0$ stellar mass (different lines). Error bars show the 68 percent bayesian confidence interval estimated following Cameron (2011).

Acknowledgements: The authors thank the referee for useful comments and suggestions. They gratefully acknowledge the Gauss Centre for Supercomputing e.V. (www.gauss-centre.eu) and the Partnership for Advanced Supercomputing in Europe (PRACE, www.prace-ri.eu) for funding the MULTIDARK simulation project by providing computing time on the GCS Supercomputer SuperMUC at Leibniz Supercomputing Centre (LRZ, www.lrz.de). The MDPL2 simulation has been performed under grant pr87yi. This work was done in part using the Geryon computer at the Center for Astro-Engineering UC, part of the BASAL PFB-06, which received additional funding from QUIMAL 130008 and Fondequip AIC-57 for upgrades. SAC acknowledges funding from *Consejo Nacional de Investigaciones Científicas y Técnicas* (CONICET, PIP-0387), *Agencia Nacional de Promoción Científica y Tecnológica* (ANPCyT, PICT-2013-0317), and *Universidad Nacional de La Plata* (G11-124), Argentina. TH and CVM acknowledge CONICET, Argentina, for their supporting fellowships. AO acknowledges support from project AYA2015-66211-C2-2 of the Spanish *Ministerio de Economía, Industria y Competitividad.* This project has received funding from the European Union's Horizon 2020 Research and Innovation Programme under the Marie Sklodowska-Curie grant agreement No 734374.

References

Beckmann R.S., et al., 2017, MNRAS, 472, 949
Behroozi P.S., Wechsler R.H., Wu H.Y., 2013a, ApJ, 762, 109
Behroozi P.S., et al., 2013b, ApJ, 763, 18
Brown T., et al., 2017, MNRAS, 466, 1275
Cameron E., 2011, PASA, 28, 128
Chabrier G., 2003, PASP, 115, 763
Chan T.K., et al., 2018, MNRAS, 478, 906
Cochrane R.K., Best P.N., 2018, MNRAS, 480, 864
Cora S.A., et al., 2018, MNRAS, 479, 2
Cora S.A., et al., 2019, MNRAS, 483, 1686
Fabian A.C., 2012, ARA&A, 50, 455
Gunn J.E., Gott J.R.I., 1972, ApJ, 176, 1
Henriques B.M.B., et al., 2017, MNRAS, 469, 2626
Hopkins P.F., et al., 2014, MNRAS, 445, 581
Jian H.Y., et al., 2017, ApJ, 845, 74
Kawinwanichakij L., et al., 2017, ApJ, 847, 134
Klypin A., et al., 2016, MNRAS, 457, 4340
Lin L., et al., 2014, ApJ, 782, 33
Merritt D., 1983, ApJ, 264, 24
Muzzin A., et al., 2012, ApJ, 746, 188
Nulsen P.E.J., 1982, MNRAS, 198, 1007
Peng Y., Maiolino R., Cochrane R., 2015, Nature, 521, 192
Peng Y.j., et al., 2010, ApJ, 721, 193
Planck Collaboration, et al., 2014, A&A, 571, A16
Ruiz A.N., et al., 2015, ApJ, 801, 139
van den Bosch F.C., et al., 2008, MNRAS, 387, 79
Wetzel A.R., Tinker J.L., Conroy C., 2012, MNRAS, 424, 232
Wetzel A.R., et al., 2013, MNRAS, 432, 336

Study of the physical properties in extragalactic star-forming regions

D. Muñoz-Vergara[1], V. Firpo[1,2], G.F. Hägele[3,4], G. Bosch[3,4], D. Sanmartim[1], M. Cardaci[3,4] & G. Gimeno[1]

[1] *Gemini Observatory, La Serena, Chile*
[2] *Departamento de Física y Astronomía, Universidad de La Serena, La Serena, Chile*
[3] *Instituto de Astrofísica de La Plata, CONICET–UNLP, Argentina*
[4] *Facultad de Ciencias Astronómicas y Geofísicas, UNLP, Argentina*

Contact / daniamunozv@gmail.com

Resumen / El análisis de los procesos físicos entre una región de formación estelar y su medio requiere de un completo estudio de las componentes gaseosas. En este trabajo presentamos resultados preliminares del estudio de las propiedades físicas de regiones de formación estelar en tres galaxias: NGC 6070, NGC 5861 y Tol 1924-416. Estimamos la densidad y temperaturas electrónicas, abundancias químicas iónicas y totales y enrojecimiento usando datos de ranura larga de GMOS, obtenidos en el Telescopio Gemini Sur.

Abstract / The analysis of the physical processes between a star-forming region and its environment requires the complete study of the gaseous component. In this work we present preliminary results of a physical properties study of star-forming regions in three galaxies: NGC 6070, NGC 5861, and Tol 1924-416. We estimate the electron density and temperatures, ionic and total chemical abundances, and reddening using GMOS/Long-slit data obtained at the Gemini-South Telescope.

Keywords / galaxies: abundances — galaxies: individual(NGC 6070, NGC 5861, Tol 1924-416)

1. Introduction

The extragalactic star-forming regions are well-observed in the disks of spiral galaxies and occupy large areas in the blue compact dwarf galaxies. A large number of young and massive stars that ionizes the surrounding gas dominates the morphology and the physical conditions of their environment. The analysis of the physical processes between a star-forming region and its environment requires the complete study of the gaseous component.

We present preliminary results of the study of the physical properties and chemical abundances in a sample star-forming regions in two spiral and one Blue Compact Dwarf (BCD) galaxies.

2. Observations and data reduction

We have obtained a sample of star-forming regions located in NGC 5861, NGC 6070, and Tol 1924-416. The observations were performed with the Gemini-South Multi-Object Spectrograph (GMOS) in longslit configuration (program ID: GS-2007A-Q-30, PI: V. Firpo), using the B600 (blue) and R400 (red) gratings to cover a wavelength range ∼3350–9600 Å. Observations on each grating were made in 3 different central wavelengths so that the posterior combination would correct for chip gaps. Data reduction was performed using the GEMINI GMOS IRAF TASKS and included bias and overscan subtraction, flat fielding, wavelength calibration, and flux calibration. Observing conditions were good, with an average seeing of 0.7 arcsec. The R400 grating, centered at 7700 Å, gives a dispersion of 1.3 Åpix^{-1}. The B600 grating centered at 4800 Å gives a dispersion of 0.9 Åpix^{-1}.

3. Results

In each listed emission-lines (see Table 1), we measured the flux, continuum, and equivalent width (EW) with the respective uncertainties using the SPLOT task in IRAF and following the procedure described in Hägele et al. (2006). Table 1 shows, as example, the reddening-corrected emission-line ratios, for each measurement of the galaxy Tol 1924-416, along with the reddening constant and its error, taken as the uncertainties of the least-square fit and the reddening-corrected Hβ intensity. [S III] λ9532 flux was considered as the theoretical value 2.44×[S III] λ9069.

The physical conditions of the ionized gas in six star-forming regions (the two brightest regions observed within each slit) were derived following the methodology used in Hägele et al. (2012). The electronic density, n_e, was determined from the ratio R_{S2} of the lines [SII] $\lambda\lambda$6717,6731. The electron temperatures for each ion were derived using the Hägele et al. (2012) strategy (see discussion in its section §3.2). Table 2 shows the electron densities and temperatures, ionic and total chemical abundances derived for each observed region.

We derived the ionic chemical abundances of different species using the strongest available emission-lines

Table 1: Line intensities corrected by reddening ([F(Hβ)=I(Hβ)=10000]). 1: Measured emission-lines in region I and II of Tol 1924-416. Columns 2: Correction factor of region I and II. Columns 3 & 6: Equivalent widths of each measured line in region I and II respectively. Columns 4 & 7: intensity of each line in unities of Hβ with the corresponding error. Columns 5 & 8: Percentage error.

		Tol1924-416					
		I			II		
λ(Å)	f (λ)	–EW (Å)	I (λ)	Error (%)	–EW (Å)	I (λ)	Error (%)
3727 [OII]dob	0.271	87.82	13631±325	2.4	89.45	14065±421	3.0
3868 [NeIII]	0.238	36.64	4208±88	2.1	48.39	4957±169	3.4
3889 HeI+H8	0.233	13.58	1646±72	4.4	23.21	2027±92	4.5
3970 [NeIII]+He	0.215	47.78	3292±168	5.1	30.59	2673±133	5.0
4102 Hδ	0.188	34.26	2700±176	6.5	27.98	2664±437	16.4
4340 Hγ	0.142	74.78	4842±334	6.9	91.75	5263±149	2.8
4363 [OIII]	0.138	11.30	815±50	6.1	14.40	901±90	10.0
4471 HeI	0.106	7.32	471±30	6.4	. . .	. . .	. . .
4861 Hβ	0.000	179.99	10000±228	2.3	178.10	10000±200	2.0
4959 [OIII]	-0.024	281.76	17729±65	0.4	299.76	17691±26	0.1
5007 [OIII]	-0.035	786.43	53184±120	0.2	782.22	52661±106	0.2
5876 HeI	-0.209	25.48	971±19	1.9	34.18	1228±50	4.1
6300 [OI]	-0.276	11.33	363±18	5.1	13.57	548±19	3.5
6364 [OI]	. . .	. . .	. . .	. . .	5.80	234±19	8.3
6548 [NII]	-0.311	10.52	319±21	6.5	6.85	272±19	7.1
6563 Hα	-0.313	663.25	28366±186	0.7	767.78	29504±385	1.3
6584 [NII]	-0.316	28.02	854±30	3.5	18.01	727±30	4.1
6678 HeI	-0.329	11.86	311±13	4.3	8.87	302±53	17.7
6717 [SII]	-0.334	46.62	1283±32	2.5	43.76	1666±43	2.6
6731 [SII]	-0.336	32.97	928±29	3.1	30.51	1171±33	2.8
7065 HeI	-0.377	7.60	189±14	7.3	. . .	. . .	. . .
7136 [ArIII]	-0.385	20.23	476±18	3.7	18.48	544±22	4.1
7319 [OII]dob	-0.406	7.47	174±14	8.3	8.13	239±20	8.3
7330 [OII]dob	-0.407	7.69	179±22	12.3	5.89	174±17	9.8
7751 [ArIII]	-0.451	6.31	138±9	6.2	71.00	205±14	7.0
9069 [SIII]	-0.561	41.43	617±26	4.2	38.41	801±34	4.2
c(Hβ)		0.43 ± 0.03				0.25 ± 0.02	
I(Hβ)(erg seg^{-1} cm^{-2})		2.76×10^{-14}				1.60×10^{-14}	

detected in the analyzed spectra, and the equations given in Hägele et al. (2008), which were derived using ionic task the STSDAS package in IRAF, based in the five-level statistical equilibrium atom approximation. The ionic and total chemical abundances from forbidden lines O, S, N, Ne and Ar were derived from the measured forbidden emission-lines and using the estimated line temperatures as described in Hägele et al. (2008, 2012). The table includes the adopted value for He^+/H^+ as the average value, weighted by the errors, of the He ionic abundances derived from each HeII emission-line.

Empirical methods to determine abundances are based on the cooling system of the ionized nebulae. The most studied methods are based on the direct calibration of the relative intensities of some strong emission-lines compared with the abundances of relevant ions present in the nebula (empirical parameters). In the last seven lines of Table 2, we present the oxygen abundances of the observed regions (columns 2 to 7) derived with the strong-line empirical parameters (column 1).

4. Discussion

In all observed regions the electron densities were found to be well below the critical density for collisional de-excitation. In the two regions of Tol 1924-416 was possible to measure the auroral lines [OIII] λ4363, and [OII] λλ7319,7330, and we were able to estimate electron temperatures T([OIII]) and T([OII]) using the direct method. In both regions was possible to derive the oxygen abundances with values of ∼0.18 and ∼0.15 times the solar value ($12+\log(O/H)_\odot = 8.69$; Allende Prieto et al., 2001) for region I and II, respectively. These results, as well as the derived sulfur abundance, are in good agreement with the obtained by Kehrig et al. (2006) (0.16 times the solar value for the oxygen abundances and 6.08±0.12 for the sulfur abundances).

In the regions of the two spiral galaxies we assumed that T([OIII]) is equal to 10^4 K (as was discussed in §3.2 Hägele et al., 2012), then we estimated the oxygen abundances using photoionization models and empirical methods. The derived values for NGC 5861-I,II and NGC 6070-I are 0.1, 0.15 and 0.19 times the solar values, respectively. These oxygen abundances are consistent with the values estimated for both regions on Tol 1924-416. Meanwhile, NGC 6070-II has an oxygen abundance of 0.32 times the solar value, doubling the values of the BCD galaxy. The sulphur abundance for all regions are lower than the solar value ($12+\log(S/H)_\odot = 7.33$; Grevesse & Sauval, 1998). The log(S/O) ratio of NGC 5861-I,II and NGC 6070-I is consistent with the

Table 2: Densities in cm^{-3} and temperatures in 10^4K. [a] Derived using temperatures predicted by photionization models; [b] Derived using temperatures estimated from photoionization models and/or empirical methods; [c] Derived using Hägele et al. (2006) empirical method; [d] Derived using Díaz et al. (2007) empirical method; [e] Assumed temperature=10^4 K; [f] Derived using Pérez-Montero & Díaz (2003) empirical method.

	NGC 5861		NGC 6070		Tol 1924-416	
	I	II	I	II	I	II
n([SII])	10:	80:	10:	50:	30:	10:
T([OIII])	1.0[e]	1.0[e]	1.0[e]	1.0[e]	1.35±0.03	1.42±0.06
T([SIII])	0.87[c]	0.87[c]	0.87[c]	0.87[c]	1.29±0.03[d]	1.37±0.05[d]
T([OII])	1.21[f]	1.05[f]	1.21[f]	1.08[f]	1.29±0.12	1.47±0.12
T([SII]	0.98[f]	0.98[f]	0.98[f]	1.01[f]	1.04[b]	1.16[b]
T([NII])	1.21[a]	1.05[a]	1.21[g]	1.08[g]	1.06[c]	1.075[c]
			Total and relative abundances			
12+log(O/H)	7.67±0.01	7.87±0.03	7.96±0.01	8.20±0.02	7.95±0.06	7.87±0.06
ICF($S^+ + S^{2+}$)	1.04	1.00	1.22±0.01	1.04	1.37±0.12	1.48±0.09
12+log(S/H)	6.39±0.11	6.40±0.10	6.52±0.15	6.48±0.11	5.87±0.08	5.91±0.07
log(S/O)	-1.27±0.11	-1.47±0.10	-1.44±0.15	-1.72±0.11	-2.08±0.10	-1.96±0.09
log(N/O)	-0.49±0.02	-0.63±0.03	-0.67±0.02	-1.00±0.04	-1.31±0.18	-1.32±0.07
ICF(Ne^{2+})	. . .	. . .	. . .	. . .	1.08±0.01	1.08±0.01
12+log(Ne/H)	. . .	. . .	. . .	. . .	7.23±0.04	7.24±0.07
log(Ne/O)	. . .	. . .	. . .	. . .	-0.72±0.07	-0.64±0.09
ICF(Ar^{2+})	1.17	1.27±0.01	1.11	1.16±0.01	1.16±0.05	1.21±0.05
12+log(Ar/H)	5.73±0.21	5.50±0.30	5.99±0.18	5.69±0.59	5.10±0.05	5.04±0.07
log(Ar/O)	-1.94±0.21	-2.38±0.30	-1.97±0.18	-2.52±0.59	-2.95±0.08	-2.83±0.1
He^+/H^+(adopted)	0.11±0.01	0.06±0.01	0.08±0.002	0.08±0.001	0.08±0.01	0.1±0.1
Empirical Parameters			Oxygen abundances			
O_{23}	8.93±0.19	8.91±0.19	8.79±0.19	8.59±0.19	8.06±0.13	8.06±0.13
S_{23}	8.08±0.20	8.07±0.20	8.03±0.20	8.14±0.20	7.55±0.20	7.72±0.20
SO_{23}	8.63±0.27	8.60±0.28	8.29±0.27	8.14±0.28	7.37±0.27	7.55±0.27
O_3N_2	8.63±0.25	8.76±0.25	8.40±0.25	8.42±0.25	8.01±0.25	7.98±0.25
S_3O_3	8.46±0.25	8.54±0.25	8.27±0.25	8.18±0.25	7.55± 0.25	7.69±0.25
N_2	8.69±0.25	8.74±0.25	8.56±0.25	8.62±0.25	8.01±0.25	7.95±0.25
Ar_3O_3	8.56±0.23	8.59±0.24	8.38±0.23	8.05±0.47	7.63±0.23	7.73±0.23

solar value ($\log(S/O)_\odot$=-1.36; Grevesse & Sauval, 1998). The rest of regions present slightly lower values than solar ones. The log(N/O) ratio of NGC 5861-I,II and NGC 6070-I are slightly higher than the solar value ($\log(N/O)_\odot$=-0.88; Asplund et al., 2005). The other regions present log(N/O) values lower than the solar ones. Both regions of the Tol 1924-416 present similar log(Ne/O) ratio than the solar value ($\log(Ne/O)_\odot$=-0.61 dex; Grevesse & Sauval, 1998). The log(Ar/O) ratio of NGC 5861-I and NGC 6070-I are higher than the solar value ($\log(Ar/O)_\odot$=-2.29 dex; Grevesse & Sauval, 1998), the remaining regions have lower value than the solar one. The He total abundance estimated in all regions is similar at the typical values found for HII galaxies (Hägele et al., 2008). In all the studied regions the computed oxygen abundances using the empirical parameters are similar within the uncertainties. In both spiral galaxies, NGC 5861 and NGC 6070, the values estimated by the empirical parameters are higher than the once predicted by photoionization models and empirical methods. In both regions of Tol 1924-416 the estimated abundances are consistent with the derived abundances using the temperatures calculated by the direct method and by model-based and empirical temperature relationship.

Acknowledgements: DM gratefully acknowledges support from the Gemini Observatory, Southern Operations Centre, Internship Program. VF acknowledges support from CONICYT Astronomy Program-2015 Research Fellow GEMINI-CONICYT (32RF0002). Based on observations obtained at the Gemini Observatory, which is operated by the Association of Universities for Research in Astronomy, Inc., under a cooperative agreement with the NSF on behalf of the Gemini partnership: the National Science Foundation (United States), the National Research Council (Canada), CONICYT (Chile), Ministerio de Ciencia, Tecnología e Innovación Productiva (Argentina), Ministério da Ciência, Tecnologia e Inovação (Brazil) and the Korea Astronomy & Space Science Institute (Korea)

References

Allende Prieto C., Lambert D.L., Asplund M., 2001, ApJL, 556, L63

Asplund M., Grevesse N., Sauval A.J., 2005, T.G. Barnes III, F.N. Bash (Eds.), *Cosmic Abundances as Records of Stellar Evolution and Nucleosynthesis, Astronomical Society of the Pacific Conference Series*, vol. 336, 25

Díaz Á.I., et al., 2007, MNRAS, 382, 251

Grevesse N., Sauval A.J., 1998, SSRv, 85, 161

Hägele G.F., et al., 2006, MNRAS, 372, 293

Hägele G.F., et al., 2008, MNRAS, 383, 209

Hägele G.F., et al., 2012, MNRAS, 422, 3475

Kehrig C., et al., 2006, A&A, 457, 477

Pérez-Montero E., Díaz A.I., 2003, MNRAS, 346, 105

The VISTA variables in the vía láctea survey and the large-scale structure of the Universe

F. Milla[1], J.L. Nilo Castellón[1,2], L. Baravalle[3,4], M.V. Alonso[3,4], C. Valotto[3,4], J. Díaz Tello[5], G. Damke Calderón[1,2] & D. Minniti[6]

[1] *Departamento de Física y Astronomía, Facultad de Ciencias, Universidad de La Serena, Chile*
[2] *Instituto de Investigación Multidisciplinario en Ciencia y Tecnología, La Serena, Chile*
[3] *Instituto de Astronomía Teórica y Experimental, CONICET–UNC, Argentina*
[4] *Observatorio Astronómico de Córdoba, UNC, Argentina*
[5] *Pontificia Universidad Católica de Chile, Chile*
[6] *Universidad Andrés Bello, Santiago, Chile*

Contact / fmilla@userena.cl

Resumen / Presentamos algunos resultados respecto a la búsqueda de fuentes extragalácticas localizadas detrás de la Vía Láctea, basado en datos en el infrarrojo cercano proporcionados por el relevamiento público VISTA Variables en la Vía Láctea. Aplicamos un algoritmo que combina parámetros morfológicos y fotométricos para la detección de fuentes extendidas de naturaleza extragaláctica en cuatro regiones de más baja extinción Galáctica. Hemos detectado cientos de galaxias nunca antes vistas, cúmulos de galaxias y el indicio de una estructura mayor en la dirección del Cúmulo de Norma.
Los buenos resultados hasta ahora obtenidos, nos permitirán extender nuestra búsqueda de objetos extragalácticos a todo el disco Galáctico del relevamiento VVV y su extensión, VVVx.

Abstract / We present some results about the search for extragalactic sources located behind the Milky Way, based on near-IR data provided by VISTA Variables in the Vía Láctea Survey. We applied an algorithm that combines morphological and photometric parameters for the detection of extended sources of extragalactic nature in four regions at lower Galactic extinction. We have detected hundreds of galaxies never seen before, clusters of galaxies and the trace of a major structure in the direction of Norma Cluster.
The good results so far obtained, will allow us to extend our search for extragalactic objects in the Galactic disk of the VVV survey, and its extension, VVVx.

Keywords / catalogs — galaxies: fundamental parameters — galaxies: photometry — surveys

1. Introduction

The Large-Scale Structure (LSS) in the Universe is important to understand how the mass distribution at early times evolved through gravitational instabilities of small fluctuations to the *cosmic web*. This is a mixture of clustered halos, dense peaks of matter connected by filaments, sheets and voids (Zeldovich, Einasto & Shandarin, 1982). The effects generated by this composition create local disturbances to the expansion of the Universe inducing coherent flows of matter in some directions. These flows are present in the movements of the nearby Universe, printed on the map of Cosmic Microwave Background radiation (CMB; Planck Collaboration et al., 2014) as a dipole in the anisotropy distribution map.

In order to study the distribution and dynamics of the LSS of the nearby Universe, we need to find and map the extragalactic sources in all the sky regions. For many years the Milky Way (MW) put a serious limitation to the mapping of the galaxy distributions. Galactic dust distributed along the disk and bulge increases at low Galactic latitudes and towards the Galactic center dimming the radiation coming from the extragalactic sources behind the MW. This area is known as the Zone of Avoidance (ZoA; Shapley, 1961).

In the past, Kraan-Korteweg & Lahav (2000) reviewed the search of galaxies in the ZoA ($| b |< 20^{\circ}$), where they found more than 8 000 new galaxy candidates in the direction of the CMB radiation dipole using optical, near-IR, far-IR, radio and X-ray wavelengths. Also, the Two Micron All Sky Survey (2MASS; Skrutskie et al., 2006) covered the 91 % of the sky at bright limiting magnitudes. The 2MASS Redshift Survey (2RS; Huchra et al., 2012), presented one of the more detailed maps of the local Universe based on the spatial distribution of more than 43 000 galaxies within a radius of 300 Mpc (97.6 % of completeness) and limiting magnitude of $K_s = 11.75$ mag.

Although earlier efforts, the map of the LSS is still incomplete and important signs of structures encourage new studies. In this project, we propose to contribute to the study of the distribution of galaxies analyzing the near-IR data provided by one of the deepest surveys available on the bulge and the region of the disk of the MW: The VISTA Variables in the Vía Láctea Survey (VVV; Minniti et al., 2010).

2. The IR Data

The VVV is a public European Southern Observatory (ESO) near-IR variability survey carried out at the VISTA telescope in Chile, using five near-IR bands (Z, Y, J, H, K_s). VVV covered two sections of the MW divided in 196 regions (or tiles) in the bulge ($-10^\circ < l < +10^\circ$ and $-10^\circ < b < +5^\circ$), and 152 in the disk ($-65^\circ < l < -10^\circ$ and $-2^\circ < b < +2^\circ$), producing an area of 562 square degrees, with 348 of them covering an important section of the ZoA.

Since the main goal of VVV survey is to identify stellar variability in the Galaxy, the photometry generated by Cambridge Astronomy Survey Unit (CASU) is oriented to stellar types. In this frame, it becomes necessary to generate our own catalogs to obtain morphological parameters of the detected sources.

Our work is based on the application of high performance computational techniques, on near-infrared images provided by the VVV survey. We applied SExtractor v2.19.1 (Bertin & Arnouts, 1996) + PSFEx v3.17 (PSF Extractor; Bertin 2011) on the VVV images to obtain astrometric, photometric and morphological parameters of the sources in the Y, Z, J, H and K_s passbands.

To separate the extended sources from the stellar objects, we followed the procedure described in detail in Baravalle et al. (2018). The algorithm first identify extended sources by a combination of several morphological parameters such as the radius that contains 50 % of the total flux $R_{1/2}$, the concentration index (C; Conselice et al., 2000), and the parameters *CLASS_STAR* and *SPREAD_MODEL*. The magnitudes and colors obtained were corrected by extinction along the line of sight using maps of Schlafly & Finkbeiner (2011) and Catelan et al. (2011) for the VVV IR passbands. Some extended sources are detected in passbands at longer wavelengths (J, H, K_s) and are very faint or not visible at shorter wavelengths (Z, Y), while the stellar objects are visible in the five passbands of the survey. SExtractor + PSFEx may confuse faint objects with single objects or clump of stars in the MW. To minimize the false detections the color criteria were added: $0.5 < (J - K_s) < 2.0$ mag; $0.0 < (J - H) < 1.0$ mag; $0.0 < (H - K_s) < 2.0$ mag and $(J - H) + 0.9(H - K_s) > 0.44$ mag. If the source has detections in Z and Y passbands, it should also satisfy: $-0.3 < (Y - J) < 1.0$ mag and $-0.3 < (Z - Y) < 1.0$ mag.

3. Results

We applied the mentioned procedure in four regions of interest behind the MW disk.

The first two (tiles d010 and d115) are described in Baravalle et al. (2018). They are at low Galactic extinctions (K_s-values lower than 1 mag) with no previous detections in other surveys as the Extended Source Catalog (2MASSX; Jarrett et al., 2000). We found 345 and 185 extragalactic candidates, for the tiles d010 and d015, respectively, resulting in a total of 530 sources, all visually inspected and confirmed to be galaxies (Baravalle et al., 2018).

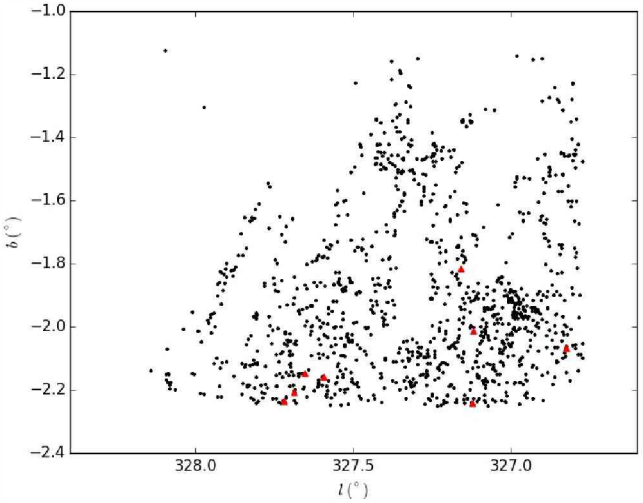

Figure 1: Spatial distribution of the extragalactic objects detected in tile d023. Red triangles correspond to the sources below.

The third studied tile, d015 contains 933 extragalactic sources detected (Baravalle et al., 2019). For the first time, using only photometric data we found a cluster of galaxies VVV-J144321-611754 based on the clustering analysis and the presence of the cluster Red Sequence (RS; Yee, Gladders & López-Cruz 1999). In a region of 30 × 30 $arcmin^2$, centered in the brightest galaxy, 25 extragalactic sources were detected and visually inspected. The median morphological parameters and near-IR colors of these galaxies are: $R_{1/2} = 1.59 \pm 0.16$ *arcsec*; $C = 3.01 \pm 0.08$; $\epsilon = 0.30 \pm 0.03$; Sersic index, $n = 4.63 \pm 0.39$; $(H - K_s) = 0.34 \pm 0.05$ mag; $(J - H) = 0.57 \pm 0.08$ mag and $(J - K_s) = 0.87 \pm 0.06$ mag. They are consistent with the properties of early-type galaxies. We estimated the photometric redshift of the brightest galaxy as $z = 0.196 \pm 0.025$ modeling the spectral energy distribution (Mancone & Gonzalez, 2012). For the two brighter galaxies we also obtained spectroscopic data using the near-IR imaging spectrograph, FLAMINGOS-2 at Gemini South telescope, in the long-slit, low resolution R ∼ 1200 mode. The estimated spectroscopic redshift of the concentration is $z = 0.234 \pm 0.022$ and we performed the K-correction to obtain the RS in the rest-frame near-IR color–magnitude diagram. The obtained slope is consistent with a galaxy cluster at redshift of 0.2. Based on all these results, we conclude that the galaxy concentration VVV-J144321-611754 found in the VVV tile d015 is a bona fide galaxy cluster.

The fourth tile, d023 was selected to start the study of the galaxy distribution in the Norma region. After a visual inspection of the tile, we applied the photometric procedure of Baravalle et al. (2018). Here we found over 500 extragalactic candidates with a half-light radius of about 5 *arcsec*. Our preliminary analysis is consistent with their results. Fig. 1 shows the distribution of the extragalactic candidates of the d023 tile in Galactic coordinates. The spatial distribution is not uniform. For instance, the left-upper part has empty regions with

higher extinctions (A_{Ks}=0.045) and the right-bottom part has clear concentrations with lower extinctions (A_{Ks}=0.018). There is also a prominent concentration at (l,b) = (326.97°, -1.96354°) corresponding to 41 detected sources. This strong distribution in the south-west region of the tile, probably is an indicative of *a bridge structure* that begins in the Norma Cluster (Kraan-Korteweg et al., 1996) and emerges at (l,b) = (323°, +2°). Fig. 2 shows color-composed images of some examples of the extragalactic sources represented with red triangles in Fig. 1. We will continue this work by analyzing an adjacent area to the tile d023 (300° < l < 330° and -2° < b < 2°), corresponding to 83 tiles in order to determine a major structure behind the disk of the MW.

4. Final Comments

Using the morphological and photometric methodology to find extragalactic sources we expect to increase the number of galaxies behind the MW. As part of this project, our main goal is to study the galaxy distribution in the projection of Norma Cluster. We will also use clustering techniques that allow us to separate real extensive, concentrated galaxy clusters from the distributions. We plan to search for extragalactic sources in the Galactic disk of the VVV survey and the extension (VVVx), and map the Large-Scale Structure in the nearby Universe beyond the Milky Way.

Acknowledgements: We are grateful to have access to the data of the ESO Public Survey (Program ID 179.B-20002) obtained with the VISTA telescope, and data products from the Cambridge Astronomical Survey Unit (CASU). Also, we thank to the organizing committee for the opportunity to present our work, the grant awarded for participation and University of La Serena for the financial support from Programa DIDULS PT17145.

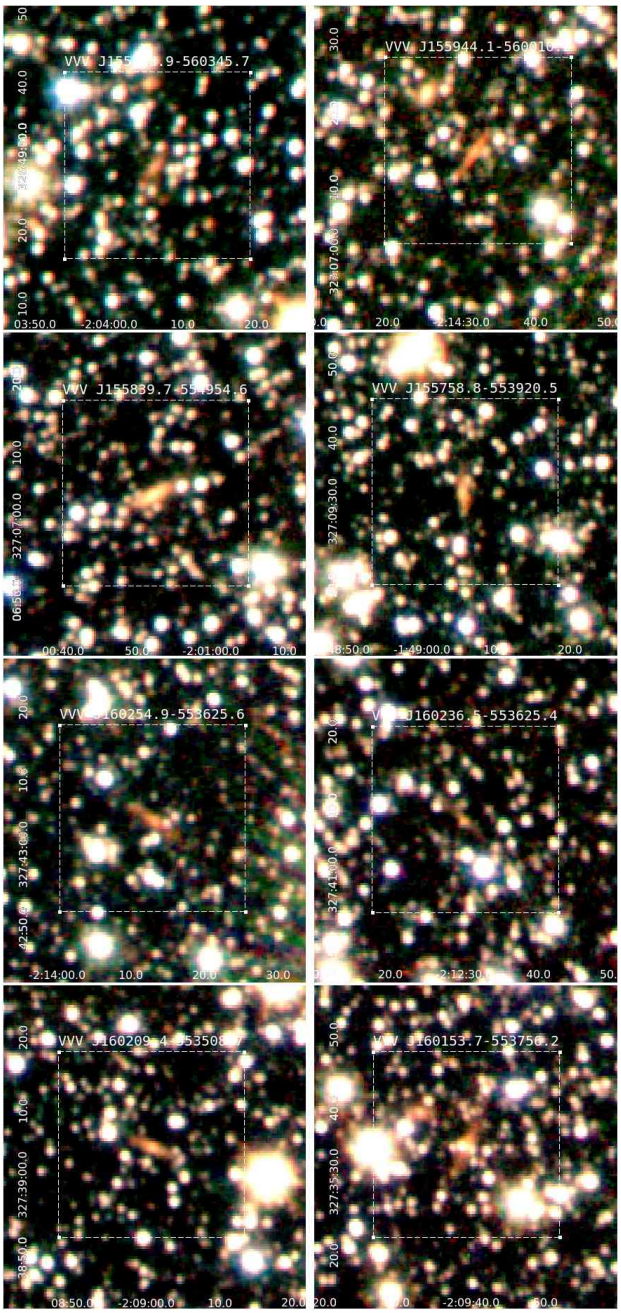

Figure 2: Color-composed images (J, H and K_s) of the extragalactic sources detected in tile d023 and represented by red triangles in Fig. 1. Each image has a box size of 44×44 arcsec^2. White dashed-line box represents an area of 25×25 arcsec^2.

References

Baravalle L.D., et al., 2018, AJ, 155, 46
Baravalle L.D., et al., 2019, arXiv e-prints
Bertin E., 2011, I.N. Evans, A. Accomazzi, D.J. Mink, A.H. Rots (Eds.), *Astronomical Data Analysis Software and Systems XX*, *Astronomical Society of the Pacific Conference Series*, vol. 442, 435
Bertin E., Arnouts S., 1996, A&AS, 117, 393
Catelan M., et al., 2011, A. McWilliam (Ed.), *RR Lyrae Stars, Metal-Poor Stars, and the Galaxy*, vol. 5, 145
Conselice C.J., Bershady M.A., Jangren A., 2000, ApJ, 529, 886
Huchra J.P., et al., 2012, ApJS, 199, 26
Jarrett T.H., et al., 2000, AJ, 119, 2498
Kraan-Korteweg R.C., Lahav O., 2000, A&A Rv, 10, 211
Kraan-Korteweg R.C., et al., 1996, The Messenger, 84, 17
Mancone C.L., Gonzalez A.H., 2012, PASP, 124, 606
Minniti D., et al., 2010, NewA, 15, 433
Planck Collaboration, et al., 2014, A&A, 571, A23
Schlafly E.F., Finkbeiner D.P., 2011, ApJ, 737, 103
Shapley H., 1961, *Galaxies*.
Skrutskie M.F., et al., 2006, AJ, 131, 1163
Yee H.K.C., Gladders M.D., López-Cruz O., 1999, R. Weymann, L. Storrie-Lombardi, M. Sawicki, R. Brunner (Eds.), *Photometric Redshifts and the Detection of High Redshift Galaxies*, *Astronomical Society of the Pacific Conference Series*, vol. 191, 166
Zeldovich I.B., Einasto J., Shandarin S.F., 1982, Nature, 300, 407

Studying the stellar field component of NGC 1316

C. Escudero[1,2], L. Sesto[1,2] & F. Faifer[1,2]

[1] *Instituto de Astrofísica de La Plata, CONICET–UNLP, La Plata, Argentina*
[2] *Facultad de Ciencias Astronómicas y Geofísicas, UNLP, La Plata, Argentina*

Contact / cgescudero@fcaglp.unlp.edu.ar

Resumen / Utilizamos la técnica de cinemática estelar a través de múltiples ranuras sobre datos espectroscópicos profundos Gemini/GMOS, a fin de calcular la cinemática y los valores de poblaciones estelares de la luz difusa de la galaxia NGC 1316 en diversas regiones. Así mismo, obtuvimos los parámetros estelares para cuatro cúmulos globulares asociados a dicha galaxia mediante la técnica de ajuste espectral completo.

Abstract / We used the Stellar Kinematics from Multiple Slits technique on deep Gemini/GMOS spectroscopic observations, in order to obtain the kinematics and stellar population values of the diffuse light of the galaxy NGC 1316 in different regions. We also obtained the stellar parameter values of four globular clusters associated with the galaxy using the full spectral fitting technique.

Keywords / galaxies: elliptical and lenticular, cD — galaxies: kinematics and dynamics

1. Introduction

The assembly history of the galaxies can be studied by mapping stellar populations at large galactocentric distances. The chemical and dynamic properties originated by accretion events that have suffered throughout its history should be preserved in these regions. In this sense, one of the tools used to study the ages and metal abundances at such distances is long-slit spectroscopy. However, the information obtained with this method is limited to the slit position. On the other hand, the low surface brightness of galaxies out to large galactocentric radii makes spectroscopic measurements difficult. In this context, we present preliminary results of using the Stellar Kinematics from Multiple Slits (SKiMS) technique (e.g., Norris et al., 2008) to map out the kinematics and stellar populations of the diffuse light of the galaxy NGC 1316.

NGC 1316 ($\alpha_{J2000} = 3^h22^m41.7^s$, $\delta_{J2000} = -37°12'30''$), located on the outskirts of the Fornax cluster ($\sim$ 20 Mpc), is a radio galaxy cataloged as a remnant of an intermediate-age merger ($\sim$ 2-3 Gyr), with a complex globular clusters (GC) system showing a dominant subpopulation of young clusters (Sesto et al., 2018).

2. Stellar Populations

Using the GMOS-S instrument of the Gemini Observatory, a MOS mask was obtained to observe the GC associated with NGC 1316 (GS-2013B-Q-24; PI: Sesto, L.). The flux incident on each MOS slitlet contains information of the observed GC, the sky background and the contribution from the diffuse light of the galaxy. Using a similar procedure as described by Norris et al. (2008), we extracted spectra from a small region (Fig. 1) of NGC 1316 ($V_{\rm helio}$=1760±10 km s^{-1}) corresponding to its stellar component.

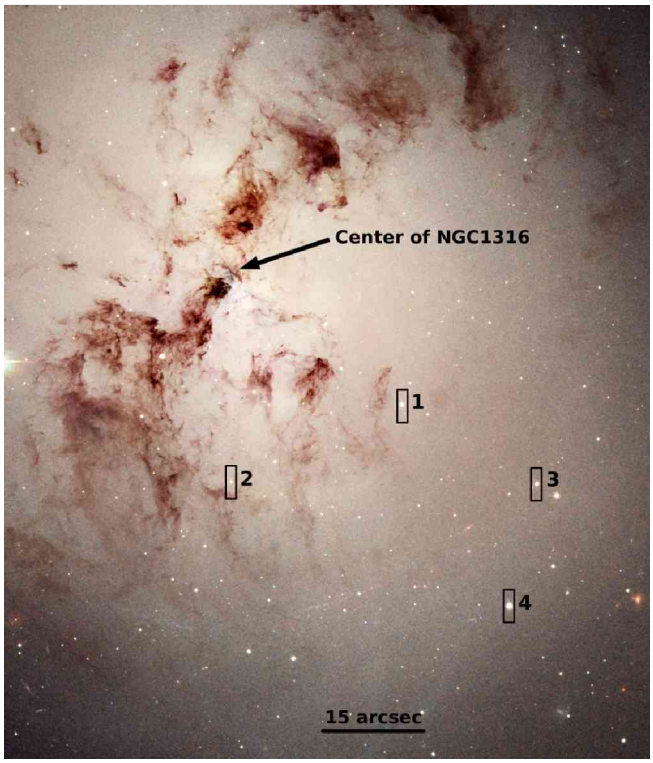

Figure 1: Hubble Space Telescope image of the central region of NGC 1316. The different rectangles indicate the slits where the spectra of the diffuse component of the galaxy and the associated GC were extracted.

We adopted the full spectral fitting technique implemented within the ULySS code (Koleva et al., 2009), in order to derive the kinematics and the simple stellar population-equivalent (SSP-equivalent) ages, total metallicities ([Z/H]), and α-element abundances

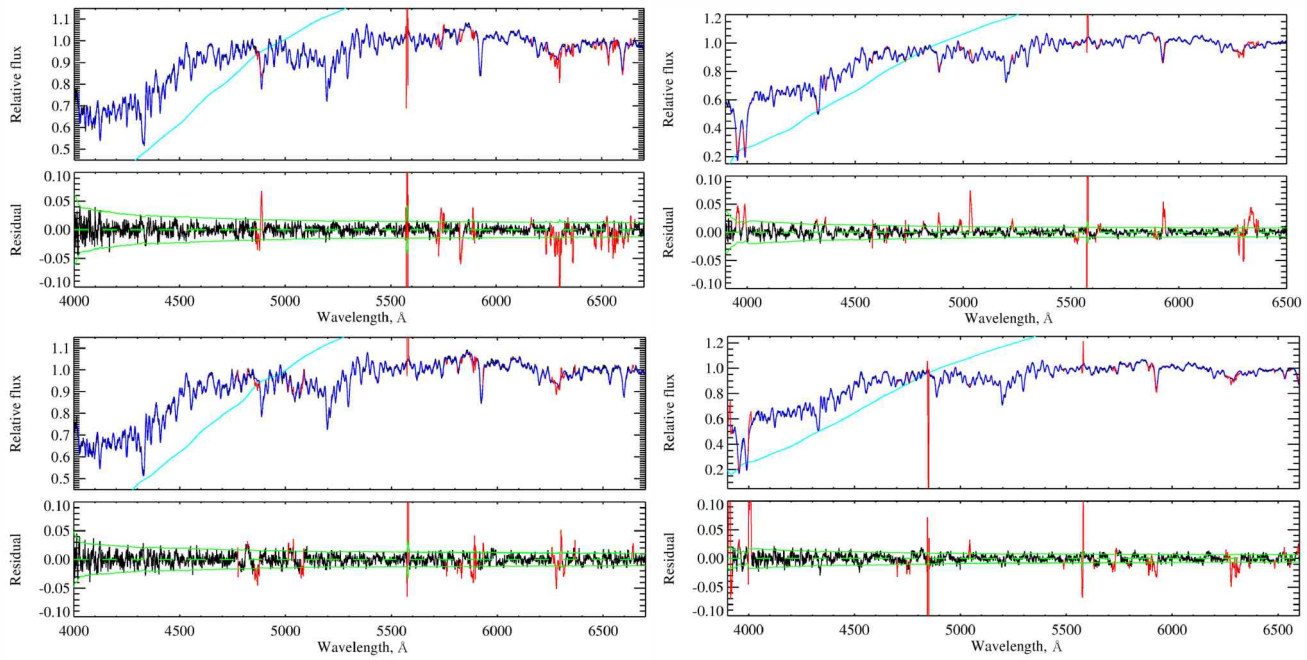

Figure 2: Representative diffuse-light spectra for NGC 1316 with the best fit obtained by ULySS (blue lines). The light blue line indicates the multiplicative polynomial. Red lines indicate the discarded lines during the fit. The residue obtained are displayed below each spectrum, where the green lines indicate the 1-σ deviation.

Table 1: Stellar population parameters obtained for the spectra of the galaxy and for the GC located in the same slitlet.

Object	V_r km s^{-1}	σ km s^{-1}	Age Gyr	[Z/H] dex	[α/Fe] dex
NGC1316(1)	1655±3	248±4	3.3±0.4	0.15±0.02	0.10±0.02
GC(1)	1265±20	—	1.7±0.5	0.20±0.20	0.15±0.05
NGC1316(2)	1687±5	252±4	4.6±0.3	0.03±0.01	0.10±0.03
GC(2)	1856±40	—	12.8±1.2	-1.1±0.17	-0.20±0.10
NGC1316(3)	1638±5	226±5	3.7±0.4	0.03±0.02	0.10±0.03
GC(3)	1640±22	—	1.8±0.5	0.11±0.20	0.05±0.05
NGC1316(4)	1621±5	213±6	4.1±0.2	0.02±0.01	0.07±0.03
GC(4)	1472±22	—	1.8±0.4	0.28±0.15	0.01±0.05

([α/Fe]) of the diffuse light of NGC 1316. For this, we use the PegaseHR models (Le Borgne et al., 2004) with ELODIE library, which span a range in age and [Z/H] of 1 to 20000 Myr and −2.3 to +0.69 dex, respectively. Fig. 2 shows the spectra for the diffuse light of the galaxy and the fit obtained by ULySS.

Table 1 lists the stellar parameter values derived for the spectra of the galaxy and for the GC located in the same slitlet.

3. Conclusions

We derive SSP-equivalent ages, metallicities and [α/Fe] ratios for the diffuse light of NGC 1316 in different regions, and compared them to those found for the GC population at the same projected radii. We find that the former presented slightly older ages (∼3-4 Gyr) than the young clusters (∼2.1 Gyr; Sesto et al., 2018), possibly as a consequence of a mixture between the young population formed during the main merger event and the oldest populations of the galaxy. On the other hand, the values of metallicity and α-element abundance between both samples are similar ([Z/H]∼0.0 dex and [α/Fe]∼0.1 dex).

We show the utility of the SKiMS method for investigating the kinematics and stellar populations in a small region of NGC 1316. As future work, all slitlets in our MOS mask will be used to study these properties and the star formation history at different galactocentric distances in the galaxy.

References

Koleva M., et al., 2009, A&A, 501, 1269
Le Borgne D., et al., 2004, A&A, 425, 881
Norris M.A., et al., 2008, MNRAS, 385, 40
Sesto L.A., et al., 2018, MNRAS, 479, 478

Hunting the polarization of the Cosmic Microwave Background using component separation methods

C. López-Caraballo[1,2], F. Rojas[3], C. Varas[1], L. Maurin[1], C. Vargas[1] & R. Dünner[1]

[1] *Instituto de Astrofísica and Centro de Astro-Ingeniería, Pontificia Universidad Católica, Santiago, Chile*
[2] *Departamento de Matemáticas, Universidad de La Serena, La Serena, Chile*
[3] *Computer Science Department, Pontificia Universidad Católica, Santiago, Chile*

Contact / lopezcaraballoch@gmail.com

Resumen / La radiación de Fondo Cósmico de Microondas (FCM) es una herramienta muy útil para estudiar el Universo primigenio. La detección de los modos B primordiales de la polarización del FCM se considera la piedra fundamental para probar la inflación. La caracterización de la polarización del FCM es un reto debido a la presencia de contaminantes astrofísicos que emiten en el mismo rango de frecuencias, lo cual requiere de métodos de separación de componentes (MSC) para recuperar la señal primordial del FCM. Aquí, presentamos el método *Hybrid Internal combination with Template Fitting* (HIT FITTING) el cual es un nuevo enfoque de los métodos de combinación lineal. Un conjunto de simulaciones en multifrecuencias se usan para evaluar la eficiencia del HIT FITTING y también se compara con otros métodos bien conocidos tales como el de combinación lineal interna y el de ajuste interno por patrones.

Abstract / The Cosmic Microwave Background (CMB) is a powerful tool to study the primitive Universe. The detection of the primordial B-modes of CMB polarization is considered a milestone for proving inflation. The characterization of primordial CMB polarization is challenging due to the contribution of astrophysical foregrounds emitting in the same frequency range, and we require of component separation methods (CSM) to recover the primordial CMB signal. Here, we present the *Hybrid Internal combination with Template Fitting* (HIT FITTING) method which is a new approach of linear combination methods. Multifrequency sets of simulations are used to assess the performance of the HIT FITTING and compare with other well-known methods, the *Internal Linear Combination* and the *Internal Template Fitting*.

Keywords / cosmology: cosmic background radiation — diffuse radiation

1. Introduction

The Cosmic Microwave Background (CMB) has been a powerful tool to study the primitive Universe. The CMB anisotropies have produced groundbreaking results, providing us cosmological parameters with a high precision supporting what is now accepted as the standard model of Cosmology (the ΛCDM, Bennett et al., 2013; Planck Col. et al., 2018, and references therein). In addition, the information contained in the CMB polarization patterns opens the door to characterize the inflation epoch. The E-modes (curl-free component) due to fluctuations in density were detected by DASI (Leitch et al., 2005) and several experiments. The B-modes (curl component) induced by primordial gravitational waves remain undetected and it is expected to be around an order of magnitude lower than E-modes. The B-modes signal induced from the gravitational lensing, a CMB foreground, were recently detected by experiments like SPT, BICEP, Keck and Planck. The detection of primordial B-modes is an important milestone in Cosmology, because it would confirm the presence of gravitational waves in the primordial Universe generated in the inflationary epoch. Moreover, the B-modes amplitude would determine the energy scale of inflation.

In the last decade, several new experiments have been deployed to measure the B-mode power spectrum, consequently improving the current constraints on the inflationary B-mode signal. In this context, the BICEP2 experiment, combined with Planck data, produced the tightest constraints to inflationary B-mode power (BICEP2/Keck Col. et al., 2015), setting an upper limit on scalar-to-tensor ration of $r < 0.12$. These results also demonstrated that the foreground emission of the Galaxy is a dominant effect that limits the determination of the signal of interest. Therefore, a comprehensive characterization of the galactic and extragalactic foregrounds is essential to clean and recover the primordial B-mode signal out of the CMB observations.

Given the relevance of the foregrounds, the use of component separation methods (CSMs) to extract the CMB signal is fundamental. There is a wide range of CSMs that can be found in the literature and that exploit different approaches to the problem. The methods are diverse as whether they operate in angular, Fourier or wavelet space, or whether they recover only the CMB component (e.g. Internal Linear Combination, or ILC) or if they extract several components (e.g. the *spectral fitting* approach). For example, the Planck team used NILC (Needlets Internal Linear Combination), SMICA, SEVEM and COMMANDER methods Planck Col. et al. (2016). However, irrespective of the approach, the per-

formance of all CSMs depends on the physical assumptions used to characterize the foregrounds. For this reason, the correct characterization of the Galactic polarized signal is a critical task in the quest to detect primordial B-modes.

Here we present a new approach called HIT FITTING, based on linear combination methods, to recover the polarized CMB and to study their impact in the characterization of the primordial B-modes.

2. Component Separation Methods

Methods based on a linear combination of maps are a simple, fast and practical methodology to recover the CMB signal. Therefore, we will consider methods focused on recovering only CMB signal and operating in the pixel space: the *Internal Linear Combination*, the *Internal Template Fitting* and the new approach HIT FITTING.

We consider that each frequency map, T_i, consists of the contribution of c astrophysical components (with amplitude A_c and frequency dependence $a_{c,i}$) and noise. In the description of each method, we assume maps are in thermodynamic temperature, i. e. the CMB spectrum is constant ($a_{CMB,i} = 1$).

2.1. Internal Linear Combination

In thermodynamic temperature, the Internal Linear Combination (ILC, Tegmark, 1998; Eriksen et al., 2004; Fernández-Cobos et al., 2016) recovers the CMB signal from a weighted linear combination of different frequency maps T_i:

$$\hat{T}_{\rm CMB,ILC} = \sum_{i=1}^{n_\nu} \omega_i \, T_i \, , \text{ and } \sum_{i=1}^{n_\nu} \omega_i = 1 \tag{1}$$

where the coefficients ω_i are estimated by minimizing the variance of the resulting map and considering the condition that ensures an unbiased measurement of the studied component (the sum of weights must be one). Using the Lagrange multipliers we obtain:

$$\omega_i = \frac{\sum_{j=1}^{n_\nu} C_{ji}^{-1}}{\sum_{i,j=1}^{n_\nu} C_{ji}^{-1}} \tag{2}$$

where C_{ij} is the covariance matrix of maps ($\langle T_i T_j \rangle - \langle T_i \rangle \langle T_j \rangle$), and $\langle \ldots \rangle$ identify the average over all pixels. The ILC only requires maps at the same resolution.

2.2. Internal Template Fitting

The Internal Template Fitting (ITF, Fernández-Cobos et al., 2012, 2016) computes an estimator of the CMB signal ($\hat{T}_{\rm CMB,ITF}$) from a map (T_{ν_c}) which is foregrounds cleaned using a lineal combination of templates ($\mathcal{T}_k$, without CMB component information):

$$\hat{T}_{\rm CMB,ITF} = T_{\nu_c} - \sum_{k=1}^{n\alpha} \alpha_k \, \mathcal{T}_k \tag{3}$$

where α_k are weights. These coefficients are estimated minimizing the variance of the $\hat{T}_{\rm CMB,ITF}$ map and assuming the same α_k for all pixel, which provides us:

$$\alpha = \mathbf{C}^{-1}\mathbf{b}, \tag{4}$$

Table 1: Simulations: frequency [GHz], Full Width at Half Maximum [arcmin] and sensitivity [μK-arcmin].

Freq	21	29	40	95	150	220	270
FWHM	120	91	66	28	18	12	10
Sensitivity	6.4	4.6	2.9	1.6	1.8	5.7	8.2

where $\mathbf{C}$ and $\mathbf{b}$ are the covariance matrix of templates ($\langle \mathcal{T}_k \mathcal{T}_j \rangle - \langle \mathcal{T}_k \rangle \langle \mathcal{T}_j \rangle$) and the covariance vector between the cleaned map and templates ($\langle T_{\nu_c} \mathcal{T}_k \rangle$), respectively.

2.3. Hybrid Internal combination with Template Fitting (HIT Fitting)

The Hybrid Internal combination with Template Fitting (HIT FITTING, López-Caraballo et al., in prep.) is a new approach combining the ILC and ITF methodology. Our CMB estimator, $\hat{T}_{\rm CMB,HIT}$, is described as:

$$\hat{T}_{\rm CMB,HITF} = \sum_{i=1}^{n\alpha} \alpha_i \, T_i \; - \; \sum_{j=1}^{n\beta} \beta_j \mathcal{T}_j \tag{5}$$

where T_i are the $n\alpha$ maps operating as the ILC approach, and $\mathcal{T}_j$ are the $n\beta$ foreground templates used in the template fitting approach. The α_i and β_j linear coefficients are estimated by minimizing the variance of the CMB estimator, and taking into account that the CMB signal is preserved when:

$$\sum_{i=1}^{n\alpha} \alpha_i = \; 1 \; . \tag{6}$$

Similar to ILC and ITF, α_i and β_j are obtained minimizing the variance of the CMB estimator and considering the Eq. 6. Using the Lagrange multipliers we obtained the solutions:

$$\alpha_i = \frac{\sum_{m=1}^{n\alpha} G_{m,i}^{-1}}{\sum_{m,i=1}^{ni} G_{m,i}^{-1}} \text{ and } \beta_j = \frac{\sum_{m=1}^{n\beta} H_{m,j}^{-1}}{\sum_{m,j=1}^{nt} G_{m,j}^{-1}} \tag{7}$$

where

$$G^{-1} = \left(A - CB^{-1}C^T\right)^{-1} \text{ and } H^{-1} = B^{-1}C^T G^{-1}$$

A, B and C are the covariance matrices of the T_i maps ($\langle T_i T_l \rangle - \langle T_i \rangle \langle T_l \rangle$), of the $\mathcal{T}_i$ templates ($\langle \mathcal{T}_j \mathcal{T}_k \rangle - \langle \mathcal{T}_j \rangle \langle \mathcal{T}_k \rangle$) and of the maps and templates ($\langle T_i \mathcal{T}_j \rangle - \langle T_i \rangle \langle \mathcal{T}_j \rangle$), respectively.

In this method, the T_i maps of the ILC approach must be smoothed to the same beam resolution. Templates contain only the foregrounds contribution, and they can be constructed from external or internal data.

The HIT FITTING, and similar to the ILC and ITF, does not require prior information about foregrounds, and the method only needs to know the behavior of the CMB's spectrum.

3. Forecasting

We use multifrequency sets of simulations to evaluate the performance of the HIT FITTING. In particular, we follow a preliminary version of Simons Observatory

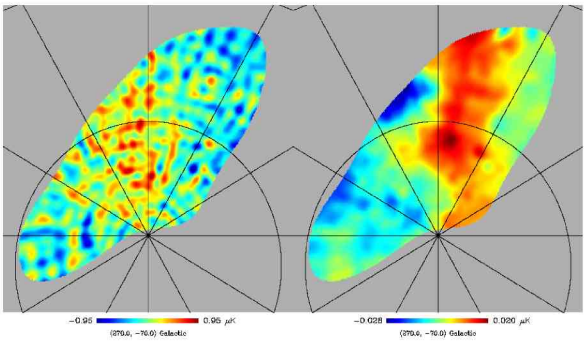

Figure 1: Stokes Q maps of the CMB input (left) and of the foreground residuals from the HIT FITTING (right).

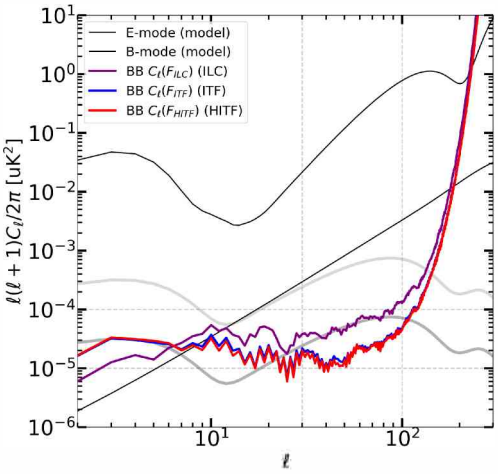

Figure 2: B-modes power spectra of the foreground residuals for the HIT FITTING (red), ILC (purple) and ITF (blue). The black lines drawn the theoretical E-modes and lensing B-modes ($r=0$) used in our simulations. The grey lines illustrate primordial B-modes with r equal to 0.01 and 0.001.

simulations consisting of seven frequency bands and covering 5 % of sky from southern hemisphere (see Table 1). In polarization, we consider the synchrotron and thermal dust emission. The free-free emission is known to be practically unpolarized. The Anomalous Microwave Emission were not included because it is expected to be weakly polarized (see e.g. Lazarian & Draine, 2000) and we only found strong constraint on their polarization ($\lesssim$1%, see e.g. López-Caraballo et al., 2011; Dickinson et al., 2018). We assume Gaussian white noise to estimate the noise maps. CMB map is computed without the primordial B-modes contribution ($r=0$), i.e. only lensing contribution. The maps were smoothed to a common resolution of 130 arcmin (see Fig. 1).

3.1. Implementation and Foreground residuals

The ILC CMB maps were computed using the seven bands. The ITF CMB maps were obtained cleaning the 95 GHz map and using four templates: $\mathcal{T}_1 = T_{20} - T_{30}$, $\mathcal{T}_2 = T_{30} - T_{40}$, $\mathcal{T}_3 = T_{220} - T_{150}$ and $\mathcal{T}_4 = T_{270} - T_{220}$.

For the HIT FITTING, we used the T_{30}, T_{95} and T_{270} (for the ILC part) and the $\mathcal{T}_2$ and $\mathcal{T}_4$ templates. The three methods are compared using the foreground residual map ($F_{\rm CSM}$), which is obtained from the propagation of foregrounds once the weights are computed. In Fig. 1, we can see the low foreground residual levels compared to the input CMB signal. HIT FITTING and ITF have similar foreground residuals level, and they are lower than those from ILC.

The power spectrum is estimated for each foreground residuals map ($F_{\ell,\rm CSM}$), which is corrected for beam and pixel window functions and the sky fraction. If the power spectrum of foreground residuals is lower than the primordial B-modes signal (with a tensor-to-scale ratio r), we consider that our estimator $T_{\rm CMB}$ allows us to establish a strong constraint (or detection) on this r. Fig. 2 shows the $F_{\ell,\rm CSM}$ for each method, where $30\lesssim \ell \lesssim 100$ is a reliable range because it is slightly affected by beam or the observed sky fraction.

The ILC shows a $F_{\ell,\rm ILC}$ residual compatible with the primordial B-modes with a $r=10^{-3}$, which could hinder the characterization of B-modes with such amplitude r. HIT FITTING and ITF have similar foreground residuals level in several multipoles (ℓ). Moreover, the foreground residuals are lower than primordial B-mode with $r=10^{-3}$. In particular, HIT FITTING appears to be a better performance than ITF in several multipoles.

4. Conclusions

The HIT FITTING is a new approach to recover the CMB signal using a linear combination. The HIT FITTING and ITF have similar foreground residuals level in several ℓ. We cannot confirm which of them has better performance, however, the HIT FITTING appears to be better performed. Our foreground residuals are lower than primordial B-modes with r=0.001. The HIT FITTING can be applied to multifrequency experiments such as liteBIRD, PICO and CORE, and in joint analysis (e.g. groundBIRD-QUIJOTE-Planck). Some other tests must be carried out (effect of gain, etc.). We expect to implement Needlet and Two Spin approaches.

Acknowledgements: C. López-Caraballo, C. Varas, C. Vargas and R. Dünner thank CONICYT for grants Anillo ACT-1417 and project Basal AFB-170002. F. Rojas thanks support from CONICYT Doctorado Nacional 23190411. L. Maurin thanks support from CONICYT, FONDECYT 3170846.

References

Bennett C.L., et al., 2013, ApJS, 208, 20
BICEP2/Keck Col., et al., 2015, PRL, 114, 101301
Dickinson C., et al., 2018, NewAR, 80, 1
Eriksen H.K., et al., 2004, ApJ, 612, 633
Fernández-Cobos R., et al., 2012, MNRAS, 420, 2162
Fernández-Cobos R., et al., 2016, MNRAS, 459, 441
Lazarian A., Draine B.T., 2000, ApJL, 536, L15
Leitch E.M., et al., 2005, ApJ, 624, 10
López-Caraballo C.H., et al., 2011, ApJ, 729, 25
López-Caraballo et al. C.H., in prep., â
Planck Col., et al., 2016, A&A, 594, A9
Planck Col., et al., 2018, ArXiv e-prints
Tegmark M., 1998, ApJ, 502, 1

Gravitational arc-tomography of the circumgalactic medium

A. Fernández-Figueroa[1], S. López[1], N. Tejos[2], C. Ledoux[3] & F. Barrientos[4]

[1] *Departamento de Astronomía, Universidad de Chile*
[2] *Instituto de Física, Pontificia Universidad Católica de Valparaíso, Chile*
[3] *European Southern Observatory, Chile*
[4] *Instituto de Astrofísica, Pontificia Universidad Católica de Chile, Santiago, Chile*

Contact / anto.f.figueroa@gmail.com

Resumen / Presentamos una aplicación de la "tomografía de arcos gravitacionales", una técnica que devela la estructura morfológica y cinemática del gas enriquecido de forma coherente en galaxias formadoras de estrellas con corrimiento al rojo intermedio. Esta técnica pone condiciones de borde nuevas e independientes para entender la física de la formación de galaxias. En este artículo estudiamos un sistema de absorción con el espectrógrafo de campo integral MUSE del VLT, mostrando absorción de metales encima del arco que está asociada con una galaxia anfitriona a z=0.77.

Abstract / We present an application of "gravitational-arc tomography", a technique that unveils the coherent morphological and kinematics structure of enriched gas surrounding star-forming galaxies at intermediate redshifts. This technique puts new and independent boundary conditions to constrain the physics of galaxy formation and evolution. In this article, we study an absorption system at z=0.77 with the integral field spectrograph MUSE on the VLT showing metal absorption on top of a gravitational arc close in projection to the absorbing galaxy.

Keywords / Galaxies: halos — Galaxies: kinematics and dynamics

1. Introduction

The gas surrounding galaxies, known as the circumgalactic medium (e.g., Tumlinson et al., 2017), is too diffuse to emit; therefore, it has to be studied through absorption against background sources. Usually, quasars are used as background sources, and this has led to the discovery of ∼100-300 kpc halos around galaxies (Churchill et al., 2000; Nielsen et al., 2013). But there is an issue with this technique: since the quasar is a point source, it can only trace one point of a given galaxy halo. This means that the QSO method is "one-dimensional", and a great amount of coherent spatial information remains inaccessible.

A new technique called "gravitational arc-tomography", has been recently developed, that uses gravitational arcs as background sources (see Fig. 1 for an explanation of the observational set up). Since gravitational arcs are extended sources (several tens of arcseconds on the sky), we can now directly map the spatial distribution of the gas around the foreground galaxies over projected distances of a few hundreds of kpc. More details about the technique can be found in Lopez et al. (2018).

2. Methodology

2.1. Data

The precious data used in this article was obtained using the Multi Unit Spectroscopic Explorer (MUSE) (Bacon et al., 2004) on the VLT, which is an integral field spectrograph operating in the visible wavelength range (4650–9300 Å), at a resolving power ranging from R=2000 at 4650 Å to R=4000 at 9300 Å.

We observed a gravitational arc at z=2.92 that extends over 10 arsec on the sky using adaptive optics, which results in better spatial resolution than previous observations.

Fig. 2 shows two images of the lensed galaxy at z=2.92: one north and one south, and a foreground galaxy in between at z=0.77 (G1). According to our *HST* imaging of the system, the galaxy is seen face-on with only a small inclination, therefore this arc is *positioned almost perfectly to study the minor axis of G1, particularly to look for outflows.*

2.2. Methods

The kinematics and parameters of G1 were studied using GalPaK, a tool to extract Galaxy Parameters and Kinematics from 3-Dimensional data, using reverse deconvolution with Markov Chain Monte Carlo analysis (Bouché et al., 2015).

3. Results

3.1. Mg II detections

Using arc-tomography, we have found strong detections of Mg II at z=0.77, on the northern and southern parts of the arc, as it can be seen in Fig. 3. The results are promising: we can clearly see that in the southern part of the arc, the absorption occurs only near the minor axis of G1.

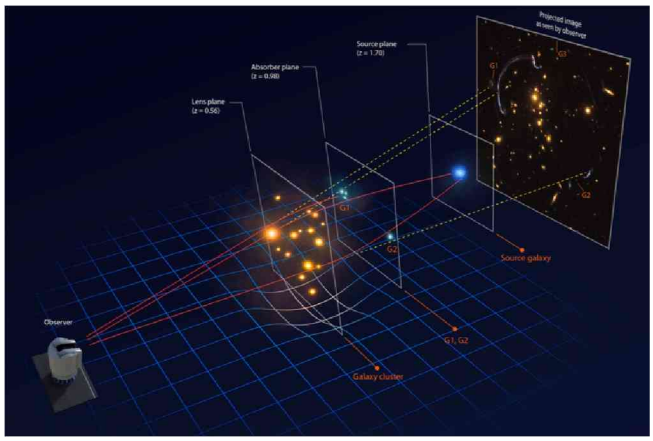

Figure 1: Illustration showing how arc tomography works (Lopez et al., 2018). We have a source galaxy, whose light gets bended as it travels towards us, because of the effect of a massive galaxy cluster. The light of this source galaxy can be absorbed by the halos of other galaxies, so that the spectra of these absorbing galaxies is imprinted on the spectrum of the source galaxy.

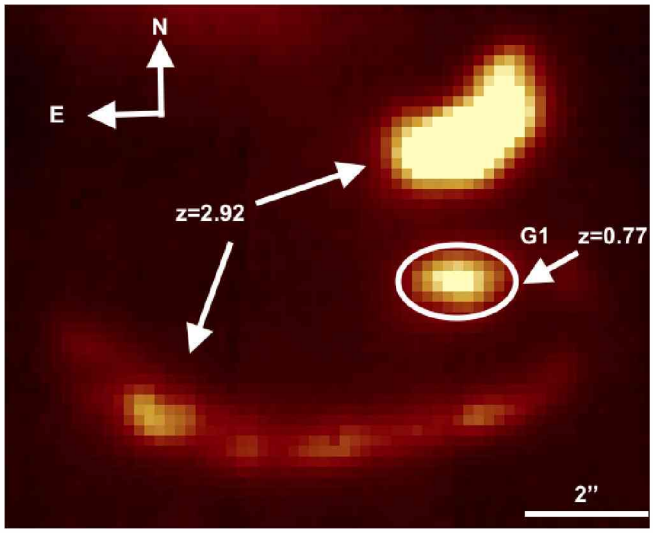

Figure 2: MUSE white image of the arc at z=2.92 and galaxy (G1) at z=0.77. This image was created by collapsing each spectrum into one flux value, in this case by calculating the sum of the flux in each pixel of the spectrum.

3.2. Kinematics and parameters

These can be seen in Fig. 4 and Table 1, respectively. As shown in Fig. 4, the western part of the galaxy is moving away from us, while the eastern part is moving towards us. This shows that G1 may be rotating counterclockwise. By contrast, Fig. 5 shows the kinematics of the gas in absorption.

4. Conclusions and forthcoming research

The results are auspicious. First, looking at preliminary results on the kinematics of the gas in the halo of the absorbing galaxy, we notice it is completely different from the kinematics of the stars found using GalPak.

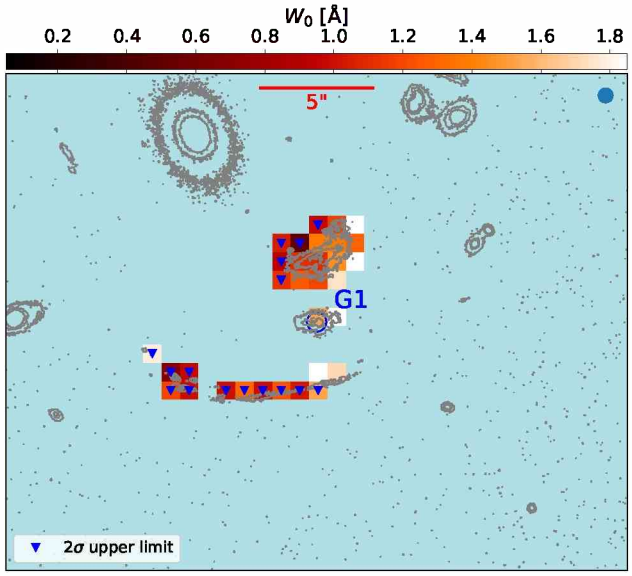

Figure 3: Preliminary Mg II absorption map. The color scale indicates the rest-frame equivalent width of Mg II λ2796.

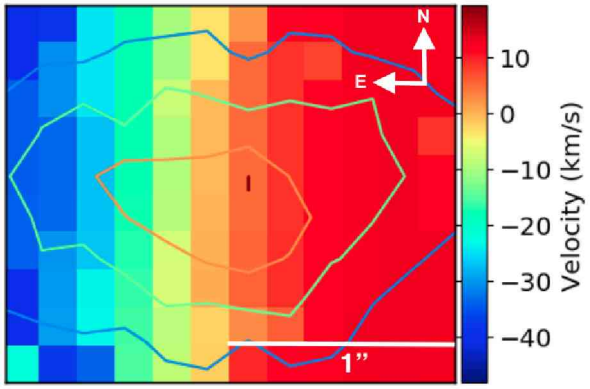

Figure 4: Velocity map of the galaxy at z=0.771. The contour lines show isophotes of G1.

Table 1: Galaxy parameters from GalPaK.

Parameter	Value	± Std. Deviation	Units
Inclination	10.4	9.9	deg
PA	90.2	8.4	deg
Maximum velocity	42.8	16.8	km s^{-1}
Velocity dispersion	3.8	2.9	km s^{-1}

Next, the Mg II absorption map is also quite interesting, as the gas seems to be concentrated near the minor axis of G1. Both results strongly suggest the presence of outflows. However there is still a considerable amount of work left to do, such as studying the kinematics of the halo of the galaxy, using absorption lines that can be found in the arc, as well as looking for other chemical species on top of the arc at the same redshift. We will achieve the latter using Magellan/MagE, which has a wider spectral coverage towards the blue.

After correcting for the magnification and distortion

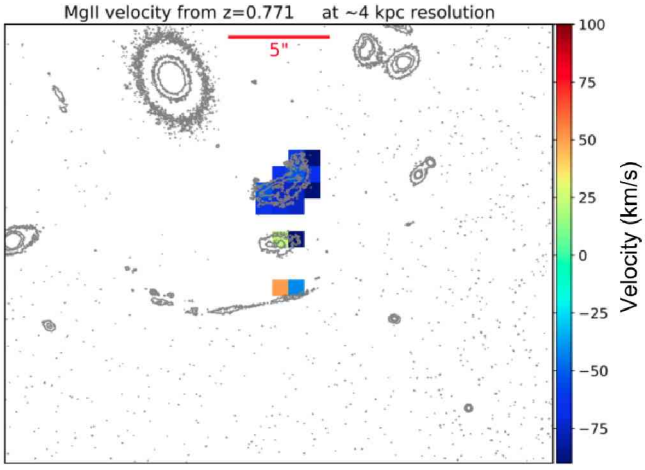

Figure 5: Velocity map of the arc made using Mg II absorption lines at z=0.771.

of the light at absorber plane (i.e., z=0.771), this research will lead to a better understanding of the kinematics relationship between galaxies and the circumgalactic medium from an unique perspective provided by the gravitational-arc tomography technique.

Acknowledgements: This work has been supported by FONDECYT grant number 1140838.

References

Bacon R., et al., 2004, A.F.M. Moorwood, M. Iye (Eds.), *Ground-based Instrumentation for Astronomy*, *Proc. SPIE,* , vol. 5492, 1145–1149

Bouché N., et al., 2015, The Astronomical Journal, 150, 92

Churchill C.W., et al., 2000, ApJS, 130, 91

Lopez S., et al., 2018, Nature, 554, 493

Nielsen N.M., Churchill C.W., Kacprzak G.G., 2013, ApJ, 776, 115

Tumlinson J., Peeples M.S., Werk J.K., 2017, Annual Review of Astronomy and Astrophysics, 55, 389

The kinematics in the inner kiloparsec of nearby active galaxies as revealed by molecular (ALMA) and ionized gas (Gemini-GMOS/IFU)

R. Slater[1,2], N. Nagar[2], D. Muñoz-Vergara[2], P. Humire[3], P. Soto-Pinto[2], A. Schnorr-Müller[4], T. Storchi-Bergmann[4], D. Lena[5,6], V. Ramakrishnan[2], C. Mundell[7] & R.A. Riffel[8]

[1] *Dirección de Formación General, Facultad de Educación y Ciencias Sociales, Universidad Andres Bello, Sede Concepción, Talcahuano, Chile*
[2] *Departamento de Astronomía, Universidad de Concepción, Chile*
[3] *Max-Planck-Institut für Radioastronomie, Bonn, Germany*
[4] *Instituto de Física, Universidade Federal do Rio Grande do Sul, Porto Alegre, Brasil*
[5] *SRON Netherlands Institute for Space Research, Utrecht, the Netherlands*
[6] *Department of Astrophysics, Institute for Mathematics, Astrophysics and Particle Physics, Radboud University, Nijmegen, the Netherlands*
[7] *Department of Physics, University of Bath, Claverton Down, UK*
[8] *Departamento de Física, Centro de Ciências Naturais e Exatas, Universidade Federal de Santa Maria, Brazil*

Contact / royslater@astro-udec.cl

Resumen / Para trazar flujos entrantes y salientes nucleares en AGNs, determinar la masa del gas involucrado y su impacto en la galaxia huésped y el agujero negro nuclear, se requieren de estudios en imágenes en 3-D tanto del gas ionizado como del molecular. Nuestro objetivo es mapear la distribución y cinemática del gas molecular e ionizado en una muestra de galaxias activas, para cuantificar los flujos entrantes y salientes nucleares. Aquí, analizamos la cinemática nuclear en la región de 1 kpc más interno de una submuestra de tres galaxias Seyfert cercanas por medio de: observaciones con ALMA de la emisión de CO J : 2–1 a resolución espacial de 0.5″ y ∼2.6 km s^{-1} de resolución espectral (NGC 1566), y observaciones por Gemini-GMOS/IFU de líneas de emisión de gas ionizado a similar resolución espacial (UGC 2024 y ESO 362–G18). Mientras el gas molecular como el ionizado muestran signos de rotación, existen movimientos no circulares significativos en el kiloparsec central de las tres fuentes. En NGC 1566, por ejemplo, existen movimientos no circulares en el 200 pc más interno, mientras lóbulos con corrimiento al azul y al rojo prominentes (∼80 km s^{-1}) son encontrados a lo largo del eje menor en las zonas más internas lo que interpretamos como la presencia de un flujo saliente molecular en el disco con velocidades reales de ∼180 km s^{-1} en el núcleo y desacelerando a 0 a 1.5″ del núcleo (∼72 pc). Este trabajo mostrará cómo las cinemática del gas perturbado en el kiloparsec central puede ser explicado de manera diferente y cómo los flujos salientes de gas molecular e ionizado parecen estar presentes con relativa frecuencia en galaxias activas cercanas en las escalas más internas.

Abstract / Tracing nuclear inflows and outflows in AGNs, determining the mass of gas involved in these, and their impact on the host galaxy and nuclear black hole, requires 3-D imaging studies of both the ionized and molecular gas. We aim to map the distribution and kinematics of molecular and ionized gas in a sample of active galaxies, to quantify the nuclear inflows and outflows. Here, we analyze the nuclear kinematics at the inner 1 kpc region of a subsample of three nearby Seyfert galaxies via: ALMA observations of the CO J : 2-1 emission at 0.5″ spatial and ∼2.6 km s^{-1} spectral resolution (NGC 1566), and Gemini-GMOS/IFU observations of ionized gas emission lines at similar spatial resolution (UGC 2024 y ESO 362–G18). While both ionized and molecular gas show rotation signatures, there are significant non-circular motions in the central kpc of the three sources. In NGC 1566 for example, there are non-circular motions in the innermost 200 pc, whereas prominent (∼80 km s^{-1}) blue and redshifted lobes are found along the minor axis in the inner arcseconds which we interpreted as the presence of a molecular outflow in the disk with true velocities of ∼ 180 km s^{-1} in the nucleus and decelerating to 0 at 1.5″ from the nucleus (∼72 pc). This work will show how the disturbed gas kinematics in the inner kpc can be differently explained and how molecular and ionized gas outflows seems to be present with relative frequency in nearby active galaxies at the innermost scales.

Keywords / galaxies: nuclei — galaxies: active — galaxies: Seyfert — galaxies: kinematics and dynamics

1. Introduction

A major topic of interest in extragalactic astronomy and cosmology these days is to understand the formation and evolution of galaxies. A primary question which the scientific community wants to address in this particular area is: How mass is transferred from galactic scales down to nuclear scales to feed the Super-Massive Black Hole (SMBH)? So far, the mechanisms regulating the transfer of material towards the galaxy core

are still poorly understood. However, in recent years, this is becoming more accessible thanks to the recent and upcoming new generation of telescopes. One of the instruments, which is playing a main role, is the Atacama Large Millimeter/submillimeter Array (ALMA) which can provided us with better spatial and spectral resolution. We are hence in the best epoch to study gas kinematics at high spatial resolution, covering almost the entire electromagnetic spectrum. One of the most attractive targets are active galaxies such as Seyferts, which have the potential to heats or disrupts the gas, and hence slows down star formation through feeding/feedback processes.

Previous studies have pointed out that a triggering mechanism which can start the nuclear activity are dusty nuclear spirals. Martini et al. (2003) show that nuclear dusty spirals occur with comparable frequency in both active and inactive galaxies. The only difference is that none of the AGNs lack this structure implying that nuclear dusty spirals are correlated with AGNs. Following this issue, Simões Lopes et al. (2007) studied a sample of normal and active galaxies and showed that dusty nuclear spirals are present in 100 % of early type AGNs whereas in only 25 % in non-AGNs. More recent studies from optical spectra of several nearby Seyferts with Integral Field Units (IFUs) have demonstrated that gas inflows are present along these dusty spirals in the inner kiloparsec (e.g.: Schnorr-Müller et al., 2014a,b). These evidences, along with the frequency detected of dusty spirals, support the hypothesis that nuclear spirals are one of the most important mechanism for fueling the SMBH, transporting gas from kiloparsec scales down to within a few tens of parsecs of the active nucleus. Several authors who follow this argument, have tried to quantify this inflows at the inner scales in nearby AGNs with optical and near-infrared observations (e.g.: Storchi-Bergmann et al., 2007; Riffel et al., 2008; Schnorr-Müller et al., 2014a,b, 2017b,a). They obtained inflow velocities ranging between 50 – 200 km s^{-1} as well as mass inflows rates around 0.1 – 1 M$_\odot$ yr^{-1}. The most accepted interpretation of the small values of mass inflow rates do not agree with the expected ones, which is necessary to initiate a nuclear activity in galaxies, is that at frequencies close to the optical band, we are able to observe only the hot skin of a much larger gas reservoir and flow, which should otherwise be dominated by cold molecular gas (e.g. CO). For this, our immediate goal is to map both the spatial distribution and kinematics of cold molecular gas in order to quantify the actual inflows/outflows at the same scale probed by the optical and near-IR observations. Some of the most recent results obtained so far, following this goal by our group, are shown in the next section.

2. Results

We have noted that outflows in nearby Seyfert galaxies are present with noticeable recurrence in the inner kiloparsec as ionized and molecular gas. Particularly, Muñoz et al. (in prep.), have detected non circular features in the central region of the Seyfert galaxy UGC 2024, interpreting this as a nuclear outflow of ionized gas. Spectra analysis of its ionized line emissions as [O III], [N II] and H$_\alpha$ observed by GMOS/IFU (see Fig. 1) show that emission lines of ionized gas lie at zero velocities at several orientations especially in [O III], postulating this scenario as concrete evidence of a spherical outflow at lower dust extinction: with the presence of dust (dominantly in the plane of the galaxy disk) we would preferably see emission from the hemisphere in front of the galaxy and moving towards us, i.e., blueshifted radial velocities. In the absence of dust one would expect a high dispersion and a median velocity close to systemic which is the case here (6790 km s^{-1}). The outflow velocity estimated was v = 250 km s^{-1} which was lower than the escape velocity estimated (300 km s^{-1}) indicating that this expanding sphere of ionized gas is not going out of the galaxy, rather it is slowing down until finally it goes back to the galactic nucleus. Analogous results were found in the nearby Seyfert galaxy ESO 153–G20 (Soto-Pinto et al., in prep.)

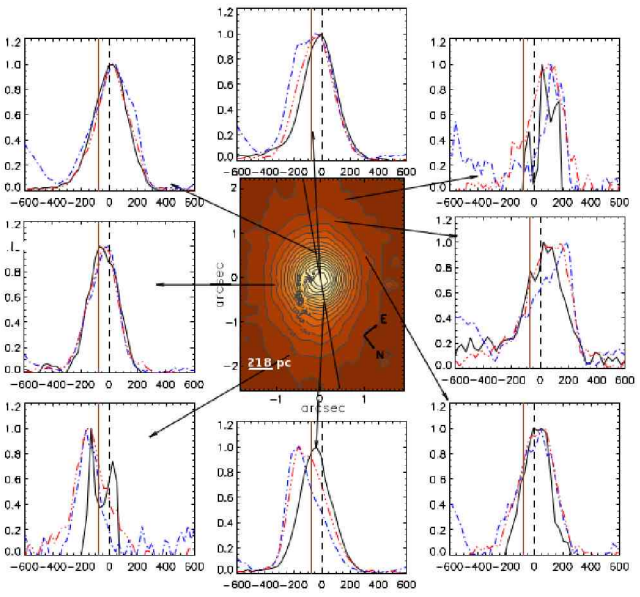

Figure 1: Line profiles in UGC 2024 of the [O III] (solid black), [N II] (triple dot-dashed red) and H$_\alpha$ (dot-dashed blue) emission lines extracted from 0.16″ radius apertures centered on the offset positions (in arcsec) indicated in each panel. The offsets are calculated from the stellar continuum peak. The central panel shows the stellar continuum flux in greyscale and contours, and the major axis as a solid black line: it is shown to illustrate the locations of the individual apertures. For easy comparison, the profiles are normalized and each panel indicates the systemic velocity (dashed black line) and the velocity expected from the best-fit H$_\alpha$ Bertola rotation model (solid brown line). The x-axis is in km s^{-1} centered on the systemic velocity.

Another study of the ionized gas was presented in Humire et al. (2018) for the Seyfert galaxy ESO 362–G18 also with GMOS/IFU. They have reported non-circular features related to an outflow in [O III]. Based on this, they proposed a toy model to explain why [O III] is preferentially redshifted to our line of sight (LOS), except at the nucleus where is blueshifted (see top panel

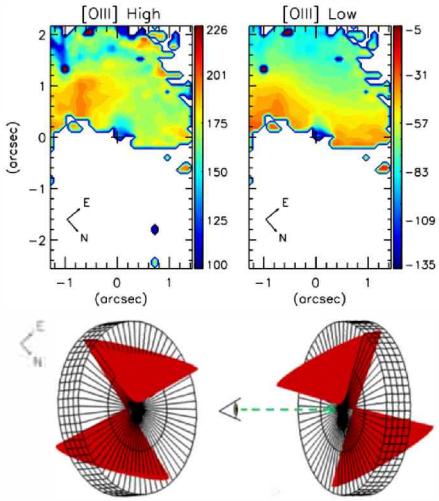

Figure 2: Top panel: Results of the double component fit in ESO 362-G18 to the [O III]. Velocity fields of the high-velocity and low-velocity narrow components. Bottom panel: Proposed configuration for the nuclear region of ESO 362–G18, where the galactic disk is shown both from our perspective (left; in the same orientation as the data cube) and in profile (right). (Source: Humire et al., 2018).

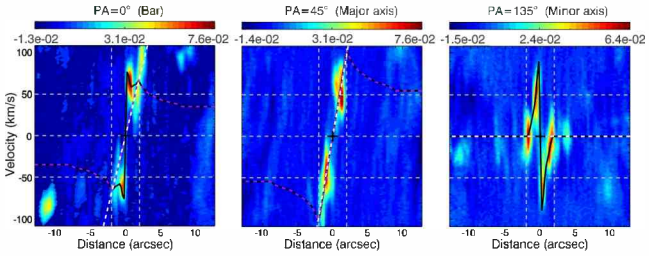

Figure 3: Position-Velocity diagrams of the CO J : 2-1 emission in NGC 1566 along three PAs are shown in color following the color bar above each panel. The PA of the "slit" over which the pv diagram was extracted is indicated above each panel, as are the PAs corresponding to the large-scale bar (left), major (middle) and minor (right) axis of the galaxy. On the x-axis, the linear scale corresponds to 48 pc arcsec^{-1}. Negative offsets correspond to the PA listed above the panel, i.e., positive offsets are along the 180° plus the listed PA. The black cross indicates the position of the 230 GHz continuum peak (presumed to be the galaxy center). The dashed white and purple lines are rotation models (see Slater et al. (2019) for details). The solid black line shows the expectation of adding our outflow model (see Slater et al. (2019) for details). (Source: Slater et al., 2019).

of Fig. 2). The best interpretation was the presence of a biconical outflow of ionized gas in the nuclear region which was modeled as shown in the bottom panel of Fig. 2. The top ionization cone intersects the galaxy disk behind the plane of the sky, generating the redshifted component of [O III] in the high velocity component noted in the top panel of Fig. 2. This cone also intersects the galaxy disk in front of the plane of the sky, but only in a very small region close to the nucleus, producing the greatest blueshift seen in the low-velocity component of [O III] (top panel of Fig. 2). The bottom ionization cone is almost always hidden by the galactic disk.

For NGC 1566, Slater et al. (2019) show, with respect to cold molecular gas, a significant outflow of CO in the nuclear region. However the outflow possibility was neglected by Combes et al. (2014) and supported later with optical observations with SINFONI in Smajić et al. (2015). Non circular features were detected for CO J : 3-2 observations of NGC 1566 using ALMA in Cycle 0 (Combes et al., 2014), however they reported no outflow arguing small amplitude owing to streamings by the large-scale bar. In spite of this, we defend an outflow scenario with one of the most significant evidence being illustrated in Fig. 3. On these, the Position-Velocity diagram of CO data along the minor axis not only shows the high velocity components, but also lower brightness emission which connects these high velocity components to the zero velocity components seen at $r \approx 1.8''$ from the nucleus. These diagrams also show velocity deviations which are consistent with a radial cold molecular outflow in the plane of the disk at different position angles (PAs) (more details in Slater et al. (2019).

3. Conclusions

It has been demonstrated that the feedback processes as nuclear outflows take part at different phases of the gas (ionized gas and cold molecular gas) with presumably the same origin but are morphologically different. Thus it is important to elucidate these components not only from one wavelength range, but also by taking multi-wavelengths observations in order to get the full picture of their physical properties, and here is where the new generations of detectors, telescopes as well as new interferometric techniques will play an important role to achieve this goal in the coming years.

Acknowledgements: This work was (partially) funded by the CONICYT PIA ACT172033. R.S. acknowledges support provided by SOCHIAS for the participation.

References

Combes F., et al., 2014, A&A, 565, A97
Humire P.K., et al., 2018, A&A, 614, A94
Martini P., et al., 2003, ApJ, 589, 774
Riffel R.A., et al., 2008, MNRAS, 385, 1129
Schnorr-Müller A., et al., 2014a, MNRAS, 437, 1708
Schnorr-Müller A., et al., 2014b, MNRAS, 438, 3322
Schnorr-Müller A., et al., 2017a, MNRAS, 471, 3888
Schnorr-Müller A., et al., 2017b, MNRAS, 466, 4370
Simões Lopes R.D., et al., 2007, ApJ, 655, 718
Slater R., et al., 2019, A&A, 621, A83
Smajić S., et al., 2015, A&A, 583, A104
Storchi-Bergmann T., et al., 2007, ApJ, 670, 959

High-energy astrophysics on compact objects Accretion on all scales

F.L. Vieyro[1,2]

[1] *Instituto Argentino de Radioastronomía, CONICET–CICPBA, Argentina*
[2] *Facultad de Ciencias Astronómicas y Geofísicas, UNLP, Argentina*

Contact / fvieyro@iar-conicet.gov.ar

Resumen / La emisión gamma es la evidencia mas fuerte de que procesos no-térmicos tienen lugar en una fuente astrofísica. Estos procesos son el resultado de la presencia de partículas relativistas que interaccionan con los diferentes campos, como el campo magnético, de radiación y de materia fría. En este trabajo, se describirán los principales procesos radiativos que las partículas sufren en ambientes extremos, que dan lugar a que gran parte de la emisión se produzca en altas energías. Se presentará la fenomenología asociada a las diferentes clases de fuentes con objetos compactos, con particular interés en aquellas sustentadas por la acreción sobre agujeros negros. Finalmente se discutirán algunos de los problemas abiertos asociados a estas fuentes.

Abstract / Gamma-ray emission is the ultimate evidence that non-thermal processes are taking place in an astrophysical source. These processes are the result of the presence of relativistic particles interacting with different fields, such as magnetic, radiation or cold matter fields. In this article, I describe the main radiative processes that particles undergo in extreme environments, that result in a significant fraction of the total emitted power to be released in the gamma-domain. I present the phenomenology related to the different classes of high-energy sources involving compact objects, with particular interest in those powered by accretion into black holes. Finally, I discuss some of the open questions associated with these sources.

Keywords / radiation mechanisms: non-thermal — gamma rays: general — stars: black holes

1. Introduction

The detection and study of gamma ray radiation allows us to explore the properties of the most extreme astrophysical sources in the Universe. Gamma-ray emission is the result of the presence of a populations of relativistic particles accelerated in energetic astrophysical scenarios. The interaction of these relativistic particles with their environment –magnetic field, radiation and cold gas– result in non-thermal emission at high energies.

Some of the sources found to be gamma-ray emitters, in particular some of the most energetic phenomena in the Universe, are powered by accretion onto black holes. The accretion process of matter onto compact objects is the most efficient mechanism know until date to convert rest mass energy into radiation. These include Active Galactic Nuclei (AGNs), which are the result of accretion onto supermassive black holes in the core of galaxies; in a smaller spatial scale, we find the X-ray binaries, which are powered by the accretion onto a compact object -stellar black hole or neutron star- in binary systems.

Although these phenomena can be described by the same basic ingredient of matter accretion (Mirabel & Rodríguez, 1999), the microphysics of these systems might differ. This is why the study of accretion on all scale –both spatial and temporal– can give us information in different astrophysical aspects.

This article is organized as follow: First, in Sec. 2., a description of solutions for different accretion regimes is presented. Then, in Sec. 3. we present the phenomenology observed in accreting stellar lack holes. In Sec. 4. we discuss some open problems associated with different classes of AGNs, and some similarities found between AGNs and XRBs. We conclude with some final remarks in Sec. 5. The relevant non-thermal processes that takes place in gamma-ray sources are briefly described in the Appendix.

2. Accretion flow models

In steady state, the structure of an accretion disk is determined by the mass and spin of the black hole, and by the accretion rate. The latter is usually written in units of the Eddington accretion rate, $\dot{M}_{\rm Edd} = 1.8 \times 10^{-8} M/M_{\odot}$, since sources with similar fraction of the Eddington luminosity are observed to present similar accretion flows (Done et al., 2007).

The structure of the accretion flows is determined by a set of conservation equations (mass, radial momentum, angular momentum and energy), and identifying the processes of heating and cooling of the gas, relevant in each regime (for a more complete discussion and description on accretion disk models the reader is referred to reviews such as Abramowicz & Fragile 2013).

There are three important solutions of the black hole accretion flows, that are valid for different ranges of ac-

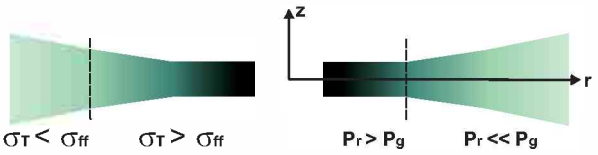

Figure 1: Different disk regions. Here, $\sigma_{\rm T}$ and $\sigma_{\rm ff}$ are the Thomson and free-free cross sections, respectively. Adaptation from Shakura & Sunyaev (1973).

cretion rate $\dot{m}$ and optical depth τ: the thin Shakura-Sunyaev disks $\dot{m} \ll 1$, $\tau \gg 1$; the slim disks $\dot{m} \sim 1$, $\tau \gg 1$; and the Advection Dominated Accretion Flow (ADAF) disks $\dot{m} \ll 1$, $\tau \ll 1$.

2.1. Standard disk

The simplest and most popular solution of accretion disk was developed by Shakura & Sunyaev (1973) and Novikov & Thorne (1973). This model, usually know as the standard disk or Shakura-Sunyaev disk, describes the structure of a Keplerian accretion disk around a point mass M. The physical parameters are vertically integrated in this model, hence the solution only depends on the radial coordinate.

In this model, a radial velocity component $v_{\rm r}$ arises as a result of viscous stress, which is responsible of converting gravitational potential into heat, which is radiated locally. The origin of viscosity in accretion disk is now thought to have its origin in the magnetic rotational instability (MRI), which is a self-sustaining dynamo process (Balbus & Hawley, 1991). In the Shakura-Sunyaev disk, however, the stress is treated using a simple approach, in which all viscous effects depends on a simple parameter α, hence the cinematic viscosity ν results in:

$$\nu = \alpha \rho c_{\rm s} h. \quad (1)$$

The solution of Shakura & Sunyaev results in a disk optically thick, that is $\tau > 1$, measured in the vertical direction, and geometrically thin, $H/r \ll 1$. Three regions are found in the solution (see Fig 1):

- An inner region where the pressure is mainly radiation pressure, and dispersion dominates over absorption.
- A central region where dispersion is still dominant, but the pressure is now dominated by the gas.
- An external region for large r, where the opacity is due to free-free absorption.

In the external regions, where the disk is optically thick and absorption dominates over dispersion, the disk is in local thermal equilibrium, hence it radiates as a black body with temperature $T(r)$, given by

$$T_{\rm s} = \left\{ \frac{3GM\dot{M}}{8\pi a c r^3} \left[1 - \left(\frac{r_{\rm in}}{r} \right)^{1/2} \right] \right\}^{1/4}. \quad (2)$$

The spectrum is obtained integrating along the disk,

$$I_\nu = 4\pi \int_{r_{\rm in}}^{r_{\rm ext}} F_\nu [T_{\rm s}(r)] r dr. \quad (3)$$

For a local black body spectrum, and a temperature profile given by Eq. 2, a dependence of $I_\nu \propto \nu^{1/3}$ is obtained. Fig. 2 shows the spectra of a Shakura-Sunyaev disk around a solar mass black hole, for two values of the accretion rate $\dot{m}$, where $\dot{m} = \dot{M}/\dot{M}_{\rm Edd}$. The spectra peak beyond keV energies, meaning that the disk around an stellar black hole is able to emit soft X-ray photons.

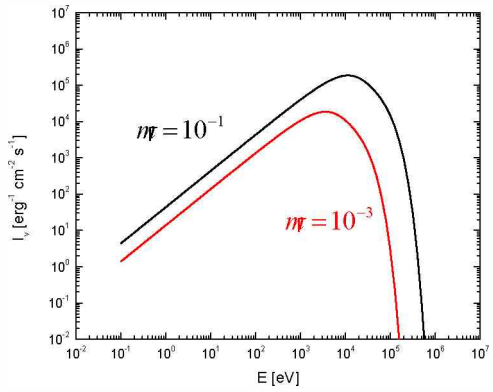

Figure 2: Standard disk spectra. The intensity scale is arbitrary and the accretion rate is in units of $\dot{M}_{\rm Edd}$.

The disk is subject to two instabilities: a thermal instability related to the ionization of hydrogen, which is responsible for the states transitions observed in some XRBs, and an instability due to the radiation pressure (Lightman & Eardley, 1974; Done et al., 2007).

2.2. Slim disk

As in the Shakura-Sunyaev model, this solution assumes that the disk is radiatively efficient. However, at higher accretion rates, advection should be considered as an additional cooling term, and the problem can no longer be solved analytically. The advection modifies the spectrum: for high accretion rates, a large fraction of the heat is advected into the black hole, hence the efficiency of the disk decreases and the disks are only moderately luminous (Abramowicz & Fragile, 2013).

2.3. Hot accretion flows: ADAF

Solutions of thin disks are valid as long as the radiative mechanism is efficient with respect to the local energy dissipation rate; for cases where this is not valid, the structure could result in a geometrically thick disk where $H/r \sim 1$. This is the case of the solutions known as advection dominated accretion flows (e.g., Ichimaru, 1977; Narayan & Yi, 1994, 1995a,b; Abramowicz et al., 1995).

These solutions are valid for sub-Eddington accretion rates ($\dot{m} \ll 1$), where the gas is not dense, hence the cooling time is longer than the accretion time. The energy released by viscosity is stored as thermal energy in the gas and advected. The plasma results optically thin, and with two temperature (e.g., Yuan & Narayan, 2014).

In the ADAF solutions the radiation pressure is neg-

ligible; the two significant contributions to pressure are the magnetic and gas pressure. A second condition is that the interaction between electrons and ions is only through Coulomb interactions and, given the low densities, it is inefficient, and the plasma adopts a two-temperature configuration, with ions much hotter than electrons. Since the energy transfer to electrons is inefficient, and radiation is mainly via electrons, the luminosities of ADAF are lower than the standard disk. Finally, the viscosity is treated as in the Shakura-Sunyaev model, with the parameter α.

Some of the main characteristics of the ADAF solutions are the following:

- the radial velocity is comparable to the free fall velocity;
- the tangential velocity component is sub-Keplerian;
- since cooling is inefficient, the heat is stored as internal energy, the plasma reaches high temperature, causing an elevation of the gas, with a mean height scale $H \sim r$;
- the electrons reach temperatures of $T_e \sim 10^9 - 10^{10}$ K, for $r < 10^3 r_g$;
- a significant fraction of the energy is advected, hence the luminosity of ADAF is low.

2.4. Other solutions

Several other solutions have been developed relaxing some of the conditions imposed by the ADAF model, for example:

- ADIOS: adiabatic inflow-outflow solutions (Blandford & Begelman, 1999; Turolla & Dullemond, 2000). This solutions contemplates the possibility that a fraction of the accreted gas is ejected in wind or jets.
- CDAF: convection dominated accretion flows (Quataert & Gruzinov, 2000; Abramowicz & Igumenshchev, 2001). In this model convective instabilities transport angular momentum to inner regions, and the transport of angular momentum outward by other mechanisms is weak.
- LHAF: Luminous hot accretion flows (Yuan, 2001). In this case, the cooling rate of protons for Coulomb interactions is higher than the heating by viscous effects, and the advective term results in heating. This solution is valid for higher accretion rates than those of the ADAF, and results in more luminous and hotter flows.

3. X-ray binaries

X-ray binaries (XRBs) are systems composed by a compact object (a stellar black hole or a neutron star), that accretes material from a companion star. The accretion disk formed in these sources radiates a high fraction of the energy on the X-rays, hence the name of the systems. XRBs are often observed in different spectral states, the most canonical ones being the *high* state and the *low* state. In these states, the X-ray spectrum usually presents two main components: a thermal and a non-thermal component. The thermal component is associated with the emission of a thin standard disk,

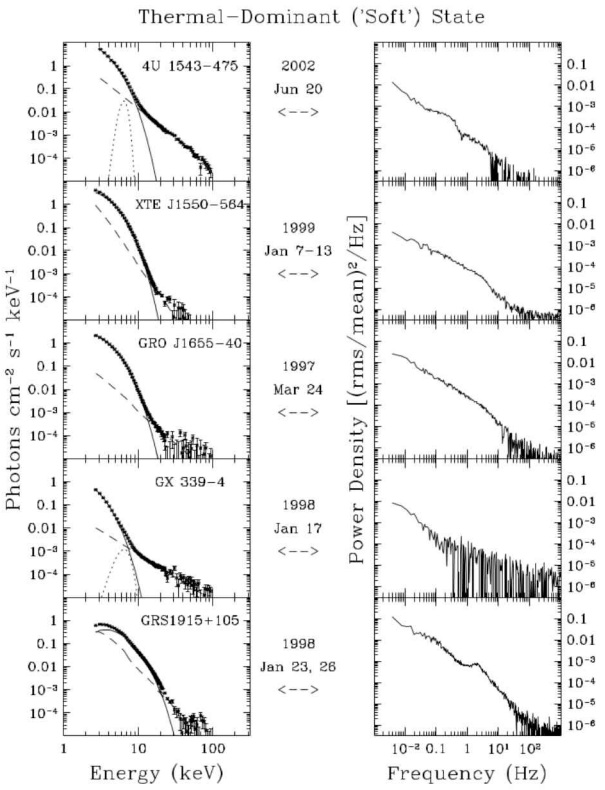

Figure 3: XRBs spectra in the HS state. From McClintock & Remillard (2006).

with an extended black body spectra, whereas the non-thermal component is evidence of a geometrically thick and hot flow, which could be an ADAF, or a component usually known as a *corona* (Stern et al., 2001; Poutanen & Vurm, 2009; Poutanen, 1998; Poutanen et al., 1997). The power-law component is the result of Comptonization of soft photons from the disk by this hot flow.

The phenomenology of the states is the following:

- *High-soft* (HS) state
  The X-ray spectrum in this state is dominated by the thermal component, with a characteristic temperature of $kT \sim 0.7 - 1.5$ keV. The power law is soft, with an index of $\alpha \sim 2.1 - 4.8$ and low intensity. Fig. 3 shows the spectra of several sources in this state.
  This state occurs for high accretion rates, $0.09 < \dot{m}$, where the accretion disk can be described by an optically thick Shakura-Sunyaev solution (Esin et al., 1997).
- *Low-hard* (LH) state
  This state takes place for lower accretion rates, $10^{-2} < \dot{m} < 0.08$, where the geometry of the accretion flow becomes similar to an ADAF in the inner regions, hence the spectra is dominated by the non-thermal component. The thermal component if shifted towards lower energies, $kT < 0.8$ keV, since the standard disk is truncated at larger radii. Fig. 3 shows several examples of the LH state.
  Sources that spend a long period in this state are associated with radio emission, which is attributed

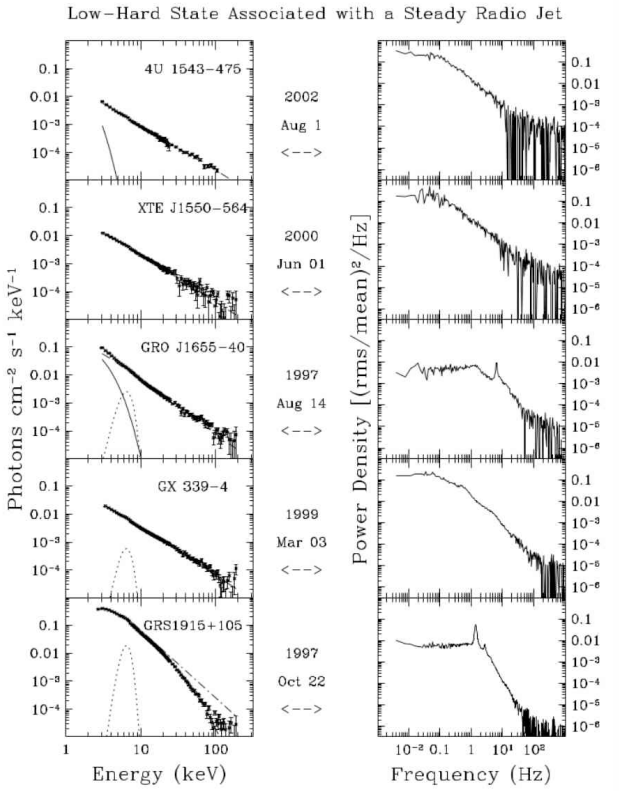

Figure 4: XRBs spectra in the LH state. From McClintock & Remillard (2006).

to the presence of a relativist jet. In these cases the systems are known as *microquasars* (Mirabel et al., 1992). In some sources, as the well studied microquasar Cygnus X-1, VLBI has allowed to resolved the structure of the jet (Stirling et al., 2001).

- *Quiescent* state
  XRBs spent most of their life in a quiescence state, with very low accretion rates $\dot{m} < 10^{-2}$, and ADAF type accretion regime. The spectra during the period of inactivity is similar to the LH state, but with lower luminosities.

3.1. Jets and the dynamical cycle

As mentioned above, the LH state is associated with the presence of steady jets. In addition, state transitions also show radio activity, but in this case the ejections are discrete, more luminous and with higher Lorentz factor than those observed in the LH state.

Fender et al. (2004) proposed a model to describe the dynamical cycle or outbursts that XRB might undergo. In a first phase, and at very low accretion rates, the source is in a low luminous state which correspond to quiescence. When the source enters an activity period, it moves vertically on the diagram towards the LH state, where it shows persistent jets with Lorentz factor mildly relativistic. In the transition from the LH to the HS state, powerful and relativistic jets are launched, which can be the result of the ejection of the inner accretion

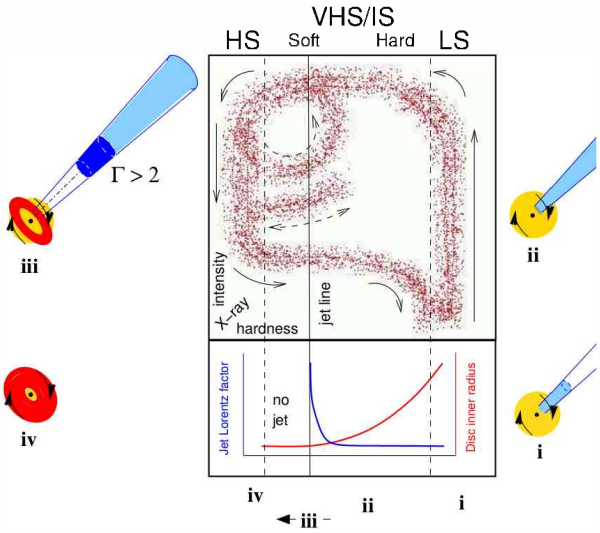

Figure 5: Dynamical cycle in XRBs. From (Fender et al., 2004).

flow. The disk extends up to the last stable orbit, and the source is in the HS state. During this phase no radio emission is observed. The accretion rate decreases, and the source returns to the quiescent state. Fig. 5 shows the diagram of the model, where the solid line marks the cycle.

3.2. Gamma-ray emission from microquasars

Microquasars are known to be variable gamma-ray sources. At least five source are known to emit MeV gamma-rays (McConnell et al., 2000; Cadolle Bel et al., 2006; Paredes & Bordas, 2019), and three of them are also GeV emitters. The MeV emission is found to be polarized, showing a very likely jet origin (Laurent et al., 2011; Jourdain et al., 2012; Zdziarski et al., 2014; Pepe et al., 2015). Alternative models where this emission is originated in a hot accretion flow have also been proposed (Vieyro & Romero, 2012; Romero et al., 2014; Vieyro et al., 2016). The GeV emission is found to be originated far from the compact object, also favoring jet models (Bosch-Ramon, 2007; Zanin et al., 2016).

In the TeV energy range, there was only a 4σ detection of Cygnus X-1 by the MAGIC Collaboration (Albert et al., 2007), by it needs to be confirmed by a higher significance detection. Hence if microquasars are TeV emitter is still an open question.

4. Accretion onto supermassive black holes

Active galactic nuclei (AGN) are composed of a supermassive black hole that accretes material from the inner region of the galaxy host. Their emission –both thermal and non-thermal– covers the full electromagnetic spectrum, from radio to gamma-rays (see the example in Fig. 6). They present a rich phenomenology, with sources such as Seyfert galaxies, quasars, blazars, radiogalaxies, among others (see, e.g., Padovani et al. 2017 for a detailed review on these sources).

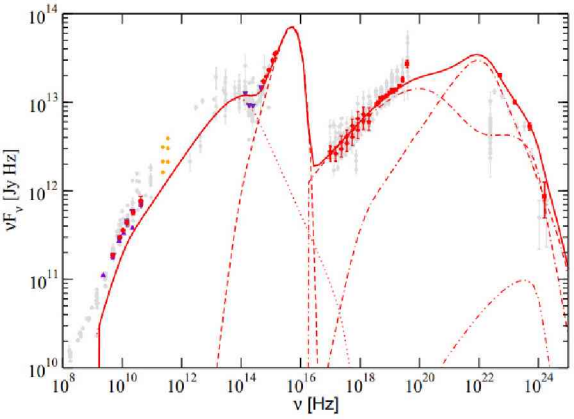

Figure 6: Spectral energy distribution of the blazar 3C 273. The solid line corresponds to a leptonic model, in which the low energy component is synchrotron emission, and the high-energy components are due to inverse Compton interactions. The dashed line is the contribution of the accretion disk. In hadronic models, $p\gamma$ emission and synchrotron of protons can also contribute significantly to the high energy component. From Böttcher et al. (2013).

According to their radiowavelength activity, they can be classified in two main groups: radio-loud and radio-quiet. Since the radio emission is dominated by leptonic synchrotron radiation of the relativistic jet (see the Appendix for a description of the main non-thermal processes), this rough classification is an indicator of the jet power. Within the radio-loud AGNs, the most currently accepted classification system is based principally in three characteristics (Urry & Padovani, 1995): the inclination angle of the jet with the line of sight, the optical spectrum and the radio emission. These AGNs are mainly classified in two groups: blazars, where the jet is almost parallel to the line of sight, hence its luminosity is enhanced by Doppler boosting effects, and radio-galaxies, with large inclination angles, and beaming effects negligible.

The third *Fermi* catalog includes 1591 AGNs, which represents a 71 % increment of source in only two years (Ackermann et al., 2015). The 98 % of these sources are blazars. However the new generation of Cherenkov instruments has allowed the identification of new classes of AGNs that emit very high-energy (VHE) radiation. In 2009, VHE emission was detected from Seyfert galaxies, in particular Narrow-Line Seyfert 1 (NLS1, Abdo et al. 2009), showing that relativistic jets can be present in AGNs with galaxy host of relatively low mass. The power of these jets is lower than those associated with blazars. This has open new questions in the identification of AGN classes with different evolutionary state in their galaxy hosts in which the classification system of Urry & Padovani was based (Falcke et al., 2004; McHardy et al., 2006; Romero et al., 2017). In addition, this is a problem involving more AGN classes besides NLS1, since *Fermi* surveys show evidence of the existence of other type of AGN with jets, where both the galaxy host and the central black hole have low mass. The detailed classification of AGNs is, thus, being revised continuously, and there are many efforts to replace a purely phenomenological classification by one based on the underlying physics of these complex sources (see, e.g., Foschini 2017 for a more complete discussion).

Regarding the relation between the mass of the central black hole, the AGN activity, and the nature of the galaxy host, there is growing evidence that supports the idea that AGN play a fundamental role in the evolution of its galaxy host (Fabian, 2012). The outflows (both winds and jets) associated with the active nucleus regulate the stellar formation in the galaxy host, effect known as AGN feedback. It is then fundamental to have a more comprehensive view on the properties of different AGN host, to understand the role of feedback on the galaxy evolution, and more generally, on the cosmological evolution (Croton et al., 2006; Bower et al., 2006; McCarthy et al., 2010; Fabian, 2012).

The problems for studying AGNs in different epochs of their evolution are the long timescales involved. For a simple scaling of $\Delta t \propto M_{\rm BH}$, what lasts a fraction of a year for a $10 M_\odot$ black hole, it could last $\sim 10^7$ yr for a $10^9 M_\odot$ black hole. Assuming that the physics behind the accretion process is scale-invariant, the idea is using XRBs as a tool for studying accretion physics, jet launching mechanism, accretion modes, effects of outflows on their ambient media, etc.

Based on the different kinds of AGNs observed in the Universe, and in the so-called fundamental plane of black hole activity, which is a relation between black hole masses, radio and X-ray luminosities across several decades in magnitude in the black hole mass (Merloni et al., 2003; Falcke et al., 2004), it was suggested that different types of AGNs are equivalent to different spectral states of XRBs (Körding et al., 2006). Radio loudness in AGNs could be simple the parallel of the LH states in XRBs, where a persistent jet is found, whereas radio-quiet quasars could be identified with XRBs in the HS state, where no radio emission is observed (Maccarone et al., 2003).

During the last years new evidence supporting the common accretion states in both XRBs and AGNs (Svoboda et al., 2017; Ruan et al., 2019, e.g.,) has grown. However, there are still many questions that remain to be answered and further research is needed.

5. Final remarks

Multiwavelength studies are fundamental to better understand the underlying physics behind accretion. The evidence so far seems to indicate that the accretion process onto black holes is scale invariant (McHardy et al., 2006). If this is correct, then XRB studies might help us understand different states of supermassive black holes and their role on shaping the Universe.

Acknowledgements: This work was supported by the Argentine Agency CONICET (PIP 2014-00338) and the National Agency for Scientific and Technological Promotion (PICT 2017-0898). The author also acknowledges support from the Spanish Ministerio de Economía y Competitividad (MINECO/FEDER, UE) under grants AYA2013-47447-C3-1-P and AYA2016-76012-C3-1-P with partial support by the European Regional Development

Fund (ERDF/FEDER), MDM-2014-0369 of ICCUB (Unidad de Excelencia 'María de Maeztu'), and the Catalan DEC grant 2014 SGR 86.

References

Abdo A.A., et al., 2009, ApJL, 707, L142
Abramowicz M.A., Fragile P.C., 2013, Living Reviews in Relativity, 16, 1
Abramowicz M.A., Igumenshchev I.V., 2001, ApJL, 554, L53
Abramowicz M.A., et al., 1995, ApJL, 438, L37
Ackermann M., et al., 2015, ApJ, 810, 14
Albert J., et al., 2007, ApJ, 665, L51
Atoyan A.M., Dermer C.D., 2003, ApJ, 586, 79
Balbus S.A., Hawley J.F., 1991, ApJ, 376, 214
Begelman M.C., Rudak B., Sikora M., 1990, ApJ, 362, 38
Blandford R.D., Begelman M.C., 1999, MNRAS, 303, L1
Blumenthal G.R., Gould R.J., 1970, Rev. Mod. Phys., 42, 237
Bosch-Ramon V., 2007, Ap&SS, 309, 321
Böttcher M., et al., 2013, ApJ, 768, 54
Bower R.G., et al., 2006, MNRAS, 370, 645
Cadolle Bel M., et al., 2006, A&A, 446, 591
Croton D.J., et al., 2006, MNRAS, 365, 11
Done C., Gierliński M., Kubota A., 2007, A&A Rv, 15, 1
Esin A.A., McClintock J.E., Narayan R., 1997, ApJ, 489, 865
Fabian A.C., 2012, ARA&A, 50, 455
Falcke H., Körding E., Markoff S., 2004, A&A, 414, 895
Fender R.P., Belloni T.M., Gallo E., 2004, MNRAS, 355, 1105
Foschini L., 2017, Frontiers in Astronomy and Space Sciences, 4, 6
Ichimaru S., 1977, ApJ, 214, 840
Jourdain E., Roques J.P., Malzac J., 2012, ApJ, 744, 64
Kelner S.R., Aharonian F.A., Bugayov V.V., 2006, PhRvD, 74, 034018
Körding E.G., Jester S., Fender R., 2006, MNRAS, 372, 1366
Laurent P., et al., 2011, Science, 332, 438
Lightman A.P., Eardley D.M., 1974, ApJL, 187, L1
Maccarone T.J., Gallo E., Fender R., 2003, MNRAS, 345, L19
McCarthy I.G., et al., 2010, MNRAS, 406, 822
McClintock J.E., Remillard R.A., 2006, *Black hole binaries*, 157–213
McConnell M.L., et al., 2000, ApJ, 543, 928
McHardy I.M., et al., 2006, Nature, 444, 730
Merloni A., Heinz S., di Matteo T., 2003, MNRAS, 345, 1057
Mirabel I.F., Rodríguez L.F., 1999, Annual Review of Astronomy and Astrophysics, 37, 409
Mirabel I.F., et al., 1992, Nature, 358, 215
Narayan R., Yi I., 1994, ApJL, 428, L13
Narayan R., Yi I., 1995a, ApJ, 444, 231
Narayan R., Yi I., 1995b, ApJ, 452, 710
Novikov I.D., Thorne K.S., 1973, C. Dewitt & B. S. Dewitt (Ed.), *Black Holes (Les Astres Occlus)*, 343–450
Padovani P., et al., 2017, Astronomy and Astrophysics Review, 25, 2
Paredes J.M., Bordas P., 2019, [2019arXiv190209898P], arXiv:1902.09898
Pepe C., Vila G.S., Romero G.E., 2015, A&A, 584, A95
Poutanen J., 1998, M.A. Abramowicz, G. Bjornsson, J.E. Pringle (Eds.), *Theory of Black Hole Accretion Disks*, 100, Cambridge Contemporary Astrophysics, Cambridge University Press, Cambridge, UK
Poutanen J., Krolik J.H., Ryde F., 1997, MNRAS, 292, L21
Poutanen J., Vurm I., 2009, ApJL, 690, L97
Quataert E., Gruzinov A., 2000, ApJ, 539, 809
Romero G.E., Vieyro F.L., Chaty S., 2014, A&A, 562, L7
Romero G.E., et al., 2017, SSRv, 207, 5
Ruan J.J., et al., 2019, [2019arXiv190302553R]
Shakura N.I., Sunyaev R.A., 1973, A&A, 24, 337
Stecker F.W., 1973, Ap&SS, 20, 47
Stern B.E., Beloborodov A.M., Poutanen J., 2001, ApJ, 555, 829
Stirling A.M., et al., 2001, MNRAS, 327, 1273
Svoboda J., Guainazzi M., Merloni A., 2017, A&A, 603, A127
Turolla R., Dullemond C.P., 2000, ApJL, 531, L49
Urry C.M., Padovani P., 1995, PASP, 107, 803
Vieyro F.L., Romero G.E., 2012, A&A, 542, A7
Vieyro F.L., Romero G.E., Chaty S., 2016, A&A, 587, A63
Yuan F., 2001, MNRAS, 324, 119
Yuan F., Narayan R., 2014, Annual Review of Astronomy and Astrophysics, 52, 529
Zanin R., et al., 2016, A&A, 596, A55
Zdziarski A.A., et al., 2014, MNRAS, 442, 3243

A Non-thermal processes

A.1 Leptonic processes

There are two main non-thermal processes of relativistic electrons with the different fields in the source: synchrotron radiation, and inverse Compton (IC) scattering. For sources with a high cold matter density, relativistic Bremsstrahlung could be also relevant.

The synchrotron radiation of ultra-relativistic electrons dominates much of the high-energy astrophysics. One of the general features of the radiation of relativistic electrons is that the radiation is beamed in the direction of motion of the electron. The synchrotron cooling rate for a particle of mass m, charge e, and energy E in a region of magnetic energy density U_B is

$$t_{\rm synchr}^{-1} = \frac{4}{3}\left(\frac{m_e}{m}\right)^3 \frac{c\sigma_T U_B}{m_e c^2}\frac{E}{mc^2}. \quad (A.1)$$

Expressions to calculate the synchrotron spectrum can be found, for example, in Blumenthal & Gould (1970). The power radiated by a single particle of energy E and pitch angle α is given by

$$P_{\rm synchr}(E, E_\gamma) = \frac{\sqrt{3}e^3 B\sin\alpha}{hmc^2}\frac{E_\gamma}{E_{\rm c}} \int_{E_\gamma/E_{\rm c}}^{\infty} K_{5/3}(\xi)d\xi, \quad (A.2)$$

where $K_{5/3}(\xi)$ is a modified Bessel function and the characteristic energy is

$$E_{\rm c} = \frac{3}{4\pi}\frac{ehB\sin\alpha}{mc}\left(\frac{E}{mc^2}\right)^2. \quad (A.3)$$

For a particle distribution with a power-law spectrum, i.e., $N(E) \propto E^{-\alpha}$, the synchrotron spectrum results in

$$L_\gamma(E_\gamma) \propto E_\gamma^{-\frac{\alpha-1}{2}}, \quad (A.4)$$

which is also a power-law spectrum.

In both Thomson and Klein-Nishina regimes, the IC cooling rate for an electron is given by (Blumenthal & Gould, 1970)

$$t_{\rm IC}^{-1} = \frac{1}{E_e}\int_{\epsilon_{\rm min}}^{\epsilon_{\rm max}}\int_{\epsilon}^{\frac{\Gamma E_e}{1+\Gamma}} (\epsilon_1 - \epsilon)\frac{dN}{dtd\epsilon_1}d\epsilon_1. \quad (A.5)$$

Here ϵ is the energy of the incident photon, ϵ_1 is the energy of the scattered photon, and

$$\frac{dN}{dtd\epsilon_1} = \frac{2\pi r_0^2 m_e^2 c^5}{E_e^2}\frac{n_{\rm ph}(\epsilon)d\epsilon}{\epsilon}F(q), \quad (A.6)$$

where $n_{\rm ph}(\epsilon)$ is the density of target photons, r_0 the classical radius of the electron, and

$$\begin{aligned} F(q) &= 2q\ln q + (1+2q)(1-q) + \frac{1}{2}(1-q)\frac{(\Gamma q)^2}{1+\Gamma q}, \\ \Gamma &= 4\epsilon E_e/(m_e c^2)^2, \\ q &= \epsilon_1/[\Gamma(E_e-\epsilon_1)]. \end{aligned} \quad (A.7)$$

According to Blumenthal & Gould (1970), the spectrum of photons scattered by an electron of energy $E_e = \gamma_e m_e c^2$ in a target radiation field of density $n_{\rm ph}(\epsilon)$ is

$$P_{\rm IC}(E_e, E_\gamma, \epsilon) = \frac{3\sigma_{\rm T} c (m_e c^2)^2}{4E_e^2}\frac{n_{\rm ph}(\epsilon)}{\epsilon}F(q), \quad (A.8)$$

where $F(q)$, q, and Γ are given by Eq. (A.7) (in this case $\epsilon_1 = E_\gamma$). The allowed range of energies for the scattered photons is

$$\epsilon \leq E_\gamma \leq \frac{\Gamma}{1+\Gamma}E_e\ . \quad (A.9)$$

The total luminosity can then be obtained from:

$$L_{\rm IC}(E_\gamma) = E_\gamma^2 \int_{V_c} d^3r \int_{E_{\rm min}}^{E_{\rm max}} dE_e N_e(E_e) \times \int_{\epsilon_{\rm min}}^{\epsilon_{\rm max}} d\epsilon P_{\rm IC}. \quad (A.10)$$

This equation takes into account the Klein-Nishina effect on the cross-section with energy.

A.2 Hadronic processes

For sources where an hadronic component can also be accelerated up to relativistic energies, the main hadronic processes for gamma emission are synchrotron radiation, photohadronic interactions and proton-proton inelastic collisions in some cases. Hadronic interactions produce neutral pions, which have a short mean lifetime of 8.4×10^{-17} s, and then they decay with a probability of 98.8 % into two gamma rays

$$\pi^0 \rightarrow \gamma + \gamma. \quad (A.11)$$

The photomeson production takes place for photon energies above $\epsilon_{\rm th} \approx 145$ MeV (measured in the rest-frame of the proton). Near the threshold, a single pion is produced per interaction; at higher energies, the production of multiple pions dominates.

The cooling rate due to photopion production for a proton of energy E_p in an isotropic photon field of density $n_{\rm ph}(\epsilon)$ is given by (Stecker, 1973)

$$t_{p\gamma}^{-1}(E_p) = \frac{m_p^2 c^5}{2E_p^2}\int_{\frac{\epsilon_{\rm th}}{2\gamma_p}}^{\infty} d\epsilon \frac{n_{\rm ph}(\epsilon)}{\epsilon^2} \int_{\epsilon_{\rm th}}^{2\epsilon\gamma_p} d\epsilon' \sigma_{p\gamma}(\epsilon')K_{p\gamma}(\epsilon')\epsilon', \quad (A.12)$$

where ϵ' is the photon energy in the rest-frame of the proton and $K_{p\gamma}$ is the inelasticity of the interaction. Atoyan & Dermer (2003) introduced a simplified approach to treat the cross-section and the inelasticity, which can be written as

$$\sigma_{p\gamma}(\epsilon') \approx \begin{cases} 340\ \mu{\rm barn} & 200{\rm MeV} \leq \epsilon' \leq 500{\rm MeV} \\ 120\ \mu{\rm barn} & \epsilon' \geq 500{\rm MeV}, \end{cases}$$

and

$$K_{p\gamma}(\epsilon') \approx \begin{cases} 0.2 & 200{\rm MeV} \leq \epsilon' \leq 500{\rm MeV} \\ 0.6 & \epsilon' \geq 500{\rm MeV}. \end{cases}$$

At energies below the threshold for photomeson production, the main channel of proton-photon interaction is the direct production of electrons or positrons. The cooling rate is also given by Eq. (A.12), and the corresponding cross-section and inelasticity. The cross-section for this channel - also known as the Bethe-Heitler cross-section- increases with the energy of the photon. Both the cross-section and inelasticity approximations in the limits of low and high energies can be found in Begelman et al. (1990).

The cooling rate for inelastic collisions of protons with nuclei of the source is given by:

$$t_{pp}^{-1} = n_i c \sigma_{pp} K_{pp}, \quad (A.13)$$

where n_i is the cold matter density, K_{pp} is the total inelasticity of the process, of value ~ 0.5. The total cross-section σ_{pp} can be approximated by (Kelner et al., 2006)

$$\sigma_{\rm inel}(E_p) = (34.3 + 1.88L + 0.25L^2)\left[1 - \left(\frac{E_{\rm th}}{E_p}\right)^4\right]^2, \quad (A.14)$$

where

$$L = \ln\left(\frac{E_p}{1\ {\rm TeV}}\right). \quad (A.15)$$

The proton threshold kinetic energy for π^0 production is $E_{\rm th}^{\rm kin} \approx 280$ MeV.

Hybrid magnetized stars within the Field Correlator Method

M. Mariani[1,2], M.G. Orsaria[1,2], I.F. Ranea-Sandoval[1,2] & O.M. Guilera[3,4,5]

[1] *Grupo de Gravitación, Astrofísica y Cosmología, Facultad de Ciencias Astronómicas y Geofísicas, UNLP, Argentina.*
[2] *Consejo Nacional de Investigaciones Científicas y Técnicas, Argentina.*
[3] *Facultad de Ciencias Astronómicas y Geofísicas, UNLP, Argentina.*
[4] *Instituto de Astrofísica de La Plata, CONICET–UNLP, Argentina.*
[5] *Instituto de Astrofísica, Pontificia Universidad Católica de Chile, Santiago, Chile.*

Contact / mmariani@fcaglp.unlp.edu.ar

Resumen / Presentamos resultados preliminares del estudio de los efectos de campos magnéticos intensos en estrellas híbridas. Para la descripción de la fase hadrónica, utilizamos la aproximación de campo medio relativista. Para la materia de quarks, empleamos el formalismo del Field Correlator Method. Construida la ecuación de estado, discutimos la anisotropía de las presiones debido a la presencia del campo magnético. Finalmente, calculamos la estructura de las estrellas compactas utilizando las ecuaciones de estado híbridas magnetizadas y sus modos de oscilación relacionados con la emisión de ondas gravitacionales.

Abstract / We present preliminary results of the study of intense magnetic fields effects on hybrid stars. For the description of the hadronic phase, we use the relativistic mean field approximation. For the quark matter phase, we employ the Field Correlator Method formalism. Once the the equation of state is built, we discuss the pressure anisotropy due the presence of the strong magnetic field. Finally, we calculate the structure of the compact stars using magnetized hybrid equations of state and their oscillation modes related with the emission of gravitational waves.

Keywords / stars: magnetars — asteroseismology — equation of state

1. Introduction

Neutron stars (NSs) or hybrid stars (HSs) are extremely compact ($M \sim 1.4$ M$_\odot$, $R \sim 10$ km) remnants of high-mass stars. In their inner cores, matter is compressed to densities larger than 10^{15} g/cm^3 so new exotic particles like mesons, hyperons and/or deconfined quarks can appear. The discovery of the 2 M$_\odot$ pulsars PSR J1614-2230 (Demorest et al., 2010) and PSR J0348-0432 (Antoniadis & et al., 2013) has imposed restrictions to the equation of state (EoS) needed to describe matter inside compact objects and has forced astrophysics to rethink the internal composition of NSs.

On the other hand, it is well known that at the surface of NSs there exist magnetic fields (MFs) of the order of 10^{11-13} Gauss, i.e., the classical pulsars. However, there is evidence of NSs with ultra strong MFs, called magnetars, in which the surface MF could be higher than 10^{14-15} G.

In addition, the recent direct detections of gravitational waves (GWs) have made GW astronomy become highly relevant. In this way, it is known that NS oscillation modes are directly related to its interior composition (Vásquez Flores & Lugones, 2014). In particular, non-radial oscillation modes may emit GWs. For this reason, the study of non-radial pulsations and their associated GW emission could shed some light on the behavior of matter inside NSs.

2. Hybrid EoS and phase transition

We model cold HSs using a hybrid-magnetized EoS by combining the magnetized BPS EoS for the crust (Lai & Shapiro, 1991), the magnetic non-linear relativistic mean field model (Rabhi et al., 2009) for the outer hadronic core and a magnetized version of the Field Correlator Method (FCM) EoS of quark matter for the inner core (Simonov & Trusov, 2007; Strickland et al., 2012). We consider a chemical potential, μ_b, dependent magnetic field in the z-direction given by (Dexheimer et al., 2012):

$$B(\mu_b) = B_{\rm surface} + B_{\rm center}[1 - e^{\beta \frac{(\mu_b - m_n)^\alpha}{m_n}}] \qquad (1)$$

where $\alpha = 2.5$ and $\beta = -4.08\ 10^{-4}$ are fixed parameters, and m_n is the nucleon mass.

The FCM quark model is characterized by two parameters: the gluon condensate, G_2, and the large distance static $\bar{q}q$ potential, V_1.

As we are studying cold hybrid stars, the only leptons present in neutron star matter in chemical equilibrium are electrons and muons.

To build the phase transition between hadronic and quark matter, we use the Maxwell construction in which no mixed phase exists and there is a sharp discontinuity. Electric charge is conserved locally and β-equilibrium condition, which establishes equilibrium among weak interaction processes, is also taken into account.

We study two different MF configurations (consistent with a "classical pulsar", A1 and B1 cases, and

with a "magnetar", A2 and B2 cases) and two sets of FCM parameters. Details of the parameter values for each case are given in Table 1.

Considering these conditions, it is possible to construct hybrid EoS which determine the particle population of magnetized HSs, as shown in Fig. 1. It can be seen that the MF shifts the phase transition to high densities. This is more noticeable by comparing B1 and B2 cases in which a Δ^- appears in the hadronic phase as the phase transition to quark matter occurs later. The strong MF also increases the electron population in the quark phase.

One of the strong MF effects is to produce an anisotropy on the pressure, related to its axial direction (Menezes et al., 2015, 2018):

$$P_{\parallel} = P_{matter} - \epsilon_{matter} - \frac{B^2}{2}\,, \tag{2}$$

$$P_{\perp} = P_{matter} - \epsilon_{matter} + \frac{B^2}{2} - \mathcal{M}B\,, \tag{3}$$

where $\mathcal{M} = -\frac{\partial\Omega}{\partial B}$ (Ω is the Grand canonical potential) is the matter magnetization and ϵ_{matter} is the matter energy density. As we will explain in detail later, we have considered an average of the pressure tensor components to obtain the total pressure of the system.

In the top panel of Fig. 2, we show the resulting hybrid EoS for the four cases considered.

Table 1: Parameters values and labels for each studied case.

Case	$B_{\rm surface}$ [Gauss]	$B_{\rm center}$ [Gauss]	V_1 [MeV]	G_2 [GeV^4]
A1	1.0 10^{13}	1.0 10^{15}	15	0.006
A2	1.0 10^{15}	5.0 10^{18}	15	0.006
B1	1.0 10^{13}	1.0 10^{15}	20	0.006
B2	1.0 10^{15}	5.0 10^{18}	20	0.006

3. Hybrid star structure

Once the hybrid EoS is obtained, we construct the family of stationary stellar configurations. The Tolman-Oppenheimer-Volkoff (TOV) equations are the relativistic structure equations of hydrostatic equilibrium and mass conservation for a spherically symmetric spacetime. These equations determine the mass-radius relationship for each family of stars.

In our case, the MF breaks the spherical symmetry. Including the breaking of the spherical symmetry in a consistent way would lead to 2D calculations. To avoid this complication, we have considered the total pressure as the average of the pressure contributions in different directions, maintaining in this way the isotropy of the system (Dexheimer et al., 2012). With this choice, we are able to use TOV equations without any change and study the effect on the M-R relationships for magnetized HSs. We present our results in Fig.2.

In addition, we study stellar polar pulsations within the relativistic Cowling approximation (Vásquez Flores & Lugones, 2014; Sotani et al., 2011; Ranea-Sandoval et al., 2018) where metric perturbations are neglected. In Fig. 3 we present the frequencies of the fundamental (f) and first pressure (p_1) modes as a function of the stellar mass. The four cases show non distinguishable frequencies. As the frequency calculations are possible only for the -purely hadronic- stable stars, because the appearance of quark matter immediately destabilizes the star, and as the MF increases for higher densities, these results are consequence of the negligible effect of the low MF in the hadronic phase.

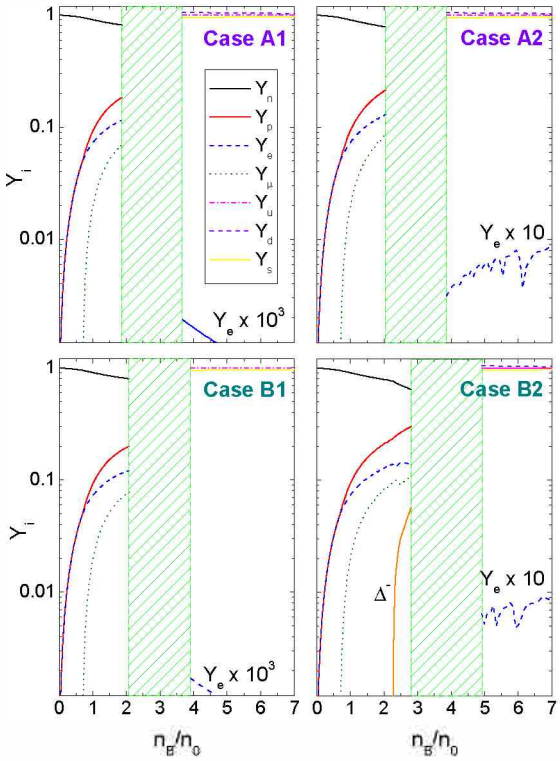

Figure 1: Particle populations as a function of baryon number density in nuclear density units ($n_0 = 0.16$ fm^{-3}). The left region of each panel corresponds to the hadronic phase and the right one shows the quark phase population. The green area represents the jump in the density corresponding to the phase transition.

4. Conclusions and discussion

We have calculated magnetic hybrid EoSes and we have obtained stable magnetars that reach 2 $M_\odot$ for the maximum mass star. According to these results, the magnetic field would increase the maximum mass star of the stable branch of the HSs family in comparison to the classical pulsars. This is a consequence of a late phase transition from hadronic to quark matter in the magnetized neutron star matter.

Regarding the FCM parameters, the increase of V_1 produces an increase in the maximum mass of the last stable star. Remains to analyze the effect of a G_2 variation.

In the four studied cases, the appearance of the quark matter destabilizes the star. In this way, all the stable stars obtained are pure hadronic stars.

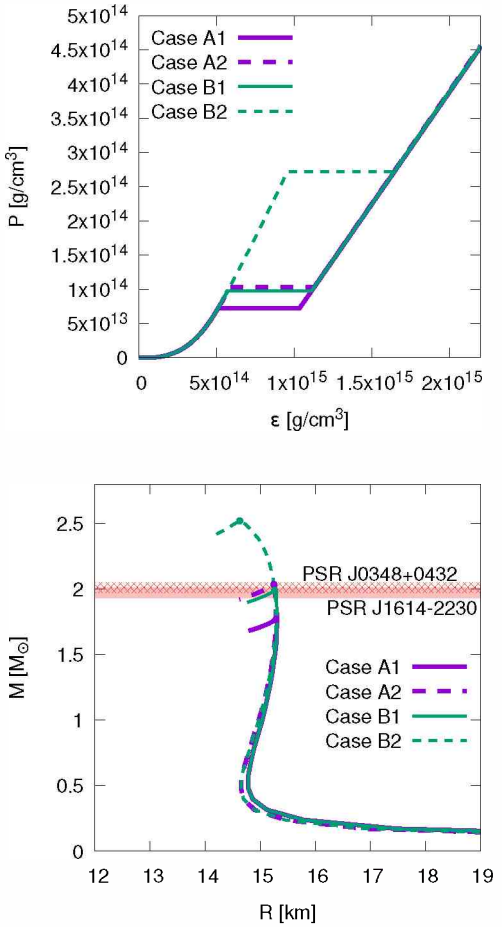

Figure 2: Hybrid EoSes (top panel) and M-R relationship (bottom) for the four cases. In the EoS curves, the constant pressure regions correspond to the transition phase. It can be seen that the effect of the strong MF delays the phase transition and stiffens the EoSes. In the M-R curves, the rounded dot indicates where the quark mater core appears. After the peaks, towards smaller radii, the stars become unstable. The horizontal bars are the measured masses of the 2 $M_\odot$ pulsars with their corresponding errors. It can be seen that the magnetars reach higher maximum masses than the classical pulsars.

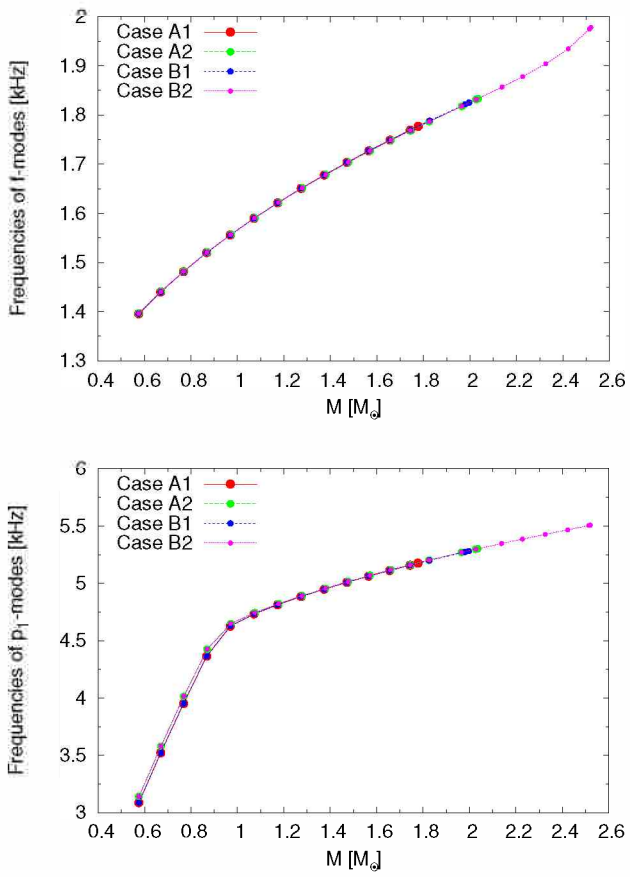

Figure 3: Frequencies of f (top panel) and p_1 (bottom) modes for the four cases. The results are almost coincident due to the low MF along the hadronic phase.

From the analysis of the oscillation modes, as we have explained before, it turns out that all the studied cases show very similar frequency values. These results suggest that the detection of f and p_1 modes would not be enough to distinguish between classical pulsars or magnetars. Nevertheless, as these are preliminary results, it is necessary to study new values for the model parametrization, consider the existence of a mixed hadron-quark phase and calculate other frequency oscillation modes, such as the g-mode.

Acknowledgements: MM, MGO and IFRS acknowledge support from Universidad Nacional de La Plata and CONICET under Grants G140, G157 and PIP-0714. OMG thanks ANPCyT and UNLP for financial support under Grants PICT 2006-0053 and G157.

References

Antoniadis J., et al., 2013, Science, 340, 448
Demorest P.B., et al., 2010, Nature, 467, 1081
Dexheimer V., Negreiros R., Schramm S., 2012, European Physical Journal A, 48, 189
Lai D., Shapiro S.L., 1991, ApJ, 383, 745
Menezes D.P., Pinto M.B., Providência C., 2015, PhRvC, 91, 065205
Menezes D.P., Pinto M.B., Providência C., 2018, PhRvC, 97, 029904
Rabhi A., et al., 2009, J. Phys. G, 36, 115204
Ranea-Sandoval I.F., et al., 2018, JCAP, 2018, 031
Simonov Y.A., Trusov M.A., 2007, J. Exp. Theor. Phys. Letters, 85, 598
Sotani H., et al., 2011, PhRvD, 83, 024014
Strickland M., Dexheimer V., Menezes D.P., 2012, PhRvD, 86, 125032
Vásquez Flores C., Lugones G., 2014, Class. Quantum Gravity, 31, 155002

Formation of massive black holes via collisions and accretion

D.R.G. Schleicher[1], M. Fellhauer[1], T.C.N. Boekholt[2], B. Reinoso[1], R.S. Klessen[3,4], M.Z.C. Vergara[1], P.J. Alister Seguel[1], S. Bovino[1], C. Olave[1], V.B. Díaz[1], P. FFibla[1], R. Riaz[1], B. Bandyopadhyay[1], R.I. San Martín-Pérez[1], J. Zamponi[1] & L. Haemmerle[5]

[1] *Departamento de Astronomía, Facultad Ciencias Físicas y Matemáticas, Universidad de Concepción, Concepción, Chile*
[2] *CIDMA, Departamento de Física, Universidade de Aveiro, Aveiro, Portugal*
[3] *Universität Heidelberg, Zentrum für Astronomie, Institut für Theoretische Astrophysik, Heidelberg, Germany*
[4] *Universität Heidelberg, Interdisziplinäres Zentrum für Wissenschaftliches Rechnen, Heidelberg, Germany*
[5] *Observatoire de Genève, Université de Genève, Sauverny, Switzerland*

Contact / bidisharia@gmail.com

Resumen / Para explicar la población de agujeros negros supermasivos en $z \sim 7$, se necesitan semillas de agueros negros muy masivas o, alternativamente, escenarios de acreción super-Eddington a fin de alcanzar masas finales del orden de 10^9 $M_\odot$. El modelo del colapso directo predice la formación de un solo objeto masivo debido al colapso directo de una nube de gas masiva. Las simulaciones en los últimos años han demostrado que este escenario es muy difícil de lograr. Un modelo realista de formación de agujeros negros debería tener en cuenta la fragmentación y considerar la interacción entre los procesos estelar-dinámicos y la dinámica del gas. Presentamos aquí una simulación numérica aplicada con el código AMUSE, realizando un tratamiento aproximado del gas. Según estas simulaciones, mostramos que se pueden formar agujeros negros muy masivos, $10^4 - 10^5$ $M_\odot$, dependiendo del sumistro del gas y la acreción en las protoestrellas.

Abstract / To explain the observed population of supermassive black holes at $z \sim 7$, very massive seed black holes or, alternatively, super-Eddington scenarios are needed to reach final masses of the order of 10^9 $M_\odot$. A popular explanation for massive seeds has been the direct collapse model, which predicts the formation of a single massive object due to the direct collapse of a massive gas cloud. However, simulations over the last years have shown that such a scenario is very difficult to achieve. Therefore, a realistic model of black hole formation should take fragmentation into account, and consider the interaction between stellar-dynamical and gas-dynamical processes. We present here numerical simulations performed with the AMUSE code, employing an approximate treatment of the gas. Based on these simulations, we show that very massive black holes of $10^4 - 10^5$ $M_\odot$ may form depending on the gas supply and the accretion onto the protostars.

Keywords / black hole physics - stars: Population III - methods: numerical

1. Introduction

At present, more than 100 quasars are known at $z > 5.6$ (Bañados et al. 2016; Schleicher 2018), with the currently known highest-redshift quasar at $z \sim 7.5$, hosting a supermassive black hole with about 8×10^8 $M_\odot$ (Bañados et al. 2018). To explain such early and supermassive black holes, one needs to assume almost continuous Eddington accretion since redshifts $z \sim 20$, bursts of Super-Eddington accretion or rather massive seeds at the beginning of the accretion process (e.g. Shapiro 2005). The pathways to produce massive seeds have already been laid out by Rees (1984). These include the formation via direct collapse of a massive gas cloud into one single object and also black hole formation, via stellar-dynamical processes resulting from runaway-collisions either in stellar clusters or clusters of stellar-mass black holes.

The direct collapse seemed initially very promising, due to its capacity of producing very high-mass seeds with up to 10^5 $M_\odot$ (e.g. Bromm & Loeb 2003; Wise et al. 2008; Schleicher et al. 2010; Latif et al. 2013, 2014). However, to reach the required conditions, the collapse should basically be isothermal under atomic cooling, requiring very large ambient UV fluxes (Latif et al. 2015). On the other hand, even tiny amounts of dust can already trigger strong fragmentation through the enhanced cooling (e.g. Omukai et al. 2008; Dopcke et al. 2011; Klessen et al. 2012; Bovino et al. 2016; Latif et al. 2016).

Under realistic conditions, it is then almost unavoidable for fragmentation to occur, at least initially preventing the formation of a single massive object. However, also star clusters can produce massive black holes by collisions, as discussed e.g. by Devecchi et al. (2012); Sakurai et al. (2017), showing that black holes of ~ 500 $M_\odot$ are able to form. It has been established over the last years that the radii of primordial protostars can be considerably enhanced while accreting, thereby effectively behaving like red giants (Hosokawa et al. 2013; Haemmerlé et al. 2018). As known already from present-

day protostellar clusters (Baumgardt & Klessen 2011), such an enhancement of the protostellar radii increases the probability for collisions, and may favor the formation of massive objects. In the context of primordial stellar clusters, Reinoso et al. (2018) recently explored the implications of such enhanced radii for the collisions, showing that indeed both the fraction of collisions as well as the mass of the central massive object, increases significantly with protostellar radii. They also provide scaling relations that allow to infer the black hole mass as a function of the ambient condition.

The presence of gas in the first proto-cluster may have further implications. Firstly, it provides an additional gravitational potential, which enhances the velocity dispersion of the embedded stellar cluster. Secondly, the protostars may accrete and change their masses during the run-time of the simulations. The interaction between gas-dynamical and stellar-dynamical processes may thus be quite relevant for the formation of very massive objects in the first stellar clusters, however, it has hardly been considered so far. In the following, we present a set of simulations performed with the publicly available AMUSE framework* (Pelupessy et al. 2013) to approximately account for such effects. A more detailed description of the simulations has been presented by Boekholt et al. (2018).

2. Numerical setup

We adopt here a simplified initial condition, where both protostars and the gas follow a Plummer distribution (Plummer 1911). In our reference model, the initial gas mass corresponds to 10^5 $M_\odot$, the Plummer radius is 0.1 pc and the initial number of stars is 256, with very low masses of initially 0.1 $M_\odot$. The system is thus initially gas-dominated. We also introduce a cut-off radius after which the density is set to zero. The latter corresponds to five times the Plummer radius. The gravitational interaction between the stars is modeled via the N-body code PH4 by McMillan & Hut (1996), using a fourth-order Hermite algorithm by employing the time-symmetric integration scheme developed by Hut et al. (1995). The gravitational potential of the gas cloud is described as an analytic background potential, which is coupled to the stars using the `BRIDGE` method (Fujii et al. 2007).

The accretion of the gas onto the stars is described by the simplified models outlined in Table 1 (Boekholt et al. 2018). Models with an infinite gas reservoir indicate that the gas is efficiently resupplied during the evolution, so that gas accreted onto the protostars is not removed from the gas (models 1-2), while it is removed in the models with a finite gas reservoir (models 3-6). In case of position-dependent accretion, we assume that the accretion rate is proportional to the gas density in the Plummer sphere. If the accretion rate is also time-dependent, we assume it to be proportional to the mass in the gas reservoir. In models 3-6, the accretion is switched off when the gas reservoir is exhausted. Our fiducial accretion rate is 0.03 $M_\odot$ yr^{-1}, as suggested through numerical simulations (e.g. Latif et al. 2013, 2014), but we also explored other values.

*Webpage AMUSE: http://amusecode.org/

Model	Gas reservoir	Position dep. accretion	Time dep. accretion
1	Infinite	no	no
2	Infinite	yes	no
3	Finite	no	no
4	Finite	yes	no
5	Finite	no	yes
6	Finite	yes	yes

Table 1: The gas accretion models for Pop. III protostars embedded in their natal gas cloud, as presented by Boekholt et al. (2018).

The stellar radii have been determined using approximate fits to the mass-radius relations given by Hosokawa et al. (2013) and Haemmerlé et al. (2018), where both prescriptions yield similar results. To model collisions, we adopt the so-called "sticky-sphere" approximation, replacing two protostars by one if the distance between two protostars becomes less than their radii. During the collision, we assume the conservation of mass, and the new radius is determined from the mass-radius parametrization. Using this setup, we follow the evolution of the system until no further collisions occur. The latter usually corresponds to a physical time of less than one million years.

3. Results

The results for our fiducial parameters, providing the time evolution of the mass of the most massive central object, are presented in Fig. 1 for the different accretion models (Boekholt et al. 2018). Clearly, the most optimistic models are models 1 and 2 with an infinite gas reservoir, so that the central mass can continue to grow unimpededly. Such a scenario is only feasible in case of a strong external mass supply, which needs to be transported through the protogalaxy, for instance as a result of gravitational torques. In case the gas reservoir is finite, the mass of the resulting object is lower by a factor of 2 or 3. The most conservative model with respect to the black hole mass is our model 5, with the finite gas reservoir and a time-dependent accretion rate, which is however independent of position. In this case, large fractions of the mass are accreted in the outer parts of the cluster, where they do not strongly participate in collision events. As a result, they do not contribute to the mass of the most massive object. Nevertheless, even in the most conservative scenario, the central object reaches a mass of 10^4 $M_\odot$.

We have checked the dependence of these results on various parameters, as presented in detail by Boekholt et al. (2018). We found that the most crucial parameter is the initial gas reservoir. In case a gas mass of 10^5 $M_\odot$ is available, the results only weakly depend on other parameters, but the mass of the central massive object decreases significantly if less gas is available. The size of the cluster as well as the accretion rate, on the other hand, were found to be of minor relevance and to

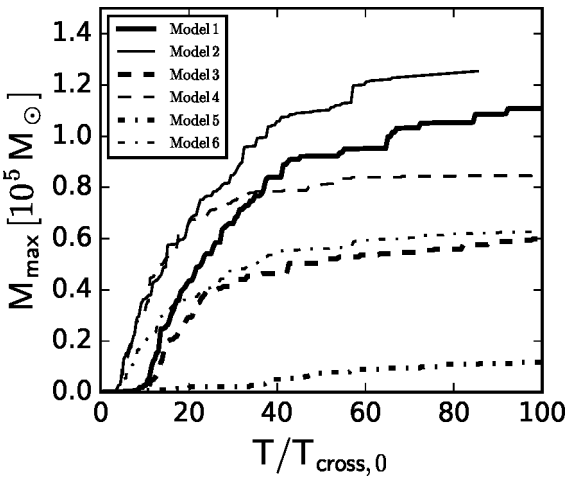

Figure 1: Time evolution of the most massive object mass. Shown are the results for the six different accretion models given in Table 1. Figure from Boekholt et al. (2018).

primarily affect the timescale until the process is completed. Therefore, the model has the advantage to potentially be robust, at least under conditions where a sufficiently large gas masses are available for accretion.

4. Summary and discussion

We find that our scenario provides a potentially promising pathway for the formation of very massive black holes, with masses between 10^4 and 10^5 $M_\odot$. Our gas-dynamical model, however, is still based on highly simplifying assumptions, considering an analytic gravitational potential and very simple prescriptions for the accretion of the protostars. For the future, it will be central to gradually relax some of the assumptions, and to explore how a detailed dynamical treatment of the gas and the accretion will affect the results. Additional uncertainties concern the geometry of the star and gas distribution, which was here assumed to be spherical. Numerical simulations frequently suggest that fragmentation will occur preferentially in flattened geometries including rotation. The presence of such an ordered velocity component could potentially somewhat alter the results presented here, as collisions may become less likely in such a case. On the other hand, the presence of gas is also expected to lead to dynamical friction, which we neglected in the simulations presented here. Such friction could further affect the motions of the stars and increase the probability of collisions.

As semi-analytic models indeed suggest that massive seeds are needed to form supermassive black holes (Valiante et al. 2016), it will be important to explore realistic formation scenarios.

Acknowledgements: We thank for funding via Conicyt, in particular via Conicyt PIA ACT172033, Fondecyt regular (project code 1161247), the "Concurso Proyectos Internacionales de Investigación, Convocatoria 2015" (project code PII20150171) and the CONICYT project Basal AFB-170002. MF thanks for funding via Fondecyt regular 1180291. BR and VBD thank Conicyt for financial support on their Master studies through CONICYT-PFCHA/MagísterNacional/2017-22171385 and CONICYT-PFCHA/MagísterNacional/2017-22171293. RSK acknowledges financial support from the Deutsche Forschungsgemeinschaft via SFB 881, "The Milky Way System" (sub-projects B1, B2 and B8). He also thanks for support from the European Research Council via the ERC Advanced Grant "STARLIGHT: Formation of the First Stars" (project number 339177). TB acknowledges support from Fundação para a Ciência e a Tecnologia (grant SFRH/BPD/122325/2016), and support from Center for Research & Development in Mathematics and Applications (CIDMA) (strategic project UID/MAT/04106/2013), and from ENGAGE SKA, POCI-01-0145-FEDER-022217, funded by COMPETE 2020 and FCT, Portugal.

References

Bañados, E., Venemans, B. P., Decarli, R., et al. 2016, ApJS, 227, 11
Bañados, E., Venemans, B. P., Mazzucchelli, C., et al. 2018, Nature, 553, 473
Baumgardt, H. & Klessen, R. S. 2011, MNRAS, 413, 1810
Boekholt, T. C. N., Schleicher, D. R. G., Fellhauer, M., et al. 2018, MNRAS, 476, 366
Bovino, S., Grassi, T., Schleicher, D. R. G., & Banerjee, R. 2016, ApJ, 832, 154
Bromm, V. & Loeb, A. 2003, ApJ, 596, 34
Devecchi, B., Volonteri, M., Rossi, E. M., Colpi, M., & Portegies Zwart, S. 2012, MNRAS, 421, 1465
Dopcke, G., Glover, S. C. O., Clark, P. C., & Klessen, R. S. 2011, ApJL, 729, L3
Fujii, M., Iwasawa, M., Funato, Y., & Makino, J. 2007, PASJ, 59, 1095
Haemmerlé, L., Woods, T. E., Klessen, R. S., Heger, A., & Whalen, D. J. 2018, MNRAS, 474, 2757
Hosokawa, T., Yorke, H. W., Inayoshi, K., Omukai, K., & Yoshida, N. 2013, ApJ, 778, 178
Hut, P., Makino, J., & McMillan, S. 1995, ApJL, 443, L93
Klessen, R. S., Glover, S. C. O., & Clark, P. C. 2012, MNRAS, 421, 3217
Latif, M. A., Bovino, S., Grassi, T., Schleicher, D. R. G., & Spaans, M. 2015, MNRAS, 446, 3163
Latif, M. A., Omukai, K., Habouzit, M., Schleicher, D. R. G., & Volonteri, M. 2016, ApJ, 823, 40
Latif, M. A., Schleicher, D. R. G., & Schmidt, W. 2014, MNRAS, 440, 1551
Latif, M. A., Schleicher, D. R. G., Schmidt, W., & Niemeyer, J. C. 2013, MNRAS, 436, 2989
McMillan, S. L. W. & Hut, P. 1996, ApJ, 467, 348
Omukai, K., Schneider, R., & Haiman, Z. 2008, ApJ, 686, 801
Pelupessy, F. I., van Elteren, A., de Vries, N., et al. 2013, A&A, 557, A84
Plummer, H. C. 1911, MNRAS, 71, 460
Rees, M. J. 1984, ARA&A, 22, 471
Reinoso, B., Schleicher, D. R. G., Fellhauer, M., Klessen, R. S., & Boekholt, T. C. N. 2018, A&A, 614, A14
Sakurai, Y., Yoshida, N., Fujii, M. S., & Hirano, S. 2017, MNRAS, 472, 1677
Schleicher, D. R. G. 2018, ArXiv e-prints
Schleicher, D. R. G., Spaans, M., & Glover, S. C. O. 2010, ApJL, 712, L69
Shapiro, S. L. 2005, ApJ, 620, 59
Valiante, R., Schneider, R., Volonteri, M., & Omukai, K. 2016, MNRAS, 457, 3356
Wise, J. H., Turk, M. J., & Abel, T. 2008, ApJ, 682, 745

Accretion models for LLAGNs: model parameter estimation with M87 as an example

B. Bandyopadhyay[1], D.R.G. Schleicher[1], N. Nagar[1], F.G. Xie[2] & V. Ramakrishnan[1]

[1] *Departamento de Astronomía, Facultad Ciencias Físicas y Matemáticas, Universidad de Concepción, Concepción, Chile*

[2] *Key Laboratory for Research in Galaxies and Cosmology, Shanghai Astronomical Observatory, Chinese Academy of Sciences, Shanghai, China*

Contact / bidisharia@gmail.com

Resumen / El Telescopio de Horizonte de Eventos (EHT por sus siglas en inglés) brinda una oportunidad única para explorar la física de los agujeros negros supermasivos por medio de la interferometría de muy larga base (VLBI por sus siglas en inglés), incluyendo la existencia del horizonte de eventos y los procesos de acreción así como la formación de chorros. Hemos construído un modelo teórico que incluye un flujo de acreción dominado por advección (ADAF por sus siglas en inglés) y un flujo en chorro de radio simple. La distribución espectral de energía (SED por sus siglas en inglés) predicha por este modelo se puede comparar con observaciones para obtener las mejores estimaciones de los parametros del modelo. Además, los perfiles de emisión radial predichos por el modelo en diferentes bandas de frecuencia, pueden ser usados para predecir la posibilidad de resolver el flujo de entrada con el EHT u otros telescopios. En esta publicación aplicamos el modeo a la radio galaxia M87 como ejemplo.

Abstract / The Event Horizon Telescope (EHT) provides a unique opportunity to probe the physics of supermassive black holes through Very Large Baseline Interferometry (VLBI), such as the existence of the event horizon, the accretion processes as well as jet formation in low luminosity AGN (LLAGN). We build a theoretical model which includes an advection-dominated accretion flow (ADAF) and a simple radio jet outflow. The predicted spectral energy distribution (SED) of this model can be compared to observations to get the best estimates of the model parameters. Additionally, the model-predicted radial emission profiles at different frequency bands, can be used to predict whether the inflow can be resolved by the EHT or other telescopes. In this proceeding we demonstrate this process using M87 as an example.

Keywords / Galaxies:active, Accretion:accretion disks, Black hole physics, Relativistic processes

1. Introduction

Active Galactic Nuclei (AGN) are among the brightest sources in the sky, with a central engine consisting of a compact object with accreting gas surrounding it. The accretion process is expected to be the primary power source illuminating the AGN. The existence of a highly massive compact object in the center of our galaxy (Sgr A*) has been confirmed from observations of stellar motions near the center (Meyer et al., 2012). Based on the predictions of General Relativity, the compact object is assumed to be a black hole, i.e. an object with an event horizon, from which not even light can escape. To rule out the existence of a surface for the compact object in Sgr A* and M87 (CD galaxy in the Virgo cluster), Broderick et al. (2009, 2015) pursued a comparison of the observed fluxes in the central regions with the expected fluxes in the presence of a putative surface. They have shown that, for realistic accretion rates, the existence of such a surface is highly implausible. However, this still presents an indirect argument. The detection of the shadow of the black hole would provide direct and firm evidence of the existence of an horizon. Imaging the shadow of the supermassive black holes in Sgr A* and M87, thus detecting their horizons, is one of the main goals of the Event Horizon Telescope (EHT) which has a resolution of 15-20 μarcsec. In addition, the EHT will study the accretion of supermassive black holes in other nearby Low-Luminosity AGN (LLAGN). While the Global 3-mm VLBI Array (GMVA) and the European VLBI Network (EVN) observe at lower frequencies and offer lower resolutions (50-70 μarcsec), observing nearby LLAGN with them will enable the characterization of emission from a greater part of the accretion disk. Our primary aim is to build a simple theoretical framework to predict, for a large sample of LLAGN, the spectrum and the morphology of the emitting region when varying the model parameters. In this work we demonstrate this process with M87 as an example.

2. Model Description

2.1. Dynamical Equations

The accretion disks in LLAGN can be described by an advection dominated accretion flow (ADAF), which is a sub-Eddington accretion flow (Shapiro et al., 1976; Ichimaru, 1977; Rees et al., 1982). The accretion rate is much smaller than the Eddington rate and the gas

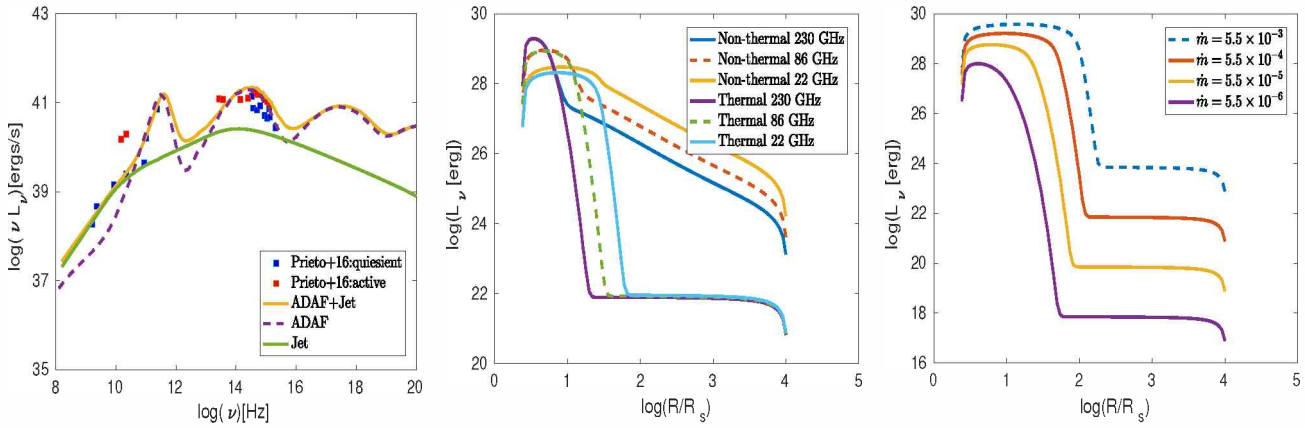

Figure 1: *Left Panel*: We show the best fit ADAF+JET model SED for M87 (yellow line) and compare the result with the observational data given in Prieto et al. (2016). The individual components are ADAF (purple dashed) and JET (green line). *Middle Panel*: The radial profile for emission at 22 GHz, 86 GHz and 230 GHz with the ADAF disk models in cases with and without the inclusion of non-thermal electrons. Here R_s is the Schwarzchild radius. *Right Panel*: Variation in the radial profile of emission at 22 GHz for different accretion rates. Here $\dot{m} = \dot{M}/\dot{M}_{\rm Edd}$ *i.e.* the ratio of true accretion rate to the Eddington rate.

reaches its virial temperature. Such disks are geometrically thick but optically thin, and are often accompanied by outflows. The small accretion rate leads to a low density in the disk. The excess heat generated due to viscous dragging is unable to escape due to inefficient radiative cooling, and is advected into the black hole. As a consequence of low opacity, a two-temperature plasma forms, where the ions are much hotter than the electrons. We investigate the evolution of the dynamical equations in an ADAF model tailored to LLAGN (Yuan et al., 2005). From the laws of conservation of mass, radial momentum, angular momentum and energy, we set up the following dynamical equations (Yuan & Narayan, 2014):

$$\dot{M}(R) = \dot{M}_{\rm R_{out}} \left(\frac{R}{R_{\rm out}}\right)^{s} = 4\pi\rho RH|v| \quad (1)$$

$$v\frac{dv}{dR} - \Omega^2 R = -\Omega_K^2 R - \frac{1}{\rho}\frac{d}{dR}(\rho c_s^2) \quad (2)$$

$$\frac{d\Omega}{dR} = \frac{v\Omega_K(\Omega R^2 - j)}{\alpha R^2 c_s^2} \quad (3)$$

$$\rho v\left(\frac{de_i}{dR} - \frac{p_i}{\rho^2}\frac{d\rho}{dR}\right) = (1-\delta)q^+ - q^{ie}$$

$$\rho v\left(\frac{de_e}{dR} - \frac{p_e}{\rho^2}\frac{d\rho}{dR}\right) = \delta q^+ + q^{ie} - q^- \quad (4)$$

The variables have their usual meaning. It should be noted that Eq. 1 includes the case of outflows, while Eq. 4 is the modified energy conservation equation for two temperature plasmas. Comparing the modeled spectrum with the available SED data, allows us to constrain important model parameters like the accretion rate $\dot{M}$, the strength of the outflow parameter s, the relative magnetic strength β (which is embedded in the energy equation) and the electron heating factor δ (Xie & Yuan, 2012; Chael et al., 2018b). For M87, using a black hole mass of 6.4×10^9 $M_\odot$ and a distance of 14.9 Mpc, the best fit parameter values, by comparing our models with observational data (left panel of Fig. 1), are: $\dot{M}_{R_{out}} = 5.5 \times 10^{-4}\ M_{Edd}$, $\beta = 0.9$, $s = 0.1$ and $\delta = 0.09$.

2.2. The Jet

The accretion dynamics is more complex due to turbulence, the presence of magnetic fields, hot spots and outflows. Narayan & Yi (1994, 1995) and Blandford & Begelman (1999) postulate that hot accretion flows should have strong winds followed by the formation of jets. This is supported by observational evidence which suggests that almost all LLAGN are radio-loud (Falcke & Markoff, 2000; Nagar et al., 2000; Ho, 2002). The jet dynamics is generally assumed to arise from a combination of magnetic fields and rotation. The most accepted theoretical models are the Blandford-Znajek model (BZ, Blandford & Znajek, 1977) which states that the primary source of energy in the jet is the rotational energy of the black hole, while the Blandford-Payne model (BP, Blandford & Payne, 1982) suggests that it is due to the rotational energy of the accretion flow. Independent of the origin of the jet, it is often necessary to include a jet to explain the observed SED of most LLAGN (Nemmen et al., 2014; Li et al., 2016). The most powerful jet can be produced by a highly-magnetized version of ADAF, i.e. the magnetically arrested disk (MAD, Tchekhovskoy et al. (2011); Chael et al. (2018a)). In this work, we do not aim to explore the origin of the jet, but use a phenomenological model to describe its properties (Spada et al. 2001; Yuan et al. 2005), which is sufficient to model the 1D spectrum. Owing to the supersonic radial velocity of accretion near the supermassive black hole, the bending of the gas into the jet causes a standing shock at the bottom. Post shock properties, like the temperature and densities, are determined from the shock jump condition. The shock accelerates a fraction of the electrons yielding a power law energy distribution. These are the electrons that contribute most to the emis-

sion of the jet. The emission from the jet depends on the mass loss rate, $\dot{m}_j$, the Lorentz factor, Γ_j and the energy densities, ϵ_e and ϵ_B, for the accelerated electrons and the amplified magnetic fields respectively. For M87 we obtain: $\dot{m}_j = 1.0 \times 10^8$, $\Gamma_j = 6.0$, $\epsilon_e = 0.0006$ and $\epsilon_B = 0.001$ (left panel of Fig. 1).

2.3. The Spectral Energy Distribution (SED) and emission profiles

The temperature, electron density and velocity profiles of the gas, are the parameters that we obtain from the solution of the dynamical equations. Assuming the disk is isothermal in the vertical direction, the spectrum of non scattered photons at a given radius is calculated by solving the radiative transfer equation in the vertical direction of the disk, based on the two-stream approximation (Rybicki & Lightman, 1979). Since the gas near to the black hole is hot, optically thin and magnetized, the processes which significantly contribute to the emission are synchrotron and bremsstrahlung (Manmoto et al., 1997). The presence of electrons comptonizes (Coppi & Blandford, 1990) these photons to modify the total SED. Processes such as magnetic reconnection, weak shocks and turbulent dissipation can accelerate a fraction of the thermal electrons to a non-thermal, power-law distribution, which also emits via synchrotron emission (Yuan et al., 2005). The power-law electrons in the jet lead to an enhanced contribution of the synchrotron emission. In our model we have included the emission of power-law electrons from the disk (following the method of Özel et al. (2000)) which has not been included in the works of Li et al. (2016).

3. Discussion and Conclusion

We showed how to obtain the best fit parameter values of our model, by comparing the simulated SED with the observed dataset. As a specific example, we have calculated the SED of M87 and the expected radial profiles of the emission from the disk at three different frequencies (22 GHz, 86 GHz and 230 GHz), shown in the middle panel of Fig. 1. The radial profile changes depending on the parameter values as well as the adopted physics in the disk (mass of the black hole, Eddington ratios, presence of non-thermal electrons, etc.). Potentially allowing us to constrain the physics of the accretion disk through a comparison with observations from the EHT (230 GHz), the GMVA (86 GHz) and the EVN (22 GHz). As an example we have shown in right panel of Fig.1, the variation in the radial profile of emission from the disk at 22 GHz for different accretion rates. This analysis is the first step towards predicting the resolvability of the region in the proximity of the black hole. The summary of our analysis for M87 is as follows:

- The emission from power-law electrons in the disk is important especially to explain the Compton peak in the SED of M87.
- The radial profile of emission varies significantly when including the power-law electrons, hence showing their significant contribution to emission at low frequencies, even from the outer regions of the disk.
- For a system like M87, it is important to include the emission from the jet in order to explain the flux at lower frequencies. Any synchrotron emission from the disk will be highly self-absorbed.

Acknowledgements: We acknowledge funding from Conicyt, in particular through ALMA-Conicyt (Project No. 31160001), Fondecyt regular (Project No. 1161247), the 'Concurso Proyectos Internacionales de Investigación, Convocatoria 2015' (project code PII20150171) , Conicyt PIA ACT172033 and the CONICYT project Basal AFB-170002.

References

Blandford R.D., Begelman M.C., 1999, MNRAS, 303, L1
Blandford R.D., Payne D.G., 1982, MNRAS, 199, 883
Blandford R.D., Znajek R.L., 1977, MNRAS, 179, 433
Broderick A.E., Loeb A., Narayan R., 2009, ApJ, 701, 1357
Broderick A.E., et al., 2015, ApJ, 805, 179
Chael A., Narayan R., Johnson M.D., 2018a, arXiv e-prints
Chael A., et al., 2018b, MNRAS, 478, 5209
Coppi P.S., Blandford R.D., 1990, MNRAS, 245, 453
Falcke H., Markoff S., 2000, A&A, 362, 113
Ho L.C., 2002, ApJ, 564, 120
Ichimaru S., 1977, ApJ, 214, 840
Li Y.P., Yuan F., Xie F.G., 2016, ApJ, 830, 78
Manmoto T., Mineshige S., Kusunose M., 1997, ApJ, 489, 791
Meyer L., et al., 2012, Science, 338, 84
Nagar N.M., et al., 2000, ApJ, 542, 186
Narayan R., Yi I., 1994, ApJL, 428, L13
Narayan R., Yi I., 1995, ApJ, 444, 231
Nemmen R.S., Storchi-Bergmann T., Eracleous M., 2014, MNRAS, 438, 2804
Özel F., Psaltis D., Narayan R., 2000, ApJ, 541, 234
Prieto M.A., et al., 2016, MNRAS, 457, 3801
Rees M.J., et al., 1982, Nature, 295, 17
Rybicki G.B., Lightman A.P., 1979, *Radiative processes in astrophysics*
Shapiro S.L., Lightman A.P., Eardley D.M., 1976, ApJ, 204, 187
Tchekhovskoy A., Narayan R., McKinney J.C., 2011, MNRAS, 418, L79
Xie F.G., Yuan F., 2012, MNRAS, 427, 1580
Yuan F., Cui W., Narayan R., 2005, ApJ, 620, 905
Yuan F., Narayan R., 2014, ARA&A, 52, 529

Weak detonations from baryonic matter to strange quark matter

S. Morales[1] & D. Sevilla[1]

[1] *Grupo de Astrofísica, Facultad de Ciencias Exactas, Ingeniería y Agrimensura, UNR, Argentina*

Contact / dsevilla@fceia.unr.edu.ar

Resumen / Consideramos el escenario en el cual materia de bariones se transforma en materia extraña en el núcleo de una estrella de neutrones. Suponemos que la combustión ocurre en una zona estrecha que puede ser modelada como una discontinuidad matemática. Prestamos especial atención al mecanismo de combustión conocido como detonación, y mostramos que para altas presiones pueden ocurrir detonaciones débiles. Este resultado permite calcular el estado del fluido detrás del frente de combustión en función de la densidad delante del frente para rangos de densidad más amplios que en trabajos previos.

Abstract / We consider the scenario in which baryonic matter burns to strange quark matter in the core of a neutron star. We suppose that the combustion occurs in a narrow zone which can be modeled as a mathematical discontinuity. We pay special attention to the combustion mechanism of detonation, and we show that for high pressures weak detonations can be reached. This result allows to calculate the state of the fluid after the combustion front as a function of the density before the combustion front for wider density ranges that in previous works.

Keywords / stars: neutron — dense matter — shock waves — supernovae: general

1. Introduction

It has been proposed that strange quark matter is the ground state of the matter (Witten, 1984), but this state can only be reached under extreme conditions that can be found in some supernovae or neutron stars cores. The phase transition from baryonic matter to strange quark matter in a neutron star must release about 10^{47} J of energy, so it could be the engine of some high luminosity astrophysical phenomena (Ouyed et al., 2002). But the reaction rate is unknown—proposals go from the diffusive regime to detonation—, as it depends on physical parameters of uncertain values.

There are many proposals of equations of state (EOSs) for baryon and strange quark matter. In this work we consider the polytropic EOS BJ1 by Bethe & Johnson (1974) for the baryonic matter

$$\begin{cases} P = K\, n_B^{\gamma} \\ E = m_B\, n_B + \dfrac{P}{\gamma - 1} \end{cases} \tag{1}$$

being P the pressure, E the energy density, n_B the baryon density, m_B the baryon rest energy, $\gamma = 2.54$ and $K = 364$ if $[P] = [E] = \mathrm{MeV\,fm^{-3}}$ and $[n_B] = \mathrm{fm^{-3}}$.

On the other hand, we consider the MIT Bag Model for mass-less non-interacting particles for the strange quark matter (Cleymans et al., 1986):

$$\begin{cases} P = \dfrac{1}{c^3\,\hbar^3}\left(\dfrac{19}{36}\,\pi^2\,T^4 + \dfrac{3}{2}\,T^2\,\mu^2 + \dfrac{3}{4\pi^2}\,\mu^4\right) - B \\ E = 3\,P + 4\,B \\ n_B = \dfrac{1}{c^3\,\hbar^3}\left(T^2\,\mu + \dfrac{1}{\pi^2}\,\mu^3\right) \end{cases} \tag{2}$$

being T the temperature and μ the chemical potential, both in energy units. We use $B = 60\,\mathrm{MeV\,fm^{-3}}$ as the bag constant (Farhi & Jaffe, 1984). These two EOSs, besides being simple, are supported by the M-R relation observed for neutron stars (Steiner et al., 2013). Later we will see that the results obtained by using more sophisticated EOSs should be qualitatively the same.

The energy per baryon is always lower for strange quark matter described within the MIT Bag Model (Haensel et al., 2007), but only a fraction of the baryonic matter of a neutron star can be transformed to strange quark matter (Benvenuto et al., 1989). That depends on the progenitor star structure and the burning dynamics. So, the result of the star transformation is an hybrid star with a strange quark matter core enveloped by baryonic matter.

Currently there are no conclusive results regarding the duration of the transformation (Haensel et al., 2007). If the combustion occurs in the diffusive regime, a timescale of about 10 min is expected, but under certain conditions it could be as low as 0.1 s. On the other hand, some authors argue that the instabilities in the combustion front must speed it up. If deflagration to detonation transition does not occur, the timescale of the conversion is about 10 ms. But if the detonation scenario takes place, the timescale results ∼0.1 ms.

In any case, if the combustion is fast enough, it must occur in a narrow zone that can be mathematically approximated by a discontinuity. The theory of these reactions, developed by Ya. B. Zeldovich in 1940 (Landau & Lifshitz, 1959), can be extended to the relativistic case considering the Taub adiabat (Benvenuto et al., 1989).

2. The detonation mechanism

A discontinuity in a relativistic fluid must satisfy the Taub equation (Thorne, 1973)

$$E_2\,X_2 - E_1\,X_1 = P_2\,X_1 - P_1\,X_2 \tag{3}$$

where $X_i = \mu_i\,V_i$ is called *generalized volume* (Lugones et al., 1994), being $V_i = n_{Bi}^{-1}$. We use subscript 1 for the fluid immediately before the discontinuity, and subscript 2 for the fluid immediately after it. From Eq. 3 and an initial state (X_1, P_1)—which corresponds to baryon matter—and considering no phase transition—i.e. the matter after the front is also described by EOS 1—a function $P_2(X_2)$ known as shock adiabat results defined. But when the shock triggers a phase transition subscript 2 corresponds to strange quark matter. The function $P_2(X_2)$ obtained from Eq. 3, EOS 2 and the initial state (X_1, P_1) is called detonation adiabat.

In the detonation process, the unburnt fluid at state 1 is heated up by the shock wave to state 1' on the shock adiabat. Then, the fluid evolves from state 1' to state 2 on the detonation adiabat due to the combustion. Fig. 1 shows the path follows by the detonation process for an initial state of $n_B = 0.35\,\mathrm{fm}^{-3}$. The evolution from state 1' to state 2 follows the segment that connects 1' with 1, up to state 2 on the detonation adiabat is reached. There is a special final state for which the segment that joins state 1 and 2 is tangent to the detonation adiabat. This is the *Chapman-Jouguet* point, and it is the final state of self-sustained detonations, which are the only ones that occur in nature. The detonation process shown in Fig. 1 has the Chapman-Jouguet point as final state. The mechanism of deflagrations is different, but the final state must also lie on the detonation curve. For detonations $X_2 < X_1$ and $P_2 > P_1$, and for deflagrations $X_2 > X_1$ and $P_2 < P_1$. Deflagrations also have Chapman-Jouguet points which are not usually the final state, but they represent the strongest possible deflagrations with the highest velocity of propagation. On the other hand, the weakest deflagrations are these in which the reaction rate is as low as possible. We call *slow combustion limit* to the deflagrations with ΔP and velocity of propagation zero, which of course cannot be reached if the combustion occurs in a narrow zone.

But there is a peculiarity of the detonations of baryonic matter to strange quark matter: for some initial conditions, the shock and the detonation adiabats cross each other between the corresponding Chapman-Jouguet point and the initial state. In these situations the final state cannot be the Chapman-Jouguet point, but it must be the crossing point itself. Fig. 2 shows the case for $n_B = 0.75\,\mathrm{fm}^{-3}$. This occurs because the adiabatic index of strange quark matter varies significantly with the baryon density from infinity at $n_B \sim 0.287\,\mathrm{fm}^{-3}$ to 4/3 at high density, while the adiabatic index of baryonic matter does not—it is constant in this case—. In particular, this allows the final state could reach the weak detonations branch of the detonation adiabat, which is usually forbidden. The goal of this paper is to highlight this issue which is not discussed in previous works on detonations of baryonic matter to strange quark matter.

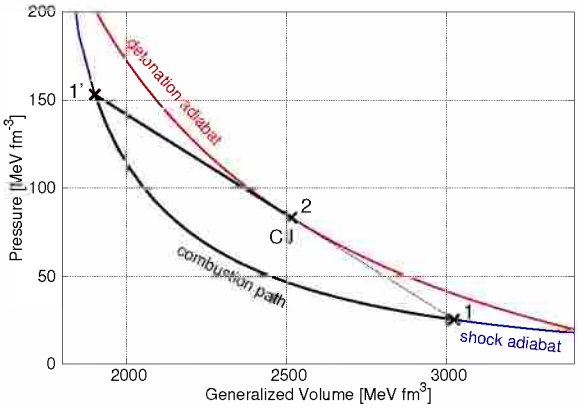

Figure 1: Shock adiabat, detonation adiabat and the path from initial state 1 to final state 2 for $n_B = 0.35\,\mathrm{fm}^{-3}$. In this case the final state is the Chapman-Jouguet point.

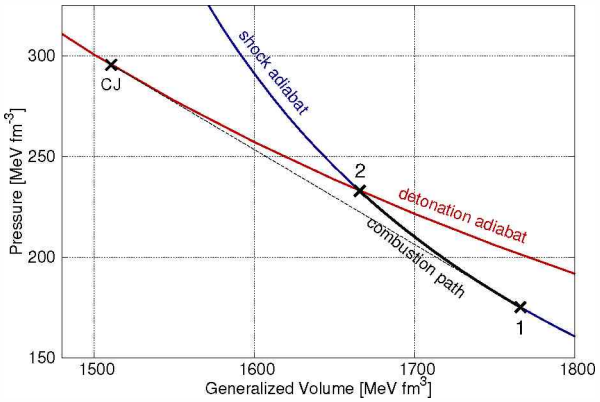

Figure 2: Shock adiabat, detonation adiabat and the path from initial state 1 to final state 2 for $n_B = 0.75\,\mathrm{fm}^{-3}$. Here the final state is the crossing point between the adiabats.

3. Results and discussion

Fig. 3 shows the numerical results for the pressure of the strange quark matter after the combustion front as function of the baryon density of the baryonic matter before it, for detonations and deflagrations. As detonations in nature have well defined final states that depend only on initial states, they are represented by a single curve. On the other hand, the final state of deflagrations depends on several physical factors that determine the rate of the reaction, but it must be limited by two curves: the slow combustion limit curve—the weakest case—, and a the curve corresponding to the strongest possible deflagrations.

We can see that the three curves are defined into an interval of baryon densities between 0.297 and $0.839\,\mathrm{fm}^{-3}$. Outside this interval the reaction is not longer exothermic, so it results inhibited (Lugones et al., 1994). We can see that the curves for detonations and the strongest deflagrations have one breaking point each one: at $n_B = 0.563\,\mathrm{fm}^{-3}$ for the former and $n_B = 0.523\,\mathrm{fm}^{-3}$ for the later. For detonations to the left of the breaking point the final states are obtained from the Chapman-Jouguet points, and for detonations

to the right of the breaking point, from the crossing points between the shock and detonation adiabats. In this particular case, the branch of the curve corresponding to the crossing points has constant a pressure of $233\,\mathrm{MeV\,fm^{-3}}$. The curve for the strongest deflagrations is similar, but now the branch corresponding to the crossing points is to the left, and the branch corresponding to the Chapman-Jouguet points is to the right. The branch of the curve corresponding to the crossing points has a constant pressure of $16.7\,\mathrm{MeV\,fm^{-3}}$.

Fig. 4 shows the results for the velocity of the front for detonations, and the fastest deflagrations—the strongest ones—as function of the baryon density before it. As we stated before, the lower limit of propagation velocity for deflagrations is zero. Fig. 4 also shows the sound velocity in baryonic matter and the velocity of the strange quark matter with respect to the front, for comparison. As we can see, detonations are always supersonic and deflagrations are always subsonic.

Now the question is what happens if different—and more realistic—EOSs are considered. If the baryonic matter EOS is too stiff, the phase transition is not longer exothermic and it results inhibited (Lugones et al., 1994). But if the phase transition results exothermic only into a pressure interval, there are arguments to support that the behaviour shown here should happen. On one hand, it has been suggested that all the EOSs for strange quark matter in compact stars are well fitted by a generic linear form on only two parameters (Haensel et al., 2007). So, the dependence of the adiabatic index on density is qualitatively the same for all of them, particularly, it results infinity at $n_B \sim 0.3\,\mathrm{fm^{-3}}$. On the other hand, the adiabatic index of most accepted realistic EOSs for npeμ matter actually depends on pressure, but its value remains between 2 and 4 for baryon densities between 0.1 and $1.5\,\mathrm{fm^{-3}}$ (Haensel et al., 2007). Therefore, it is expected that for several different choices of EOSs the corresponding shock and detonation adiabats cross each other inside the baryon density interval at which the phase transition is possible. So, the behaviour shown in this paper—in which weak detonations result possible for phase transitions from baryonic matter to strange quark matter—should be typical.

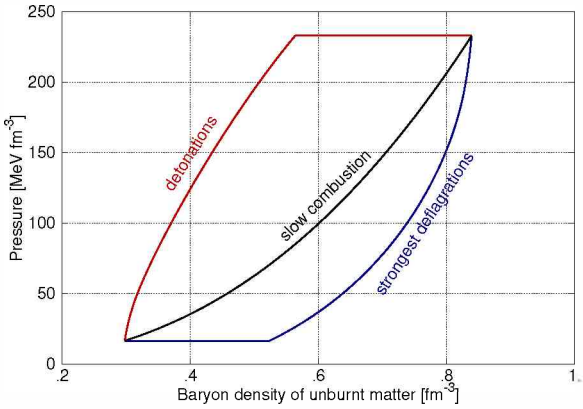

Figure 3: Pressure of the strange quark matter after the combustion front for detonations and deflagrations, as function of the baryon density of the baryonic matter before it. While the pressure for detonations is represented by a single curve, deflagrations can have pressures into an interval limited by the strongest deflagrations and the slow combustion curves.

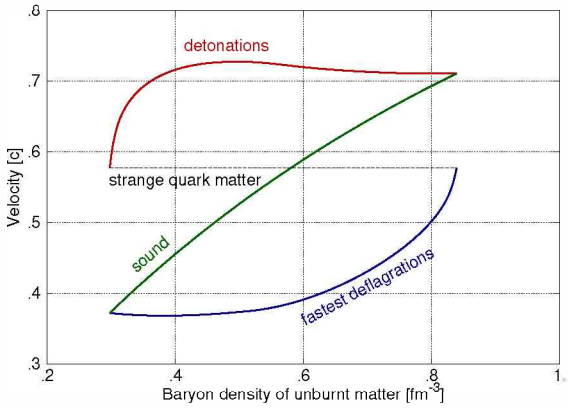

Figure 4: Velocity of the combustion front for detonations and the fastest deflagrations, and velocity of sound in baryonic matter. The velocity of the slowest deflagrations is zero. The first two curves also represent the velocity of the incoming baryonic matter with respect to the combustion front. The velocity of the outcoming strange quark matter is shown by the dashed segment.

Conclusions

We show that for typical equations of state for baryonic matter and strange quark matter, the shock and the detonation adiabats cross each other before the Chapman-Jouguet points on the detonations adiabat for some initial conditions. This fact forbids that the corresponding Chapman-Jouguet point can be reached in the combustion process, so it can no longer be the final state, which is now the crossing point itself. As a consequence, the final states for detonations at high pressure lie on the branch of weak detonations. On the other hand, the same occurs to the strongest limit for deflagrations at low pressure, which now is weaker than the Chapman-Jouguet condition. We conclude that this behaviour must be typical for phase transitions from baryonic matter to strange quark matter that are modeled as mathematical discontinuities.

References

Benvenuto O.G., Horvath J.E., Vucetich H., 1989, International Journal of Modern Physics A, 4, 257
Bethe H.A., Johnson M.B., 1974, Nucl. Phys. A, 230, 1
Cleymans J., Gavai R.V., Suhonen E., 1986, PhR, 130, 217
Farhi E., Jaffe R.L., 1984, PhRvD, 30, 2379
Haensel P., Potekhin A.Y., Yakovlev D.G. (Eds.), 2007, *Neutron Stars 1 : Equation of State and Structure*, *Astrophysics and Space Science Library*, vol. 326
Landau L., Lifshitz E., 1959, *Course of theoretical physics. vol. 6: Fluid mechanics*, London
Lugones G., Benvenuto O.G., Vucetich H., 1994, PhRvD, 50, 6100
Ouyed R., Dey J., Dey M., 2002, A&A, 390, L39
Steiner A.W., Lattimer J.M., Brown E.F., 2013, ApJL, 765, L5
Thorne K.S., 1973, ApJ, 179, 897
Witten E., 1984, PhRvD, 30, 272

Radiation from hot accretion flows onto black holes

E.M. Gutiérrez[1], F.L. Vieyro[1] & G.E. Romero[1,2]

[1] *Instituto Argentino de Radioastronomía, CONICET-CICPBA, Argentina*
[2] *Facultad de Ciencias Astronómicas y Geofísicas, UNLP, Argentina*

Contact / egutierrezposse@gmail.com

Resumen / Los flujos de acreción calientes que tienen lugar alrededor de agujeros negros consisten en plasmas ópticamente delgados, en donde los electrones pueden alcanzar temperaturas de hasta 10^{10} K y producir radiación por sincrotrón, bremsstrahlung y Compton inverso, y los iones pueden alcanzar temperaturas de hasta 10^{12} K y producir emisión gamma a través de interacciones protón-protón. En este trabajo, consideramos un modelo particular de un flujo de acreción caliente y estimamos las distribuciones espectrales de energía que resultan de la emisión de ambas especies de partículas.

Abstract / The hot accretion flows upon black holes are usually optically thin two-temperature plasmas in which electrons can achieve temperatures up to 10^{10} K, producing radiation via synchrotron, bremsstrahlung and inverse Compton, and the ions can reach temperatures up to 10^{12} K. The hottest ions might produce gamma emission through proton-proton interactions. In this work, we considered a particular model of a hot accretion flow and estimate the spectral energy distributions produced by both species of particles.

Keywords / stars: black holes — accretion, accretion disks — radiation mechanisms: thermal

1. Introduction

Black hole accretion is a fundamental physical process in the universe and it is the primary power source behind Active Galactic Nuclei (AGNs), Black Hole Binaries (BHBs) and possibly Gamma Ray Bursts (GRBs). This process occurs via an accretion disk, or more generally an accretion flow, where fluid particles slowly lose energy and angular momentum and move inwards to the black hole. Accretion flows can be classified into two broad classes: cold and hot. Cold accretion flows, with temperatures in the range $10^4 - 10^7$ K, are radiatively efficient, optically thick flows, and hence they typically emit as a multi-temperature blackbody (Shakura & Sunyaev, 1973; Page & Thorne, 1974). Cold disk models are capable to explain the spectrum of quasars and BHBs in the high-soft state but they fail under other circumstances; for example they cannot explain the spectrum of BHBs in the low-hard state. This gave rise to a family of different accretion models characterized by the presence of a much hotter plasma (Bisnovatyi-Kogan & Blinnikov, 1977). These hot accretion flows are optically thin and the energy exchange between ions and electrons is inefficient yielding that these particle species have different equilibrium temperatures. In the central regions of these flows temperatures might be as high as 10^{9-10} K for electrons, and up to 10^{12} K for ions (Narayan & Yi, 1995). One of the most useful models of hot accretion flows are those of the family of Advection Dominated Accretion Flows (ADAFs) that, being radiatively inefficient, are dominated by advection onto the black hole (Narayan & Yi, 1994, 1995). In these flows the radiation that is locally produced by synchrotron and free-free (thermal bremsstrahlung) emission escape with none or little interaction. However, in some scenarios comptonization of photons by the hottest electrons can significantly modify the spectrum. In this article we investigate the thermal emission produced by electrons and ions in a particular analytical model of a hot accretion flow.

The article is organized as follows: in Sec. 2. we present the main characteristics of the accretion model and we briefly discuss the relevant processes taken into account that produce thermal emission. In Sec. 3. we show some spectral energy distributions for different set of parameters.

2. Accretion flow model

We consider the accretion model applied to Sgr. A* by Straub et al. (2012), which is based on the formalism developed by Abramowicz et al. (1978). The flow consists in a perfect fluid torus orbiting a Kerr black hole. The equation for conservation of energy and momentum can be easily solved yielding an expression for the gravitational potential function:

$$W(r,\theta) = \frac{1}{2}\ln\left[-\frac{g_{tt}+2\Omega g_{t\phi}+g_{\phi\phi}}{(g_{tt}+\Omega g_{t\phi})^2}\right]. \quad (1)$$

Here, Ω is the angular velocity of the torus and $g_{\alpha\beta}$ are the metric components. The equipotential surface that defines the torus boundaries crosses itself in a cusp through which accretion onto the black hole may occur without the need of viscosity and the subsequent loss of angular momentum (it is a Roche lobe overflow). Assuming a two-temperature gas and a polytropic equation of state we can obtain analytical expressions for the temperatures of both species:

$$T_{\rm e} = \Big[(1-\omega)\mathcal{M}+\omega\mathcal{M}_\xi\Big]\mu_{\rm e}\frac{(1-\beta)m_{\rm u}P}{k_{\rm B}\epsilon}, \quad (2)$$

Table 1: Parameter values in Fig. 1.

Parameter	Value
M	4×10^8 M$_\odot$
a	$0.9M$
λ	0.7
$T_{\rm e,c}$	10^{10} K
ξ	10^{-2}
$\epsilon_{\rm c}$	10^{-16} g cm^{-3}
β	0.5
n	3/2

$$T_{\rm i} = \left[\frac{\mu_{\rm e}}{\mu_{\rm i}}\mathcal{M} + \omega(\mathcal{M} - \mathcal{M}_\xi)\right]\mu_{\rm i}\frac{(1-\beta)m_{\rm u}P}{k_{\rm B}\epsilon}, \qquad (3)$$

where ω is a dimensionless potential, β is the magnetic pressure to total pressure fraction, $\beta = P_{\rm mag}/P$, ϵ is the mass density, $\mu_{e,i}$ are the mean molecular weights for each species, $m_{\rm u}$ is the atomic mass unit, $k_{\rm B}$ is the Boltzmann constant, $\mathcal{M} = \mu_{\rm i}/(\mu_{\rm e} + \mu_{\rm i})$, and $\mathcal{M}_\xi = \mu_{\rm i}\xi/(\mu_{\rm e} + \mu_{\rm i}\xi)$.

In order to calculate the thermal spectrum of the torus, we divided it in cells distributed equispacedly in radii and polar angles (there is axial symmetry). We considered that electrons produce radiation via free-free emission by the interaction with both electrons and ions and, as the flow might be considerably magnetized, the hottest emit synchrotron radiation. We also take into account synchrotron self-absorption at low frequencies. The photons produced by these two local processes can be Compton-scattered to higher energies by the most energetic electrons. This process is non-local and to treat it we adopt the scheme developed by Narayan et al. (1997) for ADAFs, in which multiple comptonization is included and radiative transfer is solved iteratively. In addition, we take into account the gravitational redshift of the radiation.

On the other hand, ions can achieve temperatures up to 10^{12} K and hence those on the tail of the Maxwellian distribution have energies high enough to produce neutral pions through proton-proton interactions. These neutral pions decay with a lifetime of 10^{-16} s almost always into two gamma rays; therefore we consider this emission process.

3. Spectral energy distributions

The analytical model considered depends on a set of free parameters, namely the dimensionless specific angular momentum of the torus λ, the central electron temperature $T_{\rm e,c}$, the electron to ion temperature ratio at the torus center ξ, the central mass density $\epsilon_{\rm c}$, the magnetic pressure to total pressure fraction $\beta = P_{\rm mag}/P$, the polytropic index n, and the mass and specific spin of the black hole, M and a, respectively.

Fig. 1 shows the spectrum for the particular set of parameter values showed in Table 1. It can be seen that synchrotron emission is self-absorbed at low frequencies and there the spectrum follows the Rayleigh-Jeans law. The blue line is the inverse Compton spectrum, which

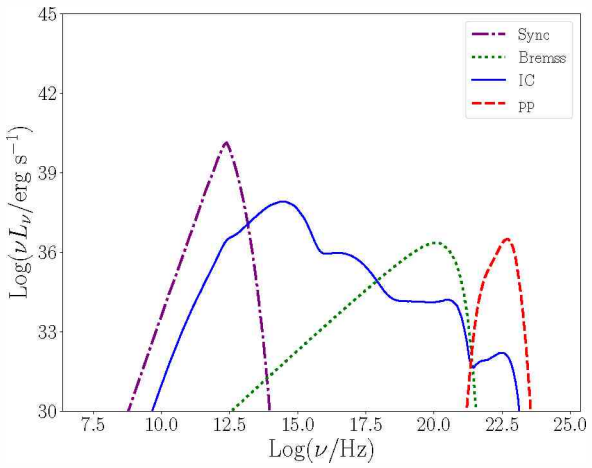

Figure 1: Thermal spectrum for $M = 4\times10^8$ M$_\odot$, $a = 0.9M$, $\lambda = 0.7$, $\epsilon_{\rm c} = 10^{-16}$ g cm^{-3}, $T_{\rm e,c} = 10^{10}$ K, $\xi = 0.2$

presents several well-defined peaks corresponding to the multiple scattering that a photon can suffer before leaving the torus. In this scenario ions at the center of the torus have a temperature of 10^{12} K and produce MeV photons.

Fig. 2 shows different spectra obtained by changing one parameter and keeping fixed the others to the values in Table 1. In the upper-left panel the central electron temperature is changed implying significant variations on the spectrum. In particular, comptonization tends to harden the spectrum as the temperature increases. Additionally, as the electron to ion temperature is keeping fixed, ions also have different temperatures and the pp emission is significantly modified. In the upper-right panel the torus specific angular momentum is changed. Though the effect is not very significant, the higher the value of λ, the larger the torus extension and hence the luminosity. In the lower-left panel the central mass density is changed. As it is expected, higher densities produce an enhancement of the whole spectrum but specially of the inverse Compton one. Finally, in the lower-right panel the magnetic pressure to total pressure fraction is changed and only the synchrotron spectrum and its correspondent Compton-scattered spectrum are modified.

This preliminary work will be extended by including non-thermal population of particles in order to have a robust model that can be applied to different kind of sources such as Seyfert galaxies or BHBs.

Acknowledgements: This work was supported by the Argentine Agency CONICET (PIP 2014-00338). E.M. Gutiérrez thanks the Local Organizing Committee for the grant received in order to attend the conference.

References

Abramowicz M., Jaroszynski M., Sikora M., 1978, A&A, 63, 221

Bisnovatyi-Kogan G., Blinnikov S., 1977, A&A, 59, 111

Narayan R., Barret D., McClintock J.E., 1997, The Astrophysical Journal, 482, 448

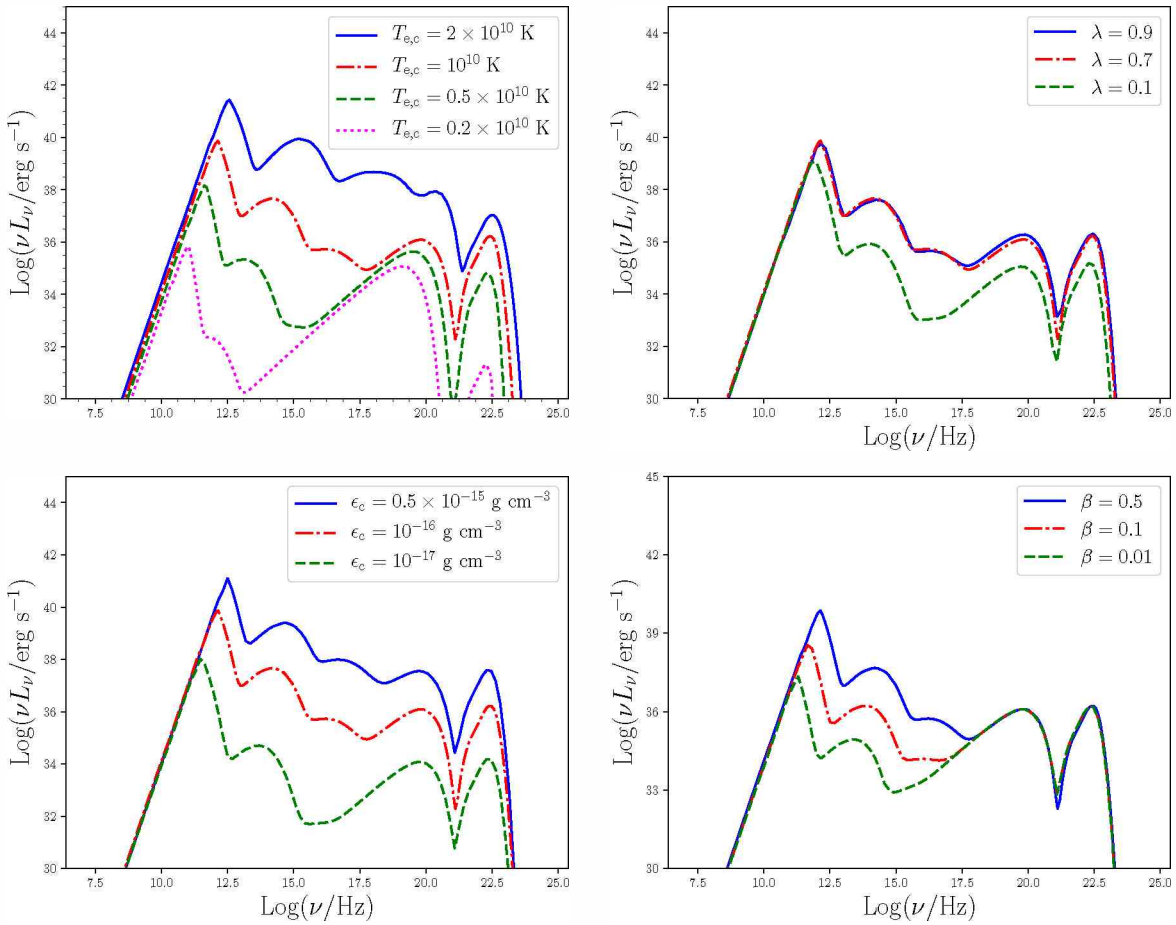

Figure 2: Different plots of the torus spectrum. The parameters are the same as in Figure 1 except those explicitly mentioned. *Upper-left panel:* the central electron temperature is changed. *Upper-right panel:* the dimensionless specific angular momentum parameter is changed. *Lower-left panel:* the central mass density is changed. *Lower-right panel:* the magnetic field pressure to total pressure fraction is changed.

Narayan R., Yi I., 1994, ApJL, 428, L13
Narayan R., Yi I., 1995, ApJ, 452, 710
Page D.N., Thorne K.S., 1974, The Astrophysical Journal, 191, 499
Shakura N.I., Sunyaev R.A., 1973, A&A, 24, 337
Straub O., et al., 2012, A&A, 543, A83

Neutrino production in Population III microquasars

A.M. Carulli[1] , M.M. Reynoso[1] , G.E. Romero[2,3]

[1] *Instituto de Investigaciones Físicas de Mar del Plata, CONICET–UNMdP, Argentina*
[2] *Instituto Argentino de Radioastronomía, CONICET–CICBA, Argentina*
[3] *Facultad de Ciencias Astronómicas y Geofísicas, UNLP, Argentina.*

Contact / aguscaru@hotmail.com

Resumen / *Contexto* Los microcuásares de población III (Pop III MQs) pudieron haber sido uno de los principales contribuyentes al proceso de reionización del medio intergaláctico. Se cree que las estrellas de población III fueron formadas a corrimientos al rojo altos, aproximadamente $z \sim 20 - 30$, lo cual impide la posibilidad de detectar rayos gamma de muy alta energía ($E > 100$ GeV); y por lo contrario, los neutrinos podrían ser detectados en la actualidad, debido a que solo sufren interacciones débiles.
Objetivo Desarrollamos un modelo para la producción de neutrinos en Pop III MQs y comparamos el flujo difuso obtenido con los datos disponibles del telescopio de neutrinos IceCube.
Método Resolvemos ecuaciones de transporte para obtener las distribuciones de partículas en diferentes zonas consideradas a lo largo de los chorros. Calculamos las distribuciones de partículas primarias (esto es protones y electrones) en cada zona, las cuáles se enfrían debido a procesos radiativos y a la interacción con otras partículas blanco, para dar una distribución de partículas secundarias (esto es muones y piones). Luego, obtenemos las distribuciones de muones y piones y calculamos sus decaimientos, que nos permiten calcular la producción de neutrinos. Finalmente, integramos con respecto al corrimiento al rojo z y con respecto al ángulo con la visual, para obtener el flujo difuso de neutrinos que podría ser observado desde la Tierra.

Abstract / *Context* Population III microquasars (Pop III MQs) may have been one of the main contributors to the reionization of the intergalactic medium. It is thought that PopIII stars were formed at redshifts $z \sim 20 - 30$, which prevents the possibility of detecting gamma rays of very high energy ($E > 100$ GeV). Conversely, it would be possible to detect neutrinos at the present, since they interact with matter only via the weak interaction.
Aims We develop a model that accounts for neutrino production in Pop III MQs and compare the diffuse neutrino fluxes obtained with the available data from IceCube neutrino telescope.
Method We solve transport equations to obtain the particle distributions at the different zones considered along the jets. We compute the distributions of primary particles (i.e. protons and electrons) in each zone, which cool down due to radiative processes and also interact with other particle targets, to give a distribution of secondary particles (i.e. muons and pions). We then obtain the muon and pion distributions and compute their decays, from which we obtain a neutrino output. Finally, we integrate with respect to the redshift z and over the line-of-sight angle in order to obtain the diffuse neutrino flux that may be observed from the Earth.

Keywords / neutrinos — X-rays: binaries — stars: Population III — dark ages, reionization, first stars

1. Introduction

At the period of recombination (0.37 Myr after the Big Bang), the plasma of electrons and protons went through a phase transition that coupled them together for the first time to form atomic hydrogen. This was followed by a period commonly named as "Dark Ages", during which no structures capable of producing radiation had yet been formed. This period ended $\sim$ 1 Gyr after the Big Bang due to the ultraviolet (UV) radiation produced by the first formed stars, and the "Epoch of Reionization" began. However, it is thought that in order to reionize the intergalactic medium (IGM), the UV radiation produced by massive stars was not enough, since the ionizing UV photons must have escaped from the primordial galaxies at higher rates than the observed. Astrophysical sources like active galactic nuclei, cosmic rays, and X-ray binaries, have been proposed as possible contributors to the reionization of the IGM. In particular, it has been suggested that Pop III microquasars (MQ) could have contributed enough radiation as required to ionize the IGM. In the present work we aim to obtain the possible neutrino emission from these systems in order to compare with current data from IceCube. The model adopted here is based in previous works on microquasar jets and their interaction with the external medium (Bordas et al., 2009; Bosch-Ramon et al., 2011; Romero & Sotomayor Checa, 2018), which allows the possibility of taking into account different zones or regions along the jet where particle acceleration and emission can take place.

2. Outline of the model

The microquasar jets are modeled considering different emission zones along them, where particles are being accelerated by some mechanism. We account for all the main interactions of particles by solving a particular transport equation corresponding to each zone, in order to finally compute a total neutrino output.

The first zone considered (base zone) is located at the inner jet, which is launched at a distance $z_0 = 100R_g$ from the central black hole (BH). The magnetic field along the jet is supposed to vary as $B = B_0(z_0/z)^{1.5}$, where z is the distance to the BH, and B_0 is the magnetic field at z_0. This implies that the magnetic energy density decreases faster than the kinetic one. We place the position of the base zone at $z_{\rm acc}$ where the kinetic energy density is in sub-partition with the magnetic energy density by a fraction q_m, i.e. $\rho_m = q_m\rho_k$, with $\rho_k = L_k/[(\Gamma-1)\Gamma\pi R_{\rm jet}^2 v_{jet}]$. Here, $R_{\rm jet}$ is the radius of the jet and v_{jet} is its bulk velocity. Primary particles (protons and electrons) are injected as power laws in the energy. The injection as a function of the energy for the particle type i (that stands for protons or electrons) is $Q_i(E_i) = K_i E_i^{-\alpha}\exp(-E_i/E_{{\rm max},i})$, where K_i is a normalizing constant that is fixed with the luminosities L_i. The maximum energies $E_{{\rm max},i}$ are found by the balance of the cooling rates with an acceleration rate given by $t_{\rm acc}^{-1} = \eta cB/E$, where η is the acceleration efficiency. The transport equation for the primary particles distributions at the base zone $N_{i,{\rm b}}$ of type $i = \{e, p\}$, corresponds to a typical one-zone approximation:

$$-\frac{d(b_i N_{i,{\rm b}})}{dE_i} + \frac{N_{i,{\rm b}}}{T_{\rm esc}} = Q_i \tag{1}$$

where $b_i \equiv dE/dt = Et_{\rm cool}^{-1}$ accounts for the continuous energy losses of particles due to the cooling processes: synchrotron, Inverse Compton (IC), adiabatic expansion, pp and $p\gamma$ interactions. The photon target for IC and $p\gamma$ interactions is considered to be given by the synchrotron emission of the electrons. The thickness of the zone is $\Delta z \sim R_{\rm jet}$, and the escape timescale in the comoving jet frame is $T_{\rm esc} \simeq \Gamma\Delta z/c$, where Γ is the Lorentz factor of the jet. Pions are generated via $p\gamma$ and pp interactions, and the corresponding injection Q_π can be computed as in (Reynoso & Romero, 2009), using approximations for the SOPHIA code for $p\gamma$ interactions (Atoyan & Dermer, 2003), and using fits based on the SIBYLL code in the case of pp interactions (Kelner et al., 2006). The pion distribution is obtained as a solution of

$$-\frac{d(b_i N_{i,{\rm b}})}{dE_i} + \frac{N_{i,{\rm b}}}{T_{\rm esc}} + \frac{N_{i,{\rm b}}}{T_{\rm dec}} = Q_i \tag{2}$$

where $T_{\rm dec}$ is the typical decay time. Muons, in turn, are produced by the decay of pions, and the corresponding injection Q_μ is obtained following the above references. The muon distribution N_μ is then found solving Eq. 2 for the base zone.

For the typical values of jet power and magnetic field adopted in the present context, we found that for electrons injected at the base zone, cooling dominates over escape. Hence, all the power injected in electrons at this zone, is essentially radiated there. This is not the case for protons, which undergo a not so efficient cooling as compared to the escape. This is the main reason why it becomes necessary to consider the effect of the protons that were originally injected at the base zone but did not get to efficiently cool there, and rather escaped to continue their propagation along the jet. The second zone is then an extended conical one due to the lateral expansion of the jet as it propagates. We consider a transport equation with a convection term, which expressed in spherical coordinates reads (Zdziarski et al., 2014):

$$\frac{\Gamma v_{\rm jet}}{r^2}\frac{\partial(r^2 N_{i,{\rm c}})}{\partial r} - \frac{\partial(b_i N_{i,{\rm c}})}{\partial E} = Q_{i,{\rm c}}, \tag{3}$$

where the injection term is $Q_{i,{\rm c}} = N_{i,{\rm b}}/T_{\rm esc}$. Pions are produced by pp interactions in this zone, and after computing the injection along the conical jet, we solve Eq. 3 including also a decay term to obtain the pion distribution. A similar procedure is carried out to obtain the muon distribution in this zone.

The third zone considered is a reconfinement one, placed at a position $z_{\rm rec}$, where expansion ends due to the external pressure of the IGM (Bordas et al., 2009). This forces the cone shaped jet to become a cylinder. Since we found that a significant fraction of the relativistic protons can reach the reconfinement point by convection, we added an extra term of acceleration to Eq. 1, $b = \eta Bc$, and applied it in this reacceleration zone. The magnetic field in this and in the rest of the terminal regions of the jet were considered to represent a magnetic energy equal to 10 % of the kinetic energy density. The thickness of this zone is taken to be the jet radius at $z_{\rm rec}$, and the escaping particles are injected in a fourth zone which corresponds to the rest of the reconfined jet and extends down to the the region where the jet is finally stopped.

Two other zones are present at the terminal jet, one due to the forward shock produced by the interaction with the IGM, and the reciprocal reverse shock. These are called bow shock and cocoon, respectively and are placed at a distance $l_{\rm b}$ from the BH. This value, along with $z_{\rm rec}$ are computed following Bordas et al. (2009), and they depend on the IGM density, the jet power, and the MQ age $t_{\rm MQ}$.

Table 1: Parameters of the model

Symbol	Description	Value
$M_{\rm bh}$	black hole mass [$M_\odot$]	30
Γ	jet Lorentz factor	1.67
L_k	jet kinetic power [erg s^{-1}]	10^{41}
ξ	jet half-opening angle [°]	5.7
$q_{\rm rel}$	ratio $(L_p + L_e)/L_k$	~ 0.07
a	ratio L_p/L_e	1
q_m	ratio ρ_m/ρ_k at $z_{\rm acc}$	0.001
B	magnetic field at $z_{\rm acc}$ [G]	4.8×10^3
α	index for injection $\propto E^{-\alpha}$	2
z_0	jet launching point [cm]	4.4×10^8
$z_{\rm acc}$	position of base zone [cm]	4.4×10^{11}
$z_{\rm rec}$	jet reconfinement point [cm]	1.2×10^{20}
$l_{\rm b}$	bow shock position [cm]	3.5×10^{20}
$t_{\rm MQ}$	maximum MQ age [yr]	10×10^5

3. Results

Once we have the pion and muon distributions for each zone, we obtain the different neutrino emissivities following (Lipari et al., 2007; Reynoso & Romero, 2009). The contributions are: direct pion decays to $\nu_\mu + \bar{\nu}_\mu$

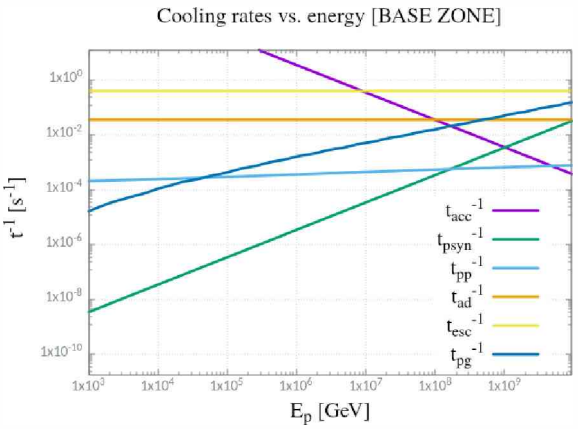

Figure 1: Acceleration and cooling rates for protons at $z_{\rm acc}$.

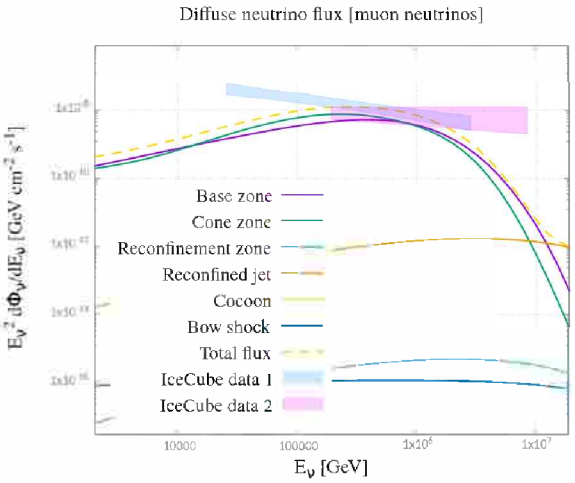

Figure 2: Diffuse flux of muon neutrinos for the different parameter set adopted.

($Q_{\pi\to\nu_\mu}$), muon decays to $\nu_\mu + \bar{\nu}_\mu$ ($Q_{\mu\to\nu_\mu}$), and muon decays to $\nu_e + \bar{\nu}_e$ ($Q_{\mu\to\nu_e}$).

These neutrino emissivities are in particular dependent on the viewing angle $i_{\rm j}$, and the total emission is found to depend on the length of the conical zone, which in turn depends on the MQ age $t_{\rm MQ}$ and the redshift through the IGM density. Taking this into account, and in order to estimate a total diffuse neutrino flux to be observed at present, we consider that the rate of formation of Pop III MQs as a function of the redshift is a fraction of the rate of formation of Pop III stars:

$$R_{\rm MQ} = f_{\rm BH} f_{\rm bin} R_{\rm PopIII}(z) [M_\odot {\rm Mpc}^{-3} {\rm yr}^{-1}] \quad (4)$$

We suppose $R_{\rm PopIII}(z)$ as given by de Souza et al. (2011), and we consider that the typical mass of Pop III stars is $\sim 50 M_\odot$, a fraction $f_{\rm BH} \simeq 0.9$ of them produced BHs, and a fraction $f_{\rm bin} \simeq 0.5$ were part of a close binary system.

At a given redshift z, in order to account for the effects of having a MQ population with jets pointing at different angles i_j with the line of sight, we perform an integration over such angle. We also integrate on the possible MQ ages up to $t_{\rm MQ} \simeq 10^5$ yr, to account for the fact that the neutrino emission is not constant along the MQ life. We obtain the total neutrino spectrum for MQs at a redshift z as:

$$\frac{dN'_\nu}{dE'_\nu} = 4\pi \int_0^{\Delta V} dV \int_0^{t_{MQ}} dt_{MQ} \int_0^{\frac{\pi}{2}} di_j \sin(i_j) \times \left[Q'_{\nu_\mu} P_{\nu_\mu\to\nu_\mu} + Q'_{\nu_e} P_{\nu_e\to\nu_\mu} \right]), \quad (5)$$

where the primed variables are evaluated in a reference system at rest with respect to the BH. $P_{\nu_\mu\to\nu_\mu} \simeq 0.369$ is the probability that the generated ν_μ or $\bar{\nu}_\mu$ keep the same flavor, and $P_{\nu_e\to\nu_\mu} \simeq 0.255$ is the probability that ν_e or $\bar{\nu}_e$ oscillate into ν_μ or $\bar{\nu}_\mu$. These probabilities are derived from the unitary mixing matrix $U_{\alpha j}$, which is determined by three mixing angles: $\theta_{12} \simeq 34^\circ$, $\theta_{13} \simeq 9^\circ$, and $\theta_{23} \simeq 45^\circ$ (Gonzalez-Garcia et al., 2012).

Using the neutrino spectrum, the diffuse flux originated in Pop III MQs is found as (Ando & Sato, 2004)

$$\frac{d\Phi_\nu(E_\nu)}{dE_\nu} = \frac{c}{4\pi H_0} \int_{z_{\rm min}}^{z_{\rm max}} \frac{dz\, R_{\rm MQ}(z)}{\sqrt{\Omega_\Lambda + \Omega_{\rm m}(1+z)^3}} \frac{dN'_\nu}{dE'_\nu} \quad (6)$$

We present some of the results obtained for a typical Pop III MQs with the parameters shown in Table 1. In Fig. 1, we show the acceleration and cooling rates for protons at the base zone, placed at a distance $z_{\rm acc}$ from the BH. In Fig. 2, we show the diffuse flux of muon neutrinos.

4. Conclusions

We have studied the consequences regarding neutrino emission of particle acceleration to relativistic energies in the jets of Pop III MQs. Using a set of parameters considered appropriate for such systems, we took into account the different zones in the jets where particle acceleration can be expected. Using transport equations, we found that the most relevant zones for neutrino production in the jets are the jet base and the conical jet zone. Finally, with the aid of an estimate for the rate of formation of Pop III stars, we obtained a rate of formation of Pop III MQs as a function of the redshift, and we integrated the diffuse neutino flux that can be at the level of the IceCube data.

References

Ando S., Sato K., 2004, New J. Phys., 6, 170
Atoyan A.M., Dermer C.D., 2003, ApJ, 586, 79
Bordas P., et al., 2009, A&A, 497, 325
Bosch-Ramon V., Perucho M., Bordas P., 2011, A&A, 528, A89
de Souza R.S., Yoshida N., Ioka K., 2011, A&A, 533, A32
Gonzalez-Garcia M.C., et al., 2012, J. High Energy Phys., 12, 123
Kelner S.R., Aharonian F.A., Bugayov V.V., 2006, PhRvD, D74, 034018
Lipari P., Lusignoli M., Meloni D., 2007, PhRvD, D75, 123005
Reynoso M.M., Romero G.E., 2009, A&A, 493, 1
Romero G.E., Sotomayor Checa P., 2018, Int. J. Mod. Phys. D, D27, 1844019
Zdziarski A.A., et al., 2014, MNRAS, 440, 2238

An update on the observational facilities at CASLEO

J.L. Aballay[1], S.A. Cellone[1,2], G.E.L. Fernández[1], M.A. Giménez[1], B.G. Giuliani-Ramos[1], J.L. Giuliani[1], R.A. Godoy[1], L.A. Mammana[1,2], H.R. Molina[1,3], P.G. Ostrov[1], P.F. Pereyra[1] & J.D. Pinto[1]

[1] *Complejo Astronómico El Leoncito, CONICET–UNLP–UNC–UNSJ, Argentina*
[2] *Facultad de Ciencias Astronómicas y Geofísicas, UNLP, Argentina*
[3] *Facultad de Ingeniería, UNSJ, Argentina*

Contact / direccion@casleo.gov.ar

Resumen / Presentamos una puesta al día sobre los diferentes telescopios e instrumentos disponibles en el Complejo Astronómico El Leoncito (CASLEO), Argentina. Todos los telescopios y sus instrumentos están completamente automatizados, y se operan rutinariamente en modo remoto. Los observadores pueden utilizar el telescopio Jorge Sahade (JS) de 2.15 m para imágenes, polarimetría CCD, y espectroscopía (tanto en baja como alta resolución), mientras que se encuentran en estudio nuevos desarrollos instrumentales. Actualmente, cerca del 70 % de los astrónomos optan por observar en forma remota. El telescopio Helen Sawyer Hogg (HSH) de 0.6 m también se encuentra disponible para observación remota, y puede usarse para obtener imágenes con un campo de 9.26×9.26 arcmin^2. También operan en el CASLEO dos telescopios menores, a través de sendos convenios con el Nicolaus Copernicus Astronomical Centre (NCAC, Polonia) y el Instituto de Astrofísica de Andalucía (IAA, España). La comunidad argentina tiene acceso al 20 % del tiempo disponible en cada uno de estos instrumentos (solo en modo servicio).

Abstract / We present an update on the different telescopes and instruments available at the Complejo Astronómico El Leoncito (CASLEO), Argentina. All the telescopes and their instruments are fully automated, and are routinely operated in remote mode. Observers can use the 2.15 m Jorge Sahade (JS) telescope for imaging, CCD polarimetry, and spectroscopy (both low and high resolution), future instrumental developments are also in progress. Presently, about 70 % of the astronomers opt to observe remotely. The Helen Sawyer Hogg (HSH) 0.6 m telescope is now also available for remote observing, and it can be used to obtain images with a 9.26×9.26 arcmin^2 field of view. Two smaller telescopes, operated under agreements with NCAC (Poland) and IAA (Spain), respectively, are also operational at CASLEO. The Argentine community has access to 20 % of the available time at each of these instruments (only in service mode).

Keywords / astronomical instrumentation, methods and techniques — telescopes

1. Introduction

The Complejo Astronómico El Leoncito (El Leoncito Astronomical Complex, CASLEO) is Argentina's national facility, operating astronomical telescopes. Access to CASLEO is open to the whole Argentine scientific community, as well as to foreign projects.

CASLEO began its observations in 1986, and it operates under an agreement between CONICET and the National Universities of La Plata, Córdoba, and San Juan, Argentina.

2. Optical telescopes and instruments

The main telescope at CASLEO is the 2.15 m Jorge Sahade reflector, belonging to the National University of La Plata (UNLP). It is an $f/15$ Ritchey-Chrétien system, which can be used either at its Cassegrain or Nasmyth foci. Its present instrumentation is:

- Imaging camera: Roper Scientific Versarray 2048B, 2048×2048 pix; its maximum field of view (FOV) using a focal reducer is 9 arcmin in diameter, with a scale of 0.45 arcsec pix^{-1} (see Fernández-Lajús et al., 2016, for further details).
- CasPol CCD polarimeter (presently used with a Tektronix 1024×1024 pix chip).
- Reosc spectrograph: for long-slit spectroscopy with low- and medium- ($R = 12600$) resolutions.
- EBaSim bench (fiber-fed) spectrograph: high-resolution ($R \approx 40000$) (Pintado & Adelman, 2003).

All instruments are equipped with liquid Nitrogen-cooled CCDs.

The JS telescope can be used either in visitor, remote, or service modes. A new TILT (telescope free time) mode has recently been implemented, in order to fill-in unused time slots.

Three smaller telescopes are operating at Cerro Burek ($\sim$ 7 km from the main CASLEO buildings); all of them are used solely for imaging. Table 1 lists the main characteristics of these telescopes, along with their respective cameras. Columns 1-8 show, respectively: name, primary mirror diameter, system focal ratio, owner institution, field of view with the currently installed camera, plate scale, available filter set(s), and the observing mode(s) currently offered. The HSH telescope is on loan from the University of Toronto, Canada —which has up to 25 % guaranteed observing time—, and is operated by CASLEO. The other two telescopes

are operated by their respective owners, and the Argentine community has access to 20 % of the available time on each of them.

3. Remote observing

CASLEO gives principal investigators (PIs) of successful proposals at the JS (2.15 m) and HSH (0.6 m) telescopes the possibility of observing in remote mode, accessing from anywhere with an Internet connection. The observer accesses a Linux server located at CASLEO headquarters in San Juan city, and uses a VNC client through a SSH tunnel to connect to the computers at the mountain: one controlling the telescope and its dome, and a second one controlling the instrument (and acquisition camera, in the case of spectrographs).

Figure 1 shows the graphic interface of TELESCO, the software that controls telescope and dome, at both telescopes. The observer has visual access to useful information (coordinates, Universal and sidereal times, pointing), and can use buttons to control both the telescope an dome (the latter can be set either in manual or automatic mode). Technical information is also displayed, allowing the staff to check critical parameters.

Each instrument has its dedicated control software, which is also remotely accessed by the observer. As an example, we show in Fig. 2 the control interface for the Roper imaging camera at the JS telescope. The observer is able to control all relevant parameters regarding data acquisition (integration time, filter, telescope focus, etc.) as well as visualization and a fast check of the displayed image.

The observer has also on-line access to meteorological and sky-quality information, which is updated every 12 min. A GUARD system has been set-up for the Burek telescopes, which automatically closes the domes in case of unfavorable meteorological conditions, and/or power or Internet failures.

The PI can download the data at the end of the observing night, while a quick on-line examination of the data is also possible.

Remote observing is the preferred option for about 70 % of the observers. Besides convenience for the observer, its advantages also include costs and time savings, and better flexibility for time scheduling. The technical staff is also able to check the telescope, dome, and instrument behaviors in real time, allowing for a rapid response in case of technical issues.

The smaller telescopes (Solaris-4 and ASH2) are also remotely operated by staff of their respective institutions (NCAC, IAA).

4. Solar and Geophysical instruments

The development of the Solar-Geophysical Mountain Laboratory (LHM) started in the mid '90s, through a collaboration between Brazilian institutions and CONICET (Argentina), with the installation at CASLEO of the Solar Sub-millimeter Telescope (SST). This instrument has a 1.5 m dish, and was used to observe the Sun at 212 and 405 GHz frequencies. The SST is presently operating remotely from Sao Paulo, Brasil.

The following instruments are also part of the LHM:

- SAVNET (ionospheric studies)
- EFM (atmospheric electric field measurements)
- CARPET (measurements of cosmic rays modulation)
- Solar Neutron Telescope (solar and atmospheric neutrons)
- Spectrometer for hard X-rays and γ-rays
- Meteorological station (installed in 2018).

Additional Geophysics and meteorological instruments are presently acquiring data at CASLEO, through different national and international collaborations:

- All-sky photometer (Boston Univ., USA)
- Fabri-Perot Interferometer (Boston Univ., USA)
- Airglow spectrometer (IAFE, Argentina)
- 1-D Seismograph (INPRES, Argentina)
- GPS (NASA)
- Flux Magnetometer (Instituto Geofísico del Perú - ICATE, Argentina)
- Burek peak meteorological station (CASLEO)
- Cloud sensor (IAA, Spain)
- Sky Quality Meter (SQM)
- Differential Image Motion Monitor (DIMM)
- TESS-W sky photometer (STARS4ALL).

These instruments are operated by their respective institutions; collected data may be available upon request.

5. Calls for proposals

Regular calls for proposals, to apply for observing time at the four optical telescopes, are open in September and March for semesters A (Feb/01-Jul/31) and B (Aug/01-Jan/31), respectively. Proposals for DD (Director's Discretionary) time can be submitted anytime during the current semester.

It is possible to ask for more than one instrument at the JS telescope, while different proposals should be submitted if more than one telescope is asked for.

On-line forms to ask for telescope time are available at CASLEO's web page (`https://www.casleo.conicet.gov.ar`). Detailed information on instruments, observing modes, visits to the observatory, etc., are found at the same site. For any other information, please contact CASLEO staff at direccion@casleo.gov.ar or turnos@casleo.gov.ar.

References

Fernández-Lajús E., et al., 2016, BAAA, 58, 190
Pintado O.I., Adelman S.J., 2003, A&A, 406, 987

Table 1: Three telescopes operating at CASLEO (Cerro Burek).

Name	D [m]	f-ratio	owner	FOV [arcmin^2]	plate scale [arcsec pix^{-1}]	filter set	obs. mode
HSH	0.6	f/15	Univ. Toronto	9.2 × 9.2	0.54	$UBVRI$ (Johnson-Cousins)	visitor – service
Solaris-4	0.5	f/15	NCAC	12.7 × 12.7	0.37	$UBVRI$ (Johnson-Cousins) $u'g'r'i'z'$ (Sloan)	service
ASH2	0.46	f/2.8	IAA	97.8 × 65.2	1.47	L (Luminance)	service

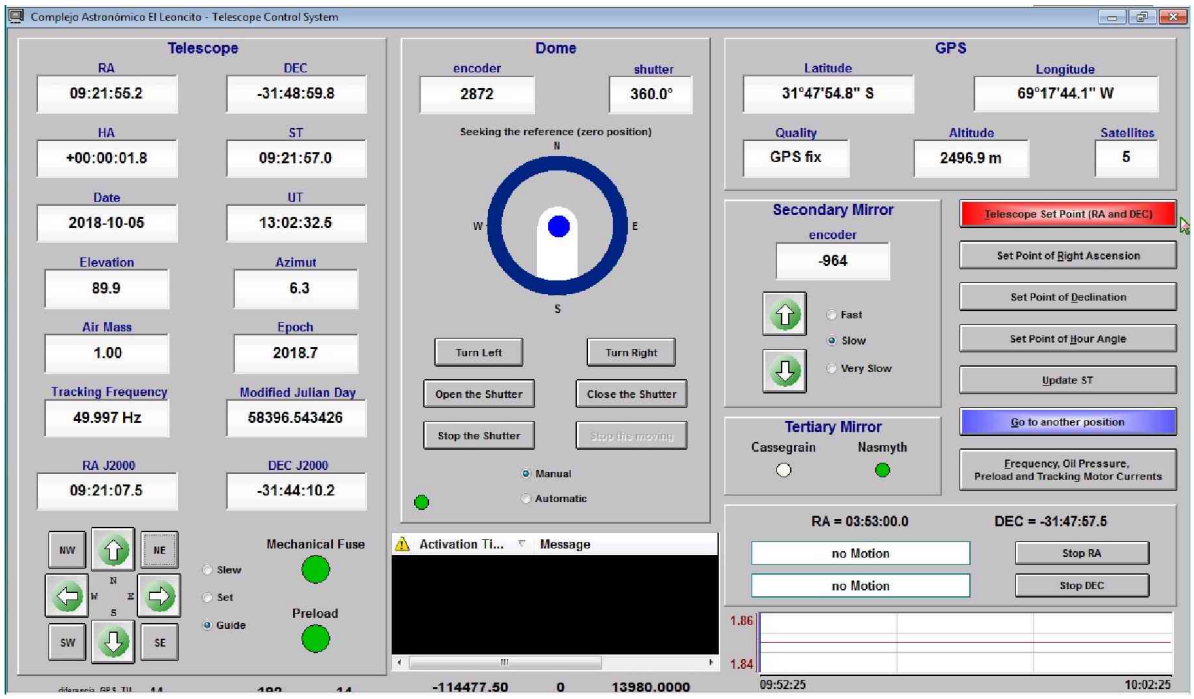

Figure 1: Graphic interface of TELESCO, the software used to control telescope and dome at the JS telescope. The same interface is used for the HSH telescope.

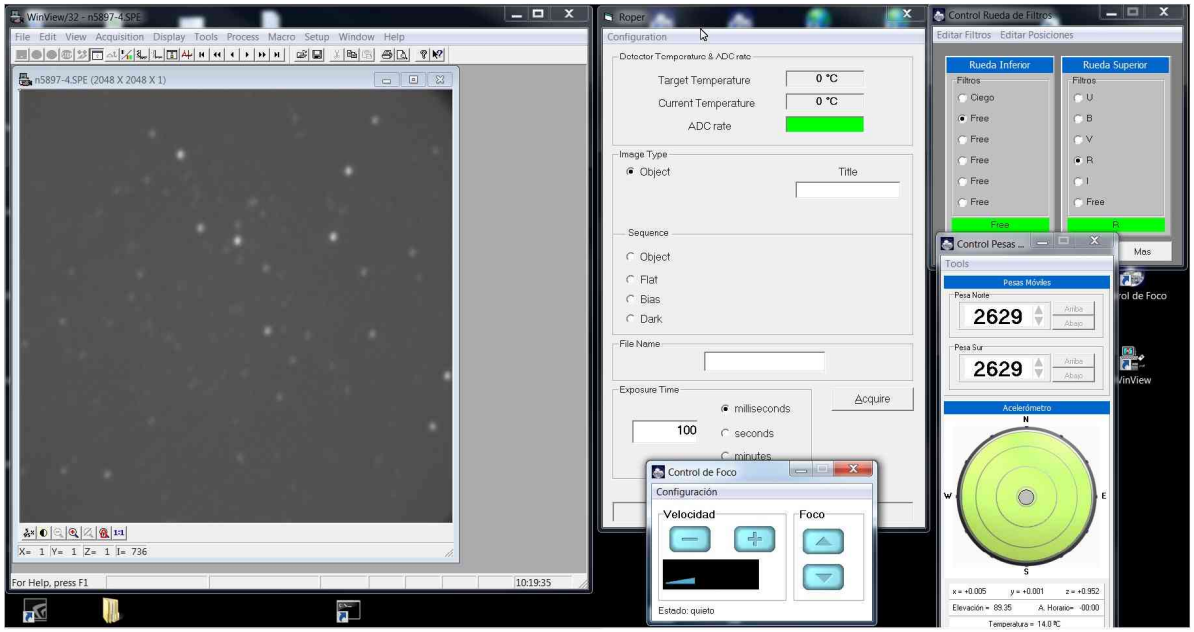

Figure 2: Graphic interface of the Roper imaging camera at the JS telescope. Similar interfaces are used for the HSH telescope and the remaining JS telescope instruments.

GMOS at Gemini: an update

G. Gimeno[1], V. Firpo[1] & H. Kim[1]

[1] *Gemini Observatory, La Serena, Chile*

Contact / ggimeno@gemini.edu

Resumen / Se presenta una descripción de las novedades acerca del espectrógrafo GMOS del observatorio Gemini, en particular sobre el desempeño y mejoras recientes, asi como de su impacto en la calidad de los datos cienttíficos. Se destacan el mantenimiento óptico de GMOS-S en 2018 y la actualización de los detectores en GMOS-N en 2017, entre otros

Abstract / An update is presented on the GMOS instruments at Gemini, in particular about performance, recent upgrades and their impact on the delivered science data. Highlights are the GMOS-S optical maintenance in 2018 and the GMOS-N detector upgrade in 2017, among others.

Keywords / instrumentation: spectrographs — instrumentation: detectors — techniques: image processing

1. Introduction

The Gemini Multi-Object Spectrographs (GMOS; Hook et al. (2004)) are the workhorse instruments at both Gemini Observatory 8 m telescopes. The GMOS instruments at both Gemini North and South have proved to be the most heavily requested Gemini instruments contributing to more than half of the observing queue. After a few years of continuous operation, Gemini has been planning and executing upgrades for both instruments, notably several detector upgrades in order to improve the on-sky efficiency (Gimeno et al., 2016; Roth et al., 2012). We present here an update on the GMOS instruments at Gemini, in particular about performance, recent upgrades and their impact on the delivered science data. Highlights are:

- GMOS-S optical maintenance in 2018
- GMOS-S/N new narrow band filters in 2018
- GMOS advanced reduction tips
- GMOS-N detector upgrade in 2017.

2. GMOS-S optical fix

The optical system of GMOS is comprised of a collimator and a camera, each of which has three groups of lenses. In turn, these lens groups are formed by three to four lenses. Within each lens group, the lenses are not in contact but separated by a 0.1 mm gap, filled with index-matching oil.

Over the years, air bubbles have developed when oil is lost from the lens interfaces. These can have a measurable impact on light transmission and image quality, in the affected parts of the field of view. In particular, the flat-fielding in imaging mode had become particularly difficult due to the presence of such air bubbles in the collimator lens groups. This has been a long-standing problem, affecting both GMOS-N and GMOS-S.

Fig. 1 (top) shows as an example an image of one lens group, in which the air bubbles are clearly visible.

While some of the lens interfaces can be refilled during regular instrument maintenance (this is the case for the lenses of the camera), other refill ports are inaccessible without major intervention. Such an intervention, in which the collimator was removed for the first time since the instrument was built, was performed on GMOS-S between July 17 and August 30 at the Cerro Pachon (CP) Instrument Lab. It involved not only refilling the lens interfaces but also modifying the oil piping, so that the refilling ports of the innermost lens groups can be accessed from the outside, thus eliminating the need of removing the collimator again in the event of potential future oil leaks.

Once installed again in the instrument, the realignment of the collimator was performed with the aid of two independent techniques, namely an alignment telescope and a laser beam propagated through the optical axis. Final alignment resulted better than 4 pixels as measured on the CCD. Fig. 1 (bottom) shows the collimator after the intervention. As a result of the optical fix, the flat-fielding performance of GMOS-S is restored.

3. New narrow-band filters

As part of the Gemini Instrument Upgrades Program (IUP, https://www.gemini.edu/sciops/future-instrumentation-amp-current-development/instrument-upgrade-projects), two pairs of narrow band filters were acquired for both GMOS-S and GMOS-N. These are OVI (683.5 nm) and OVIC (678 nm), for the project ORaman OVI narrow-band imaging with Gemini/GMOS.O (see R. Angeloni et al. in this bulletin).

Fig. 2 shows the transmission curves for the set of filters at GMOS-S, measured at the CP Instrument Lab. The performance on-sky was tested successfully in 2017. The filters acceptance tests have been completed, and the new capability will be offered to users in 2019.

Figure 1: Top: Bubbles in collimator lens group 3 before the intervention. Bottom: Collimator after the oil refill (as seen from lens group 1). Bubbles are gone.

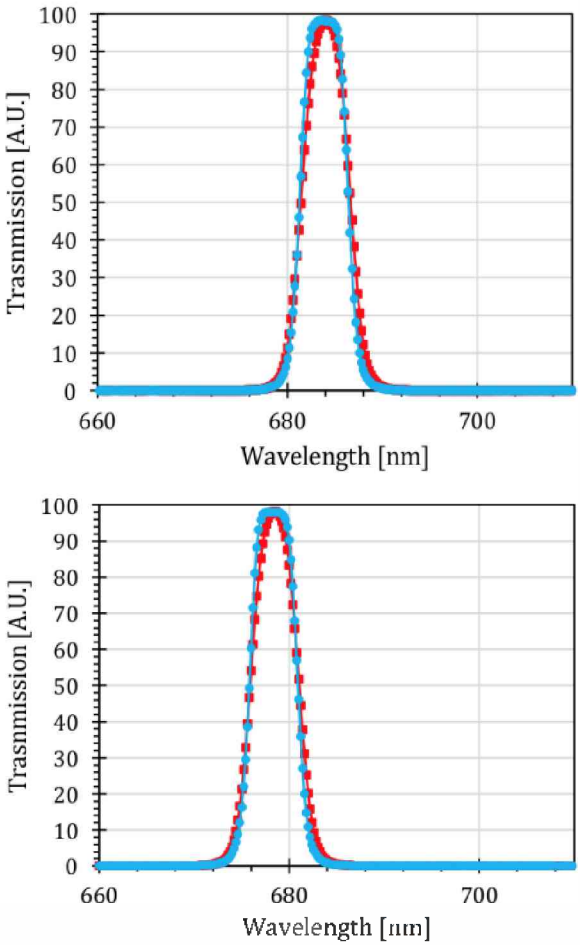

Figure 2: Transmission of the OVI - 683.5 nm (top) and OVIC - 678 nm (bottom) new filters, as measured at GS with the CARY 500 spectrometer (red), and as provided by the manufacturer (blue).

4. GMOS-N new CCDs

The installation of fully-depleted Hamamatsu CCDs in GMOS-N in February/March 2017 marked the conclusion of the CCD upgrade project for the two Gemini Multi-Object Spectrographs. The new CCDs have superior quantum efficiency (QE) at wavelengths longer than 680 nm, with significant sensitivity extending beyond 1 μm (Scharwaechter et al., 2018), similar to that in GMOS-S. Fig. 3 presents the focal plane array. It includes three CCD types with different anti-reflective coatings, referred to as "HSC" in reference to the Subaru Hyper Suprime-Cam instruments, and "BB" for "BetterBlue" (Gimeno et al., 2016). The spectral response of the Hamamatsu chips extends from roughly 360 to 1030 nm, with slightly different relative quantum efficiency characteristics due to the different arrangement of CCD types in the focal plane array. The Hamamatsu CCDs provide a significant improvement in sensitivity (especially at longer wavelengths) compared to the original EEV devices. Compared to the interim GMOS-N e2v DD devices (Roth et al., 2012), the Hamamatsu CCDs show an obvious higher throughput (see Fig. 4), albeit at the expense of 0.8 e^- higher readout noise. Fringing in the i' and Z filters is found to be negligible for the Hamamatsu CCDs. The GMOS-N upgrade concluded the Hamamatsu CCD upgrade project for both GMOS instruments.

5. GMOS advanced data reduction tips

A new tutorial on some advanced GMOS data reduction has been assembled by the instrument team. This tutorial will provide some tips that will hopefully help users to solve some of the most serious issues that may arise during data processing, as a consequence of the problems related to the detectors and the instrument. These solutions were compiled from the numerous requests from the user community within the last few years, coming mainly from GMOS-S users. In particular it provides some techniques on how to deal with difficulties with flat fielding issues, detector effects, bad columns, etc. These are not universal, fail-proof solutions; they may work well with some datasets and not so well on others, depending on what was the initial observing strategy and the quality of the raw data. It is available for imaging mode only (https://gmos-data-reduction-problems-and-solutions.readthedocs.io/en/latest/), however it is to be

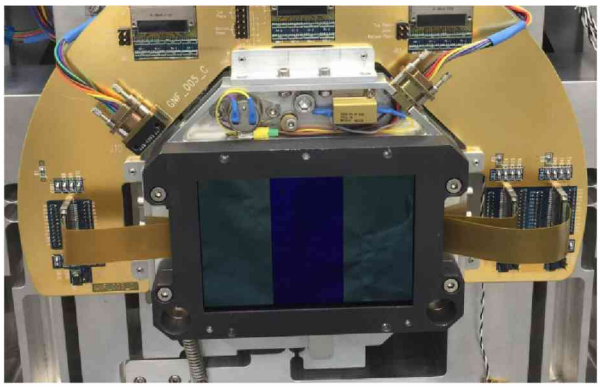

Figure 3: Photograph of the GMOS-N Hamamatsu focal plane array. The left- and right-most CCDs (CCDr and CCDb) are of type "BB". The middle CCD (CCDg) is of type "HSC". The golden semi-circular plate behind is the electrostatic discharge (ESD) protection board.

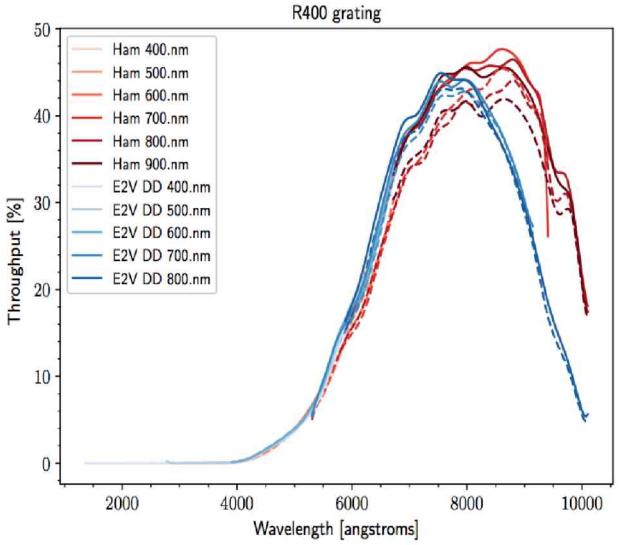

Figure 4: Comparison of spectroscopic throughput measurements for the GMOS-N Hamamatsu (red) and interim e2v DD (blue) CCDs based on two different sets of spectrophotometric standard star observations, respectively. All observations were obtained under photometric conditions using a 5 arcsec-wide slit. The central wavelength settings are indicated in the legend. All data sets using central wavelength settings $\leq$ 700 nm were obtained through the OG515 order-blocking filter and clipped at $<$ 530 nm where the filter cuts off. All data observed without OG515 were clipped at $>$ 673 nm to remove residual 2nd-order overlap. At the long-wavelength end, all data were clipped at $>$ 1030 nm, where the upturn of the throughput is due to 2nd-order overlap from the wavelength region beyond the OG515 cut-off wavelength.

extended to spectroscopy in the future.

Acknowledgements: Gemini Observatory is operated under a cooperative agreement with the NSF on behalf of the Gemini partnership: the National Science Foundation (United States), the National Research Council (Canada), CONICYT (Chile), Ministerio de Ciencia, Tecnología e Innovación Productiva (Argentina), and Ministério da Ciência, Tecnologia e Inovação (Brazil).

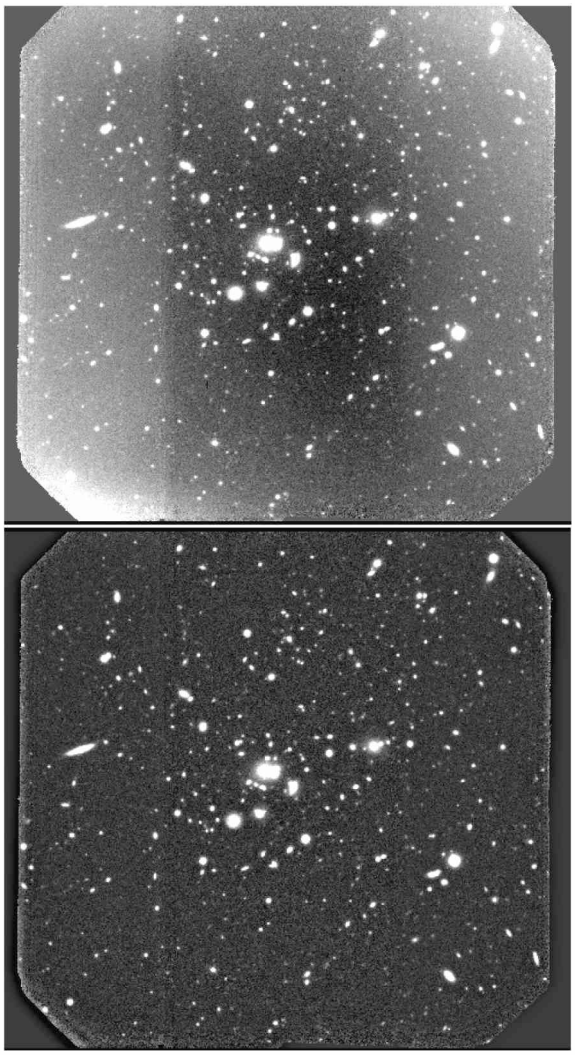

Figure 5: Example flat-fielded image obtained using the standard procedure (top) and the improved flat-fielding (bottom) described in the GMOS advanced data reduction tips tutorial (Sec.5).

References

Gimeno G., et al., 2016, *Ground-based and Airborne Instrumentation for Astronomy VI, Proc SPIE 99082, Proc. SPIE*, vol. 9908, 99082S

Hook I.M., et al., 2004, PASP, 116, 425

Roth K.C., et al., 2012, *Ground-based and Airborne Instrumentation for Astronomy IV, Proc SPIE 84463, Proc. SPIE*, vol. 8446, 84463V

Scharwaechter J., et al., 2018, *Ground-based and Airborne Instrumentation for Astronomy IV, Proc SPIE 10702, Proc. SPIE*, vol. 10702, 107022T

Construcción y caracterización de detectores auxiliares para la calibración de un observatorio de rayos gamma

G. Barboza[1], T. Codina[1], A. Pichel[2] & A.C. Rovero[2]

[1] *Departamento de Física, Facultad de Ciencias Exactas y Naturales, UBA, Argentina*
[2] *Instituto de Astronomía y Física del Espacio, UBA–CONICET, Argentina*

Contacto / anapichel@iafe.uba.ar

Resumen / Los arreglos de detectores utilizados en astronomía gamma deben ser calibrados; una forma es mediante el uso de detectores auxiliares. Se construyeron dos detectores auxiliares de partículas con un área de 20x20 cm^2, utilizando barras plásticas de centelleo, cada una con dos fibras ópticas "waveshifter" que llevan la luz a un fotomultiplicador que registra los pulsos de luz producidos por una partícula cargada que pasa por la barra de centelleo. El comportamiento de cada detector se estudió por separado, analizando su homogeneidad y la respuesta de la electrónica. Luego, colocando los detectores en coincidencia, se estudió el flujo de partículas atmosféricas y su dependencia con el ángulo cenital.

Abstract / Detector arrays used in gamma-ray astronomy must be calibrated; one way is by using auxiliary detectors. We built two auxiliary particle detectors with an area of 20x20 cm^2, using plastic scintillator bars, each one with two optical "waveshifter" fibers that guide the light to a photomultiplier, which in turn records the light pulses produced by a charged particle passing through the scintillator bar. The behavior of each detector was studied separately, analyzing its homogeneity and the response of the electronics. Then, by operating both detectors in coincidence, the flux of atmospheric particles and its dependency with the zenith angle were studied.

Keywords / rayos cósmicos – centelladores de muones – instrumentación astronómica, métodos y técnicas

1. Introducción

La astronomía gamma estudia los fenómenos más energéticos del Universo mediante el registro de los fotones gamma que llegan a la Tierra. Según la energía de estos fotones los instrumentos que los detectan pueden estar montados en satélites (como *Fermi-LAT*) o en arreglos de detectores en tierra. Los rayos gamma de mayor energía producen cascadas de partículas en la atmósfera terrestre que, a su vez, producen radiación Cherenkov en el rango óptico-UV. Los observatorios en tierra que utilizan arreglos de telescopios Cherenkov actualmente en operación son: VERITAS (EEUU), MAGIC (Canarias) y HESS (Namibia).

Hay otra forma de registrar los fotones gamma sin utilizar telescopios, es por medio de arreglos de detectores de partículas en la superficie terrestre, los cuales registran directamente las componentes cargadas de las cascadas. Los más utilizados son los *Water Cherenkov Detectors* (WCD): tanques de agua con detectores sensibles que registran la luz Cherenkov producida por partículas cargadas relativistas que lo atraviesan. Los trabajos pioneros en astronomía gamma utilizando este tipo de instrumentos fueron los de Milagro Gamma-ray Observatory, en EEUU (Abdo et al., 2012). Con esa base, se construyó el observatorio HAWC en México, el cual consistente en un arreglo de 300 WCD a 4100 m de altitud, con resultados sorprendentes (v.g., Abeysekara et al., 2017). Actualmente, la comunidad internacional está planeando la implementación de su contraparte en el hemisferio sur (Southern Gamma-ray Survey Observatory, SGSO), desde donde se podrá observar en plenitud la Vía Láctea y el Centro Galáctico.

No solo los rayos gamma producen cascadas de partículas en la atmósfera, sino también los rayos cósmicos (RC). Los RC son núcleos atómicos que vienen del espacio exterior viajando a velocidades relativistas; se trata mayormente de protones, aunque también núcleos más pesados, desde Helio hasta Hierro, y sus energías van desde alrededor de 1 GeV hasta cientos de EeV (10^{18} eV). Dependiendo de su energía, estos RC pueden haberse generado tanto dentro como fuera de nuestra galaxia, siendo su origen aún hoy en día un tema abierto en astrofísica, después de más de cien años de su descubrimiento.

El flujo de RC es órdenes de magnitud más elevado que la fuente gamma más intensa y, como se trata de partículas cargadas, sus trayectorias son desviadas por los campos magnéticos en su viaje a la Tierra, formando un fondo de radiación sobre el cual las fuentes gamma deben ser identificadas. Así, los componentes secundarios producidos en las cascadas atmosféricas constituyen el fondo de partículas que cualquier detector situado en la superficie de la Tierra registra en forma continua. Los componentes de una cascada producida por RC pueden verse en la Fig. 1, en donde se aprecia el desarrollo en la atmósfera y los flujos verticales de cada componente en función de la profundidad atmosférica. Se puede apreciar que a nivel del mar los "muones atmosféricos" son mayoría y, así, los que se utilizan para la calibración de instrumentos como los WCDs ya mencionados.

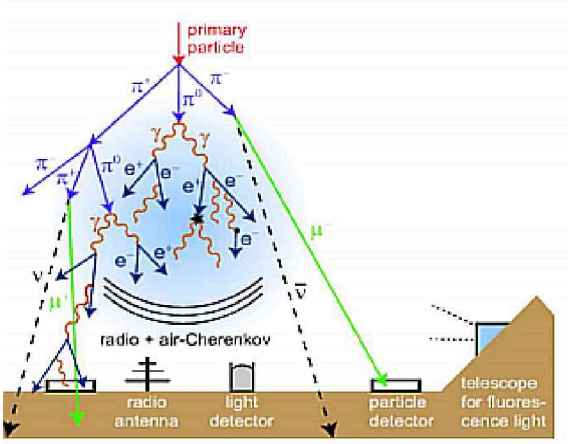

Figura 1: Desarrollo de cascada atmosférica hadrónica.

En estos detectores la señal obtenida es proporcional a la distancia recorrida por la partícula cargada dentro del tanque, de modo que la calibración consiste en caracterizar la señal del WCD para muones de trayectoria conocida. Para lograr esto se utilizan dos detectores auxiliares en coincidencia temporal, ubicados en la trayectoria deseada; cuando estos detectores registran el paso de un muón dentro de una ventana temporal dada (algunos ns), entonces se registra la señal del WCD y se estudian sus características.

El flujo de muones atmosféricos utilizables para este tipo de calibración está modulado por el espesor de la atmósfera en función del ángulo cenital de incidencia del muón. A los flujos verticales mostrados en la Fig. 1, se le debe agregar este efecto para obtener el flujo a un ángulo cenital dado (Rossi, 1964), siendo :

$$I(\theta) = I(0)\, cos^2(\theta), \qquad (1)$$

en la cual $I(0) = 7 \times 10^{-3}\ cm^{-2}\, s^{-1}\, sr^{-1}$.

En este trabajo describimos el diseño, construcción y caracterización de dos detectores auxiliares, del tipo comúnmente llamado "paleta centelladora", un detector pequeño que consta de un centellador plástico con un detector óptico adosado que registra los pulsos de luz producidos por una partícula cargada que lo atraviesa.

2. Diseño experimental y construcción

Cada detector fue construido utilizando centelladores de plástico orgánico de 20.5 cm×4.1 cm×1 cm y un PMT Hamamatsu de 16 píxeles (H8711-06), montado sobre una placa electrónica con la fuente de alto voltaje. Fue diseñado con una distribución de 2 capas superpuestas de 5 barras centelladoras cada una, haciendo una superficie detectora de aproximadamente $20\times20\,\mathrm{cm}^2$. Las barras poseen una ranura sobre una de las caras en la cual se colocaron dos fibras ópticas acopladas con grasa óptica; las fibras son del tipo "waveshifter", que es necesario para que las mismas puedan absorber los fotones producidos en los centelladores y, convertidos a una longitud de onda adecuada, transportarlos hacia el PMT sin ser atenuados. Las diez fibras fueron dirigidas hacia un colector, o "cookie" (Fig. 2). Para alojar el PMT con

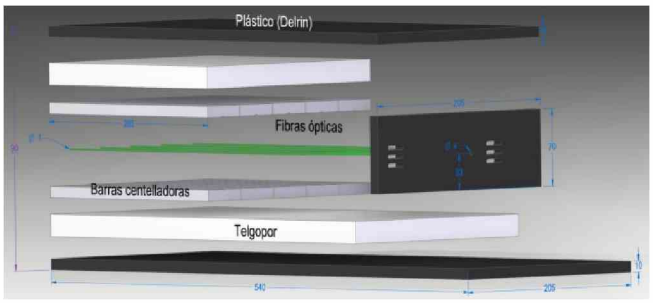

Figura 2: Esquema del recinto construido para contener a las placas centelladoras y fibras. De arriba hacia abajo: Plástico, telgopor, barras, fibras, barras, telgopor y plástico.

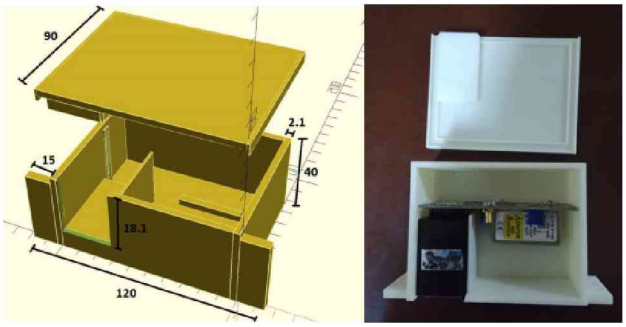

Figura 3: Plano y foto de la caja impresa en 3D. El PMT y la electrónica se ven ubicados en su lugar.

Figura 4: Un detector una vez terminada su construcción.

la electrónica y poder ubicar un pixel dado frente al cookie, se diseñó e imprimió una caja en 3D (Fig. 3), que va anclada frente al cookie. El diseño de la caja incluyó un sistema de rendijas que permite un movimiento X-Y entre el cookie y los píxeles del PMT, el cual permite utilizar cualquiera de éstos si fuese necesario. Luego de cerrar las partes, se recubrió el detector con dos capas de aluminio y posteriormente con tela "blackout", dejando los orificios necesarios para la salida de las fichas BNC y de alimentación de 12 V. De esta forma el detector queda sellado a la luz completamente y resulta sencillo de manipular (Fig. 4).

3. Resultados y discusión

Como primer paso para caracterizar al detector se colocaron ambas paletas una sobre la otra distanciadas por 88 cm de altura. Para los pulsos de las paletas (ancho ∼10 ns) se registraron las coincidencias utilizando el método Setup & Hold de un osciloscopio Tektronik DPO3054 (ventana de 30 ns). Así, se obtuvo la curva de

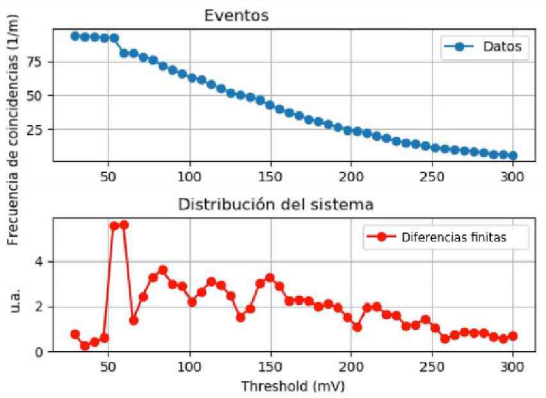

Figura 5: Paleta 1: Frecuencia integral de coincidencias en función del umbral (arriba); idem diferencial (abajo).

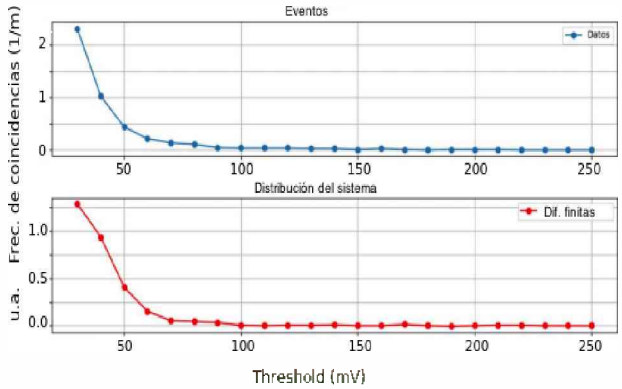

Figura 6: Paleta 2: Idem Fig. 5

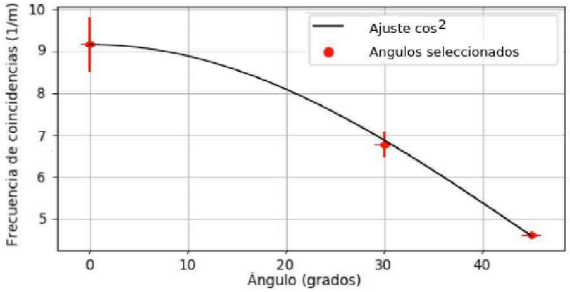

Figura 7: Distribución angular del flujo de muones medido con las paletas centelladoras separadas una altura de 88 cm.

frecuencia de coincidencias en función del umbral (tensión de trigger) para cada paleta centelladora.

Para la curva característica de la paleta centelladora 1, se midió durante 3 días obteniendo 33 puntos para umbrales entre -20 mV y -300 mV con 2 horas y 15 minutos de estadística cada uno (ver Fig. 5). Esta figura muestra las tasas de conteo integrales, o sea para eventos que superen cierto umbral. Para poder comparar esto con lo esperado para un PMT debemos computar las tasas diferenciales, lo cual se muestra en la parte inferior de la misma figura, y representa la señal que se obtiene del PMT de un detector, que en teoría se obtiene de la convolución de las respuestas del PMT a la incidencia de fotoelectrones (electrones producidos en el fotocátodo del PMT). Considerando fluctuaciones, la curva está dentro de la distribución esperada y nos permite definir un umbral de operación, que tomamos en 60 mV.

Repetimos el procedimiento anterior para la segunda paleta centelladora, barriendo 23 puntos desde 10 mV hasta 250 mV, con estadística similar al caso anterior y obtuvimos las curvas de la Fig. 6. En este caso resulta evidente que para obtener la distribución esperada se debería aumentar la amplificación para que la curva se desplace hacia los valores superiores de voltaje umbral. Sin embargo, para lograr coincidencias entre los dos detectores auxiliares, basta operar a esta paleta con un voltaje umbral de 20 mV. Debemos mencionar aquí que el PMT de esta paleta tuvo que ser reemplazado por uno de características distintas (EMI 9781B), lo cual justifica las diferencias en las curvas de respuesta.

Medir el flujo total de muones correspondería a integrar la ecuación 1 sobre el área del detector inferior A_0 teniendo en cuenta su dependencia angular y su ángulo sólido Ω_0, para detectores muy separados esto es esencialmente constante, y se puede calcular como:

$$I(t) = I(0)\, A_0\, \Omega_0. \qquad (2)$$

En nuestro caso particular se midió el flujo de muones para las paletas centelladoras a $\theta = 0$ separadas a 88 cm y 17 cm fijando umbrales de voltaje según lo mencionado anteriormente. Para 88 cm el resultado fue de (9.2 ± 0.6) eventos por minuto donde el error corresponde a fluctuaciones del valor medio (ver Fig. 7). Satisfactoriamente, dicho valor concuerda con lo predicho por la ecuación 2 al remplazar los valores $A_0 = 420.25\,\mathrm{cm}^2$ y $\Omega_0 = 0.054$, correspondientes a la configuración experimental, obteniéndose un flujo de 9.53 muones por minuto. Luego variamos el ángulo cenital a 30 y 45 grados (ver Fig. 7). Por otro lado, para una separación entre paletas de 17 cm, el valor del flujo obtenido fue de (76.2 ± 0.4) eventos por minuto, mientras que lo predicho teóricamente para los valores $A_0 = 420.25\,\mathrm{cm}^2$ y $\Omega_0 = 1.076$ es de 190 muones por minuto. El error es solo estadístico, pero la discrepancia viene porque la aproximación de la ecuación 2 no se cumple ya que se admiten incidencias de hasta 30° cenital.

Hemos construido dos detectores de muones de pequeñas dimensiones para ser utilizados como auxiliares en el proceso de calibración de detectores de partículas. En particular, se planea utilizarlos en la calibración de detectores WCD, los que serán incluidos en el futuro SGSO. El correcto funcionamiento de estos detectores auxiliares fue probado mediante mediciones en coincidencia, con lo cual se pudo reproducir el flujo conocido de muones a nivel del mar y su dependencia con el ángulo cenital.

Agradecimientos: Las barras, fibra y uno de los PMTs fueron provistos por el ITeDA. La caja fue impresa en el Dep. Física, FCEyN, UBA. El trabajo fue parcialmente solventado por ANPCyT.

Referencias

Abdo A.A., et al., 2012, ApJ, 750, 63
Abeysekara A.U., et al., 2017, ApJ, 843, 40
Rossi B., 1964, *Cosmic Rays*

Sidelobe analysis for the Atacama Cosmology Telescope: a novel method for importing models in GRASP

R. Puddu[1], N.F. Cothard[2], P.A. Gallardo[3], R. Dünner[1] & P. Fluxá[1] for the ACT Collaboration

[1] *Instituto de Astrofísica y Centro de Astro Ingeniería, Pontificia Universidad Católica, Santiago de Chile*
[2] *Department of Applied and Engineering Physics, Cornell University, Ithaca, USA*
[3] *Department of Physics, Cornell University, Ithaca, USA*

Contact / rpuddu@aiuc.puc.cl

Resumen / Los telescopios para observar el fondo cósmico de microondas suelen tener pantallas y *baffles*, con el fin de reducir la emisión del suelo. Estas estructuras pueden introducir lóbulos laterales no deseados. En este manuscripto introduciremos una herramienta en GRASP para obtener un modelo electromagnético de objectos de gran tamaño y estructura compleja, como los telescopios, y predecir la forma así como la posición de los lóbulos laterales.

Abstract / Telescopes for observing the Cosmic Microwave Background usually have shields and baffle structures in order to reduce the pickup from the ground. These structures may introduce unwanted sidelobes. We present a method to measure and model baffling structures of large aperture telescope optics to predict the sidelobe pattern.

Keywords / instrumentation: high angular resolution — cosmology: observations

1. The Atacama Cosmology Telescope

The Atacama Cosmology Telescope (ACT) is a 6 m telescope located in northern Chile, at 5200 m elevation. The high altitude and low water vapor content in the atmosphere provide excellent conditions for observing the sky in mm wavelengths. The tropical latitude allows access to more than half of the sky. The design is an off-axis Gregorian. The large aperture is required to achieve arcminute resolution, which allows to study the Sunyaev Zel'dovich effect in galaxies clusters, weak lensing and give constraints on neutrino mass (Hilton et al., 2018; Sherwin et al., 2017; Hand et al., 2015; Madhavacheril et al., 2015), as well as the CMB power spectrum up to high multipoles (Louis et al., 2017). The short focal length, 5.2 m, makes the telescope compact enough for fast scanning. To minimize ground pick-up during scanning, the telescope has two ground screens. A large, stationary outer ground screen surrounds the telescope. A second, inner comoving screen connects the edges of the primary reflector to the secondary reflector and moves with the telescope during scanning. A climate-controlled receiver cabin is situated underneath the primary and secondary reflectors (Thornton et al., 2016; Fowler et al., 2007).

Spillover at the Lyot stop can load the detectors with radiation emitted from warm, nearby structures. Theoretical estimates based on the optical design show that there is 2 % spillover past the secondary reflector (Swetz et al., 2011). To reduce this loading, the primary reflector is surrounded by a 0.75 m radial baffle that reduces the primary spillover to less than 0.2 %, by directing those rays to the sky. However, the spillover on the secondary reflector occurs at larger angles. Measurements suggested that there is as much as 2 % to 3 % power that does not get reflected to the sky. As a result, the secondary baffling was redesigned to ensure that the majority of the spillover was redirected to the sky (Swetz et al., 2011).

2. Sidelobes characterization

Diffracted and reflected power may reach the sky in arbitrary angles, forming far sidelobes. If these sidelobes get illuminated by strong sources, like the sun or the moon, they may produce spurious features in maps of the sky. For large optical systems the sidelobe response can be challenging to model and characterize (Lockman, 2002; Page et al., 2003; Tauber et al., 2010; Carlstrom et al., 2011). Nevertheless, an accurate model of this systematic effect is crucial to obtain clean maps and accurate astrophysical results (Barnes et al., 2003). In order to characterize the sidelobes of ACT, we have performed simulations with the GRASP (General Reflector Antenna Software Package⋆) physical optics software. Propagation of electromagnetic waves, as well as their reflection and refraction, is ruled by Maxwell's equations and induced currents play an important role in them. GRASP is able to compute surface currents induced by incoming radiation upon reflectors. These currents will cause the reflector to re-emit radiative power and thus can illuminate further reflectors. In this way it is possible to build any desired optical chain. The last reflector will radiate the complex fields, which will be evaluated on a grid, typically in the far field. Knowing the complex fields may give important insights on the polarization state

⋆`https://www.ticra.com/software/grasp/`

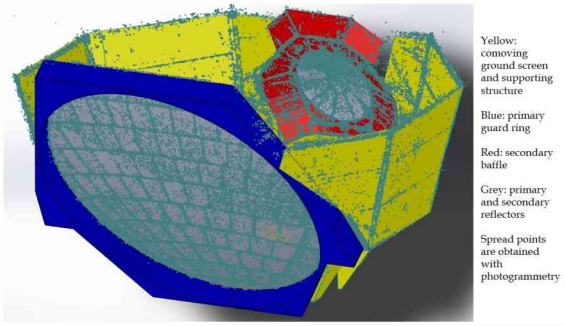

Figure 1: Point cloud obtained with photogrammetry Photoscan software, overlapped with the ACT telescope CAD model. Most relevant parts in the GRASP simulations are the primary guard ring (blue) and the secondary baffle (red).

and coherence of the signal, which are hard to obtain with other ray-trace similar software packages.

A model of the telescope is required in GRASP. This consists, in our case, in a series of (according to software notation) "geometrical objects" called "reflectors". Each element of the inner and outer shield, as well as the mirrors and the secondary baffling is treated as a reflector. Drawing the ACT model in GRASP is not trivial since every reflector must be defined with a coordinate system, a surface and a rim. This, unfortunately, cannot be done in a quick and intuitive way as it would be in Computer Aided Design (CAD) software. Information about the geometry of the model is handled with a file with specific GRASP syntax. Furthermore, while mechanical specifications are available for most of telescope parts, that is not the case for the secondary baffling. For this reason we used photogrammetry to get a *points cloud* reconstruction of the telescope, which was used to build the model within a CAD software (SOLIDWORKS). Later, we imported it into GRASP by means of a code able to read the CAD file and writing the corresponding file for the GRASP project.

3. Photogrammetry

In a photogrammetric system, a series of stickers, *photogrammetry targets*, are photographated by a camera and processed by a suitable software. We have used a Nikon 600D camera and the PHOTOSCAN software. The software combines a large amount of photos, performs triangulations for all recognized markers, and generates their 3D positions. The final result is a point cloud which reproduces the telescope shape.

We use the measured positions of the targets (the point cloud) to create a best fit model that represents the shape of the upper structure's planar faces. The planar faces fit the point cloud (see Fig. 1). The primary and secondary reflectors have been drawn following the geometrical specifications of the telescope and not using the point cloud (Fowler et al., 2007).

4. ACT in GRASP

GRASP is a software able to perform electromagnetic simulations of antennas. Its main purpose is to study the behavior of relatively simple systems composed by one or two reflectors, and a feeding device with potentially some more parts such as plates, struts, stiffeners, support rings and so on, i.e. a series of components that are useful for engineering purposes in several antenna applications. Instead, with this study we want to apply the computing potential of the software in order to investigate the systematics of the ACT, such as sidelobes. These are usually generated by interactions between optical elements such as reflections off baffling structures, scattering off optical elements, spurious reflections off support structures and panel gap diffraction. In ACT, most sidelobe contribution come from the baffle around the secondary mirror and the guard ring around the primary mirror (Gallardo et al., 2018). The geometrical definition of these structures is a tricky obstacle, since the analysis of secondary effects like telescopes sidelobes is not the main purpose of the software.

We use the CAD model of ACT obtained with the point cloud to obtain a correspondent model in GRASP. This has been accomplished by means of a dedicated code able to perform such a conversion. A powerful Python library, FreeCAD**, extracts the geometrical information contained in the CAD model. It reads the file extracting the model geometry in a hierarchical architecture, i.e. the solid body is organized in faces, each of them in lines, each line in points. All elements in the CAD file are referred to a unique coordinate systems, whilst in GRASP this is not the optimal scenario: this would both increase the computation time for currents and fields, and make the model hard to handle or modify. Thus, we assign a local coordinate system to each face of the CAD model. Local coordinate systems are referred to the global one via a suitable Euler rotation (ϕ, θ, ψ) with axes zyz (as defined in GRASP). In order to find ϕ and θ (ψ is set to zero, as two angles are enough to define a xy plane containing all the points of the face) we proceed as follows. for each face of the body:

- any three consecutive points are taken to define two non-parallel vectors. Their cross product will define the normal vector $\mathbf{n} = (n_x, n_y, n_z)$ to the plane containing the face. The normal vector will be parallel to the z axis of the local coordinate system, which will pass through the center of mass of the face.
- the center of mass of the face is set as the origin of the local coordinate system.
- ϕ is retrieved as $\arctan \frac{n_y}{n_x}$.
- θ is retrieved as $\arctan \frac{n_z}{\sqrt{n_x^2+n_y^2}}$.
- each point is translated by the vector of the center of mass and then rotated with the Euler angles ϕ and θ. This ensure that all the points will lay in the xy plane of the local coordinate system, i.e. $z_{\text{point}} = 0$.
- the local system allows to define the surface easily, being the origin $(0, 0)$ and the z axis unit vector the constant parameters.

In this way all the geometrical elements are defined in a convenient way, improving the performance of the software and making the project more readable, allowing straightforward modifications, when necessary (e.g a rim point, or the tilt of a plane with respect to the

**https://www.freecadweb.org/

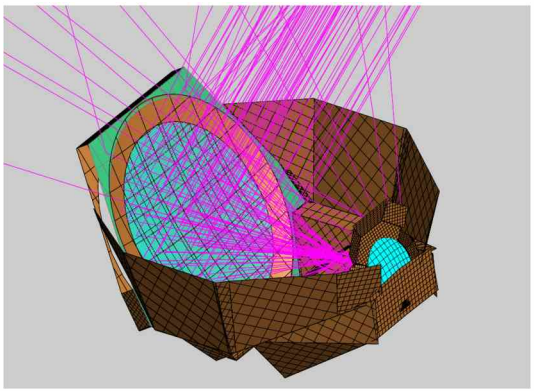

Figure 2: The same model as in Fig. 1, imported in GRASP with our Python code.

global system coordinates). The importance of this code mostly relies in allowing to perform optical simulations with GRASP physical optics, including elements not previously available and thus improving the accuracy. In particular elements such the ones responsible for the sidelobes were tricky to insert in the model because of the non-trivial definition in GRASP. The model as it has been imported into GRASP is shown in Fig. 2.

4.1. GRASP analysis

The secondary baffling, together with the large structure around the primary mirror and the outer part the primary mirror (the guard ring, highlighted in green in Fig. 2) are expected to be the most responsible of sidelobes (see Sec. 1.). The analysis has been performed in GRASP by illuminating the secondary baffle with a feed placed at the entrance window of the camera. The beam of the camera has been measured (Gallardo et al., 2018) *in situ* and it is reproduced in GRASP. The secondary baffling in turn illuminates the guard ring and finally the fields are collected on the output, far field grid. A remarkable match arises comparing the simulated maps in GRASP with the observed ones and will be released in a future publication.

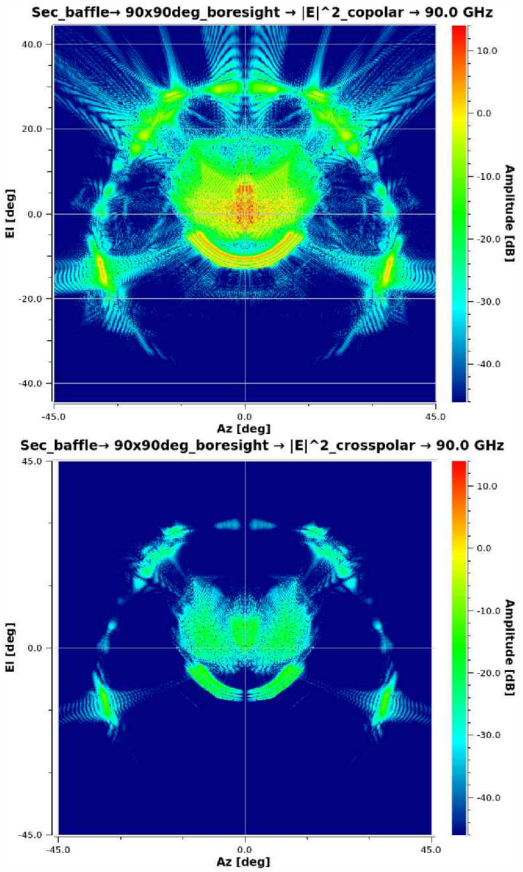

Figure 3: Far field of the telescope, as observed illuminating the baffle around the secondary mirror with subsequent scattering off the primary mirror and its guard ring structure. The angular coordinates azimuth and elevation are referred to the boresight, whilst the dB scale is referred to the injecting power.

5. Conclusions and future steps

The utility developed to import CADs in GRASP makes possible to perform extensive simulations of sidelobes, thus allowing a complete characterization of the telescope. We were able to find the origin of the sidelobes, and this will let us decide the best strategy, both for scanning the sky and determining the panels that have the most trouble. In wintertime, when the humidity is very low and the weather conditions are stable, we are planning to perform extensive measurements involving all the panels, as well as to make sidelobes maps with the eccosorb on the panels to verify that contributors to the sidelobe structure have been appropriately identified and mitigated.

Acknowledgements: This work was supported by the CONYCIT award Anillo ACT-1147, BASAL CATA PFB-06, Anillo ACT-86, FONDEQUIP AIC-57 and QUIMAL 160009. We also acknowledge the U.S. National Science Foundation through awards AST-0408698 for the ACT project and PHY-0355328. We gratefully thank the supporting TICRA staff for their technical suggestions.

References

Barnes C., et al., 2003, ApJS, 148, 51
Carlstrom J.E., et al., 2011, Publications of the Astronomical Society of the Pacific, 123, 568
Fowler J.W., et al., 2007, ApOpt, 46, 3444
Gallardo P.A., et al., 2018, in Millimeter, Submillimeter, and Far-Infrared Detectors and Instrumentation for Astronomy IX. *Society of Photo-Optical Instrumentation Engineers (SPIE) Conf. Series*, vol. 10708
Hand N., et al., 2015, PhRvD, 91, 062001
Hilton M., et al., 2018, ApJS, 235, 20
Lockman F.J., 2002, in Single-Dish Radio Astronomy: Techniques and Applications, *Astronomical Society of the Pacific Conf. Series*, vol. 278, 397–411
Louis T., et al., 2017, JCAP, 6, 031
Madhavacheril M., et al., 2015, PhRvL, 114, 151302
Page L., et al., 2003, ApJ, 585, 566
Sherwin B.D., et al., 2017, PhRvD, 95, 123529
Swetz D.S., et al., 2011, ApJS, 194, 41
Tauber J.A., et al., 2010, A&A, 520, A2
Thornton R.J., et al., 2016, ApJS, 227, 21

Data-driven education and public outreach with the Sloan Digital Sky Survey

B. Lundgren[1], R. Tojeiro[2], R. L. Beaton[3], M. R. Blanton[4], J. Borissova[5], M. Cano-Díaz[6], K. Grabowski[7], R. Kurtev[5], N. MacDonald[8], S. R. Majewski[9], K. L. Masters[10,11], K. Meredith[12], C. Nitschelm[13], T. O'Reilly[14], J. Raddick[15], D. Skinner[16], A. Thakar[15], A. Weijmans[2], D. G. Whelan[17] & the Sloan Digital Sky Survey IV Collaboration

[1] *Department of Physics, University of North Carolina, USA*
[2] *School of Physics and Astronomy, University of St Andrews, North Haugh, UK*
[3] *Hubble Fellow, Department of Astrophysical Sciences, Princeton University, Princeton, New Jersey, USA.*
[4] *Center for Cosmology and Particle Physics, Department of Physics, New York University, USA*
[5] *Instituto de Física y Astronomía, Universidad de Valparaíso, Chile; Millennium Institute of Astrophysics (MAS), Santiago, Chile*
[6] *Instituto de Astronomía, Universidad Nacional Autónoma de México, Mexico D.F., Mexico*
[7] *Apache Point Observatory, New Mexico, USA*
[8] *University of California Observatories, UC Santa Cruz, USA*
[9] *Department of Astronomy, University of Virginia, Charlottesville, USA*
[10] *Haverford College, Department of Physics and Astronomy, Haverford, USA*
[11] *Institute of Cosmology & Gravitation, Univ. of Portsmouth, UK*
[12] *Geneva Lake Astrophysics and STEAM, Williams Bay, Wisconsin, USA*
[13] *Centro de Astronomía, Universidad de Antofagasta, Chile*
[14] *Department of Astronomy, University of Washington, Seattle, USA*
[15] *Institute for Data Intensive Engineering and Science, Johns Hopkins University, Baltimore, USA*
[16] *Center for Relativistic Astrophysics, School of Physics, Georgia Institute of Technology, Atlanta, USA*
[17] *Department of Physics, Austin College, Sherman, USA*

Contact / blundgre@unca.edu

Resumen / Durante más de quince años, la colaboración internacional de *Sloan Digital Sky Survey* (SDSS) ha puesto a disposición del mundo terabytes de datos astronómicos profesionales. Las vastas imágenes de archivo y los conjuntos de datos espectroscópicos del SDSS, junto con sus múltiples puntos de acceso e interfaces adecuados para los usuarios de todos los niveles de experiencia, proporcionan un novedoso recinto de pruebas para audiencias de una amplia gama de entornos para explorar y relacionarse con los datos mientras cultivan intereses y dominio de la astronomía. Los científicos, educadores, técnicos y observadores de SDSS que participan en el grupo de trabajo Educación y Difusión Pública de la colaboración han colaborado durante la última década para desarrollar un conjunto amplio y diverso de actividades educativas y exposiciones basadas en los datos de SDSS y los conceptos de ingeniería. La reciente expansión de las operaciones SDSS-IV APOGEE-2 al Observatorio Las Campanas en Chile ha impulsado un nuevo énfasis en la ampliación de la accesibilidad de estos recursos educativos para las audiencias de habla hispana.

Abstract / For over fifteen years, the international collaboration of the Sloan Digital Sky Survey (SDSS) has made terabytes of professional astronomical data freely available to the world. The vast archival imaging and spectroscopic datasets of the SDSS, coupled with its multiple access points and interfaces suitable for users of all levels of experience, provide a novel sandbox for audiences from a wide range of backgrounds to explore and engage with the data while cultivating interests and proficiency in astronomy. SDSS scientists, educators, technicians, and observers involved in the collaboration's Education and Public Outreach working group have collaborated over the past decade to develop a large and diverse set of educational activities and exhibits built around SDSS data and engineering concepts. The recent expansion of SDSS-IV APOGEE-2 operations to Las Campanas Observatory in Chile has prompted a new emphasis on broadening the accessibility of these educational resources for Spanish-speaking audiences.

Keywords / editorials, notices — miscellaneous — astronomical databases: miscellaneous

1. Introduction

For nearly two decades the Sloan Digital Sky Survey (SDSS; York & SDSS Collaboration, 2000) has collected the images and spectra of millions of stars, galaxies, and quasars. Through regular data releases, the fully reduced astronomical data and value-added catalogs have been published and made freely available to the world via `http://www.sdss.org`. The sheer scale of the data has enabled new statistical understandings of the physical processes shaping the evolution of galaxies and the

large-scale structure of the universe.

The SDSS Collaboration, now in its fourth generation (SDSS-IV; Blanton et al., 2017), is composed of hundreds of astronomers, engineers, technicians, and observers in dozens of institutions around the world. As an indication of the survey's global impact, the SDSS was cited over 700,000 times by authors in 52 countries in its first 10 years of operations (Chen et al., 2009). Over the past decade, the SDSS data and related products have become even more prolific, with research applications extending well beyond the international membership of the SDSS collaboration.

The SDSS Education and Public Outreach (E/PO) working group is charged with advancing education and public outreach in astronomy through SDSS-related activities and, increasingly, the direct engagement of the public with SDSS data. The SDSS E/PO group has leveraged the SDSS data products and research tools to produce inquiry-based activities for thousands of students learning science, technology, engineering and mathematics (STEM) subjects, from elementary through graduate school, and through after-school and informal education programs. SDSS data have been used to enhance the understanding of science among the general public as well, by enabling citizen science projects like Galaxy Zoo (Lintott et al., 2011) and appearing in museum exhibits and planetaria around the world.

2. SDSS Data as a Tool for Astronomy Education

While astronomy has always been at the forefront of data-intensive research, instrumental and computational advances over the past two decades have made terabyte-scale datasets the norm. With even more expansive surveys on the horizon (from e.g., the Large Synoptic Survey Telescope and the Wide Field Infrared Survey Telescope), astronomy – along with other data-rich areas of science and industry – will increasingly rely on individuals who are equipped with the skills to visualize and analyze data of ever-increasing scale. As such, a modern astronomy education should include computational methods as an integral part of the experimental and theoretical core curriculum. Teaching these methods with the use of authentic scientific data can further enhance the learning process and positively affect student attitudes and persistence in STEM (Nagda et al., 1998; Russell et al., 2007)

2.1. SDSS *SkyServer* and *Voyages*

The SDSS *SkyServer*[1] provides the astronomy community and the public with access to the latest SDSS data releases, which currently include:

- Full color images and photometric measurements for >930 million unique objects
- Optical spectra of >4 million stars, galaxies, and quasars
- Infrared spectra of ∼263 000 stars
- Spatially resolved optical spectra of nearly 5000 galaxies in the nearby universe

Since the earliest SDSS data releases, educational materials have been developed and made freely available as part of the *SkyServer*, with the aim of helping students, teachers, and the public explore the growing SDSS dataset and develop a better understanding and appreciation for astronomy. The intentionally broad scope of the SDSS survey has accommodated the development of a diverse set of educational activities, with topics ranging from the structure of our solar system and the Milky Way to the properties of distant quasars and the large-scale structure of the universe.

SkyServer activities have been developed for a variety of educational levels, spanning elementary (i.e., primary) school through introductory college courses. The activities are designed to give educators flexibility to implement them in ways that will fit the time constraints of their classes and the abilities of their students. To assist with lesson planning, teaching guides have also been made available to accompany the *SkyServer* activities.

Since 2012, significant efforts have been committed to developing a new set of online activities with an updated pedagogy and aesthetic. The new flagship SDSS education site, *Voyages*[2], houses a collection of new educational activities and explorations based on the latest SDSS survey data, as well as an updated set of the original *SkyServer* educational activities. The aim of *Voyages* is to provide the pathways and supporting resources to enable student-led discovery of a variety of astronomical phenomena using the same data utilized by professional astronomers. Use of the site has steadily grown since its launch in mid-2017. Currently, ∼900 users interact with the site each month, 25 % of whom reside outside of the U.S.

2.1.1. Translation Efforts

Given the international membership of the SDSS Collaboration and its intent to reach a global user base, the first generation of the SDSS undertook a substantial effort to translate the *SkyServer* website into multiple languages. Versions on the web published prior to the Data Release 8 can be accessed in English, German, Hungarian, Japanese, Spanish, and Portuguese. Limited translations of a some original *SkyServer* educational activities were also published as part of the Data Release 7.

As the survey diversified and broadened its scope in its third and fourth generations, the effort of translating the frequently revised and updated *SkyServer* website was not actively maintained. The current version of the *SkyServer* website (serving Data Release 15) is available only in English, although thanks to the the improved automatic translations of modern web browsers (e.g., Google Chrome), the site can still be broadly accessed by an international audience.

The expansion of SDSS-IV APOGEE-2 operations to Las Campanas Observatory in Chile provided new motivation for making the SDSS educational resources

[1] `http://skyserver.sdss.org`

[2] `http://voyages.sdss.org/`

```
slice1_red = np.where( (all_gals.z_spec > 0.02) & (all_gals.z_spec < 0.03) & (all_gals['u'] - all_gals['g'] > red))[0]
slice1_blue = np.where( (all_gals.z_spec > 0.02) & (all_gals.z_spec < 0.03) & (all_gals['u'] - all_gals['g'] < blue))[0]

plt.figure(figsize=(20,8))
plt.subplot(121)
plt.scatter(all_gals.loc[slice1_blue]['ra'], all_gals.loc[slice1_blue]['dec'],  marker='.', s=10, color='blue')
plt.xlabel('RA')
plt.ylabel('Dec')
plt.ylim(-5,70)

plt.subplot(122)
plt.scatter(all_gals.loc[slice1_red]['ra'], all_gals.loc[slice1_red]['dec'],  marker='.', s=10, color='red')
plt.xlabel('RA')
plt.ylabel('Dec')
plt.ylim(-5,70)
```

```
(-5, 70)
```

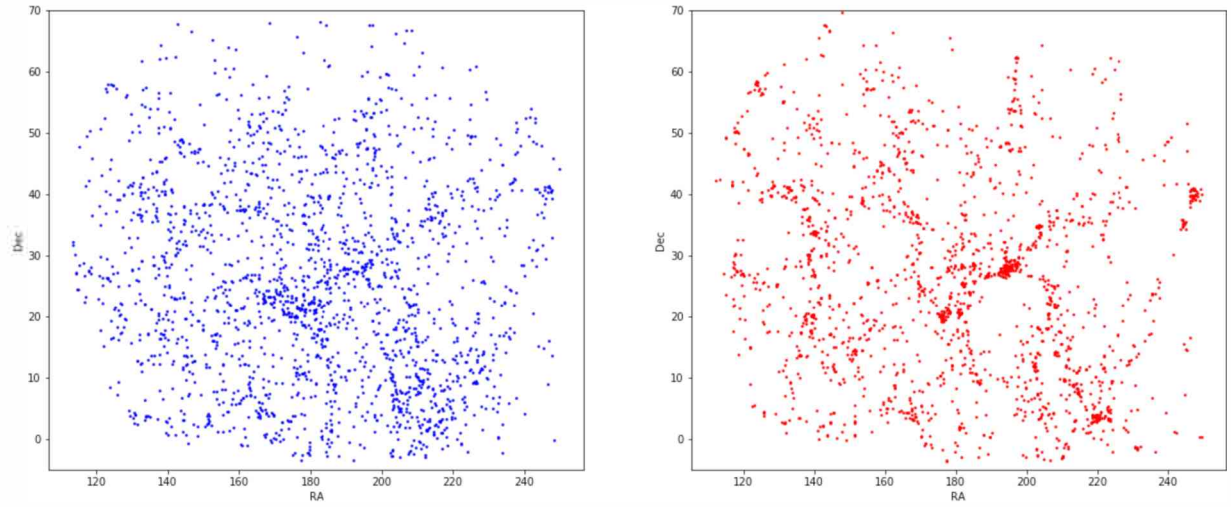

Figure 1: An example cell from a SciServer notebook activity exploring the color-density relation of SDSS galaxies.

accessible to Spanish-speaking audiences with more carefully curated translations. Through the volunteer efforts of Spanish-speaking SDSS astronomers, the SDSS *Voyages* website was translated and launched in a Spanish version[3] in 2017. Further development of the Spanish site is still underway, in parallel with continued updates to the English site.

2.2. SciServer

Basic competency in computer programming has become an essential skill required of any aspiring astronomer. Still, there remains a dearth of accessible university-level activities that teach coding within a context of real astronomical investigations.

Over the past two years the SDSS E/PO working group has been partnering with the developers of SciServer[4], a science platform of the SDSS, to produce innovative and accessible Python-based data explorations for astronomy classrooms and labs, with a focus on undergraduate-level students. Operated by the Institute for Data Intensive Engineering and Science at Johns Hopkins University, SciServer is a fully integrated cyberinfrastructure system encompassing related tools and services to enable researchers to cope with the challenges of big data. SciServer enables a new approach that allows researchers to work with terabytes or petabytes of scientific data via web-based notebooks, without downloading any large datasets or installing any software. This flexibility is particularly useful in educational settings that have traditionally lacked the computational resources to take advantage of large-scale datasets like the SDSS.

The university-level SciServer curriculum developed by the SDSS E/PO team consists of free, highly accessible, and modernized activities using SDSS data for a broad community of astronomy educators. A set of introductory-level activities has been piloted with 80 students at the University of St Andrews, in the UK, and a complementary laboratory curriculum for upper-level astronomy undergraduates has been piloted at the University of North Carolina Asheville in the U.S.

These pilot programs have demonstrated the power of SciServer in undergraduate teaching at all levels. Using web-based notebooks, the first-year class at the University of St Andrews was able to discover the large-scale structure of the Universe and color-density relation of galaxies using only very simple Python statements (e.g., Fig. 1). The new 5-hour lab was a significant departure from teaching methods traditionally used in that course, but it was a success. A large majority of the class completed bonus exercises in their own time, driven by interest and enabled by the free and easy access to SciServer. Following the pilot, the SciServer lab was adopted as an integral part of the course, and has run for a second year with equal success. SciServer-based teaching has

[3] `http://voyages.sdss.org/es/`
[4] `http://www.sciserver.org/`

also since been adopted in later years of the undergraduate curriculum at the same institution.

At more advanced levels, SciServer equips students to engage in meaningful astronomy research projects with ease. In upper-level observational astronomy courses at the University of North Carolina Asheville and the University of St Andrews, SDSS SciServer activities are providing students with a strong foundation of Python-based data analysis, within the context of SDSS science. Some students who completed these pilot courses have already gone on to produce original independent research, which has been presented at national meetings of the American Astronomical Society.

The first release of the SDSS SciServer activities was made available to participants at a half-day workshop at the 2018 Winter Meeting of the American Astronomical Society in National Harbor, Maryland. These activities, along with new curricula currently in development, are available on *github*[5][6]. SciServer's latest release (v2.0.0; Betelgeuse) in July 2018 solidifies the team's commitment to classroom use, via the introduction on classroom-friendly features. Educators can now easily set up a classroom in SciServer Compute[7] for each of their classes using the new group sharing capabilities. A customizable Jupyter notebook is also available to automate setting up a user space, group configuration, and sharing privileges for a class. These features allow for the easy set-up and sharing of a library of notebooks with a course or workshop, along with the ability to add or modify notebooks as needed during a course.

2.3. Plates for Education

Millions of SDSS spectroscopic observations have been acquired to date using tens of thousands of aluminum plates. Each plate has as many as 1000 fiber-optic cables plugged to transmit light from astronomical sources captured by the telescope to the spectrographs. Each plate is custom-designed to correspond to objects that are visible in a specific area of the sky at a certain time of night for optimal observation. Once the affiliated observations are complete, the plates are retired. In 2015, the SDSS began distributing the growing number of retired plates to educators through *Plates for Education* workshops. Attending educators each receive a plate and a poster of matching scale, which shows either a single filter image from the SDSS or a 2MASS image of the unique region of the affiliated with the plate (an example is shown in Fig 2). Supporting exercises hosted on *Voyages* offer ways for students to explore the images and spectra corresponding to objects on each plate in greater depth.

The distribution of retired plates is typically conducted by astronomers at SDSS partner institutions, who host plate workshops for educators in their local communities. Workshops have also been held in affiliation with SDSS collaboration meetings and at meetings of professional societies. Through these workshops

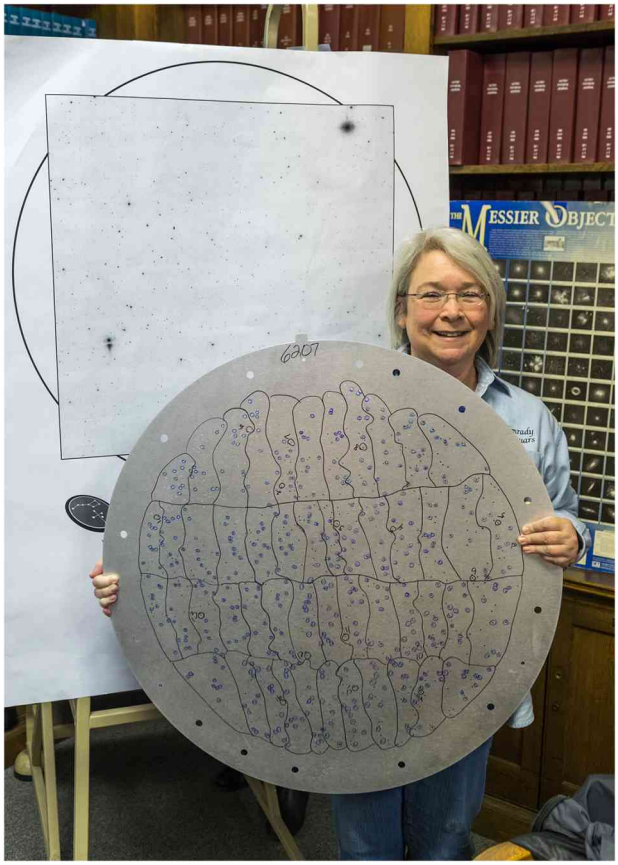

Figure 2: Chicago-area teacher and SDSS-IV pre-college educational consultant Peggy Piper stands with a retired SDSS plate and its accompanying poster, two of the primary resources distributed to teachers as part of the SDSS-IV Plates for Education Program.

teachers and informal educators are connected with mentors in the SDSS, who can provide further assistance with using the plate and associated SkyServer tools.

A new Scottish-based plate distribution program led by the University of St Andrews is also being undertaken to train secondary science teachers to use SDSS educational activities, data, and science in their classrooms. Retired plates and associated materials are being made available for lending in libraries across Scotland. Special training sessions are also being organized to help increase teacher confidence in specialist subjects and concepts. The program aims to promote engagement in science, and astronomy in particular, by giving students a backdrop of exciting activities, built around the engineering concept of the SDSS plates.

To date, plate distribution has occurred in the United States and Europe, and efforts are underway to begin distributing APOGEE-2S plates in South America after they are retired from Las Campanas Observatory. A survey of thirty-seven U.S.-based plate recipients in 2017 indicated that over ninety-five percent of respondents had used the plate in an education lesson using SDSS data and that the lessons were effective in connecting the SkyServer resources with the survey's engineering concepts and data collection methods. An equal

[5] https://github.com/brittlundgren/SDSS-EPO
[6] https://github.com/ritatojeiro/SDSSEPO
[7] https://apps.sciserver.org/compute/

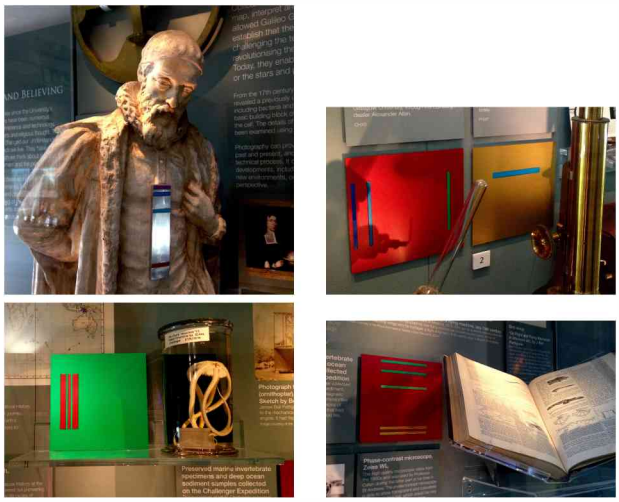

Figure 3: Examples of artwork inspired by SDSS spectra, from the exhibit 'Code for Everything' (2018) in the Museum of the University of St Andrews, by SDSS artist in residence Tim Fitzpatrick. For this exhibit, the artwork was embedded within the permanent collection of the museum. Image credit: T. Fitzpatrick.

number of respondents said the program was a useful engagement tool and effective in generating student questions. Most respondents also planned to continue to use the plate in the future.

3. Collaborations with Artists

Collaborations between scientists and artists can be a fruitful means for reaching new audiences that traditionally have not been engaged with science and technology. Art and music offer new ways to explore complex scientific data and concepts, and provide a different context for audiences to learn more about the underlying ideas.

The SDSS has inspired a number of artists to design artwork around its scientific ideas and data collection; examples include *Transient Objects* by British artist, Xavier Poultney (exhibited in Prague in 2014), *The Universe* by Chinese artist Jian Yan (exhibited in Beijing, 2016) and SDSS plates incorporated into artwork by US artists Adrienne Outlaw (exhibited in Nashville, 2015) and Sarah Ruether (exhibited in Seattle, 2014).[8]

As of 2017, the SDSS has an official artist in residence, Tim Fitzpatrick. Tim Fitzpatrick is based in Scotland and works with astronomers at the University of St Andrews on the *Shine* project:[9] exploring light through science, music and art. His work based on SDSS spectra has been on display in the UK in St Andrews, Dundee, Hull and Oxford, and was presented at the Sharing One Sky conference in Santiago, Chile, in 2017. Currently Fitzpatrick is preparing SDSS art for the Las Cruces Space Festival in New Mexico (which will feature a visit to the SDSS Telescope at Apache Point Observatory) and is developing an SDSS collaboration-

[8]For more examples see: `https://blog.sdss.org/2014/09/19/sdss-plates/`

[9]`http://shine.wp.st-andrews.ac.uk/`

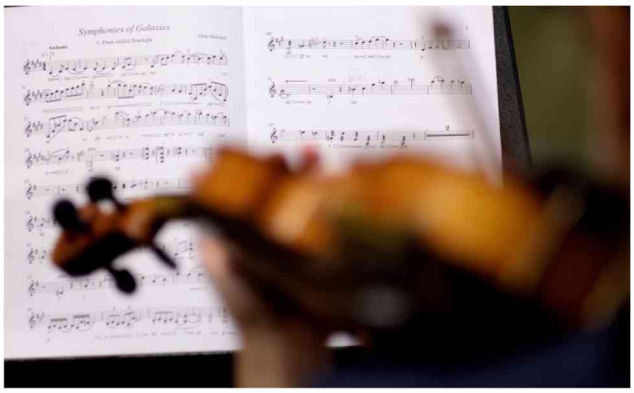

Figure 4: First rehearsal of the MaNGA Galaxy Symphonies by Scottish composer Eddie McGuire. The piece was performed in St Andrews by the New Music Ensemble of the Music Centre at the University of St Andrews, under direction of Bede Williams. Image credit: T. Fitzpatrick.

wide art project around the periodic table. Examples of his spectra inspired work are shown in Fig. 3.

As part of *Shine*, and to celebrate the International Year of Light 2015, the School of Physics and Astronomy at the University of St Andrews commissioned Glasgow-based composer Eddie McGuire to write a short musical piece on galaxies. McGuire composed the 15 minute suite 'MaNGA Symphonies of Galaxies' (see Fig. 4), which was premiered in November 2015 in St Andrews. Since then, the music has also been performed in Antofagasta as part of the Chilean National Astronomy Meeting 2016. A description of this work and its first performance is given by (Williams et al., 2016), and the work is available for hire in the Scottish Music Library.

4. Sharing One Sky

The conference series *Sharing One Sky: SDSS, APOGEE, and Astronomy Outreach*, now planning for its third gathering, was initiated to promote public dissemination of SDSS science (APOGEE in particular) and foster the sharing of methods for education and public outreach with special attention on cross-cultural exchange, particularly within and across Latin America. Given APOGEE's strong presence in Chile, the *Sharing One Sky* meetings have all been held there, and have included a special, though not exclusive, emphasis on astronomy outreach within the Chilean community, with participants from all levels of Chilean STEM education. Begun with contributing funds from the University of Virginia's Center for Global Inquiry & Innovation and the Universidad de Valparaíso, *Sharing One Sky* seeks to bridge the language gap between North and South America and provide contributing partners with new ideas for teaching astronomy to school-age children as well as the general public.

The first *Sharing One Sky* meeting took place in Viña del Mar in May 2016, and was attended by an international complement of approximately 40 scientists, undergraduate and graduate students, museum curators, members of the press, and school teachers. The main Chilean astronomical institutions were

Figure 5: SDSS-IV observer Katie Grabowski introduces some newly drilled spectroscopic plug plates for the APOGEE-2 South survey at the 2017 *Sharing One Sky II* conference in Santiago, Chile.

represented: the Millennium Institute of Astrophysics (MAS), CONICYT and the *CONICYT Explora* program[10], the Interactive Mirador Museum (MIM), the Planetarium of Santiago, and all Chilean universities with astronomy programs. Presentations were largely given in English, but translators were on hand to facilitate Spanish-speaking presenters and audience members. The event was reported on by Chilean radio, with various participants contributing interviews.

In addition to scientific talks and demonstrations, the Viña del Mar meeting promoted discussions of a great diversity of outreach methods and techniques, and participants shared their experiences and best practices for communicating science results with secondary-level students and the general public. Members of the SDSS demonstrated various outreach methods and materials that the survey has produced. Astronomy outreach performed by students was a highlight of the meeting. Three examples include Chilean undergraduate students who showcased the primary and secondary school outreach activities of *Bling Bling Universe*[11], which include content provided by the SDSS; the creators of the *Star Tres*[12] program, run by Chilean native astronomy graduate students studying in Europe, who discussed their blog and social media initiatives to engage members of the public, particularly school-aged children; and representatives of the graduate student run *Dark Skies, Bright Kids*[13] program from the University of Virginia, which has been developing bilingual English/Spanish language astronomy materials for use in the United States.

Sharing One Sky II took place on the campus of the Pontifical Catholic University of Chile in July 2017. It was held in conjunction with the SDSS-IV collaboration meeting, and included special talks and a training course aimed at educators interested in including SDSS activities in high school and undergraduate curricula. The SDSS artist-in-residence Tim Fitzpatrick (discussed above in Section 3.) also attended and showcased artwork he created around the idea of atomic spectra.

Sharing One Sky III, which is scheduled for November 2019 in Antofagasta, Chile, will be the third convening of the conference series. It will continue the mission of bringing together SDSS astronomers and educators from English- and Spanish-speaking countries to share their work and promote bilingual collaborations. A natural continuation of the series, the meeting will include a special section for educators connected with astronomical tourism in the region as well as a workshop focused on astronomy outreach for the blind and visually impaired using three-dimensional printed galaxies from *Tactile Universe*[14] (Bonne et al., 2018) as part of the *AstroBVI* initiative[15] in South America.

5. Summary and Future Work

For nearly two decades the SDSS has been promoting public engagement with SDSS data through the development of freely accessible educational resources, workshops, and arts programming. SDSS E/PO resources continue to be developed, modified, and translated, in order to meet the evolving needs of a diverse and international community of astronomy educators, students, and interested members of the public. Future work by the SDSS E/PO group will seek to better evaluate the impact of these activities in all of the diverse settings they aim to reach.

Acknowledgements: Funding for the Sloan Digital Sky Survey IV has been provided by the Alfred P. Sloan Foundation, the U.S. Department of Energy Office of Science, and the Participating Institutions. SDSS acknowledges support and resources from the Center for High-Performance Computing at the University of Utah. The SDSS web site is `www.sdss.org`.

SDSS is managed by the Astrophysical Research Consortium for the Participating Institutions of the SDSS Collaboration including the Brazilian Participation Group, the Carnegie Institution for Science, Carnegie Mellon University, the Chilean Participation Group, the French Participation Group, Harvard-Smithsonian Center for Astrophysics, Instituto de Astrofísica de Canarias, The Johns Hopkins University, Kavli Institute for the Physics and Mathematics of the Universe (IPMU) / University of Tokyo, the Korean Participation Group, Lawrence Berkeley National Laboratory, Leibniz Institut für Astrophysik Potsdam (AIP), Max-Planck-Institut für Astronomie (MPIA Heidelberg), Max-Planck-Institut für Astrophysik (MPA Garching), Max-Planck-Institut für Extraterrestrische Physik (MPE), National Astronomical Observatories of China, New Mexico State University, New York University, University of Notre Dame, Observatório Nacional / MCTI, The Ohio State University, Pennsylvania State University, Shanghai Astronomical Observatory, United Kingdom Participation Group, Universidad Nacional Autónoma de México, University of Arizona, University of Colorado Boulder, University of Oxford, University of Portsmouth, University of Utah, University of Virginia, University of Washington, University of Wisconsin, Vanderbilt University, and Yale University.

Sharing One Sky is partially supported by the Ministry for the Economy, Development and Tourism, Programa Iniciativa Cientica Milenio grant IC120009, awarded to the Millennium Institute

[10] `https://www.explora.cl`
[11] `https://bbu.cl`
[12] `http://www.startres.net`
[13] `http://http://faculty.virginia.edu/DSBK/`
[14] `https://tactileuniverse.org/`
[15] `https://astrobvi.org/`

of Astrophysics (MAS), the Universidad de Valparaiso, Chile, and a Global Research Program of Distinction grant from the Center for Global Inquiry & Innovation of the University of Virginia to SRM.

References

Blanton M. R., et al., 2017, AJ, 154, 28
Bonne N. J., et al., 2018, Astronomy and Geophysics, 59, 1.30
Chen C., Zhang J., Vogeley M. S., 2009, IEEE Intelligent Systems, 24, 74
Lintott C., et al., 2011, Monthly Notices of the Royal Astronomical Society, 410, 166
Nagda B., et al., 1998, The Review of Higher Education, 22, 55
Russell S. H., Hancock M. P., McCullough J., 2007, Science, 316, 548
Williams B., et al., 2016, Scottish Journal of Performance, 3, 59
York D. G., SDSS Collaboration 2000, AJ, 120, 1579

AstroBVI: An Astronomical educational kit for the Blind and Vision Impaired community in Latin America

M. Argudo-Fernández[1], J.P. Colque-Saavedra[1], E. Unda-Sanzana[1], M. Boquien[1] & M. Longa-Peña[1]

[1] *Center of Astronomy, CITEVA, University of Antofagasta, Chile*

Contact / maria.argudo@uantof.cl

Resumen / AstroBVI es un proyecto de Astronomía inclusiva financiado por la Oficina de la Astronomía para el Desarrollo de la Unión Astronómica Internacional (IAU–OAD). BVI responde a las siglas en inglés de la comunidad formada por personas con discapacidad visual (*Blind and Visually Impaired*), quienes a menudo se ven excluidas de las actividades educativas y de divulgación en relación a áreas de conocimiento visualmente intensivas, como en el caso de la Astronomía. Con este proyecto queremos ayudar a derribar las barreras entre la ciencia y la discapacidad, para llevar la belleza de la Astronomía a un público con discapacidad visual, independientemente de su género, su riqueza y su estatus social. En AstroBVI estamos creando y distribuyendo *kits* educativos compuestos por mapas táctiles de galaxias en 3D acompañados por un manual y material multimedia es Español y Portugués. El proyecto se desarrolla desde el Centro de Astronomía de la Universidad de Antofagasta, en colaboración con un equipo de 20 colaboradores internacionales, incluyendo astrónomos profesionales y especialistas en educación inclusiva.

Abstract / AstroBVI is an inclusion Astronomy project funded by the Office of Astronomy for Development of the International Astronomy Union (IAU–OAD). BVI responds to the Blind and Visually Impaired community, which are often excluded from outreach and educational activities in relation to visually-intensive areas of knowledge such as astronomy. In this project we aim at breaking down the barriers between science and disability, to bring astronomy's beauty to a visually-impaired public, independently of gender, wealth, and social status. We are creating and distributing educational kits composed of tactile 3D maps of galaxies accompanied by a manual and multimedia material n Spanish and Portuguese. The project core team is based in the Astronomy Center of the University of Antofagasta, with a team of 20 international collaborators, including professional astronomers and specialists on education and inclusion.

Keywords / miscellaneous — galaxies: general

1. Introduction

The World Health Organization (WHO) estimated 285 million people are visually impaired worldwide (2014*). In spite of this large number, Blind and Visually Impaired (BVI) people are often excluded from outreach and educational activities in relation to visually-intensive areas of knowledge such as astronomy.

There are many astronomy educational resources at all levels in the web. However, the great majority are written in English. It is far less common to find resources in the dominant languages of South America, such as Spanish or Portuguese. Even fewer are specifically oriented and designed for the BVI community, where "blindness affects between 1 % and 4 % of the population of Latin American countries" (IAPB**), making it extremely difficult for BVI populations in the target region to get introduced to the wonders of the sky.

In AstroBVI***, we aim to make astronomy in general, and galaxies in particular, more accessible to children with visual impairments. We have created an educational kit composed of tactile 3D maps of galaxies accompanied by a manual and multimedia material, to be distributed to many countries in Latin America.

With this kit, we want to complement the few existing astronomical education kits in Spanish (including Portuguese), and also address the challenge on being able to bring knowledge on more complex concepts as galaxies, star formation, and electromagnetic spectrum.

2. The AstroBVI project

AstroBVI is one of the 16 projects selected to receive funding in 2018 by the IAU-Office of Astronomy for Development's (OAD) sixth annual call for proposals****, within the Task Force-2: Astronomy for Schools and Children.

Our aim is to design, create and share an astronomical educational kit (accompanying with the conception and realization of an international online workshop) that will benefit from the experience learned during past complementary OAD-funded projects, such as "Touch of

*http://www.who.int/gho/publications/world_health_statistics/2014/en/

**https://www.iapb.org/

***www.AstroBVI.org

****https://www.iau.org/news/announcements/detail/ann18003/

the Universe"* and "Astronomy with all Senses"**, and in collaboration with the "Tactile Universe"*** team, which has started to run astronomy outreach activities with the Portsmouth BVI Community, and the Galileo Teachers Training Program (GTTP****).

Chile, considered as the World Capital of Astronomy, benefits from a strong, well-established outreach program. The core team is located in the Center of Astronomy of the University of Antofagasta, in Antofagasta, which is the largest city in Northern Chile. The weather conditions in this region provide a unique quality for astronomical observations. Some of the most important observatories are located in the region, as ALMA and VLT. From this region, in close collaboration with astronomers over the world, we provide a fertile starting ground to grow and extend the understanding of the sky to children, students, and general public with vision difficulties, not only in Chile but also in Latin America. Overall, we aim at reaching no limits in research in astronomy, only the desire to learn, to feed curiosity and scientific thinking, where no child feels limited to do what they are passionate about, and promoting engaging with family, friends, teachers, and other support workers. With this aim, our team is composed of 20 collaborators located worldwide, from professional astronomers and outreach coordinators, to education specialists, on working with people with disabilities and risk for social exclusion.

3. The AstroBVI kit

All we know about galaxies so far is due to the study of the light that comes from them. But how can we bring these concepts to the BVI community?

The AstroBVI educational kit is made up of 3D tactile maps of different galaxies and different wavelengths (colors). In this regard, collaboration with the Tactile Universe team is central to the project. They have developed 3D galaxy maps, in consultation with a BVI group, and started activities to engage the BVI community in the UK. They proved that plastic tactile maps offer good cognition and excellent perception by visually impaired people (Bonne et al., 2018). We draw on their experience and work closely with them to incorporate their resources in our project. What we do is therefore transform images of galaxies from the Digitized Sky Survey (DSS Springob et al., 2007) in fits format into a format that can be read by 3D printers. So we can print galaxies!

The sample of galaxies composing the AstroBVI kit has been selected according to morphology and the experience in previous activities developed by the Tactile Universe team. The AstroBVI kit is therefore composed of tactile images of the following galaxies:

M100: a face-on spiral galaxy, observed in the photometric B-band,

M109: an inclined spiral barred galaxy, observed in the B-band,

M51: a face-on merger galaxy composed of a spiral and an elliptical galaxy, observed in the R- and the B-band,

M105: an elliptical galaxy, observed in the R-band, and

NGC5866: a lenticular galaxy, observed in the R-band.

The kit is complemented with the DSS images of the galaxies used to create the tactile maps, colored images of the galaxies, a guide to help to touch each galaxy (text and audio formats), lessons for the AstroBVI teachers, and a video-manual* of the use of the kit. All multimedia material will be hosted in the web of the project (`www.astroBVI.org`) and available in Spanish and Portuguese. The galaxy models will be also available under a creative commons (CC BY-NC-ND 3.0) license.

The AstroBVI kit was successfully tested in an activity carried out in the University of Antofagasta, in collaboration with the *Programa de Integración Escolar* (PIE**) of the Corporación *Municipal de Desarrollo Social* (CMDS***) of Antofagasta. The AstroBVI kit is also part of "Spiring Stars"****, a world exhibition on Accessible Astronomy organized by the IAU (see Fig. 1). AstroBVI participated as part of "Astronomy for All"†, a cooperation of Chilean astronomical institutions helping to bring astronomy to everyone in an accessible way.

4. The AstroBVI teachers

Our project would be meaningless without the AstroBVI teachers. We made use of the social media (facebook‡ and twitter§ accounts), to make a global call for educators working with BVI students (with and without Astronomy knowledge), and astronomers, science communicators, and outreach coordinators developing public activities with the BVI community, or willing to include them in their activities.

We have received more than 120 applications from many Latin American countries, but also from Spain and Nepal (see Fig. 2). At the present time, with the available funding from the IAU-OAD and some external funding from collaborators of the project, we have selected 100 AstroBVI teachers to receive a kit. Since the selected AstroBVI teachers come from different background, we have invited them to participate in an international online workshop in early 2019. In this workshop, the AstroBVI team and collaborators will offer capacity building by training teachers and educators working with the BVI community in the different countries. We are working with the GTTP team to provide GTTP certification. AstroBVI teachers are also invited to join

*https://astrokit.uv.es

**ttp://www.astro4dev.org/blog/category/tf3/astronomy-with-all-senses

***https://tactileuniverse.org

****http://galileoteachers.org

*https://youtu.be/fLFJ-KcV7dQ

**http://www.cmds.cl/pie/

***http://www.cmds.cl/

****https://sites.google.com/oao.iau.org/inspiringstars/

†http://astronomia.udp.cl/chilean-accessible-astronomy-on-iau-inspiring-stars-exhibitio

‡https://www.facebook.com/AstroBVI/

§https://twitter.com/AstroBVIproject


ASTROBVI
AN ASTRONOMICAL EDUCATIONAL KIT FOR THE BLIND
AND VISION IMPAIRED (BVI) COMMUNITY IN SOUTH AMERICA

Producciones audiovisuales Planetario Ciudad de La Plata "El camino eterno. En búsqueda del cielo estrellado."

C. Peri[1], P. Santamaría[1], D. Bagú[1] & M. Schwartz[1]

[1] *Planetario Ciudad de La Plata, Facultad de Ciencias Astronómicas y Geofísicas, UNLP, Argentina*

Contacto / cperi@fcaglp.unlp.edu.ar

Resumen / El Planetario Ciudad de La Plata es un proyecto de la Facultad de Ciencias Astronómicas y Geofísicas, de la UNLP. Es un centro de divulgación y extensión universitaria: un punto de contacto entre la ciencia y la sociedad. El Planetario se encuentra entre los más modernos de Latinoamérica. Además de una gran cantidad de variadas actividades, en los últimos cuatro años desarrollamos producciones audiovisuales, volviéndose ello un área fundamental. Hemos producido desde cortos hasta largometrajes, y actualmente somos un nuevo referente internacional en producción *fulldome*. En este trabajo haremos un breve repaso de nuestro camino recorrido en producción, y daremos especial atención a nuestra última gran producción, "El camino eterno. En búsqueda del cielo estrellado".

Abstract / The Planetario Ciudad de La Plata is a project of the School of Astronomical and Geophysical Sciences of the UNLP. Its main goal is to be an outreach center, thus serving as a contact point between science and society. This digital planetarium is one of the most modern in Latin America. We have developed a huge amount of activities since 2014, and the audiovisual production had become a main area in our Institution. We have done from short to long movies, and using animation, live action, timelapses techniques, among others. Planetario Ciudad de La Plata is now recognized as a producer house internationally. We will show a brief summary of our productions, and give special attention to "El camino eterno. En búsqueda del cielo estrellado.".

Keywords / miscellaneous — sociology of astronomy

1. Introducción

La Universidad Nacional de La Plata es una de las más grandes de nuestro país. Durante 2008, junto a la Universidad de Buenos Aires y la Universidad Nacional de Córdoba, ha entrado en la lista de las mil mejores universidades del mundo. En su reforma estatutaria de 2008, se plantea una jerarquización de la extensión, volviéndose ésta uno de los tres pilares fundamentales de la institución, sumado a la enseñanza y la investigación.

Dentro de la Universidad, la Facultad de Ciencias Astronómicas y Geofísicas se halla entre los referentes en tradición de extensión y divulgación de las ciencias. En el año 2001 se instauró formalmente la Secretaría de Extensión de la Facultad, y desde entonces las actividades y personal dedicado han crecido de forma exponencial, fortaleciendo aún más la historia de este área.

Las actividades de extensión son: visitas al público general, visitas escolares y de grupos, observaciones astronómicas, conferencias abiertas, eventos especiales, talleres, cursos y proyectos, entre otras. En el año 2013, luego de años de gestión por parte de la Facultad y Universidad, y gracias a fondos públicos provenientes de la Provincia de Buenos Aires y la Nación, la Facultad de Ciencias Astronómicas inaugura el Planetario Ciudad de La Plata. Este hecho marcó un punto de inflexión en la extensión de la Facultad.

2. Planetario: un desafío

El Planetario Ciudad de la Plata (PCLP) ha sido concebido no sólo como un centro de divulgación científica, sino también como un lugar de encuentro e interacción de las múltiples disciplinas que se desarrollan en la Universidad Nacional de La Plata. Ello se ve reflejado en su lema: "Ciencia, Arte y Tecnología."

Bajo su domo de 17 metros de diámetro, las proyecciones digitales con resolución 4K transmiten a sus 175 espectadores una increíble sensación inmersiva, convirtiéndolo en un verdadero y maravilloso teatro de ciencia, arte y tecnología (Fig. 1).

Para la Secretaría de Extensión, la Facultad, y la Universidad misma, el hecho de contar con un planetario digital no sólo representaba una oportunidad única, sino también un gran desafío. El PCLP, en 2013, se convertía en el tercer planetario digital de Argentina, y más aún, el primer planetario universitario, con todas sus actividades gratuitas (Bagú et al., 2016).

2.1. Cómo llegar al público

Como un espacio de educación no formal, uno de los objetivos del planetario, tal como lo concebimos desde la gestión actual (2014-actualidad), es que el espectador reciba un estímulo sensorial inolvidable con el propósito de generar la curiosidad necesaria para indagar y/o profundizar acerca de la experiencia. Dicha concepción

abreva de una posición constructivista del aprendizaje: el conocimiento es una función de cómo el individuo crea significados a partir de sus vivencias.

Respecto al público, conocíamos *a priori* la existencia de un público cautivo: aquel público apasionado por las ciencias, y en particular por las ciencias astronómicas y de la Tierra. Además, existe otro: el público que no se ve atraído naturalmente a estos temas. Ahora bien, ¿de qué otras maneras se puede llegar a más gente? ¿cómo cautivar a un público, de por sí, con menor interés en esos temas? Múltiples áreas fueron exploradas. Realizamos una gran cantidad de eventos en los cuales en muchas oportunidades se combinó algún suceso astronómico o científico con manifestaciones artísticas o de otra índole: bandas en vivo, ilustraciones, proyecciones, presentaciones de libros, y cualquier tipo de agregado artístico-cultural que invitara a todo tipo de público con el fin de hacer llegar la ciencia a su imaginario de cultura general. Explotamos las redes sociales como Facebook, Twitter, Youtube, Instagram, más la existencia de un sitio web propio*. Sumado a ello, invitamos al público a disfrutar de realidad aumentada en el hall del PCLP a través de una aplicación llamada Planetario UNLP. En un futuro próximo, inauguraremos experiencias interactivas en el hall y asistencia presencial en hall y domo.

Habiéndose convertido en un nodo cultural de la ciudad platense, el PCLP constituye un lugar único, tanto por su impacto sensorial, como así también por lo original de sus propuestas (Santamaría et al., 2017a).

3. Producciones audiovisuales fulldome

Desde sus origenes, los planetarios se concibieron como instalaciones edilicias que permitían proyectar, sobre la parte interna de sus domos, el cielo estrellado tal como lo vería un observador en algún lugar del planeta y a una hora determinada. Cuando en la década de 1990 la tecnología implementada en los planetarios cambió de los proyectores optométricos a la proyección digital se pudo pasar de sólo proyectar puntos de luz sobre un fondo negro a proyectar cualquier tipo de imágenes en 180 grados sobre la superficie del domo. Este nuevo formato audiovisual, conocido como *fulldome*, es entonces capaz de generar entornos verdaderamente inmersivos sobre el domo, los cuales pueden desarrollarse en tiempo real o haber sido preparados con animaciones por computadora, imágenes reales, o fotocomposición.

Nuestra meta respecto a la producción *fulldome*, desde la gestión actual, es la de generar contenidos propios. Si bien existe un mercado internacional de contenidos digitales para planetarios, el hecho de producir contenidos propios nos ofrece varias ventajas. Por un lado, poder elegir los contenidos nos permite promocionar la ciencia local. En nuestro país y en el mundo se conoce mucho de proyectos internacionales o que poseen gran financiación y recursos humanos, pero a la hora de difundir la ciencia e historia nacional, incluso latinoamericana, queda un largo camino por recorrer. Por otra parte, nuestro planetario pertenece a una Facultad de ciencias. Ésto hace posible que sus científicos y docentes participen de las producciones y aporten conocimiento académico veraz. Por último, la producción propia fomenta la formación y colaboración de artistas y profesionales audiovisuales locales para este novedoso formato *fulldome*, lo que le da una gran calidad audiovisual a los productos.

Figura 1: Imagen del interior del domo del PCLP.

Los tipos de productos audiovisuales que hemos generado fueron varios: visitas escolares, cortometrajes disparadores que involucran conceptos relacionados a la astronomía y las ciencias en general, soporte a las cátedras y largometrajes. Con respecto a productos de terceros (gratuitos), hemos realizado traducciones y adaptaciones.

La formación en producción comenzó con la generación de cortometrajes. Las prestaciones del sistema propio del planetario (software Digistar, Evans&Sutherland), más el agregado paulatino de otros recursos audiovisuales, fortaleció las aptitudes y posibilidades del área audiovisual.

3.1. Largometrajes

La primera experiencia de PCLP con adaptación al formato *fulldome* y ambientación con música original, creada por compositoras de la UNLP, fue la clásica película de George Méliès "Viaje a la Luna", de 1912.

"Luminaciones" fue la primera producción audiovisual original del PCLP, e incluyó el desarrolo de imagen, música, guión y sonido. Este proyecto fue realizado junto al colectivo de artistas El sueño de los elefantes.

"Belisario, el pequeño gran héroe del cosmos", es nuestro proyecto emblema. Fue realizado en coproducción con Celeste Estudio Creativo y Cut to the chase gracias al financiamiento del Centro Tecnológico Aeroespacial de la Facultad de Ingeniería de UNLP y nuestra propia Facultad. Esta película *fulldome* es el piloto de una serie animada; su desarrollo incluyó desde la preproducción, guión original, creación de personajes, música original, y diseño de sonido. Se estrenó en mayo de 2017, y durante más de cien funciones sostuvo su público a sala llena. Belisario nació como un proyecto transmedia, por lo cual además del producto *fulldome*, se encuentran en desarrollo una serie de productos derivados que

*http://planetario.unlp.edu.ar/

completan la historia: revista, videojuego, página web, microrrelatos en realidad virtual, etc. Este ensamble de formatos es lo que se conoce como narrativa transmedia (Santamaría et al., 2017b).

"El universo de tu imaginación", destinado al público infantil de 0 a 6 años, pretende incentivar la curiosidad y el interés natural que muestran los niños de edad temprana para desarrollar la capacidad de observación del mundo que los rodea. El proyecto es producido por nuestro planetario en conjunto con el cantautor Hugo Figueras y su equipo. Desde su estreno en julio de 2018, ha demostrado ser un gran éxito para los más pequeños.

"El camino eterno. En búsqueda del cielo estrellado", es una película documental producida por el Planetario Ciudad de La Plata, en coproducción con Cut to the Chase. Su estreno vio la luz en abril de 2018, y sigue siendo fuente de emoción y reflexión para los adultos (Fig. 2). Los guaraníes identifican a la Vía Láctea con el camino recorrido por los primeros habitantes que llegaron a la Tierra, y por el cual regresarán los hombres a su origen, los confines del Cosmos. La bautizaron "Tapé-cué", el "camino eterno", de allí el título de nuestra película. La película cuenta la historia de un astrofotógrafo que busca la foto perfecta del cielo estrellado. Para ello deberá alejarse de las luces urbanas, viajar hacia cielos limpios. Su ruta estará trazada por los lugares de Argentina en donde están emplazados los instrumentos por excelencia para investigar el cielo: los telescopios de los observatorios astronómicos. Pronto descubrirá que su pasión por la noche estrellada es un viaje colectivo que involucra no sólo a investigadores, sino también a ingenieros, informáticos, mecánicos y mucho más personal para tomar imágenes del cielo. Este argumento nos sirve como pretexto perfecto para contar la historia, el presente, y el futuro de la Astronomía Óptica Argentina, y recorrer los sitios que albergan institutos, Facultades y observatorios: Córdoba, La Plata, San Juan y Buenos Aires. El trabajo de diseño de producción de esta película siguió la estructura más típica de filmación tradicional: etapa de preproducción, rodaje, y postproducción. El documental utiliza registros tomados *insitu* y el cielo es fotografiado a través de la técnica de cámara rápida (en inglés, *timelapse*). Una voz en *off* nos acompaña relatando la historia. "El camino eterno" tiene una versión *fulldome* para planetarios digitales, y una versión para medios tradicionales (cine, televisión), aún a estrenarse durante 2019.

Como complemento de la película, y siguiendo el concepto de transmedia, el día del estreno se inauguró la muestra fotográfica "El camino eterno CAPTURADO". En ella se mostró el camino de búsqueda de la foto perfecta del cielo estrellado a través de frases del guión de la película. Se expuso el detrás de escena de la filmación del documental, la contaminación lumínica de sitios muy poblados, y el cielo nocturno claramente despejado de los sitios de observación.

Durante el rodaje de la película se generó una gran cantidad de material audiovisual que incluye entrevistas a más de 60 personas, las cuales se integrarán en una serie original en formato web, a ser estrenada durante 2019. En la serie se abordarán temas que se tocan sólo tangencialmente en "El camino eterno": el día a día en cada institución, la pasión por la Astronomía, las implicancias de trabajar en la montaña, y muchas situaciones que en general, en los documentales de ciencia, no son tenidas en cuenta. Además, conoceremos en primera persona la gente que sostiene cada sitio particular.

Figura 2: Poster oficial "El camino eterno".

4. Conclusiones

El Planetario Ciudad de La Plata es actualmente un referente en divulgación de las ciencias. Prueba de ello son los diversos medios locales y nacionales que día a día se contactan por diferentes eventos y sucesos.

En materia de producción audiovisual, se han generado productos de varios tipos para cubrir distintas necesidades: cortos, visitas escolares, apoyo a las cátedras y largometrajes. Gracias a esto, el PCLP posee renombre nacional e internacional como productor de contenidos. A través de los diversos productos, no sólo se ha realizado divulgación, sino que también se han formado recursos humanos especializados en el tema, y se han generado vínculos con instituciones y personas dentro y fuera de la Facultad, lo cual enriquece la tarea diaria y proyectos futuros.

Referencias

Bagú D., Schwartz M., Santamaría, 2016, Memorias del XI Congreso de Educación en Tecnología y Tecnología en Educación

Santamaría P., et al., 2017a, Memorias del IX Congreso Argentino de Tecnología Espacial.

Santamaría P., et al., 2017b, Libro de memorias 15to. Congreso CONEXIONES RedPOP, 96 100

Computational Astrochemistry: importance, pitfalls and applications

S. Bovino[1], D.R.G. Schleicher[1] & T. Grassi[2]

[1] *Departamento de Astronomía, Universidad de Concepción, Chile,*
[2] *University Observatory Munich Ludwig-Maximilians-University, Germany*

Contact / stefanobovino@astro-udec.cl

Resumen / La astroquímica se encuentra actualmente en su edad de oro gracias a la gran cantidad de datos que proporcionan los telescopios de plato único e interferométricos como APEX y ALMA. Para permitir una mejor comparación y interpretación de los datos de observación, es indispensable hacer un esfuerzo notable también en el aspecto teórico/computacional. Los modelos astroquímicos de última generación son una herramienta poderosa para la interpretación de los datos observacionales y permiten probar las condiciones físicas de las regiones de formación estelar, proporcionando una ventana única para comprender cómo se forman y evolucionan estas regiones. Sin embargo, la inclusión de la microfísica y la química en las simulaciones hidrodinámicas que se basan en la computación requiere información detallada y conocimiento de los procesos químicos básicos. Esto, junto con la amplia gama de escalas espaciales y temporales implicadas en la astrofísica, conduce a un problema computacionalmente costoso. Presentamos aquí las ventajas y los inconvenientes de los modelos astroquímicos y mostramos algunas aplicaciones importantes.

Abstract / Astrochemistry is currently in its golden age thanks to the huge amount of data that single-dish and interferometric telescopes like APEX and ALMA are providing. To allow for a better comparison and interpretation of the observational data it is indispensable to make a noteworthy effort also on the theoretical/computational side. State-of-the-art astrochemical models are a powerful tool for the interpretation of observational signatures and allow to probe the physical conditions of star-forming regions, providing a unique window to understand how these regions are formed and evolved. However, including microphysics and chemistry in computationally intensive hydrodynamical simulations requires detailed information and knowledge of the basic chemical processes. This, together with the wide range of involved spatial and temporal scales in astrophysics, leads to a computationally expensive problem. We introduce here the advantages and pitfalls of astrochemical models, and show some important application.

Keywords / ISM: molecules — hydrodynamics — astrochemistry

1. Introduction

Chemistry is very important for the interpretation of observational data as the entire Universe is permeated by atoms and molecules. The latter are excellent diagnostics of the physical conditions and processes in the regions where they reside, and control the ionization balance, affecting the coupling of magnetic fields to the gas, through important processes like ambipolar diffusion. In addition, molecules are fundamental for the cooling of the gas, which regulates the star formation process.

While observations are very powerful and already provide a lot of information about the observed regions, they only give us a snapshot in time of their evolution. Astrochemical models are then needed to retrieve information on the evolution prior and after the observed stage.

Astrochemistry is a complex multidisciplinary research area, which is now living its golden age in particular thanks to the radio facilities we developed over the last decade. With the advent of ALMA, this discipline has grown exponentially, and has attracted many scientists from different areas, from astrophysicists to biologists. Since its birth, which goes back to fifties with the development of the first astrochemical models (Kramers & Ter Haar, 1946; Bates & Spitzer, 1951), astrochemistry has changed its objectives and has now become an incredible tool to interpret observational data. This is particularly true for Computational Astrochemistry, i.e. the study of how chemical processes affect the dynamics of galaxies, stars and planets formation via hydrodynamical simulations.

In the following sections, we will present the main pitfalls of computational astrochemistry, and some interesting results.

2. The problem

Chemistry *per se* is a complex problem, which involves many different processes. Beyond the standard gas-phase reactions, indeed, in regions where freeze-out surface chemistry could strongly impact the chemical evolution of the gas.

In the simple case where only gas-phase reactions are considered, we have to face with the solution of a system of coupled ordinary differential equations (ODEs) of the

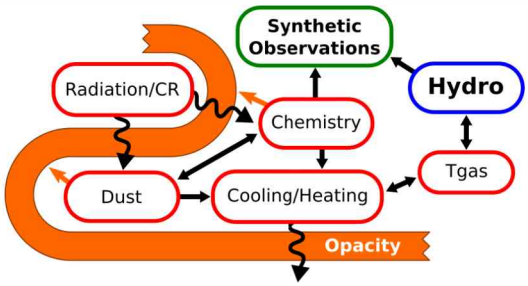

Figure 1: Sketch of chemistry and microphyscis complexity.

following form:

$$\frac{dn_i}{dt} = \overbrace{\sum_{lm} k_{lm}(T) n_l(t) n_m(t)}^{formation} - \overbrace{\sum_{j} k_{ij} n_i(t) n_j(t)}^{destruction} \quad (1)$$

where n_i are the chemical abundances number density, k_{lm} and k_{ij} represent the formation and destruction reaction rate coefficients. The above system is extremely CPU demanding, and requires accurate implicit solvers (Bovino et al., 2013). In addition, to build a chemical network is not an easy task, because the uncertainties affecting the rate coefficients are related to the accuracy of the rates itself, and in most of the cases the rates are not available.

Chemistry is also strongly coupled with other physical processes, very interconnected (see Fig. 1), as for instance processes involving radiation, dust-grain physics/chemistry, and in particular the thermal processes, i.e. cooling and heating. When the latter processes are included the system reported in eq. 1 should include the rate change of the temperature in time:

$$\frac{dT}{dt} = \frac{\gamma - 1}{k_B \sum_i n_i} (\Gamma(n,T) - \Lambda(n,T)) \quad (2)$$

with $\Gamma(n,T)$ and $\Lambda(n,T)$ being the cooling and the heating functions in erg cm^{-3} s^{-1}, γ the adiabatic index, and k_B the Boltzmann's constant. For an overview of different cooling and heating functions see Grassi et al. (2014); Bovino et al. (2016).

As already mentioned in the Introduction, computational astrochemistry is that branch of Astrochemistry which refers to the solution of chemical models necessary to interpret observations. However, models can go from very simple single-zone, which only provide qualitatively results to more complex ones. While the dimension of the problem increases, the chemistry becomes more and more computationally expensive as it should be solved many times, and for many different time-step. Three-dimensional hydrodynamics simulations suffer memory problems because of the huge amount of data that should be stored over the entire time domain. For this reason coupling the chemistry with the hydrodynamics has been, for a very long time, an off limit topic. Furthermore, the chemistry included in hydrodynamical simulations has been kept very simple, with a few species, and some tens of reactions.

With the development of larger and more powerful supercomputing centers it is nowadays possible to include comprehensive chemical networks, and the necessary microphysics to accurately follow the evolution of the gas in complex simulations (e.g. Glover et al., 2010; Körtgen et al., 2018).

Chemistry couples with hydrodynamics through the energy equation as a source term. Two of the prevailing problems when coupling chemistry and hydrodynamics are i) the adiabatic index (γ), and ii) the mean molecular weight (μ). The first is strongly dependent on the chemical composition of the gas while the second is used to convert pressure $\rightarrow$ energy $\rightarrow$ temperature. In adaptive mesh refinement codes for instance multi-fluid advection and conservation of abundances could provide problems if not handled in the correct way (e.g. loss of chemical flux).

2.1. The package Krome

To alleviate the problem to couple hydrodynamical codes with chemistry, chemical packages have been developed (e.g. Smith et al., 2017). Unfortunately, these codes are still limited to very few and simple species/reactions, and are not prepared to properly describe the chemistry/microphysics in complex environment like galaxies and star-forming regions.

In Grassi et al. (2014), we have presented the package KROME, which is optimised to be included in hydrodynamics codes, and contains a lot of processes. In the last four years, KROME has been employed in several works, exploring a variety of astrophysical problems and conditions. This allows people to avoid a series of typical problems when employing chemistry in simulations, as for instance the environment-dependent assumptions, or the use of numerically unstable solvers.

3. Chemistry in Hydrodynamics: results

Some of the results obtained with KROME, through different hydrodynamical codes are reported in Fig. 2 and Fig. 3, where we show star-forming filaments with deuteration, and a turbulent molecular cloud simulation.

3.1. Star-forming filaments

Deuterium fractionation, i.e. the enrichment of deuterated molecules towards the non deuterated, is considered to be an important chemical tracer of the initial conditions of star-forming regions (Caselli et al., 2003). In highly depleted environments, H_2D^+ is the main ion still available in gas phase. Whether or not H_2D^+ can be used to trace the different evolutionary stages of star-forming regions is not clear. We have recently performed high-resolution three-dimensional MHD simulations of star-forming filaments following deuteration chemistry (Körtgen et al., 2018). We have found that a high-level of deuteration can be reached within one million years, and that dynamical parameters do not strongly affect the results. A typical time-evolution sequence for deuterium enrichment is reported in Fig. 2.

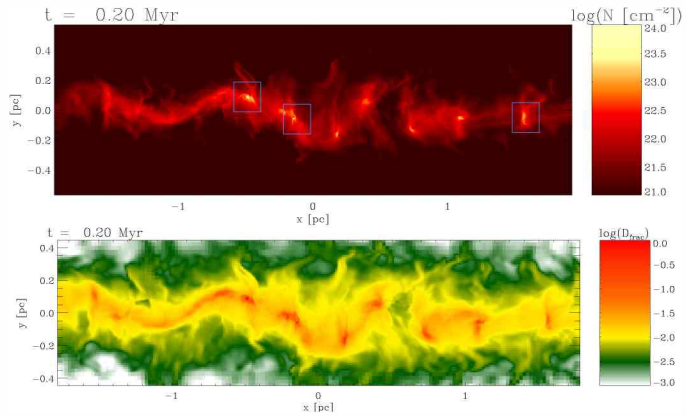

Figure 2: Total column density (top panel) and deuteration (bottom panel). Re-arranged from the collapsing filament simulations of Körtgen et al. (2018). The blue squares represent the most evolved clumps.

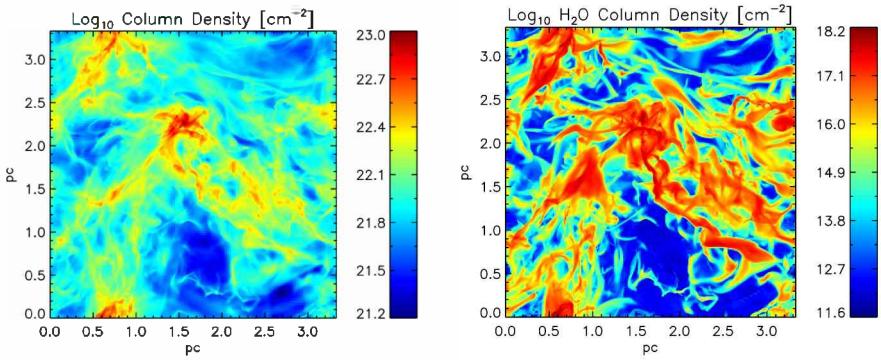

Figure 3: Total column density (left panel) and water column density (right panel), from turbulent molecular cloud simulations. Details of the setup are reported in Grassi et al. (2017); Frostholm et al. (2018).

3.2. Molecular clouds chemistry

In Fig. 3 we report the results of high-resolutions simulations of a molecular cloud patch where we have included a comprehensive H-C-O chemical model. The latter includes 34 species, and 227 reactions and it is an update of the network reported in Glover et al. (2010). We are in particular interested in following CO and H_2O evolution. We employ RAMSES (Teyssier, 2002) to simulate a (3.3 pc)^3 box with an average density of $\rho_0 = 4 \times 10^{-21}$ g cm^{-3}, with an initial magnetic field of 7 μG. A constant cosmic ray flux of 1.3 $\times 10^{-17}$ s^{-1} and a UV interstellar radiation field of 1.69 in units of Habing flux have been used. The initial temperature is set to 20 K. We add six adaptive mesh refinement levels. In Fig. 3 we report the total and the H_2O column density after 5.6 Myr of evolution as plotted from the data of Grassi et al. (2017).

4. Conclusions

We have presented an overview of recent developments of astrochemistry, with particular focus on its computational aspects. The main pitfalls when coupling chemistry with hydrodynamics have been discussed, and the package KROME introduced. Recent results from three-dimensional hydrodynamics simulations have been presented. In particular, results from high-resolution turbulent molecular cloud simulations where we follow a large CO network, and collapsing filaments with deuteration chemistry have been discussed. The results show the importance of including chemistry in hydrodynamics simulations, and the efficiency of doing that via highly optimised packages like KROME.

Acknowledgements: SB and DRGS acknowledge for funds through CONICYT programa de Astronomia Fondo Quimal 2017 QUIMAL170001, and BASAL Centro de Astrofisica y Tecnologias Afines (CATA) AFB-17002. SB is financially supported by Fondecyt Iniciación (project code 11170268), and DRGS by CONICYT Fondecyt regular (project code 1161247) and the international collaboration project PII20150171.

References

Bates D.R., Spitzer Jr. L., 1951, ApJ, 113, 441
Bovino S., et al., 2013, MNRAS, 434, L36
Bovino S., et al., 2016, A&A, 590, A15
Caselli P., et al., 2003, A&A, 403, L37
Frostholm T., Haugbølle T., Grassi T., 2018, ArXiv e-prints
Glover S.C.O., et al., 2010, MNRAS, 404, 2
Grassi T., et al., 2014, MNRAS, 439, 2386
Grassi T., et al., 2017, MNRAS, 466, 1259
Körtgen B., et al., 2018, MNRAS, 478, 95
Kramers H.A., Ter Haar D., 1946, BAN, 10, 137
Smith B.D., et al., 2017, MNRAS, 466, 2217
Teyssier R., 2002, A&A, 385, 337

Astro-acústica para no videntes

J. Retondo[1], G. Londonio[1], L. Medina[1] & R. Girola[1]

[1] *Artes Electrónicas, Universidad Nacional de Tres de Febrero, Buenos Aires, Argentina*

Contacto / rafaelgirola@yahoo.com.ar

Resumen / Este proyecto tiene por objetivo ofrecer a personas no videntes o con capacidades visuales disminuidas, la oportunidad de experimentar el cielo nocturno y sus cuerpos celestes a través del sonido. Para ello se utilizaron datos astronómicos de las veinticinco estrellas más brillantes observadas desde la Tierra, los cuales fueron modelizados con parámetros sonoros mediante síntesis y procesamiento de sonidos: las frecuencias con las magnitudes aparentes y la reverberación con las distancias estelares.

Abstract / The purpose of this project is to offer blind and visually impaired people the opportunity to experience the night sky and its celestial bodies through sound. To do so, astronomical data were used of the twenty-five brightest stars observed from Earth and modelled with sound parameters by synthesis and sound processing: frequencies with apparent magnitudes and reverberations with stellar distances.

Keywords / methods: miscellaneous — stars: fundamental parameters

1. Introducción

La Astronomía es una ciencia de carácter observacional. Es por ello que usualmente se asume que es imprescindible que tanto la comunidad científica como el público general dispongan de una correcta visión, excluyendo a personas con capacidades visuales disminuidas. Estas personas estarían limitadas por la falta de herramientas específicamente desarrolladas.

Para poder superar esta limitación, aquí presentamos una propuesta que hace posible transmitir un dado paisaje celeste mediante la modelización sonora de ciertos parámetros estelares.

Los efectos de sonido que se pueden usar en la traducción de las características generales de las estrellas son el *eco*, la *reverberación* y el *timbre*. La *reverberación* es un fenómeno sonoro producido por la reflexión y que consiste en una ligera permanencia del sonido una vez que la fuente original ha dejado de emitirlo. Cuando el sonido reflejado es inteligible por el ser humano como un segundo sonido, se denomina *eco*, pero cuando es percibido como una adición, modificando el sonido original, se denomina *reverberación* (Miyara, 2004).

Respecto al *timbre*, este no puede analizarse desde un único plano, ya que no tiene necesariamente relación con la fuente sonora sino que es una propiedad de todos los sonidos. Dado que el *timbre* es el resultado de una percepción compleja que surge de la unión de varios planos espacio-temporales (e. g., la envolvente, la sonoridad, la duración, las formantes del sonido y el comportamiento en el tiempo de estas últimas, Miyara, 2004), no es posible considerarlo para nuestra propuesta.

Teniendo esto en cuenta, los parámetros estelares que proponemos interpretar acústicamente son la magnitud aparente, la distancia y la posición respecto al Sol. La magnitud aparente puede ser interpretada como una frecuencia fundamental del sonido, mientras que la distancia y posición se pueden interpretar a través de porcentajes del efecto de *reverberación*. El objetivo es generar una instalación inmersiva donde los sonidos (equivalentes a la magnitud y distancia de las estrellas) provengan de puntos específicos, siendo equivalentes a las posiciones de las estrellas en el cielo. Esta experiencia incluye el uso de altoparlantes para poder direccionar espacialmente las posiciones de las estrellas (respecto de una posición dada) y los respectivos brillos mediante variaciones de frecuencias sonoras (similares al efecto Doppler).

A continuación resumimos los lineamientos generales de nuestra propuesta. En la sección 2. describimos en detalle los aspectos metodológicos, así como también las modelizaciones realizadas. En la sección 3. comentamos las primeras experiencias realizadas. Finalmente presentamos las primeras conclusiones y perspectivas para mejorar el proyecto en la sección 4..

2. Sonorización de parámetros estelares

Para este trabajo se consideraron las 25 estrellas más brillantes del cielo (excluyendo al Sol). La información sobre su distancia, magnitud (aparente y absoluta) y tipo espectral fueron extraídos de Dolan (1989) y se muestran en la Tabla 1, con el fin de generar sonidos de acuerdo a sus características físicas más importantes. Sobre esta población de estrellas realizamos diferentes procesos de normalización de acuerdo a las relaciones presentadas en (Schaeffer, 2008).

En primer lugar normalizamos las distancias a las estrellas a valores entre 0 y 100. Luego se realizó la conversión de todos los valores de la magnitud aparente (A) en números positivos (C) usando la relación:

$$C = A \cdot 100 + B \tag{1}$$

seleccionando un valor de B para que el resultado sea

positivo. De esta forma podemos usar el valor C para establecer una relación directa entre el menor de los valores obtenidos y la frecuencia audible más baja que podemos usar en nuestro proyecto (45 Hz):

$$D = C \cdot 45, \tag{2}$$

donde ahora C representa los valores positivos de la magnitud aparente y D los valores finales de la frecuencia a sintetizar. Si además implementamos el efecto de *reverberación*:

$$F = (E \cdot 100)/1500, \tag{3}$$

siendo E la distancia en años-luz, donde E=1500 representa el máximo valor correspondiente a la estrella αCyg, y 100 su valor máximo de distancia normalizado.

Este proceso se realizó de forma sucesiva para el resto de los datos. En la últimas dos columnas de la Tabla 1 se muestran la conversión de datos con las frecuencias sonoras y el volumen de *reverberación* resultante para cada estrella. Se observa que la frecuencia va disminuyendo a mayor magnitud aparente (menor brillo aparente), con una disminución más lineal para magnitudes m> -0.5 mag.

Adicionalmente, se aplicaron procesos individuales a cada sonido con el fin de representar propiedades físicas de cada estrella (como las configuraciones binarias o la existencia de vientos estelares) con el objetivo de complementar la información de las mismas con un contexto sonoro específico. A continuación mostramos algunos ejemplos:

- *Capella*: sistema cuádruple formado por Capella A y B, dos estrellas gigantes amarillas, mientras que C y D son de menor tamaño. Por ello se les asignó una frecuencia fundamental y 3 armónicos, con un timbre adicional.
- *Shaula*: estrella azul múltiple de tres componentes y de tipo variable pulsante. Se les asignó una frecuencia fundamental y dos armónicos, con espectro sonoro variable.
- *Acrux*: estrella doble separada por 4 ″. Se le asignó una frecuencia fundamental y una adicional.
- *Spica*: sistema binario de componentes muy próximas entre sí. Se le asignó un armónico parcial. Como presenta intensos vientos estelares emitidos por ambas estrellas, se le adicionó un ruido. Debido también a su metalicidad, se le agregó un *flanger* o "ruido metálico".

3. Experiencia inmersiva

Como ya mencionamos en la Sección 1., proponemos la creación de una experiencia inmersiva en la que realizamos la simulación acústica de las estrellas presentadas en la Tabla 1 mediante la parametrización sonora de sus propiedades físicas. Pero, además, esto requiere el montaje de una instalación específica, la que incluye una sala oscura con sillones personalizados para cada asistente y altoparlantes direccionables. Para seleccionar y regular los sonidos de cada una de las estrellas usamos el controlador *Launchpad* que se muestra en la Fig. 1.

Figura 1: Captura de pantalla del controlador *Launchpad* empleado en las experiencias. En la parte superior se aprecia el listado de las estrellas de trabajo y los diferentes comandos que permiten seleccionarla; en la parte central se encuentran los comandos para seleccionar las frecuencias fundamentales para cada una y sus armónicos; mientras que en la parte inferior se regulan los parámetros de reverberación para simular las distancias.

Adicionalmente, la experiencia incluye una parte cultural, en la que se introduce el significado de las estrellas en diferentes culturas.

Antes de probar nuestra propuesta de experiencia inmersiva con personas con discapacidad visual, primero hemos hecho algunos ensayos con la ayuda del público general. Para ayudarles a vivenciar la descripción de cómo el no vidente construye el cielo acústicamente, se dispusieron de mascarillas de obstrucción visual. Los ensayos se realizaron en el espacio áulico de Física en la Universidad Nacional de Tres de Febrero (UNTREF), y en el "Parque Cielos del Sur" (Chivilcoy, Prov. de Bs.As.), éste último durante las Jornadas de Enseñanza y Divulgación de la Astronomía. En ambas experiencias los participantes (tanto alumnos como asistentes a las Jornadas) simularon diferentes grados de dificultades visuales mediante mascarillas y pudieron percibir distintas frecuencias y matices de sonidos, visualizando desde esta nueva perspectiva el paisaje celeste.

Los ensayos nos han demostrado que resulta difícil recrear la experiencia de observar el cielo nocturno literalmente sin el uso de la imagen. Sin embargo, al hacerlo de manera interpretativa es posible sumar información acerca de cada astro que de otra forma no se encontraría. Por ello, el recurso sonoro enriqueció la forma de percibir ciertas características de las estrellas por parte de los participantes que realizaron las primeras experiencias. De este modo, nuestro proyecto está planeado a futuro con la idea de ser montado en una instalación holofónica, donde los sonidos correspondientes a cada cuerpo celeste provengan de la ubicación precisa donde el mismo se encontrara en el firmamento.

Tabla 1: Lista de las 25 estrellas más brillantes utilizadas en este trabajo (ordenadas por magnitud aparente en orden creciente). Información extraída de Dolan (1989). Las últimas dos columnas corresponden a la parametrización sonora generada en nuestro experimento.

Desig.	Nombre	Distancia (a.l.)	Magnitud Aparente	Magnitud Absoluta	Tipo Espectral	Frecuencia (Hz)	Dry/Wet Volume
α CMa	Sirius	8,6	−1,46	+1,4	A1Vm	13950,0	0,57
α Car	Canopus	74,0	−0,72	−2,5	A9II	186,0	4,93
α Cen	Rigil Kentaurus	4,3	−0,27	+4,4	G2V+K1V	116,3	0,29
α Boo	Arcturus	34,0	−0,04	+0,2	K1,5IIIp	97,6	2,27
α Lyr	Vega	25,0	+0,03	+0,6	A0Va	93,0	1,67
α Aur	Capella	41,0	+0,08	+0,4	G6III+G2III	90,0	2,73
β Ori	Rigel	1400,0	+0,12	−8,1	B81ae	87,7	93,33
α CMi	Procyon	11,4	+0,38	+2,6	F5IV-V	75,4	0,76
α Eri	Achernar	69,0	+0,46	−1,3	B3Vnp	72,3	4,60
α Ori	Betelgeuse	1400,0	+0,50	−7,2	M2Iab	70,8	93,33
β Cen	Hadar	320,0	+0,61	−4,4	B1III	67,1	21,33
α Cru	Acrux	510,0	+0,76	−4,6	B0,5Iv+B1Vn	62,6	34,00
α Aql	Altair	16,0	+0,77	+2,3	A7Vn	62,3	1,07
α Tau	Aldebaran	60,0	+0,85	−0,3	K5III	60,1	4,00
α Sco	Antares	520,0	+0,96	−5,2	M1,5Iab	57,4	34,67
α Vir	Spica	220,0	+0,98	−3,2	B1V	56,9	14,67
β Gem	Pollux	40,0	+1,14	+0,7	K0IIIb	53,4	2,67
α PsA	Fomalhaut	22,0	+1,16	+2,0	A3Va	53,0	1,47
β Cru	Becrux	460,0	+1,25	−4,7	B0,5III	51,3	30,67
α Cyg	Deneb	1500,0	+1,25	−7,2	A2Ia	51,3	100,00
α Leo	Regulus	69,0	+1,35	−0,3	B7Vn	49,5	4,60
ϵ CMa	Adhara	570,0	+1,50	−4,8	B2II	47,0	38,00
α Gem	Castor	49,0	+1,57	+0,5	A1V+A2V	45,9	3,27
γ Cru	Gacrux	120,0	+1,63	−1,2	M3,5III	45,0	8,00
λ Sco	Shaula	330,0	+1,63	−3,5	B1,5IV	45,0	22,00

4. Conclusiones y perspectivas de desarrollo

Hasta el momento se han sonorizado parámetros básicos de las estrellas y seleccionando un mapa estelar en concreto. Nuestro objetivo es con mostrar un cielo lo más real posible, además de introducir y poder explicar otros parámetros estelares más complejos. De este modo, en una siguiente instancia del proyecto, se utilizarán parámetros estelares tales como su masa, temperatura superficial, radio, luminosidad y movimiento propio. Para ello éstos parámetros serán descriptos también con códigos que establecen rangos auditivos selectivos, pero con un parámetro a la vez. Además, para poder realizar el mapeado de una constelación completa de acuerdo al brillo de las estrellas que la componen, nuestra idea es acotar un rango de frecuencias correlacionadas con la magnitud aparente, así como también los colores (de acuerdo a su tipo espectral), asignando frecuencias específicas. Respecto al movimiento propio, se trabajará con la direccionalidad del sonido de acuerdo al efecto Doppler. La masa también será acotada en un rango de frecuencias correlacionadas con las mismas, y, finalmente, los tamaños estarán reflejadas en un conjunto de valores discretos de frecuencias.

Si queremos realmente lograr en el público no vidente, o con capacidades visuales disminuidas, una sensación auditiva lo más objetiva posible, deberíamos tener en cuenta que la posibilidad de establecer alguna relación matemática específica, lineal como en nuestro caso, que modele de alguna forma esta percepción, es un tema controversial y todavía sin resultados concretos (ver, por ejemplo Zimmer, 2005). Además, dado que las magnitudes aparentes escalan logarítmicamente con el flujo luminoso, a través de la ecuación de Pogson, que no es más que la aplicación astronómica de la ley fisiológica de Weber-Fechner, si la diferencia en brillos no es pequeña, podría producir sensaciones auditivas relativas muy diferentes al de las sensaciones visuales. Este tema será analizado a futuro.

Agradecimientos: Los autores agradecen al árbitro anónimo por las valiosas sugerencias realizadas, las cuales enriquecieron y mejoraron la presentación de este trabajo.

Referencias

Dolan C., 1989, *The 26 Brightest Stars DataBase*, Longman Group UK

Miyara F., 2004, *Acústica, sistemas y sonido 3a edic*, UNR Editora, Argentina

Schaeffer P., 2008, *Tratado de los objetos musicales 2a edic*, Alianza Editorial, España

Zimmer K., 2005, *Perception & Psychophysics*, 67, 569

Índice alfabético

E

F

G

H

I

J

K

Q

R

S

T

U

V

W

X

Y

Z